Development of Cyclometalated Iron Complexes as Sustainable Photosensitizers

Dissertation

Vorgelegt von

Jakob Steube

Fakultät für Naturwissenschaften

Universität Paderborn

zur Erlangung des akademischen Grades

Doktor der Naturwissenschaften

(Dr. rer. Nat.)

im Department Chemie

2023

Für Evelyn, Henry und Emmy.

I may not have gone where I intended to go,
but I think I have ended up where I needed to be.
Douglas Adams

Promotionskomission

Diese Dissertation wurde von Oktober 2017 bis März 2023 an der Universität Paderborn im Fachbereich Chemie der naturwissenschaftlichen Fakultät im Arbeitskreis von Prof. Dr. Matthias Bauer angefertigt.

Jun.-Prof. Dr. Hans-Georg Steinrück	Vorsitz
Prof. Dr. Matthias Bauer	Erstgutachter
Prof. Dr. Thomas Werner	Zweitgutachter
PD Dr. Hans Egold	Drittprüfer

Einreichung:	28.03.2023
Disputation:	08.05.2023

Eidesstattliche Erklärung

Hiermit versichere ich, dass ich die vorliegende Arbeit selbstständig verfasst habe und keine anderen als die von mir angegebenen Hilfsmittel verwendet habe. Ich versichere, dass ich keine anderen als die angegebenen Quellen benutzt und alle wörtlich oder sinngemäß aus anderen Werken übernommenen Aussagen als solche gekennzeichnet habe. Genehmigungen zur Veröffentlichung der urheberrechtlich geschützten Publikationen wurden eingeholt.

Paderborn, 28.03.2023 .....

Jakob Steube

Abstract

Photocatalytic reactions are becoming established in more and more areas of chemistry. They require photosensitizers that convert the energy of light into chemically usable energy, which are often based on platinum group metal complexes. However, these show only a low abundance. Thus, their extraction is resource-intensive, which makes their use economically and ecologically problematic. Therefore, the aim of this work was to develop iron complexes that can complement and replace noble metal photosensitizers. To achieve this goal, the complexes must have long lifetimes of catalytically active excited states and ideally be emissive. For this reason, cyclometalating functions (anionic carbon donor ligands) were integrated into the ligand framework.

In a first approach, a terminal pyridine of a terpyridine ligand was replaced by a carbon donor function. The aim was to prepare heteroleptic complexes with one cyclometalating function and homoleptic complexes with two cyclometalating functions. In the heteroleptic complex synthesized *via* a new synthetic route, the lifetimes of the catalytically active states were improved. However, these were still too short for photoreactions. Therefore, the synthesis of homoleptic complexes was investigated. The controlled synthesis was not successful, but provided valuable insights into the decomposition mechanisms of these compounds.

In order to stabilize the iron-carbon binding motif, the second approach was to incorporate the C-donor function in *N*-heterocyclic carbene ligands. Using this method, it was possible to obtain an iron (III) complex that fulfills the requirements of a photosensitizer. It exhibits emission from the opposite metal-to-ligand charge transfer (MLCT) and ligand-to-metal charge transfer (LMCT) states. In addition, the MLCT state has a long lifetime and exhibits high redox potentials. This makes it an ideal candidate to complement existing photosensitizers. Furthermore, the stable oxidation states +II and +IV were investigated to obtain a comprehensive picture of the electronic structure in all accessible oxidation states. Based on this, first experiments in photoredox catalysis were carried out to bridge the gap between the development of active systems and their application in catalysis.

Subsequently, a series of complexes was synthesized to investigate the influence of ligand backbone functionalization on the overall properties. These were studied by various spectroscopic methods to obtain a detailed picture of the electronic structure, photoproperties and photodynamics. Understanding the underlying structure-property relationships is a fundamental step for the application of these iron photosensitizers in various areas of photochemistry.

Kurzzusammenfassung

Photokatalytische Reaktionen etablieren sich in immer mehr Bereichen der Chemie. Sie benötigen Photosensitizer, die die Energie des Lichts für chemische Reaktionen nutzbar machen. Häufig werden dafür Komplexe auf der Basis von Platingruppenmetallen eingesetzt. Diese zeigen jedoch nur ein geringes Vorkommen. Ihre Gewinnung ist daher ressourcenintensiv, was ihren Einsatz ökonomisch und ökologisch problematisch macht. Ziel dieser Arbeit war es daher, Eisenkomplexe zu entwickeln, die Edelmetallphotosensitizer ergänzen und ersetzen können. Um dieses Ziel zu erreichen, müssen die Komplexe lange Lebenszeiten der katalytisch aktiven Zustände aufweisen und im Idealfall emittieren. Aus diesem Grund wurden in dieser Arbeit cyclometallierende Funktionen (anionische Kohlenstoffdonorliganden) in Liganden integriert. In einem ersten Ansatz wurde ein terminales Pyridin eines Terpyridin-Liganden durch eine Kohlenstoffdonorfunktion ersetzt. Ziel war es, sowohl heteroleptische Komplexe mit einer cyclometallierenden Funktion als auch homoleptische Komplexe mit zwei cyclometallierenden Funktionen darzustellen. Im heteroleptischen Komplex, der mit einer neuen Syntheseroute dargestellt wurde, konnten die katalytisch aktiven Zustände verlängert werden. Da diese für Photoreaktionen dennoch zu kurzlebig sind, wurde die Synthese von homoleptischen Komplexen untersucht. Die kontrollierte Synthese war jedoch nicht erfolgreich, obwohl wertvolle Erkenntnisse über die Zersetzungsmechanismen dieser Verbindungen gewonnen werden konnten.
Aus diesem Grund wurde, zur Stabilisierung des Eisen-Kohlenstoff-Bindungsmotivs, in einem weiteren Ansatz die Integration der C-Donor-Funktion in *N*-Heterocyclische Carbenliganden untersucht. Mit dieser Methode konnte ein Eisen(III)-Komplex erhalten werden, der die Anforderungen an einen Photosensitizer erfüllt. Dieser zeigt eine Emission aus den entgegengesetzten Metall-zu-Ligand Charge Transfer (MLCT) und Ligand-zu-Metall Charge Transfer (LMCT) Zuständen. Der MLCT-Zustand weist zudem eine lange Lebenszeit, sowie hohe Redoxpotentiale des angeregten Zustandes auf. Somit ist diese Verbindung ein idealer Kandidat, um bestehende Photosensitizer zu ergänzen. Ferner wurden die weiteren stabilen Oxidationsstufen +II und +IV untersucht um ein umfassendes Bild der elektronischen Struktur zu erhalten. Darauf aufbauend wurden erste Experimente in der Photoredoxkatalyse durchgeführt, um die Entwicklung aktiver Systeme mit der Anwendung in der Katalyse zu verknüpfen.
Abschließend wurde eine Komplexreihe synthetisiert, in der Einflüsse des Ligandenrückgrats auf die Eigenschaften zu untersuchen. Diese wurde mit Vielzahl an spektroskopischen Methoden untersucht, um ein detailliertes Bild der elektronischen Strukturen, der Photoeigenschaften und der Photodynamik zu erhalten. Das Verständnis der zugrunde liegenden Struktur-Eigenschafts-Beziehungen ist ein grundlegender Schritt für die Anwendung dieser Eisenphotosensitizer in verschiedenen Bereichen der Photochemie.

Danksagungen

Zuallererst möchte ich Prof. Dr. Matthias Bauer danken, dass er mich in den Arbeitskreis aufgenommen hat und mir die Möglichkeit geboten hat, auch schon seit dem Bachelor (nahezu) eigenständig an spannenden Themen zu arbeiten. Deshalb möchte ich mich bei ihm bedanken, dass er das Vertrauen in mich hatte, dieses anspruchsvolle Thema zu bearbeiten und dass er mir mit mehr oder weniger guten Sprüchen und Ratschlägen bei Problemen zur Seite stand. Für die freundliche Übernahme des Zweitgutachtens möchte ich mich bei Prof. Dr. Thomas Werner bedanken.
Besonderer Dank gilt den Mitarbeitern im Arbeitskreis Bauer, den Leuten, die sowohl am Anfang, als auch am Ende dieser Reise dabei waren. Allen voran gehört dabei mein Dank Dr. Peter Zimmer, der zuerst als Mentor und Betreuer, später als Kollege und Freund mit Rat und Tat zur Seite stand. Den Laborkollegen möchte ich für den Spaß, die netten Unterhaltungen und die unterhaltsamen Mittags- und Kaffeepausen danken.
Allen Hilfskräften, Projekt- und Abschlussarbeitern (René Rodrigues, Linus Kuckling, Jan Locher, Jennifer Klaucke, Fan Yang, Nicole Dickmann und Nils Düsterhues) gilt besonderer Dank, da ohne sie viele Projekte nicht möglich gewesen wären. Großer Dank geht an die Analytik-Abteilung des Instituts. Zuerst bedanke ich mich bei Dr. Roland Schoch für die Röntgenstrukturanalyse und seine Bemühungen auch bei schwierigen Ansätzen eine Lösung zu finden. Für die NMR-Spektroskopie bedanke ich mich bei Karin Stolte, Andrea Harbarth und Herrn PD Dr. Hans Egold. Die Massenspektrometrie wurde von Dr. Adam Neuba und Christiane Gloger gemessen, ihnen möchte ich für die Suche nach dem $[M]^+$-Peak danken. Letztere hat, genau wie Maria Busse, für die Messung der Elementaranalysen gesorgt, wofür ich danken möchte.
Ferner möchte ich auch der Deutschen Bundesstiftung Umwelt (DBU) für die finanzielle und ideelle Unterstützung danken, besonders Frau Dannhauer und Herrn Dr. Schaefer für die Betreuung. Auch den Kooperationspartnern möchte ich danken, allen voran Ayla Kruse aus dem Arbeitskreis von Prof. Dr. Lochbrunner, welche Transiente Absorptions- sowie Streak-Kamera-Messungen durchgeführt hat und immer die Ohren für Diskussionen um den Ursprung der dualen Fluoreszenz offen hatte, sowie Miguel A. Argüello Cordero, welcher diese Messungen weitergeführt hat. Auch Dr. Olga Bokareva aus dem Arbeitskreis von Prof. Dr. Kühn möchte ich für die Rechnungen und theoretischen Betrachtungen danken.
Besonderer Dank geht an die "Druncles" Benni und Bene. Ihr seid die Besten. Wirklich. Der größte Dank allerdings geht an meine bessere Hälfte Evelyn, die mir stets den Rücken freigehalten hat und für mich da war. Ohne dich wäre ich nicht an dieser Stelle. Zu guter Letzt möchte ich mich bei Henry und Emmy bedanken, welche für willkommene Abwechslung vom Laboralltag gesorgt haben.

List of Publications

Publications

- Isostructural cyclometalated iron complex in three oxidation states:
  Jakob Steube, Ayla Kruse, Lorena Fritsch, Olga Bokareva, Serhiy Demeshko, Roland Schoch, Mohammad Alaraby, Stephan Hohloch, Thomas Kühne, Franc Meyer, Oliver Kühn, Stefan Lochbrunner, Matthias Bauer*, **2023**, manuscript submitted

- Janus-type emission from a cyclometalated iron(III) complex:
  Jakob Steube, Ayla Kruse, Olga Bokareva, Thomas Reuter, Serhiy Demeshko, Roland Schoch, Stephan Hohloch, Franc Meyer, Katja Heinze, Stefan Lochbrunner, Matthias Bauer*, Nature Chemistry, **2023** (DOI: 10.1038/s41557-023-01137-w)

- Ultrafast Dynamics of Photosensitizers based on Fe(II):
  Ayla Päpcke, Jakob Steube, Yannik Vukadinovic, Matthias Bauer, Stefan Lochbrunner*, International Conference on Ultrafast Phenomena, **2020**, Tu4A. 32

- Excited-State Kinetics of an Air-Stable Cyclometalated Iron(II) Complex:
  Jakob Steube, Lukas Burkhardt, Ayla Päpcke, Johannes Moll, Peter Zimmer, Roland Schoch, Christoph Wölper, Katja Heinze, Stefan Lochbrunner, Matthias Bauer*, Chemistry - A European Journal, **2019**, 25 (51), 11826–11830

Talks

- Janus-Type Emission in Cyclometalated Iron(III) Complexes:
  Jakob Steube, Matthias Bauer, 28th PhotoIUPAC, Amsterdam, 21.07.2022

- Dual Emission of a Cyclometalated Iron(III) Complex:
  Jakob Steube, Ayla Päpcke, Olga S. Bokareva, Thomas Reuter, Serhiy Demeshko, Roland Schoch, Stephan Hohloch, Franc Meyer, Katja Heinze, Oliver Kühn, Stefan Lochbrunner, Matthias Bauer, SPP 2102 Meeting, Online, 30.11.2020

- Cyclometallierte Eisenkomplexe - Nachhaltige Photosensitizer für photokatalytische Anwendungen:
  Jakob Steube, Matthias Bauer, DBU Jour fixe, Online, 20.10.2020

- Cyclometallierte Eisenkomplexe - Nachhaltige Photosensitizer für photokatalytische Anwendungen:
  Jakob Steube, Matthias Bauer, DBU Stipendiatenseminar, Feldberg-Falkau, 16.09.2019

- Control of the ultrafast photodynamics of iron complexes by ligand design:
  Ayla Päpcke, Jakob Steube, Matthias Bauer, Stefan Lochbrunner, Katja Heinze, Oliver Kühn, SPP 2102 1st regular meeting, Bonn, 21.03.2019

- Cyclometallierte Eisenkomplexe als vielversprechende Photosensitizer:
  Jakob Steube, Matthias Bauer, 15. Koordinationschemikertreffen, München, 05.03.2019

- Cyclometallierte Eisenkomplexe - Nachhaltige Photosensitizer für photokatalytische Anwendungen:
  Jakob Steube, Matthias Bauer, DBU Einführungsseminar, Osnabrück, 28.09.2018

- Cyclometallierte Eisenkomplexe - Nachhaltige Photosensitizer für photokatalytische Anwendungen:
  Jakob Steube, Matthias Bauer, 2. Ligandendesignworkshop, Köln, 23.07.2018

Posters

- Janus-emitting cyclometalated NHC-iron(III) complexes:
  Jakob Steube, Ayla Kruse, Miguel A. Argüello Cordero, Nicole Dickmann, Nils Düsterhues, Stefan Lochbrunner, Matthias Bauer, 'Bring-your-own-poster'-session JCF Paderborn, Paderborn, 24.10.2022

- The effect of phenyl-substitution on Janus-emitting cyclometalated NHC-iron(III) complexes:
  Jakob Steube, Ayla Kruse, Miguel A. Argüello Cordero, Stefan Lochbrunner, Matthias Bauer, SPP2102 regular meeting, Jena, 11. - 13.05.2022

- Unprecedented Luminescence in a Cyclometalated Iron(III) Complex:
  Jakob Steube, Ayla Päpcke, Olga Bokareva, Thomas Reuter, Serhiy Demeshko, Roland Schoch, Franc Meyer, Katja Heinze, Oliver Kühn, Stefan Lochbrunner, Matthias Bauer, 16. Koordinationschemikertreffen, Freiburg, 01. - 03.03.2020

- A Luminescent Cyclometalated Iron(III) Complex:
  Jakob Steube, Ayla Päpcke, Thomas Reuter, Roland Schoch, Stephan Hohloch, Katja Heinze, Stefan Lochbrunner, Matthias Bauer, SPP2102 regular meeting, Düsseldorf, 29.09. - 02.10.2019

- Cyclometalated Iron Complexes as promising Photosensitizers:
  Jakob Steube, Lukas Burkhardt, Ayla Päpcke, Johannes Moll, Peter Zimmer, Stefan Lochbrunner, Katja Heinze, Matthias Bauer, 'Bring-your-own-poster'-session JCF Paderborn, Paderborn, 05.12.2018

Cooperations and Tools

NMR and ESI spectra were analyzed with the software MestReNova 11.0.4 © 2017 Mestrelab Research S.L.. Chemical structures were drawn with ChemDraw 20.1.1 © 1998-2021 PerkinElmer Informatics, Inc. Visualization and data processing was done with OriginPro 2019 © 1991-2018 OriginLab Corporation. This thesis was written in LaTeX with TeXstudio 4.3.1.

The excited state properties were determined *via* transient absorption spectroscopy, streak camera measurements and quenching experiments. These were performed in the work group of Prof. Dr. Stefan Lochbrunner at the University of Rostock by Ayla Kruse and Miguel A. Argüello Cordero. Spectroelectrochemical measurements were performed by the work group of Prof. Dr. Katja Heinze in Mainz by Johannes Moll and Thomas Reuter. (TD)DFT calculations were performed in our work group (Prof. Dr. Matthias Bauer in Paderborn) by Lukas Burkhardt, the group of Prof. Dr. Thomas Kühne (Mohammad Alaraby) in Paderborn and the group of Prof. Dr. Oliver Kühn in Rostock (Dr. Olga Bokareva). Mößbauer and SQUID measurements were performed by the group of Prof. Dr. Franc Meyer in Göttingen (Dr. Serhiy Demeshko). Crystal structures were measured and analyzed by Dr. Roland Schoch (Workgroup of Prof. Dr. Matthias Bauer in Paderborn), Dr. Christoph Wölper (University of Duisburg-Essen) and Ass.-Prof. Dr. Stephan Hohloch (University of Innsbruck). X-ray spectroscopy was analyzed by Lukas Burkhardt and Lorena Fritsch (Workgroup of Prof. Dr. Matthias Bauer in Paderborn). Following students contributed to this thesis as either student assistants or by joint research within their bachelor or master thesis: René Rodrigues, Linus Kuckling, Jan Locher, Jennifer Klaucke, Fan Yang, Nicole Dickmann and Nils Düsterhues.

Contents

Index of Abbreviations

bimp	2,6-bis(imidazole-2-ylidene)pyridine
bpy	2,2'-biypridine
bpz	2,2'-bipyrazine
CT	Charge-transfer
CtC-XES	Core-to-Core X-ray emission spectroscopy
dcpp	2,6-bis(2-carboxypyridyl)pyridine
DFT	Density functional theory
DIPEA	Diisopropylethylamine
DMF	Dimethylformamide
DSSC	Dye-sensitized solar-cell
EnT	Energy-transfer
ESI-MS	Electron-spray ionization mass spectrometry
GS	Ground state
HERFD-XANES	High energy resolution fluorescence detected X-ray absorption near edge structure
HImP	1,1'-(1,3-phenylene)bis(3-methyl-1-imidazol-2-ylidene)
HMDS	Hexamethyldisilazane
Hpbpy	6-phenyl-2,2'-bipyridine
Hppy	2-phenylpyridine
IC	Internal conversion
ISC	Intersystem crossing
LIESST	Light-induced excited spin-state trapping
LMCT	Ligand-to-metal charge-transfer
MC	Metal-centered
Me	Methyl
MeCN	Acetonitrile
MLCT	Metal-to-ligand charge-transfer
MO	Molecular orbital
NBO	Natural bond orbital
NHC	*N*-Heterocyclic carbene
NIR	Near infrared
NMR	Nuclear magnetic resonance
PGM	Platinum metal group
phtmeimb	phenyl(tris(3-methylimidazol-1-ylidene))borate
SOMO	Singly occupied molecular orbital

PS	Photosensitizer
S	Substrate
SCE	Saturated calomel electrode
SXRD	Single crystal X-ray diffraction
tBu	tert-butyl
TCSPC	Time-correlated single-photon counting
TDDFT	Time-dependant density functional theory
TEOA	Triethanolamine
THF	Tetrahydrofuran
TMP	2,2,6,6-Tetramethylpiperidine
tpy	2,2';6',2"-Terpyridine

1. Introduction

With almost 8 billion people inhabiting the earth and a further increasing population, the energy demand keeps rising. This is coupled with an ongoing industrialization, leading to high demand of fossil resources, as energy from renewable resources makes up only 17.1 % as of 2018.[1] This is problematic, since the availability of fossil resources is declining constantly, geopolitical tensions lower the supply further and climate change is progressing. Especially the latter, caused by CO_2 and NO_x emissions, bears high conflict potential, as it leads to increasing maximum temperatures, a greater frequency of weather extremes and rising sea levels, resulting in humanitarian crises, especially in developing countries.[2] Hence, apart from the economical reasons, reducing fossil resource consumption is urgent. To achieve this goal, a green adequate substitute for fossil fuels needs to be found. One important factor for this is the green generation of hydrogen, since it is a key building block in the chemical industry and is needed for many processes and applications. These include the formation of ammonia and methanol as base chemicals for fertilizer production and further formation of the important chemicals formaldehyde and acetic acid. The chemical industry in Germany alone required around 1.1 million tons of hydrogen in 2020,[3] which was mostly produced by steam reforming of natural gas. Therefore, replacing this with green hydrogen is an important step towards limiting climate change.

Apart from the importance of hydrogen as a basic building block, it also has the highest gravimetric heating value of 119 MJ/kg.[4,5] In theory, hydrogen is an ideal theoretical fuel, but it suffers from its low density. This results in a very low volumetric heating value (0.01 MJ/L),[i] lower than methane (0.04 MJ/L)[7] and methanol (15.8 MJ/L),[ii] which represent better fuels. Even though the heating values of those two are still lower than in fossil fuels like gasoline (31.5 MJ/L) or diesel fuel (35.9 MJ/L),[7] they can be obtained by reaction of green hydrogen and CO_x, hence do not depend on fossil resources and are thus carbon neutral.

Electrolysis of water, powered by renewable energies like wind and solar power, is the current source of green hydrogen. Another theoretical source of green hydrogen are photocatalytic reactions. In these, light is used to reduce protons.[4] In theory, this omits the step of generating electricity from sunlight to use it for electrolysis of water. Therefore, sunlight-driven photocatalytic proton reduction would be an improvement. Even though this reaction has been studied thoroughly since the late 70s,[4,9–16] an industrial application still seems to be inaccessible. This can be explained by the following: On the laboratory scale, the reaction (Eq. (1.1) in Scheme 1) can be divided into its two main steps, the water oxidation (Eq. (1.2)) and the proton reduction (Eq. (1.3)). Producing only oxygen

[i] Obtained by multiplication with the the density (0.0000899) kg/L).[6]

[ii] Calculated from the gravimetric heating value[8] and the density of methanol.[6]

or hydrogen works well on this scale, since electron acceptors and donors can be added to the respective reaction, but makes it uneconomical on a large scale. Yet for an industrial application, and to help limiting climate change, the reactions have to be combined. A great challenge of this combination is the need for a concerted 4-electron-transfer.

$$2\,H_2O \xrightarrow{hv} 2\,H_2 + O_2 \tag{1.1}$$

$$2\,H_2O \longrightarrow O_2 + 4\,H^+ + 4\,e^- \tag{1.2}$$

$$2\,H_2O + 4\,e^- \longrightarrow 2\,H_2 + 2\,OH^- \tag{1.3}$$

Scheme 1: Chemical equations for water splitting with the overall reaction (1.1), the water oxidation (1.2) and water reduction (1.3) part. If the reactions are investigated separately, electron-acceptors have to be added for the water oxidation and electron-donors for the water reduction.

But other sectors can also profit from light-driven reactions, e.g. organic transformations can be carried out using light from energy-efficient LEDs in visible-light photocatalysis.[17,18] This reaction type is usually carried out under ambient temperature and pressure, thus does not require additional energy input, since the light carries the energy for the reaction. This can reduce the needed energy in chemical reactions drastically. Therefore, these reactions are of high interest especially for the pharmaceutical industry, not only as they and the chemical industry were responsible for 8 % of the nation-wide energy consumption of Germany,[19] but also since they provide for efficient and selective transformations, as well as late-state functionalizations.[20–23] A good overview on the use of photoredox catalysis in medicinal chemistry is given by Zbieg *et al.*[23] from Genentech (associated with Roche), reporting research cooperations of various photochemists like Stephenson and MacMillan with pharmaceutical companies like Merck, Novartis, or Eli Lilly. Some transformations were not possible before, like some peptide functionalizations and protein bioconjugations,[23] or required stochiometric amounts of chemicals for radical generation, but can now be performed catalytically and therefore in an economically and ecologically more viable way. However, just as the photocatalytic water splitting, this reaction type has also no large-scale application yet, as the pivotal research done by the groups of Yoon,[24] MacMillan[25] and Stephenson[26] was published in the years 2008 and 2009, barely over a decade ago. The limiting factors of large-scale applications are the high costs of the required iridium-photosensitizers and that increasing the scale of reactions remains problematic.[27] Yet, the latter challenge is addressed by many groups, and first results show a scalability of some reactions into the kg/day regime by smart reactor

design.[28] The first challengm, which is addressed by several groups, is subject of this work. With the goal of obtaining catalytic activity, tailoring the excited state landscape of base metals is much more difficult. Hence it is of great importance to understand the underlying fundamental mechanisms of photocatalysis, since it allows adapting and improving current systems. Therefore, the mechanisms will be discussed in the following chapters, with emphasis on the diffusion limit and photophysics of photosensitizers, especially with focus on iron-based systems.

1.1. Mechanisms of Photocatalysis

In photocatalysis, a fundamental reagent is the photosensitizer (PS), which converts light into chemically usable energy. The PS can react in two different ways: It can transfer either an electron or energy onto a substrate (S) (Scheme 2). The transfer of an electron (Scheme 2 a) is the more common mechanism and is usually referred to as photoredox catalysis. In the first step the PS absorbs a photon, which excites it from the electronic ground state into an excited state. The excited state possesses different redox potentials than the ground state, and can be more easily reduced or oxidized. Therefore, it can react by electron transfer with a substrate (S_1), which can be an electron donor or acceptor (Scheme 2 a, red or blue arrow, respectively), depending on the redox potential of the excited state. This is either another catalyst, an organic substrate, or a sacrificial electron donor or acceptor, dependent on the reaction type.[17] In the second step, the oxidized or reduced PS reacts with another substrate (S_2), returning to the ground state of the original oxidation state. Sacrificial reagents are needed in non-redox-neutral reactions, as they close the catalytic cycle.

Sacrificial reagents are not needed in energy transfer (EnT) catalysis (Scheme 2 b), which differs from photoredox catalysis, since it transfers energy from the excited state.[29,30] The two types of energy transfer can be Förster or Dexter. In Förster resonance energy transfer, the energy donor (PS) and energy acceptor (S) are coupled by dipole-dipole interactions. A spectral overlap of the emission spectrum of the donor and the absorption spectrum of the acceptor is required for energy transfer to occur.[31] Energy transfer of the Dexter type involves an exchange of electrons and is the primary mechanism in EnT-catalysis.[29] The transfer usually follows a concerted mechansim (Fig. 2 b), where an electron from the excited state of the PS is transferred onto the S, while an electron from the ground state of the substrate is transferred onto the PS. Even though it is a formal electron transfer, the effect itself relies on spectral overlap between the donor and acceptor and leads to the transfer of energy. While photoredox catalysis is more common than EnT catalysis, singlet oxygen generation dominated the early applications of EnT catalysis and is still a common photocatalytic reaction.[32]

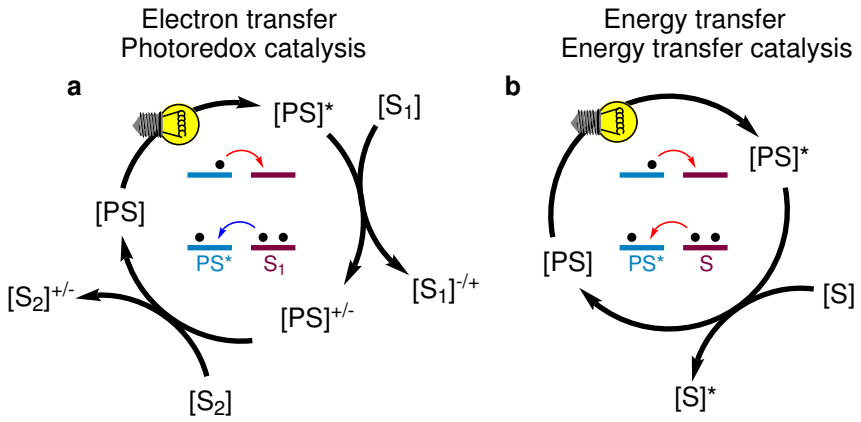

Scheme 2: The two pathways of photocatalysis. **a**: Photoredox catalysis; the photoexcited photosensitizer acts as a redox reagent to participate in single electron transfer processes (red arrow: photoreduction of S_1, blue arrow: photooxidation of S_1). **b**: Energy transfer catalysis; the photoexcited photosensitizer transfers energy in a Dexter way (red arrows).

The formation of excited states itself is not sufficient for reactions to occur, since the excited photosensitizer and the substrate have to collide to react. Hence, the excited-state lifetimes have to be sufficiently long, otherwise a low reaction rate or no reaction at all will be observed. The excited states of molecules follow common decay laws, where the lifetime τ describes the time, where the population of the excited states has decreased to 1/e. Therefore, a closer look on "sufficiently long" is needed. The distance a substrate can diffuse during τ, depends on its diffusion coefficient D Eq. (1.4):[31]

$$\sqrt{\bar{x^2}} = \sqrt{2D\tau} \tag{1.4}$$

A typical xanthene dye like rhodamine B has a fluorescence lifetime of 90 ps in water.[33] During this time, a potential quencher like oxygen,[iii] covers only a distance of 6.7 Å, making a collision with the excited dye improbable. This changes when the triplet excited state of the same dye, with a lifetime of 1.6 μs, is considered.[34] During this lifetime, oxygen can diffuse roughly 900 Å. This results in a drastically increased probability of quenching, as the larger traveled distance increases the probability of collision. For $[Ru(bpy)_3]^{2+}$ (bpy = 2,2'-bipyridine), a common metal-organic photosensitizer, with a triplet excited state lifetime of 0.58 μs in water,[35] a diffusion distance of 540 Å is obtained. This seems to be sufficient, as oxygen quenches the excited state efficiently.[36] While oxygen shows a high diffusion coefficient, larger substrates diffuse more slowly, as the diffusion coefficient is inversely proportional to the molecular radius R_M (Eq. (1.5)). The diffusion coefficient D can be derived from the Stokes-Einstein equation:[31]

[iii] The diffusion coefficient of oxygen in water at 25°C is $2.5 \cdot 10^{-5} cm^2 s^{-1}$.[31]

$$D = \frac{k_B T}{6\pi\eta R_M} \tag{1.5}$$

The diffusion coefficient also depends on the temperature T, the solvent viscosity η and Boltzmann's constant k_B. Hence, for a bigger substrate with a radius of around 3.5 Å in acetonitrile,[37] a common solvent for photocatalysis,[17] a value of $D = 1.7 \cdot 10^{-5} cm^2 s - ^1$ is obtained. Therefore, the traveled distance will be reduced for this larger compound. Yet it is necessary to connect the diffusion of a single molecule to the collision rate of two molecules. This can be done with the diffusion-controlled bimolecular rate constant k_0, which is also present in the Stern-Volmer equation for dynamic quenching. It is derived from the Smoluchowski equation and connects the molecular radii and diffusion coefficients of both excited molecule and the corresponding quencher.[31,38]

$$k_0 = 4\pi R D \frac{N_A}{1000} = 4\pi \frac{N_A}{1000}(R_{M_1} + R_{M_2})(D_{M_1} + D_{M_2}) \tag{1.6}$$

R is the radius in which the two molecules will collide and is the sum of the two individual molecular radii R_{M_x}. D is the sum of diffusion coefficients D_{M_x} of the respective molecules. The factor $\frac{N_A}{1000}$ with Avogadro's number N_A was introduced to convert the rate constant to the more widely used concentration in mol/L instead of molecules per cubic centimeter.[31] Known molecular radii can be taken from the literature, while unknown can be calculated from crystal structures.

Based on these equations, an exemplary k_0 can be calculated for the reaction of oxygen with $[Ru(bpy)_3]^{2+}$. The diffusion coefficients for both $[Ru(bpy)_3]^{2+}$[39] and oxygen[40] in acetonitrile are literature-known. The radius of the complex is 5.7 Å.[39] This value is comparable to most organometallic polypyridine complexes, therefore, the resulting rate constant approximately fits for many of those complexes. The overall collision radius $(R_{M_1} + R_{M_2})$ results in 6.3 Å, with the radius of oxygen obtained from half the O−O bond length.[6] The resulting rate constant is $4.85 \cdot 10^{10} s^{-1} M^{-1}$. From this, the collision frequency Z can be calculated, which gives the collisions of the PS and the substrate per second:[31]

$$Z = k_0 c \tag{1.7}$$

The frequency depends on the concentration c of the substrate, as more collisions happen, when more reactant is available. For the average time t_{coll} it takes for one collision to happen, the reciprocal of Z can be formed.

$$t_{coll} = \frac{1}{Z} = \frac{1}{k_0 c} \tag{1.8}$$

Hence, using a photosensitizer with a radius of 5.7 Å and air-saturated acetonitrile as a solvent, an average collision time of 8.9 ns is obtained. Thus, for diffusion-controlled oxygen quenching reactions to occur, a τ of around 9 ns is needed. This can be challenging for fluorophores with short excited state lifetimes. Fortunately, this can be counteracted by increasing the concentration of the quenching substrate in other reactions. Hence, photosensitizers with lower excited-state lifetimes can participate in photoreactions. Since the fundamentals of the diffusion-controlled reactivity and the resulting time-scales are resolved, a further look into the photosensitizers and the processes after photoexcitation is needed to understand the reactivity and the lifetimes of excited states.

1.2. Photosensitizers

As previously mentioned, photosensitizers convert light into chemically usable energy, by either electron or energy-transfer upon photoexcitation. They can be either heterogeneous or homogeneous, meaning suspended as a solid or in solution. Heterogeneous sensitizers are usually inorganic semiconductors like TiO_2, CdS, $BiVO_4$ or WO_3,[41,42] with carbon nitrides such as C_3N_4, C_2N and related (sub)structures as organic semiconductors being the major exception.[43] Even though the field of heterogenous sensitizers is very interesting and promising, this work focuses on homogeneous photosensitizers, due to the easy tunability of the excited states[44–50] and the broad means to follow the photodynamics.[51–54] Widely used are organic sensitizers like xanthene dyes,[55,56] perylene diimides,[57] or riboflavines.[58] Due to their increased photostability and wider range of excited-state redox potentials, organometallic complexes are more popular. $[Ru(bpy)_3]^{2+}$ is one ofthe best investigated photoactive compounds (Fig. 1a).[36,59]

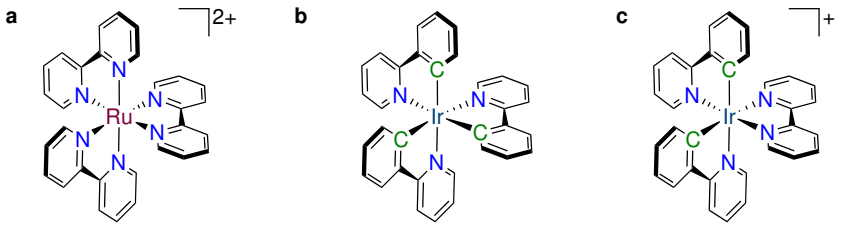

Figure 1: Overview of different organometallic photosensitizers. **a**, $[Ru(bpy)_3]^{2+}$, the prototypical photosensitizer used in many photoreactions. **b**, $[Ir(ppy)_3]$, a strongly reducing iridium(III)-based sensitizer. **c**, $[Ir(bpy)(ppy)_2]^{+}$, a heteroleptic and tunable iridium-based photosensitizer.

Taking this compound as example, fundamental photodynamic processes of photosenisitzers will be explained (Fig. 2). By absorption of a photon, an electron is excited from the ground state to a singlet metal-to-ligand charge-transfer (^{1}MLCT) state. In this charge-

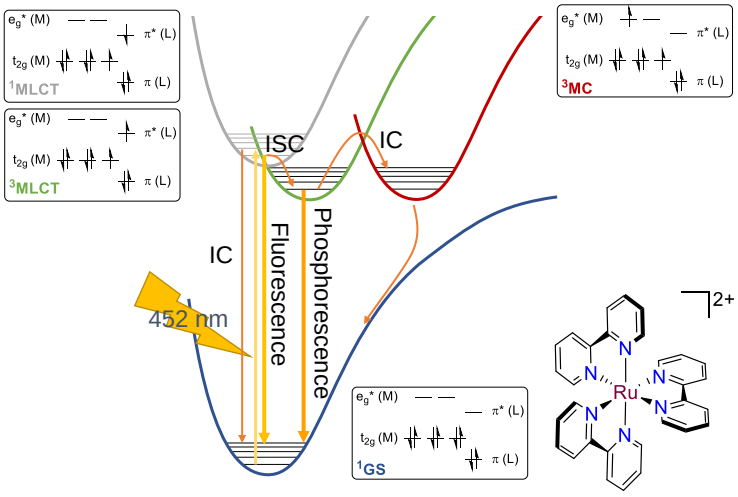

Figure 2: Schematic representation of the processes in $[Ru(bpy)_3]^{2+}$ after photoexcitation. Yellow arrows indicate radiative processes such as excitation, fluorescence and phosphorescence. Orange arrows indicate non-radiative processes such as internal conversion (IC) and intersystem crossing (ISC).

separated state, an electron from the filled t_{2g}-based d-orbitals of the metal is transferred into the empty π^*-orbitals of the ligands. Relaxation back to the ground state can be either non-radiative via internal conversion (IC) or radiative via spin-allowed fluorescence. In the case of transition metal photosensitizers, the ^{1}MLCT typically undergoes intersystem crossing (ISC) into the triplet state (^{3}MLCT) with almost unity.[60] This state has a much higher lifetime than singlet states, since deactivation into the ground state is spin-forbidden. In consequence, these states are the ideal candidate for a catalytically active state and can either participate in electron or energy transfer reactions. Deactivation from this state can be either radiative via phosphorescence, which can be used for light-emitting applications, or non-radiative by internal conversion into a metal centered (MC) state. These are usually energetically higher than MLCT states in ruthenium compounds, but can be thermally populated. These states are in general catalytically inactive, since electron and energy transfer is not possible from them. Luminescence is also not observed, therefore relaxation into the ground state occurs non-radiative.

The MLCT excited state of ruthenium compounds has excellent properties, in terms of longevity and excited state redox-potentials, but in the past two decades, iridium-based systems started to complement and replace ruthenium-based photosensitizers. This is based on the higher excited state redox potentials of these compounds, as well as their high triplet energies. Photoredox catalysis relies on the same principles as normal redox reactions. Therefore, reactions will proceed faster with an increased potential difference between electron donor and acceptor.[61] The homoleptic $[Ir(ppy)_3]$ (Hppy = 2-phenylpyridine, cf. Fig. 1**b**) shows a highly reducing triplet state and high excited state

lifetimes.[62] The heteroleptic $[Ir(bpy)(ppy)_2]^+$ (cf. Fig. 1**c**) on the other hand, shows excellent tunability of the excited state energies, as both the energy of the HOMO (highest occupied molecular orbital) and LUMO (lowest unoccupied molecular orbital) can be tuned independently by varying the substitution pattern at the ppy or bpy ligand, respectively.[62] The combination of the high redox potentials, the tunability of the excited states and the long lifetimes makes this compound class more suitable for different applications than ruthenium photosensitizers. Iridium sensitizers do generally show a higher activity, as screenings of different sensitizers in proton reduction experiments by the Bernhard group showed.[11,47]

They belong to the platinum group metals (PGM), which show the lowest abundance in the earth's crust. Hence, they have a high price, since extraction of the metals is a tedious process as the ore in the main mining region of south africa contains typically around 5 g/t of PGMs (Ru, Rh, Pd, Os, Ir and Pt **combined**).[63] But apart from high prices, the low concentration results in serious environmental issues due to the high energy consumption and waste production. The debris alone for the approximately 34 tons pure ruthenium per year amounts to at least 34 million tons.[64] Thus, a more ideal photosensitizer would utilize base-metals with higher abundance. While the examples of luminescent base-metal photosensitizers are dominated by copper compounds,[65–67] the recent past showed a great increase in other base-metals.[68–71] Especially one element shows great potential: Iron.

1.3. Iron(II) Photosensitizers

Iron makes up 5.6 % of the earth's crust,[6] being the fourth most abundant element after oxygen, silicon and aluminum. This makes it much easier to extract and inexoensive. Another major advantage is the low toxicity of most iron compounds.[72] Chemically advantageous is the perfectly reversible redox pair of iron(II)/iron(III).[73] The latter can help in photoredox catalysis, where stability in a consecutive change of oxidation states is a necessity (Scheme 2). But its photophysics, due to iron being a 3d-element, are more challenging.

Photophysical properties of iron complexes are related to the more contracted 3d orbitals, compared to 4d-orbitals in Rutheniums, an issue caused by the primogenic effect.[74] A graphical representation is shown in Fig. 3. The name goes back to Pyykkö,[75] who named the 1s, 2p, 3d and 4f-shells primogenic, from the latin words primus (first) and genitus (born). The effect describes that the radial parts of the first-shell atomic orbitals of an angular momentum quantum number are nodeless and hence contracted. Therefore, valence 3d-orbitals do not extend as far from the core electron sphere (s- and p-orbitals) as 4d-orbitals. Concequently, this affects bonding of these metals to ligands. Due to repulsion of the metal 3p-orbitals, which show a similar extend as the 3d-orbitals, an

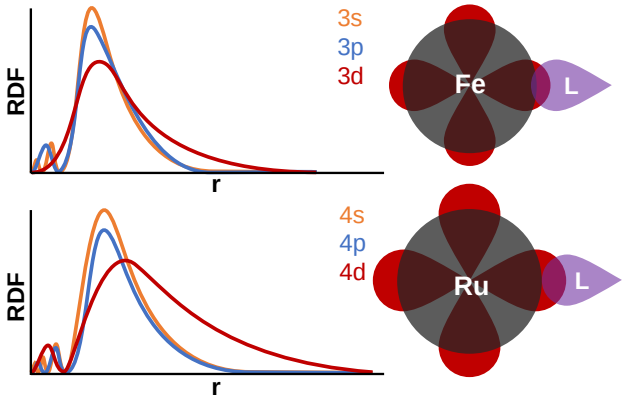

Figure 3: Schematic representation of the primogenic effect. On the left, the radial distribution function (RDF) of the electron density in dependence on the radius r is shown. The 4d electron density extends further from the core electron sphere, hence overlap with ligand orbitals (right) is better.

optimal overlap with the ligand orbitals is not possible.[76] These stretched bonds are easier to break, hence a lower stability of 3d-complexes is usually observed. It also leads to a smaller separation of bonding and antibonding orbitals, meaning that the ligand field splitting is smaller. Since the MC states correspond to the energetic position of the antibonding e_g* orbitals, they are energetically low-lying for these complexes (cf. Fig. 4).

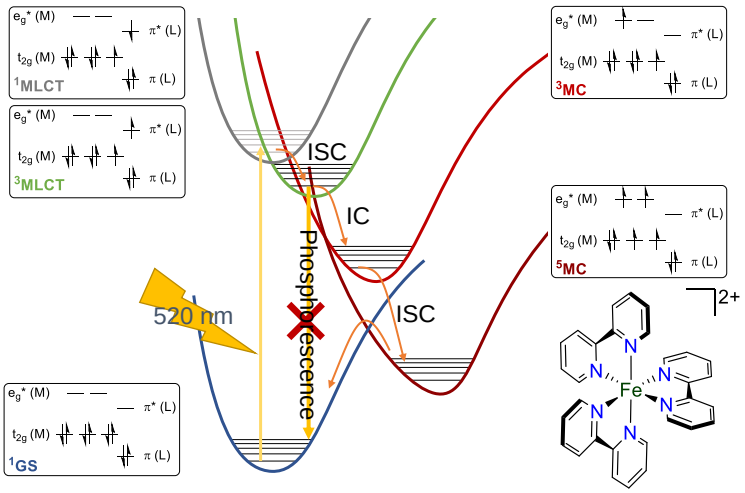

Figure 4: Schematic potential energy curves for $[Fe(bpy)]^{2+}$. Contrary to $[Ru(bpy)]^{2+}$, MC states dominate the deactivation cascade after photoexcitation. Due to the small ligand field splitting in iron, MC states are energetically lower than the MLCT states.

Hence, the relaxation cascade in $[Fe(bpy)]^{2+}$, which is isoelectronic to $[Ru(bpy)]^{2+}$, shows a different structure. After photoexcitation into the ^{1}MLCT, ISC into the ^{3}MLCT state is followed by an ISC into a ^{5}MC state, with the whole process taking place in less than

50 fs.[77] For other iron complexes, a transitional ^{3}MC state may be observed.[78] While the MLCT state is very short-lived, the ^{5}MC state shows a lifetime of around 1 ns, due to a high activation barrier back into the ground state. Even though this behavior can be exploited for light induced excited spin state trapping (LIESST) where iron complexes can be trapped in a meta-stable high-spin state,[79] this effect is not wanted in photocatalysis, as it inhibits further reaction due to trapping the PS in a long-lived MC state. Nonetheless, a new approach of utilizing these states emerged recently, where McCusker *et al.* showed electron-transfer reactions from presumably a ^{5}MC state[80] and Bauer *et al.* singlet oxygen sensitization from a ^{3}MC state.[81] Although this approach is new, it has huge potential, as most iron complexes so far possess long-lived MC states. However, research in iron-photochemistry of the past decade has been focussed on eliminating the deactivation of MLCT states by MC states.

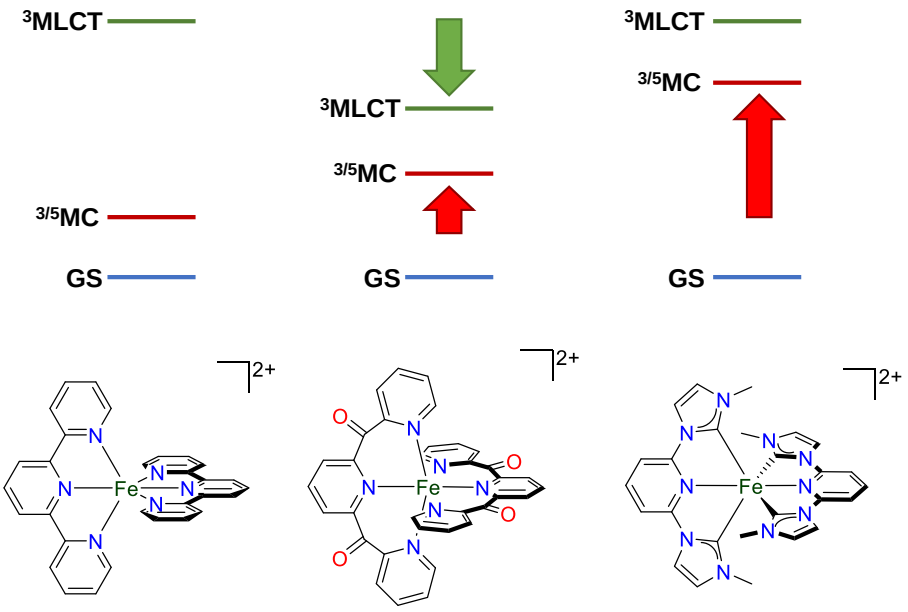

Figure 5: Schematic representation of the energy levels in three different iron complexes, to show the influence of ligand design on the excited states. Left: $[Fe(tpy)_3^{2+}]$ as reference compound for tridentate iron complexes. Here, the MC states are much lower than the MLCT states. Middle: $[Fe(dcpp)_2]^{2+}$, where π-accepting moieties are introduced and hence MLCT states are stabilized. Increased octahedricity leads to a moderate destabilization of the MC states. Right: $[Fe(bimp)_2]^{2+}$, where NHCs as strong σ-donors are introduced. They lead to a significant destabilization of the MC states.

The only way to change the electronic structure of complexes is to make use of different ligand effects, which will be discussed in the following. The first discussed approach is the

utilization of π-acceptor ligands. Strongly π-accepting moieties lower the energy of π*-orbitals, corresponding to stabilizing MLCT states respective to the MC states. A good example for this is the $[Fe(dcpp)_2]^{2+}$ (dcpp = 2,6-bis(2-carboxypyridyl)pyridine) complex, where a drastically reduced MC lifetime of 0.3 ns is observed compared to the 1.0 ns of $[Fe(bpy)_3^{2+}]$ or the 5.4 ns of $[Fe(tpy)_3^{2+}]$ (tpy = 2,2':6',2"-terpyridine) (Fig. 5).[82] A further look at the coordination of this complex reveals a another approach: Because the ligand is a six-membered chelate ligand, an increase in octahedricity is obtained. A perfectly octahedral complex is characterized by the highest overlap of metal and ligand orbitals. Thus, the ligand field splitting is increased. While this has been proven to be very effective for ruthenium complexes,[83] purely pyridyl coordonated iron complexes utilizing these strategies still do not show long-living MLCT states.[84,85]

Consequently, another strategy has to be followed: The introduction of stronger σ-donor ligands. The ligand field is increased in these complexes, since the anti-bonding e_g* orbitals, which correspond to the MC states, are destabilized by these ligands. The initial research, done by the Wärnmark group was published 2013. They introduced *N*-heterocyclic carbenes (NHCs) into an iron complex, resulting in the tetra-NHC compound $[Fe(bimp)_2]^{2+}$ (bimp = 2,6-bis(imidazole-2-ylidene)pyridine).[86] Wärnmark *et al.* observed an MLCT lifetime of 9 ps (Fig. 5), almost 2 magnitudes higher than the MLCT lifetime of the structurally related $[Fe(tpy)_3]^{2+}$. Due to the strong destabilization of the MC states, the ^{5}MC states cannot be populated anymore.[87] Other approaches have included the introduction of electron withdrawing groups such as carboxyl groups, leading to longer lifetimes, and electron injection into TiO_2 for application in dye sensitized solar cells (DSSCs).[88–90] Another variation of this concept included increased octahedricity in the ligands, where an increase in lifetime was observed.[91] NHC complexes of iron were even tested in photocatalytic proton reduction reactions, showing turn over numbers of up to 10, compared to 30 in a noble-metal photosensitizer.[92,93] In general, MLCT lifetime increased with a growing number of NHCs.[94] Consequently, an iron(II) complex with six NHC-donors by the Wärnmark group showed an MLCT lifetime of around 0.5 ns.[95] To further understand the influence of NHCs on the properties of iron compounds, a deeper look into the molecular orbitals (MOs) of iron complexes is needed (cf. Fig. 6).

The MO diagram shows the orbitals, which are involved in the previously discussed MLCT and MC states, as well as ligand-to-metal charge-transfer (LMCT) states, common in d^5-complexes.

1.3.1. N-Heterocyclic Carbenes as Donor-Ligands

The interactions of the carbene with the metal center can be generally divided into σ- and π-interactions. The first involves the overlap of the σ-orbital lobe of the ligand with

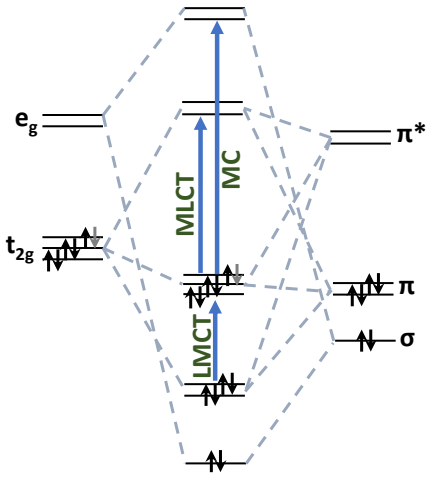

Figure 6: Schematic molecular orbitals of octahedral low-spin d^5 and d^6 complexes with the main possible transitions of MC, LMCT and MLCT.

the metal center. Based on the symmetry, it can only overlap with the e_g*-orbitals (cf. Fig. 7), resulting in σ-bonds between metal and ligand. NHCs are, like for photoactive compounds typical pyridine-moieties, a neutral two-electron donor ligand. However, due to the lower electronegatvity of carbon compared to nitrogen, the carbene lone-pair is higher in energy. The result is a more covalent bond of *C*-donors in comparison to *N*-donors.[96] The resulting increased σ-donation leads to a more destabilized e_g* orbital and therefore, energetically higher MC states. π-interactions only play a minor role in NHC-metal complexes (Fig. 8, left), but are pronounced enough to be mentioned. The free electron pairs of the nitrogens in this NHC donate electron density to the empty p_z-orbital of the carbene (Fig. 8). This results in a partially filled π-orbital of the carbene function to the metal center, leading to minor π-donating properties. However, the π-backbonding of the metal into these empty orbitals outweighs these effects, hence acting as π-accepting ligands.[97]

1.3.2. Cyclometalating Donor-Ligands

π-interactions play a major role in another type of strong donor ligand: Cyclometalating ligands show strong σ-donor properties and are important ligands in PGM photosensitizers (cf. Fig. 1).[11,13,98–103] Cyclometalated complexes have anionic carbon-atoms bound to the metal center. The lone electron pair of the anionic carbon donor is even higher in energy then the corresponding donor function centered at the neutral charged carben, therefore resulting in a pronounced covalent bond the metal. Thus, the destabilization of the e_g*-orbitals is even more prominent (Fig. 7). For these ligands, π-donor properties are a distinct feature.[104] The result is a destabilization of the t_{2g}-based ground state (Fig. 8),

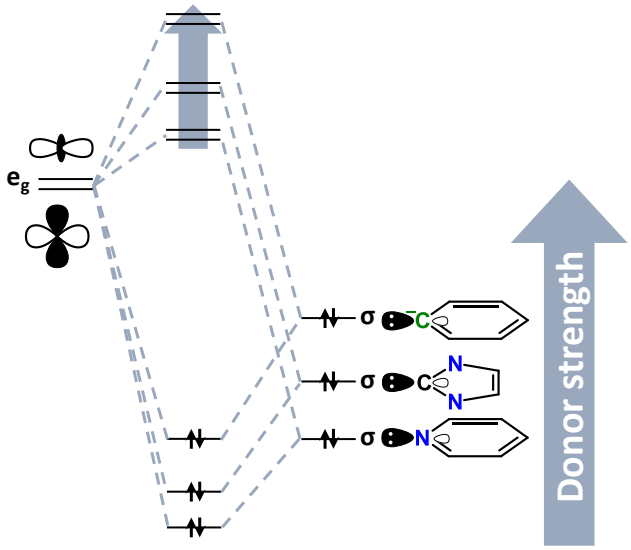

Figure 7: Schematic molecular orbitals for the σ-interactions of ligands and the metal center. The depicted pyridyl, NHC, and cyclometalating fragments posses different amounts of σ-donor-strength, influencing the energetic position of the e_g*-orbitals.

by interactions of the phenyl-π-orbitals with the respective t_{2g}-orbital. These effects can be observed in all cyclometalated complexes, e.g. with ruthenium[99,103] and iridium.[62] For iron compounds specifically, this leads to an unexpected result: If the central pyridine in terdentate ligands, analogous to terpyridine, is replaced by a phenyl moiety (Fig. 9 a), an overall stabilization of MC states is observed respective to the parent iron terpyridine complex (Fig. 9 c).[105] Even though this seems counterintuitive at first, since two strong donors are introduced, it can be explained by the σ-interactions of the ligands with the d-orbitals. In the case of the NCN coordination, the σ-orbital of the cyclometalating moiety overlaps with the d_z^2-orbital of the metal. Therefore, it is destabilized more than the d_{x2-y2} orbital, which stays mostly unaffected. The result is a smaller separation of the π-donation destabilized t_{2g}-based ground state and the d_z^2-orbital. Preservation of the symmetry has another result: Since pyridine-moieties are weak donors and are much more loosely bound than carbon-donors, the metal-nitrogen-bonds of the d_{x2-y2}-type can be easily elongated in symmetric vibrations. These elongated bonds are a necessity for energetically low ^{3}MC-states. Another factor coming into play here, is the trans-effect. Since both strong cyclometalating donors are on the same axis, the electron density cannot be counteracted by a *trans*-standing ligand. The effect is a longer metal-carbon bond than in the heteroleptic NCN/NNN compound and the same length as the central N-Fe-bond in $[Fe(tpy)_2]^{2+}$.[105]

If the phenyl-donor is located on the outside of the ligand (cf. Fig. 9 b), the symmetry of the complex is disturbed.In this CNN coordination, the effect on the e_g* orbitals is greater because the carbon donors are not on the same axis. Therefore, the destabilization

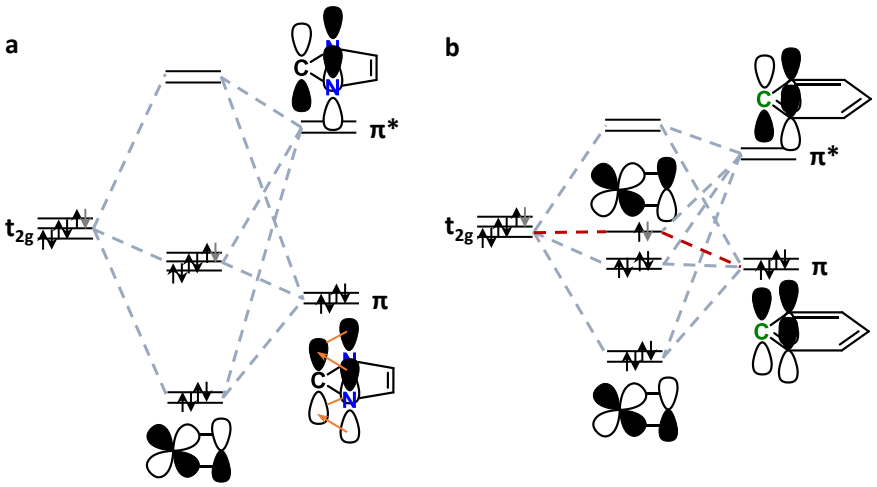

Figure 8: Schematic molecular orbitals for π-interactions (donating and accepting) of ligands and the metal center. **a**, interactions between an NHC and the t_{2g}-orbitals are depicted. **b**, interactions between a cyclometalating ligand and the t_{2g}-orbitals are shown, where the π-donor-properties lead to significant destabilization of the interacting t_{2g}-orbital (red).

caused by the strong donor functions cannot be counteracted by symmetric vibrations. The results are higher-lying ^{3}MC states, as predicted by Dixon *et al.*.[105] In this case, the metal-carbon bond is also stronger than in $[Fe(tpy)_2]^{2+}$, since the cyclometalating functions are *trans* to a pyridine, good acceptor ligands.

Therefore, this complex should be an ideal candidate for a luminescent iron(II)-compound with long-living ^{3}MLCT states, since it is the energetically lowest-lying excited state. The results of this prediction were essential for this dissertation and are responsible for the experimental approach in chapter 3.2. Recently, such a complex was published. It is the first monometallic iron(II) complex showing a 2.4 ns long NIR-emission from its ^{3}MLCT state and reactivity in photocatalytic reactions.[106]
Since cyclometalating moieties destabilize the ground state, they lower the oxidation potential of the complex, as shown in iridium complexes.[62] Hence, the oxidation state of the previously discussed iron CNN-complex will be in the +III state under ambient atmospheric conditions. The analogous NCN-complex was reported by Lagadec *et al.* and is obtained as iron(III) under atmosphere.[107] Unfortunately, there are no reports on the photophysical properties of either the iron(II) nor iron(III). But as reports from Wärnmark *et al.* show, iron(III) may be a viable alternative to iron(II) or even superior to it.[108,109]

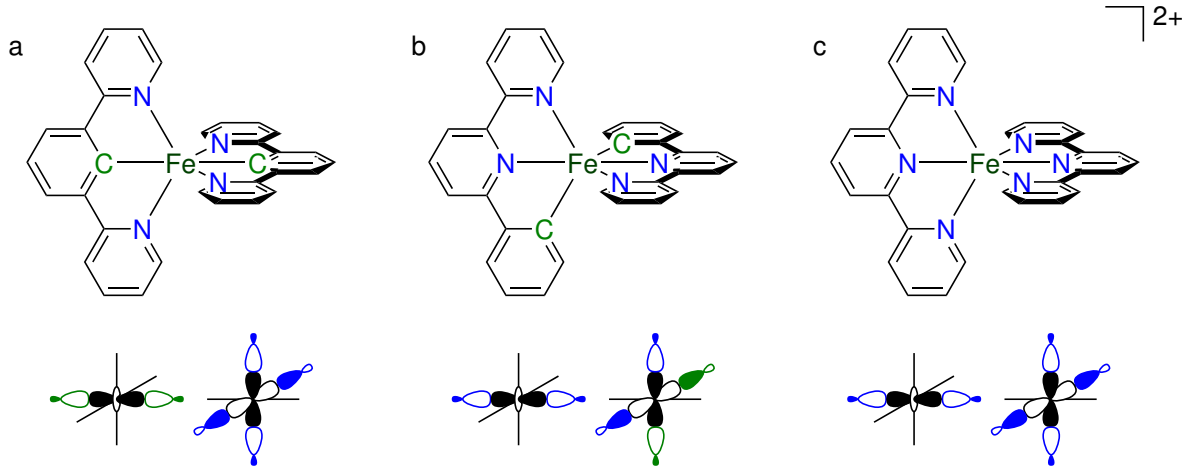

Figure 9: Cyclometalated iron complexes of the NCN type (a), the CNN type (b), and the reference complex $[Fe(tpy)_2]^{2+}$(c). The overlap of the ligand σ-orbitals and the e_g*-orbitals is shown for the respective complexes.

1.4. Iron(III)-Photosensitizer

Even though they reported a ^{3}MLCT lifetime of 528 ps for a hexacarbene iron(II) complex,[95] they were not able to detect luminescence. The analogous iron(III) complex however showed the first charge-transfer-based luminescence in iron compounds. The emission with a lifetime 100 ps originates from a spin-allowed ^{2}LMCT (ligand to metal charge transfer) state. This rare example of a fluorescent d^5-complex is analogous to previously reported rhenium and technetium(II) compounds,[110–113] and to hexacyanoruthenate(III)[114] which show high fluorescence quantum yields with a short excited-state lifetime, comparable to organic singlet-emitting chromophors.

In this case, the lowest ^{2}LMCT state cannot undergo intersystem crossing into a ^{4}LMCT state, the only accessible quartet state is the ^{4}MC state. This is accompanied by a bond elongation, since MC states, regardless of the spin-state, involve the population of an antibonding e_g*-orbital. Therefore, the radiative relaxation back into the ground state dominates the relaxation cascade, even though population of the MC states is possible when it is not resolved in optical spectroscopy (cf. Fig. 10). To get more insight on their population, time resolved X-ray spectroscopy is needed.[52] Further research by the Wärnmark group resulted in an iron(III) complex with a fluorescence lifetime of 2 ns and a quantum yield of 2 %, which can undergo bimolecular quenching.[109] Further studies suggest, that even though the complex is quenched by substrates, a fast charge-recombination inhibits the formation of photoproducts.[115] Nonetheless, very recently it was shown that this can be bypassed by performing photoreactions in halogenated solvents such as dichloromethane because it can potentially create partial state mixing with

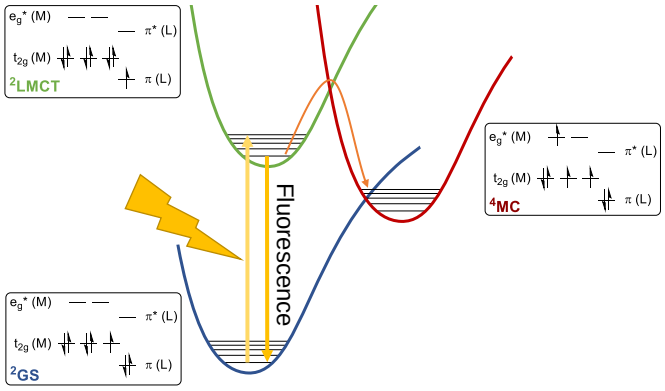

Figure 10: Schematic potential energy curves of a low-spin iron(III) complex in a strong ligand field. Photoexcitation from the doublet ground state leads to population of a ^{2}LMCT state. This can relax back into the ground state via fluorescence or undergo ISC into a quartet metal-centered state. From there, it can relax non-radiative back into the ground state.

higher spin-states. This proved to be effective in a benchmark dehalogenation reaction, showing that ns-lifetimes are sufficient for photoredox catalysis.[116]

2. Objectives and motivation

As climate change progresses and causes humanitarian problems, sustainable methods such as photochemical applications like photoredox catalysis are gaining more and more interest. As this field requires both effective and sustainable photosensitizers, the aim of this work is to develop new iron-based photosensitizers, as current photosensitizers are mostly based on platinum group metals. These are both expensive and environmentally problematic, therefore should be substituted in the long-term. However, iron complexes are typically characterized by short-lived catalytically active excited states due to energetically low metal-centered states. Previous research has shown that these can be overcome by strong donor ligands. Theoretical calculations suggest that cyclometalating ligands as strong donor functions have the ability to prolong the excited states. However, no complexes had been reported at the beginning of this work. This work helps to bridge the gap between theoretical considerations and experimental results to provide access to an entirely new class of iron photosensitizers with promising photopysical and photocatalytic properties.

To rationalize the impact of cyclometalation and the effects of different coordination environments, the ground and excited states have to be characterized. Electrochemical methods, such as cyclic voltammetry, are a powerful tool to gain a deeper insight into the changes in the electronic ground state structure. This is complemented by modern X-ray spectroscopic methods such as HERFD-XANES (high energy resolution fluorescence detected X-ray absorption near edge spectroscopy) and VtC-XES (valence to core X-ray emission spectroscopy). These provide further insight into the electronic structure. The excited states and their dynamics are investigated by transient absorption spectroscopy, which allows a detailed time-resolved analysis of the excited state landscape. Luminescent complexes are characterized by streak camera measurements and time-correlated single photon counting (TCSPC).

Scheme 3 summarizes the strategies pursued for the octahedral bis-tridentate iron complexes in this dissertation, which will be discussed shortly as they divide the approaches and chapters of this work.

The first strategy (A-complexes) is based on $[Fe(tpy)_2]^{2+}$, where a pyridine of the terpyridine ligand is replaced by a phenyl moiety. This strategy is applied to the monocyclometalated complex A1 (Ch. 3.2.2), followed by the class of biscyclometalated complexes A2 (Ch. 3.2.3). The second complex class is based on the $[Fe(bimp)_2]^{2+}$ complex, which combines *N*-heterocyclic carbenes with a central pyridine moiety, popular in iron photosensitizer research. In this work, the central pyridine fragments are replaced by phenyl moieties, resulting in the CCC-coordinated iron(III) complex B. First, the ground state, excited state and photodynamics are investigated (Ch. 3.3.2). Then, the electronic struc-

ture changes upon reduction and oxidation (Ch. 3.3.3) will be studied. To bridge the gap between development and application of cyclometalated iron photosensitizers, first catalytic experiments are performed (Ch. 3.3.4). Further insights into the structure-property relationship are obtained by systematic substitution of the complexes with electron withdrawing and donating groups in the ligand backbone (Ch. 3.3.5).

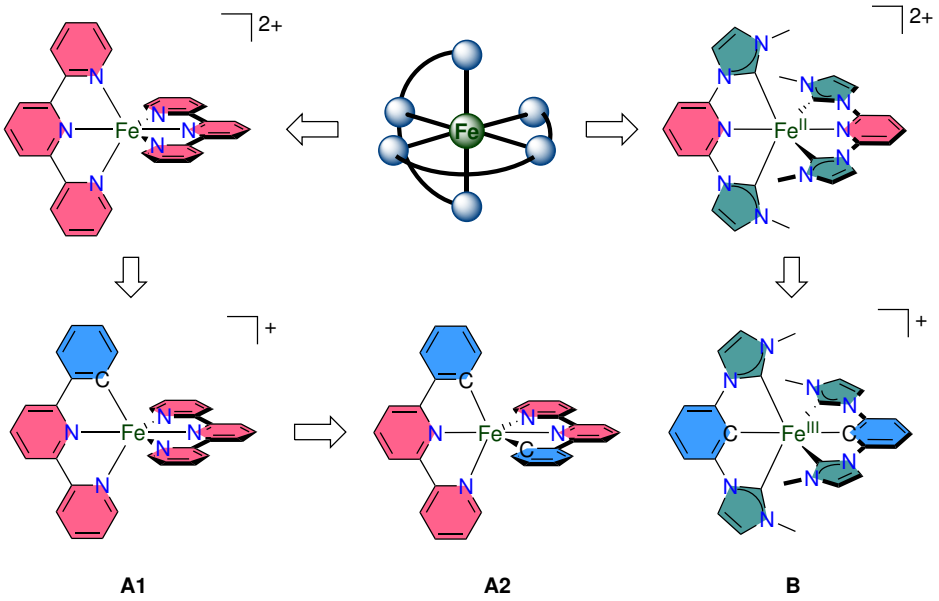

Scheme 3: Design of cyclometalated complexes with CNN (A-Complexes) and CCC ligands (B complex).

The overall goal of this work is to develop new iron-based cyclometalated complexes and to gain insight into their energetic structure in the ground and excited states and their photodynamics. With this knowledge, they can be modified and established among other photosensitizers. The long-term goal is to contribute to the replacement of ecologically and economically problematic noble-metal photosensitizers.

3. Results and Discussion

3.1. Synthetic approach to cyclometalation

The reported complexes within this work bear covalent metal-carbon bonds, located in CNN and CCC ligand motifs. Hence, formation of these bonds is a necessity for the success of this work, irrelevant whether the complexes contain CNN or CCC ligands. Different approaches may lead to the formation of these metal-carbon bonds.[117] Of these, C-H activations of the ligand are the most common reaction and can be subdivided into different mechanisms (Scheme 4). They all start with a metal M, which is precoordinated by a donor D to the ligand, on which cyclometalation will occur (**I**). Another ligand (X) is coordinated, which is usually anionic and acts as a base. The first discussed mechanism is the electrophilic aromatic substitution (Scheme 4, left).

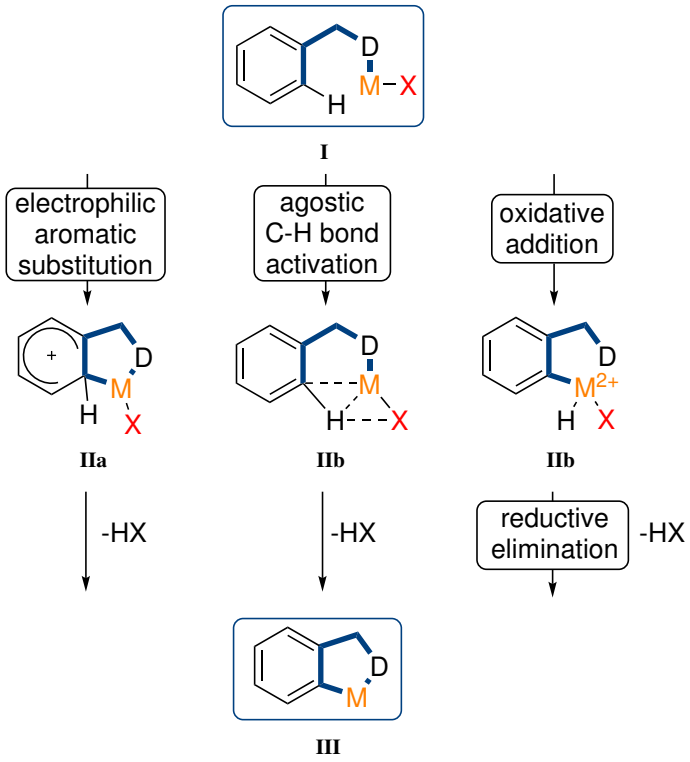

Scheme 4: Mechanisms of C-H activations for metal-carbon formation. Replicated and adjusted from Albrecht.[117]

It involves the formation of a σ-complex **IIa**, similar to typical organic electrophilic aromatic substitutions. But contrary to these, no intermediate π complex can be observed in the organometallic reaction. In the other aspects, the reactions follow the same rules. Elimination of the protonated ligand X transfers the intermediate σ complex to the desired

cyclometalated complex **III**. These reactions proceed more quickly with electron-donating substituents.

The second mechanism is the agostic C-H bond activation (Scheme 4, middle). In this case, an intermediate complex **IIb** involving the metal center and the C-H bond is formed.[117] The anionic ligand X stabilizes this complex, leading to metalation and deprotonation of the carbon. This reaction competes with the aromatic substitution and both can occur in the same reaction mixture. A special case is the σ-bond metathesis. It follows the same pathway as the agostic activation, but X in this case is a different anionic carbon species, such as a methyl group. The difference between the two pathways is, that σ-bond metathesis predominates in electron-poor systems, while the others dominate in electron rich systems.

Another mechanism for C-H activation reactions is the oxidative addition (Scheme 4, right), which is not only found in C-H activations, since other bonds like carbon-(pseudo)-halogen- or carbon-heteroatom-bonds can be activated via this route as well. Contrary to the electrophilic bond activations, the antibonding σ^* orbital of the C-H bond is directly populated in oxidative addition reactions, thus involving a formal two-electron transfer. The intermediate **IIc** may undergo further reductive elimination going back to the original oxidation state and resulting in the final complex **III**. For this case, the overall reaction is the same to the previous reactions. It differs from them by the influence substituents, as electron withdrawing groups lead to faster product formation.[118]

The last option to form a metal-carbon bond is transmetalation. There, an organic group is transferred from one metal to another. This is an important step in cross-coupling reactions, where different organometallic species are transferred onto the catalyst. This includes organozinc,[119] -magnesium,[120] -tin[121] and -boron[122] species,[iv] which also can be used to transfer organic groups onto other metals, apart from cross-coupling. Other common reagents for this application include organolithium species.[123] These metathesis-transmetalations differ from redox-transmetalations, as they are redox-neutral. Here, transmetalation occurs from the more electropositive metal to the more electronegative metal.[124] This is the reason why the previously mentioned metals work so well in trans-metalation reactions.

In summary, the starting material is mostly responsible for the mechanism in the formation of a C-M-bond. Applications of these different approaches is discussed in chapter 3.2.3.

[iv] For the Negishi, Kumada, Stille and Suzuki coupling, respectively.

3.2. Complexes with CNN-Ligands

3.2.1. Ligand design

Due to the high interest in cyclometalated iridium complexes, many bidentate phenylpyridine proligands are commercially available. This is unfortunately not the case for tridentate ligands, which were used in this project. Hence, different synthesis routes for the ligands of the A-complexes with CNN ligands (phenylbipyridine derivatives, Hpbpy = 6-phenyl-2,2'-bipyridine) will be described in the following (Fig. 5). The first route is based on a condensation reaction, starting from acetylpyridine, acetophenone and a C1-building block. From these and an ammonia donor, the central pyridine ring is formed. The second route is building the phenylbipyridine by a Suzuki-Miyaura coupling of a halo-bipyiridine with a phenyl boronic acid.

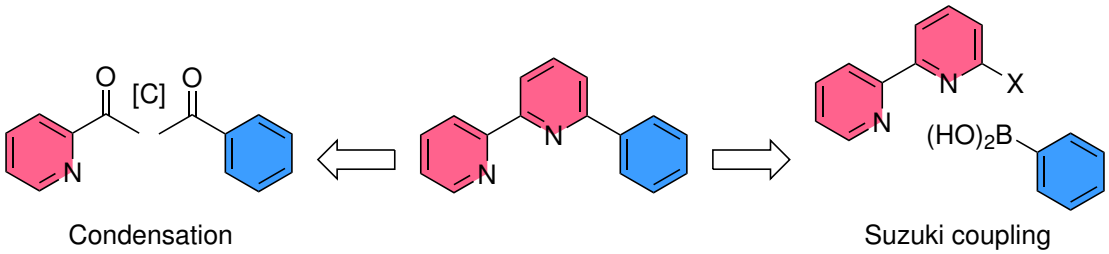

Scheme 5: Retrosynthetic routes for CNN-ligands. The first route is the condensation route. There, the central pyridine is built up via condensation, starting from acetylpyridine, acetophenone and a C1 building block. The second route is based on a Suzuki-Miyaura coupling of halo-bipyridines and phenyl boronic acids.

The overview of performed condensation reactions is displayed in Scheme 6. Two CNN ligands were obtained by this general mechanism. The first approach is based on the Jameson-terpyridine synthesis.[125] In this route, an acetyl functionalized aryl compound is treated with dimethylformamide dimethyl acetal to form a dimethylamino vinyl ketone **1** in an Aldol condensation. This was done for both acetophenone and acetylpyridine, forming the respective dimethylamino vinyl ketone in 53 % (**1a**) and 70 % (**1b**) yield. In the second step of the reaction, the other acetyl compound (acetylpyridine or acetophenone) was deprotonated with potassium *tert*-butoxide in tetrahydrofurane (THF). This was reacted with the previously synthesized vinyl ketone in a michael reaction to form an intermediate diketone, which was not isolated. In a second step, ammonium acetate and acetic acid were added, while THF was distilled off to form the central pyridine. The reaction yields phenylbipyridine **2** with around 20 % for both reactions. The aldol reaction works better for acetylpyridine, while the michael reaction does not seem to be influenced by the reagents. Hence, the optimal way is to first convert the acetylpyridine into the

vinyl ketone, followed by reaction with acetophenone. Using that method, the analogous bromophenylbipyridine, needed for C-Br activations and metalations, **3** was synthesized in a 25 % yield. A later approach for this ligand is based on the Kröhnke synthesis.[126] In a first step, a so called "Kröhnke reagent" is formed by the reaction of acetylpyridine, iodine and pyridine. The acetylpyridine is iodinated to ω-iodoacetylpyridine, which then reacts with pyridine in a nucleophilic substitution to pyridinium-acetylpyridine with a yield of 45 %. In the literature, yields of around 80 % are more common.[126] The second reagent is the Mannich adduct of 2'-bromoacetophenone, formaldehyde and dimethylamine hydrochloride, which was obtained in a yield of 50 %. These two reagents were combined in methanol with ammonium acetate as a nitrogen source, resulting in **3** in a yield of 32 %. The overall yield for this process is a bit lower (14 %) than for the Jameson method (20 %) and involves one step more. Nonetheless, this reaction type is preferred, since the last step is more efficient and show, as reported in the literature, high tolerance for functional groups.[126,127]

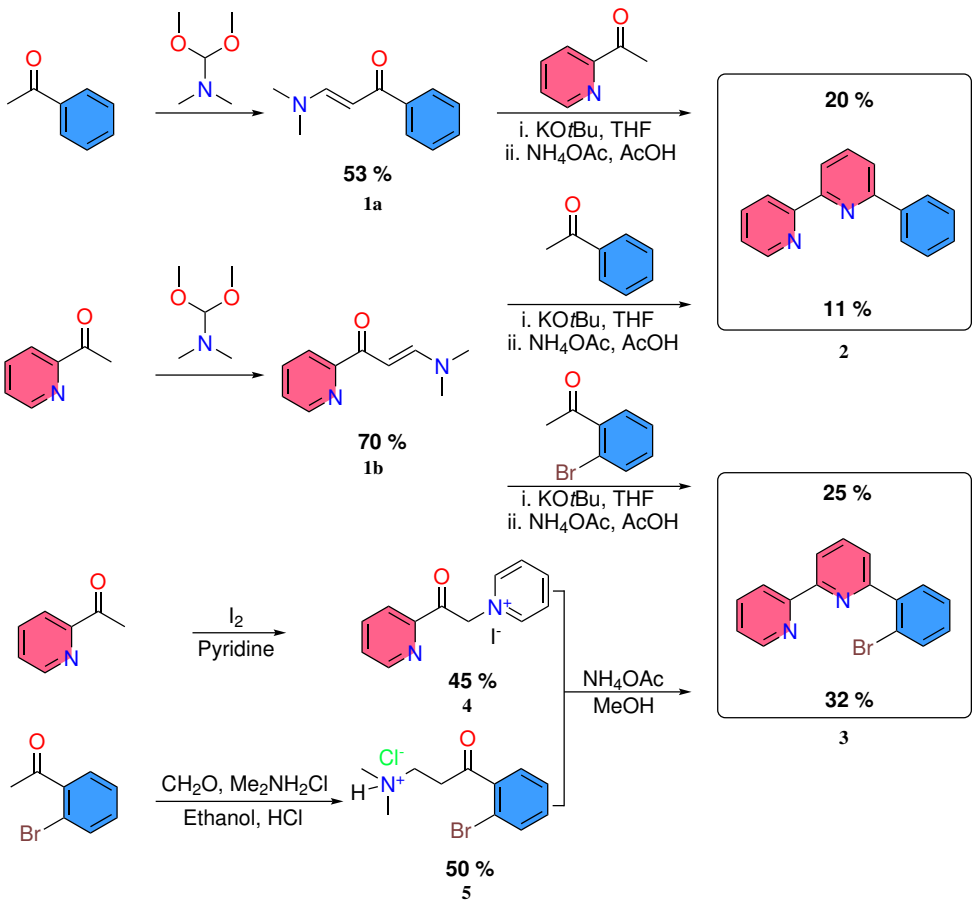

Scheme 6: Synthesis of proligands **2** and **3**, based on condensation reactions.

Even though this route provides an easy path to cyclometalating ligands, it is difficult to incorporate many substitution patterns into the ligands, since an acetyl functionality is needed. These are often not commercially available and cannot be incorporated easily in many cases, like for the fluorinated ligands (Fig. 7). For CNN ligands, palladium-catalyzed cross-coupling was chosen as a second reaction route. This reaction route does not tolerate bromide or iodide in the ligand backbone due to their high reactivity. Therefore, some form of C-H activation must be used for these ligands, or they must be be functionalized subsequently in a palladium-catalyzed bromination.[128] The cross-coupling reaction employed to obtain the following ligands is the Suzuki-Miyaura coupling. There, organoboronates and halides,[v] are coupled under mild conditions.[122]

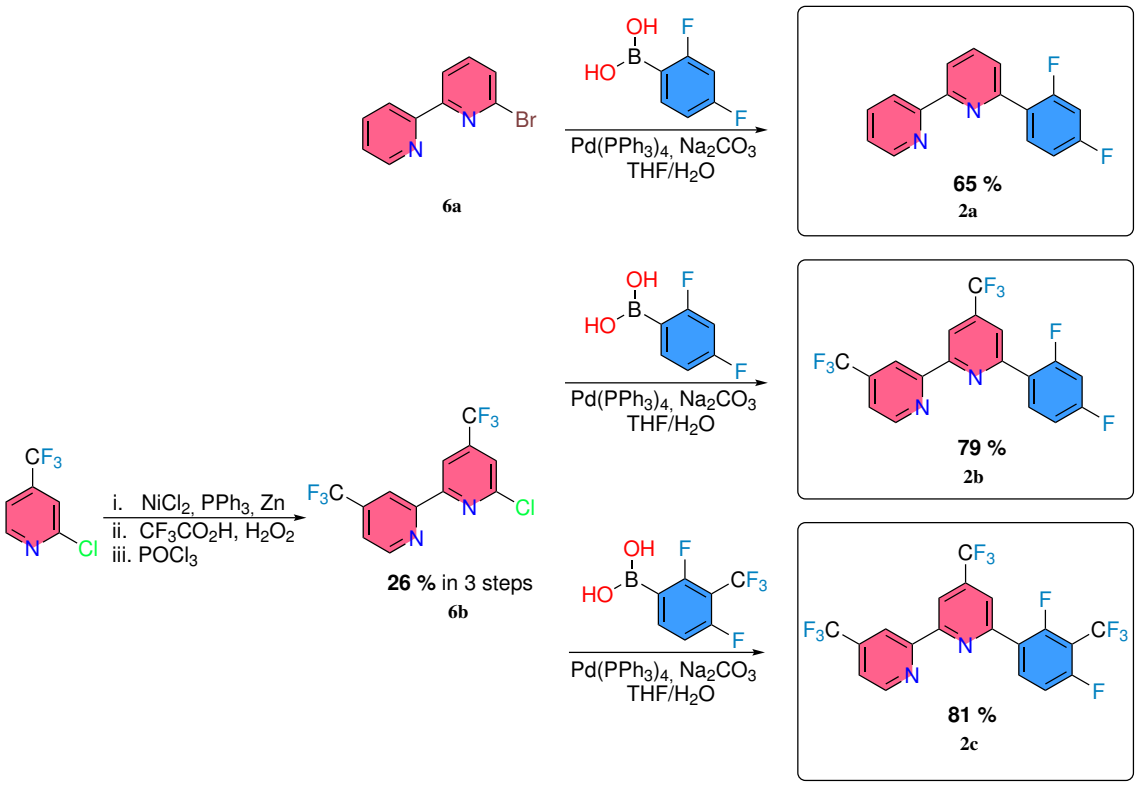

Scheme 7: Synthesis of fluorinated proligands based on the Suzuki-Miyaura reaction.

The three proligands synthesized this way are electron-deficient, due to electron withdrawing fluoro and trifluoromethyl substituents. The general procedure is based on a procedure by Baranoff *et al.*,[129] where a halobipyridine **6**, a boronic acid and sodium carbonate are suspended in a THF/water mixture and degassed, before tetrakis(triphenylphosphane)palladium is added to the mixture (Fig. 7). This shows the great advantage of

[v] In most cases, bromo or iodo compounds are used, but also chloro compounds work in some cases. Pseudohalides such as triflates can be used as well.

this coupling, since other cross-coupling reactions require water-free conditions. The first proligand **2a** includes an F_2-substitution at the phenyl ring of phenylbipyridine. The reaction uses the commercially available 6-bromo-2,2'-bipyridine **6a** and 2,4-difluorophenylboronic acid and leads to the ligand in 65 % yield. Additional electron withdrawing functions were introduced by trifluoromethyl groups in the bipyridine backbone (**6b**). This substituted bipyridine was obtained by the homocoupling of commercially available 2-chloro-4-trifluoromethylpyridine, with subsequent oxidation and chlorination in 26 % yield over the three steps.[129] It was reacted with 2,4-difluoro-phenylboronic acid to **2b**, with a yield of 79 %. The most electron deficient ligand further decreases the electron density on the phenyl moiety by introducing a CF_3-group at the F_2-phenylene unit. This was done by using the corresponding boronic acid, which was obtained by lithiation and subsequent boronation of 2,6-difluorobenzotrifluoride. Reaction of this and **6b** gave **2c** with a yield of 81 %. Overall, the yields of these reactions were much higher than for the condensation pathways described before. This is slightly overshadowed by the high cost of **6c** (95.60 €/g as cheapest option).[130] Synthesis of **6c** via Stille or Negishi coupling was not performed in the lab due to the toxic organotin reagents and the highly reactive organzic compounds, respectively.[131,132] Another downside is the preparation of **6b**, which involves working with two equivalents of nickel chloride per CF_3-bpy and large amounts of phosphoroxychloride. Nevertheless, the overall synthetic ease of this reaction, the high tolerance towards functional groups and availability of different boronic acids makes this preferable over the condensation reaction. The use of these ligands is discussed in the next chapters.

3.2.2. Monocyclometalated CNN-complexes

In this project, the first air- and water stable cyclometalated iron(II) complex was obtained and characterized in its ground and excited state. The results were compared to the $[Fe(tpy)_2]^{2+}$complex. Using the mechanism of oxidative addition (Ch. 3.1) of bromophenylbipyridine **3** by the low-valent iron precursor $[Fe(PMe_3)_4]$ and further reaction with terpyridine, the target complex $[Fe(tpy)(pbpy)]^+$ was obtained. Ground state analysis by electrochemistry and X-ray spectroscopy supports the results of DFT calculations[104,105,133] that the t_{2g} levels are destabilized due to the strong σ- and π- donating effect of the cyclometalated moiety. The result is a panchromatic absorption over the whole UV-Vis range up into the NIR region. The excited state behavior was probed by transient absorption spectroscopy, revealing two time-constants of 0.8 and 12 ps, respectively. Their decay associated amplitude spectra are similar in shape, making an unambiguous assignment impossible without further examination with fs-X-ray pump-probe experiments. Nevertheless, the presented data suggests that the shorter time constant can be assigned to a ^{3}MLCT state and the longer time constant to a ^{3}MC state. This is supported by the calculations of Dixon,[105,133] who predicted a ^{3}MC state energetically lower than the ^{3}MLCT state. In comparison to the iron terpyridine complex, the MLCT lifetime is increased by a factor of 5.5, while the MC lifetime is reduced drastically.

Excited-State Kinetics of an Air-Stable Cyclometalated Iron(II) Complex

Contributing authors:

Jakob Steube: Design and synthesis of the title molecule, its standard characterization (NMR, MS, IR), cyclic voltammetry, UV-Vis spectroscopy, interpretation of the data, wrote the manuscript.

Dr. Lukas Burkhardt: (TD)DFT calculations, analysis of X-ray spectroscopy data.

Ayla Päpcke (now Kruse), Prof. Dr. Stefan Lochbrunner: Transient absorption spectroscopy.

Dr. Johannes Moll, Prof. Dr. Katja Heinze: Spectro-electrochemistry.

Dr. Peter Zimmer: Involved in the design of the title molecule, synthesized $[Fe(PMe_3)_4]$, involved in discussing the results.

Dr. Roland Schoch, Dr. Christoph Wölper: Single-crystal X-ray diffraction.

Prof. Dr. Matthias Bauer: Corresponding author and wrote the manuscript.

Supplementary Information for this publication is found in the Appendix in Ch. C.1.

Photochemistry

Excited-State Kinetics of an Air-Stable Cyclometalated Iron(II) Complex

Jakob Steube,[a] Lukas Burkhardt,[a] Ayla Päpcke,[b] Johannes Moll,[c] Peter Zimmer,[a] Roland Schoch,[a] Christoph Wölper,[d] Katja Heinze,[c] Stefan Lochbrunner,[b] and Matthias Bauer*[a]

Abstract: The complex class $[Fe(N^N^C)(N^N^N)]^+$ with an Earth-abundant metal ion has been repeatedly suggested as a chromophore and potential photosensitizer on the basis of quantum chemical calculations. Synthesis and photophysical properties of the parent complex $[Fe(pbpy)(tpy)]^+$ (Hpbpy = 6-phenyl-2,2′-bipyridine and tpy = 2,2′:6′,2″-terpyridine) of this new chromophore class are now reported. Ground-state characterization by X-ray diffraction, electrochemistry, spectroelectrochemistry, UV/Vis, and X-ray spectroscopy in combination with DFT calculations proves the high impact of the cyclometalating ligand on the electronic structure. The photophysical properties are significantly improved compared to the prototypical $[Fe(tpy)_2]^{2+}$ complex. In particular, the metal-to-ligand absorption extends into the near-IR and the ^{3}MLCT lifetime increases by 5.5, whereas the metal-centered excited triplet state is very short-lived.

The long-standing quest for iron complexes that substitute noble metals in photochemical applications as photosensitizers in photocatalytic reactions and as luminescence emitters, is currently carried out with great effort. To this end, long-lived metal-to-ligand charge transfer (MLCT) states have to be achieved in Fe^{II} complexes. Ruthenium(II) provides this essential property more or less intrinsically with suited ligands, whereas this is not the case in iron(II) complexes. Because of the much smaller t_{2g}–e_g* ligand field splitting in iron(II) complexes, the metal e_g* levels are usually lower in energy, which favors a very fast deactivation of the MLCT states into nonemissive and catalytically inactive metal-centered (MC) states.[1,2]

Approaches to establish iron(II) complexes as emissive or photocatalytically active materials follow two fundamental strategies to prolong MLCT lifetimes: the stabilization of MLCT states and the destabilization of the MC states. From an application point of view, bis(tridentate) ligand–iron(II) combinations are superior to tris(bidentate) iron(II) complexes, as the former ones are typically more inert toward substitution.[3] Since recorded ^{3}MLCT lifetimes are so far reported for bidentate complexes,[4] further lifetime engineering in tridentate-coordinated Fe^{II} complexes[5,6] and derivatives thereof are thus highly important.

An overview of the conceptual approaches to increase the ^{3}MLCT lifetime of Fe^{II} complexes was recently given by Wenger.[7] Optimized octahedral symmetry in combination with π-accepting ligands to lower the t_{2g}-levels, or a push–pull ligand combination to stabilize MLCT states while destabilizing the MC states, are successful concepts established by McCusker[8] and Heinze[9] for $[Fe(N^N^N)_2]^{2+}$ chromophores. Exchange of pyridyl units by N-heterocyclic carbene (NHC) ligands by Wärnmark, Gros, and Bauer lead to $[Fe(C_{NHC}^N^C_{NHC})_2]^{2+}$ and related complexes.[10,11,12] NHCs are stronger σ-donors, destabilizing the MC states and thus extending MLCT lifetimes. In combination with polypyridine ligands in heteroleptic complexes the undesired properties of bis(NHC) ligands to raise the ^{3}MLCT energy can be partially compensated.[11] For all these compounds of the type $[Fe(N^N^N)_2]^{2+}$ and $[Fe(C_{NHC}^N_{\wedge}C_{NHC})_2]^{2+}$ experimental and theoretical studies complement and support each other.[6,13]

In contrast, quantum chemical predictions provided by Jakubikova et al. and Dixon et al.[14,15,16] for the effects of exchanging an N-donor by a cyclometalating ligand could not be confirmed experimentally so far. Although aryl carbanion ligands in the form of 2-phenylpyridine, 1,3-di(2-pyridinyl)benzene, and 6-phenyl-2,2′-bipyridine (Hpbpy already found applications in the context of noble metal complexes,[17,18] air- and water-stable cyclometalated Fe^{II} compounds, allowing for photochemical applications, are lacking up to date.[19] With this work we will fill this gap and present a) a synthetic access to heteroleptic, cyclometalated $[Fe(N^N^N)(N^N^C_{cm})]^+$ complexes, here in the form of $[Fe(pbpy)(tpy)]^+$ (tpy = 2,2′:6′,2″-terpyri-

[a] J. Steube, Dipl.-Chem. L. Burkhardt, Dr. P. Zimmer, Dr. R. Schoch, Prof. Dr. M. Bauer
Institute of Inorganic Chemistry and Center for Sustainable Systems Design (CSSD), University of Paderborn, Warburger Straße 100 33098 Paderborn (Germany)
E-mail: matthias.bauer@upb.de

[b] A. Päpcke, Prof. Dr. S. Lochbrunner
Institute of Physics and Department of Life, Light and Matter
University of Rostock, 18051 Rostock (Germany)

[c] J. Moll, Prof. Dr. K. Heinze
Institute of Inorganic Chemistry and Analytical Chemistry
Johannes Gutenberg University
Duesbergweg 10–14, 55128 Mainz (Germany)

[d] Dr. C. Wölper
Institute for Inorganic Chemistry and Center for Nanointegration Duisburg-Essen (Cenide), University of Duisburg-Essen
Universitätsstraße 5-745117 Essen (Germany)

Supporting information and the ORCID identification number(s) for the author(s) of this article can be found under: https://doi.org/10.1002/chem.201902488.

dine) and b) thoroughly investigate the ground- and excited-state characteristics in comparison to the prototypical complex $[Fe(tpy)_2]^{2+}$ to prove the high potential of cyclometalating ligands for increasing MLCT lifetimes.

The established synthesis of cyclometalated complexes by C–H-activation,[20,21] as with ruthenium(II) and other 4d/5d transition metals, could not be transferred to iron(II) complexes. Instead, an oxidative addition involving the low valent $[Fe(PMe_3)_4]$ precursor has been developed (Scheme 1). This approach is similar to that developed by Klein et al. for cyclometalated nickel(II) complexes.[22] The phosphane iron(0) complex is treated with the ligand precursor 6-(2-bromophenyl)-2,2′-bipyridine (Brpbpy).[23] This results in the octahedral cyclometalated phosphane bromido iron(II) intermediate *trans*-FeBr(pbpy)$(PMe_3)_2$ (**1**), which can be isolated under inert conditions. Addition of a stoichiometric amount of terpyridine substitutes the phosphanes and the halide yielding the air- and water-stable complex [Fe(pbpy)(tpy)](PF_6) **2** PF_6 after anion exchange (Scheme 1).

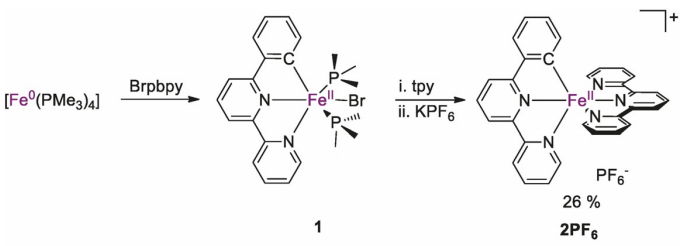

Scheme 1. Synthesis of cyclometalated complex **2** PF_6.

Single crystals suitable for X-ray diffraction could be obtained with BPh_4 as the counterion (Figure 1). As the phenyl ring is disordered over the two ligands in a one to one ratio, the Fe–C distance is the mean value of a Fe–N1 and a Fe–C1 bond length. Also, the Fe–N3 distances are the average of the tpy–Fe–N and pbpy–Fe–N values. Still, a shorter Fe–C1/N1 bond of 1.944 Å and a slightly elongated Fe–N3 bond of 1.981 Å *trans* to the Fe–C bond compared to the outer Fe–N bond lengths in $[Fe(tpy)_2]^{2+}$ are observed due to the *trans* effect of the strong Fe–C bond.[24] These structural results are in good accordance with the structure calculated by DFT.

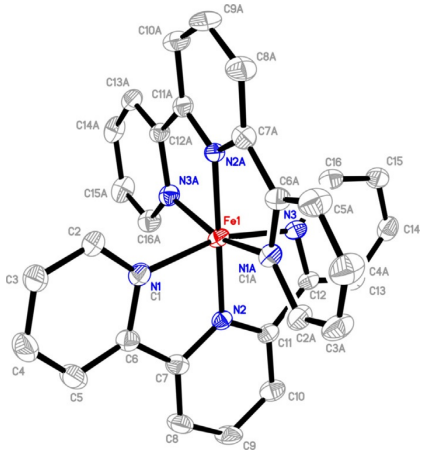

Figure 1. Single-crystal structure of [Fe(tpy)(pbpy)](BPh_4) (**2**BPh_4) drawn with anisotropic displacement ellipsoids at a 50% probability level. Hydrogen atoms and the counterion are not displayed for reasons of clarity.

The ground-state of **2** is characterized by optical spectroscopy, electrochemistry, and spectroelectrochemistry, combined with advanced hard X-ray spectroscopic techniques. The latter is less established for photochemical research yet offers a multitude of information about core-excited states. This in turn allows to calibrate and validate the selected theoretical approach for the ground state.[25,26]

A low-spin (LS) configuration of **2** is confirmed by NMR and core-to-core X-ray emission spectroscopy (CtC-XES)[26] at the iron K-edge, similar to the reference complex $[Fe(tpy)_2]^{2+}$ (**3**). The LUMO and HOMO levels are probed in detail by HERFD-XANES (high energy resolution fluorescence detected XANES)[27] and VtC-XES (valence-to-core X-ray emission spectroscopy) in combination with TD-DFT calculations.[25,26,28] From the HERFD-XANES prepeak analysis of **2** and **3** it can be deduced that the core-excited MC states, formed by the metal-centered e_g* acceptor orbitals, are destabilized significantly in the cyclometalated complex. This result nicely confirms the chosen approach of using cyclometalating ligands to destabilize MC excited states of iron(II) as has been found in the homologous ruthenium(II) complex $[Ru(tpy)(pbpy)]^+$.[21,29,30] In contrast, no significant effect on the t_{2g} levels by cyclometalation is observed with VtC-XES. With VtC-XES, the occupied levels of lower energy are probed that prove the σ-bonding interaction of the $pbpy^-$ ligand and the Fe $3d_{z^2}$ orbital, as well as the stabilization of the phenyl/polypyridyl σ and π fragment orbitals in **2** as compared to **3**.

Consequently, the Kohn–Sham molecular orbital diagrams (Figure 2) obtained by DFT calculations with MeCN as the solvent using the SMD solvation model[31] show a significant destabilization of the HOMO-t_{2g} levels of reduced degeneracy,[15] in agreement with the strong π-donor properties of the cyclometalating ligand. The LUMO is located at the tpy ligand in **2**, whereas the $pbpy^-$ ligand only contributes to molecular orbitals of higher energy,[29] similar to the Ru^{II} congener.[30] Since the LUMO is less destabilized than the HOMO, the HOMO–LUMO gap is decreased by 0.44 eV in **2** compared to **3**. The unoccupied metal-centered e_g* orbitals of **2** are destabilized, the d_{z^2} orbital to a larger extent than the $d_{x^2-y^2}$ orbital due to the covalent Fe–C bond located on the *z*-axis.[32]

According to the MO diagrams, the HOMO and LUMO levels of **2** are significantly affected by the cyclometalating ligand (Figure 2). This is furthermore reflected in the electrochemical properties of **2**. The redox potential is significantly lowered by −0.83 V for the reversible $Fe^{II/III}$ redox wave compared to **3** (−0.11 and 0.72 V vs. FcH/FcH^+, respectively) as a result of the larger π-donor strength of the cyclometalating moiety.[15,16,32] This agrees with the theoretically predicted destabilization of the t_{2g}-orbitals by 0.76 eV (Figure 2). A similar value for the

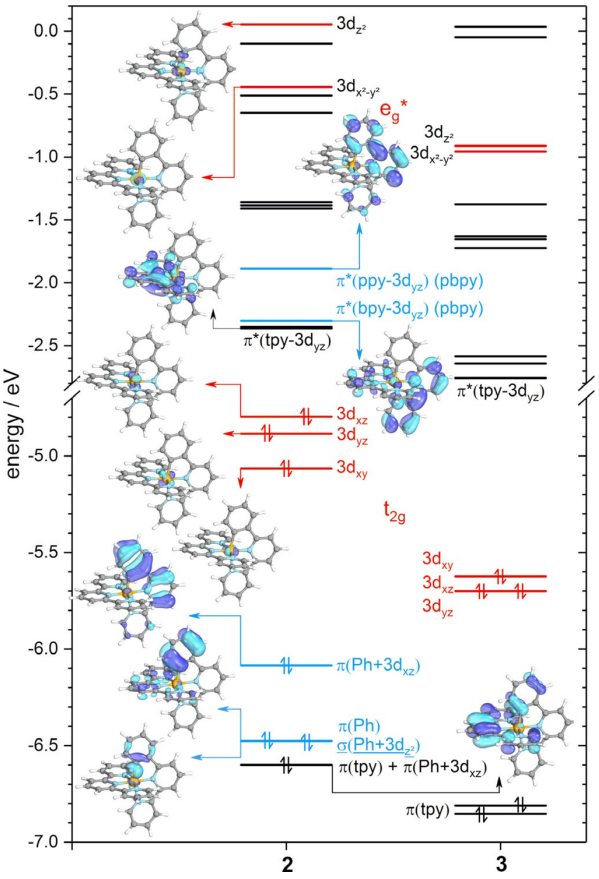

Figure 2. DFT-calculated molecular orbital diagrams of **2** and **3** (def2-TZVPP, TPSSh, SMD). Levels with significant Fe 3d contribution are shown in red, levels with significant pbpy contributions in blue.

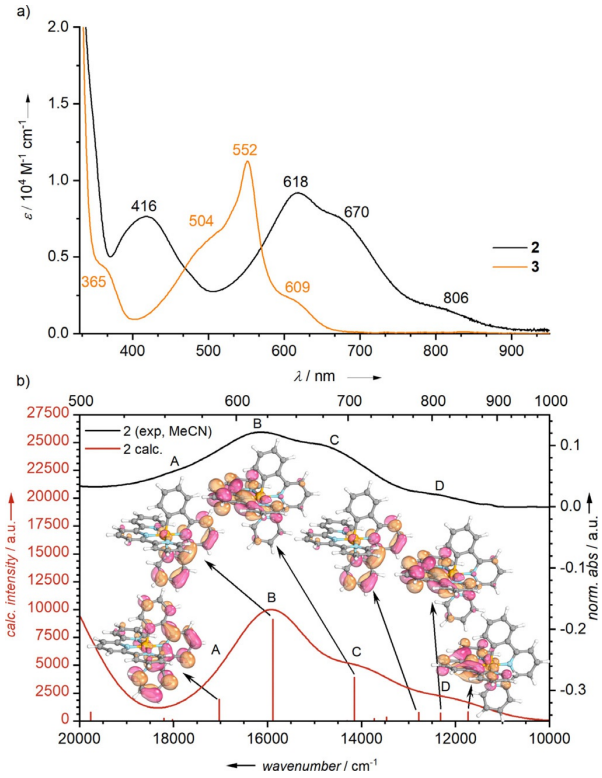

Figure 3. a) Electronic absorption spectra of **2** and **3** (10^{-5} M in MeCN) b) Comparison of the normalized experimental spectrum of **2** with the TDDFT calculated spectrum. Dominant acceptor orbitals are shown.

cathodic shift of 0.74 V is known for the $[Ru(pbpy)(tpy)]^{+/2+}$ and $[Ru(tpy)_2]^{2+/3+}$ redox couples.[29] The ligand-centered reduction waves of **2** are also cathodically shifted (−1.97 and −2.25 V) in comparison to **3**, but to a smaller extent. This is due to a weaker influence of the cyclometalating ligand on the LUMO levels, which are dominated by the tpy ligand. Consequently, the HOMO–LUMO gap in **2** is smaller than that in **3**.

In the electronic absorption spectra, **2** shows a strong panchromatic absorption up into the NIR region (Figure 3) with broadened peaks due to the lower symmetry[18,21,33] and concomitant larger t_{2g} splitting in comparison to **3**.[15] The MLCT maximum of **2** at λ_{max} = 618 nm (ε_{max} = 0.92 10^4 $M^{-1}cm^{-1}$) is redshifted compared to that of **3** (λ_{max} = 552 nm, ε_{max} = 1.12 10^4 $M^{-1}cm^{-1}$) due to the destabilized t_{2g} orbitals (Figure 2).

The MLCT absorption bands were assigned using TD-DFT calculations. The high energy shoulder A (Figure 3 b) at around 550 nm is mainly characterized by a transition to a π*-type orbital delocalized on the $pbpy^-$ ligand, whereas the final state of B is dominated by a π*-type acceptor orbital located on the bpy fragment of the $pbpy^-$ ligand. Complementary, C results from a transition to a tpy π*-type acceptor orbital. Finally, the low energy shoulder D is composed of three acceptor orbitals, two with mainly tpy π*- and one with bpy π*-character at $pbpy^-$. Solvatochromic shifts in different solvents (MeCN, MeOH, EtOH, acetone, DCM, and DMSO) confirm the asymmetric charge distribution in these MLCT states.

In luminescence measurements of **2** at 293 K in MeCN, no emission could be detected. This either points to low-lying MC states[11] or highly distorted MLCT states,[30] which cause an efficient nonradiative decay. Excited-state dynamics were thus probed by ultrafast pump–probe spectroscopy.[11,34,35] Transient absorption spectra of **2** in MeCN with a time resolution of about 50 fs and excitation pulses centered at 615 nm are shown for selected delay times in the Supporting Information. Decay associated amplitude spectra (DAS) obtained by a global fit are depicted in Figure 4.

After optical excitation, the transient absorption spectra of complex **2** exhibit a maximum at 500 nm and two negative bands with minima at 425 and 620 nm. The transient signals decay completely within less than 20 ps. The dynamics were analyzed by globally fitting a double exponential decay to the data. The fit reproduces the measurement very well, resulting in time constants of τ_1 = 0.8 and τ_2 = 12 ps. The corresponding DAS are compared to the difference spectrum between the oxidized $\mathbf{2}^+$ and **2** obtained from spectroelectrochemical measurements (Figure 4). For *N*-heterocyclic carbene iron(II) complexes MLCT states have been identified by comparison with the combination of difference spectra between oxidized

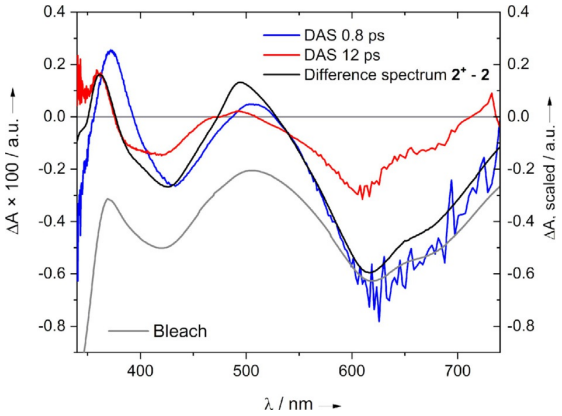

Figure 4. Decay associated amplitude spectra (DAS) of the two exponential components with time constants of 0.8 and 12 ps resulting from a double-exponential global fit (left scale) to the ultrafast absorption measurements. The DAS are compared to the scaled bleach and scaled difference spectrum obtained from spectroelectrochemical oxidation measurements (right scale) of complex **2**.

and reduced species and the ground-state spectrum, respectively.[11,35,36] Unfortunately, this procedure cannot be directly transferred to the cyclometalated complex **2** due to the irreversibility of the reduction process in spectroelectrochemical experiments and the fact, that no characteristic intense, low-energy LMCT transition is found for the electrochemically generated Fe^{III} species but merely a rather weak absorption around 500 nm (Supporting Information, Figure S17; difference spectrum "$\mathbf{2}^{+}-\mathbf{2}$" in Figure 4).

The short-lived component (τ_1) exhibits indeed a weak excited-state absorption (ESA) signal around 500 nm (Figure 4). The difference spectrum "$\mathbf{2}^{+}-\mathbf{2}$" reasonably matches the DAS (τ_1) and consequently, we assign this lifetime to a MLCT state (Figure 4). Together with the very short lifetime of 0.8 ps, this component is, therefore, assigned to a ^{3}MLCT state with high confidence. This triplet state is populated after excitation into a ^{1}MLCT state, followed by ultrafast intersystem crossing.[1,11,37] With this assignment, the $[Fe(N^N^N)(N^N^C_{cm})]^+$ complex $[Fe(pbpy)(tpy)]^+$ (**2**), therefore, shows an MLCT lifetime of 0.8 ps increased by a factor of 5.5 compared to its $[Fe(N^N^N)_2]^{2+}$ counterpart $[Fe(tpy)_2]^{2+}$ **3** exhibiting a MLCT lifetime of 145 fs.[35]

The longer-lived component is assigned to a ^{3}MC state due to its similarity to the ground-state bleach. Wärnmark[10,35] and Gros[38] pointed out for NHC complexes that such behavior indicates a missing population of the ^{5}MC state. For a ^{5}MC state typically a nanosecond lifetime is expected due to the double spin state change required in the relaxation. Thus, the very short lifetime of 12 ps for **2** makes a contribution of a quintet ^{5}MC state unlikely[8,9] as it would additionally require an elongation of all iron–ligand bonds, which is unlikely due to the presence of the Fe–C_{cm} bond.

A conceivable alternative interpretation of the longer-lived component assigns a second ^{3}MLCT state to the τ_2 lifetime, resulting from an independent excitation of the tpy^- and $pbpy^-$ ligands. The excitation wavelength of 615 nm is indeed exciting transitions involving different acceptor ligands (Figure 3). After relaxation and ISC of the individual MLCT states, internal conversion between ^{3}MLCT(tpy) and ^{3}MLCT(pbpy) states might be hindered due to the orthogonal arrangement of the tpy and $pbpy^-$ ligands. Although the DAS of the two components resemble each other (apart from the ESA at 500 nm), we consider the scenario of parallel ^{1}MLCT(tpy)→^{3}MLCT(tpy)→$^1A_1$ and ^{1}MLCT(pbpy)→^{3}MLCT(pbpy)→$^1A_1$ relaxation pathways as rather unlikely. This possibility would require direct relaxation pathways from both ^{3}MLCT states into the $^1A_1$ ground state bypassing the typically involved ^{3}MC state. This is very much at odds with theoretical predictions for such complexes.[16,32]

Consequently, the effects of the terminal cyclometalation in **2** are as follows. First, we observe a ^{1}MLCT→^{3}MLCT→^{3}MC→$^1A_1$ deactivation cascade, which differs significantly from **3** featuring a long-lived ^{5}MC state as the finally populated excited state.[35] Second, the ^{3}MLCT lifetime in **2** ($\tau_1 = 0.8$ ps) increases by a factor of 5.5 compared to that of **3** ($\tau_1 = 145$ fs).[35,38] This effect is significant, as complexes with even two NHC ligands $[Fe(C^N^C)(tpy)]^2+$ or $[Fe(N^N^C)_2]^{2+}$ merely yield ^{3}MLCT lifetimes below 100 fs.[11] In principle, the ^{5}MC state could still be lower in energy than the ^{3}MLCT state, but would remain unpopulated due to a high activation barrier caused by strong distortions. Still, our time-resolved measurements confirm the theoretical calculations of Dixon et al.[16] and Jakubikova et al.[15] predicting a $^3MC < {}^3MLCT < {}^5MC$ ordering of states in **2**, which is our third conclusion.

In summary, an oxidative addition synthetic access to cyclometalated iron(II) complexes was developed. This allowed the ground state, and, in particular, the excited state characterization of such chromophores with an Earth-abundant metal ion filling the so-far existing theory–experiment knowledge gap. The ^{3}MLCT stabilization of 0.95 eV with respect to the reference bis(terpyridine) iron(II) complex predicted by theoretical calculations[16] resulted in an increased ^{3}MLCT lifetime by a factor of 5.5 accompanied by a bathochromic shift of the absorption bands into the NIR. Both beneficial effects are mandatory for future photochemical applications of iron(II) complexes. To this end, ^{3}MLCT distortion needs to be further probed and finally controlled to increase the ^{3}MLCT lifetime of iron(II) complexes with tridentate ligands.

Acknowledgements

This work was supported by Deutsche Forschungsgemeinschaft [DFG, Priority Program SPP 2102 "Light-controlled reactivity of metal complexes" (BA 4467/7-1, LO 714/11-1, HE2778/14-1)]. The European Synchrotron Radiation Facility is acknowledged for provision of beamtime at beamline ID26. J. S. thanks the Deutsche Bundesstiftung Umwelt (DBU) for a PhD scholarship.

Conflict of interest

The authors declare no conflict of interest.

Keywords: iron · photochemistry · excited-state kinetics · transient absorption spectroscopy · DFT calculations

[1] E. A. Juban, A. L. Smeigh, J. E. Monat, J. K. McCusker, *Coord. Chem. Rev.* **2006**, *250*, 1783.

[2] A. Cannizzo, C. J. Milne, C. Consani, W. Gawelda, C. Bressler, F. van Mourik, M. Chergui, *Coord. Chem. Rev.* **2010**, *254*, 2677.

[3] a) P. Zimmer, P. Müller, L. Burkhardt, R. Schepper, A. Neuba, J. Steube, F. Dietrich, U. Flörke, S. Mangold, M. Gerhards, M. Bauer, *Eur. J. Inorg. Chem.* **2017**, *11*, 1504; b) T. Duchanois, L. Liu, M. Pastore, A. Monari, C. Cebrián, Y. Trolez, M. Darari, K. Magra, A. Francés-Monerris, E. Domenichini, M. Beley, X. Assfeld, S. Haacke, P. C. Gros, *Inorganics* **2018**, *6*, 63.

[4] a) P. Chabera, K. S. Kjær, O. Prakash, A. Honarfar, Y. Liu, L. A. Fredin, T. B. Harlang, S. Lidin, J. Uhlig, V. Sundstrom, et al., *J. Phys. Chem. Lett.* **2018**, *9*, 459; b) Y. Liu, K. S. Kjaer, L. A. Fredin, P. Chábera, T. Harlang, S. E. Canton, S. Lidin, J. Zhang, R. Lomoth, K.-E. Bergquist et al., *Chem. Eur. J.* **2015**, *21*, 3628.

[5] a) S. M. Fatur, S. G. Shepard, R. F. Higgins, M. P. Shores, N. H. Damrauer, *J. Am. Chem. Soc.* **2017**, *139*, 4493; b) S. Mukherjee, D. E. Torres, E. Jakubikova, *Chem. Sci.* **2017**, *8*, 8115.

[6] M. Pápai, G. Vankó, T. Rozgonyi, T. J. Penfold, *J. Phys. Chem. Lett.* **2016**, *7*, 2009.

[7] O. S. Wenger, *Chem. Eur. J.* **2019**, *25*, 6043.

[8] L. L. Jamula, A. M. Brown, D. Guo, J. K. McCusker, *Inorg. Chem.* **2014**, *53*, 15.

[9] A. K. C. Mengel, C. Förster, A. Breivogel, K. Mack, J. R. Ochsmann, F. Laquai, V. Ksenofontov, K. Heinze, *Chem. Eur. J.* **2015**, *21*, 704.

[10] L. A. Fredin, M. Pápai, E. Rozsályi, G. Vankó, K. Wärnmark, V. Sundström, P. Persson, *J. Phys. Chem. Lett.* **2014**, *5*, 2066.

[11] P. Zimmer, L. Burkhardt, A. Friedrich, J. Steube, A. Neuba, R. Schepper, P. Müller, U. Flörke, M. Huber, S. Lochbrunner, M. Bauer, *Inorg. Chem.* **2018**, *57*, 360.

[12] a) Y. Liu, P. Persson, V. Sundstrom, K. Wärnmark, *Acc. Chem. Res.* **2016**, *49*, 1477; b) D. Leshchev, T. C. B. Harlang, L. A. Fredin, D. Khakhulin, Y. Liu, E. Biasin, M. G. Laursen, G. E. Newby, K. Haldrup, M. M. Nielsen, K. Wärnmark, V. Sundström, P. Persson, K. S. Kjær, M. Wulff, *Chem. Sci.* **2018**, *9*, 405; c) M. Pastore, T. Duchanois, L. Liu, A. Monari, X. Assfeld, S. Haacke, P. C. Gros, *Phys. Chem. Chem. Phys.* **2016**, *18*, 28069.

[13] D. C. Ashley, E. Jakubikova, *Inorg. Chem.* **2018**, *57*, 9907.

[14] a) S. Mukherjee, C. Liu, E. Jakubikova, *J. Phys. Chem. A* **2018**, *122*, 1822; b) I. M. Dixon, G. Boissard, H. Whyte, F. Alary, J.-L. Heully, *Inorg. Chem.* **2016**, *55*, 5089.

[15] S. Mukherjee, D. N. Bowman, E. Jakubikova, *Inorg. Chem.* **2015**, *54*, 560.

[16] I. M. Dixon, F. Alary, M. Boggio-Pasqua, J.-L. Heully, *Dalton Trans.* **2015**, *44*, 13498.

[17] a) H. Kisserwan, A. Kamar, T. Shoker, T. H. Ghaddar, *Dalton Trans.* **2012**, *41*, 10643; b) R. Kaneko, G. Wu, K. Sugawa, J. Otsuki, A. Islam, L. Han, I. Bedja, R. K. Gupta, *J. Organomet. Chem.* **2017**, *833*, 61; c) L. L. Tinker, S. Bernhard, *Inorg. Chem.* **2009**, *48*, 10507; d) P. Coppo, E. A. Plummer, L. de Cola, *Chem. Commun.* **2004**, 1774; e) M. S. Lowry, S. Bernhard, *Chem. Eur. J.* **2006**, *12*, 7970; f) T. Tsuzuki, N. Shirasawa, T. Suzuki, S. Tokito, *Adv. Mater.* **2003**, *15*, 1455.

[18] P. G. Bomben, K. C. D. Robson, B. D. Koivisto, C. P. Berlinguette, *Coord. Chem. Rev.* **2012**, *256*, 1438.

[19] A. S. Estrada-Montaño, A. D. Ryabov, A. Gries, C. Gaiddon, R. Le Lagadec, *Eur. J. Inorg. Chem.* **2017**, *12*, 1673.

[20] a) M. Albrecht, *Chem. Rev.* **2010**, *110*, 576; b) S. Fernandez, M. Pfeffer, V. Ritleng, C. Sirlin, *Organometallics* **1999**, *18*, 2390; c) E. C. Constable, J. M. Holmes, *J. Organomet. Chem.* **1986**, *301*, 203.

[21] P. G. Bomben, K. C. D. Robson, P. A. Sedach, C. P. Berlinguette, *Inorg. Chem.* **2009**, *48*, 9631.

[22] D. L. Jameson, L. E. Guise, *Tetrahedron Lett.* **1991**, *32*, 1999.

[23] L. A. Barrios, C. Bartual-Murgui, E. Peyrecave-Lleixà, B. Le Guennic, S. J. Teat, O. Roubeau, G. Aromí, *Inorg. Chem.* **2016**, *55*, 4110.

[24] M. Bauer, *Phys. Chem. Chem. Phys.* **2014**, *16*, 13827.

[25] P. Glatzel, U. Bergmann, *Coord. Chem. Rev.* **2005**, *249*, 65.

[26] a) M. Agote-Arán, I. Lezcano-González, A. G. Greenaway, S. Hayama, S. Díaz-Moreno, A. B. Kroner, A. M. Beale, *Appl. Catal. A* **2019**, *570*, 283; b) P. Eisenberger, P. M. Platzman, H. Winick, *Phys. Rev. Lett.* **1976**, *36*, 623; c) O. V. Safonova, M. Tromp, J. A. van Bokhoven, F. M. F. de Groot, J. Evans, P. Glatzel, *J. Phys. Chem. B* **2006**, *110*, 16162; d) A. J. Atkins, M. Bauer, C. R. Jacob, *Phys. Chem. Chem. Phys.* **2015**, *17*, 13937.

[27] a) M. U. Delgado-Jaime, S. DeBeer, M. Bauer, *Chem. Eur. J.* **2013**, *19*, 15888; b) A. J. Atkins, M. Bauer, C. R. Jacob, *Phys. Chem. Chem. Phys.* **2013**, *15*, 8095; c) K. M. Lancaster, K. D. Finkelstein, S. DeBeer, *Inorg. Chem.* **2011**, *50*, 6767; d) B. Lassalle-Kaiser, T. T. Boron, V. Krewald, J. Kern, M. A. Beckwith, M. U. Delgado-Jaime, H. Schroeder, R. Alonso-Mori, D. Nordlund, T.-C. Wenig, D. Sokaras, F. Neese, U. Bergmann, V. K. Yachandra, S. DeBeer, V. L. Pecoraro, J. Yano, *Inorg. Chem.* **2013**, *52*, 12915; e) C. J. Pollock, S. DeBeer, *J. Am. Chem. Soc.* **2011**, *133*, 5594.

[28] S. H. Wadman, M. Lutz, D. M. Tooke, A. L. Spek, F. Hartl, R. W. A. Havenith, G. P. M. van Klink, G. van Koten, *Inorg. Chem.* **2009**, *48*, 1887.

[29] C. Kreitner, K. Heinze, *Dalton Trans.* **2016**, *45*, 13631.

[30] A. V. Marenich, C. J. Cramer, D. G. Truhlar, *J. Phys. Chem. B* **2009**, *113*, 6378.

[31] I. M. Dixon, S. Khan, F. Alary, M. Boggio-Pasqua, J.-L. Heully, *Dalton Trans.* **2014**, *43*, 15898.

[32] T. C. Motley, L. Troian-Gautier, M. K. Brennaman, G. J. Meyer, *Inorg. Chem.* **2017**, *56*, 13579.

[33] P. Zimmer, L. Burkhardt, R. Schepper, K. Zheng, D. Gosztola, A. Neuba, U. Flörke, C. Wölper, R. Schoch, W. Gawelda, S. E. Canton, M. Bauer, *Eur. J. Inorg. Chem.* **2018**, *48*, 5203.

[34] Y. Liu, T. Harlang, S. E. Canton, P. Chábera, K. Suárez-Alcántara, A. Fleckhaus, D. A. Vithanage, E. Göransson, A. Corani, R. Lomoth, V. Sundström, Kenneth Wärnmark, *Chem. Commun.* **2013**, *49*, 6412.

[35] A. M. Brown, C. E. McCusker, J. K. McCusker, *Dalton Trans.* **2014**, *43*, 17635.

[36] W. Gawelda, A. Cannizzo, V.-T. Pham, F. van Mourik, C. Bressler, M. Chergui, *J. Am. Chem. Soc.* **2007**, *129*, 8199.

[37] T. Duchanois, T. Etienne, C. Cebrián, L. Liu, A. Monari, M. Beley, X. Assfeld, S. Haacke, P. C. Gros, *Eur. J. Inorg. Chem.* **2015**, *14*, 2469.

[38] J. E. Monat, J. K. McCusker, *J. Am. Chem. Soc.* **2000**, *122*, 4092.

Manuscript received: May 29, 2019

Accepted manuscript online: June 1, 2019

Version of record online: June 26, 2019

3.2.3. Biscyclometalated CNN-complexes

Based on the success with the monocyclometalated CNN-complex, synthesis of the biscyclometalated CNN-complex [Fe(pbpy)$_2$] **7** was approached, utilizing the different C-H and C-X activation mechanisms discussed in Chapter 3.1. The experiments are presented in this chapter, even though the syntheses were not successful. During the experimental work, which lasted for 1.5 years and involved more than 100 experiments, much information about the underlying mechanisms was obtained.

The first discussed approach for cyclometalation utilizes the method of transmetalation. This method allows to transfer of organic ligands from one metal to another. In this case, organomercury Hgpbpy (**8a**), organolithium Lipbpy (**8b**) and organomagnesium Mgpbpy (**8c**) species were employed (Scheme 8).

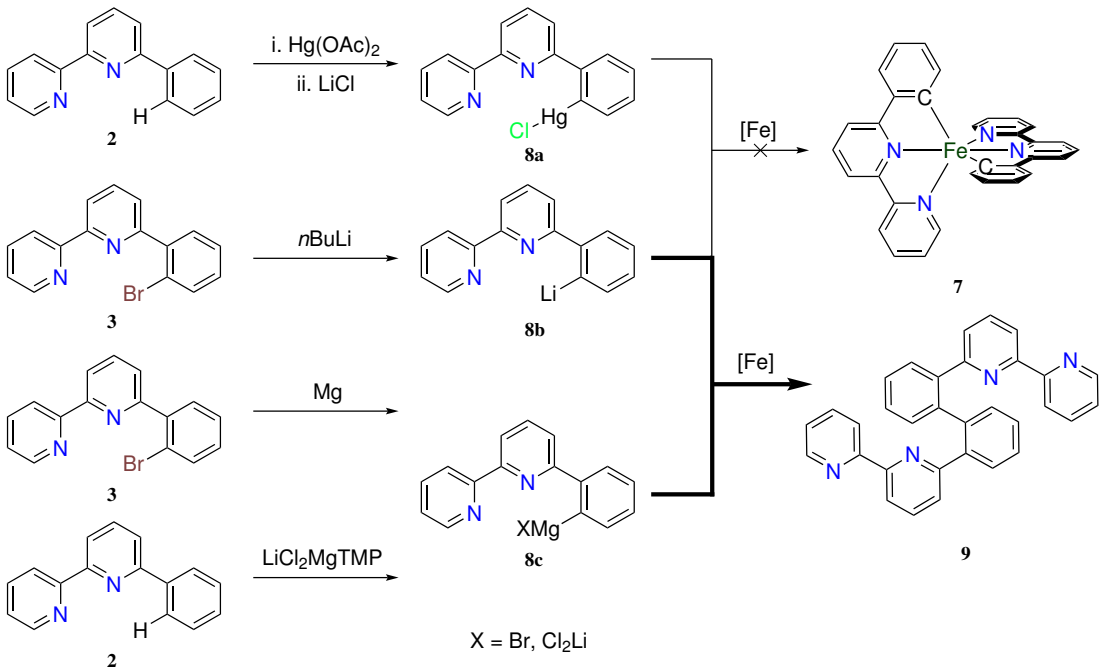

Scheme 8: Trials to synthesize the biscyclometalated complex **7** *via* the transmetalation route.

Although the usage of organomercury compounds is generally inadvisable due to their high toxicity,[72] they have a great history in transmetalation. Constable showed in 1987 that the ppy$^-$ ligand can be readily transferred from mercury onto ruthenium, iridium and palladium.[134] Based on this, organomercury reagents are still important in the synthesis of photoactive cyclometalated complexes, such as gold(III) compounds.[135] Recently, an NCN ligand, the anion of 1,3-dipyridylbenzene, was transferred from mercury onto iron,

resulting in an biscyclometalated NCN iron complex complex.[107] Hence, this approach was promising. Hgpbpy **8a** was obtained easily by the reaction of mercury acetate with **2** in ethanol and subsequent addition of lithium chloride in methanol, to exchange the remaining acetate group by a chlorido ligand. The compound was isolated with a yield of 26 %, but still suffered from impurities in the NMR. Most likely, these stem from the homoleptic [Hg(pbpy)$_2$]. The next step was the reaction with an iron precursor. The group around Le Lagadec used iron dodecacarbonyl in a mixture of hexane/toluene.[107] For the reaction of **8a** and $Fe_3(CO)_{12}$ only iron oxide was obtained after work-up. No transmetalation was also observed for the reaction with $Fe(CO)_5$, even under light irradiation. Reaction of **8a** with iron chloride resulted in an immediate color change of the reaction mixture, Nevertheless, the desired iron complex **7** was not isolated. Via mass spectrometry, the orange solid was identified as mainly ligand.

The next approach was the reaction of Lipbpy **8b** with an iron salt. Organolithium species are often used in transmetalation reactions. Utilizing an organolithium reagent, a five-coordinated biscylcometalated iron complex was obtained by the group of Ritter.[123] The organolithium species was formed *in situ* by reaction of bromophenylbipyridine **3** with *n*-butyllithium. It was directly reacted with the iron precursors $FeBr_2$ and $FeCl_2$. Even though no **7** was observed in ESI-MS, the reaction product of *n*-BuLi with the ligand, similar to the synthesis of phenylpyridine by arylation of pyridine,[136] was observed. Apart from this, the homocoupling product **9** of the ligand was observed as well. It is most likely coupled at the 2-phenyl positions, since also the mono- and bisbutylated variants of this compound are observed in ESI-MS. This hints towards an intermediate formation of a biscyclometalated iron species, followed by a reductive elimination, as has been found for iron catalyzed cross-coupling reactions.[137] Something similar has also been found for a bidentate approach of biscyclometalation. An analogous decomposition was observed by the group of Le Lagadec.[138] Using an organomercury species, they found a way to synthesize a biscyclometalated dicarbonyl iron complex. Under light irradiation, this compound decomposed to the carbonyl-bridged homocoupled ligand.

Another reaction leading to the homocoupling product may be a Wurtz-type coupling of **8b** and **3**, hence further studies of the reaction were conducted. This included the transmetalation reaction of an organomagnesium reagent. This was obtained by two different methods. The first aims at synthesis of the corresponding Grignard reagent by reacting **3** with magnesium shavings, following textbook knowledge.[139] The other method is based on the research of the Knochel group, utilizing the so called Turbo-Hauser base of tetramethylpiperidine (TMP), a mixed lithium magnesium amide. Their research showed that it can activate 2-phenylpyridine,[140] thus an activation of **2** should also be possible. Again, reaction of this organomagnesium reagent with iron bromide led to the formation of **9**,

as observed by ESI-MS measurements. No iron complexes were identified in the mass spectra. Hence, the formation of **9** and the inability to detect any iron compounds seems to be a mechanistic problem, originating from the instability of the intermediate species **7**. Parallel to the transmetalation reactions, the formation of **7** was attempted using C-H bond activations.

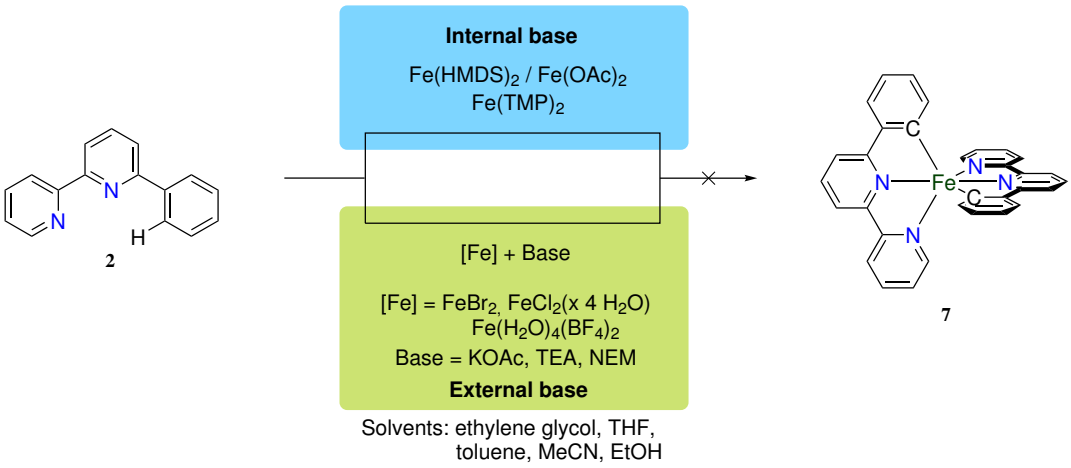

Scheme 9: Trials to synthesize biscyclometalated complex **7** using C-H activations with an internal base (top) and external base (bottom).

As described in Chapter 3.1, a basic coligand is commonly used in these reactions. In iridium and platinum precursors, a chlorido-ligand is sufficient,[50] but basic ligands like acetate are more common.[117] Hence, iron acetate is one example for iron precursors with an internal base function. Another iron precursor with an internal base function is FeHMDS ($[Fe(N(SiMe_3)_2)_2]$; HMDS = Hexamethyldisilazane, Bistrimethylsilylamide), a green, oily and pyrophoric substance.[141] Analogous to this, a TMP congener can be prepared from a mixture of iron chloride, lithium chloride and the $LiCl_2$MgTMP base. Since TMP is an even stronger base, an activation of aryls should be possible. Investigations from the Knochel group showed the ability to form aryl iron complexes from this precursor, if a directing group is present, proving the potential of this precursor.[142] The reaction with iron acetate was performed in dry and degassed ethylene glycol and was heated at 200 °C for 48 hours. Unfortunately, no product was obtained. Similar results were observed in different solvents such as acetonitrile and toluene. That is also the case for the other precursors, where the reaction was performed in THF. The reactions with $Fe(TMP)_2$ were also conducted with the electron withdrawing functionalized **2b** and **2c**. Reaction mixtures were charactzerized by a promising color change, yet no complexes were observed. In these cases, also no coupling products such as **9** were observed.

The use of a precursor with an internal base is not the only way to prepare cyclometalated complexes. Another possibility is to add a base like potassium acetate, triethylamine or *N*-ethylmorpholine to a metal source. Here, iron bromide, iron chloride (both water free and the tetrahydrate) and iron tetrafluoroborate hexahydrate were chosen as metal sources. The combination of different iron sources, bases and solvents was tested in screening reactions. Doing so, iron sources, solvents and bases were combined in vials, degassed and heated in an aluminium block, providing identical conditions during the experiments. Work up was also done parallel, resulting in fast results, even though they were negative in all cases. Similar to the reactions with an internal base, no coupling products were detected. Hence, typical C-H activation conditions known from cyclometalation reactions of 4d and 5d metals seem to be not transferable to iron.

Thus, the only reaction type leading to results so far was transmetalation. Consquently, the next step was the identification of factors leading to reductive elimination via careful substitution in the ligand backbone. For transmetalations, ususally the bromo-functionalized proligand is necessary. Hence, these ligands are hard to obtain due to the low commercial availability and synthetic inaccessibility of substituted phenyl and pyridine precursors with acetyl functions. These are needed, as cross-coupling of bromo- or iodo-substituted phenyl precursors is no viable approach due to side reactions and preferred coupling at these positions. Hence, another method for synthesizing these complexes had to be found. As previously discussed, another common approach for cyclometalation reactions is the σ-bond metathesis. Inspiration for this was found in the literature: Klein *et al.* started from the $[Fe(Me)_2(PMe_3)_4]$ complex, which reacted in different cyclometalation reactions, forming both mono- and biscyclometalated products.[143–145] As experience with the formation of monocyclometalated complexes has shown, PMe_3 can be difficult to exchange for polypyridines. Hence, a comparable synthesis was developed (Scheme 10). In the first step, 2 equivalents of a phenylbipyridine react in with an iron source, providing the intermediate complex **10a** coordinated by two bipyridine moieties and two halogens. In all cases, the reaction mixture had to be heated for a short period of time to produce the clear, intensely colored solution of **10a** in THF. Even though the intermediate product was not characterized, the consumption of all solids indicate the formation of a neutral complex, which is expected to be soluble in THF. At low temperatures, methyl lithium was added to the reaction mixture to form the dimethyl complex **10b**. This is analogous to $[Fe(Me)_2(PMe_3)_4]$, but with the supporting donor ligands in form of the bipyridines and the phenyl moieties combined. While the reaction mixture warms up slowly, development of methane gas ist expected due to deprotonation of the phenyl moieties, resulting in complex **7**.

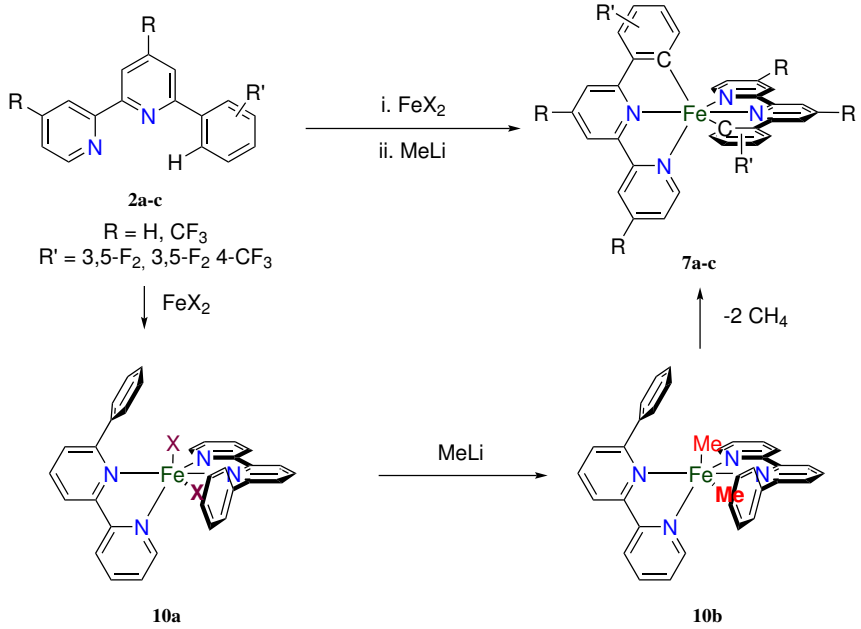

Scheme 10: Proposed reaction mechanism for the σ-metathesis synthesis route, leading to biscyclometalated complexes **7**.

To improve the stability of the resulting biscyclometalated complex, more electron withdrawing substituents were introduced into the ligand backbone, as shown in Scheme 7. These can help to supress reductive elimination and stabilize the iron(II) complex towards oxidation. First reactions using **2a** as starting material and iron bromide as iron source resulted in an air-sensitive violet material, which was handled in a glovebox. NMR spectra in acetonitrile showed many signals (Fig. 11), indicating a variety of species. Nevertheless, between 5.0 and 5.3 ppm signals are found which indicate a successful cyclometalation reaction. These result from the protons adjacent to the cyclometalated position, which are strongly shielded by the metal center and often found in this spectral region.[99,101–103,146] A doublet of doublets (dd) would be expected for this position, since this proton can couple with the neighboring fluorine and the proton next to it. A total of five dds are found in this region, suggesting five different cyclometalated ligands in different coordination environments in this mixture. Since two of those signals show the same integral, heteroleptic complexes with different cyclometalating environments can not be excluded. ^{19}F-NMR measurements support the assumption of many different complexes.

As the attempts of purifiying this mixture in a glovebox failed, an isolation and purification of the oxidized products was attempted. Upon contact with oxygen, the solution changed color from purple to orange immediately. After a few minutes, iron oxide precipitated and a yellow solution remained. This hints towards a instability of the respective iron(III) compound(s) towards reductive elimination. Even though this may seem counterintuitive, since this would result in iron(I) compounds, Chi *et al.* recently made similar

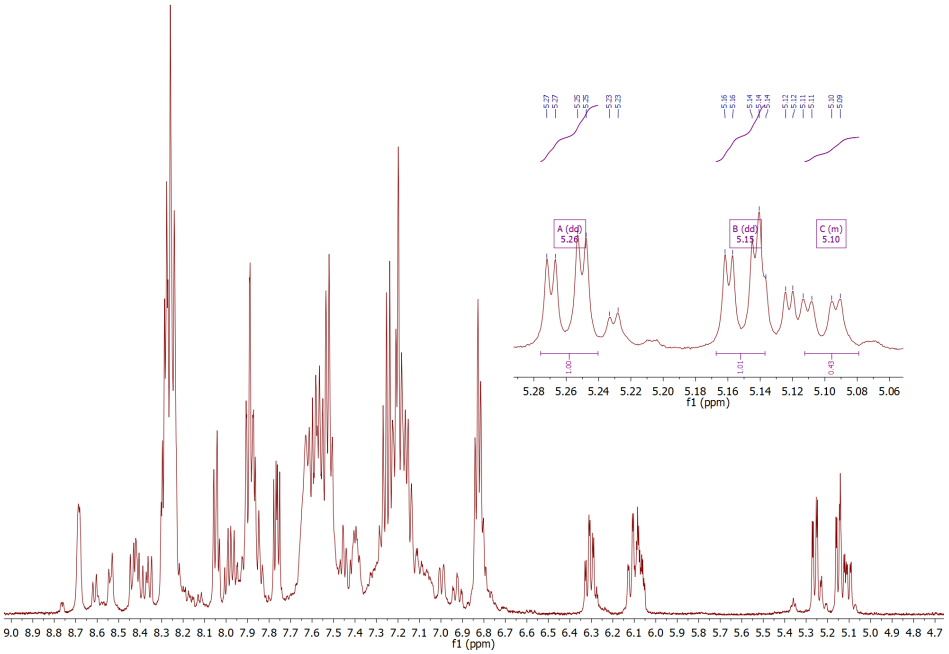

Figure 11: ^{1}H-NMR of the aromatic region of the crude product, obtained from σ-bond metathesis with proligand **2d**, with the typical region for protons adjacent to cyclometalating bonds enhanced.

observations for heteroleptic cyclometalated NHC complexes.[147]

In an attempt to enhance the stability towards oxygen and to avoid the reductive elimination, the more electron-deficient ligand **2b** was used. Methylation of **10a** was also achieved with methyl magnesium bromide, to examine wether the methyl source influences the formation of **7**. The violet reaction mixture was also unstable towards atmospheric conditions and decomposed quickly after turning yellow upon contact with oxygen. Residual solids were analyzed and identified as pure organic products (homocoupled ligands and a methylated ligand, respectively). The first has been observed in the transmetalation reaction, but not in the C-H activation reaction so far. Hence, the magnesium may contribute towards this behavior. Therefore, the alkylation reagent was changed back to methyl lithium. NMR analysis of the purple reaction indicated the formation of at least three complex species and organic products. These could not be removed by washing with an unpolar solvent such as pentane or hexane, since it also dissolved the purple complexes. Again, these decomposed under atmospheric conditions.

Therefore, the reaction with the most electron-poor ligand **2c** was attempted under the same conditions. This resulted in a purple solution, which stayed purple even under atmosphere and after addition of water. After a short workup of filtering and extraction, a dark residue was obtained. ^{1}H- and ^{19}F-NMR analysis suggests that a variety of different complex species is present (Fig. 12).

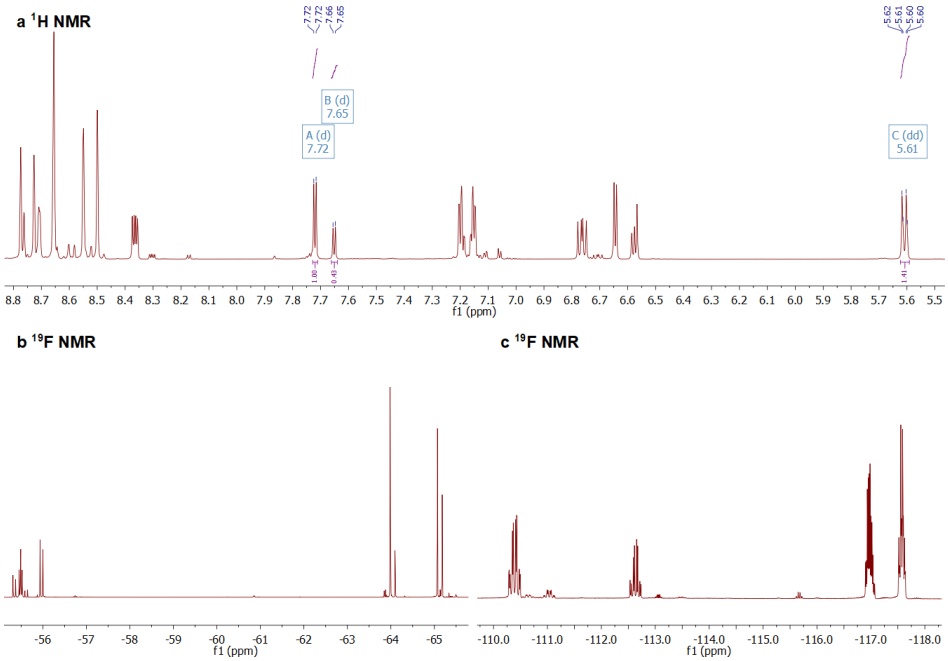

Figure 12: **a**: ^{1}H NMR spectrum in the aromatic region of the crude product in CD_3CN obtained in the synthesis of **7c**. **b**: ^{19}F NMR spectrum in the range of CF_3-groups, where the low field signals correspond to the CF_3-groups on the phenyl moiety and the high field signals to the bipyridine moiety. **c**: ^{19}F NMR spectrum of the fluoride region on the phenyl moieties.

In the ^{1}H-NMR, as depicted in Fig. 12 a, the three exemplary integrated peaks show that at least two species with protons adjacent to a carbon-iron bond are present. This is evident by comparing the integral of the protons next to the metal carbon bond at 5.61 ppm with the protons at 7.72 and 7.65 ppm, which add up to the same integral. Other signals yield the same integrals, indicating that two main species are present.

Investigations with mass spectrometry support this assumption, as many complexes were found with the exception of the desired **7c**. In Fig. 13 is shown how the substitution on the ligands had to change for the complexes to obtain these masses. It becomes apparent that at least one defluorination had to take place. In exchange for the fluorines, either one or two protons, or a methyl group has to be added.

Separation of the different complexes by crystallization proved to be inefficient, as the structural similarity caused the different products to crystallize under identical conditions. Column chromatography with a mixture of pentane and dichloromethane was attempted, but separation was insufficient. Solvent mixtures with decreased polarity like pentane diethylether 8:1 resulted in good separation of both compounds in thin-layer chromatography. Unfortunately, this strategy could not be transferred to column chromatography, where separation was also insufficient because the complexes showed a strong tailing on the column. Higher percentages of pentane resulted in a better separation; due to the long retention time, products decomposed on the column. Consequently, no clean prod-

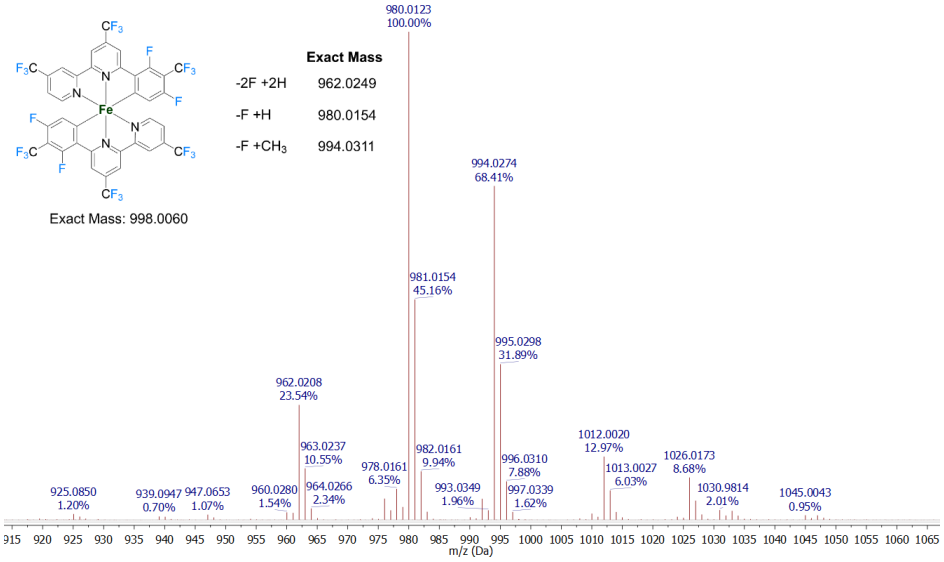

Figure 13: ESI-MS of the crude product obtained from the σ-bond metathesis reaction with proligand **2c**.

uct was obtained. However, the slow evaporation of the $CDCl_3$ solutions of the fractions after separation with pentane:ether (8:1) led to the formation of single crystals, from which two SXRD structures could be confirmed (Fig. 14), corresponding to the m/z of 962 (**11**) and 980 (**12**). The latter structure was of poor quality, but good enough to show a connectivity of the atoms and confirm the product.

The SXRD data supports the assumption that the ligand has been defluorinated during the reaction. The only viable mechanism, as fluorine-lithium exchange is not expected to happen, is an oxidative addition of the C-F-bond. Hence, a mechanism based on Scheme 10 is envisioned. Here, a dimethyl intermediate **10b** reductively eliminates ethane, forming a low-valent iron(0) center **10c** (Scheme 11). This can undergo oxidative addition with the C-F bond, resulting in a monocyclometalated fluorido complex **10d**. This can be transformed into the methyl complex **10e** with methyl lithium. Deprotonation of the aryl ring, via σ-bond metathesis, leads to **12**. The only reasonable explanation for the formation of **11** would involve the defluorination of **10e** with the elimination of CH_3F.

Unfortunately, the crystals could not be separated. Hence a photophysical characterization of these complexes could not be achieved. In an attempt to circumvent the formation of **10c**, a synthesis route using $LiCl_2MgTMP$ was explored. This did not lead to results, contrary to the attempts with the more electron-rich ligand. This may be explained by the mechanistic basis (Ch. 3.1), since this reaction step would follow either the agostic C-H-bond activation or the electrophilic substitution. These are slower and more effective in electron-rich ligands, while the σ-bond metathesis and oxidative addition reactions work better for electron-poor ligands like **2c**.

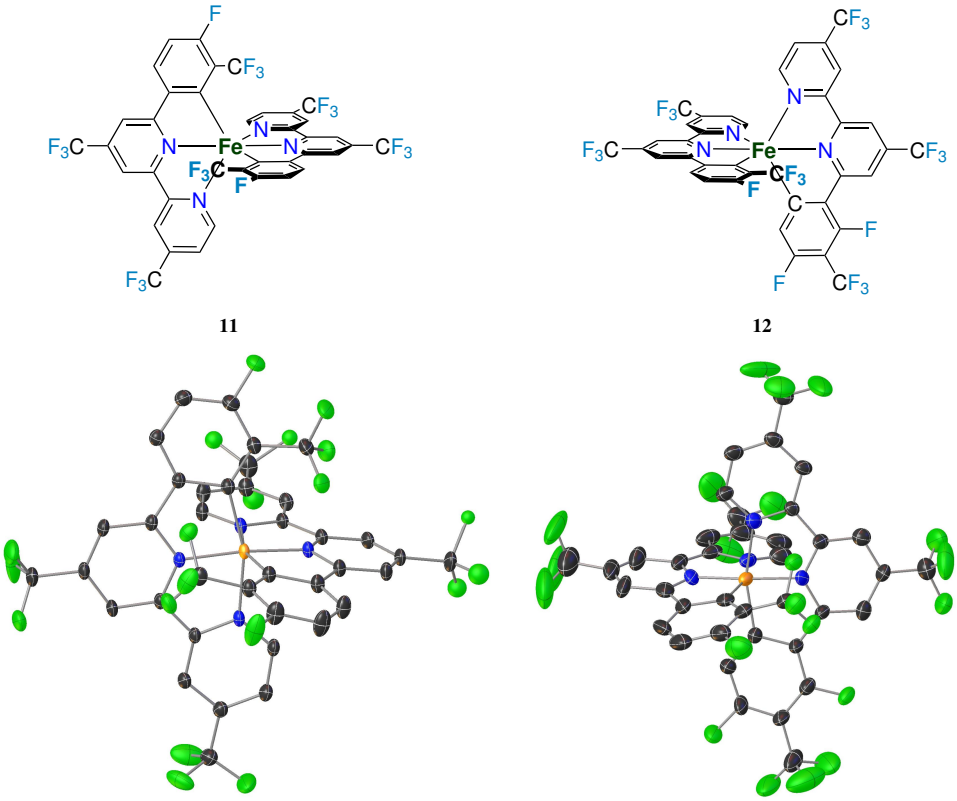

Figure 14: Top: Complexes **11** and **12**, identified by SXRD after the complex synthesis with ligand **2c**. Bottom: Crystal structures of complexes **11** and **12**, hydrogen atoms omitted for clarity. Due to the low quality, the structure of **12** can just be used to show the connectivity of the atoms.

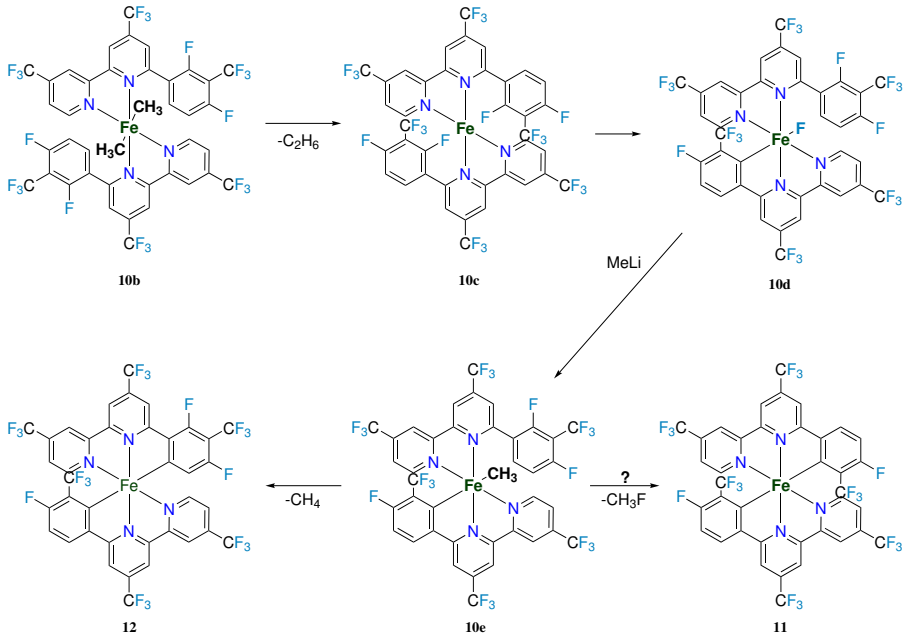

Scheme 11: Tentative reaction mechanism leading to **12**. The mechanism leading to **11** remains elusive.

Chapter Summary

In summary, no synthesis route for the controlled formation of biscyclometalated CNN complexes has been found, even though many attempts, based on transmetalation reactions and C-H-bond activations, were made. While the method of σ-bond metathesis led to the formation of cyclometalated complexes, reductive elimination of reaction intermediates gave rise to an uncontrollable variety of products. These are structurally very similar, making them demanding to separate. Thus, no photophysical investigation of the air-stable biscyclometalated iron(II) complexes was achieved.
As this project was unsuccessful, a different way to incorporate two cyclometalating functions was approached. For stabilization of the C-Fe binding motif, *N*-heterocyclic carbenes were incorporated as terminal ligand fragments, shifting the cyclometalating moieties to the central position of the ligand.

3.3. Complexes with CCC-Ligands

3.3.1. Ligand design

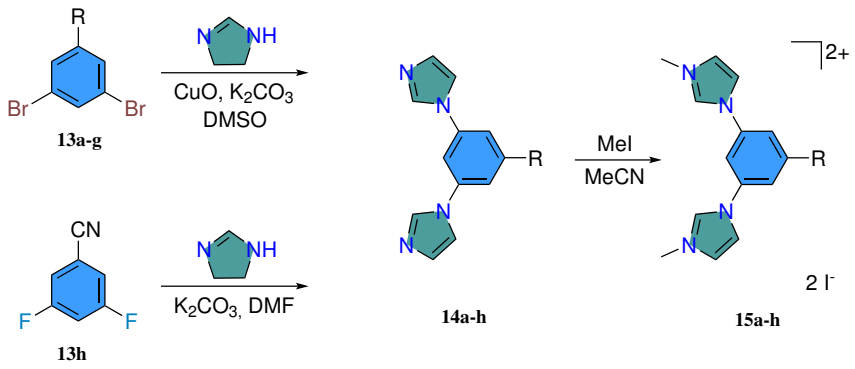

Scheme 12: Synthesis of CCC-proligands.

A key step in the synthesis of CCC complexes, in which NHCs and cyclometalated functions are combined, is a reliable way to obtain ligands with high functional group tolerance. This enables precise adjustments to the electronic structure by substitution in the ligand backbone. While CNC ligands with a central pyridine function can be easily obtained by S_NAr reactions,[92,94] this is not applicable to CCC-ligands. They have to be synthesized *via* C-N-coupling reactions. A typical example is the copper-catalyzed Ullman-type reaction, where copper species couple aryl halides with different nucleophiles, such as amines, alcohols and thiols. Thus, reaction of substituted dibromobenzenes **13a**–**g** with imidazole resulted in a variety of substituted bisimidazolebenzenes **14a**–**g**.[148]

Table 1: Yields for the synthesis of CCC-proligands.

	−R	Yield **14**	Yield **15**
a	−H	29 %	99 %
b	−Br	23 %	74 %
c	−Me	73 %	80 %
d	−tBu	50 %	62 %
e	−OMe	75 %	70 %
f	$-CF_3$	50 %	63 %
g	$-OCF_3$	36 %	92 %
h	−CN	77 %	70 %

In the case of **14h**, no copper catalyst is needed. It is accessible *via* nucleophilic substitution from **13h**, due to the strongly electron withdrawing nitrile functionality. The yields of the resulting compounds are listed in table 1. Typically, they range between 50 and 75 %, with the exception of the tribromobenzene, OCF_3-functionalized and unfunctionalized diboromobenzene.
The proligands **15a**–**h** are formed by methylation of the respective bisimidazoles mostly in typically high yields (Tab. (1)).

3.3.2. Janus-type emission from a cyclometalated iron(III) complex

In this chapter, the synthesis and characterization of the first iron(III) CCC-complex $[Fe(ImP^H)_2]^+$ ($HImP^H$ = 1,1'-(1,3-phenylene)bis(3-methyl-1-imidazol-2-ylidene)) **16a** in its ground and excited states is presented. It was synthesized based on methods developed by Hollis *et al.*[149,150] *via* ligand activation of **15a** with a zirconium reagent followed by transmetalation. Ground state characterization confirms that the complex is in a low-spin d^5 state, analogous to previously reported photoactive iron(III) complexes.[108,109] This compound differs from them in that it exhibits not only ^{2}LMCT emission, but also fluorescence originating from the fundamentally opposite ^{2}MLCT state. This unprecedented property in iron complexes is made possible by the ligand design. The energetically low π^* levels of the cyclometalating functions lead to accessible MLCT states that cannot relax into the energetically lower LMCT states. The lifetimes of both states have been determined by transient absorption spectroscopy, streak camera measurements, as well as time correlated single photon counting (TCSPC). The LMCT state has a lifetime of 0.2 ns lifetime and the MLCT state a lifetime of 4.6 ns. The excited state landscape has been studied with (TD)DFT calculations, showing potential trapping of the MLCT states. Quenching experiments confirm the reactivity of the MLCT state, which can act as a strong photoreductant and -oxidant. Thus, this complex shows promising results for establishing a class of photoactive iron complexes.

Janus-type emission from a cyclometalated iron(III) complex

Contributing authors:

Jakob Steube: Design and synthesis of the title molecule, chemical characterization (NMR, MS, IR), cyclic voltammetry, UV-Vis and fluorescence spectroscopy, TCPSPC, interpretation of the data, wrote the manuscript.

Ayla Kruse, Miguel A. Argüello Cordero, Prof. Dr. Stefan Lochbrunner: Transient absorption and streak camera measurements, interpretation of TCSPC data, quenching experiments.

Dr. Olga S. Bokareva, Prof. Dr. Oliver Kühn: (TD)DFT calculations.

Thomas Reuter, Prof. Dr. Katja Heinze: Spectroelectrochemical measurements, variable-temperature emission spectroscopy.

Athul Krishna: Synthesis of the cobalt complex analogous to the title molecule, its chemical characterization (NMR, MS) and the corresponding UV-Vis spectra.

Dr. Roland Schoch, Ass.-Prof. Dr. Stephan Hohloch: Single-crystal X-ray diffraction.

Dr. Serhiy Demeshko, Prof. Dr. Franc Meyer: SQUID and Mößbauer measurements.

Prof. Dr. Matthias Bauer: Conceivement and planning of the research, contribution to the design of the title molecule, wrote the manuscript, corresponding author.

Supplementary Information for this publication is found in the Appendix in Ch. C.2.

nature chemistry

Article

https://doi.org/10.1038/s41557-023-01137-w

Janus-type emission from a cyclometalated iron(III) complex

Received: 24 October 2021

Accepted: 19 January 2023

Published online: 27 February 2023

Check for updates

Jakob Steube[1,2], Ayla Kruse[3,4], Olga S. Bokareva[4,5], Thomas Reuter[6], Serhiy Demeshko[7], Roland Schoch[1,2], Miguel A. Argüello Cordero[3,4], Athul Krishna[1,2], Stephan Hohloch[8], Franc Meyer[7], Katja Heinze[6], Oliver Kühn[3,4], Stefan Lochbrunner[3,4] & Matthias Bauer[1,2]

Although iron is a dream candidate to substitute noble metals in photoactive complexes, realization of emissive and photoactive iron compounds is demanding due to the fast deactivation of their charge-transfer states. Emissive iron compounds are scarce and dual emission has not been observed before. Here we report the Fe^{III} complex $[Fe(ImP)_2][PF_6]$ (HImP = 1,1′-(1,3-phenylene)bis(3-methyl-1-imidazol-2-ylidene)), showing a Janus-type dual emission from ligand-to-metal charge transfer (LMCT)- and metal-to-ligand charge transfer (MLCT)-dominated states. This behaviour is achieved by a ligand design that combines four *N*-heterocyclic carbenes with two cyclometalating aryl units. The low-lying π^* levels of the cyclometalating units lead to energetically accessible MLCT states that cannot evolve into LMCT states. With a lifetime of 4.6 ns, the strongly reducing and oxidizing MLCT-dominated state can initiate electron transfer reactions, which could constitute a basis for future applications of iron in photoredox catalysis.

The greatest challenge in the search for photoactive iron complexes is posed by the weak ligand field splitting of t_{2g}- and e_g*-based orbitals, which is smaller in 3*d* transition metal complexes compared with their 4*d* and 5*d* counterparts[1]. The low-energy metal-centred states act as dark excited-state traps, quenching potentially emissive metal-to-ligand charge-transfer (MLCT) or ligand-to-metal charge-transfer (LMCT) states. Consequently, short lifetimes are observed for charge-transfer states[2]. Attempts to invert the order of metal-centred and charge-transfer states focus on the destabilization of metal-centred levels by strong σ donors[3–5] or the stabilization of charge-transfer states by π acceptors[6–9]. In Fe^{II} complexes, these strategies typically lead to MLCT lifetimes in the picosecond range. Exceptionally long MLCT lifetimes could be obtained: (1) with six *N*-heterocyclic carbene (NHC) donor groups (τ = 0.5 ns)[10]; and (2) using the HOMO inversion concept[11] (τ = 2.7 ns)[12]. Only recently, one emissive mononuclear Fe^{II} complex was reported[13,14], while two emissive Fe^{III} complexes possessing six electron-donating carbene donor units have been reported so far[15,16]. The Fe^{III} congener of the Fe^{II} complex with an MLCT lifetime of 0.5 ns presented by Wärnmark et al.[15] exhibits fluorescence from a ^{2}LMCT state with a lifetime of ~100 ps. Rigid anionic tripodal carbenes achieve a ^{2}LMCT lifetime of 2 ns, with a quantum yield of 2% in aerated MeCN solution[16]. Due to the electron-rich nature of NHC ligands and the electron-poor nature of the d^5 electron configuration, MLCT emission could not yet be observed in emissive Fe^{III} complexes. Cyclometalating phenyl-containing ligands offer strong σ-donor but also π-donor properties. More importantly, they show lower-energy and thus more easily accessible π^* orbitals than NHC donors. Fe^{II} complexes with such ligand types were extensively studied in theoretical investigations by Jakubikova and Dixon[17–20]. These predictions were recently supported by experimental studies[14,21]. The Fe^{II} complex, derived from $[Fe(tpy)_2]^{2+}$ (tpy = 2,2′:6′,2″-terpyridine) by exchanging one tpy with a deprotonated phenylbipyridine, showed an extension of the MLCT lifetime by

[1]Institute of Inorganic Chemistry, Paderborn University, Paderborn, Germany. [2]Center for Sustainable Systems Design, Paderborn University, Paderborn, Germany. [3]Department of Life, Light and Matter, University of Rostock, Rostock, Germany. [4]Institute for Physics, University of Rostock, Rostock, Germany. [5]Institute of Physics, University of Kassel, Kassel, Germany. [6]Department of Chemistry, Johannes Gutenberg University, Mainz, Germany. [7]Institute of Inorganic Chemistry, University of Göttingen, Göttingen, Germany. [8]Institute of General, Inorganic and Theoretical Chemistry, University of Innsbruck, Innsbruck, Austria. e-mail: matthias.bauer@uni-paderborn.de

https://doi.org/10.1038/s41557-023-01137-w

a factor of five and a decrease of the metal-centred state lifetime, while cyclometalating phenylphenanthroline ligands deliver a luminescent Fe^{II} complex with a ^{3}MLCT lifetime of ~1 ns[14]. Here we demonstrate that cyclometalating ligands in combination with NHC donors coordinated to Fe^{III} enable dual emission—namely from ^{2}LMCT excited states and additionally from ^{2}MLCT excited states at higher energy, enabled by stabilization of the Fe^{IV} oxidation state and energetically accessible π^* orbitals, due to the unique ligand design.

Results and discussion

Ground-state characterization

The complex $[Fe(ImP)_2][PF_6]$ (HImP = 1,1′-(1,3-phenylene)bis(3-methyl-1-imidazol-2-ylidene)) **1** is obtained by transmetalation of the ligand ImP^- (Fig. 1a)[22–24], resulting in a blue air- and water-stable Fe^{III} complex as $[PF_6]^-$ salt after workup under atmospheric air. Chemical integrity and purity were confirmed by NMR spectroscopy (Supplementary Fig. 1), mass spectrometry (Supplementary Fig. 2) and elemental analysis.

In the crystal structure (Fig. 1b), the C_{NHC}–Fe–C_{NHC} bite angle of 155° is smaller than in terpyridine analogues[4] and leads to a more distorted octahedral geometry. The ligand-to-ligand dihedral angle is 86°. The doublet found in the Mössbauer spectrum of Fig. 1c with an isomer shift of −0.12 mm s^{-1} and a quadrupole splitting of 1.59 mm s^{-1} indicates an $S = ½$ configuration, corresponding to a d^5 low-spin complex. Low isomer shifts are common for iron complexes with multiple NHC donors[15,16] and the very low value for **1** can be explained by the short Fe–C bonds (1.98 Å for Fe–C_{NHC} and 1.94 Å for Fe–C_{CM}), which lead to a compressed 4*s* orbital and hence a higher 4*s* electron density at the iron nucleus[25]. Temperature-dependent magnetic susceptibility measurements (Supplementary Fig. 6) show the typical behaviour of a low-spin Fe^{III} compound with molar magnetic susceptibility and temperature product $\chi_M T$ values higher than the spin-only value (0.375 cm^3 mol^{-1} K versus 0.49–0.64 cm^3 mol^{-1} K in **1**) and the expected deviation from the Curie law due to non-quenched orbital momentum of the $^2T_2$ ground state.

The tremendous effect of cyclometalation on the electronic structure is revealed by cyclic voltammetry (Fig. 2a). A reversible $Fe^{II/III}$ redox wave is found at −1.16 V versus $FcH^{0/+}$. Compared with the value of 0.31 V for the analogous iron complex with two C^N^C ligands (2,6-bis(3-methyl-imidazole-1-ylidine)-pyridine), a cathodic shift of ~1.5 V is observed[26]. This corresponds to the behaviour of the $[Fe(tpy)_2]^{2+}/[Fe(pbpy)(tpy)]^+$ (Hpbpy = 6-phenyl-2,2′-bipyridine) pair with a cathodic shift of ~0.8 V[21]. A quasi-reversible wave at the anodic peak potential of $E_{p,a} = 0.08$ V assigned to the $Fe^{III/IV}$ couple is additionally detected. The irreversible wave at $E_{p,a} = 1.31$ V is attributed to ligand oxidation. An irreversible reduction of the ligand can be suspected at around −2.7 V, close to the solvent reduction (Supplementary Fig. 7).

The absorption spectrum of **1** (Fig. 2b) can be divided into three parts: the first at $\lambda > 450$ nm ($\lambda_{\varepsilon,max} = 585$ nm; $\varepsilon = 540$ M^{-1} cm^{-1}; red in Fig. 2b), the second at 300 nm $< \lambda < 450$ nm ($\lambda_{\varepsilon,max} = 351$ nm; $\varepsilon = 6{,}000$ M^{-1} cm^{-1}; blue in Fig. 2b) and the third at $\lambda < 300$ nm (purple in Fig. 2b). Time-dependent density functional theory (TDDFT) calculations with optimally tuned range-separated functionals suited for the description of charge-transfer states[27,28] reveal the nature of the underlying transitions (Fig. 2b,c). Previously, it had been shown that iron complexes with NHC ligands could be reasonably described by this method unless metal-centred transitions play an important role[29]. The low-energy part of the spectrum of **1** is of charge-transfer character by design, which justifies the use of TDDFT for the assignment of the absorption spectrum (Fig. 2b,c).

The low-energy part above 450 nm is dominated by LMCT transitions caused by transitions from the ligand π orbital involving both imidazole and phenyl donors to the singly occupied metal-centred d_π acceptor orbital. The transitions contain a small amount of ligand-centred character due to the covalency of the iron–phenyl bonds. The intermediate spectral range is dominated by MLCT transitions. Contributions of ligand-centred character cannot be neglected,

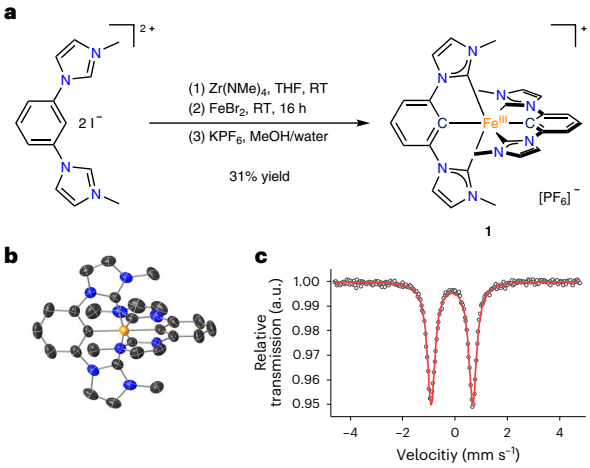

Fig. 1 | Synthesis, X-ray structure and Mössbauer spectrum of 1. a, Activation of the pro-ligand using a zirconium reagent with subsequent transmetalation onto iron. MeOH, methanol; RT, room temperature; THF, tetrahydrofuran. Due to the donor strength of the ligand, the Fe^{II} complex is oxidized under air to the Fe^{III} complex **1**. **b**, Structure of the cation of **1**, as determined by X-ray diffraction. Hydrogen atoms and counter ion are omitted for clarity. **c**, Mössbauer spectrum of **1** at 80 K showing the characteristic doublet of a low-spin Fe^{III} complex.

but predominant ligand-based transitions can be excluded since the analogous Co^{III} complex does not show transitions above 350 nm (Supplementary Fig. 8). In the MLCT band, transitions originate from singly and doubly occupied Fe^{III} *d* orbitals to the π^* orbitals of the ligand, which extend over the phenyl and NHC moieties. These transitions possess some ligand-centred character, which is more pronounced than in the LMCT transitions. This is again caused by covalent iron–phenyl bonds, leading to ligand contributions in the t_{2g}-based donor orbitals. The high-energy absorbance below 300 nm is finally dominated by ligand-centred transitions, with only minor contributions from ligand-to-ligand charge-transfer and MLCT states. For simplicity, we denote the low-, mid- and high-energy bands as LMCT, MLCT and ligand centred, respectively, and imply a mixed character with predominant contributions. The frontier orbitals are depicted in Supplementary Fig. 10 and the contributions of the metal and ligand fragments to the transitions are provided in Supplementary Fig. 12. The complementary spectra of the electrochemically generated singly reduced and oxidized species $\mathbf{1}^-$ and $\mathbf{1}^+$ are shown in Supplementary Fig. 13. According to DFT calculations on $\mathbf{1}^-$ and $\mathbf{1}^+$, these are essentially metal-centred redox processes, showing the mainly Fe^{II} and Fe^{IV} character of $\mathbf{1}^-$ and $\mathbf{1}^+$, respectively. These results indicate that iron-involved charge-transfer bands should be energetically lower than ligand-centred transitions. This assignment also agrees with the absence of low-energy charge-transfer transitions in the analogous Co^{III} complex (Supplementary Fig. 8).

Excited-state characterization

Excitation of **1** into the low-energy LMCT absorption band at 520 nm results in a broad emission mirroring the LMCT absorption band (Fig. 3a). In contrast, excitation into the high-energy absorption at 350 nm, which is dominated by MLCT contributions, results in two emission bands (Fig. 3a), leading to a visible sky-blue emission (Supplementary Fig. 14), which shows sensitivity towards oxygen (Supplementary Fig. 15). Such dual room temperature luminescence is a rare observation[30,31], particularly for first-row transition metal complexes, and has not been observed in iron complexes. Several experimental observations provide evidence for the dual emission coming from two different emissive states in a single complex and thus violating Kasha's

https://doi.org/10.1038/s41557-023-01137-w

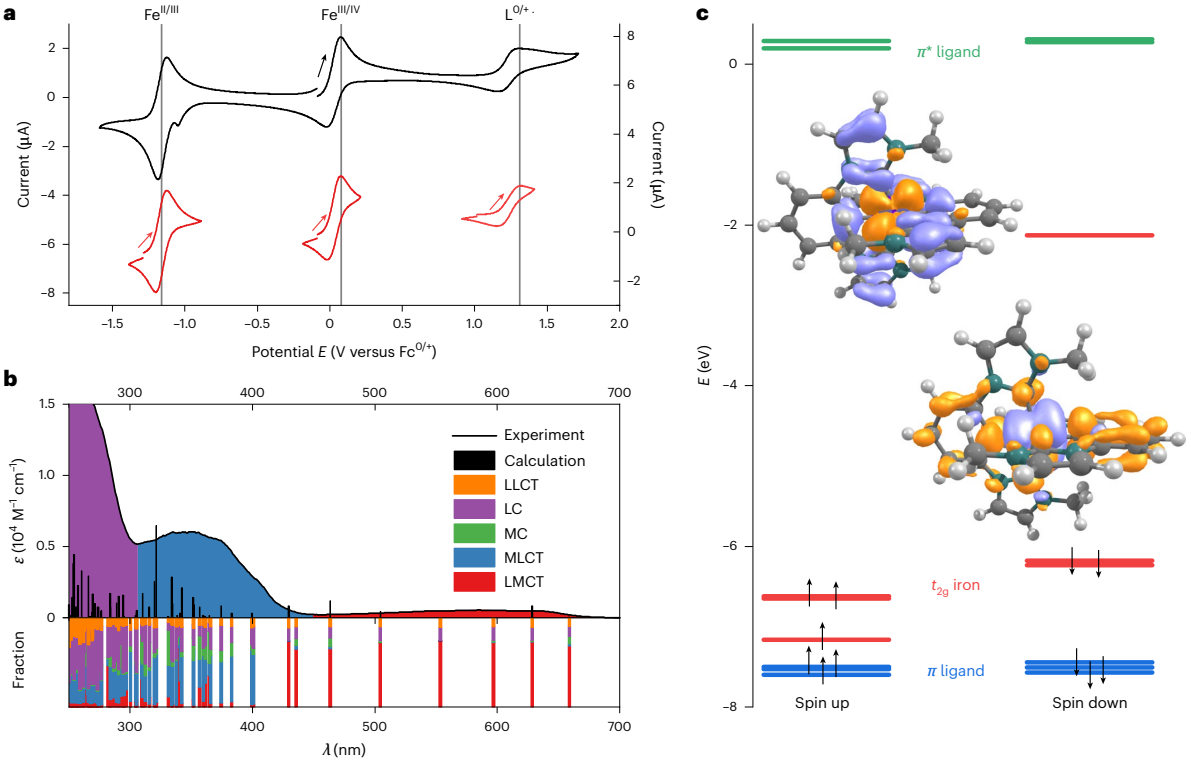

Fig. 2 | Electrochemical, optical and electronic properties of 1. a, Cyclic voltammogram of **1** (10^{-3} M) in MeCN with 0.1 M [nBu$_4$N][PF$_6$] as the electrolyte at a scan rate of 100 mV s^{-1}. Left y axis, whole voltammogram; right y axis, individual voltammograms. **b**, Ultraviolet–visible spectrum of **1** in MeCN (10^{-4} M) with TDDFT-calculated transitions and contributions from ligand-to-ligand charge-transfer (LLCT), ligand-centred π–π^* (LC), metal-centred (MC), LMCT and MLCT states. **c**, Molecular orbital scheme showing the highest occupied orbitals (t_{2g} orbitals (red) and ligand-based orbitals (blue)) and the lowest unoccupied orbitals (π^* orbitals of the ligand moiety (green)). The transition densities of the dominant LMCT (left) and MLCT (right) transitions are also depicted (hole, purple; electron, orange).

rule[32]. The high-energy emission at λ_{max} = 430 nm and the broad band emission at λ_{max} = 735 nm reflect the corresponding absorption bands at 351 and 585 nm, respectively. The excitation spectra (Fig. 3a) recorded with λ_{em} = 450 and 735 nm match the absorption spectrum, proving that the observed dual photoluminescence indeed originates from complex **1**. The two-dimensional excitation–emission plot is shown in Supplementary Fig. 16. In agreement with the two-colour absorption composed of the two main bands at 351 and 585 nm, the high-energy emission vanishes with decreasing excitation energy.

Independent of the exact nature of the emissive states, this dual emission represents a milestone in the fields of photoactive complexes of Earth-abundant elements for which luminescence is rarely observed[33]. Following the discussion on the nature of the states contributing to the absorption bands and the shape of the emission bands, it is justified to assign the low-energy luminescence to a predominantly LMCT emissive state, while the high-energy emission originates from MLCT-dominated states for which ligand contributions cannot be fully neglected. Considering the major MLCT and LMCT contributions, the moderate Stokes shifts (80 nm/0.65 eV and 150 nm/0.43 eV, respectively, determined by the difference of the maxima in the respective broad bands) indicate ^{2}MLCT and ^{2}LMCT states as fluorescent states.

Excited-state dynamics

The excited-state dynamics and excited-state landscape of complex **1** are explored by ultrafast spectroscopy. The transient absorption spectra after excitation in the MLCT-dominated band at 330 nm and the decay-associated amplitude spectra (DAAS) of a global fit are shown in Fig. 3b. The DAAS are compared with the difference spectra of the reduced **1**$^-$ − **1** and oxidized **1**$^+$ − **1** species obtained by spectroelectrochemistry as rough models for LMCT and MLCT state spectral characteristics, neglecting the radical cation and radical anion character of the ligands in these excited states, respectively (full spectra are shown in Supplementary Fig. 13)[34]. The transient spectra (Fig. 3b, inset) are dominated by a strong excited-state absorption (ESA) below 550 nm, increasing in intensity until 400 nm. Towards the red, a second, weaker ESA band follows. Three time constants are obtained from the global fit: τ_1 = 236 ps ± 20 ps, τ_2 = 6 ± 1 ps and τ_3 = 0.5 ± 0.1 ps. The slowest component (τ_1) describes the general decay of the ESA features (Fig. 3b). The strong ESA band in the blue spectral region resembles the spectrum of the Fe^{II} species **1**$^-$ very well while oxidation of **1** to the Fe^{IV} complex **1**$^+$ results only in weak absorption changes around 400 nm and is consequently not responsible for the ESA band at 400 nm. Accordingly, this time constant is assigned to the ^{2}LMCT state with Fe^{II} character, which decays with a rate of 236 ps^{-1} back to the ground state. Interestingly, in the blue spectral region of the 0.5 ps component (τ_3), the DAAS is a negative mirror image of the LMCT DAAS. It therefore corresponds to a rise of the dominant blue ESA band in the DAAS of τ_1 and seems to reflect a population rise in the LMCT state. The DAAS of the intermediate decay component with a time constant of 6 ps (τ_2) exhibits an ESA band at 420 nm, resembling signatures of neither the Fe^{II} nor Fe^{IV} species. It might be caused by an electronic relaxation from higher-lying MLCT states. Transient absorption measurements applying pump pulses

https://doi.org/10.1038/s41557-023-01137-w

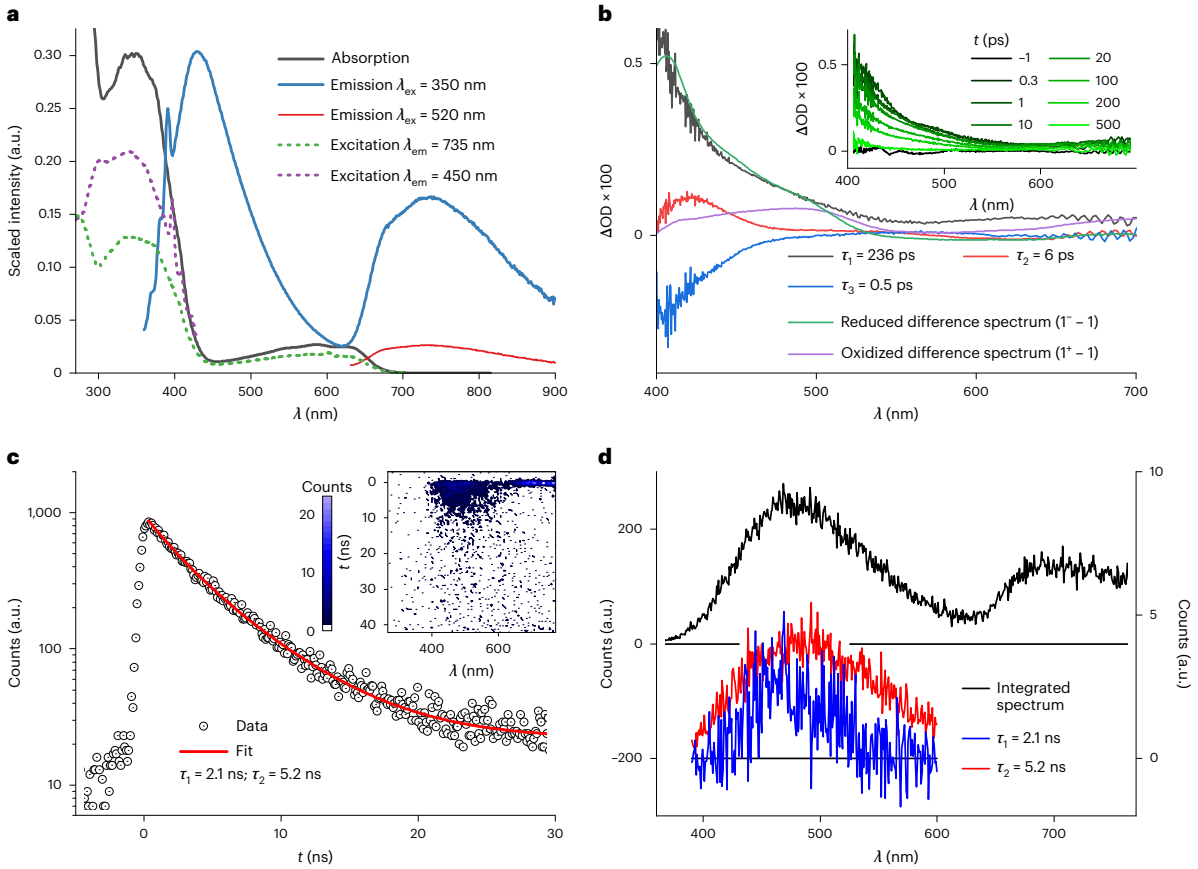

Fig. 3 | Excited-state spectroscopy and characterization of 1. a, Absorption and emission spectra of **1** at λ_{ex} = 350 and 520 nm. The excitation spectra measured at 735 and 450 nm are shown as dashed lines. **b**, DAAS with τ_1 = 236 ps, τ_2 = 6.1 ps and τ_3 = 0.5 ps, obtained from femtosecond transient absorption data after excitation at 330 nm and compared with the reduction and oxidation difference spectra obtained from spectroelectrochemical measurements as rough models for LMCT and MLCT excited states neglecting the radical cation and radical anion character of the ligands in these excited states. Inset, transient absorption spectra at the given delay times. ΔOD, change in the optical density. **c**, Decay of the fluorescence between 390 and 600 nm obtained from SCMs (inset) of a degassed solution of **1** in MeCN after 330 nm excitation, showing a double exponential decay with time constants of 2.1 ns (27.3%) and 5.2 ns (72.7%). **d**, Time-integrated spectrum obtained from SCMs with λ_{ex} = 330 nm (left y axis), showing a close resemblance with the fluorescence spectrum and the amplitude spectra of the 2.1 and 5.2 ns components (right y axis).

into the LMCT-dominated absorption band at 600 nm, as shown in Supplementary Fig. 18, reveal the same ESA bands observed at 330 nm excitation but a single exponential signal decay. The time constant is 240 ps, proving the assignment to a ^{2}LMCT state, which is directly optically excited here.

Streak camera measurements (SCMs) with excitation at 330 nm (time resolution = 50 ps) reveal a luminescence in the spectral region above 640 nm, reflecting the ^{2}LMCT emission (Fig. 3c). An additional signal in the spectral range 390–600 nm, which persists over a few nanoseconds, corresponds to the fluorescence above attributed to the ^{2}MLCT states. A time constant of 220 ps is found for the ^{2}LMCT emission, which is in excellent agreement with the transient absorption results. For the ^{2}MLCT state, two time constants of 2.1 and 5.2 ns are obtained with fractions of 27 and 73%, respectively. The spectrally integrated signal of the ^{2}MLCT emission and the corresponding fit are shown in Fig. 3d. Time-correlated single-photon counting (TCSPC) experiments support this result (Supplementary Fig. 19). However, the experimental error in the lifetime determination of the ^{2}MLCT luminescence is comparably high due to the low count rate per time bin. Amplitude spectra for the two decay components were extracted from the SCM data by a global fit, as shown in Fig. 3d. The two spectra are very similar, suggesting that the two emission components result from the same state. This similarity might indicate that the decay is non-exponential, and the double exponential fit is only an approximation, resulting in an averaged lifetime of 4.6 ns. Speculatively, this behaviour can be attributed to the flexibility of the ligands, which might cause a distribution of slightly different conformations[31,35]. The ^{2}MLCT decay is likely to be sensitive to conformational variations in the ensemble of complexes probed, since these variations should go along with subtle changes in the crossings between different electronic states.

The spectroscopic results can be summarized in the following scenario of the excited-state landscape of complex **1** (Fig. 4a). Optical excitation in the near ultraviolet addresses a high density of charge-transfer states. Branching of the electronic relaxation pathways occurs shortly after the excitation. The population majority is transferred within 0.5 ps to the lowest ^{2}LMCT state. This state is emissive but decays to the ground state primarily by internal conversion resulting in a lifetime of 240 ps. The weak absorption band at 600 nm (ε = 540 M^{-1} cm^{-1}), associated with the ^{2}LMCT state, shows that the corresponding transition dipole moment is small. In combination with the limited lifetime, a low

https://doi.org/10.1038/s41557-023-01137-w

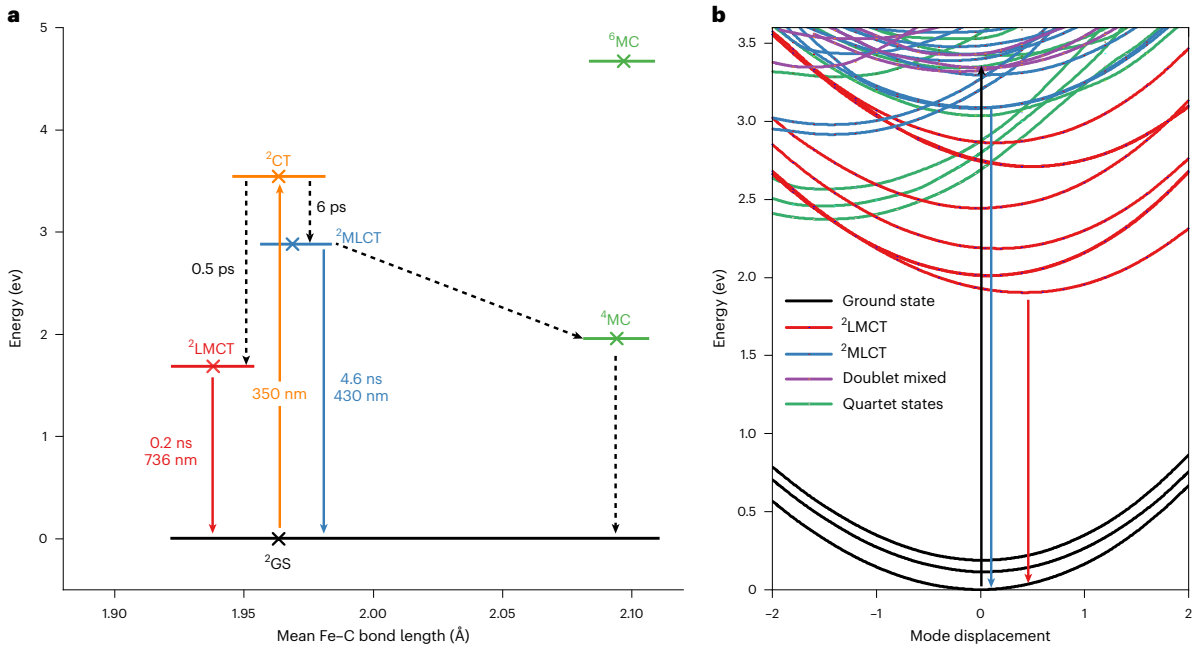

Fig. 4 | Summary of deactivation pathways and associated time scales of 1. a, Jablonski diagram based on the experimental results and calculated ground-state DFT energies of the optimized doublet, quartet and sextet states in their respective geometries (crosses). The ^{2}LMCT and ^{2}MLCT geometries are approximated from the calculated geometries of $\mathbf{1}^-$ and $\mathbf{1}^+$. The orange arrow indicates the excitation at 350 nm, the dotted arrows indicate non-radiative transitions, the blue arrow indicates the MLCT emission and the red arrow indicates the LMCT emission. GS, ground state; CT, charge transfer; MC, metal centred. **b**, TDDFT potential energy curves for displacement along with the a_1 symmetry vibrational mode (in D_{2d} symmetry), showing doublet LMCT, MLCT and mixed LMCT/ligand-centred states, as well as quartet metal-centred states. The black arrow indicates the excitation at 350 nm, the blue arrow indicates the MLCT emission and the red arrow indicates the LMCT emission.

quantum yield of <1% results. A minor fraction of the excited population evolves to the lowest ^{2}MLCT state. The 6 ps component in the transient absorption measurements can be a signature of this relaxation. The ^{2}MLCT state exhibits a lifetime of 4.6 ns and relaxes non-radiatively as well as radiatively back to the ground state, resulting in the weak but observable MLCT emission in the blue spectral region.

To rationalize the behaviour after photoexcitation, quantum chemical TDDFT calculations of potential energy curves, Huang–Rhys factors and non-adiabatic couplings were performed. The results indicate that a description of the dynamics by a simple few-state scheme, which follows from the results of TCSPC measurements and SCMs, might be an oversimplification. This consideration, together with the limited accuracy of the TDDFT method, provides a considerable bottleneck for quantitative theoretical analysis. Hence, only a qualitative picture can be drawn with the help of the potential energy curves along the symmetric mode having the strongest Huang–Rhys factor in the given energy range shown in Fig. 4b. Excitation at 350 nm targets a dense population of different doublet charge-transfer states. The many state crossings facilitate a one-electron branching into both LMCT and MLCT states. The lower-lying ^{2}LMCT states are populated by a fast 0.5 ps relaxation pathway. Although quartet states (^{4}MC) would, in terms of state crossings, qualify for participating in this relaxation channel, no support for the involvement of higher spin states has been found in this or other cases of luminescent d^5 systems[15,16,36]. The second pathway leading to an emissive ^{2}MLCT state would require transient structural and electronic stabilization. A possible candidate for such a state has been tentatively assigned in Fig. 4. Here, already rather small energetic corrections to the potential curves beyond TDDFT could increase the barrier due to the crossing curves so as to provide a transient trapping of the population.

Excited-state reactivity

In addition to the unique property of dual luminescence, which opens up exciting opportunities for optical applications with Earth-abundant metals, such as ratiometric O_2 sensing[37], the high MLCT energy and long lifetime also offer the chance for photocatalytic reactions initiated by complex **1** as a photosensitizer complementing the carbene-only ^{2}LMCT sensitizer[38,39]. A first estimation of the reactivity is possible by means of excited-state potentials, which can be extracted from the electrochemical potentials and E_{0-0} values[40]. These were determined to be $E_{0\text{-}0,1}$ = 1.9 eV for the low-energy LMCT emission and $E_{0\text{-}0,2}$ = 3.1 eV for the high-energy MLCT emission. This results in excited-state redox potentials of E^0_1(III*/II) = 0.74 V and E^0_1(IV/III*) = −1.82 V versus FcH (1.12 V and −1.44 V versus the saturated calomel electrode) for the LMCT excited state and E^0_2(III*/II) = 1.94 V and E^0_2(IV/III*) = −3.02 V versus FcH (2.32 V and −2.64 V versus the saturated calomel electrode) for the MLCT excited state. According to these values, its excited LMCT state oxidation potential is similar to that of $[Ru(bpy)_3]^{2+}$ while its excited LMCT state reduction potential exceeds that of $[Ru(bpy)_3]^{2+}$ (ref. [41]). Reduction reactions should thus be facilitated from a thermodynamic point of view. However, LMCT reactivity is kinetically disfavoured due to the sub-nanosecond lifetime. In contrast, the high-energy MLCT state combines both strongly reducing and oxidizing excited-state potentials and a nanosecond lifetime. MLCT-sensitized bimolecular reactions should thus be possible. This type of reactivity was investigated in quenching experiments using SCMs (Supplementary Fig. 20). Oxidative quenching was investigated with an excess of triethanolamine (1.0 M; E_{ox} = 0.46 V versus Fc)[42], showing a reduction of the MLCT lifetime from 4.6 to 0.7 ns. An analogous result was obtained for triethylamine (2.3 M; E_{ox} = 0.62 V)[43], where the MLCT lifetime was also reduced to 0.7 ns.

These results agree with the excited-state potentials of **1*** calculated above. Reductive quenching was investigated using benzonitrile (1.6 M; E_{red} = −2.76 V)[44]. Here, quenching could be observed as well, with a reduction of the MLCT lifetime to 1.0 ns. Further support for the reactivity of this state is given by the sensitization of $^1O_2$. Although no direct observation of $^1O_2$ emission was possible, a decrease of the fluorescence of 1,3-diphenylisobenzofuran (DPBF) under irradiation at 350 nm in the presence of **1** was observed as a probe for $^1O_2$ generation. This corresponds to the decomposition of DPBF, which is slower than in the presence of $[Ru(bpy)_3]^{2+}$, but faster than without added sensitizer (Supplementary Fig. 21).

In summary, coordination of a phenylene-bis-imidazolylidene ligand to an Fe^{III} centre yields an air- and water-stable cyclometalated complex that shows two-colour luminescence from MLCT- and LMCT-dominated states. Such a unique behaviour is enabled by the ligand design incorporating strong NHC and cyclometalating σ and π donors, leading to LMCT luminescence. The phenyl/NHC π^* orbitals and the stabilization of the Fe^{IV} oxidation state by NHCs/phenyl donors lead to a high-energy, yet accessible, MLCT state. Pure ligand-centred states are higher in energy. The ^{2}MLCT state does not evolve into the ^{2}LMCT state, probably due to the fundamental electronic differences of these states, namely Fe^{IV}/radical anion versus Fe^{II}/radical cation. While the ^{2}LMCT state has a considerable lifetime of 240 ps, the ^{2}MLCT state shows an even longer lifetime of 4.6 ns, which is the longest charge-transfer excited-state lifetime of iron complexes reported so far. Reductive and oxidative quenching experiments, as well as $^1O_2$ sensitization, confirm an excited-state reactivity of **1**. Based on the presented data, white light emitters and multifunctional photoredox catalysts based on Earth-abundant iron might become accessible.

Online content

Any methods, additional references, Nature Portfolio reporting summaries, source data, extended data, supplementary information, acknowledgements, peer review information; details of author contributions and competing interests; and statements of data and code availability are available at https://doi.org/10.1038/s41557-023-01137-w.

References

1. McCusker, J. K. Electronic structure in the transition metal block and its implications for light harvesting. *Science* **363**, 484–488 (2019).
2. Monat, J. E. & McCusker, J. K. Femtosecond excited-state dynamics of an iron(II) polypyridyl solar cell sensitizer model. *J. Am. Chem. Soc.* **122**, 4092–4097 (2000).
3. Liu, Y., Persson, P., Sundstrom, V. & Wärnmark, K. Fe *N*-heterocyclic carbene complexes as promising photosensitizers. *Acc. Chem. Res.* **49**, 1477–1485 (2016).
4. Zimmer, P. et al. The connection between NHC ligand count and photophysical properties in Fe(II) photosensitizers. An experimental study. *Inorg. Chem.* **57**, 360–373 (2018).
5. Zimmer, P. et al. Towards noble-metal-free dyads: ground and excited state tuning by a cobalt dimethylglyoxime motif connected to an iron *N*-heterocyclic carbene photosensitizer. *Eur. J. Inorg. Chem.* **2018**, 5203–5214 (2018).
6. Liu, L. et al. A new record excited state ^{3}MLCT lifetime for metalorganic iron(II) complexes. *Phys. Chem. Chem. Phys.* **18**, 12550–12556 (2016).
7. Darari, M. et al. Iron(II) complexes with diazinyl–NHC ligands: impact of π-deficiency of the azine core on photophysical properties. *Dalton Trans.* **48**, 10915–10926 (2019).
8. Jamula, L. L., Brown, A. M., Guo, D. & McCusker, J. K. Synthesis and characterization of a high-symmetry ferrous polypyridyl complex. Approaching the 5T2/3T1 crossing point for Fe(II). *Inorg. Chem.* **53**, 15–17 (2014).
9. Mengel, A. K. C. et al. A heteroleptic push–pull substituted iron(II) bis(tridentate) complex with low-energy charge-transfer states. *Chem. Eur. J.* **21**, 704–714 (2015).
10. Chabera, P. et al. Fe^{II} hexa *N*-heterocyclic carbene complex with a 528 ps metal-to-ligand charge-transfer excited-state lifetime. *J. Phys. Chem. Lett.* **9**, 459–463 (2018).
11. Mukherjee, S., Torres, D. E. & Jakubikova, E. HOMO inversion as a strategy for improving the light-absorption properties of Fe(II) chromophores. *Chem. Sci.* **8**, 8115–8126 (2017).
12. Braun, J. D. et al. Iron(II) coordination complexes with panchromatic absorption and nanosecond charge-transfer excited state lifetimes. *Nat. Chem.* **11**, 1144–1150 (2019).
13. Jiang, T. et al. Electronic structure and photophysics of a supermolecular iron complex having a long MLCT-state lifetime and panchromatic absorption. *Proc. Natl Acad. Sci. USA* **117**, 20430–20437 (2020).
14. Leis, W., Argüello Cordero, M. A., Lochbrunner, S., Schubert, H. & Berkefeld, A. A photoreactive iron(II) complex luminophore. *J. Am. Chem. Soc.* **144**, 1169–1173 (2022).
15. Chabera, P. et al. A low-spin Fe(III) complex with 100-ps ligand-to-metal charge transfer photoluminescence. *Nature* **543**, 695–699 (2017).
16. Kjær, K. S. et al. Luminescence and reactivity of a charge-transfer excited iron complex with nanosecond lifetime. *Science* **363**, 249–253 (2019).
17. Bowman, D. N., Bondarev, A., Mukherjee, S. & Jakubikova, E. Tuning the electronic structure of Fe(II) polypyridines via donor atom and ligand scaffold modifications. A computational study. *Inorg. Chem.* **54**, 8786–8793 (2015).
18. Mukherjee, S., Bowman, D. N. & Jakubikova, E. Cyclometalated Fe(II) complexes as sensitizers in dye-sensitized solar cells. *Inorg. Chem.* **54**, 560–569 (2015).
19. Dixon, I. M., Khan, S., Alary, F., Boggio-Pasqua, M. & Heully, J.-L. Probing the photophysical capability of mono and bis(cyclometallated) Fe(II) polypyridine complexes using inexpensive ground state DFT. *Dalton Trans.* **43**, 15898–15905 (2014).
20. Dixon, I. M., Alary, F., Boggio-Pasqua, M. & Heully, J.-L. Reversing the relative ^{3}MLCT–^{3}MC order in Fe(II) complexes using cyclometallating ligands: a computational study aiming at luminescent Fe(II) complexes. *Dalton Trans.* **44**, 13498–13503 (2015).
21. Steube, J. et al. Excited-state kinetics of an air-stable cyclometalated iron(II) complex. *Chem. Eur. J.* **25**, 11826–11830 (2019).
22. Reilly, S. W., Webster, C. E., Hollis, T. K. & Valle, H. U. Transmetallation from CCC–NHC pincer Zr complexes in the synthesis of air-stable CCC–NHC pincer Co(III) complexes and initial hydroboration trials. *Dalton Trans.* **45**, 2823–2828 (2016).
23. Hollis, T. K. & Webster, C. E. Unsymmetrical salts, CCC–NHC pincer metal complexes and methods of making the same. International patent WO 2018/175659 (2018).
24. Rubio, R. J. et al. Toward a general method for CCC *N*-heterocyclic carbene pincer synthesis: metallation and transmetallation strategies for concurrent activation of three C–H bonds. *J. Organomet. Chem.* **690**, 5353–5364 (2005).
25. Neese, F. Prediction and interpretation of the ^{57}Fe isomer shift in Mössbauer spectra by density functional theory. *Inorg. Chim. Acta* **337**, 181–192 (2002).
26. Liu, Y. et al. Towards longer-lived metal-to-ligand charge transfer states of iron(II) complexes: an *N*-heterocyclic carbene approach. *Chem. Comm.* **49**, 6412–6414 (2013).
27. Bokareva, O. S., Grell, G., Bokarev, S. I. & Kühn, O. Tuning range-separated density functional theory for photocatalytic water splitting systems. *J. Chem. Theory Comput.* **11**, 1700–1709 (2015).

28. Möhle, T., Bokareva, O. S., Grell, G., Kühn, O. & Bokarev, S. I. Tuned range-separated density functional theory and Dyson orbital formalism for photoelectron spectra. *J. Chem. Theory Comput.* **14**, 5870–5880 (2018).
29. Bokareva, O. S., Baig, O., Al-Marri, M. J., Kühn, O. & González, L. The effect of *N*-heterocyclic carbene units on the absorption spectra of Fe(II) complexes: a challenge for theory. *Phys. Chem. Chem. Phys.* **22**, 27605–27616 (2020).
30. Dorn, M. et al. A vanadium(III) complex with blue and NIR-II spin–flip luminescence in solution. *J. Am. Chem. Soc.* **142**, 7947–7955 (2020).
31. Herr, P., Kerzig, C., Larsen, C. B., Häussinger, D. & Wenger, O. S.Manganese(I) complexes with metal-to-ligand charge transfer luminescence and photoreactivity. *Nat. Chem.* **13**, 956–962 (2021).
32. Kasha, M. Characterization of electronic transitions in complex molecules. *Discuss. Faraday Soc.* **9**, 14–19 (1950).
33. Förster, C. & Heinze, K. Photophysics and photochemistry with Earth-abundant metals—fundamentals and concepts. *Chem. Soc. Rev.* **49**, 1057–1070 (2020).
34. Brown, A. M., McCusker, C. E. & McCusker, J. K. Spectroelectrochemical identification of charge-transfer excited states in transition metal-based polypyridyl complexes. *Dalton Trans.* **43**, 17635–17646 (2014).
35. Büldt, L. A., Guo, X., Vogel, R., Prescimone, A. & Wenger, O. S. A Tris(diisocyanide)chromium(0) complex is a luminescent analog of Fe(2,2′-bipyridine)$_3^{2+}$. *J. Am. Chem. Soc.* **139**, 985–992 (2017).
36. Chábera, P. et al. Photofunctionality of iron(III) *N*-heterocyclic carbenes and related d^5 transition metal complexes. *Coord. Chem. Rev.* **426**, 213517 (2021).
37. Wang, X. & Wolfbeis, O. S. Optical methods for sensing and imaging oxygen: materials, spectroscopies and applications. *Chem. Soc. Rev.* **43**, 3666–3761 (2014).
38. Aydogan, A. et al. Accessing photoredox transformations with an iron(III) photosensitizer and green light. *J. Am. Chem. Soc.* **143**, 15661–15673 (2021).
39. Rosemann, N. W. et al. Tracing the full bimolecular photocycle of iron(III)–carbene light harvesters in electron-donating solvents. *J. Am. Chem. Soc.* **142**, 8565–8569 (2020).
40. Rehm, D. & Weller, A. Kinetics of fluorescence quenching by electron and H-atom transfer. *Isr. J. Chem.* **8**, 259–271 (1970).
41. Prier, C. K., Rankic, D. A. & MacMillan, D. W. Visible light photoredox catalysis with transition metal complexes: applications in organic synthesis. *Chem. Rev.* **113**, 5322–5363 (2013).
42. Sun, H. & Hoffman, M. Z. Reductive quenching of the excited states of ruthenium(II) complexes containing 2,2′-bipyridine, 2,2′-bipyrazine, and 2,2′-bipyrimidine ligands. *J. Phys. Chem.* **98**, 11719–11726 (1994).
43. Wayner, D. D., Dannenberg, J. J. & Griller, D. Oxidation potentials of α-aminoalkyl radicals: bond dissociation energies for related radical cations. *Chem. Phys. Lett.* **131**, 189–191 (1986).
44. Li, K. et al. Air-stable blue phosphorescent tetradentate platinum(II) complexes as strong photo-reductant. *Angew. Chem. Int. Ed.* **57**, 14129–14133 (2018).

Methods

Synthesis

Dry tetrahydrofuran was obtained from an MBraun SPS-800 solvent-drying system and was subsequently stored over a 4 Å molecular sieve. ^{1}H NMR spectra were recorded using Bruker Avance 500 and Bruker Ascent 700 spectrometers. Chemical shifts were calibrated to the resonance of residual undeuterated solvent. Electrospray ionization mass spectrometry spectra were recorded with a Waters Synapt G2 Quadrupole Time-of-Flight spectrometer. Iron(II) bromide (99.8%) was purchased from Sigma–Aldrich and tetrakis(dimethylamino)zirconium was purchased from abcr. 1,1′-(1,3-phenylene)bis(3-methyl-1-imidazolium) diiodide was synthesized based on literature methods[45].

The synthesis of bis(2,6-bis(3-methylimidazol-1-ylidene) phenyl)iron(III) hexafluorophosphate ([Fe(ImP)$_2$][PF$_6$]) was based on a modified literature synthesis[22,23]. 1,1′-(1,3-phenylene) bis(3-methyl-1-imidazolium) diiodide (1,976 mg; 4 mmol) and tetrakis(dimethylamino)zirconium (1,124 mg; 4.2 mmol) were suspended in dry tetrahydrofuran (20 ml) in a glovebox. The yellow suspension was stirred for 2 h, then iron(II) bromide (432 mg; 2 mmol) was added. The mixture was stirred for another 16 h. The red/orange mixture was worked up under atmosphere. First, methanol (2 ml) was added. The now blue suspension was stirred under air for 1 h until no further precipitation of a pale solid was observed. The suspension was filtered through a cotton pad and through a porous glass frit. The respective filter cakes were washed with acetonitrile until the filtrate turned colourless. The solvent of the filtrate was evaporated using a rotary evaporator. The blue solid was dissolved in dichloromethane and filtered over a silica column. The column was washed thoroughly with dichloromethane. The blue band was then eluted from the column with acetonitrile. The solvent of the blue fraction was evaporated. The solid was dissolved in methanol (20 ml), and KPF_6 (2 equiv.; 736 mg; 4 mmol) was added. The desired compound **1** was precipitated by adding water (20 ml) and filtered off. It was redissolved in methanol (50 ml), treated again with KPF_6 (2 equiv.) and precipitated again with water (50 ml) to ensure a full exchange of the counterion. The suspension was filtered and the blue solid was dried under reduced pressure. It was then dissolved in a minimal amount of dichloromethane and pentane was allowed to diffuse into the solution. Dark blue long needles of **1** were obtained (415 mg; 0.61 mmol; 31%) after crystallization overnight, which were dried under reduced pressure (10^{-3} mbar) for 6 h before elemental analysis and spectroscopic measurements. The results of ^{1}H NMR (500 MHz; CD_3CN) were δ = 24.70 (4H), 9.68 (12H), 2.90 (4H), −2.39 (4H) and −35.79 ppm (2H). The electrospray ionization mass spectrometry results for [1-PF$_6$]$^+$ ($C_{28}H_{26}FeN_8$) were 530.1625 m/z (calculated) and 530.1621 m/z (found). Infrared (attenuated total reflection) analysis of **1** gave measurements of 3,166, 3,141, 2,926, 1,587, 1,470, 1,455, 1,405, 1,344, 1,263, 1,232, 1,075, 874, 824, 769, 714, 682, 555, 394, 354 and 258 cm^{-1}. Finally, elemental analysis of **1** ($C_{28}H_{26}F_6FeN_8P$) gave calculated and found values of 49.80 and 49.76% (C), 3.88 and 4.25% (H) and 16.59 and 16.30% (N), respectively.

The synthesis of [Co(ImP)$_2$][PF$_6$] (bis(2,6-bis(3-methylimidazol-1-ylidene)phenyl)cobalt(III) hexafluorophosphate) was analogous to the synthesis of [Fe(ImP)$_2$][PF$_6$] and was based on the same literature synthesis[22]. 1,1′-(1,3-phenylene)bis(3-methyl-1-imidazolium) diiodide (200 mg; 0.405 mmol) and tetrakis(dimethylamino)zirconium (100 mg; 0.445 mmol) were suspended in dry dichloromethane (10 ml) in a glovebox. The yellow suspension was stirred for 1 h, then cobalt(II) chloride (26 mg; 0.203 mmol) was added. The mixture was stirred for another 16 h. To quench the reaction, water (1 ml) was added. The suspension was filtered through a cotton pad and a porous glass frit. The respective filter cakes were washed with dichloromethane (10 ml) three times. The red solution was evaporated under reduced pressure. The solid (84 mg; 0.126 mmol) was dissolved in methanol (5 ml), and KPF_6 (6 equiv.; 140 mg; 0.75 mmol) was added. The compound was precipitated by the addition of water (20 ml) and filtered off. The process was repeated four times to ensure full exchange of the counterion. The suspension was filtered and the light-yellow solid was dried under reduced pressure. It was then dissolved in a minimal amount of acetone and allowed to crystallize under a normal atmosphere. Yellow crystals were obtained (60 mg; 0.0879 mmol; 69% yield). The results of ^{1}H NMR (700 MHz; CD_3CN) were δ = 7.72 (d; J = 2.0 Hz; 2H), 7.47 – 7.37 (m; 3H), 6.75 (d; J = 2.0 Hz; 2H) and 2.52 ppm (s, 6H). The results of ^{13}C NMR (706 MHz; CD_3CN) were δ = 207.48, 186.44, 177.78, 149.36, 125.14, 118.31, 116.01, 108.12, 35.86, 30.89 and 1.32 ppm. Finally, elemental analysis of [Co(ImP)$_2$][PF$_6$] with one molecule of acetone ($C_{28}H_{26}F_6CoN_8P \times C_3H_6O$) gave calculated and found values of 50.55 and 50.49% (C), 4.38 and 4.32% (H) and 15.21 and 15.22% (N), respectively.

X-ray diffraction analysis and crystallographic data deposition

The single-crystal data were recorded using a Bruker SMART CCD area detector diffractometer equipped with a graphite monochromator. The measurements were carried out using Mo $K\alpha$ radiation (λ = 0.71073 Å) at T = 200(2) K, with the temperature variations of the last digit during the measurements in brackets, since at lower temperatures a phase transition occurred, which caused a vaguer diffraction pattern. The structure solution process was carried out following direct methods[46], and structure refinement was conducted using full-matrix least-squares refinement based on F^2 (ref. [46]). All non-H atoms were refined anisotropically. The hydrogen atom positions were derived based on geometry, except the hydrogens of methyl groups. These were located from the Fourier map using HFIX 137 by SHELX[46]. All hydrogen atoms were refined at idealized positions riding on the carbon atoms with isotropic displacement U_{iso}, which are in case of aromatic carbon atoms 1.2 fold larger than the corresponding displacement parameters of the carbon and in case of hydrogens of a methyl group 1.5 fold larger. The bond lengths of carbon and hydrogen were limited to a range of 0.93 to 0.96 Å. All CH_3 hydrogen atoms were allowed to rotate but not to tip. One dichloromethane solvent molecule could not be modelled during refinement and was treated using SQUEEZE from the Platon software package[47–49].

The single crystal of the complex $C_{28}H_{26}N_8FePF_6$ (molar mass M_r = 675.40 Da) was obtained in form of a purple block with the size 0.42 × 0.37 × 0.25 mm^3. The substance crystallizes in the monoclinic space group $P2_1/c$ with a multiplicity Z = 4 and the cell parameters a = 13.6367(12) Å, b = 8.7801(8) Å, c = 27.099(3) Å and the angle β = 96.285(2)°, resulting in a cell volume V = 3225.2(5) Å^3, a density D_c = 1.391 mg/mm^{-3}and a total number of electrons in the cell F(000) = 1,380; 28,802 reflections of the single crystal were recorded during the measurement to a maximum angle θ_{max}= 26.462°, whereby 6,622 reflections are independent. This leads to in internal error R_{int} = 0.0455 and the refinement converged to a final error R1 = 0.0571 (for all reflections I, which were more intense than two times the standard deviation of the reflexes σ(I)) and to wR2 = 0.1683 (referring to all obtained data). As a result, the maximum residual electron density (with 0.804 eÅ^3) is located 0.62 Å from the F-atom F123 and the minimum residual electron density (−0.578 eÅ^3) in a distance of 0.61 Å from F123.

Crystallographic data have been deposited in the Cambridge Crystallographic Data Centre (CCDC) database, assigned to the deposition number CCDC 2002774. Copies are available free of charge via www.ccdc.cam.ac.uk.

Mössbauer spectroscopy and magnetic susceptibility measurements

^{57}Fe Mössbauer spectra were recorded with a ^{57}Co source in an Rh matrix using an alternating constant acceleration WissEL Mössbauer spectrometer operated in transmission mode and equipped with a Janis closed-cycle helium cryostat. Isomer shifts are given relative to iron metal at ambient temperature. Simulation of the experimental data was performed with the Mfit program using Lorentzian line doublets (E. Bill, Max Planck Institute for Chemical Energy Conversion).

Temperature-dependent magnetic susceptibility measurements were carried out with a Quantum Design MPMS3 SQUID magnetometer in the range from 300 to 2.0 K at a magnetic field of 0.5 T. The powdered sample was contained in a polycarbonate capsule and fixed in a non-magnetic sample holder. Each raw data file for the measured magnetic moment was corrected for the diamagnetic contribution of the sample holder and the capsule. The molar susceptibility data were corrected for the diamagnetic contribution. The simulation of the magnetic data was carried out with the program julX (E. Bill, Max Planck Institute for Chemical Energy Conversion) by applying a fitting procedure to the spin Hamiltonian $\hat{\mathcal{H}} = g\mu_B\vec{B} \times \vec{S}$ for Zeeman splitting of the $S = ½$ spin ground state with Landé factor g, the Bohr magneton μ_B, the magnetic flux density B and the electron spin S.

Cyclic and square wave voltammetry

Dry acetonitrile was obtained by passing HPLC-grade acetonitrile (Fisher) over a column of MP Biomedicals MP Alumina N - Super I, which was activated in an oven at 150 °C for multiple days. The cyclic and square wave voltammetry measurements were performed at room temperature in 0.1 M [(nBu)$_4$N][PF$_6$] dry acetonitrile with an analyte concentration of 0.001 M under a solvent-saturated argon atmosphere. A three-electrode arrangement with a 1 mm Pt working electrode and a Pt wire counter electrode (both Metrohm) and an Ag/AgCl reference electrode (custom built) was used, with the PGSTAT101 potentiostat from Metrohm. Ferrocene was added after the measurements as an internal standard. All potentials were referenced against the FcH$^{0/+}$ couple. The voltammograms were analysed using the NOVA software (version 2.1.3). The diagnostic criteria for reversibility were based on those proposed by Nicholson[50,51] and the Randles–Sevcik[52,53] equation.

Absorption spectroscopy (steady state)

Acetonitrile of spectroscopic grade (SPECTRONORM VWR Acetonitrile) was used as the solvent for steady-state absorption spectroscopy.

Steady-state absorption spectra were recorded using solutions with concentrations of ~10^{-5}–10^{-4} M in quartz cuvettes (path length = 10 mm) using a Cary 50 or PerkinElmer Lamda 45 spectrometer.

Theoretical calculations

Quantum chemical calculations were performed at D_{2d} symmetry with DFT and linear response TDDFT using the optimally tuned long-range separation functional LC-BLYP together with a combined basis set: def2TZVP (Fe) and 6-311 G(d,p) (all other atoms). Tuning of the functional was done using the so-called delta self-consistent field method[54–56]. The details can be found in the work of Bokarev et al.[28]. The following parameters were obtained for the present complex: $\alpha = 0$ (that is, the percentage of the exact exchange in the short range) and 0.15 Bohr^{-1} (long-range separation parameter). Solvent effects (acetonitrile) were taken into account within the polarized continuum model approach[57]. Calculations were done with the G16 (ref. [58]) and Q-Chem 5.3 (ref. [59]) packages. Excited-state analysis was performed using the TheoDORE package[60]. Analysis of Huang–Rhys factors, tuning of the functional and generation of geometries along normal modes were done with in-house codes. Further information on the calculations can be found in the Supplementary Information.

Fragment-based excited-state analysis

To consider the localization of excitations involving ligand orbitals in a more precise way, excited-state analysis with the TheoDORE package was performed for the molecule split into five moieties: a central iron atom, two phenyl unities and two imidazole unities. All possible types of excitation were considered (see Supplementary Fig. 11). The resulting analysis is shown in Supplementary Fig. 12. As one can see, the excitations within the LMCT band are spread over the entire ligand, with a slightly dominant imidazole unity. In turn, the MLCT band also consists of the excitations to the entire ligand.

Spectroelectrochemistry

Ultraviolet/visible/near-infrared spectroelectrochemical experiments were performed using a BioLogic SP-50 voltammetric analyser and a Specac Omni-Cell liquid transmission cell with CaF_2 windows equipped with a Pt gauze working electrode, a Pt gauze counter electrode and an Ag wire as the pseudo reference electrode, melt-sealed in a polyethylene spacer (approximate path length = 1 mm) in CH_3CN containing 0.1 M [nBu$_4$N][PF$_6$][61].

Room temperature emission spectroscopy

For steady-state emission spectroscopy, acetonitrile of spectroscopic grade was used as the solvent.

Steady-state emission spectra were recorded in 10 mm quartz cuvettes on an Edinburgh Instruments FLS1000 spectrometer with single monochromators and a red-extended PMT-980 detector or a HORIBA Scientific FluoroMax-4 spectrofluorometer. The solutions for the measurements under argon were degassed using the freeze–pump–thaw technique.

For determination of the Stokes shift, the highest-intensity features of the respective absorption and emission bands were used. Nonetheless, excitation at lower energies, such as 410 and 630 nm, also led to the observation of the respective MLCT and LMCT emission bands.

Variable-temperature emission spectroscopy

Variable-temperature emission spectra were recorded on a Varian Cary Eclipse spectrometer. For low-temperature photoluminescence measurements, a solution of the complex in butyronitrile (refluxed over Na_2CO_3 and $KMnO_4$, distilled and stored over aluminium oxide) was filled into a quartz cuvette in an argon-filled glovebox and the cuvette was sealed and transferred to an Oxford cryostat (Oxford instruments OptistatDN). Measurements were conducted between 297 and 87 K.

Femtosecond transient absorption spectroscopy

Femtosecond transient absorption spectra were recorded using excitation wavelengths in three different optical regions and thereby somewhat different pump–probe setups. In all cases, they were based on regenerative Ti:sapphire laser systems operating at a frequency of 1 kHz and at a centre wavelength of either 775 nm (CPA 2001; Clark MXR) or 800 nm (Spitfire Pro; Spectra-Physics). For probing, a white light continuum generated by focusing a small fraction of the Ti:sapphire output into a CaF_2 crystal was used. Pump and probe beams were focused onto the sample to overlapping spots with diameters in the range of 200–400 µm for the pump and of 100 µm for the probe. The polarizations of the pump and probe pulses were set to the magic angle with respect to each other. After the sample, the probe was dispersed by a prism and transient absorption changes were spectrally resolved and recorded by an array detector.

For pumping the sample with an excitation wavelength of 400 nm, the output of the Ti:sapphire system (Spitfire Pro) was frequency doubled using a beta barium borate (BBO) crystal. The resulting time resolution was ~150 fs.

To obtain ultrashort excitation pulses in the visible range with a centre wavelength of 600 nm, a non-collinear optical parametric amplifier (NOPA) pumped by the Ti:sapphire system (CPA 2001) was applied. The dispersion of the NOPA pulses was minimized by a compressor based on fused silica prisms, resulting in an overall time resolution of better than 100 fs.

For excitation in the ultraviolet range (that is, at a centre wavelength of 330 nm), the NOPA was tuned to 660 nm and its output was frequency doubled by a 100-µm-thick BBO crystal cut for type I phase matching.

For all measurements, the iron complex was dissolved in acetonitrile under argon and the sample solution was filled into a fused silica cuvette with a thickness of 1 mm.

The obtained data were fitted using a global fit. In the global fit, the multi-exponential model function $F(\lambda,t)=\sum_{i}^{N}\mathrm{DAAS}_i(\lambda)\times\exp(-t/\tau_i)$, convoluted with the temporal response of the pump–probe setup, was fitted to the complete set of time-dependent transient absorption spectra, yielding the decay associated amplitude spectra DAAS_i and the associated time constants τ_i. In the present case, three exponential decay components were necessary to reproduce the data with satisfying accuracy (that is, $N=3$).

SCMs

To investigate the time-resolved luminescence, a streak camera (Streakscope C10627; Hamamatsu Photonics) was applied. The samples were prepared and measured under argon in 1 cm cuvettes. For excitation at 388 nm, ultrashort laser pulses generated by frequency doubling the output of a Ti:sapphire laser system (CPA 2001; Clark MXR) were used. For excitation at 330 nm, a NOPA was set to a centre wavelength of 660 nm and its output pulses were frequency doubled using a BBO crystal. To ensure that only radiation at 330 nm reached the sample, a fused silica prism was applied to separate the ultraviolet pulses from the fundamental.

The luminescence lifetimes were determined by fitting a mono-exponential decay to the data in the spectral region 640–840 nm and a double exponential decay to the data of the region 390–600 nm.

Averaged lifetimes τ_{av} were obtained using:

$$\tau_{av}=\frac{A_1\times\tau_1+A_2\times\tau_2}{A_1+A_2}$$

With A_1 and A_2 being the integrals and τ_1 and τ_2 being the lifetimes of the respective amplitude spectra.

TCSPC and time-resolved emission spectroscopy

Time-resolved emission spectroscopy (TRES) was employed through TCSPC using a HORIBA Ultima 01-DD (HORIBA Jobin Yvon). The degassed sample solution was excited at 374 nm using a HORIBA DD375L laser diode with a maximum repetition rate of 100 MH. The emission was recorded in 5-nm steps between 440 and 520 nm in reverse mode with a slit of 6 nm of the emission monochromator. Repetitive start–stop signals were recorded using a multi-channel analyser over the course of 1 h per wavelength. A histogram of photons was recorded as a function of 16,383 channels on a time range of 100 ns (0.012 ns per channel). To evaluate the TRES data, a global fitting procedure was applied to the data, similar to the analysis of the transient absorption data.

Quenching experiments

The experimental setup for the quenching experiments was the same as in the SCMs. The quencher was one-sixth of the solution, resulting in a concentration of 1.0 M for triethanolamine, 1.6 M for benzonitrile and 2.3 M for triethylamine.

Singlet oxygen sensitization

DPBF was used to indirectly detect the generation of $^1O_2$[62,63]. The reaction was carried out in air-saturated MeOH solutions at room temperature. For the reactions, 2.4 ml of a **DPBF** solution (20 µM) was mixed with 0.5 ml solutions of either **1** (10^{-4} M), $[Ru(bpy)_3]^{2+}$ (10^{-4} M) or pure MeOH in a Hellma 1-cm-path fluorescence cuvette. The reaction mixtures were illuminated in an Edinburgh Instruments FLS1000 fluorescence spectrophotometer at 350 nm with a slit of 2.5 nm. The decomposition of DPBF was detected by monitoring the luminescence intensity at 450 nm after excitation at 350 nm. The emission spectra were recorded at 5-min intervals with a dwell time of 0.2 s in the range of 420–600 nm.

Data availability

Crystallographic data have been deposited in the CCDC database, assigned to the deposition number CCDC 2002774. Copies are available free of charge via www.ccdc.cam.ac.uk. Source data are provided with this paper.

Code availability

The codes used for the analysis of Huang–Rhys factors, functional tuning and the generation of geometries along normal modes is available from O.K. (oliver.kuehn@uni-rostock.de) upon reasonable request.

References

45. Collado, A. et al. Synthesis of Au I– and Au III–Bis(NHC) complexes: ligand influence on oxidative addition to Au I species. *Eur. J. Inorg. Chem.* **2016**, 4111–4122 (2016).
46. Sheldrick, G. M. A short history of SHELX. *Acta Crystallogr. A Found. Crystallogr.* **64**, 112–122 (2008).
47. Spek, A. L. Structure validation in chemical crystallography. *Acta Crystallogr. D* **65**, 148–155 (2009).
48. Spek, A. L. *PLATON—A Multipurpose Crystallographic Tool* (Utrecht Univ., 2011).
49. Spek, A. L. PLATON SQUEEZE: a tool for the calculation of the disordered solvent contribution to the calculated structure factors. *Acta. Crystallogr. C Struct. Chem.* **71**, 9–18 (2015).
50. Nicholson, R. S. & Shain, I. Theory of stationary electrode polarography. Single scan and cyclic methods applied to reversible, irreversible, and kinetic systems. *Anal. Chem.* **36**, 706–723 (1964).
51. Heinze, J. Cyclovoltammetrie—die "spektroskopie" des elektrochemikers. *Angew. Chem.* **96**, 823–840 (1984).
52. Randles, J. E. B. A cathode ray polarograph. Part II.—The current-voltage curves. *Trans. Faraday Soc.* **44**, 327–338 (1948).
53. Scholz, F. et al. *Electroanalytical Methods* (Springer Berlin Heidelberg, 2010).
54. Livshits, E. & Baer, R.A well-tempered density functional theory of electrons in molecules. *Phys. Chem. Chem. Phys.* **9**, 2932–2941 (2007).
55. Stein, T., Kronik, L. & Baer, R. Reliable prediction of charge transfer excitations in molecular complexes using time-dependent density functional theory. *J. Am. Chem. Soc.* **131**, 2818–2820 (2009).
56. Stein, T., Kronik, L. & Baer, R. Prediction of charge-transfer excitations in coumarin-based dyes using a range-separated functional tuned from first principles. *J. Chem. Phys.* **131**, 244119 (2009).
57. Tomasi, J., Mennucci, B. & Cammi, R. Quantum mechanical continuum solvation models. *Chem. Rev.* **105**, 2999–3093 (2005).
58. Frisch, M. J. et al. *Gaussian 16 Rev. C.01* (2016).
59. Shao, Y. et al. Advances in molecular quantum chemistry contained in the Q-Chem 4 program package. *Mol. Phys.* **113**, 184–215 (2015).
60. Plasser, F. TheoDORE: a toolbox for a detailed and automated analysis of electronic excited state computations. *J. Chem. Phys.* **152**, 084108 (2020).
61. Krejčik, M., Daněk, M. & Hartl, F. Simple construction of an infrared optically transparent thin-layer electrochemical cell. *J. Electroanal. Chem. Interf. Electrochem.* **317**, 179–187 (1991).
62. Dierks, P. et al. Distinct photodynamics of κ-N and κ-C pseudoisomeric iron(II) complexes. *Chem. Commun.* **57**, 6640–6643 (2021).
63. Carloni, P. et al. On the use of 1,3-diphenylisobenzofuran (DPBF). Reactions with carbon and oxygen centered radicals in model and natural systems. *Res. Chem. Intermed.* **19**, 395–405 (1993).

Acknowledgements
J.S. thanks the German Federal Environmental Foundation (Deutsche Bundesstiftung Umwelt) for a PhD scholarship. This work was performed in the framework of the SPP 2102, funded by the German Research Foundation (Deutsche Forschungsgemeinschaft; BA 4467/7-1, HE 2778/14-1, KU 952/12-1, LO 714/11-1 and ME 1313/15-1). Financial support from the Deutsche Forschungsgemeinschaft via the collaborative research centre SFB 1477 (Light–Matter Interactions at Interfaces; project number 441234705) is gratefully acknowledged. We received no specific funding for this work.

Author contributions
J.S. carried out the synthesis of the title molecule, provided and analysed the NMR, mass spectrometry, cyclic and square wave voltammetry, optical absorption and emission spectroscopy data and performed the TCSPC spectroscopy. A.K. and S.L. recorded and analysed the emission, transient absorption and SCMs and analysed the TCSPC data. O.S.B. and O.K. performed and analysed the DFT and TDDFT calculations. T.R. and K.H. performed and analysed the spectroelectrochemical measurements and variable-temperature emission and electron paramagnetic resonance spectroscopy. R.S. solved the single-crystal structure. S.D. and F.M. recorded and analysed the SQUID and ^{57}Fe Mössbauer data. S.H. recorded single-crystal X-ray diffraction data for the title compound. M.A.A.C. conducted the quenching experiments. A.K. carried out the synthesis of the analogous Co^{III} compound and provided and analysed NMR, mass spectrometry and optical absorption spectroscopy data. The principal investigator, M.B., conceived of and planned the research and contributed to the design of the title molecule. J.S., A.K., S.L., O.S.B., O.K., T.R., K.H., R.S. and M.B. wrote the manuscript.

Competing interests
The authors declare no competing interests.

Additional information
Supplementary information The online version contains supplementary material available at https://doi.org/10.1038/s41557-023-01137-w.

Correspondence and requests for materials should be addressed to Matthias Bauer.

Peer review information *Nature Chemistry* thanks the anonymous reviewer(s) for their contribution to the peer review of this work.

3.3.3. Investigation of a CCC complex in three oxidation states

Electrochemical investigations in the previous chapter showed the accessibility of $[Fe(ImP^H)_2]^+$ **16a** in both the one-electron reduced (**16a**$^-$) and one-electron oxidized (**16a**$^+$) congener. The complex in its three oxidation states was synthesized and then characterized by different ground and excited state techniques such as magnetic measurements, modern X-ray spectroscopy and transient absorption spectroscopy. The results are presented in this chapter. Reduction of **16a** with sodium amalgam resulted in the highly air-sensitive **16a**$^-$, while oxidation with $NOPF_6$ led to the air- and moisture-stable **16a**$^+$. The sensitivity of **16a**$^-$ can be explained by only miniscule structural differences between the structures of the congeners, enabling a fast electron transfer due to small activation barriers.
The ground state characterization proves that oxidation and reduction are indeed metal-based, leading to the first isostructural series of a homoleptic iron complex in the low-spin d^6, d^5 and d^4 configuration with spin-states of S = 0, 1/2, and 1, respectively. Excited state characterization leads to the conclusion that neither the iron(II) or (IV) congeners have the photoactive abilities of the parent iron(III) complex. Nevertheless, a great insight into the properties and electronic structure of this compound class was obtained by these investigations.

Isostructural cyclometalated iron complex in three oxidation states

The attached manuscript is submitted to the Journal of the American Chemical Society and currently under review.

Contributing authors:

Jakob Steube: Design and synthesis of the compounds, chemical characterization (NMR, MS, IR), UV-Vis spectroscopy, interpretation of the data, wrote the manuscript.
Lorena Fritsch: Valence to Core and Core to Core X-ray emission spectroscopy, high-energy-resolution fluorescence detected X-ray absorption near edge spectroscopy.
Ayla Kruse, Prof. Dr. Stefan Lochbrunner: Transient absorption spectroscopy.
Dr. Olga S. Bokareva, Prof. Dr. Oliver Kühn: (TD)DFT calculations.
Dr. Serhiy Demeshko, Prof. Dr. Franc Meyer: SQUID and Mößbauer measurements.
Dr. Hossam Elgabarty, Dr. Mohammad Alaraby, Prof. Dr. Thomas D. Kühne: NBO analysis and advanced DFT analysis.
Dr. Roland Schoch, Ass.-Prof. Dr. Stephan Hohloch: Single-crystal X-ray diffraction.
Prof. Dr. Matthias Bauer: Corresponding author, wrote the manuscript.

Supplementary Information for this publication is found in the Appendix in Ch. C.3.

Journal of the American Chemical Society

Isostructural cyclometalated iron complex in three oxidation states

Journal:	*Journal of the American Chemical Society*
Manuscript ID	Draft
Manuscript Type:	Article
Date Submitted by the Author:	n/a
Complete List of Authors:	Steube, Jakob; Universität Paderborn Department Chemie, Department Chemie; Center for Sustainable Systems Design Fritsch, Lorena; Universität Paderborn Department Chemie, Department Chemie; Center for Sustainable Systems Design Päpcke, Ayla; Universität Rostock, Physik Bokareva, Olga; Universitat Rostock, Institut für Physik Demeshko, Serhiy; Institut für Anorganische Chemie, Georg-August-Universität Göttingen Elgabarty, Hossam; Universität Paderborn Department Chemie, Department Chemie; Center for Sustainable Systems Design Schoch, Roland ; Universität Paderborn Department Chemie, Department Chemie; Center for Sustainable Systems Design Alaraby, Mohammad; Universität Paderborn Department Chemie, Department Chemie Hohloch, Stephan; University of Innsbruck, Centre for Chemistry and Biomedicine Kuehne, Thomas; Paderborn University; Center for Sustainable Systems Design Bauer, Matthias; Universität Paderborn Department Chemie, Department Chemie Meyer, Franc; Georg-August-Universitat Gottingen, Institute of Inorganic Chemistry; Georg-August-University Göttingen, Institute of Inorganic Chemistry Kühn, Oliver; Universitat Rostock, Institut fuer Physik Lochbrunner, Stefan; Universitat Rostock, Institut für Physik

Page 1 of 12 Journal of the American Chemical Society

Isostructural cyclometalated iron complex in three oxidation states

Jakob Steube[1,2], Lorena Fritsch[1,2], Ayla Kruse[3,4], Olga Bokareva[3†], Serhiy Demeshko[5], Hossam Elgabarty[2,6], Roland Schoch[1,2], Mohammad Alaraby[2,6], Stephan Hohloch[1‡], Thomas D. Kühne[2,6], Franc Meyer[5], Oliver Kühn[3,4], Stefan Lochbrunner[3,4], Matthias Bauer[1,2]*

1: Institute for Inorganic Chemistry, Paderborn University, 33098 Paderborn, Germany

2: Center for Sustainable Systems Design (CSSD), Paderborn University, 33098 Paderborn, Germany

3: Department of Life, Light and Matter, University of Rostock, Rostock, Germany

4: Institute for Physics, University of Rostock, Rostock, Germany

5: Institute of Inorganic Chemistry, University of Göttingen, Göttingen, Germany

6: Institute for Theoretical Chemistry, Paderborn University, 33098 Paderborn, Germany

ABSTRACT: An isostructural series of Fe^{II}, Fe^{III} and Fe^{IV} complexes $[Fe(ImP)_2]^{0/+/2+}$ utilizing the ImP (1,1'-(1,3-phenylene)bis(3-methyl-1-imidazol-2-ylidene) ligand is presented. In these complexes, a uniquely strong donor ligand set is formed by the combination of four *N*-heterocyclic carbenes (NHCs) and two cyclometalating functions. These stabilize the high-valent Fe^{IV} oxidation state, but also keep the Fe^{II} oxidation state accessible from the parent Fe^{III} compound. Chemical oxidation of $[Fe(ImP)_2]^+$ with $NOPF_6$ yields chemically stable $[Fe^{IV}(ImP)_2]^{2+}$. In contrast, $[Fe^{II}(ImP)_2]^0$, obtained by reduction with sodium amalgam, is highly sensitive towards oxygen. Exhaustive ground state characterization with a broad array of methods, namely single-crystal X-ray diffraction (scXRD), ^{1}H-NMR, Mössbauer spectroscopy, temperature-dependent magnetic measurements, a combination of X-ray absorption near edge structure (XANES) and Valence-to-Core, as well as Core-to-Core X-ray emission spectroscopy, complemented by detailed DFT analysis, reveals that the three complexes $[Fe(ImP)_2]^{0/+/2+}$ can be unequivocally attributed to low-spin d^6, d^5 and d^4 complexes, respectively, with spin-states of 0, ½ and 1. The excited state behavior of the Fe^{II} and the Fe^{IV} complexes, as characterized by transient optical spectroscopy, is radically different from the parent Fe^{III} complex. Short ^{3}MLCT and ^{3}LMCT excited state lifetimes of 5.1 and 1.4 ps, respectively, are revealed. An energetically low-lying MC state with a lifetime of 10.8 ps was identified in the relaxation cascade of $[Fe^{II}(ImP)_2]^0$, leading to the fast deactivation of the ^{3}MLCT state.

Introduction

The chemistry of iron offers a huge variety due to the broad range of possible formal oxidation states in its complex chemistry. From the -II state in Collman's reagent[1] up to the +VI state in either the ferrate anion (FeO_4^{2-})[2] or the recently published example of a bis(carbene) bis(imido) complex from the group of Smith *et al.*,[3] every oxidation state has been observed. However, isostructural series of more than two metal-based oxidation states are still rare,[4,5] often due to ligand non-innocence.[6–12] Another important factor is the stabilization of higher oxidation states, which requires strong donor ligands. Typically, strong π-donors, such as oxo or imido ligands[13,14] but also corroles are employed for this purpose.[15,16] Besides such anionic nitrogen π-donors, anionic carbon ligands in the form of alkyl and aryl anions can also be used.[17–19] Here the σ-donor character dominates, but they also show a significant amount of π-donation in the case of aryl carbanions.[20,21] Therefore, compared to neutral nitrogen counterparts such as pyridines, higher oxidation states are more stabilized. Noteworthy examples are Au(III) and Pt(IV) compounds,[22,23] where cyclometalating functions play a role in stabilizing these high oxidation states. Another good example for the stabilization of higher oxidation states is a series of Os(II) complexes, based on $[Os(bpy)_3]^{2+}$ (bpy = 2,2'-bipyridine). Here, bpy ligands are exchanged for cyclometalating 2-phenylpyridine (ppy^-) ligands. Each ppy-ligand leads to a destabilization of the Os(II)-state of around 0.5 V.[24] Such a trend has also been observed in recently realized cyclometalated iron complexes. Substitution of one of the outer pyridines in the parent bis(terpyridine)iron(II) by a cyclometalating phenylene leads to a significant decrease of the $Fe^{II/III}$ redox potential by about 0.8 V.[25] This trend continues for the replacement of the two central pyridine rings in $[Fe(bimp)_2]^{2+}$ (bimp = (2,6-bis(3-methylimidazol-1-ylidene)pyridine))[26] by phenylene in $[Fe(ImP)_2]^+$ (ImP =1,1'-(1,3-phenylene)bis(3-methyl-1-imidazol-2-ylidene)), with a cathodic shift of the $Fe^{II/III}$ potential of around 1.5 V.[27] This complex is additionally characterized by a $Fe^{III/IV}$ transition at a potential of 0.1 V vs $Fc^{0/+}$. Accordingly, $[Fe(ImP)_2]^+$ shows a rather rare property of both a MLCT (metal-to-ligand charge-transfer) and LMCT

(ligand-to-metal charge-transfer) optical absorption. As a unique feature in iron complex chemistry, an emission from both states is observed. Due to the ligand

Table 1: Comparison of the important structural parameters of 1^-, 1 and 1^+ obtained from their crystal structures with their respective error in brackets.

Compound	1^- ($[Fe(ImP)_2]^0$)	1 ($[Fe(ImP)_2]^+$)	1^+ ($[Fe(ImP)_2]^{2+}$)
Fe-C_{CM} mean distance (Å)	1.918(2)	1.948(3)	1.955(7)
Fe-C_{NHC} mean distance (Å)	1.938(8)	1.983(3)	2.005(8)
C_{NHC}-Fe-C_{NHC} bite angle (°)	156.00(60)	155.36(15)	154.30(30)
Ligand/Ligand torsion angle (°)	90	86	88

design combining *N*-heterocyclic carbenes (NHCs) with a cyclometalating functionality in the ImP-ligand, three oxidations states are in an accessible range. Therefore, a series of the isostructural homoleptic complexes $[Fe(ImP)_2]^{0/+/2+}$ was realized.

The electronic structure of the complexes was investigated with respect to the physical oxidation state of the iron center using various analytical and spectroscopic methods, including single crystal X-ray diffraction, Mössbauer and temperature dependent superconducting quantum interference device (SQUID) magnetization. Special emphasis was placed on synchrotron-based X-ray absorption (XAS) and emission spectroscopy (XES), as these provide high sensitivity to the local electronic structure of the iron center. The excited state dynamics were studied by transient optical absorption spectroscopy. Theoretical calculations are used to understand and consolidate the spectroscopic results.

Results and Discussion

Figure 1 shows the synthesis for the discussed complexes. The synthesis of $[Fe^{III}(ImP)_2]PF_6$ (HImP =1,1'-(1,3-phenylene)bis(3-methyl-1-imidazol-2-ylidene)) **1** was published beforehand.[27] From this, $[Fe^{II}(ImP)_2]$ $\mathbf{1}^-$ is obtained by reduction of **1** with sodium amalgam in THF. For better solubility in THF, **1** was converted to its BPh_4 salt prior to reduction (cf. Supplementary Information, Synthesis). The orange compound was stored in the cold (-30°C) in the glovebox, since miniscule amounts of oxygen at room temperature led to reoxidation to the blue Fe^{III} counterpart, which is, as expected, faster in solution as in the solid. Single crystals suitable for X-ray diffraction were grown by diffusion of pentane into a DCM solution of $\mathbf{1}^-$ (cf. Supplementary Information, Single Crystal X-Ray Analysis).

Dark $[Fe^{IV}(ImP)_2](PF_6)_2$ $\mathbf{1}^+$ can be obtained by oxidation of **1** under inert conditions in acetonitrile (MeCN) using $NOPF_6$. Fine crystalline material is yielded by diffusion of chloroform into a solution of $\mathbf{1}^+$ in acetone, black single crystals suitable for X-ray diffraction were obtained by diffusion of diethyl ether into a solution of $\mathbf{1}^+$ in methanol.

In table 1, the selected metric parameters of $\mathbf{1}^-$ and $\mathbf{1}^+$ are compared to the literature values of **1**.[27,28] The corresponding molecular structures are depicted in Figure 1. The bond lengths of $\mathbf{1}^-$ are generally similar, but shorter than those of the analogous Fe^{II} complex with pyridines in the center of the tridentate ligands (mean Fe-N distance: 1.929 Å, mean Fe-C distance: 1.962 Å).[26]

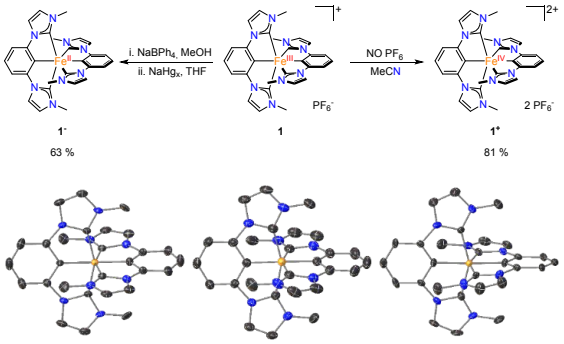

Figure 1: Synthesis of complexes $\mathbf{1}^-$ and $\mathbf{1}^+$ which are obtained by reduction via sodium amalgam (0.3 %) and oxidation via nitrosonium hexafluorophosphate, respectively, and the molecular structures of $\mathbf{1}^-$, **1** and $\mathbf{1}^+$ determined by scXRD (electron density on a 50% probability level).

The mean Fe-C_{NHC} bond-length is also shorter than in the $[Fe^{II}(btz)]^{2+}$ complex (btz =3,3′-dimethyl-1,1′-bis(*p*-tolyl)-4,4′-bis(1,2,3-triazol-5-ylidene)), where a similar mean Fe-C bond-length of 1.963 Å is observed.[29] The mean Fe-C_{NHC} bond-lengths of **1** and $\mathbf{1}^+$ are both comparable to the mean Fe-C bond-lengths of $[Fe(phtmeimb)_2]^+$ and $[Fe(phtmeimb)_2]^{2+}$ (phtmeimb) = [phenyl(tris(3-methylimidazolin-2-ylidene))borate]$^-$) (1.979 and 2.002 Å, respectively.[30,31] Therefore, comparison with literature-known compounds shows that the ligand type has a greater influence on the bond-length than the oxidation state, although slightly longer bonds are observed in higher oxidation states.

A comparison of the different oxidation states in the $[Fe^{n+}(ImP)_2]^{(n-2)+}$ series shows only minor structural changes (Table 1). While there is a correlation between oxidation states and an increase in bond length, the changes between adjacent oxidation states are not significant. This leads to two conclusions: 1. All complexes are in a low-spin environment, since high-spin complexes usually show longer bond lengths, which are usually at least 0.1 Å longer.[32,33] 2. The covalency of the iron-carbon bonds and the rigidity of the (ImP) ligand lead to a stability of the

structural motif, where only small structural changes are possible upon oxidation state change. This induces only small structural reorganization energies between the different oxidation states, allowing fast electron transfer processes, as described by Wärnmark *et al.*[31] This also explains the fast reaction of **1**$^-$ with oxygen, leading to reoxidation to **1**.

Therefore, acquisition of NMR data for **1**$^-$ was a challenging task. Nevertheless, NMR data matches the expectation of a low-spin Fe^{II} complex and does not show residues of **1** or protonated ligand. ^{1}H-NMR proved also useful for the examination of **1**$^+$, as again all signals except for the central proton in the phenyl backbone can be observed. With the broadest peak showing reasonable FWHM values of 125 Hz/ 0.179 ppm and data indicating symmetric ligands, the NMR data supports that oxidation of **1** occurs on the metal center and **1**$^+$ is a low-spin Fe^{IV} compound.

First insights into the electronic structure is provided by Mössbauer spectroscopy. The spectra of **1**$^-$ and **1**$^+$ in comparison to the literature values of **1**[27] are shown in Figure 2.

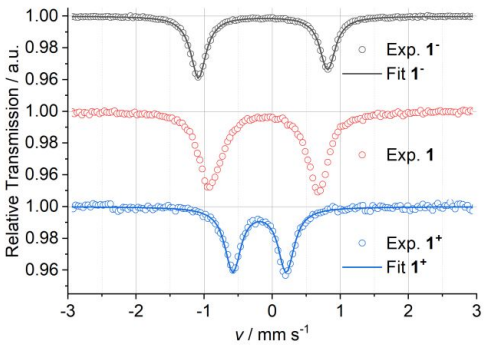

Figure 2: ^{57}Fe zero-field Mössbauer spectra of **1**$^-$ (black), **1** (red)[27] and **1**$^+$ (blue) at 80 K.

The Mössbauer spectra of the three compounds are all composed of doublets, characterized by their isomer shift and quadrupole splitting parameters. Usually, the isomer shift is a revealing parameter for the oxidation state of iron compounds. It is typically lower for the higher oxidation state, as it reflects the contribution of the 4s electrons to the electron density at the Fe nucleus, which is mainly influenced by the 4s population and by shielding effects due to the 3d population.[34] On the other hand, the isomer shift depends strongly on the iron–ligand distances, i.e., shorter iron–ligand distances cause lower isomer shifts due to the decreased radial extension of the 4s-orbital.[35] After oxidation from **1** to **1**$^+$, the isomer shift decreases from –0.12 mm s^{-1} to –0.19 mm s^{-1}, as expected for the increased metal oxidation state, since the shielding effect of the 3d-electrons (less for **1**$^+$ compared to **1**) on the 3s- and 4s-electrons decreases while all iron–C distances remain comparable upon going from **1** to **1**$^+$ (see Table 1). Hence, the difference in the isomer shift between **1** to **1**$^+$ follows the expected trend and can be attributed to the changes in 3d-orbital population. However, after reduction from **1** to **1**$^-$, the isomer shift decreases slightly from –0.12 mm s^{-1} to –0.14 mm s^{-1}. This counterintuitive isomer shift change can be explained by the significant contraction of the iron–C distances in **1**$^-$ (see Table 1) due to enhanced π-backdonation, hence the data are still in line with metal based reduction.[36] All three isomer shift values are quite low, in accordance with a low spin configuration of the investigated compounds.

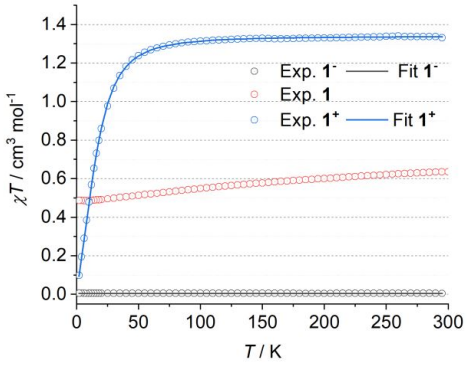

Figure 3: Temperature-dependent magnetic susceptibility measurements of **1**,[27] **1**$^-$, and **1**$^+$.

Temperature-dependent magnetic susceptibility measurements confirm these considerations. Experimental $c_M T$ values at room temperature are 0.005, 0.63[27] and 1.33 cm^{3}mol^{-1}K for **1**$^-$, **1**, and **1**$^+$, respectively, which is close to the theoretically expected spin-only values of 0, 0.375 and 1 cm^{3}mol^{-1}K for S = 0, ½ and 1, respectively, and indicative of some orbital contributions in case of **1** and **1**$^+$. For **1**$^+$, global fitting of the temperature dependent susceptibility data and the variable temperature – variable field measurements (Fig. S1) allowed the determination of the zero -field splitting parameter D = +39.5 cm^{-1}; see SI for more information.

Further analysis of the electronic structure is obtained by hard X-ray spectroscopy in form of X-ray absorption near-edge structure spectroscopy (XANES)[37–39] and X-ray emission spectroscopy (XES).[40–43] XANES spectra of 3d-metal complexes exhibit prepeak signals originating from 1s → LUMO transitions, thus probing typically nd/(n+1)p states. As pure s→d transitions are dipole forbidden and the resulting signal would be very weak, the prepeak intensity in these distorted octahedral complexes gain intensity from hybridization of the d-orbitals with ligand p-orbitals.[44,45] Thus, the prepeaks can provide information about the coordination geometry and the electronic structure of the absorbing atom. Due to the isostructural nature of the investigated complexes, it is employed here to gain information on the local electronic structure at the iron centers. With increasing oxidation states from ([Fe(ImP)$_2$]^0) to ([Fe(ImP)$_2$]$^{2+}$), a higher prepeak energy is expected for purely metal-based oxidation events, which is indeed found

in the experimental spectra of Figure 4. Only one prepeak in the range of 7110-7116 eV can be observed for complex **1**$^-$, whereas **1** and **1**$^+$ show two. Since the prepeaks result from excitations into the d-orbitals, the signal at higher energies around 7114 eV is assigned to transition into the e_g states (d_z^2 and $d_{x^2-y^2}$) and the one at lower energies at about 7112 eV to t_{2g} states. DFT calculations,[46,47] presented in Figure 4, confirm this assignment. In complex **1**$^-$, no transitions to this final state are observed, as t2g are fully occupied,

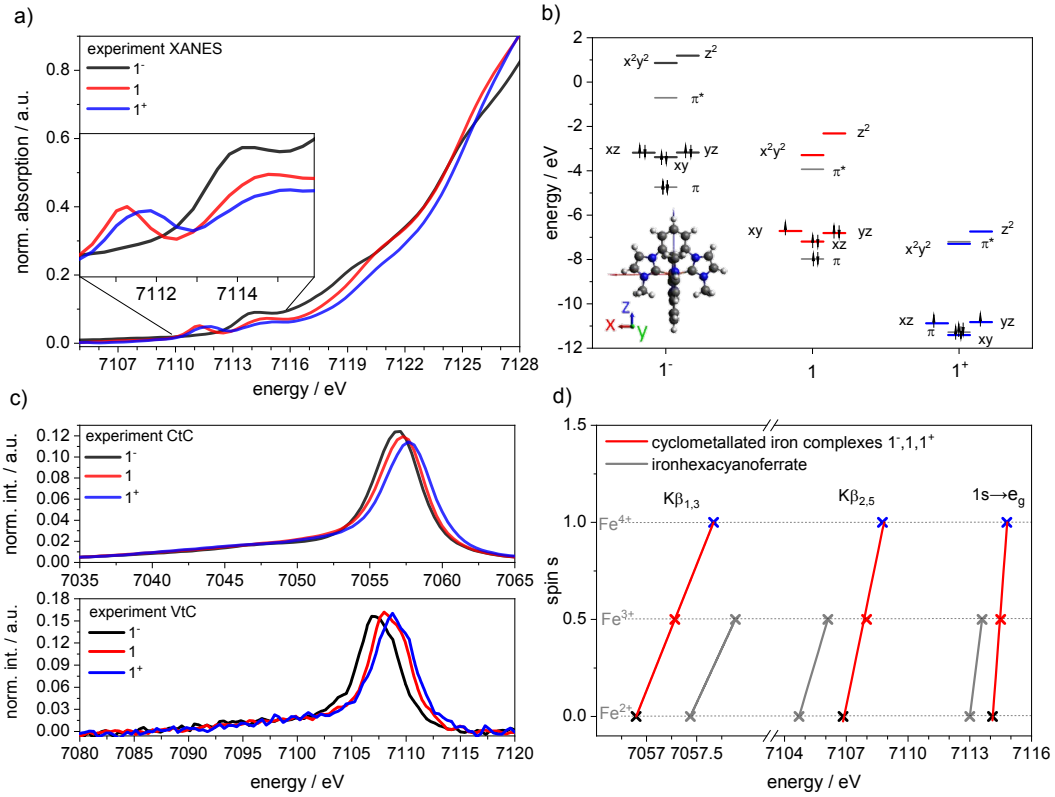

Figure 4: a) Experimental XANES spectra of complexes **1**$^-$, **1** and **1**$^+$. Inset: Magnification of the pre-edge region. b) Selected molecular orbital levels of d-orbitals, highest π and lowest π* orbital based on TPSS/def2-TZVPP DFT calculations. c) Experimental CtC (top) and VtC (bottom) spectra of complexes **1**$^-$, **1** and **1**$^+$. d) Plot spin vs. energy of the $K\beta_{1,3}$, $K\beta_{2,5}$ and pre-peak ($1s\rightarrow e_g$) maxima of complexes **1**$^-$, **1** and **1**$^+$ in comparison to $Fe(CN)_6^{3+/4+}$. Parameters for linear regression are listed in Tab. S3.

confirming **1**$^-$ as low-spin Fe^{II}-d_6 complex.

In contrast both low spin Fe^{III}-d^5 (**1**) and $[Fe(ImP)_2]^{2+}$ (**1**$^+$) exhibit t_{2g} vacancies that cause the additional low energy prepeak signal. According to DFT results in Figure 4, a constant and nearly identical energy increase of both the t_{2g} and e_g levels with decreasing iron oxidation state is predicted. Experimental values confirm this prediction: The t_{2g} prepeak energy increases by 0.6 eV from ($[Fe(ImP)_2]^+$) (**1**: 7111.3 eV) to ($[Fe(ImP)_2]^{2+}$) (**1**$^+$: 7111.9 eV), while the e_g prepeak energy increases by 0.4 and 0.3 eV respectively, from **1**$^-$ (7114.1 eV) to **1** (7114.5 eV) and **1**$^+$ (7114.8 eV). In particular, the last row of values suggests a constant change of charge at the iron center, or a stepwise iron-localized oxidation, supporting that the observed redox-events are metal-based and **1**$^+$ is indeed a low-spin Fe^{IV}-complex.

To further prove this stepwise oxidation state change on the metal-center, the more metal localized K-edge Core-to-Core X-ray emission spectroscopy (CtC-XES) is applied in the following. Here the emission caused by radiative relaxation from the metal 3p to 1s orbital after excitation at energies above the absorption edge is observed. The resulting signal splits into two peaks: The intense Kβ mainline ($K\beta_{1,3}$), and a weaker peak shifted to lower energies, the Kβ satellite (Kβ'). The reason for the splitting and therefore the spectral shape is the 3p-3d exchange interaction. The higher the effective electron spin in the d orbitals, the larger the exchange interaction and thus the splitting.[40,41,48]

In the experimental CtC-XES spectra shown in Figure 4 c, the first thing to notice is that the intensity of the Kβ' satellite is rather low. This indicates a small splitting and thus a small number of unpaired electrons in agreement with a low-spin configuration for all complexes. Therefore only the energy of the Kβ mainline can be used properly as parameter to describe the splitting.[40] Although the main line

energy is not only dependent on the spin state but also covalency, ligand and metal-metal interactions effects,[49,50] such influences can be nearly fully ruled out in the presented isostructural row of mononuclear complexes.

The $K\beta_{1,3}$ signal shows a linear correlation between the number of unpaired electrons and the main line energy (Figure 4d), as reported for purely ionic compounds with increasing oxidation states by Glatzel and Bergman.[40] Accordingly these results support the prepeak analysis and the conclusion of a stepwise oxidation state change at the metal center, since a ligand centered oxidation will not have the exact same effect on the spin state as a metal centered oxidation. To further substantiate this claim, the identical analysis is shown in Figure 4d for Fe^{II} and Fe^{III} hexacyanoferrate. The slope of the spin-energy correlation is very similar to the investigated row of isostructural carbene complexes.

Table 1: Computed spin-up and spin-down orbital occupation numbers and the derived oxidation state of the iron center. The shaded boxes mark the occupied orbitals with n≈1. The atomic charges based on Mulliken and natural populations are also listed together with the corresponding spin populations.

	Spin	d-orbital occupation numbers					Configuration	Spin multiplicity	Natural charges (total/ per Spin)	Mulliken charge	Mulliken spin population	Natural spin population
1⁻	α	0.33	0.36	**0.99**	**0.99**	**0.99**	d^6	0	-1.427	-0.0546	0	0
									α: -0.713			
	β	0.33	0.36	**0.99**	**0.99**	**0.99**			β: -0.713			
1	α	0.65	0.69	**0.97**	**0.97**	**0.98**	d^5	1	-0.969	0.765	1.189	0.96
									α: -0.975			
	β	0.19	0.69	0.73	**0.95**	**0.95**			β: 0.006			
1⁺	α	0.75	0.81	**0.98**	**0.98**	**0.99**	d^4	2	-0.615	0.693	2.171	1.75
									α: -1.204			
	β	0.19	0.20	0.69	0.78	**0.97**			β : 0.590			

The hard X-ray investigation of the isostructural complex row is complemented by Valence-to-Core X-ray emission spectroscopy (VtC-XES). Here the emitted signal serves as a probe of valence levels including occupied 3d-orbitals and ligand-centered orbitals.[51] In the experimental VtC-XES spectra of Figure 4c a nearly constant shift of the $K\beta_{2,5}$ signal from 7107.0 (**1**⁻) to 7108.0 eV (**1**) to 7108. 8 eV (**1**⁺) is observed with increasing oxidation state, thus supporting the previous findings. To further analyze the spectrum and explain the origin of this shift, DFT calculations were performed (Fig. S3). The calculations show that the weak Kβ'' signal in the range of 7095-7102 eV originates from transitions of orbitals with mainly C-s and -p character, as well as N-p contributions from the imidazolylidene. In this range, the low energy transitions involve the s- and the higher energy transitions mainly involve the p-orbitals of carbon delocalized over the ligand. The $K\beta_{2,5}$ peak is composed by transitions from the C p-orbitals with a small admixture of Fe p-orbitals. As demonstrated in Figure S3 transitions from the NHC carbon constitute the lower energy side of the signal, while the higher-energy side is dominated by the phenyl fragment. It is important to note that according to the calculations the orbital composition of the transitions does not change (see Fig. S3 and SI Fig. S4/Tab. S2). Instead, the metal orbitals are stabilized with higher oxidation state (Figure 4b)) but the ligand based π molecular orbitals are less affected confirming the metal-based oxidation.

The quantum chemical characterization of **1**, **1**⁻, and **1**⁺ regarding their oxidation states and associated changes in the electronic charge densities was performed with DFT calculations on the isolated complexes (See Computational details in SI). In molecular systems, as opposed to isolated ions, there is no correlation between formal charges invoked by oxidation states and the charge localized around the atomic center. The reason behind this widely reported observation was explained by Raebiger *et. al.*[52] (schematic depiction in Figure S9). Whenever an electron is added or removed at the d-orbitals of a transition metal (TM) center, there is an inevitable change in the energies of the d-orbitals. Hence, the hybridization of the metal-ligand bonding orbitals, such that the contribution of the TM center to the bonding orbitals decreases or increases, respectively. This leads to a negative feedback charge self-regulation that stabilizes the amount of charge localized around the TM center.

For characterizing the oxidation state in each molecule, the wave function projection method suggested by Sit et al.[53] was chosen (See computational details). With this method the occupancy (n) of each iron atomic d-orbital in each complex can be obtained. As in the case of a free atom, only fully occupied d-orbitals (n≈1) are relevant for determining the oxidation state of the TM. The oxidation state is determined by simply counting the fully occupied d-

orbitals. All other d-orbitals with weaker occupations (n≈0) are due to ligand donation to empty d-orbitals and do not contribute to the determination of the oxidation state. The results are reported in Table 1, where it is indeed found that the oxidation state and electronic configuration of each molecule can be unambiguously identified, ranging from d^6 in the case of $\mathbf{1}^-$ down to d^4 in the case of $\mathbf{1}^+$.

Interestingly, the signature of the strong ligand field in these molecules also manifests in the analysis. The ideal case of n=1 for fully occupied and n=0 for vacant d-orbitals is only achieved in the limit of a weak-field ligand.[53,54] For strong-field ligands as is the case here, the occupation numbers deviate from this ideal. The deviations mainly arise from the larger distortions in the atomic d-orbitals due to the stronger ligand field and larger orbital mixing. The presence of π-backdonation from ligand to the TM center is contributing here as well (cf. Computational details, NBO analysis results in the SI). Nevertheless, the assignment of the oxidation state in each case remains easy and non-ambiguous, with the occupied orbitals all having n > 0.95.

A common method for characterization of the charge distribution in a molecule is to compute partial atomic charges, which are obtained through a partitioning of the total electron density into atomic contributions. Because this partitioning can be accomplished in different ways, there is always an ambiguity in the definition of the charges and different methods can yield widely differing values. As already mentioned, they are a rather poor measure of the oxidation state, if a measure at all.[55,56] In most cases, because of the aforementioned negative feedback mechanism, first-principles quantum mechanical calculations show only negligible changes in the total charge localized around the TM center as the oxidation state is altered. A change of +/- 0.5 in any direction, or sometimes much less, is rather common.[57,58] It seems that transition metal atomic charges are rather more sensitive to the nature of the complexing ligand than to the formal oxidation state.[59] For compounds in a low oxidation state and coordinated to a highly electronegative ligand, a higher charge at the metal atom can be observed than for a complex with a higher oxidation state and a less electronegative ligand.[59]

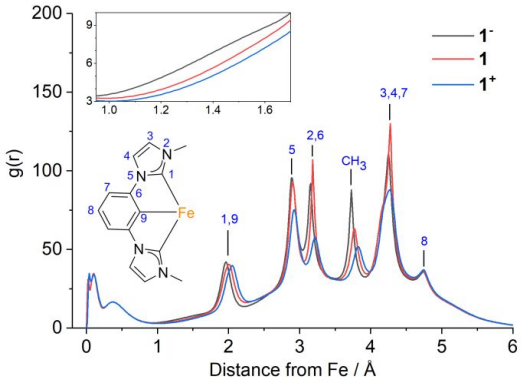

Figure 5: Radial distribution function of the electron density of the complex, with the iron at the center.

The partial atomic charges and spin populations obtained from Mulliken and from natural bond orbital analyses (NBO[60,61]) are listed in Table 1. The atomic charges not only give information about the charge distribution but also carry the fingerprint of the charge self-regulation process. Upon oxidation of $\mathbf{1}^-$ to $\mathbf{1}$ (removing a spin-down electron), the Fe atom loses a natural charge of 0.7e from the beta (spin-down) channel, but concomitantly gains 0.25e in the alpha (spin-up) spin channel, leading to the more modest net loss of 0.45e. The difference between the natural spin populations however now amounts to almost one full electron, explaining the previously reported observation that spin populations usually perform much better than atomic charges in characterizing the oxidation state of a compound particularly in high spin states.[62,63] This is merely a consequence of the negative feedback charge regulation. The same behavior and arguments are also valid for the iron-center in $\mathbf{1}^+$, which loses 0.6e in one spin channel and gains back 0.25e in the other, for a net loss of only 0.35e. Again, the charge self-regulation working in the different spin channel leads to a change in the spin population of almost 1e. We conclude that, for the same reason that partial atomic charges do not correlate with the oxidation state, the spin populations can be a very cheap and efficient method for its characterization. This is also true for Mulliken population analysis, even though the Mulliken charges are known to occasionally have several problematic features like basis-set sensitivity and chemically non-intuitive values.[61]

For a more detailed understanding of the oxidation-induced charge reorganization in the three complexes, Figure 5 depicts the radial distribution function of the electron density, with the Fe atom at the origin. By far the most significant charge redistribution is taking place at the aromatic π-system at the second- and third- neighbor atoms to the Fe. At the vicinity of the Fe atom, oxidation leads to a depletion in the charge density at the bond between the metal atom and the six nearest neighbors. There is also radial charge redistribution at the Fe atom itself, particularly obvious in the case of $\mathbf{1}^+$, and consistent with a shrinking in the ionic radius at higher oxidation states.

Therefore, the theoretical approach also shows that the redox events of $\mathbf{1}$ lead to metal-centered reduction and oxidation, respectively, as judged by the populations of the d-orbitals in Table 1. The overall observed effects, which may suggest partial ligand-non-innocence, are due to charge redistribution within the system. A driving force behind this is the strong donor ligand, which is able to redistribute electron density from the ligand backbone into the metal-ligand bond. The characterization of the electronic structures of the complex in its three oxidation states thus concludes that the complexes $\mathbf{1}^-$, $\mathbf{1}$ and $\mathbf{1}^+$ are indeed low-spin iron +II, +III and +IV, respectively.

To get further information on the optical properties of this interesting compound class, electronic absorption

spectra of **1**$^{-}$, **1** and **1**$^{+}$ were recorded in solutions of acetonitrile (Figure 6). The electronic transitions in **1**$^{-}$, **1** and **1**$^{+}$ were assigned using TD-DFT calculations (reference [27] for **1**). Because of the covalent cyclometalating bond, the orbitals contain electron density from both ligands and metals. This mixing results in the LMCT and MLCT transitions including some LC, ILCT and LLCT characters and vice versa. In both **1** and **1**$^{+}$, LMCT transitions can be observed in the low energy part of the spectra above 450 and 380 nm (Fig. 6c), respectively. Contrary to **1**, the Fe^{IV} complex **1**$^{+}$ shows two LMCT bands. The transitions are around five times more intense (ε_{791nm} = 0.24 10^4 M^{-1} cm^{-1} and ε_{496nm} = 0.26 10^4 M^{-1} cm^{-1}) than the LMCT transition in **1** (ε_{585nm} = 0.05 10^4 M^{-1} cm^{-1}). MLCT transitions can be observed in all three oxidation states between 320 and 420 nm and for **1**$^{+}$ over 500 nm. In the Fe^{IV} compound **1**$^{+}$, the MLCT shows just as a shoulder at 330 nm. The intensities of the MLCT band decrease with increasing oxidation state, as it is expected.

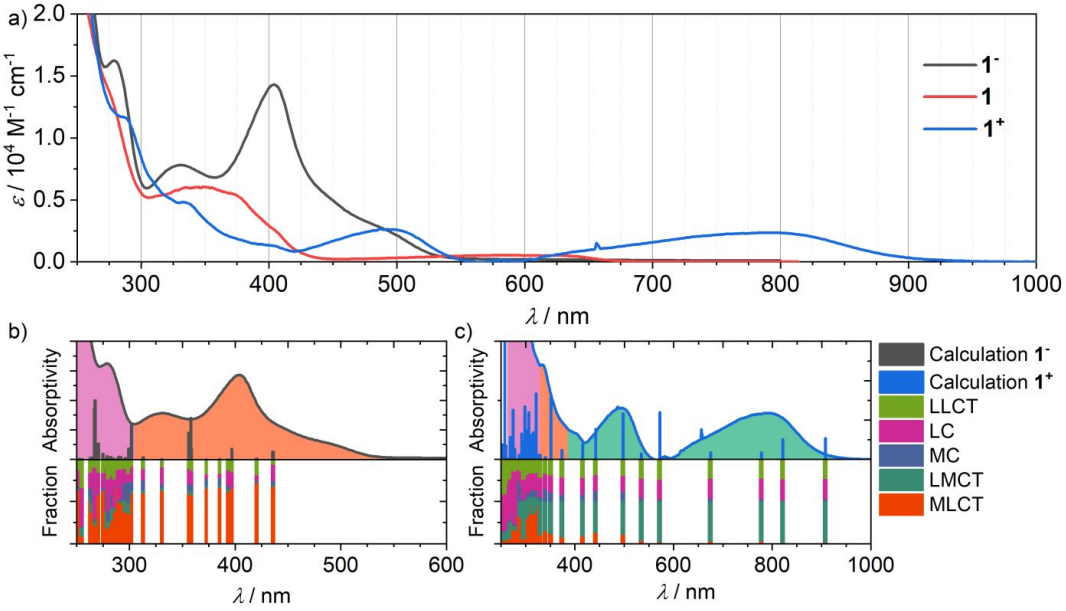

Figure 6: a) UV-Vis spectra of **1**$^{-}$, **1**[27] and **1**$^{+}$ in comparison (measured at 10^{-5} M for **1** and **1**$^{+}$ and 10^{-4} M for **1**$^{-}$ in MeCN). b) Calculated transitions of **1**$^{-}$ compared to and the fractional composition of the transitions. c) Calculated transitions of **1**$^{+}$ and the fractional composition of the transitions.

The MLCT absorption of Fe^{II} **1**$^{-}$ shows a molar extinction of ε_{404nm} = 1.43 10^4 M^{-1} cm^{-1}, Fe^{III} as reported ε_{351nm} = 0.60 10^4 M^{-1} cm^{-1} and Fe^{IV} ε_{333nm} = 0.48 10^4 M^{-1} cm^{-1}. Besides, a further blue-shift of the maximum is observed for increasing oxidation states. This is supported by the observation of a relative stabilization of the metal-orbitals to the ligand orbitals (Figure 4 b) in the VtC-spectra. Below 310 nm, ligand-based transitions are observed in all three compounds. Contrary to **1,** which exhibits a unique emissive behavior with luminescence from both MLCT and LMCT states, no emission from **1**$^{-}$ and **1**$^{+}$ could be observed. Thus, the excited state dynamics could only be investigated with Transient Absorption Spectroscopy (TA).

The transient absorption measurements of the $[Fe(ImP)_2]^0$ complex **1**$^{-}$ (figure 7) show a negative signal in the range below 450 nm with a minimum beyond the measured 400 nm. Towards longer wavelengths from 450 nm the signal is positive with a maximum at about 535 nm, which can be attributed to ESA (see Figure 8, right). The fit of the transient absorption spectra shows a biexponential decay with time components of around 5 ps and 10 ps. The contribution of the ESA at longer wavelengths than 550 nm decays with the short time constant of 5 ps. At shorter wavelengths than 550 nm, the two decay associated spectra show a certain mirror symmetry. This may indicate that with the short time constant from the optically excited state, an energetically lower intermediate state is first populated, which is responsible for the ESA components between 400 and 550 nm, and which subsequently relaxes to the ground state within the slower decay time of 10 ps. The bleach is clearly imprinted on the TA spectra at short times but is masked by the new ESA at longer delay times between the pump and the probe pulses.

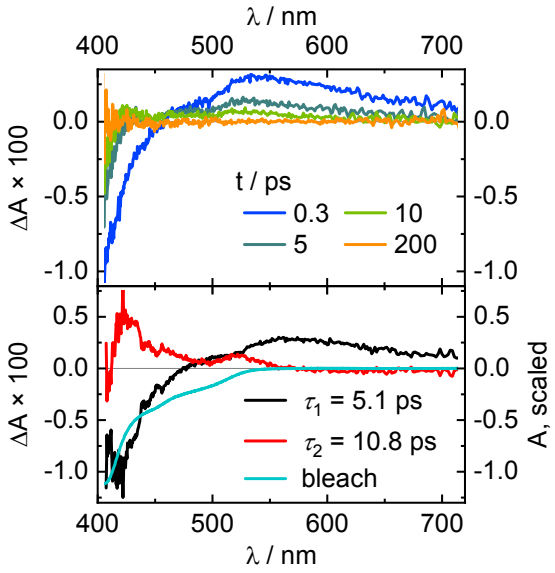

Figure 7: Transient absorption spectra (top) at different delay times between pump and probe pulse measured in the magic angle between the pulses and the decay associated spectra (bottom) compared to the bleach (negative, scaled absorption spectrum) for complex $\mathbf{1}^{-}$.

Here, the short τ_1 lifetime can be attributed to a ^{3}MLCT state, as the ESA red to the MLCT absorption (figure 8) stems from the LMCT absorption of the oxidized metal center in the charge-separated state and is comparable to what is seen in the absorption spectrum of **1** (Figure 6). In contrast, the longer τ_2 can be attributed to an MC state, most likely a ^{3}MC state. This is deduced from the absence of ESA components, indicative of charge transfer states.

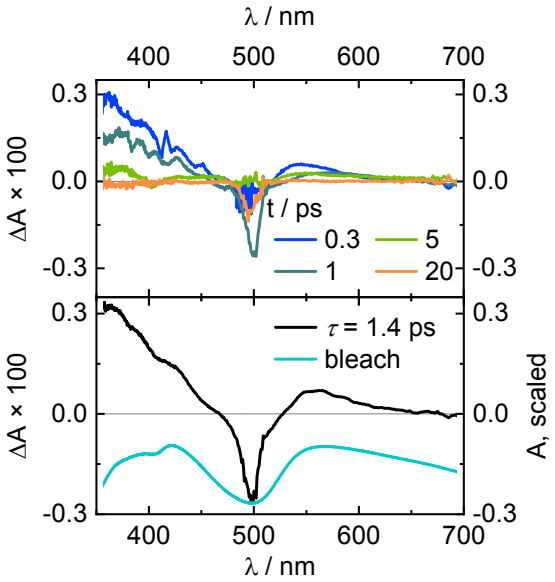

Figure 8: Transient absorption spectra (top) at different delay times between pump and probe pulse measured in the magic angle between the pulses and the decay associated spectra (bottom) compared to the bleach (negative, scaled absorption spectrum) for complex $\mathbf{1}^{+}$.

In the transient absorption measurements of the $[Fe(ImP)_2]^{2+}$ complex $\mathbf{1}^{+}$ (Figure 8) a negative signal could be observed in the range of 470-530 nm with a minimum at 500 nm. At this point, the bleach also shows a minimum. Going from the negative signal to shorter and longer wavelengths, the signal is positive with a maximum at about 355 and 560 nm, which can be attributed to excited state absorption (ESA) (Figure 9). The course of the transient absorption spectra shows a fast, monoexponential decay with a time constant of about 1.4 ps. The narrow-band negative signal component at 500 nm is possibly related to scattered light, since the spectral position and band width match the excitation pulses. However, if the narrowband component is ignored, the impression arises that there is a broadband ESA that spans the entire visible spectral range. The shape of the transient spectra suggests that the bleach is imprinted on the ESA, which overlaps with it. The shape of the decay associated amplitude spectrum (DAS) indicates that this component belongs to an ^{3}LMCT, since the ESA fits the absorption profile of **1** well (cf. Figure 6). This is expected for an LMCT, since it involves a reduction of the metal center ($Fe^{IV} \rightarrow Fe^{III}$), from which the known LMCT bands arises.

These results become even more interesting when compared to known compounds in different oxidation states. The Fe^{II}/Fe^{III} pair $[Fe(btz)_3]^{2/3+}$ is an ideal reference.[29,64] The MLCT lifetime of $[Fe(btz)_3]^{2+}$ with 0.5 ns is much longer than the LMCT lifetime in the Fe^{III} congener (0.1 ns), which is a diametral behaviour to results. Here, the LMCT of the Fe^{III} compound shows a lifetime of 0.2 ns, whereas the MLCT of the Fe^{II} shows around half of the MLCT lifetime of the Fe^{II} complex it is derived from ($[Fe(bimp)_2]^{2+}$ with 9 ps MLCT lifetime).[26] A possible explanation is the destabilization of the MLCT states by the π-donor strength of the cyclometalating moieties, which outweighs the σ-donor strength of the C^C^C donor-set, enabling energetically low MC-states. This can be further supported by the symmetry of the complex, since the cyclometalating moieties are in trans position. This enables an energetically low MC-state where the Fe-Carbene bonds are elongated. This is analogous to the calculations Dixon made on an $[Fe(NCN)_2]$ complex,[65] predicting exactly this behavior, even though the Fe-carbene bonds should be harder to elongate than the Fe-pyridine bonds presented in the work. Overall, an interplay of these two effects is believed to be the main cause for the short MLCT lifetime and a pronounced MC lifetime. The lifetime of the ^{3}LMCT state in the Fe^{IV} complex on the other hand is a bit longer than in the other known Fe^{IV} ^{3}LMCT lifetime (0.8 ps),[31] but still far off from a region where photophysical applications are possible.

Conclusions

To conclude, an iron compound was fully characterized in its three accessible oxidation states to provide a full image of the electronic structures and the charge-induced changes. Overall, the methods conclude that the oxidation processes are metal centered and that the iron complex remains in its low-spin configuration from d^6 to d^4. Therefore, this is one of the very few isostructural series, showing solely metal-centered redox events and, to the best of our knowledge, the first isostructural series for homoleptic iron complexes. These results are supported by a variety of DFT calculations and NBO analysis. The results suggest that charge-redistribution within the strong donor-ligand is responsible for effects, which can be mistaken as ligand non-innocence. Nevertheless, based on the population of the d-orbitals, the experimental results of metal-centered redox events are supported. Optical characterization shows a panchromatic absorption of $\mathbf{1}^+$ with the absorption ranging up until 900 nm. The excited states of $\mathbf{1}^+$ and $\mathbf{1}^-$ were investigated using streak camera measurements. $\mathbf{1}^+$ exhibits an ^{3}LMCT lifetime of around a picosecond, which is slightly longer than the observed ^{3}LMCT lifetime in a comparable low-spin Fe^{IV} complex, which has been previously reported. $\mathbf{1}^-$ on the other hand shows a very short-lived MLCT state, contrary to the expectations from the strong donor ligands. This can be explained by an energetically more favorable MC state, which is caused by the destabilization of the MLCT state by the strong π-donating cyclometalating functions, outweighing the σ-donating capabilities. While this results in a dual-emissive compound with ns-lifetime in the +III oxidation state, the effects on the +II and +IV oxidation states are not sufficient to lead to photoactive complexes. All in all, an exhaustive spectroscopic and theoretical approach led to the full characterization of this interesting compound in three stable oxidation states.

ASSOCIATED CONTENT

Supporting Information. Synthesis and experimental details, spectra and computational details.
This material is available free of charge via the Internet at http://pubs.acs.org

AUTHOR INFORMATION

Corresponding Author

* Matthias Bauer; Email: matthias.bauer@upb.de

Present Addresses

† Institute of Physics, University of Kassel, Kassel, Germany
‡ Institute of General, Inorganic and Theoretical Chemistry, University of Innsbruck, Innsbruck, Austria

Author Contributions

The manuscript was written through contributions of all authors. All authors have given approval to the final version of the manuscript.

Notes

The authors declare no competing financial interest.

ACKNOWLEDGMENT

J.S. thanks the German Federal Environmental Foundation (Deutsche Bundesstiftung Umwelt - DBU) for a PhD scholarship. Wolfgang Caliebe and Aleksandr Kalinko of Petra III-beamline P64 (Deutsches Elektronensynchrotron Desy, Hamburg) is acknowledged for support and provision of beamtime. The grant of computer time at the Paderborn Center for Parallel Computing PC2 is acknowledged. This work was performed in the framework of the SPP 2102 funded by the Deutsche Forschungsgemeinschaft (BA 4467/7-1 and BA 4467/7-2, KU 952/12-1 and KU 952/12-2, LO 714/11-1 and LO 714/11-2, ME 1313/15-1).

REFERENCES

(1) Collman, J. P. Disodium tetracarbonylferrate, a transition metal analog of a Grignard reagent. *Acc. Chem. Res.* **1975**, *8* (10), 342–347. DOI: 10.1021/ar50094a004.

(2) Sharma, V. K. Potassium ferrate(VI): an environmentally friendly oxidant. *Advances in Environmental Research* **2002**, *6* (2), 143–156. DOI: 10.1016/S1093-0191(01)00119-8.

(3) Martinez, J. L.; Lutz, S. A.; Yang, H.; Xie, J.; Telser, J.; Hoffman, B. M.; Carta, V.; Pink, M.; Losovyj, Y.; Smith, J. M. Structural and spectroscopic characterization of an Fe(VI) bis(imido) complex. *Science* **2020**, *370* (6514), 356–359. DOI: 10.1126/science.abd3054

(4) Gravogl, L.; Heinemann, F. W.; Munz, D.; Meyer, K. An Iron Pincer Complex in Four Oxidation States. *Inorg. Chem.* **2020**, *59* (8), 5632–5645. DOI: 10.1021/acs.inorgchem.0c00355. Published Online: Apr. 9, 2020.

(5) Sinha, W.; Sommer, M. G.; Deibel, N.; Ehret, F.; Bauer, M.; Sarkar, B.; Kar, S. Experimental and Theoretical Investigations of the Existence of Cu(II), Cu(III), and Cu(IV) in Copper Corrolato Complexes. *Angew. Chem. Int. Ed.* **2015**, *54* (46), 13769–13774. DOI: 10.1002/anie.201507330. Published Online: Sep. 25, 2015.

(6) Garai, A.; Sobottka, S.; Schepper, R.; Sinha, W.; Bauer, M.; Sarkar, B.; Kar, S. Chromium Complexes with Oxido and Corrolato Ligands: Metal-Based Redox Processes versus Ligand Non-Innocence. *Chemistry (Weinheim an der Bergstrasse, Germany)* **2018**, *24* (48), 12613–12622. DOI: 10.1002/chem.201801452. Published Online: Jul. 19, 2018.

(7) Wittwer, B.; Dickmann, N.; Berg, S.; Leitner, D.; Tesi, L.; Hunger, D.; Gratzl, R.; van Slageren, J.; Neuman, N. I.; Munz, D.; Hohloch, S. A mesoionic carbene complex of manganese in five oxidation states. *Chem. Commun.* **2022**, *58* (41), 6096–6099. DOI: 10.1039/d2cc00097k. Published Online: May. 20, 2022.

(8) Keilwerth, M.; Mao, W.; Jannuzzi, S. A. V.; Grunwald, L.; Heinemann, F. W.; Scheurer, A.; Sutter, J.; DeBeer, S.; Munz, D.; Meyer, K. From Divalent to Pentavalent Iron Imido Complexes and an Fe(V) Nitride via N-C Bond Cleavage. *Journal of the American Chemical Society* **2023**, *145* (2), 873–887. DOI: 10.1021/jacs.2c09072. Published Online: Dec. 30, 2022.

(9) Kosog, B.; La Pierre, H. S.; Denecke, M. A.; Heinemann, F. W.; Meyer, K. Oxidation state delineation via U L(III)-edge XANES in a series of isostructural uranium coordination complexes. *Inorg. Chem.* **2012**, *51* (14), 7940–7944. DOI: 10.1021/ic3011234. Published Online: Jul. 5, 2012.

(10) Keilwerth, M.; Hohenberger, J.; Heinemann, F. W.; Sutter, J.; Scheurer, A.; Fang, H.; Bill, E.; Neese, F.; Ye, S.; Meyer, K. A Series of Iron Nitrosyl Complexes {Fe-NO}6-9 and a Fleeting {Fe-NO}10 Intermediate en Route to a Metalacyclic Iron Nitrosoalkane. *Journal of the American Chemical Society* **2019**, *141* (43), 17217–17235. DOI: 10.1021/jacs.9b08053. Published Online: Oct. 17, 2019.

(11) Akbar Ali, M.; Bernhardt, P. V.; Brax, M. A. H.; England, J.; Farlow, A. J.; Hanson, G. R.; Yeng, L. L.; Mirza, A. H.; Wieghardt, K. The trivalent copper complex of a conjugated bis-dithiocarbazate Schiff base: stabilization of Cu in three different oxidation states. *Inorg. Chem.* **2013**, *52* (3), 1650–1657. DOI: 10.1021/ic302596h. Published Online: Jan. 16, 2013.

(12) Bigi, J. P.; Harman, W. H.; Lassalle-Kaiser, B.; Robles, D. M.; Stich, T. A.; Yano, J.; Britt, R. D.; Chang, C. J. A high-spin iron(IV)-oxo complex supported by a trigonal nonheme pyrrolide platform. *Journal of the American Chemical Society* **2012**, *134* (3), 1536–1542. DOI: 10.1021/ja207048h. Published Online: Jan. 4, 2012.

(13) Meyer, S.; Klawitter, I.; Demeshko, S.; Bill, E.; Meyer, F. A Tetracarbene-Oxoiron(IV) Complex. *Angew. Chem.* **2013**, *125* (3), 935–939. DOI: 10.1002/ange.201208044.

(14) Zou, H.-B.; Yang, H.; Liu, Z.-Y.; Mahmood, M. H. R.; Mei, G.-Q.; Liu, H.-Y.; Chang, C.-K. Iron(IV)-Corrole Catalyzed Stereoselective Olefination of Aldehydes with Ethyl Diazoacetate. *Organometallics* **2015**, *34* (12), 2791–2795. DOI: 10.1021/acs.organomet.5b00069.

(15) Simkhovich, L.; Goldberg, I.; Gross, Z. Iron(III) and iron(IV) corroles: synthesis, spectroscopy, structures, and no indications for corrole radicals. *Inorg. Chem.* **2002**, *41* (21), 5433–5439. DOI: 10.1021/ic020118b.

(16) Casitas, A.; Rees, J. A.; Goddard, R.; Bill, E.; DeBeer, S.; Fürstner, A. Two Exceptional Homoleptic Iron(IV) Tetraalkyl Complexes. *Angew. Chem., Int. Ed.* **2017**, *56* (34), 10108–10113. DOI: 10.1002/anie.201612299. Published Online: Mar. 2, 2017.

(17) Lewis, R. A.; Smiles, D. E.; Darmon, J. M.; Stieber, S. C. E.; Wu, G.; Hayton, T. W. Reactivity and Mössbauer spectroscopic characterization of an Fe(IV) ketimide complex and reinvestigation of an Fe(IV) norbornyl complex. *Inorg. Chem.* **2013**, *52* (14), 8218–8227. DOI: 10.1021/ic401096p. Published Online: Jun. 21, 2013.

(18) Bower, B. K.; Tennent, H. G. Transition metal bicyclo[2.2.1]hept-1-yls. *Journal of the American Chemical Society* **1972**, *94* (7), 2512–2514. DOI: 10.1021/ja00762a056.

(19) Kreitner, C.; Heinze, K. Excited state decay of cyclometalated polypyridine ruthenium complexes:Insight from theory and experiment. *Dalton. Trans.* **2016**, *45* (35), 13631–13647. DOI: 10.1039/c6dt01989g.

(20) Dixon, I. M.; Khan, S.; Alary, F.; Boggio-Pasqua, M.; Heully, J.-L. Probing the photophysical capability of mono and bis(cyclometallated) Fe(ii) polypyridine complexes using inexpensive ground state DFT. *Dalton. Trans.* **2014**, *43* (42), 15898–15905. DOI: 10.1039/c4dt01939c.

(21) Newman, C. P.; Casey-Green, K.; Clarkson, G. J.; Cave, G. W. V.; Errington, W.; Rourke, J. P. Cyclometallated platinum(II) complexes: oxidation to, and C-H activation by, platinum(IV). *Dalton Trans.* **2007** (29), 3170–3182. DOI: 10.1039/b705609e. Published Online: Jun. 15, 2007.

(22) Kumar, R.; Nevado, C. Cyclometalated Gold(III) Complexes: Synthesis, Reactivity, and Physicochemical Properties. *Angew. Chem. Int. Ed.* **2017**, *56* (8), 1994–2015. DOI: 10.1002/anie.201607225. Published Online: Jan. 23, 2017.

(23) Cerón-Camacho, R.; Hernández, S.; Le Lagadec, R.; Ryabov, A. D. Cyclometalated Os(C-N)x(N-N)(3-x)m+ mimetics of tris(2,2'-bipyridine)osmium(II): covering a 2 V potential range by known (x = 0, 1) and new (x = 2, 3) species (C-N = o-2-phenylpyridinato). *Chem. Commun.* **2011**, *47* (10), 2823–2825. DOI: 10.1039/c0cc04582a. Published Online: Jan. 14, 2011.

(24) Steube, J.; Burkhardt, L.; Päpcke, A.; Moll, J.; Zimmer, P.; Schoch, R.; Wölper, C.; Heinze, K.; Lochbrunner, S.; Bauer, M. Excited-State Kinetics of an Air-Stable Cyclometalated Iron(II) Complex. *Chem. Eur. J.* **2019**, *25* (51), 11826–11830. DOI: 10.1002/chem.201902488.

(25) Liu, Y.; Harlang, T.; Canton, S. E.; Chábera, P.; Suárez-Alcántara, K.; Fleckhaus, A.; Vithanage, D. A.; Göransson, E.; Corani, A.; Lomoth, R.; Sundström, V.; Wärnmark, K. Towards longer-lived metal-to-ligand charge transfer states of iron(II) complexes: an N-heterocyclic carbene approach. *Chem. Comm.* **2013**, *49* (57), 6412–6414. DOI: 10.1039/C3CC43833C.

(26) Steube, J.; Kruse, A.; Bokareva, O. S.; Reuter, T.; Demeshko, S.; Schoch, R.; Argüello Cordero, M. A.; Krishna, A.; Hohloch, S.; Meyer, F.; Heinze, K.; Kühn, O.; Lochbrunner, S.; Bauer, M. Janus-type emission from a cyclometalated iron(III) complex. *Nat. Chem.* **2023.** DOI: 10.1038/s41557-023-01137-w. Published Online: Feb. 27, 2023.

(27) *CCDC database, entry 2002774*.

(28) Chabera, P.; Kjær, K. S.; Prakash, O.; Honarfar, A.; Liu, Y.; Fredin, L. A.; Harlang, T. B.; Lidin, S.; Uhlig, J.; Sundstrom, V.; Lomoth, R.; Persson, P.; Wärnmark, K.; Chábera, P.; Kjaer, K. S.; Harlang, T. C. B.; Sundström, V. A FeII Hexa N-Heterocyclic Carbene Complex with a 528 ps Metal-to-Ligand Charge-Transfer Excited-State Lifetime // FeII Hexa N-Heterocyclic Carbene Complex with a 528 ps Metal-to-Ligand Charge-Transfer Excited-State Lifetime. *J. Phys. Chem. Lett.* **2018**, *9* (3), 459–463. DOI: 10.1021/acs.jpclett.7b02962.

(29) Kjær, K. S.; Kaul, N.; Prakash, O.; Chábera, P.; Rosemann, N. W.; Honarfar, A.; Gordivska, O.; Fredin, L. A.; Bergquist, K.-E.; Häggström, L.; Ericsson, T.; Lindh, L.; Yartsev, A.; Styring, S.; Huang, P.; Uhlig, J.; Bendix, J.; Strand, D.; Sundström, V.; Persson, P.; Lomoth, R.; Wärnmark, K. Luminescence and reactivity of a charge-transfer excited iron complex with nanosecond lifetime. *Science* **2019**, *363* (6424), 249–253. DOI: 10.1126/science.aau7160.

(30) Prakash, O.; Chábera, P.; Rosemann, N. W.; Huang, P.; Häggström, L.; Ericsson, T.; Strand, D.; Persson, P.; Bendix, J.; Lomoth, R.; Wärnmark, K. A Stable Homoleptic Organometallic Iron(IV) Complex. *Chem. Eur. J.* **2020**, *26* (56), 12728–12732. DOI: 10.1002/chem.202002158. Published Online: Sep. 11, 2020.

(31) Constable, E. C.; Baum, G.; Bill, E.; Dyson, R.; van Eldik, R.; Fenske, D.; Kaderli, S.; Morris, D.; Neubrand, A.; Neuburger, M.; Smith, D. R.; Wieghardt, K.; Zehnder, M.; Zuberbühler, A. D. Control of Iron(II) Spin States in 2,2′:6′,2″-Terpyridine Complexes through Ligand Substitution. *Chem. Eur. J.* **1999**, *5* (2), 498–508. DOI: 10.1002/(SICI)1521-3765(19990201)5:2<498:AID-CHEM498>3.0.CO;2-V.

(32) Toftlund, H. Spin equilibria in iron(II) complexes. *Coord. Chem. Rev.* **1989**, *94*, 67–108. DOI: 10.1016/0010-8545(89)80045-1.

(33) Bunker, G. *Introduction to XAFS*; Cambridge University Press, 2010. DOI: 10.1017/CBO9780511809194.

(34) Bauer, M. HERFD-XAS and valence-to-core-XES:New tools to push the limits in research with hard X-rays? *Phys. Chem. Chem. Phys.* **2014**, *16* (27), 13827–13837. DOI: 10.1039/C4CP00904E.

(35) Zimmer, P.; Burkhardt, L.; Schepper, R.; Zheng, K.; Gosztola, D.; Neuba, A.; Flörke, U.; Wölper, C.; Schoch, R.; Gawelda, W.; Canton, S. E.; Bauer, M. Towards Noble-Metal-Free Dyads: Ground and Excited State Tuning by a Cobalt Dimethylglyoxime Motif Connected to an Iron N-Heterocyclic Carbene Photosensitizer. *Eur. J. Inorg. Chem.* **2018**, *2018* (48), 5203–5214. DOI: 10.1002/ejic.201800946.

(36) Glatzel, P.; Bergmann, U. High resolution 1s core hole X-ray spectroscopy in 3d transition metal complexes—electronic and structural information. *Coord. Chem. Rev.* **2005**, *249* (1-2), 65–95. DOI: 10.1016/j.ccr.2004.04.011.

(37) Bergmann, U.; Glatzel, P. X-ray emission spectroscopy. *Photosynthesis research* **2009**, *102* (2-3), 255–266. DOI: 10.1007/s11120-009-9483-6.

(38) Burkhardt, L.; Holzwarth, M.; Plietker, B.; Bauer, M. Detection and Characterization of Hydride Ligands in Iron Complexes by High-Resolution Hard X-ray Spectroscopy and Implications for Catalytic Processes. *Inorg. Chem.* **2017**, *56* (21), 13300–13310. DOI: 10.1021/acs.inorgchem.7b02063.

(39) Burkhardt, L.; Vukadinovic, Y.; Nowakowski, M.; Kalinko, A.; Rudolph, J.; Carlsson, P.-A.; Jacob, C. R.; Bauer, M. Electronic Structure of the Hieber Anion Fe(CO)3(NO)- Revisited by X-ray

Emission and Absorption Spectroscopy. *Inorg. Chem.* **2020**, *59* (6), 3551–3561. DOI: 10.1021/acs.inorgchem.9b02092. Published Online: Mar. 3, 2020.

(40) Matthias Bauer; Helmut Bertagnolli. X-Ray Absorption Spectroscopy – the Method and Its Applications. In *Methods in Physical Chemistry*; John Wiley & Sons, Ltd, 2012; pp 231–269. DOI: 10.1002/9783527636839.ch7.

(41) Yamamoto, T. Assignment of pre-edge peaks in K-edge x-ray absorption spectra of 3d transition metal compounds: electric dipole or quadrupole? *X-Ray Spectrom.* **2008**, *37* (6), 572–584. DOI: 10.1002/xrs.1103.

(42) Staroverov, V. N.; Scuseria, G. E.; Tao, J.; Perdew, J. P. Comparative assessment of a new nonempirical density functional: Molecules and hydrogen-bonded complexes. *The Journal of Chemical Physics* **2003**, *119* (23), 12129–12137. DOI: 10.1063/1.1626543.

(43) Weigend, F.; Ahlrichs, R. Balanced basis sets of split valence, triple zeta valence and quadruple zeta valence quality for H to Rn: Design and assessment of accuracy. *Phys. Chem. Chem. Phys.* **2005**, *7* (18), 3297–3305. DOI: 10.1039/b508541a.

(44) Kenjiro Tsutsumi; Hiroo Nakamori; Kouichi Ichikawa. X-ray Mn Kβ emission spectra of manganese oxides and manganates. *Phys. Rev. B* **1976**, *13* (2), 929. DOI: 10.1103/PhysRevB.13.929.

(45) Pollock, C. J.; Delgado-Jaime, M. U.; Atanasov, M.; Neese, F.; DeBeer, S. Kβ mainline X-ray emission spectroscopy as an experimental probe of metal-ligand covalency. *J. Am. Chem. Soc.* **2014**, *136* (26), 9453–9463. DOI: 10.1021/ja504182n.

(46) Kowalska, J. K.; Hahn, A. W.; Albers, A.; Schiewer, C. E.; Bjornsson, R.; Lima, F. A.; Meyer, F.; DeBeer, S. X-ray Absorption and Emission Spectroscopic Studies of [L2Fe2S2]n Model Complexes: Implications for the Experimental Evaluation of Redox States in Iron–Sulfur Clusters. *Inorganic Chemistry* **2016**, *55* (9), 4485–4497. DOI: 10.1021/acs.inorgchem.6b00295.

(47) Lee, N.; Petrenko, T.; Bergmann, U.; Neese, F.; DeBeer, S. Probing valence orbital composition with iron Kbeta X-ray emission spectroscopy. *J. Am. Chem. Soc.* **2010**, *132* (28), 9715–9727. DOI: 10.1021/ja101281e.

(48) Raebiger, H.; Lany, S.; Zunger, A. Charge self-regulation upon changing the oxidation state of transition metals in insulators. *Nature* **2008**, *453* (7196), 763–766. DOI: 10.1038/nature07009.

(49) Sit, P. H.-L.; Car, R.; Cohen, M. H.; Selloni, A. Simple, unambiguous theoretical approach to oxidation state determination via first-principles calculations. *Inorg. Chem.* **2011**, *50* (20), 10259–10267. DOI: 10.1021/ic2013107. Published Online: Sep. 16, 2011.

(50) Knizia, G. Intrinsic Atomic Orbitals: An Unbiased Bridge between Quantum Theory and Chemical Concepts. *J. Chem. Theory Comput.* **2013**, *9* (11), 4834–4843. DOI: 10.1021/ct400687b. Published Online: Oct. 17, 2013.

(51) Walsh, A.; Sokol, A. A.; Buckeridge, J.; Scanlon, D. O.; Catlow, C. R. A. Electron Counting in Solids: Oxidation States, Partial Charges, and Ionicity. *J. Phys. Chem. Lett.* **2017**, *8* (9), 2074–2075. DOI: 10.1021/acs.jpclett.7b00809.

(52) Walsh, A.; Sokol, A. A.; Buckeridge, J.; Scanlon, D. O.; Catlow, C. R. A. Oxidation states and ionicity. *Nature materials* **2018**, *17* (11), 958–964. DOI: 10.1038/s41563-018-0165-7. Published Online: Oct. 1, 2018.

(53) Štekláč, M.; Breza, M. On the relation between oxidation states and d-electron populations of the 1st row transition metal complexes I. Tetrachloro complexes. *Polyhedron* **2021**, *201*, 115172. DOI: 10.1016/j.poly.2021.115172.

(54) Chaudhari, A.; Lee, S.-L. Theoretical study of 3d-metal mononitrides using DFT method. *Int. J. Quantum Chem.* **2007**, *107* (1), 212–218. DOI: 10.1002/qua.21060.

(55) Aullón, G.; Alvarez, S. Oxidation states, atomic charges and orbital populations in transition metal complexes. *Theor Chem Acc* **2009**, *123* (1-2), 67–73. DOI: 10.1007/s00214-009-0537-9.

(56) Glendening, E. D.; Landis, C. R.; Weinhold, F. Natural bond orbital methods. *WIREs Comput Mol Sci* **2012**, *2* (1), 1–42. DOI: 10.1002/wcms.51.

(57) Reed, A. E.; Curtiss, L. A.; Weinhold, F. Intermolecular interactions from a natural bond orbital, donor-acceptor viewpoint. *Chem. Rev.* **1988**, *88* (6), 899–926. DOI: 10.1021/cr00088a005.

(58) Fredin, L. A.; Pápai, M.; Rozsályi, E.; Vankó, G.; Wärnmark, K.; Sundström, V.; Persson, P. Exceptional Excited-State Lifetime of an Iron(II)-N-Heterocyclic Carbene Complex Explained. *J. Phys. Chem. Lett.* **2014**, *5* (12), 2066–2071. DOI: 10.1021/jz500829w.

(59) Thom, A. J. W.; Sundstrom, E. J.; Head-Gordon, M. LOBA: a localized orbital bonding analysis to calculate oxidation states, with application to a model water oxidation catalyst. *Physical chemistry chemical physics : PCCP* **2009**, *11* (47), 11297–11304. DOI: 10.1039/b915364k. Published Online: Oct. 19, 2009.

(60) Chabera, P.; Liu, Y.; Prakash, O.; Thyrhaug, E.; Nahhas, A. E.; Honarfar, A.; Essen, S.; Fredin, L. A.; Harlang, T. C. B.; Kjaer, K. S.; Handrup, K.; Ericson, F.; Tatsuno, H.; Morgan, K.; Schnadt, J.; Haggstrom, L.; Ericsson, T.; Sobkowiak, A.; Lidin, S.; Huang, P.; Styring, S.; Uhlig, J.; Bendix, J.; Lomoth, R.; Sundstrom, V.; Persson, P.; Wärnmark, K. A low-spin Fe(iii) complex with 100-ps ligand-to-metal charge transfer photoluminescence. *Nature* **2017**, *543* (7647), 695–699. DOI: 10.1038/nature21430.

(61) Dixon, I. M.; Alary, F.; Boggio-Pasqua, M.; Heully, J.-L. The (N4C2)2- donor set as promising motif for bis(tridentate) iron(II) photoactive compounds. *Inorg. Chem.* **2013**, *52* (23), 13369–13374. DOI: 10.1021/ic402453p.

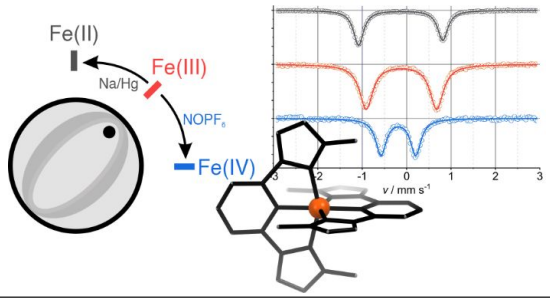
Fe(II)
Na/Hg
Fe(III)
NOPF6
Fe(IV)
-3
-2
-1
0
1
2
3
v / mm s-1

3.3.4. Photocatalysis with CCC complexes

As presented in chapter 3.3.2, the CCC-iron(III) complex **16a** ($[Fe(ImP^{H})_2]^{+}$) shows a 4.6 ns lifetime of its excited MLCT state and reactivity towards both oxidative and reductive quenchers. The possible photoredox reaction pathways together with the obtained results of the quenching experiments are summarized in Scheme 14. The potentials of the excited states (given vs. SCE as reference) were determined by the following equations for the excited state reduction potential $E^{*/-}$ (Eq. (3.1)) and oxidation potential $E^{+/*}$ (Eq. (3.2)), respectively, with the reduction potential E_{red}, the oxidation potential E_{ox} and the 0-0 transition energy $E_{0,0}$, obtained by the center of the overlap of the absorption and emission bands.

$$E^{*/-} = E_{red} + E_{0,0} \tag{3.1}$$

$$E^{+/*} = E_{ox} - E_{0,0} \tag{3.2}$$

As becomes apparent, the strongly oxidizing and reducing MLCT state should be capable of many different photocatalytic transformations, while the LMCT state still should be able to partake in some photocatalytic reactions, as the excited state redox potentials are comparable to those of $[Ru(bpy)_3]^{2+}$. The limitation will be the sub-ns lifetime, rendering diffusion-limited photocatalytic transformations unlikely (1.1). Hence, the MLCT excited state is more promising to show catalytic activity.

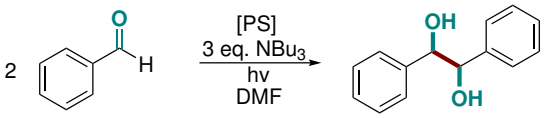

17 **18**

Scheme 13: Reductive coupling of aromatic aldehydes using the transformation of benzaldehyde to hydrobenzoin as an example, as described by the group of Rueping.[151]

Hence, a test reaction exploiting the strongly reducing MLCT excited state was chosen. Of particular interest is a C-C coupling reaction, the homocoupling of benzaldehyde **17** to hydrobenzoin **18** (Scheme 13). It was first described by the Rueping group,[151] requires strongly reducing excited states and is easily followed *via* NMR-spectroscopy.

For the experiments performed here, PS (**16a**, 1 mol-%) and diisopropylethylamine (DIPEA, 3 eq.) were used. The reactions were carried out in deuterated solvents and illumi-

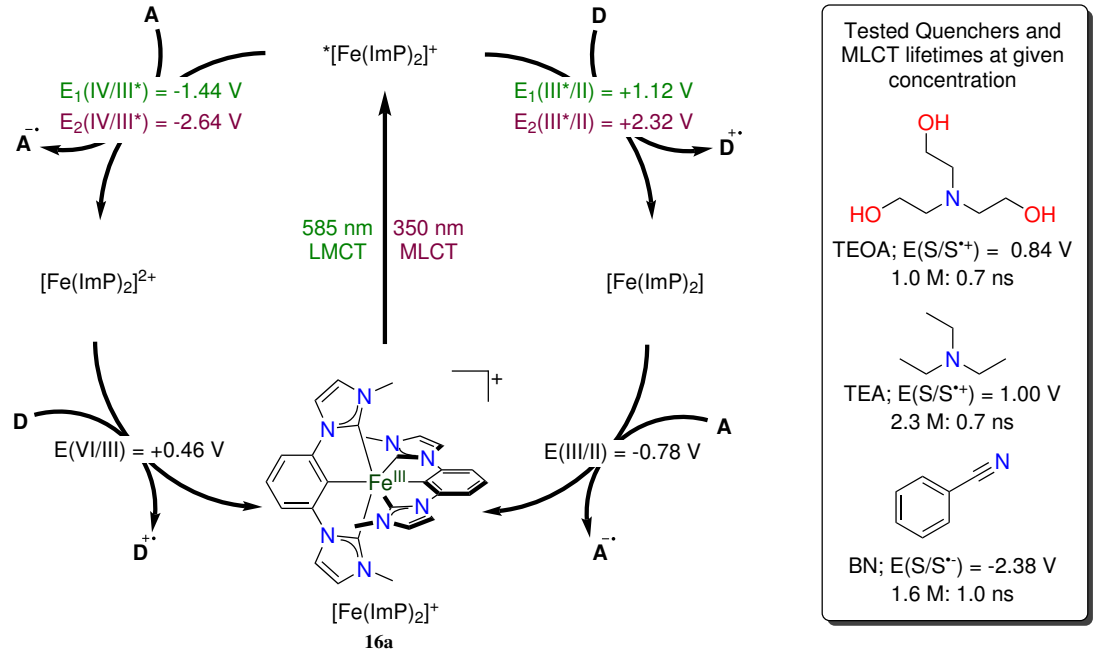

Scheme 14: Photocatalytic reaction pathways following oxidative and reductive quenching, as a graphical summary of the results of Scheme 3.3.2. The excited-state potentials for the LMCT and MLCT are shown in green and purple, respectively. The quenching agents triethylamine (TEA), triethanolamine (TEOA), and benzonitrile (BN), their oxidation or reduction potential, as well as the concentration used and the resulting MLCT lifetime obtained by streak-camera measurements in the quenching experiments are shown on the right side.

nated with a 300 W Xenon lamp (LOT LS0400), equipped with an AM1.5 filter, which leads to a light intensity of approximately 300 mW $\cdot$ cm^{-2}. The conversion of benzaldehyde was examined after 17 hours, analysing the reaction solution via NMR spectroscopy. This was done by comparing the integral of the aldehyde peak of benzaldehyde to the integral of the benzylic protons of hydrobenzoin.

$$X = \frac{n_{BA,0} - n_{BA}}{n_{BA,0}} \tag{3.3}$$

$$n_{BA,0} = n_{BA} + 2n_{HB} \tag{3.4}$$

$$n_{BA} \widehat{=} I_{BA}; n_{HB} \widehat{=} \frac{1}{2} I_{HB} \tag{3.5}$$

$$X = \frac{I_{HB}}{I_{HB} + I_{BA}} \tag{3.6}$$

As the radical reaction produces a mixture of *meso*- and *D/L*-hydrobenzoin, two singlets are observed, one for each diastereomer. The conversion X is calculated by equation 3.3. If side reactions are neglected, the amount of benzaldehyde at the start ($n_{BA,0}$) equals the current amount of benzaldehyde (n_{BA}) and two times the amount of hydrobenzoin (n_{HB}) (Eq. (3.4)). The relation between the integrals of the NMR signals I_{BA} and I_{HB} and their

corresponding amount is given in Eq. (3.5). Inserting Eq. 3.4 and 3.5 into Eq. 3.3 results in Eq. 3.6, which allows to calculate X directly from the NMR signals intensities. Even though this method neglects side reactions and does not give yields, it provides good and quick results for optimization reactions.

Selected optimization parameters and corresponding X, calculated from at least three reactions under identical conditions, are given in Tables 2 and 3. The first step was to find the optimal solvent (entries 1-4, Table 2). Typically, dry solvents give significantly higher yields. Although DMF gave the best results for Rueping and Che,[151,152] the best conversions in this test were obtained in acetonitrile (84 %) and THF (80 %). Besides a working photocatalytic reaction with an iron compound, something rather unusual was observed. The ratio of the diastereomers *meso* and *D/L*-**18**, as observed in the NMR spectra, deviated from 1:1, which would be expected for a standard radical reaction. In this case, the D/L-diastereomer was formed dominantly, up to a ratio of 4:1. This means that it is unlikely that the reaction proceeds according to the previously published mechanisms. Since the mechanism remains elusive, further optimization was performed. After finding the best solvent, the illumination was improved. All following reactions (Table 3) were performed under these improved conditions.

Table 2: Solvent optimization for the homocoupling of benzaldehyde.

Entry	PS mol-%	Solvent	Electron donor	Conversion
1	1	MeCN (not dried)	Diisopropylethylamine	25 %
2	1	MeCN (dry)	**Diisopropylethylamine**	84 %
3	1	THF (dry)	**Diisopropylethylamine**	80 %
4	1	DMF (dry)	Diisopropylethylamine	50 %

The next optimization step was testing different electron donors (entries 5-9), where both tributylamine and triethanolamine (TEOA) provided almost quantitative conversions (98 % and 95 % respectively). Since the results are similar but the latter is less toxic and more environmentally compatible,[153,154] it was chosen as the electron donor for further experiments. The next step was optimizing the equivalents of added electron donor (entries 10 and 11). An increase to six equivalents led to a conversion of 98 %. Similarly, a decrease in photosensitizer concentration to 0.5 mol-% led to a yield of 97 % (entry 12). This shows that a higher ratio of quencher to photosensitizer, whether obtained by increasing the quencher concentration or decreasing the photosensitizer, leads to better results. This may be explained by the relatively low lifetime of the excited state, where

Table 3: Further optimization parameters for the homocoupling of benzaldehyde under improved lighting conditions.

Entry	PS mol-%	Solvent	Electron donor	Conversion
5	1	MeCN (dry)	Triethylamine	88 %
6	1	MeCN (dry)	**Tributylamine**	98 %
7	1	MeCN (dry)	Diisopropylethylamine	92 %
8	1	MeCN (dry)	Hantzsch ester	-
9	1	MeCN (dry)	**Triethanolamine**	95 %
10	1	MeCN (dry)	**Triethanolamine (6 equiv)**	98 %
11	1	MeCN (dry)	Triethanolamine (2 equiv)	94 %
12	**0.5**	MeCN (dry)	**Triethanolamine (3 equiv)**	97 %
13	1 $[Ru(bpy)_3]^{2+}$	MeCN (dry)	Triethanolamine (3 equiv)	80 %
14	1 $[Ir(ppy)_2(bpy)]^{+}$	MeCN (dry)	Triethanolamine (3 equiv)	85 %
15[a]	1	MeCN (dry)	Triethanolamine (3 equiv)	-
16	-	MeCN (dry)	Triethanolamine (3 equiv)	80 %
17	1	MeCN (dry)	-	-
18[b]	1	MeCN (dry)	Triethanolamine (3 equiv)	-
19	1 $FeCl_3$	MeCN (dry)	Triethanolamine (3 equiv)	-
20	1 **16a**$^{-}$ (Fe^{II})	MeCN (dry)	Triethanolamine (3 equiv)	-

a: No light. b: 400 nm longpass filter.

a certain concentration of the quencher is needed to provide diffusion-controlled quenching (Ch. 1.1, eq. 1.7), or by the self-quenching of the excited MLCT state at higher concentrations. Hence, almost quantitative conversion of the substrate is possible under the right conditions. A comparison to the noble-metal photosensitizers $[Ru(bpy)_3]^{2+}$ and $[Ir(ppy)_2(bpy)]^{+}$ was made. Under conditions with 3 equiv. TEOA, they showed a conversion of 80 and 85 % respectively, lower than that achieved by using the iron sensitizer. Without light, no reaction was observed, but with light and without photosensitizer, a conversion of 80 % was observed as well. This result was surprising, but under these conditions, benzaldehyde itself may be able to act as a photosensitizer, as it absorbs light up to 370 nm. If a 400-nm longpass filter is used for the reaction to exclude excitation of benzaldehyde, no conversion is observed. This was expected since the MLCT states of the iron complex can only be accessed with UV-light as well, with an absorption maximum at 350 nm. Therefore, the complex and benzaldehyde cannot be excited individually to identify the photoactive compound in this reaction. But from the increased yield and the change in the *meso*- to *D/L*-ratio of hydrobenzoin, as well as the high dependency on the quencher concentration, it becomes apparent that the iron complex plays a major role.
To rule out that the iron does not act solely as a catalyst instead of a photocatalyst, $FeCl_3$ was added to the reaction mixture instead of the photosensitizer. This did not yield any product, hence inhibits the reaction. Thus, **16a** itself is needed to increase the yield and

to lead to the observed ratio of diastereomers. To examine whether an iron(II) intermediate plays a role in the catalytic cycle (as in reductive quenching, Scheme 14, right side of the cycle), the reduced complex **16a**$^-$ was added to the solution. In this case, no product formation was observed as well, showing that the iron(II) complex does not play a role in the catalytic cycle and actually inhibits product formation. Although the exact mechanism of this reaction remains still ambiguous, a potential application was shown for this first dual-emitting iron photosensitizer, demonstrating the immense potential of this compound class.

Chapter Summary

In this chapter, the first application of the iron(III) complex **16a** as a photosensitizer in reductive homocoupling of benzaldehyde with hydrobenzoin was investigated, which is a well-established photoreaction and therefore suitable as a benchmark for highly reductive photosensitizers. The conversion of the reaction was followed by ^{1}H-NMR, providing fast results. Optimization of reaction parameters showed that dry solvents were indispensable for high yields. Almost quantitative conversions were achieved in acetonitrile with triethanolamine as a quencher. Both 1 mol-% **16a** with 6 equivalents of quencher and 0.5 mol-% **16a** with 3 equivalents triethanolamine were found to be optimal. This shows that a higher ratio of quencher to photosensitizer is needed for an efficient reaction. An interesting observation is that formation of the *D/L*-hydrobenzoin diastereomer is preferred (4:1 *D/L*:*meso*) when **16a** is used, since reference measurements with different systems show an equal distribution of diastereomers. High yields are also observed without photosensitizers, which may be the result of direct excitation of benzaldehyde, which leads to the formation of benzaldehyde radicals. Nevertheless, **16a** is necessary for higher yields and the diastereomer ratio. The cause of the latter is still unknown, and experiments trying to resolve the origin were unsuccessful. Hence, further studies have to be conducted: laser-flash photolysis to resolve the mechanism of this reaction, or X-ray spectroscopic methods to identify the reactive species.

3.3.5. Backbone-functionalized CCC-complexes

Based on the promising results obtained for the parent CCC-complex, backbone-substituted complexes were synthesized from the ligands introduced in chapter 3.3.1. There are two ways to obtain the desired complexes **16a**–**h** (Scheme 15). The first possibility is the previously presented route via transmetalation with a zirconium reagent (Ch. 3.3.2). The second route was developed together with Ulises Carillo. With this approach, the proligand is deprotonated with lithium hexamethyldisilazane (LiHMDS, $LiN(SiMe_3)_2$) to generate the free carbene. This reacts with iron(II) hexamethyldisilazane (FeHMDS, $[Fe(N(SiMe_3)_2)_2]$), which can be formed *in situ* by reacting $FeBr_2$ and LiHMDS. Due to the release of dimethylamine during the reaction, the transmetalation route does not work well with substrates sensitive to nucleophilic substitution.

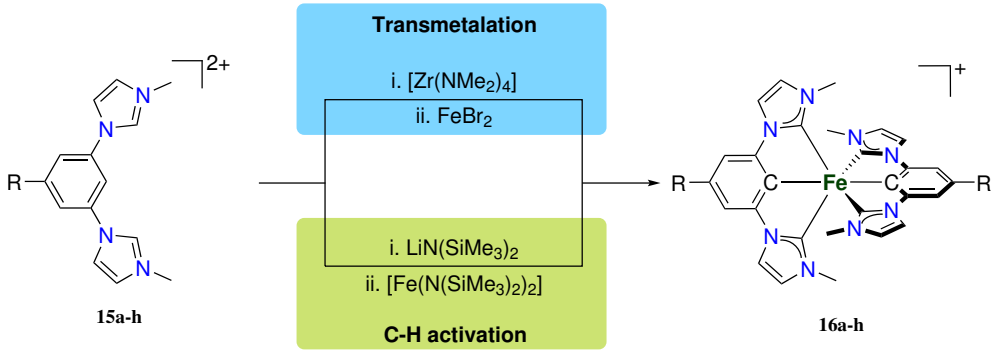

Scheme 15: Formation of cyclometalated carbene complexes **16a**–**h** via the route of transmetalation and CH-activation.

This was the case for ligand **15f**, with a CF_3-function in the ligand backbone. Transmetalation did not lead to the desired compound. Instead, a complex with an amidinium group in the backbone was obtained (Scheme 16), as the fluorides were substituted by the *in situ* formed dimethylamine. A similar observation was made by Nicole Dickman during the work for her Master's thesis, where carboxy-functionalized CCC-complexes were approached. Starting with an ester-functionalized ligand, a complex with a carboxyamide-functionalization was obtained in the end. This slowly decomposed further towards the beforehand described amidinium complex. The heteroleptic complex with one amide and one amidinium group was also observed, presumably being a transitional product. Obviously, the reactivity of the backbone towards nucleophiles is induced by coordination, even though the exact mechanism remains elusive. This makes these complexes attractive to functionalization on the complex, as nucleophiles are able to change the electronic

properties, enable coupling with catalysts, or heterogenization on semiconductor surfaces.

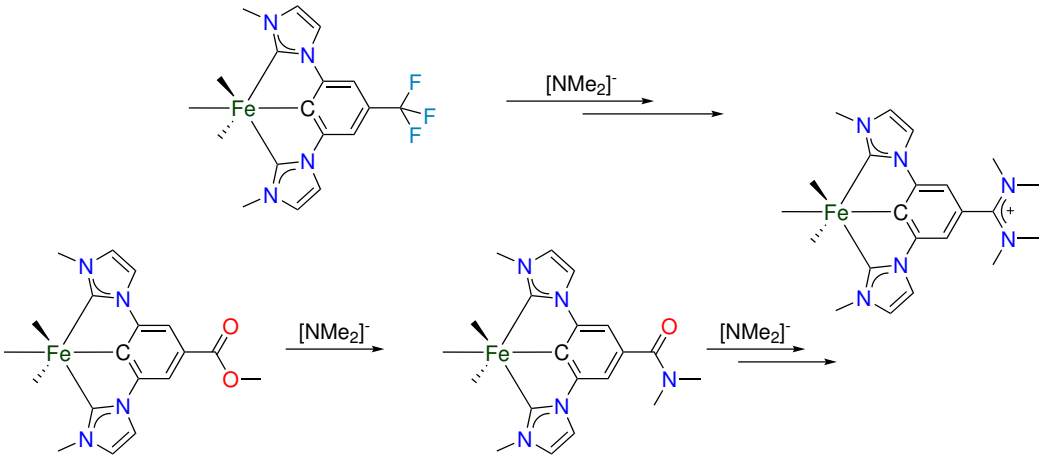

Scheme 16: Observed nucleophilic substitution reactions.

Yet to achieve a specific functionalization, substitution has to be avoided in the beginning. Hence, the zirconium reagent $Zr(NMe_2)_4$ was first exchanged for one with a non-nucleophilic base instead of NMe_2^-. The $Zr(TMP)_4$ reagent, developed by the Knochel group,[155] seems like a perfect candidate for this, as arylation reactions were described for this compound. Unfortunately, only very low yields (< 1 %) were obtained for both the CF_3 and the ester functionalized ligand, presumably due to the sterically crowded metal center. Therefore, a new method based on C-H-activation of the deprotonated ligand by FeHMDS was developed.

With this method, CF_3-functionalized complex **16f** could finally be obtained in 57 % yield. Unfortunately, the reaction was developed late in this project. Therefore, the coordination of ester-functionalized ligands was not repeated with this method and will not be discussed further. The yields for complexes **16a**–**h** are shown in table 4. The amidine complex is not included, since it was isolated in pure form. In most cases, yields are quiet low, the reason is still unknown. The chemical identity of these complexes was confirmed with ^{1}H-NMR, ESI-MS, elemental analysis and single-crystal X-ray diffraction analysis, with the exception of **16g** and **16h**, where no single crystals could be obtained due to formation of fine needles. While ESI-MS and ^{1}H-NMR suggest a clean **16g**, the elemental analysis shows large deviations from the calculated value. Therefore, if the elemental analysis result is not the result of a faulty measurement, the impurities should be of an inorganic nature without any redox transitions, since no additional transitions

were observed in CV. Thus, the complex will be treated as formally clean.

Table 4: Yields for the synthesis of CCC-complexes.

16	−R	Yield for **16**
a	−H	47 %
b	−Br	15 %
c	−Me	20 %
d	−*t*Bu	8 %, 63 %[a]
e	−OMe	27 %, 7[a] %
f	$-CF_3$	57 %[a]
g	$-OCF_3$	7 %, 8 %[a]
h	−CN	16 %[a]

a: obtained with the C-H-activation route.

Despite complexes **16a**–**h** being paramagnetic, ^{1}H-NMR is a viable tool to determine the purity of these complexes. Impurities like solvent residues could be easily detected and were found at the ususal shifts. Signals of all ligand protons were detected and integrated, with the exception of the backbone methyl protons in **16c**. X-ray diffraction shows that the substitution does not change the Fe-C bond lengths or other structure parameters significantly. Hence, all observed substitution effects stem from the electronic structure.

Table 5: Potentials of the metal-centered redox events of the substituted complexes **16a**–**h**, obtained by cyclic voltammetry of the respective compound (10^{-3} M in 0.1 M nBu$_4$PF$_6$ MeCN solution).

16	−R	$E(Fe^{III/II})$	$E(Fe^{IV/III})$
		[V vs Fc.]	
a	−H	-1.16	0.08[a]
b	−Br	-1.10	0.19
c	−Me	-1.22	0.00
d	−*t*Bu	-1.36	-0.06
e	−OMe	-1.35	-0.11
f	$-CF_3$	-0.96	0.32
g	$-OCF_3$	-0.93	0.16
h	−CN	-0.78	0.26

a: quasireversible transition

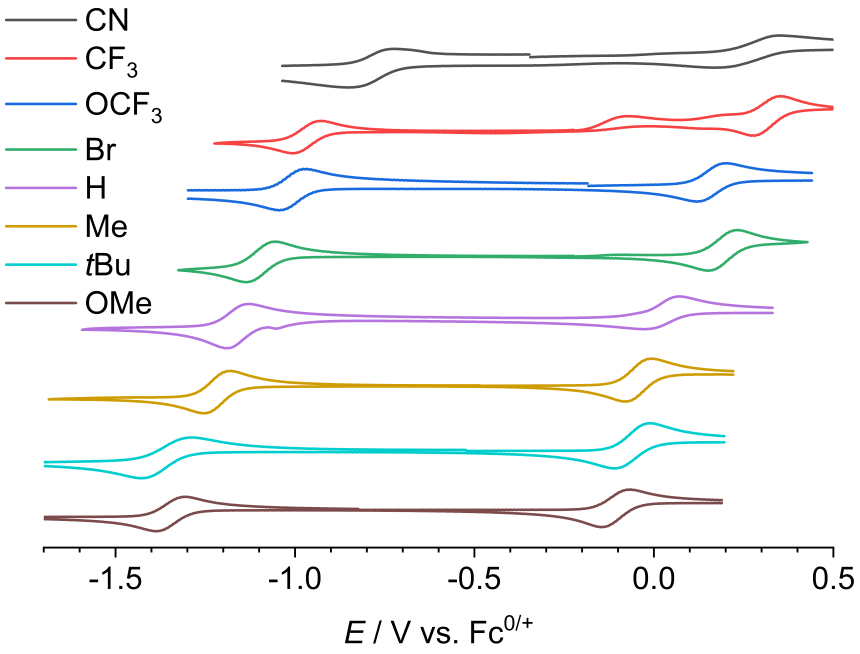

Figure 15: Cyclic voltammetry in comparison for complexes **16a**–**h** at a concentration of 1 mM in 0.1 M $N(Bu)_4(PF_6)$ MeCN solution with a scan rate of 100 mV/s.

To get a first insight on this, the ground state properties of these complexes were investigated. First, cyclic voltammetry was performed (Fig. 15). The potentials of the reduction to iron(II) and oxidation to iron(IV) are given in table 5. As expected, electron donating substituents like -OMe or -*t*Bu shift both oxidation and reduction potential cathodically. This can be explained by an increase of electron density on the metal center, which destabilize the ground state and resulting in lowered potentials. The opposite effect is observed for electron withdrawing groups like -CF_3 and -CN, leading to reduced electron density on the metal center, shifting the potentials anodically. In the case of the CF_3 group, irreversible oxidation processes are observed before the metal oxidation event. These are possibly located on the ligand. Further studies using spectroelectrochemistry can be performed to investigate the effect.

Based on these results, the influence of substituents on the electronic transitions was investigated with UV-Vis spectroscopy (Fig. 16). The broad LMCT absorption band, which can be observed between 450 and 750 nm, shows a comparable structure for all complexes and a clear: With increasing electron donor strength (from CF_3 to OMe), the energetically lowest absorption feature of the LMCT band gets shifted towards lower energies (Tab. (6)). Since both the Br and CN functionalized complexes deviate from this trend, approximate π-energies were calculated. The energy of the LMCT (E_{LMCT}) is equal to the difference of the energy of the singly occupied t_{2g} orbital (E_{SOMO}, SOMO: singly

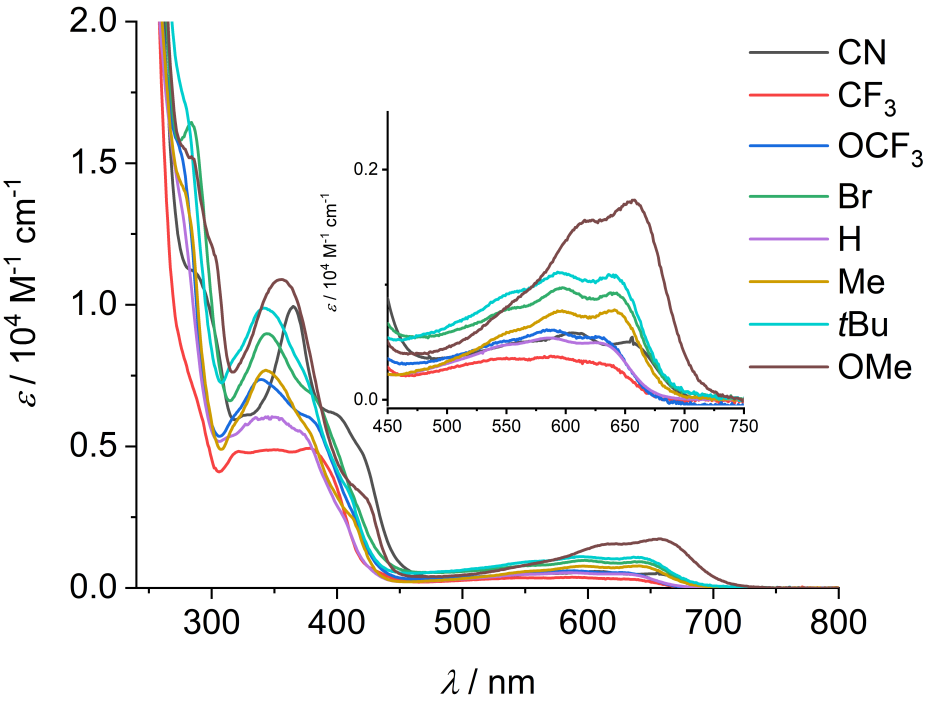

Figure 16: UV-Vis spectra of **16a**–**h** ($2.5{\cdot}10^{-5}$ M in MeCN) with the LMCT absorption bands enlarged in the inset.

occuppied molecular orbital), into which LMCT transitions occur,[156] and the π-energy E_π (Eq. 3.7). The energy of the SOMO can be approximated from cyclic coltammetry as $-E_{Fe^{III/II}}$ (Eq. 3.8). Since going to positive (anodic) potentials in cyclic voltammetry corresponds to a shift to negative energies, the negative value of the redox potential has to be taken. Inserting Eq. (3.8) into Eq. (3.7) and solving for E_π leads to Eq. (3.9) (Tab. (7)).

$$E_{LMCT} = E_{SOMO} - E_\pi \tag{3.7}$$

$$E_{SOMO} \mathrel{\widehat{=}} - E_{Fe^{III/II}} \tag{3.8}$$

$$E_\pi = -E_{\mathrm{Fe^{III/II}}} - E_{LMCT} \tag{3.9}$$

Here, a destabilization of the π-energies with increasing donor strength can be observed. Whether the influence on the π or metal energies is predominant depends on the functional group. For the Me-, *t*Bu-, and OMe-complexes, destabilization of the π-orbital dominates, while for the Br- and CN-complexes a greater effect on the metal center is observed. Hence, the LMCT energy is in most cases smaller than in the unfunctionalized complex. Both CF_3- and OCF_3-functionalized complexes show only small deviations in the LMCT

Table 6: Wavelength and Extinction coefficients of the maxima in the LMCT and MLCT band.

16	−R	$\lambda_{max}(\epsilon_{LMCT})$ [nm (10^4 M^{-1} cm^{-1})]	$\lambda_{max}(\epsilon_{MLCT})$
a	−H	585 (0.054)	351 (0.60)
b	−Br	597 (0.097)	344 (0.90)
c	−Me	641 (0.078)	343 (0.77)
d	−*t*Bu	593 (0.11)	342 (0.99)
e	−OMe	657 (0.17)	355(1.09)
f	$-CF_3$	587 (0.038)	378 (0.49)
g	$-OCF_3$	589 (0.060)	339 (0.74)
h	−CN	605 (0.055)	365 (0.99)

absorption, since comparable shifts in metal and ligand energies are observed. Not only does the LMCT energy change upon substitution, but the extinction coefficients also change. While they remain below 2000 $M^{-1}cm^{-1}$, introduction of electron donor groups leads to a drastic increase (Tab. (6)). The effect is most pronounced in the case of the OMe-functionalized complex **16e**, where the extinction coefficient is found to be more than three times higher than that of the non-functionalized complex. This may be due to additional the π-electrons from the ether functionality.

Table 7: Energetically lowest LMCT transition, the respective energy, the MLCT transition energy, π and π^* energies and π-π^* gap energy.

16	-R	$\lambda_{LMCT,Emin}$ [nm]	$E_{LMCT,Emin}$	E_{MLCT}	E_π [eV]	$E_{\pi*}$	$\Delta E_{\pi-\pi*}$
a	-H	630	1.97	3.53	-0.81	3.61	4.42
b	-Br	640	1.94	3.60	-0.84	3.79	4.63
c	-Me	641	1.93	3.62	-0.71	3.62	4.33
d	-*t*Bu	639	1.94	3.63	-0.58	3.57	4.15
e	-OMe	657	1.89	3.49	-0.54	3.38	3.92
f	$-CF_3$	633	1.96	3.57	-1.00	3.89	4.89
g	$-OCF_3$	628	1.97	3.66	-1.04	3.82	4.86
h	-CN	654	1.90	3.40	-1.12	3.66	4.77

The increase in absorptivity is also found in the MLCT band. Here, the methoxy-compound again shows the highest extinction coefficient. The trifluoromethyl-substituted complex shows the lowest extinction coeffecient, which is often observed for these substituents.[129] This results in a nearly flat MLCT absorption band. In general, a slight shift of the absorption maximum towards higher energies for electron donors can be observed.

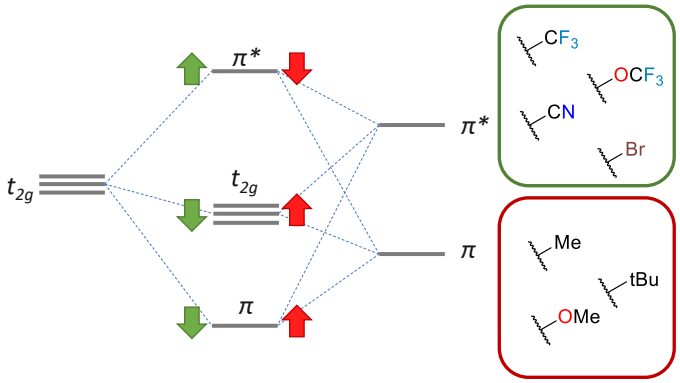

Figure 17: Schematic MO diagram to show the influences of functional groups on energy levels. Electron-withdrawing groups (green arrows) destabilize the t_{2g} levels, as well as the π and π*-levels. The opposite is true for electron-donating groups (red arrows).

$$E_{MLCT} = E_{\pi*} - E_{HOMO} \tag{3.10}$$

$$E_{HOMO} \widehat{=} - E_{Fe^{IV/III}} \tag{3.11}$$

$$E_{\pi*} = E_{MLCT} - E_{\mathrm{Fe^{IV/III}}} \tag{3.12}$$

From the energies of the MLCT transitions E_{MLCT} (Eq. (3.10)) and $E_{\mathrm{Fe^{IV/III}}}$ (Eq. (3.11)), approximate π*-energies were calculated (Eq. (3.12), Tab. (7)). It was more difficult to determine the energetically lowest transition in the MLCT band. Therefore $\lambda_{MLCT,max}$ was chosen, except for the CF_3 functionalized complex. In this case the energy of the central transition (347 nm) was chosen. It corresponds with high certainty to the transition of $\lambda_{MLCT,max}$ in the other complexes. In this case, electron donating substituents lead to stabilization and electron withdrawing substituents to destabilization of the π* energies. This effect is also observed for various ruthenium and iridium systems, where electron withdrawing groups on the cyclometalating ligand lead to an increase in the MLCT energy while increasing the redox potential.[11,47,48,99,100]

Consequently, a shift in the π-π* gap is observed for complexes **16a**–**h**. The OMe-complex shows the smallest gap, as it is expected due to the additional π-electrons of the ether function. Generally, the gap decreases with stronger donors, since π-energies are increased and π*-energies are decreased. From these observations, a schematic MO diagram can be constructed to summarize the influences of the functional groups on the metal center and the ligand (Fig. 17). When these influences are compared, it becomes clear that there is no obvious trend in when the influence is more pronounced on the metal or ligand energies and is highly dependent on the functional group. Therefore, it can not be predicted how the LMCT or MLCT shifts upon substitution. As a result, this constitutes

a basis for further (TD)DFT analysis. Here, possible effects leading to this behavior may be identified, as well as identifying pathways in the excited state landscape.

Table 8: Wavelength of the emission maxima for both low energy ($\lambda_{Em,LMCT}$) and high energy ($\lambda_{Em,MLCT}$) emission band, the high-energy shoulder of the LMCT emission ($\lambda_{Em,LMCT,shoulder1}$), and the stokes shifts ΔE for the LMCT and MLCT, obtained by fluorescence spectroscopy ($2.5 \cdot 10^{-5}$ M in MeCN) after excitation between 340 and 360 nm.

16	−R	$\lambda_{Em,LMCT,max}$	$\lambda_{Em,LMCT,shoulder1}$ [nm]	$\lambda_{Em,MLCT}$	ΔE_{LMCT} [eV]	ΔE_{MLCT}
a	−H	735	675	430	0.43	0.65
b	−Br	741	683	433	0.40	0.74
c	−Me	730	682	435	0.24	0.76
d	−*t*Bu	722	684	425	0.37	0.71
e	−OMe	738	710	448	0.21	0.73
f	$-CF_3$	748	672	423	0.45	0.35
g	$-OCF_3$	733	674	425	0.41	0.74
h	−CN	760	691	446	0.42	0.62

The excited state behavior was first investigated *via* emission spectroscopy. Excitation into the LMCT band of all the complexes led to a low-intensity emission, as previously observed for the parent complex **16a** (chapter 3.3.2).[156] It becomes more intense, if the MLCT band is excited (Fig. 18, a.), which shows a much higher absorptivity. Then, also a second emission band is visible, like observed for the parent complex, proving that the dual emission is no singular event, but a property inherent to this compound class. The LMCT emission will be discussed first. It is broad and represents the mirrored band structure of the LMCT absorption profiles for all complexes. It ranges from 630 nm up into the NIR region beyond 900 nm, with the peak maxima[vi] between 720 and 750 nm (Tab. (8)). Hence, the influence on the energetic position of the LMCT state is rather small. Still, a trend can be observed, if the position of the first shoulder is considered (Fig. 18 bottom right). The Stokes shifts of the LMCT ΔE_{LMCT} remain in the region of 0.4 eV, comparable to the parent complex. Both Me- and OMe-functionalized complexes show a smaller Stokes shift of about 0.2 eV. This is due to the fact that the energetically lowest absorption band shows the highest intensity in these compounds.

The high-energetic shoulder of the LMCT band follows roughly the trend described previously for the absorption spectra for the differences in ligand and metal energy. Thus,

[vi] The emission bands are very broad (Fig. 18), thus the maximum itself does not differ too much from the rest of the peak.

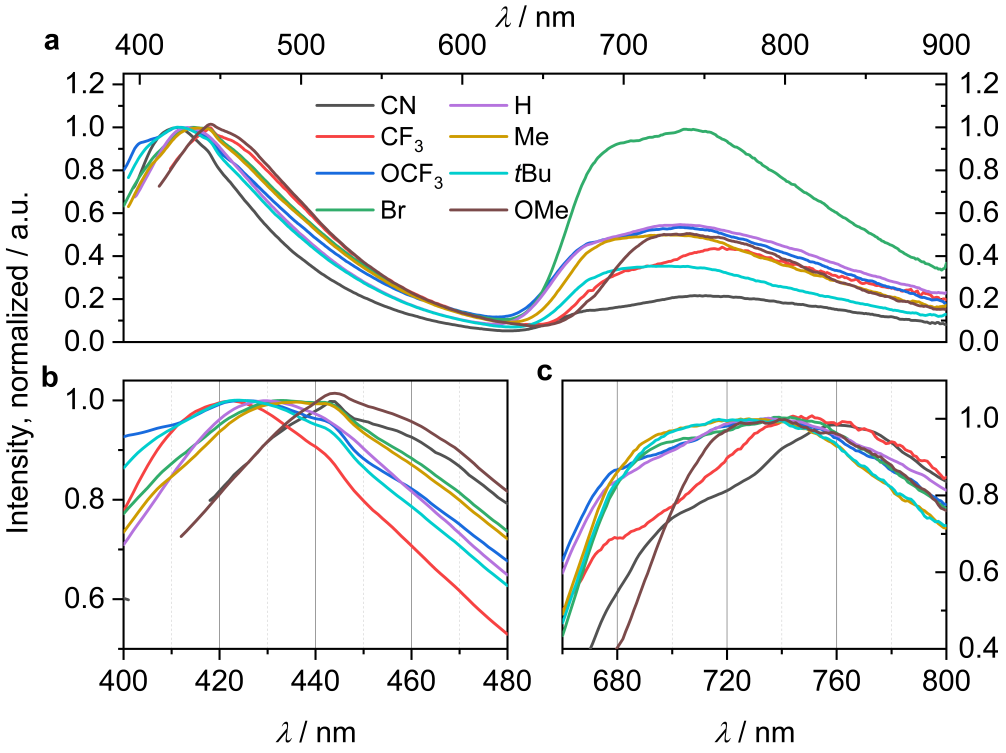

Figure 18: Emission spectra of **16a**–**h** (2.5 10^{-5} M in degassed MeCN, excited in the high-energy absorption band). **a**, Complete spectra normalized on the high-energy emission. **b**, High-energy bands, normalized. **c**, Low-energy bands, normalized.

nitrile and methoxy functionalized complexes show the energetically lowest LMCT transitions. Likewise, CF_3, as well as OCF_3, show the energetically highest LMCT emission band. The MLCT band on the other hand behaves differently (Tab. (8)). Here, the different Stokes shifts ΔE_{MLCT} lead to differences of up to 0.14 eV, with the exception of the CF_3-functionalized complex. Here, the energetically lowest band is the most intense, leading to a small Stokes shift of 0.35 eV. In the other complexes, moderate ΔE_{MLCT} between 0.62 and 0.76 eV are observed, indicating stronger excited state distortions than in the LMCT. Interestingly, the Me functionalized complex shows a higher Stokes shift than the *t*Bu-complex. Altough they show the same maximum in the MLCT absorption band, a difference of 10 nm between their emission bands is observed. This behavior may have two reasons. Either, distortion of the excited states leads to different Stokes shifts, or the absorption maximum in the MLCT band does not correspond to the emissive state and only few of the underlying transitions of the MLCT band lead to the high-energy emission. From the current results, both reasons are viable. Yet, the excitation spectra for the MLCT-emissions are inconconclusive. Although they follow the general absorption profile, they show small deviations in the band structure. This supports the hypothesis that not all transitions in the MLCT band lead to MLCT emission.

Despite the observed differences in emission energies, the $E_{0,0}$ transitions of the LMCT

and MLCT states remain in the same range of around 1.9 and 3.1 eV (± 0.1 eV), respectively. Hence, the ground state redox potentials (calculated *via* Equations 3.2 and 3.1) determine the excited state potentials (tab. 9). These are discussed in the following.

Table 9: Excited state potentials for the LMCT and MLCT of the substituted complexes.

16	−R	E_{LMCT}(III*/II)	E_{LMCT}(IV/III*)	E_{MLCT}(III*/II)	E_{MLCT}(IV/III*)
		[V vs. Fc] / [V vs. SCE]			
a	−H	0.74 / 1.12	-1.82 / -1.44	1.94 / 2.32	-3.02 / -2.64
b	−Br	0.77 / 1.15	-1.68 / -1.30	2.07 / 2.45	-2.98 / -2.60
c	−Me	0.66 / 1.04	-1.87 / -1.49	1.98 / 2.36	-3.19 / -2.81
d	−*t*Bu	0.51 / 0.89	-1.93 / -1.55	1.85 / 2.23	-3.27 / -2.89
e	−OMe	0.46 / 0.84	-1.92 / -1.54	1.82 / 2.20	-3.28 / -2.90
f	$-CF_3$	0.94 / 1.32	-1.58 / -1.20	2.14 / 2.52	-2.78 / -2.40
g	$-OCF_3$	0.97 / 1.35	-1.74 / -1.36	2.17 / 2.55	-2.94 / -2.56
h	−CN	1.02 / 1.40	-1.54 / -1.16	2.32 / 2.70	-2.84 / -2.46

Considering LMCT states, the electron-withdrawing substituted complexes **16f**–**h** show a stronger oxidizing state than the unfunctionalized complex, being in the range of $[Ru(bpz)_3]^{2+}$ (bpz = 2,2'-bipyrazine)($E(PS^*/PS^-)$ = 1.07 V),[17] which is commonly used for oxidative transformations. The -OMe and -*t*Bu-complexes show strongly reducing LMCT states, which are comparable to the $[Fe(phtmeimb)_2]^+$ (phtmeimb = phenyl(tris(3-methylimidazol-1-ylidene))borate) complex ($E(PS^+/PS^*)$ = -1.9 V),[109] which recently was tested in photocatalytic applications.[116] The question remains if the lifetime of the LMCT state is sufficient for photocatalytic reactions, as it was determined to be 0.24 ns for **16a**. This combined with a low quantum yield, may result in non-optimal conditions for photocatalysis. The MLCT lifetime of the parent complex on the other hand showed a lifetime of around 4.6 ns, making this state more promising, which was proven by first catalytic experiments (Ch. 3.3.4). Here, the electron-withdrawing functionalized complexes **16f**–**h** are the most oxidizing compounds again and the OMe and *t*Bu-complexes the most reducing, showing a shift of around -0.25 V respective to the unsubstituted complex. These should be able to react in most known reduction reactions, like reductive dehalogenations of aryl bromides and activated aryl chlorides, since they exceed the reduction potential of even chlorobenzene (-2.78 V vs. SCE).[157] To see whether the excited state lifetimes remain in the region of catalytic activity, TCSPC measurements were employed. The fluorescence decays were measured at 720 nm for the LMCT and 550 nm for the MLCT state, respectively, after excitation at 374 nm. For a better comparison, the previously

investigated **16a** was measured again under the same conditions. The results are shown in table 10.

Table 10: Excited-state lifetimes of the LMCT (τ_{LMCT}) and MLCT ($\overline{\tau}_{MLCT}$ for the intensity-weighted average lifetime and $\langle\tau_{MLCT}\rangle$ for the amplitude-weighted average lifetime) obtained by TC-SPC measurements at 374 nm excitation and detection at 720 nm (LMCT) and 550 nm (MLCT). The experimental details and specifics on the analysis are found in chapter 5.2.10.

16	−R	τ_{LMCT}	$\overline{\tau}_{MLCT}$ [ns]	$\langle\tau_{MLCT}\rangle$
a	−H	0.24	4.51	2.61
b	−Br	0.29	3.23	2.97
c	−Me	0.21	4.73	2.94
d	−*t*Bu	0.23	5.20	2.96
e	−OMe	0.26	4.86	3.02
f	$-CF_3$	0.37	4.25	3.10
g	$-OCF_3$	0.29	4.46	3.33
h	−CN	0.28	4.79	3.48

For the LMCT lifetime, usually two exponentials were needed to provide a good fit ($\chi^2 \leq 1.2$). The decay with the highest amplitude can be attributed to the LMCT-state, while the smaller amplitude corresponds to the tail of the MLCT emission. This lifetime was excluded from the discussion of the LMCT states, as it does not belong to the LMCT. The impact of backbone-functionalization on the LMCT-lifetimes is relatively low, those are in a range of 0.21 and 0.29 ns. The notable exception is complex **16f** ($-CF_3$), where the lifetime is prolonged to 0.37 ns, an increase of around 50 % respective to **16a**. The determination of MLCT lifetime at 550 nm has proven to be more demanding, as four exponentials were required in the fit for a $\chi^2 \leq 1.2$. In every fit, a low ps lifetime was required. This can be attributed to scattering and fitting artifacts, and was thus excluded from the analysis of the decays. The other lifetimes were in the ranges of 0.7 ns, 3-4 ns and 10-13 ns (Table 11 in the experimental part). The origin of these different lifetimes is still unclear as is their physical significance. A possible explanation is that torsion of the ligands is leading to different environments, in which deactivation is more or less favored, hence leading to these lifetimes. Another explanation involves three independent states, emitting in the same energetic region. Further research has to be done to exclude one of these hypotheses. It becomes apparent that the emission behavior is complex, both in the spectral and the temporal domain and that even the description of two emitting states is just a model of the actual behavior.

For this necessary simplification, it is important to average the lifetimes, also due to the

nature of multiexponential fits. To understand the issue, a closer look on the processing of the data is needed. The formula shown in (3.13) describes the fitting function. $I(t)$ is the intensity of the whole decay curve at time t, the pre-exponential factor B_i describes the amplitude of a lifetime τ_i at a given time.

$$I(t) = \sum_i B_i \cdot exp(t/\tau_i) \tag{3.13}$$

$$\overline{\tau} = \frac{\sum_i B_i \tau_i^2}{\sum_i B_i \tau_i} \tag{3.14}$$

$$\langle \tau \rangle = \frac{\sum_i B_i \tau_i}{\sum_i B_i} \tag{3.15}$$

The problem of multi-exponential decays and the applied least-square fitting is that it can lead to parameter correlation of amplitudes and lifetimes, resulting in imprecise values.[31] Hence, the single lifetimes and their amplitudes have to be regarded with some suspicion and have to be interpreted conservatively. Therefore, the averaged lifetime has more informative value, since the whole decay is considered. There are two average lifetimes found in the literature, the intensity-weighted average lifetime $\overline{\tau}$ and the amplitude-weighted lifetime $\langle \tau \rangle$ (Eq. 3.14 and 3.15).[158,159] $\overline{\tau}$ can be explained as different excited state populations weighted by their relative contribution to the whole fluorescence.[160] $\langle \tau \rangle$ on the other hand describes the lifetime of a fluorophore, which has the same steady-state fluorescence as the multicomponent fluorophore.[160] Sillen and Engelborghs discussed in great detail which average fluorescence lifetime is appropriate for which case.[160] While $\overline{\tau}$ is the actual description of how long a fluorophore spends in the excited state before the average population reaches 1/e, $\langle \tau \rangle$ is the proper average lifetime for discussing reactivity and obtaining radiative rate and quenching constants.

As given in table 10, the amplitude-weighted lifetimes are much shorter than the intensity-weighted lifetimes. Yet the latter are similar to those obtained from streak-camera measurements (Scheme 3.3.2).[156] This is good, as the lifetimes were obtained in a similar manner and validate these results. As shown in table 10, a trend for $\overline{\tau}_{MLCT}$ is observable. While the electron-donating *t*Bu, OMe and Me functionalized complexes result in a higher lifetime than the unfunctionalized compound, $\overline{\tau}_{MLCT}$ is shorter in the OCF_3 and CF_3 complexes. The CN and Br-functionalized complexes do not follow this trend. The first shows a higher lifetime, while the latter shows the lowest $\overline{\tau}_{MLCT}$. This may be due to Br causing ISC through heavy-atom effect, which would make a deactivation by quartet states of excited MLCT states into LMCT or MC states possible. Since the LMCT-lifetime decays monoexponentially, it is more likely that the Br leads to different branching dynamics by incorporating ISC. That could give a smaller population of the

longer-lived MLCT states and a higher population of the energetically-low LMCT states. This would also be an explanation for the higher relative population of the LMCT state (Fig. 18).
$\langle\tau_{MLCT}\rangle$ shows a contradictive trend, where electron-withdrawing groups lead to increased lifetimes compared to the electron-donating groups. Yet all complexes have a higher lifetime than the unfunctionalized compound.

Chapter Summary

In this chapter, the influence of phenyl backbone substitution was investigated in order to establish structure-property relationships. A series of complexes was synthesized with the electron withdrawing CN-, CF_3-, OCF_3- and Br-groups, as well as the electron donating Me-, *t*Bu- and OMe- groups. The complexes were characterized in their ground and excited states.
The experiments show that there is no simple approach to tuning the ground and excited states. This can be explained by the fact that the electron donating and withdrawing capabilities influence the metal center as well as the π- and π*-energies, leading to different energies of the two emissive states. Nevertheless, a basic understanding of the behavior was obtained. Cyclic voltammetry revealed the expected cathodic shifts (destabilization) of metal-centered redox events with increasing electron donor strength and anodic shifts (stabilization) for electron withdrawing groups. The absorption spectra indicate that electron donating functions destabilize the π-orbitals more than the metal orbitals, leading to decreased LMCT energies. Both the Br and CN functionalized complexes show the opposite behavior, where the metal is more stabilized than the ligand. In the CF_3 and OCF_3 complex, both states are affected in the same way. For the MLCT state, no clear trend was found for an increased influence on the π* or the metal center. However, the π*-energies follow the opposite trend as the π-energies: Electron-withdrawing groups destabilize the π* orbitals, while electron-donating groups stabilize them.
Although the substitution effects on the LMCT absorption can be transferred to the LMCT emission, the MLCT emission shows a different behavior. The Stokes shifts remain in the same range. However, they show differences of up to 0.14 eV. Thus, the excited states show different distortions. Nevertheless, the $E_{0,0}$ transitions remain roughly in the same energy range. Consequently, the changes in the ground state redox properties determine the excited state potentials. Due to the cathodic shifts caused by electron donating groups, the MLCT potential becomes even more reducing. Therefore, these complexes can potentially reduce even chlorobenzene.
The lifetimes of the different states were determined by TCSPC. For the LMCT state,

a higher lifetime was observed for the electron-withdrawing functionalized complexes. In contrast, the MLCT state did not show a monoexponential fluorescence decay, but had to be fitted with three meaningful lifetimes and one correlating to scattered light. This decay behavior is the same for all complexes and requires the calculation of an average lifetime. While in the literature the amplitude-averaged lifetime is the proper average lifetime, the intensity-averaged lifetime is the one that shows a clear trend. Longer lifetimes are achieved by electron donating groups, while electron withdrawing groups lead to shorter lifetimes.

4. Conclusion

The goal of the present thesis was to develop and characterize cyclometalated iron photosensitizers to rationalize the impact of cyclometalation on the ground and excited states and to determine the viability of this approach. New synthetic routes for both CNN and CCC cyclometalated iron complexes were developed, resulting in a wide variety of complexes. In the terpyridine-based compounds, the monocyclometalated complex demonstrated the strong influence of cyclometalating functions on the ground and excited states. It was shown that the catalytically active MLCT states were prolonged by exchanging a pyridine function for an anionic phenyl donor. Further development of a defined synthesis route for biscyclometalating complexes was not successful, although over a hundred different reactions were carried out. In this work, common synthetic routes for cyclometalation reactions were examined for feasibility. It was shown that complex formation is likely, but that reductive elimination from the iron(III) complex occurs, leading to decomposition of the complexes. Therefore, increasingly electron-poor ligands were used to stabilize the complex. Using the method of σ-bond metathesis and a ligand with three CF_3 and two fluoride functionalizations, an inseparable mixture of different biscyclometalated complexes was obtained. Two different products crystallized from the separation. This led to the identification of an important mechanistic step: A reductive elimination of ethane from the intermediate dimethyl complex, which led to the oxidative addition of C-F bonds, resulting in the formation of different complexes.

The CCC complexes, on the other hand, were obtained in pure form. These combine two phenylene moieties with four *N*-heterocyclic carbenes. The parent iron(III) complex of this class of compounds exhibits a Janus-type dual emission due to the fundamentally opposing metal-to-ligand and ligand-to-metal charge transfer states. The MLCT emission has a long lifetime of 4.6 ns, while the LMCT state is rather short-lived with 0.2 ns. Quenching experiments confirmed the reactivity of the MLCT state. Since DFT calculations suggest that the first oxidation and reduction events are metal-centered, the reduced and oxidized complexes were approached. Ground state characterization by Mössbauer spectroscopy, magnetic measurements, HERFD-XANES, VtC- and CtC-XES as well as NBO analysis of these complexes confirm the assumption that the first redox event, both reductive and oxidative, is metal-centered. Excited state characterization showed that both the iron(II) and iron(IV) complexes do not possess photoactive properties, as their CT states are short-lived.

Therefore, the iron(III) complex was further investigated for its reactivity in photocatalytic applications. Due to the strongly reducing nature of the MLCT states, the reductive coupling of benzaldehyde was chosen as a benchmark reaction. Here, a conversion to hydrobenzoin was observed in first experiments. Consequently, the reaction conditions were

optimized, leading to an almost quantitative conversion. This could not be achieved with either a ruthenium or an iridium photosensitizer under the same conditions. Although the reaction without photosensitizer also showed a high conversion, the iron compound was necessary for the higher conversion. In addition, it leads to increased formation of the *D/L* diastereomer of hydrobenzoin. Further investigation of this mechanism is required to rationalize the role of the iron complex. Laser flash photolysis should provide greater insight into the reaction pathway.

Since this compound shows activity in photocatalytic applications, a systematic study of substitution of electron donating and withdrawing groups on the phenyl moiety was performed. Experiments aimed at investigating the impact of different functional groups on the ground- and excited-state electronic structure and the photodynamics. Cyclic voltammetry confirmed that electron-donating groups lead to cathodically shifted potentials, whereas electron-withdrawing groups shift the potentials anodically. The effect on the absorption and emission of MLCT and LMCT is rather small and leads to unexpected effects in the MLCT emission, which does not follow the trend of the MLCT absorption maxima. Therefore, either transitions different from the absorption maximum or excited state distortions must be responsible for the observed differences. Thus, detailed (TD)DFT studies are needed to rationalize these effects.

The excited state lifetimes of these complexes were subsequently investigated by TCSPC. It was shown that electron withdrawing groups increase the lifetime of the LMCT but decrease the lifetime of the MLCT state. Since the lifetime of the MLCT state remains in the ns-range, photocatalytic activity of all complexes can be expected. Since the absorption and emission bands of the complexes remain in the same energetic region, the $E_{0,0}$ energies vary only by a negligible amount. Therefore, the excited state redox potentials are dominated by the ground state potentials. Thus, the methoxy- and *tert*-butyl-substituted complexes exhibit MLCT redox potentials, which may allow the reduction of chlorobene. This reaction is a benchmark for strongly reducing photosensitizers. Therefore, future work must focus on the photocatalytic capabilities of the photosensitizers discussed within this thesis.

The overall goal of developing new iron-based cyclometalated complexes and obtaining insight into their electronic structure and excited state behavior was achieved. The combination of a cyclometalated function with N-heterocyclic carbenes resulted in CCC complexes characterized by unprecedented dual emission and exceptionally long excited states. First structure-property relationships were established by investigating a series of functionalized complexes. It was demonstrated that these complexes can be used in photocatalytic applications and may complement or even replace noble metal photosensitizers in the future.

5. Experimental Part

5.1. General work techniques

Reactions under inert conditions were conducted in an argon-filled glovebox or using standard Schlenk techniques under argon atmosphere (Argon 5.0 was used). The vacuum of up to 10^{-3} mbar was generated with a rotary vane pump. The glassware was heated in a vacuum with a heatgun, flooded with argon and left to cool under vacuum for three times prior to use. Solids were filled in counterflow, while fluids were injected through a septum. Dry solvents were obtained from an MBraun SPS-800 solvent drying system and were subsequently stored over 3 Å molecular sieve.[161] Dry acetonitrile for spectroscopy was obtained by passing it through a column of MP Biomedicals MP Alumina N-Super I, which was activated in an oven at 150 °C for multiple days. Solvents and solutions were degassed by either bubbling a solvent-saturated argon flow through the solution or with the freeze-pump-thaw technique. There, the medium in a Schlenk flask was evacuated under vacuum, after being frozen in liquid nitrogen, until a minimum pressure was reached. Afterwards, the flask was thawed under static vacuum in a lukewarm water bath. The cycles were repeated until the pressure did not increase after freezing the medium.
Chemicals were used without further purification. Solvents were technical grade, except for acetonitrile, which was HPLC grade, and solvents for spectroscopy. Reactions were heated in oil baths, sand baths, and on aluminum blocks, and the temperatures given are the set temperatures.

5.2. Analytical and spectroscopic methods

5.2.1. Column chromatography

For manual column chromatography, silica with 60 Å pore size, neutral alumina or C18-silica was used. Automatic column chromatography was performed with a CombiFlash RF+ MPLC from Teledyne Isco, with prepacked silica columns. For fraction control and determination of the ideal eluents, thin layer chromatography with silica plates and fluorescence indicator was used.

5.2.2. NMR spectroscopy

NMR spectra were recorded on a Bruker Avance 300, a Bruker Avance 500 and a Bruker Ascent 700. The chemical shifts are given in [ppm], the coupling constants in [Hz]. The chemical shifts are referenced to the residue of the non-deuterated solvents.[162]

5.2.3. IR spectroscopy

IR-spectra were obtained with the Vertex 70 FT-IR spectrometer from Bruker in ATR mode, which enables the measurement without an additional medium.

5.2.4. Mass spectrometry

ESI mass spectra were measured on a SYNAPT G2 quadropole TOF mass spectrometer from Waters. The solutions were around c = 10^{-5} M in acetonitrile.

5.2.5. Elemental analysis

Elemental analysis was measured with a vario MicroCube from elementar, giving the content of carbon, nitrogen, hydrogen, and sulfur in the sample.

5.2.6. Single-crystal X-ray diffraction

The single-crystal data were recorded using a Bruker SMART CCD area detector diffractometer equipped with a graphite monochromator. The measurements were carried out using Mo K_α radiation ($\lambda = 0.71073\,\text{Å}$) at a temperature T = 120(2) K.

5.2.7. Cyclic voltammetry

The cyclic and square wave voltammetry measurements were performed at room temperature in 0.1 M $[(nBu)_4N][PF_6]$ dry acetonitrile with an analyte concentration of 0.001 M under a solvent-saturated Argon atmosphere. A three electrode arrangement with a 1 mm Pt working electrode and Pt-wire counter electrode (Metrohm) and a custom-built Ag/AgCl reference electrode was used, with the PGSTAT101 potentiostat from Metrohm. Ferrocene was added after the measurements as an internal standard. All potentials were referenced against the $Fc^{0/+}$ couple. The voltammograms were analyzed using the NOVA software (version 2.1.3), reversibility was investigated with the criteria proposed by Nicholson[163,164] and the Randles-Sevcik[165,166] equation.

5.2.8. UV-Vis spectroscopy

UV-Vis spectra were recorded on a Varian Cary 50 and a PerkinElmer Lambda 465 single-beam spectrophotometer at a concentration of around 10^{-5} M in acetonitrile in 10 mm pathlength quartz cuvettes. The precise concentration was determined by weighing both the solvent and the sample and calculating the exact solvent volume from the corresponding density. From this, the extinction coefficient was determined with the Beer-Lambert law, which was plotted against the wavelength.

5.2.9. Steady-state emission spectroscopy

Samples for emission spectroscopy were degassed by the previously described techniques (Ch. 5.1). The emission spectra were recorded with an Edinburgh Instruments FLS1000 spectrometer with single monochromators and a red-extended PMT-980 detector.

5.2.10. Time-Correlated Single Photon Counting

The samples were prepared analogous to the steady-state emission samples (Scheme 5.2.9). Time correlated single photon counting was measured using a Horiba Ultima-01-DD (Horiba Jobin Yvon GmbH). The sample solution was excited at 374 nm using a Horiba DD375L laser diode with a maximum repetition rate of 100 MHz. The decays of the emission were measured at the specified wavelengths. Repetitive start-stop signals were recorded by a multi-channel analyzer until one of the channels reached 10000 counts. A histogram of photons was recorded as a function of 16383 channels on a time-range of 100 ns (6.4 ps per channel). The decays were analyzed together with the instrument response function (IRF) in the EzTime software from Horiba. The IRF was measured at 374 nm using a scatter solution of dispersed LUDOX in water. Fitting of the decays followed the procedure of increasing the number of fitted exponentials (Equation (3.13), also depicted below), until the χ^2 parameter was smaller than 1.2. The goodness of the fit was reviewed by looking at the residuals, to see, whether they are statistically aligned around 0. The MLCT emission of the complexes in Ch. 3.3.5 required four exponentials, the LMCT emission 2-3 exponentials. Of the four exponentials of the MLCT fit, one was always in a range of 3-60 ps. This very short lifetime can attributed to artifacts and/or stray light. Hence, it was not included in the calculations of the average lifetimes ($\overline{\tau}$ and $\langle\tau\rangle$, Eq. 3.14 and 3.15, shown below). Of the exponentials required to fit the LMCT emission decay, only the sub-ns lifetime is attributed to the LMCT band, since the longer lifetime(s) originate from the spectral tail of the MLCT emission.

$$I(t) = \sum_i B_i \cdot exp(t/\tau_i)$$

$$\overline{\tau} = \frac{\sum_i B_i \tau_i^2}{\sum_i B_i \tau_i}$$

$$\langle\tau\rangle = \frac{\sum_i B_i \tau_i}{\sum_i B_i}$$

The results from these Equations are presented in Table 11, together with the relative amplitudes of the decay, obtained from $A_i = \frac{B_i}{\sum_i B_i}$ for both two and three exponentials.

Table 11: Results for Time-Correlated Single Photon Counting of complexes **16a**–**h**. B_i represents the amplitudes and τ_i the lifetimes obtained from Eq. 3.13. The relative Amplitudes A_i show the fraction of the respective amplitude to the sum of amplitudes with the exclusion of an ultrashort component. give the value for either three or two exponentials (A_1 excluded from the calculation) with the associated average lifetime $\tau_{av,i}$.

16	-R	λ	B_1	B_2	B_3	τ_1	τ_2	τ_3	A_1	A_2	A_3	$\overline{\tau}$	$\langle\tau\rangle$
		[nm]	[a.u.]			[ns]			[a.u.]			[ns]	
a	−H	550	$6.50{\cdot}10^{-3}$	$3.89{\cdot}10^{-3}$	$6.96{\cdot}10^{-4}$	0.69	3.85	13.60	0.59	0.35	0.06	4.51	2.61
		720	1.00			0.24			1.00			0.24	
b	−Br	550	$9.74{\cdot}10^{-3}$	$1.37{\cdot}10^{-2}$	$2.33{\cdot}10^{-3}$	0.66	3.42	10.03	0.38	0.53	0.09	3.23	2.97
		720	1.00			0.29			1.00			0.29	
c	−Me	550	$1.2{\cdot}10^{-2}$	$9.76{\cdot}10^{-3}$	$2.80{\cdot}10^{-3}$	0.67	3.53	11.00	0.50	0.39	0.11	4.73	2.94
		720	1.00			0.21			1.00			0.21	
d	−*t*Bu	550	$1.12{\cdot}10^{-2}$	$7.45{\cdot}10^{-3}$	$1.90{\cdot}10^{-3}$	0.64	3.97	12.76	0.55	0.36	0.09	5.20	2.96
		720	1.00			0.23			1.00			0.23	
e	−OMe	550	$1.21{\cdot}10^{-2}$	$8.24{\cdot}10^{-3}$	$1.86{\cdot}10^{-3}$	0.76	4.08	13.05	0.55	0.37	0.08	4.86	3.02
		720	1.00			0.26			1.00			0.26	
f	$-CF_3$	550	$1.24{\cdot}10^{-3}$	$1.04{\cdot}10^{-2}$	$1.93{\cdot}10^{-3}$	0.80	4.06	12.72	0.50	0.42	0.08	4.25	3.10
		720	1.00			0.37			1.00			0.37	
g	$-OCF_3$	550	$1.05{\cdot}10^{-2}$	$8.46{\cdot}10^{-3}$	$2.26{\cdot}10^{-3}$	0.97	4.05	11.62	0.50	0.40	0.11	4.46	3.33
		720	1.00			0.29						0.29	
h	−CN	550	$1.86{\cdot}10^{-3}$	$1.33{\cdot}10^{-3}$	$3.05{\cdot}10^{-3}$	1.06	4.58	13.38	0.53	0.38	0.09	4.79	3.48
		720	1.00			0.28			1.00			0.28	

5.3. Synthesis

5.3.1. Ligand synthesis

Synthesis of 3-(Dimethylamino)-1-(2-phenyl)-2-propen-1-one (1a)

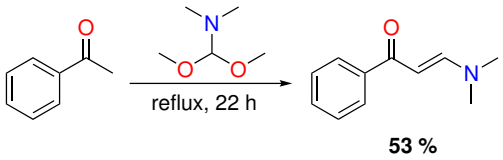

Acetophenone (9.6 g, 80 mmol) and N,N-Dimethylformamide dimethyl acetal (10.0 g, 80 mmol) were heated to reflux for 22 h. After cooling, acetone (10 mL) and pentane (20 mL) were added. The orange suspension was filtered and the residue was washed with more pentane until the filtrate ran colorless. The product (7.4 g, 42 mmol, **53 %**) was obtained after drying thoroughly under reduced pressure. The ^{1}H-NMR spectrum corresponds to the literature,[167] therefore the compound was used without further purification.
^{1}**H-NMR** (500 MHz, Chloroform-d): δ (ppm) = 7.89 (dt, J = 6.9, 1.5 Hz, 2H), 7.79 (d, J = 12.4 Hz, 1H), 7.47 – 7.37 (m, 3H), 5.71 (*d*, J = 12.4 Hz, 1H), 3.11 (s, 3H), 2.92 (s, 3H).

Synthesis of 3-(Dimethylamino)-1-(2-pyridyl)-2-propen-1-one (1b)

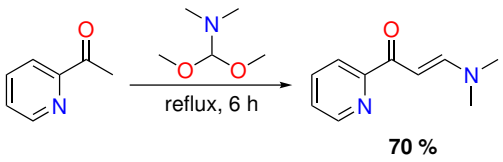

The synthesis is described in the supplementary information of the publication "Excited-State Kinetics of an Air-Stable Cyclometalated Iron(II) Complex", see C.1 under "Synthesis".

Synthesis of 6-phenyl-2,2'-bipyridine (2)

Synthesis using acetylpyridine and **1a**:

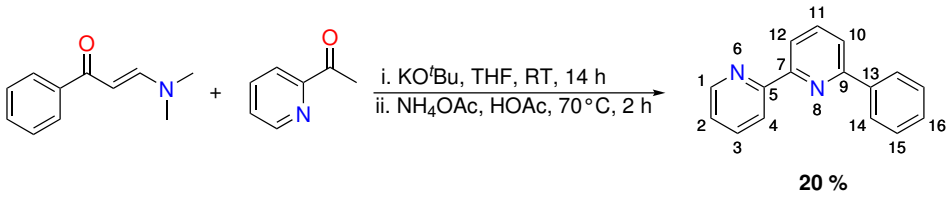

Under argon, to KOtBu (9.0 g, 80 mmol) in THF (100 mL), acetylpyridine (4.9 g, 40 mmol) was added. The solution was stirred for 2 h at room temperature. Afterwards, **1a** (7.0 g, 40 mmol) was added. The suspension was stirred for further 14 h. Afterwards, ammonium acetate (30.8 g, 400 mmol) and acetic acid (50 mL) were added. The THF was distilled off over the course of 2 h. The acetic acid was removed afterwards under reduced pressure. The black oily residue was treated with water (100 mL) and sodium carbonate. The aqueous phase was extracted with DCM (3 x 40 mL). The combined organic phases were dried over magnesium sulfate and the solvent was removed under reduced pressure. The black oil was purified by filtration over silica, with toluene as eluent. The orange oil after evaporation of the solvent was recrystallized from first hexane and then methanol, yielding **2** as a colorless solid (1.9 g, 8 mmol, **20 %**).

Synthesis using acetophenone and **1b**:

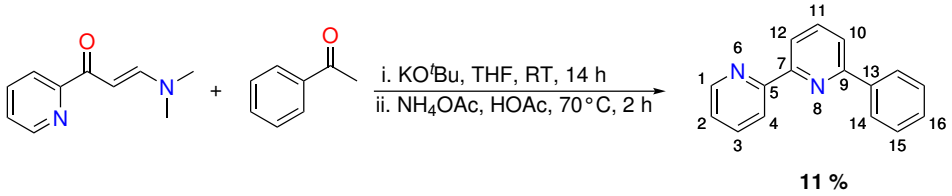

11 %

Under argon, to KOtBu (9.0 g, 80 mmol) in THF (100 mL), acetylpyridine (4.9 g, 40 mmol) was added. The solution was stirred for 2 h at room temperature. Afterwards, **1a** (7.0 g, 40 mmol) was added. The suspension was stirred for further 14 h. Afterwards, ammonium acetate (30.8 g, 400 mmol) and acetic acid (50 mL) were added. The THF was distilled off over the course of 2 h. The acetic acid was removed afterwards under reduced pressure. The black oily residue was treated with water (100 mL) and sodium carbonate. The aqueous phase was extracted with DCM (3 x 40 mL). The combined organic phases were dried over magnesium sulfate and the solvent was removed under reduced pressure. The black oil was purified by filtration over silica, with toluene as eluent. The orange oil after evaporation of the solvent was recrystallized from hexane, yielding **2** as a colorless solid (0.9 g, 4 mmol, **11 %**).

^{1}**H-NMR** (700 MHz, Chloroform-d): δ (ppm) = 8.70 (dd, J = 4.8, 1.4 Hz, 1H, **4-H**), 8.65 (dd, J = 8.0, 1.2 Hz, 1H, **1-H**), 8.39 (dd, J = 7.8, 1.1 Hz, 1H, **12-H**), 8.18 – 8.14 (m, 2H, **14-H**), 7.88 (td, J = 7.8, 1.1 Hz, 1H, **11-H**), 7.86 – 7.81 (m, 1H, **2-H**), 7.77 (dd, J = 7.6, 1.1 Hz, 1H, **10-H**), 7.58 – 7.48 (m, 2H, **15-H**), 7.48 – 7.40 (m, 1H, **16-H**), 7.32 (ddd, J = 7.5, 4.7, 1.2 Hz, 1H, **3-H**).
^{13}**C-NMR** (176 MHz, Chloroform-d): δ = 156.53 (**9-C**), 156.47 (**7-C**), 155.83 (**5-C**), 149.15 (**4-C**), 139.45 (**13-C**), 137.81 (**11-C**), 136.98 (**2-C**), 129.13 (**16-C**), 128.83 (**15-C**), 127.05 (**14-C**), 123.85 (**3-C**), 121.43 (**1-C**), 120.40 (**10-C**), 119.42 (**12-C**).
^{15}**N-NMR** (71 MHz, Chloroform-d): δ = 304.96 (**6-N**), 300.22 (**8-N**).

Synthesis of 1-(2-oxo-2-(2-pyridinyl)ethyl)pyridinium iodide (4)

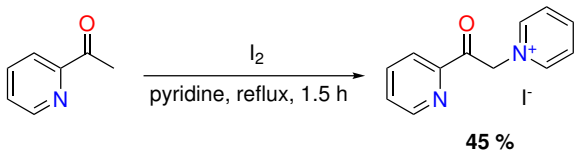

2-Acetylpyridine (15.1 g, 125 mmol) and iodine (31.7 g, 125 mmol) were refluxed in pyridine (125 mL) for 1.5 h. After cooling, more pyridine was added (25 mL) and the suspension was filtrated and washed with pyridine (50 mL) and acetone (200 mL). The dark solid was suspended in ethanol (300 mL) and heated to reflux. The suspension was filtered hot and the resulting gray solid was dried under reduced pressure (18.3 g, 56 mmol, **45 %**) and used without further purification.

Synthesis of N,N-dimethyl-3-oxo-3-phenylpropan-1-aminium chloride (5)

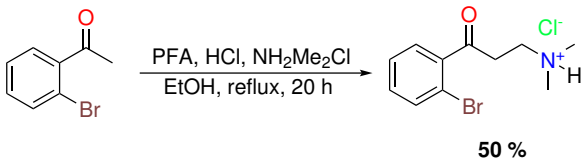

2'-Bromoacetophenone (14.6 g, 73.5 mmol), paraformaldehyde (3.1 g, 97.8 mmol) and dimethylamine hydrochloride (7.8 g, 5.9 mmol) were suspended in ethanol (40 mL), before concentrated HCl (2 mL) was added and the mixture was heated to reflux for 20 h. After cooling, 150 mL of acetone was added to the mixture, before cooling it to -20 °C for 24 h. The colorless crystals were filtered off and washed with acetone (50 mL) and dried in vacuum, yielding **5** (10.8 g, 36.7 mmol, **50 %**), which was used without further purification.

Synthesis of 6-(2-bromophenyl)-2,2'-bipyridine (3)

Jameson route

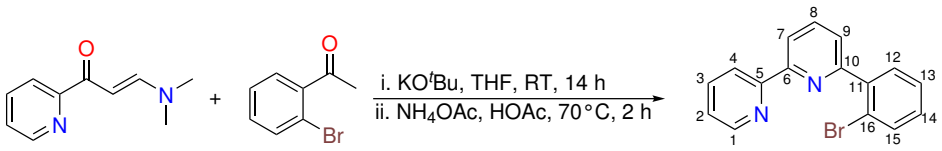

The synthesis is described in the supplementary information of the publication "Excited-State Kinetics of an Air-Stable Cyclometalated Iron(II) Complex", see C.1 in the appendix under "Synthesis".

Kröhnke route

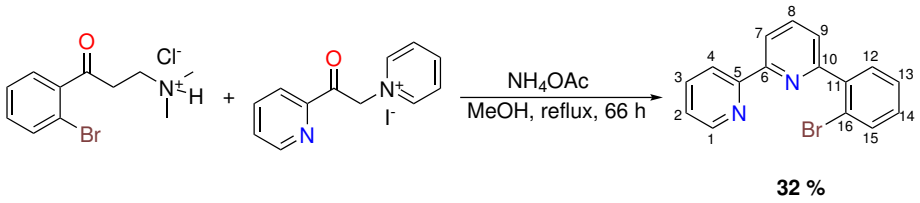

5 (10.8 g, 36.9 mmol), **4** (18.1 g, 55.4 mmol) and ammonium acetate (34.3 g, 445.0 mmol) were dissolved in methanol (180 mL) and heated for 66 h under reflux. After cooling, water (450 mL) was added and the suspension was cooled in an ice-bath and filtered. The black residue was dissolved in acetone and filtered two times over silica. The solvent of the dark solution was evaporated. The residue was extracted with hot pentane, until TLC proofed the absence of extracted product. The extract was concentrated and cooled in the freezer for 20 h. The bright yellow crystals of **3** were filtered off, washed with little cold pentane and dried in vacuum (3.7 g, 11.9 mmol, **32 %**).

^{1}**H-NMR** (500 MHz, Chloroform-d): δ (ppm) = 8.69 (ddd, J = 4.8, 1.8, 0.9 Hz, 1H,

1-H), 8.52 (dt, J = 8.0, 1.1 Hz, 1H, **4-H**), 8.42 (dd, J = 7.9, 1.0 Hz, 1H, **7-H**), 7.90 (t, J = 7.8 Hz, 1H, **8-H**), 7.80 (ddd, J = 8.0, 7.5, 1.8 Hz, 1H, 3-H), 7.74 – 7.69 (m, 1H, 12-H), 7.64 (dd, J = 7.7, 1.9 Hz, 1H, **15-H**), 7.62 (dd, J = 7.7, 1.0 Hz, 1H, **9-H**), 7.43 (td, J = 7.5, 1.2 Hz, 1H, **14-H**), 7.34 – 7.29 (m, 1H, **2-H**), 7.30 – 7.24 (m, 1H, **13-H**).

^{13}**C-NMR** (126 MHz, Chloroform-d): δ (ppm) = 157.99 (**10-C**), 156.62 (**5-C**), 156.17 (**6-C**), 149.50 (**1-C**), 141.73 (**11-C**), 137.27 (**3-C**), 137.22 (**8-C**), 133.90 (**12-C**), 132.09 (**15-C**), 130.08 (**13-C**), 127.90 (**14-C**), 124.93 (**9-C**), 124.14 (**2-C**), 122.39 (**16-C**), 121.93 (**4-C**), 120.05 (**7-C**)

Elemental analysis for $C_{16}H_{11}BrN_2$

Calculated C: 61.76, H: 3.56 N: 9.00

Found C: 61.76, H: 3.58, N: 9.08

Synthesis of 4,4'-bis(trifluoromethyl)-2,2'-bipyridine

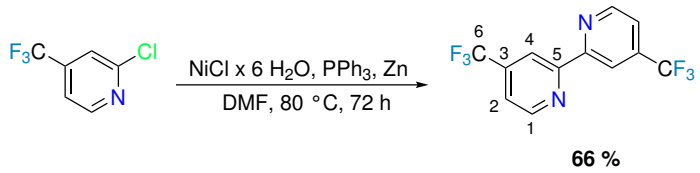

Nickel(II) chloride hexahydrate (13.1 g, 55 mmol) and triphenylphosphine (28.9 g, 110 mmol) were dissolved in DMF (150 mL) and degassed for 30 minutes with argon. To the blue solution, activated zinc dust (5.4 g, 83 mmol) was added and the resulting red-brown suspension was degassed for further 60 minutes. Afterwards, 2-chloro-4(trifluoromethyl)-pyridine (10.0 g, 55 mmol) was added to the suspension, which was then heated to 80 °C for 72 h. After cooling, the mixture was added to a large beaker with ammonia (100 mL) and ice (300 g). The suspension was extracted with diethyl ether (5 x 100 mL). The combined organic phases were dried over $MgSO_4$, before the solvent was removed. The raw product was purified with flash-chromatography (hexanes:DCM 4:1) to give 4,4'-bis(trifluoromethyl)-2,2'-bipyridine as a colorless solid (5.3 g, 18.1 mmol, **66 %**)

^{1}**H-NMR** (500 MHz, Chloroform-d): δ (ppm) 8.87 (d, J = 5.0 Hz, 1H, **1-H**), 8.76 – 8.67 (m, 1H, **4-H**), 7.57 (dd, J = 5.1, 1.7 Hz, 1H, **2-H**).
^{13}**C-NMR** (126 MHz, Chloroform-d): δ (ppm) = 156.30 (**5-C**), 150.43 (**1-C**), 139.80 (q, J = 34.5 Hz, **3-C**), 123.03 (q, J = 273.2 Hz, **6-C**), 120.02 (q, J = 3.3, 2.8 Hz, **2-C**), 117.29 (q, J = 3.7 Hz, **4-C**).
^{19}**F-NMR** (282 MHz, Chloroform-d): δ (ppm) = -64.86 (**6-F**).

Synthesis of 6-chloro-4,4'-bis(trifluoromethyl)-2,2'-bipyridine (6b)

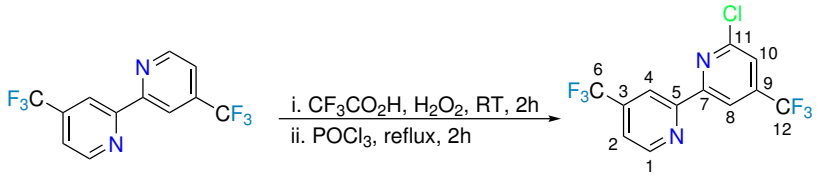

4,4'-bis(trifluoromethyl)-2,2'-bipyridine (3.5 g, 12 mmol) was dissolved carefully in trifluoroacetic acid (9.0 mL, 121 mmol). After the solution was cooled back to room temperature, hydrogen peroxide (1.7 mL, 18 mmol, 35 % in water) was added dropwise and the yellow solution was stirred for 2 h, before sodium carbonate solution was added until no further gas evolution was visible. The suspension was filtrated and the solid was washed thoroughly with water. The resulting 4,4'-bis(trifluoromethyl)-[2,2'-bipyridine] 1-oxide was used without further purification. After it was dried under vacuum, it was suspended in phosphorus oxychloride (15 mL, 161 mmol) and degassed for 10 min with argon. The suspension was heated for 2 h to reflux at 120 °C. After cooling, the phosphorous oxychloride was removed under reduced pressure. The remaining solid was washed with sodium carbonate solution and purified with flash-chromatography (hexanes:DCM 4:1), to give **6b** as an off-white solid (1.6 g, 5 mmol, **40 %**)

^{1}**H-NMR** (700 MHz, Chloroform-d): δ (ppm) = 8.85 (d, J = 5.1 Hz, 1H, **1-H**), 8.63 (s, J = 1.9 Hz, 1H, **4-H**), 8.62 (s, 1H, **10-H**), 7.59 (s, 1H, **8-H**), 7.59 (s, 1H, **8-H**), 7.58 (s, 1H, **2-H**).

^{13}**C-NMR** (176 MHz, Chloroform-d): 156.90 (**7-C**), 154.78 (**5-C**), 152.26 (**11-C**), 150.54 (**1-C**), 142.32 (q, J = 34.7 Hz, **9-C**), 139.95 (q, J = 34.4 Hz, **3-C**), 122.88 (q, J = 273.3 Hz, **6-C**), 122.25 (q, J = 273.7 Hz, **12-C**), 121.11 (q, J = 3.8 Hz, **8-C**), 120.57 (q, J = 3.3 Hz, **2-C**), 117.49 (q, J = 3.6 Hz, **4-C**), 115.94 (q, J = 3.4 Hz, **10-C**).

^{19}**F-NMR** (659 MHz, Chloroform-d): δ (ppm) = -64.92 (**12-F**), -64.94 (**6-F**).

Synthesis of (2,4-difluoro-3-(trifluoromethyl)phenyl)boronic acid

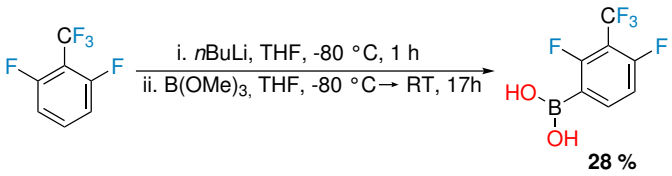

1,3-Difluoro-2-(trifluoromethyl)benzene (5.0 g, 27.5 mmol) was dissolved in dry THF (28 mL) and cooled to -80 °C, before *n*-BuLi (22 mL, 35.7 mmol, 1.6 M in hexanes) was added. The solution was stirred for 1 h at -80 °C, before trimethyl borate (4 mL, 35.7 mmol) was added. The solution was allowed to warm up to room temperature over the course of 17 h. Then, HCl (3 M, 100 mL) was carefully added and the reaction mixture was stirred for another 60 minutes, before adding sodium carbonate solution to neutralize the solution. The mixture was extracted with DCM (4 x 100 mL) and the combined organic phases were dried over $MgSO_4$. The volatiles were removed under reduced pressure and the dark brown solid was purified with flash chromatography (hexanes:EtOAc, gradient 0 to 100 % EtOAc). The main fraction was collected, yielding a colorless powder (1.7 g, 7.6 mmol, **28 %**). The product was used without further purification.

6-(2,4-difluorophenyl)-2,2'-bipyridine (2a)

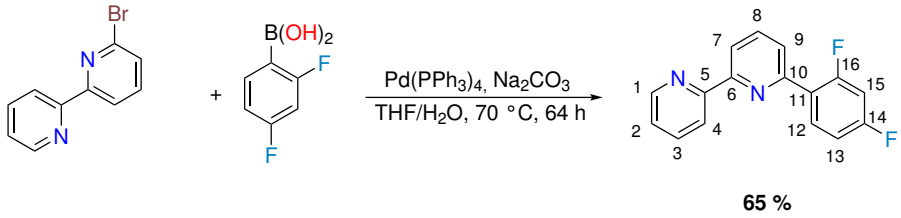

In a schlenk flask, 6-bromo-2,2'-bipyridyl (840 mg, 3.47 mmol), 2,4-difluorophenylboronic acid (657 mg, 4.16 mmol) and sodium carbonate (441 mg, 4.16 mmol) were suspended in a mixture of THF/water (75 ml/15 mL) and degassed for 20 minutes, before tetrakis-(triphenylphosphine)palladium (200 mg, 0.17 mmol) was added and the mixture was degassed for further 10 minutes. The yellow suspension was then heated to 70 °C for 64 h

under argon. After cooling, the solvent of the yellow solution was removed under reduced pressure. The resulting solid was extracted with dichloromethane (150 mL combined). The yellow solution was adsorbed onto silica and purified with flash chromatography (hexanes:EtOAc, gradient 0 to 100 % EtOAc). The resulting product was then recrystallized from acetone/pentane, resulting in off-white **2a** (600 mg, 2.24 mmol, **65 %**)

^{1}**H-NMR** (500 MHz, Chloroform-d): δ (ppm) = 8.70 (d, J = 4.8 Hz, 1H, **4-H**), 8.54 (d, J = 7.9 Hz, 1H, **1-H**), 8.40 (d, J = 7.7 Hz, 1H, **7-H**), 8.30 – 8.15 (m, 1H, **12-H**), 7.88 (t, J = 7.8 Hz, 1H, **8-H**), 7.86 – 7.82 (m, 1H, **2-H**), 7.82 – 7.78 (m, 1H, **9-H**), 7.32 (dd, J = 7.5, 4.8 Hz, 1H, **3-H**), 7.04 (td, J = 8.3, 2.5 Hz, 1H, **13-H**), 6.94 (ddd, J = 11.5, 8.7, 2.6 Hz, 1H, **15-H**).
^{13}**C-NMR** (126 MHz, Chloroform-d): δ (ppm) = 163.39 (dd, $J_{C,F}$ = 251.1, 11.9 Hz, **16-C**), 161.04 (dd, $J_{C,F}$ = 252.9, 11.9 Hz, **14-C**), 156.26,(**6-C**), 156.11 (**5-C**), 151.73 (d, $J_{C,F}$ = 2.8 Hz, **10-C**), 149.29(**4-C**), 137.61 (**8-C**), 136.97 (2-C), 132.43 (dd, $J_{C,F}$ = 9.9, 4.5 Hz, **12-C**), 128.00 (d, $J_{C,F}$ = 4.8 Hz), 124.18 (d, $J_{C,F}$ = 10.2 Hz), 123.93, 121.30, 119.80, 111.96 (dd, $J_{C,F}$ = 21.1, 3.6 Hz), 104.51 (dd, $J_{C,F}$ = 27.1, 25.7 Hz).

6-(2,4-difluorophenyl)-4,4'-bis(trifluoromethyl)-2,2'-bipyridine (2b)

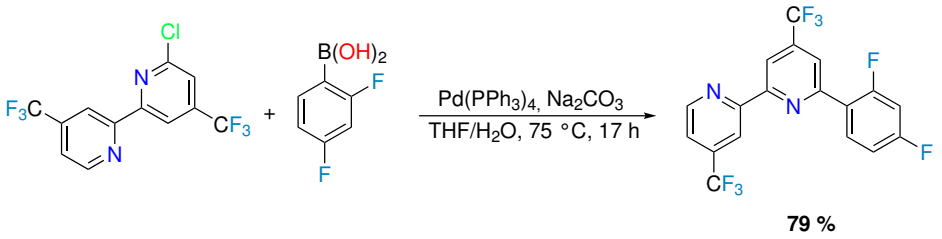

In a schlenk flask, **6b** (1307 mg, 4.0 mmol), 2,4-difluorophenylboronic acid (695 mg, 4.4 mmol) and sodium carbonate (509 mg, 4.8 mmol) were suspended in a mixture of THF/water (75 ml/15 mL) and degassed for 20 minutes, before tetrakis(triphenylphosphine)palladium (231 mg, 0.2 mmol) was added and the mixture was degassed for further 10 minutes. The yellow solution was then heated to 75 °C for 17 h under argon. After cooling, the solvent was removed. The resulting solid was extracted with dichloromethane (150 mL combined). The yellow solution was adsorbed onto silica and purified with flash chromatography (hexanes:EtOAc, gradient 0 to 100 % EtOAc), resulting in off-white **2b** (1280 mg, 3.2 mmol, **79 %**)

^{1}**H-NMR** (300 MHz, Chloroform-d): δ (ppm) = 8.93 (d, J = 5.0 Hz, 1H), 8.86 – 8.75 (m, 1H), 8.71 (d, J = 1.5 Hz, 1H), 8.24 (td, J = 8.9, 6.5 Hz, 1H), 8.09 (s, 1H), 7.63 (dd, J = 5.1, 1.6 Hz, 1H), 7.13 (tdd, J = 7.7, 2.6, 1.0 Hz, 1H), 7.01 (ddd, J = 11.3, 8.6, 2.5 Hz, 1H).
^{19}**F-NMR** (282 MHz, Chloroform-d): δ (ppm) = -64.72 (d, J = 6.9 Hz), -107.05 (p, J = 11.5, 9.7 Hz), -111.69 (q, J = 9.6 Hz).

6-(2,4-difluoro-3-(trifluoromethyl)phenyl)-4,4'-bis(trifluoromethyl)-2,2'-bipyridine (2c)

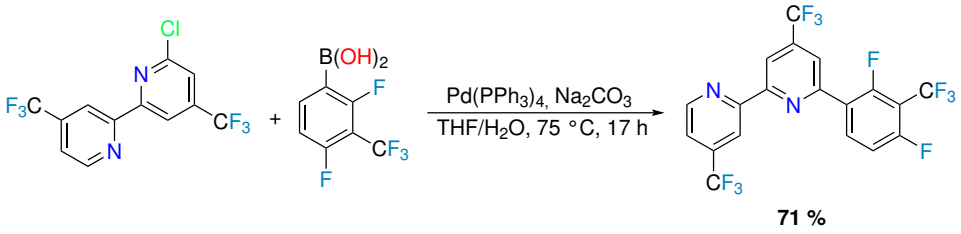

In a schlenk flask, **6b** (490 mg, 1.5 mmol), (2,4-difluoro-3-(trifluoromethyl)phenyl)boronic acid (508 mg, 1.5 mmol) and sodium carbonate (238 mg, 2.3 mmol) were suspended in a mixture of THF/water (10 ml/2 mL) and degassed for 20 minutes, before tetrakis-(triphenylphosphine)palladium (231 mg, 0.2 mmol) was added and the mixture was degassed for further 10 minutes. The yellow solution was then heated to 75 °C for 17 h under argon. After cooling, the solvent was removed. The resulting solid was extracted with dichloromethane (150 mL combined). The yellow solution was adsorbed onto silica and purified with flash chromatography (hexanes:EtOAc, gradient 0 to 100 % EtOAc), resulting in off-white **2b** (500 mg, 1.1 mmol, **71 %**)
^{1}**H-NMR** (500 MHz, Chloroform-d): δ (ppm) = 8.92 (dt, J = 5.0, 0.7 Hz, 1H), 8.76 (dd, J = 1.5, 0.7 Hz, 1H), 8.73 (dt, J = 1.6, 0.8 Hz, 1H), 8.39 (td, J = 8.8, 5.9 Hz, 1H), 8.07 (td, J = 1.7, 0.8 Hz, 1H), 7.62 (ddd, J = 5.0, 1.7, 0.8 Hz, 1H), 7.32 – 7.23 (m, 1H).
^{19}**F-NMR** (282 MHz, Chloroform-d): δ (ppm) = -56.16 (t, J = 23.3 Hz, CF_3−phenyl-F), -64.70 (CF_3−bipyridine-F), -64.74 (CF_3−bipyridine-F), -107.14 – -108.27 (m, phenyl-F), -113.71 – -114.48 (m, phenyl-F).

Synthesis of bis(imidazolyl)benzenes (14a–f)

1,3-di(1*H*-imidazol-1-yl)benzene (14a)

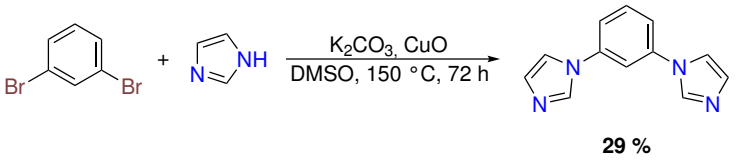

29 %

1,3-dibromobenzene (4.88 g, 20.7 mmol), imidazole (3.38 g, 49.6 mmol), potassium carbonate (7.15 g, 51.7 mmol) and cupric oxide (0.66 g, 8.27 mmol) were suspended in DMSO (20 mL) and heated to 150 °C for 72 h. After cooling, the solvent was distilled off under vacuum. The solid was extracted with a mixture of DCM/MeOH (10:1) and filtrated over silica. The product was received after distilling off the solvent as an off-white solid (1.26 g, 6.0 mmol, **29 %**). The NMR data is in agreement with previoulsy reported data.[148]
^{1}**H-NMR** (500 MHz, Chloroform-d): δ (ppm) = 7.87 (s, 2H), 7.55 (dd, J = 8.4, 7.7 Hz, 1H), 7.41 (t, J = 2.1 Hz, 1H), 7.35 (dd, J = 8.0, 2.1 Hz, 2H), 7.29 (t, J = 1.4 Hz, 2H), 7.17 (s, 2H).

1,1'-(5-bromo-1,3-phenylene)bis(1*H*-imidazole) (14b)

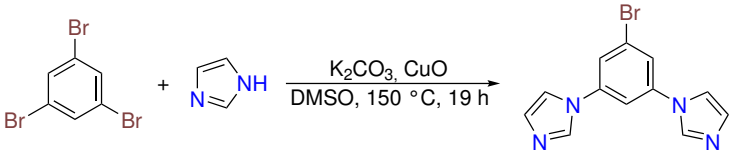

23 %

1,3,5-tribromobenzene (7.36 g, 20.7 mmol), imidazole (3.28 g, 48.1 mmol), potassium carbonate (12.15 g, 90 mmol) and cupric oxide (0.73 g, 9.16 mmol) were suspended in DMSO (40 mL) and heated to 150 °C for 19 h. After cooling, the solvent was distilled off under vacuum. The solid was extracted with DCM and the raw product was purified with flash chromatography, yielding **14b** as an off-white solid (1.51 g, 5.2 mmol, **23 %**). The NMR

data is in agreement with previoulsy reported data.[168]
^{1}**H-NMR** (700 MHz, DMSO-d_6): δ (ppm) = 8.48 (t, J = 1.1 Hz, 2H), 8.02 (t, J = 2.0 Hz, 1H), 7.96 (t, J = 1.4 Hz, 2H), 7.95 (d, J = 1.9 Hz, 2H), 7.14 (t, J = 1.2 Hz, 2H).

1,1'-(5-methyl-1,3-phenylene)bis(1*H*-imidazole) (14c)

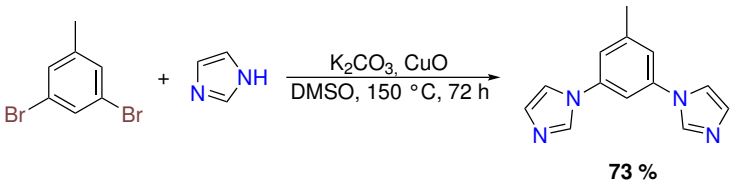

3,5-dibromotoluene (2.50 g, 10.0 mmol), imidazole (1.63 g, 24.0 mmol), potassium carbonate (3.46 g, 25.0 mmol) and cupric oxide (0.32 g, 4.0 mmol) were suspended in DMSO (15 mL) and heated under argon to 150 °C for 72 h. After cooling, the solvent was distilled off under vacuum. The solid was extracted with a mixture of DCM/MeOH (10:1) and filtrated over silica. The product was received after evaporating the solvent as an off-white solid (1.64 g, 7.3 mmol, **73 %**). The NMR data is in agreement with previoulsy reported data.[169]
^{1}**H-NMR** (500 MHz, Chloroform-d): δ (ppm) = 7.89 (s, 2H), 7.34 – 7.29 (m, 2H), 7.26 – 7.19 (m, 5H), 2.50 (s, 3H).

1,1'-(5-(*tert*-butyl)-1,3-phenylene)bis(1*H*-imidazole) (14d)

1,3-dibromo-5-*tert*-butylbenzene (2.94 g, 10.1 mmol), imidazole (1.65 g, 24.2 mmol), potassium carbonate (3.49 g, 25.2 mmol) and cupric oxide (0.32 g, 4.0 mmol) were suspended in DMSO (15 mL) and heated under argon to 150 °C for 72 h. After cooling,

the solvent was distilled off under vacuum. The solid was extracted with a mixture of DCM/MeOH (10:1) and filtrated over silica. The product was received after evaporating the solvent as an off-white solid (1.35 g, 5.1 mmol, **50 %**).
^{1}**H-NMR** (500 MHz, Chloroform-d): δ (ppm) = 7.87 (s, 2H), 7.36 (d, J = 2.0 Hz, 2H), 7.29 (s, 2H), 7.22 (t, J = 2.0 Hz, 1H), 7.20 (s, 2H), 1.37 (s, 9H).

1,1'-(5-methoxy-1,3-phenylene)bis(1*H*-imidazole) (14e)

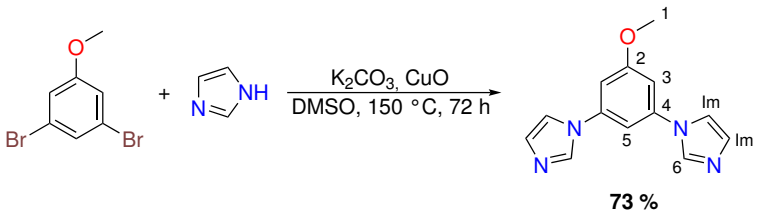

3,5-dibromoanisole (2.66 g, 10.0 mmol), imidazole (1.63 g, 24.0 mmol), potassium carbonate (3.46 g, 25.0 mmol) and cupric oxide (0.32 g, 4.0 mmol) were suspended in DMSO (15 mL) and heated under argon to 150 °C for 72 h. After cooling, the solvent was distilled off under vacuum. The solid was extracted with a mixture of DCM/MeOH (10:1) and filtrated over silica. The product was received after evaporating the solvent as an off-white solid (1.64 g, 7.3 mmol, **73 %**).
^{1}**H-NMR** (700 MHz, DMSO-d$_6$): δ (ppm) = 8.46 (s, 2H, $\mathbf{H}_{im}$), 7.95 (s, 2H, **6-H**), 7.59 (t, J = 1.9 Hz, 1H, **5-H**), 7.26 (d, J = 1.9 Hz, 2H, **3-H**), 7.16 (s, 2H, $\mathbf{H}_{im}$), 3.93 (s, 3H, **1-H**).
^{13}**C-NMR** (176 MHz, DMSO-d$_6$): δ (ppm) = 161.33 (**2-C**), 138.90 (**4-C**), 135.98 ($\mathbf{C}_{im}$), 129.95 ($\mathbf{C}_{im}$), 118.27 (**6-C**), 104.09 (**3-C**), 104.02 (**5-C**), 56.07 (**1-C**).

1,1'-(5-(trifluoromethyl)-1,3-phenylene)bis(1*H*-imidazole) (14f)

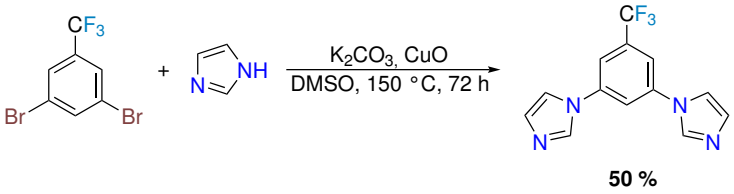

3,5-dibrombenzotrifluoride (3.04 g, 10.0 mmol), imidazole (1.63 g, 24.0 mmol), potassium carbonate (3.46 g, 25.0 mmol) and cupric oxide (0.32 g, 4.0 mmol) were suspended in DMSO (15 mL) and heated under argon to 150 °C for 72 h. After cooling, the solvent was distilled off under vacuum. The solid was extracted with a mixture of DCM/MeOH (10:1) and filtrated over silica. The product was received after evaporating the solvent as an off-white solid (1.38 g, 5.0 mmol, **50 %**). The NMR data is in agreement with previoulsy reported data.[170]

^{1}**H-NMR** (500 MHz, Chloroform-d): δ (ppm) = 7.95 (s, 2H), 7.65 (dt, J = 2.0, 0.6 Hz, 2H), 7.62 (t, J = 1.8 Hz, 1H), 7.36 (t, J = 1.4 Hz, 2H), 7.30 (t, J = 1.1 Hz, 2H).

1,1'-(5-(trifluoromethoxy)-1,3-phenylene)bis(1*H*-imidazole) (14g)

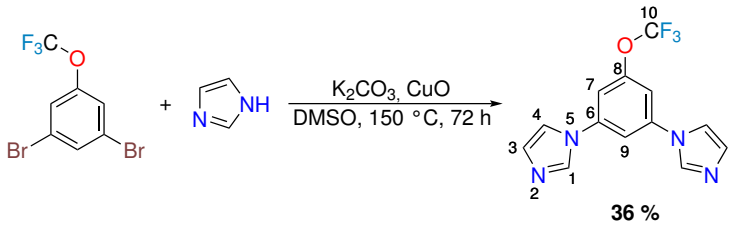

1,3-dibromo-5-trifluoromethoxybenzene (12.8 g, 40.0 mmol), imidazole (6.5 g, 96.0 mmol), potassium carbonate (13.8 g, 100.0 mmol) and cupric oxide (1.27 g, 16.0 mmol) were suspended in DMSO (80 mL) and heated under argon to 150 °C for 72 h. After cooling, the solvent was distilled off under vacuum. The solid was extracted with DCM and filtrated. After evaporation of the solvent, a saturated NaCl solution was added to the oily residue. The precipitate was filtered off and washed with water and acetone. The

solid was purified with column chromatography (silica, DCM:MeOH 10:1). The resulting solid was washed with pentane, yielding **14g** as a colorless solid (4.2 g, 14.3 mmol, 36 %).
^{1}**H-NMR** (700 MHz, DMSO-d_6): δ (ppm) = 8.51 (t, J = 1.1 Hz, 2H, **1-H**), 8.09 (t, J = 1.9 Hz, 1H, **9-H**), 7.99 (t, J = 1.4 Hz, 2H, **4-H**), 7.77 (dd, J = 1.9, 1.0 Hz, 2H, **7-H**), 7.16 (t, J = 1.2 Hz, 2H, **3-H**).
^{13}**C-NMR** (176 MHz, DMSO-d_6): δ (ppm) = 149.84 (**8-C**), 139.16 (**6-C**), 136.05 (**1-C**), 130.29 (**3-C**), 119.95 (q, J = 258.1 Hz, **10-C**), 118.16 (**4-C**), 110.93 (**7-C**), 110.52 (**9-C**).
^{19}**F-NMR** (659 MHz, DMSO-d_6): δ (ppm) = -56.78 (**10-F**).
^{15}**N-NMR** (71 MHz, DMSO-d_6): δ (ppm) = 266.61 (**2-N**), 182.49 (**5-N**).

3,5-di(1H-imidazol-1-yl)benzonitrile (14h)

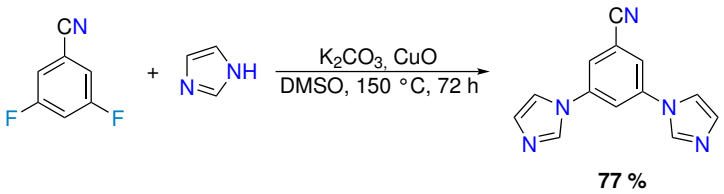

The reaction is based on a protocol by Bharadwaj *et al.*[171] 3,5-difluorobenzonitrile (11.1 g, 80 mmol), imidazole (16.3 g, 240 mmol) and potassium carbonate (33.2 g, 240 mmol) were suspended in dry DMF (80 mL) and heated under argon to 100 °C for 96 h. After cooling, the suspension was poured onto a mixture of ice and water. The colorless solid was collected by filtration and washed thoroughly with water. After drying, **14h** was obtained as a colorless solid (14.5 g, 62 mmol, **77 %**) The ^{1}H-NMR is in accordance with the literature.[171]
^{1}**H-NMR** (500 MHz, DMSO-d_6): δ (ppm) = 8.51 (dd, J = 1.4, 0.9 Hz, 2H), 8.32 (t, J = 2.1 Hz, 1H), 8.23 (d, J = 2.0 Hz, 2H), 7.99 (t, J = 1.4 Hz, 2H), 7.17 (dd, J = 1.5, 0.9 Hz, 2H).

Synthesis of CCC-proligands (15a–f)

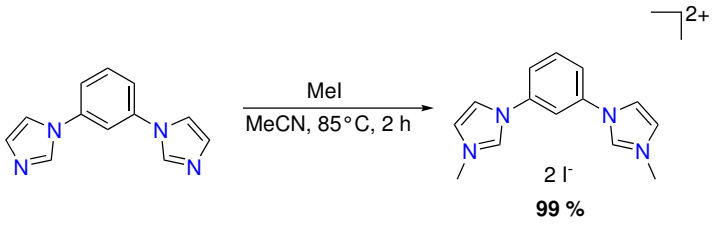

1,1'-(1,3-phenylene)bis(3-methyl-1*H*-imidazol-3-ium) diiodide (15a)

14a (4.75 g, 22.6 mmol) was suspended in acetonitrile (60 mL) and methyl iodide (5 mL, 80.3 mmol) was added. The mixture was heated to 85 °C for 2 h. After cooling to roomtemperature, the mixture was further cooled in an ice bath and filtrated. The solid was washed with acetone and pentane, yielding **15a** as a colorless solid (11.00 g, 22.3 mmol, **99 %**).

^{1}**H-NMR** (700 MHz, Acetonitrile-d_3): δ (ppm) = 8.97 (d, J = 1.7 Hz, 2H), 7.89 (dd, J = 8.7, 7.5 Hz, 1H), 7.87 (t, J = 2.2 Hz, 1H), 7.84 (t, J = 1.9 Hz, 2H), 7.81 (dd, J = 8.0, 2.2 Hz, 2H), 7.60 (t, J = 1.9 Hz, 2H), 3.97 (s, 6H).

1,1'-(5-bromo-1,3-phenylene)bis(3-methyl-1*H*-imidazol-3-ium) diiodide (15b)

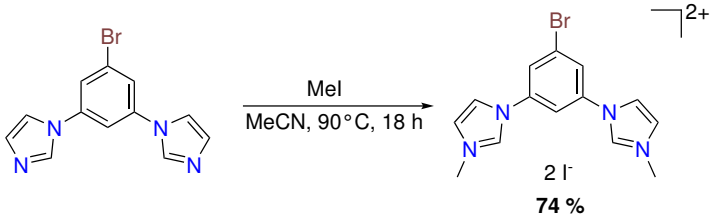

14b (1.50 g, 5.2 mmol) was suspended in acetonitrile (100 mL) and methyl iodide (2 mL, 32.1 mmol) was added. The mixture was heated to 90 °C for 18 h. After cooling, the solvent was evaporated under vacuum. The solid was washed with acetone, yielding **15b** as a colorless solid (2.21 g, 3.86 mmol, **74 %**).

^{1}H-NMR (500 MHz, DMSO-d_6): δ (ppm) = 9.94 (dq, J = 1.7, 0.8 Hz, 2H), 8.39 (t, J = 1.9 Hz, 2H), 8.36 (t, J = 2.0 Hz, 1H), 8.34 (d, J = 2.0 Hz, 2H), 3.99 (s, 6H).

1,1'-(5-methyl-1,3-phenylene)bis(3-methyl-1*H*-imidazol-3-ium) diiodide (15c)

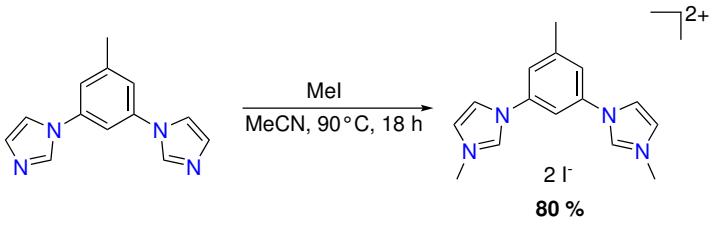

14c (1.64 g, 7.3 mmol) was suspended in acetonitrile (10 mL) and methyl iodide (1.6 mL, 26.0 mmol) was added. The mixture was heated to 90 °C for 18 h. After cooling, the solvent was evaporated under vacuum. The solid was washed with acetone, yielding **15c** as a colorless solid (2.97 g, 5.84 mmol, **80 %**).
^{1}H-NMR (500 MHz, DMSO-d_6): δ (ppm) = 9.86 (td, J = 1.6, 0.7 Hz, 2H), 8.35 (t, J = 1.9 Hz, 2H), 8.12 (td, J = 2.1, 0.7 Hz, 1H), 8.01 (t, J = 1.8 Hz, 2H), 7.88 (dd, J = 2.1, 0.8 Hz, 2H), 3.99 (d, J = 0.6 Hz, 6H), 2.53 (d, J = 0.8 Hz, 3H).

1,1'-(5-(tert-butyl)-1,3-phenylene)bis(3-methyl-1*H*-imidazol-3-ium) diiodide (15d)

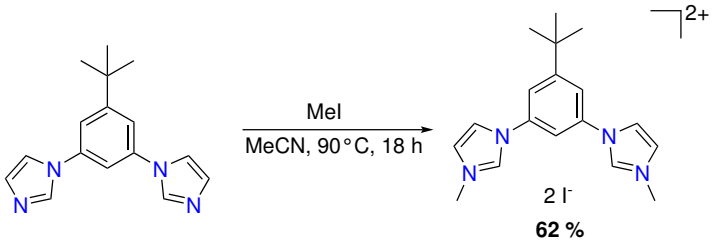

14d (1.35 g, 4.6 mmol) was suspended in acetonitrile (10 mL) and methyl iodide (1 mL, 16.4 mmol) was added. The mixture was heated to 90 °C for 18 h. After cooling, the

solvent was evaporated under vacuum. The solid was washed with acetone, yielding **15d** as a colorless solid (1.58 g, 2.87 mmol, **62 %**).
^{1}**H-NMR** (500 MHz, DMSO-d_6): δ (ppm) = 9.93 (td, J = 1.6, 0.7 Hz, 2H), 8.39 (t, J = 1.9 Hz, 2H), 8.11 (t, J = 2.0 Hz, 1H), 8.01 (t, J = 1.8 Hz, 2H), 7.98 (d, J = 2.0 Hz, 2H), 1.41 (s, 9H).

1,1'-(5-methoxy-1,3-phenylene)bis(3-methyl-1*H*-imidazol-3-ium) diiodide (15e)

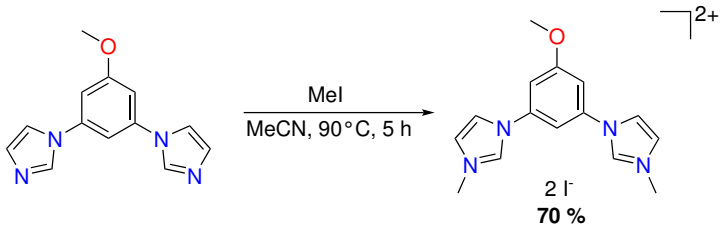

14e (1.80 g, 7.5 mmol) was suspended in acetonitrile (10 mL) and methyl iodide (1.7 mL, 26.6 mmol) was added. The mixture was heated to 90 °C for 5 h. After cooling, the solvent was evaporated under vacuum. The solid was washed with acetone, yielding **15e** as a colorless solid (2.76 g, 5.27 mmol, **70 %**).
^{1}**H-NMR** (500 MHz, DMSO-d_6): δ (ppm) = 9.92 (dt, J = 1.7, 0.8 Hz, 2H), 8.38 (t, J = 1.9 Hz, 2H), 8.01 (t, J = 1.8 Hz, 2H), 7.89 (t, J = 2.0 Hz, 1H), 7.63 (d, J = 1.9 Hz, 2H), 3.99 (s, 6H), 3.98 (s, 3H).

1,1'-(5-(trifluoromethyl)-1,3-phenylene)bis(3-methyl-1*H*-imidazol-3-ium) diiodide (15f)

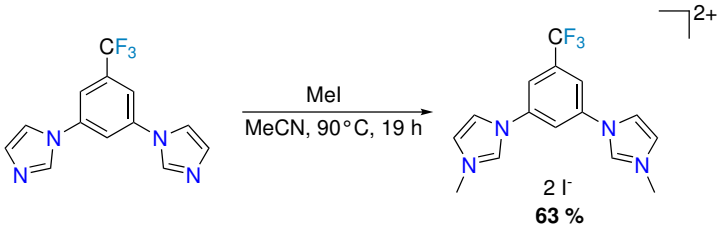

14f (3.10 g, 11.1 mmol) was suspended in acetonitrile (10 mL) and methyl iodide (2.5 mL, 39.6 mmol) was added. The mixture was heated to 90 °C for 19 h. After cooling, the solvent was evaporated under vacuum. The solid was washed with acetone, yielding **15f** as a colorless solid (3.90 g, 6.94 mmol, **63 %**).
^{1}**H-NMR** (500 MHz, DMSO-d$_6$): δ (ppm) = 10.02 (td, J = 1.6, 0.8 Hz, 2H), 8.65 (t, J = 2.1 Hz, 1H), 8.47 (dd, J = 2.0, 0.7 Hz, 2H), 8.45 (t, J = 1.9 Hz, 2H), 8.04 (t, J = 1.8 Hz, 2H), 4.01 (d, J = 0.6 Hz, 6H).

1,1'-(5-(trifluoromethoxy)-1,3-phenylene)bis(3-methyl-1*H*-imidazol-3-ium) diiodide (15g)

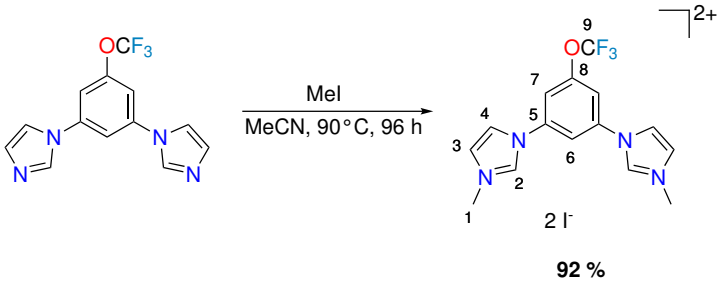

14g (3.50 g, 11.9 mmol) was suspended in acetonitrile (50 mL) and methyl iodide (6 mL, 96.4 mmol) was added. The mixture was heated to 90 °C for 96 h. After cooling, the solvent was evaporated under vacuum. The solid was washed with acetone and diethylether, yielding **15g** as a colorless solid (6.35 g, 11.0 mmol, **92 %**).
^{1}**H-NMR** (700 MHz, DMSO-d$_6$): δ (ppm) = 9.96 (q, J = 1.2, 0.8 Hz, 2H, **2-H**), 8.41 – 8.41 (m, 1H, **6-H**), 8.41 – 8.40 (m, 2H, **4-H**), 8.17 (dd, J = 2.0, 1.0 Hz, 2H, **7-H**), 8.04

(t, J = 1.8 Hz, 2H, **3-H**), 4.00 (s, 6H, **1-H**).
^{13}**C-NMR** (176 MHz, DMSO-d_6): δ (ppm) = 149.22 (**8-C**), 136.89 (**2-C**), 136.81 (**5-C**), 124.76 (**3-C**), 120.99 (**4-C**), 119.82 (q, J = 259.5 Hz, **9-C**), 115.84 (**7-C**), 114.89 (**6-C**), 36.49 (**1-C**).

1,1'-(5-cyano-1,3-phenylene)bis(3-methyl-1*H*-imidazol-3-ium) diiodide (15h)

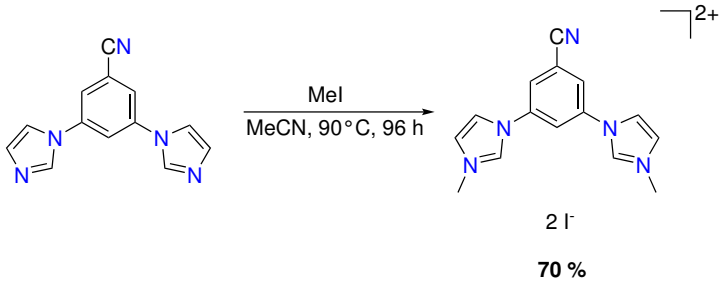

14h (11.1 g, 47.2 mmol) was suspended in acetonitrile (200 mL) and methyl iodide (8.8 mL, 142.0 mmol) was added. The mixture was heated to 90 °C for 24 h. After cooling, the solvent was evaporated under vacuum. The solid was washed with acetone, yielding **15h** as a colorless solid (17.2 g, 33.1 mmol, **70 %**).
^{1}**H-NMR** (700 MHz, DMSO-d_6): 9.91 (td, J = 1.6, 0.8 Hz, 2H), 8.60 (d, J = 2.0 Hz, 2H), 8.39 (t, J = 1.9 Hz, 2H), 8.05 (t, J = 1.8 Hz, 2H), 4.01 (d, J = 0.7 Hz, 6H).

5.3.2. Complex synthesis

Synthesis of [Fe(pbpy)$_2$] 7 via transmetalation

Organomercury route

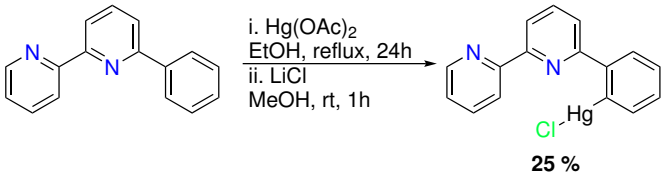

The first step in this route was the synthesis of the organomercury species Hgpbpy **8a**. This was based on the literature from Le Lagadec and Constable.[107,134] **2** (1.00 g, 4.31 mmol) and mercury acetate (1.37 g, 4.31 mmol) were heated in absolute ethanol (50 mL) under reflux for 24 h. After cooling, LiCl (0.33 g, 7.88 mmol) in methanol (15 mL) was added to the yellow suspension. The mixture was heated under reflux for another 15 minutes and then added to cold distilled water (150 mL). The colorless precipitate was filtered off and washed with water (20 mL) and ice-cold methanol (20 mL). The product was removed with DCM. The obtained solid was washed with hot methanol, from which the off-white product (25 %, 515 mg, 1.1 mmol) crystallized. Even though NMR showed still around 20 % of another compound (most probably the bismercurated product),[134] the product was used without further purification.

^{1}**H NMR** (500 MHz, $CDCl_3$): δ = 8.74 (ddd, J = 4.8, 1.8, 0.9 Hz, 1H), 8.37 (dd, J = 7.8, 1.0 Hz, 1H), 8.31 (dt, J = 7.9, 1.1 Hz, 1H), 7.97 (t, J = 7.9 Hz, 1H), 7.97 – 7.92 (m, 1H), 7.91 (td, J = 7.7, 1.8 Hz, 1H), 7.85 (dd, J = 7.9, 1.0 Hz, 1H), 7.57 – 7.54 (m, 1H), 7.48 (dtd, J = 17.7, 7.3, 1.6 Hz, 2H), 7.40 (ddd, J = 7.5, 4.8, 1.2 Hz, 1H).

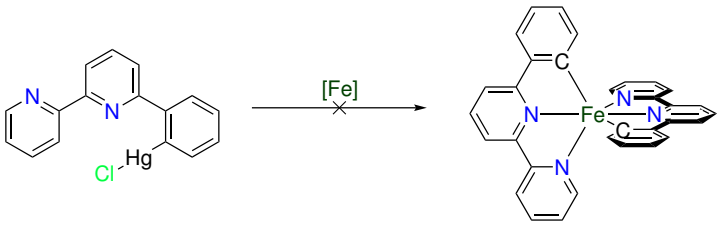

[Fe] (solvent) = Fe_3CO_{12} (toluene), $FeCO_5$ (pentane/toluene), $FeCl_2$ x 6 H_2O (MeCN)

The first attempts were made utilizing a redox transmetalation onto iron carbonyls, previously described by Le Lagadec,[107] the other attempt utilized a ligand metathesis reaction.

Reaction with iron dodecacarbonyl:

8a (290 mg, 0.62 mmol) was suspended in dry toluene (10 mL) under argon and mixed with irondodecacarbonyl (116 mg, 0.21 mmol) in toluene (30 mL). The mixture was heated to 70 °C for 16 h. After the reaction, an orange insoluble precipitate was observed, which was attributed to iron oxide. No product was observed in this reaction.

Reaction with iron pentacarbonyl: . For this, **8a** (140 mg, 0.30 mmol) was suspended in dry pentane (20 mL) and toluene (6 mL) and iron pentacarbonyl (0.1 mL, 0.76 mmol) were added. The yellow suspension was stirred for 0.5 h, before it was irradiated with a halogen lamp (150 W) for 2 h. After cooling and disposal of molten plastic residues from the stopcock stopper from the outside of the flask, the solvent was removed. No product was identified from the orange residue.

Ligand-metathesis approach: In this case, iron chloride hexahydrate (70 mg, 0.35 mmol) and **8a** (330 mg, 0.7 mmol) were dissolved in acetonitrile (10 mL). The red/orange suspension was heated under reflux for 2 h. Afterwards, 30 mL water was added and the orange solids were filtered off. The solvent of the red/violet solution was evaporated off. Analysis with ESI-MS gave no indication of product formation.

Organolithium route

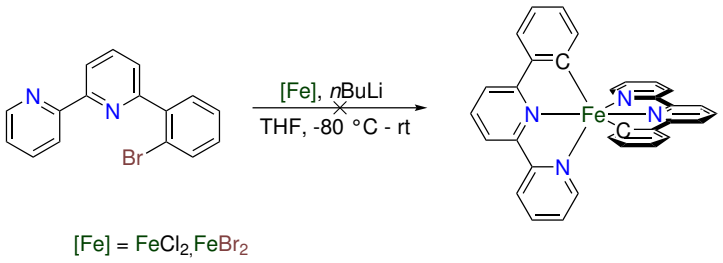

Water free iron chloride (63 mg, 0.5 mmol) and bromophenylbipyridine **3** (311 mg, 1.0 mmol) were suspended in dry THF (20 mL) under argon atmosphere. The orange suspension was cooled to -80 °C in an N_2/EtOH bath, before *n*-butyllithium (0.4 mL, 1 mmol, 2.5 M in hexanes) was added dropwise. After 2 h, the cooling bath was removed and the blue solution was let to warm to room temperature. The solution was stirred for 90 h, before the solvent was removed under reduced pressure. Acetone and water were added to the dark residue and the suspension was filtered. The solvent was removed to yield a dark residue. ESI-MS of the crude reaction mixture revealed the homocoupling produc of the ligand $pbpy_2$. Employing iron bromide as iron source resulted in the coupling product as well. Results did not change when adding the reaction product of **3** with *n*-butyllithium to an iron precursor.

ESI-MS (for $[pbpy_2]+H^+$) calc. $C_{32}H_{23}N_4^+$: 463.1917 m/z, found: 463.1881 m/z.

Organomagnesium route

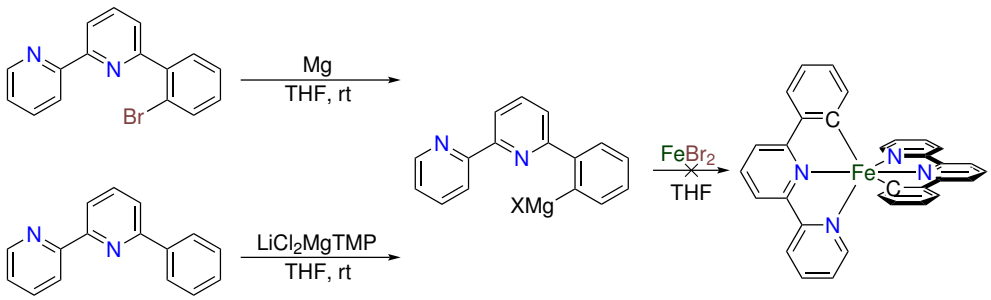

For the first attempt of the organomagnesium route, the respective Grignard was prepared. Magnesium shavings (27 mg, 1.1 mmol), which were heated in a vacuum with a

heat gun prior to the reaction, were suspended in dry THF (0.5 mL). To this, a solution of **3** (311 mg, 1.0 mmol) in THF (2.5 mL) was added dropwise. The dark suspension was stirred for half an hour. Additional THF (10 mL) was added to dissolve the precipitate formed. The purple solution was stirred for five more minutes, before it was added to iron bromide (108 mg, 0.5 mmol) in THF (2 mL) at 0 °C. After 1.5 h of reaction time, dry 1,4-dioxane (10 mL) was added to precipitate the formed magnesium bromide as the dioxane complex. The reaction mixture was heated to reflux for two hours, before 2 mL of acetone was added to quench the reaction after cooling. The solvent was removed subsequently under reduced pressure, before acetone and water were added. An orange solid was filtered off and the filtrate was concentrated under vacuum. The suspension was filtered. Analysis of the solid residue with ESI-MS revealed formation of coupling product $pbpy_2$.
ESI-MS (for $[pbpy_2]+H^+$) calc. $C_{32}H_{23}N_4^+$: 463.1917 m/z, found: 463.1912 m/z.

In order to activate pbpy **2** with $LiCl_2MgTMP$, pbpy (23 mg, 0.1 mmol) was dissolved in 1 mL dry THF and $LiCl_2MgTMP$ (0.12 mL, 0.12 mmol, 1 M in THF/toluene) was added. The solution was stirred for 18.5 h, before $FeCl_2$ (6 mg, 0.05 mmol) was added. The solvent was removed after a reaction time of 6 hours, during which the color changed to purple. Acetone and water were added to the solid. After evaporation of the solvent under reduced pressure, an orange solid was obtained. ESI-MS analysis revealed again only the coupling product $pbpy_2$.

Synthesis of [Fe(pbpy)$_2$] 7 via CH-activation

Internal base route

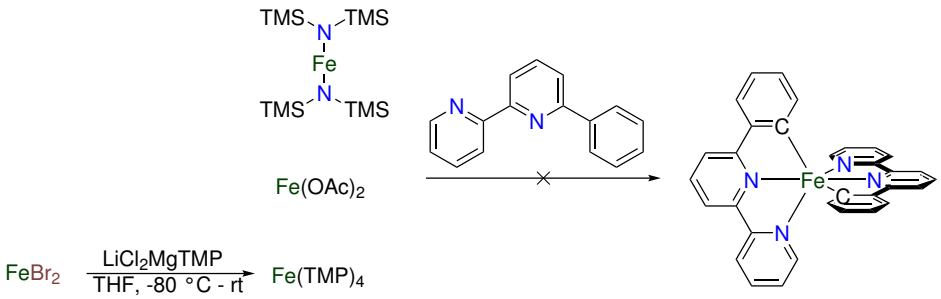

Reaction of **2** with [Fe(HMDS)$_2$]: [Fe(HMDS)$_2$] (81 mg, 0.216 mmol) was dissolved in dry THF (5 mL) at -80 °C, and **2** (100 mg, 0.431) in THF (10 mL) was added. The solution was stirred for 16 h, while the solution was let warm up to room temperature. Afterwards, the slightly green solution was heated to reflux for 24 h. From the dark brown mixture, no product was obtained.

Reaction of **2** with [Fe(OAc)$_2$]: [Fe(OAc)$_2$] (44 mg, 0.25 mmol) and **2** (116 mg, 0.5 mmol) were dissolved in degassed ethylene glycol (2 mL) and heated to 200 °C for 48 hours. After cooling, no product was obtained from the solid residue.

Exemplary for reaction of **2** with [Fe(TMP)$_2$]: At -80 °C, $FeBr_2$ (22 mg, 0.1 mmol) was suspended in dry THF (2 mL) and $LiCl_2MgTMP$ (0.2 mL, 0.2 mmol, 1 M in THF/toluene) was added dropwise. The solution was stirred for 1 h, while the reaction mixture was let to warm to -45 °C. **2** (47 mg, 0.2 mmol) in THF (1.5 mL) was added to the red reaction mixture. The reaction was stirred for additional 17 h. After removal of the solvent under vacuum, the reaction mixture was analyzed with ESI-MS and ^{1}H-NMR. No product was observed. Similar results were obtained by the reaction with **2b** and **2c** under the same reaction conditions.

External base route

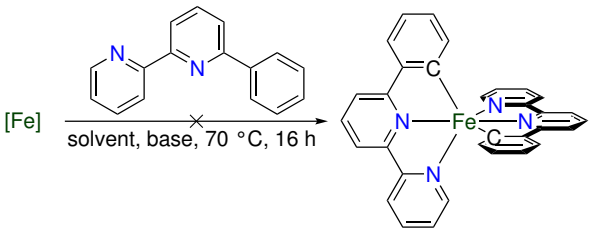

[Fe] = $FeBr_2$, $FeCl_2$, $FeCl_2$ x 4 H_2O, $Fe(H_2O)_6(BF_4)_2$
solvent = EtOH, MeCN
base = Triethylamine, *N*-ethylmorpholine

The reactions were performed parallel in screening reactions. In a vial, an iron source ($FeBr_2$, $FeCl_2$, $FeCl_2$x4 H_2O, or $Fe(H_2O)_6(BF_4)_2$, 0.05 mmol) and pbpy (23 mg, 0.1 mmol) were dissolved in a solvent (MeCN or ethanol, 2 mL). The solution was purged with argon, before a base was added (triethylamine or *N*-ethylmorpholine, 0.1 mmol). The solution was heated to 70 °C for 16 h. After filtration and removal of the solvent under vacuum, the residue was analyzed with ^{1}H-NMR. From neither of the attempts, product was observed.

σ-bond metathesis reaction

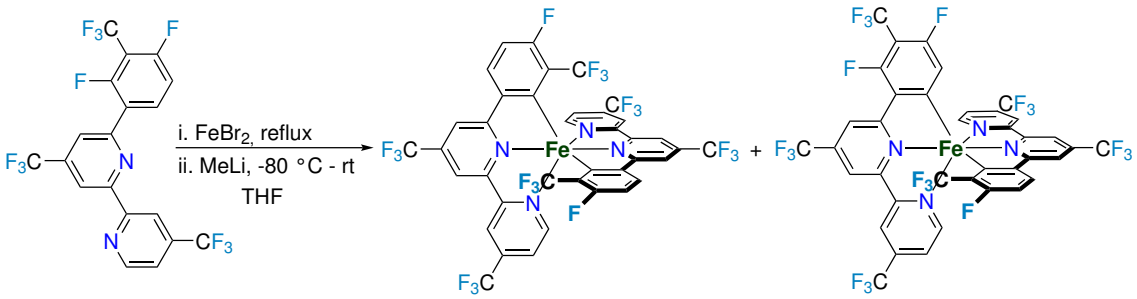

The reaction is described for the most successful attempt. $FeBr_2$ (89 mg, 0.413 mmol) and **2c** (390 mg, 0.826 mmol) were suspended in dry THF (8 mL) and heated to reflux for 5 minutes, until the solids dissolved and the solution changed color from green to violet, indicating a full coordination of the proligand. The solution was let to cool to room temperature and was cooled further to -90 °C. Methyl lithium (0.52 mL, 0.832 mmol, 1.6 M in diethylether) was added dropwise. The solution was stirred in the cold for 2 h, before

it was removed from the cold bath and stirred further for 4 h. The reaction mixture was quenched with water (2 mL) and stirred under atmosphere for 10 minutes. The solvent was removed under reduced pressure and the dark residue was treated with water and DCM (both 30 mL). The aqueous phase was extracted with DCM (2 x 30 mL) and the solvent of the combined organic phases was removed. The dark residue was separated by column chromatography (*n*-pentane:diethylether 8:1 on silica) to yield fractions of impure products, from which crystals of **11** and **12** were obtained.

ESI-MS: calc. for $[M]^+$ (**11**, $C_{38}H_{14}F_{20}N_4$): 962.0249 m/z, found: 962.0208 m/z
ESI-MS: calc. for $[M]^+$ (**12**, $C_{38}H_{13}F_{21}N_4$): 980.0154 m/z, found: 980.0123 m/z

Synthesis of CCC-complexes

Synthesis of $[Fe(ImP^{H})_2](PF_6)$ (16a)

The synthesis is shown in Chapter 3.3.2 in the Methods section, the corresponding spectra are found in C.2 in the Appendix.[156]

Synthesis of $[Fe(ImP^{Br})_2](PF_6)$ 16b

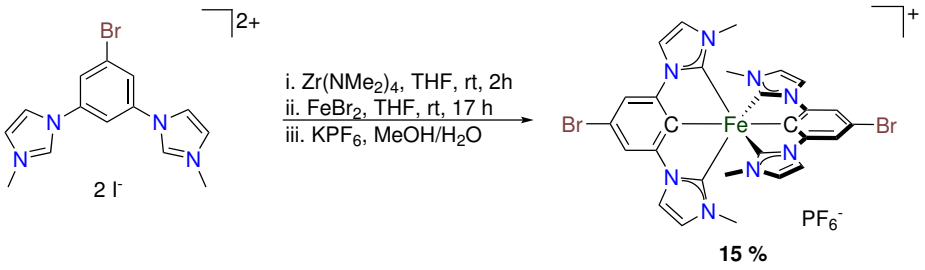

Tetrakis(dimethylamino)zirconium (0.64 g, 2.4 mmol) and **15b** (1.20 g, 2.1 mmol) were suspended in THF (20 mL) in the glovebox and stirred for 2 h. Iron bromide(II) (0.22 g, 1.0 mmol) was added to the yellow suspension, which was stirred for another 17 h, before methanol was added outside the box for quenching. The solvent was evaporated off and the residue was extracted with DCM until the color of the filtrate ran clear. The filtrate was then concentrated and passed over a plug of silica, where it was washed thoroughly with DCM. The product was then eluted with MeCN. The solvent was evaporated and the residue was redissolved in MeOH, to which an excess KPF_6 was added. After ten minutes of stirring, the product was precipitated with water. After filtrating, the product was crystallized from DCM/pentane to yield **16b** as dark blocks (128 mg. 0.15 mmol, **15 %**), which were subsequently washed with acetone/diethylether (1:5).
^{1}H NMR (500 MHz, CD_3CN): δ = 25.03 (s, 4H), 10.20 (s, 12H), 2.93 (s, 4H), -2.82 (s, 4H).
ESI-MS: Calculated for [**16b**-PF_6]$^+$ ($C_{28}H_{24}Br_2FeN_8$) 687.9820, found 687.9814.
Elemental Analysis for ($C_{28}H_{24}Br_2F_6FeN_8P$) · 0.5 ($C_3H_6O$) (0.5 eq. acetone) (Calculated, Found (%)): C (41.09, 40.81), H (3.16, 3.01), N (13.00, 13.32).x

Synthesis of $[Fe(ImP^{Me})_2](PF_6)$ 16c

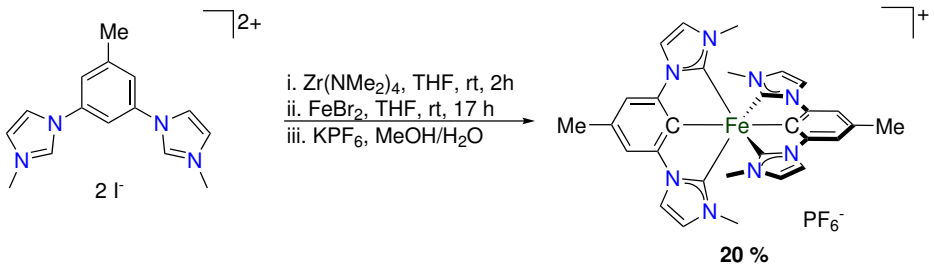

Tetrakis(dimethylamino)zirconium (0.56 g, 2.1 mmol) and **15c** (1.02 g, 2 mmol) were suspended in THF (20 mL) in the glovebox and stirred for 2 h. Iron bromide(II) (0.22 g, 1.0 mmol) was added to the yellow suspension, which was stirred for another 17 h, before methanol was added outside the box for quenching. The solvent was evaporated off and the residue was extracted with DCM until the color of the filtrate ran clear. The filtrate was then concentrated and passed over a plug of silica, where it was washed thoroughly with DCM. The product was then eluted with MeCN. The solvent was evaporated and the residue was redissolved in MeOH, to which an excess KPF_6 was added. After ten minutes of stirring, the product was precipitated with water. After filtrating, the product was crystallized from DCM/pentane to yield **16c**. In the crystal structure was observed that 1/6 of the anions were Br^- instead of PF_6. Hence, anion exchange was performed as previously described, leading to dark blue solid (143 mg. 0.20 mmol, **20 %**). Note: The methyl-group in the backbone is not resolved in the NMR.

^{1}H NMR (500 MHz, CD_3CN): δ = 25.23 (s, 4H), 9.38 (s, 12H), 3.00 (s, 4H), -2.34 (s, 4H).

ESI-MS: Calculated for [**16c**-PF_6]$^+$ ($C_{30}H_{30}FeN_8$) 558.1943, found 558.1978.

Elemental Analysis for $C_{30}H_{30}F_6FeN_8P$ (Calculated, Found (%)): C (51.22, 51.50), H (4.30, 4.21), N (15.93, 15.56).

Synthesis of $[Fe(ImP^{tBu})_2](PF_6)$ 16d

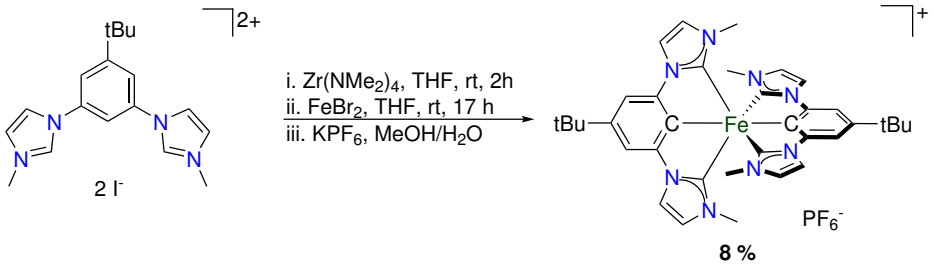

Tetrakis(dimethylamino)zirconium (0.55 g, 2.1 mmol) and **15d** (1.10 g, 2 mmol) were suspended in THF (20 mL) in the glovebox and stirred for 2 h. Iron(II) bromide (0.22 g, 1.0 mmol) was added to the yellow suspension, which was stirred for another 17 h, before methanol was added outside the box for quenching. The solvent was evaporated off and the residue was extracted with DCM until the color of the filtrate ran clear. The filtrate was then concentrated and passed over a plug of silica, where it was washed thoroughly with DCM. The product was then eluted with MeCN. The solvent was evaporated and the residue was redissolved in MeOH, to which an excess KPF_6 was added. After ten minutes of stirring, the product was precipitated with water. After filtrating, the product was crystallized from DCM/pentane, yielding **16d** (63 mg. 0.08 mmol, **8 %**).

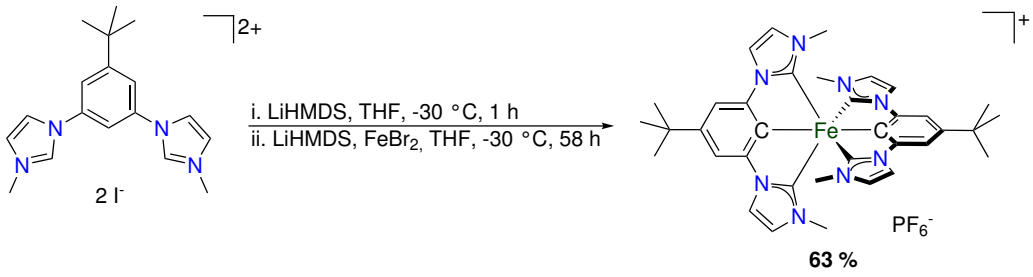

To a cooled solution (-30 °C) of **15d** (0.44 g, 0.80 mmol) in THF (4 mL), LiHMDS (0.28 g, 1.68 mmol) in THF (4 mL) was added, while to a solution of $FeBr_2$ (0.11 g, 0.50 mmol) in THF (4 mL) another solution of LiHMDS (0.17 g, 1.04 mmol) in THF (4 mL) was added in the glovebox. After stirring for 1 h, the solutions were combined and stirred for 58 h. Afterwards, methanol was added to quench the reaction. The volatiles were removed

under reduced pressure and the dark residue was redissolved in acetone. An excess KPF_6 was added and after stirring for 10 minutes, water was added. The precipitate was filtered off and purified over a silica column (DCM:MeCN, 5:1), yielding the dark **16d** (0.20 g, 0.25 mmol, **63 %**).

^{1}**H NMR** (500 MHz, CD_3CN): δ = 25.73 (s, 4H), 9.41 (s, 12H), 5.83 (s, 18H), 3.00 (s, 4H), -2.35 (s, 4H).
ESI-MS: Calculated for [**16d**-PF_6]$^+$ ($C_{36}H_{42}FeN_8$) 642.2882, found 642.2877.
Elemental Analysis for $C_{36}H_{42}F_6FeN_8P \cdot 0.5$ (C_3H_6O) (0.5 eq. acetone) (Calculated, Found (%)): C (55.15, 55.06), H (5.55, 5.17), N (13.72, 13.71).

Synthesis of $[Fe(ImP^{OMe})_2](PF_6)$ 16e

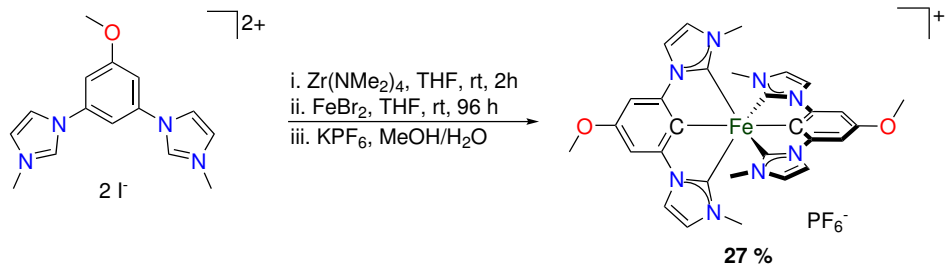

Tetrakis(dimethylamino)zirconium (0.28 g, 1.1 mmol) and **15e** (0.53 g, 1.0 mmol) were suspended in THF (10 mL) in the glovebox and stirred for 2 h. Iron(II) bromide (0.11 g, 0.5 mmol) was added to the yellow suspension, which was stirred for another 96 h, before methanol was added outside the box for quenching. The solution was stirred for 1 h under atmospheric conditions, before the solids were filtered off. The residue was washed with acetone until the filtrate ran clear. The solvent of the filtrate was removed under reduced pressure and redissolved in acetone. An excess KPF_6 was added and the solution was stirred for 10 minutes, before water was added. The precipitate was collected by filtration and washed with water. Raw **16e** was purified by column chromatography (Silica, DCM:MeCN 5:1), yielding a dark solid (0.10 g, 0.1 mmol, **27 %**).

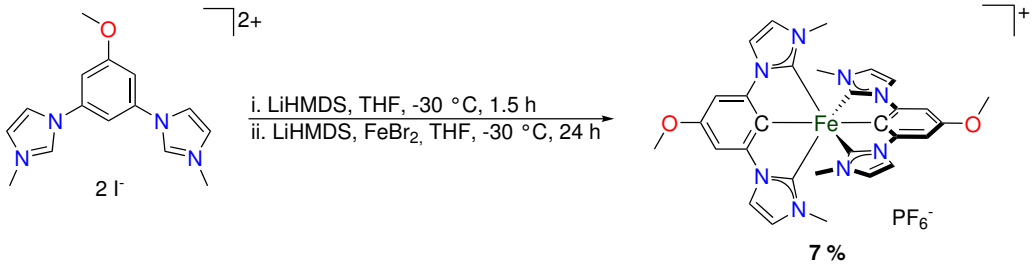

To a cooled solution (-30 °C) of **15e** (0.42 g, 0.80 mmol) in THF (4 mL), LiHMDS (0.28 g, 1.68 mmol) in THF (4 mL) was added, while to a solution of $FeBr_2$ (0.11 g, 0.5 mmol) in THF (4 mL) another solution of LiHMDS (0.17 g, 1.04 mmol) in THF (4 mL) was added in the glovebox. After stirring for 2 h, the solutions were combined and stirred for 19 h. Afterwards, methanol was added to quench the reaction. The volatiles were removed under reduced pressure and the dark residue was redissolved in acetone. An excess KPF_6

was added and after stirring for 10 minutes water was added. The precipitate was filtered off and purified over a silica column (DCM:MeCN, 5:1), yielding the dark **16e** (20 mg, 0.027 mmol, **7 %**).

^{1}**H NMR** (700 MHz, CD_3CN): δ = 23.20 (s, 4H), 15.16 (s, 6H), 9.05 (s, 12H), 3.12 (s, 4H), -2.30 (s, 4H).

ESI-MS: Calculated for [**16e**-PF_6]$^+$ ($C_{30}H_{30}FeN_8O_2$) 590.1841, found 590.1837.

Elemental Analysis for $C_{30}H_{30}F_6FeN_8O_2P \cdot C_3H_6O$ (1 eq. acetone) (Calculated, Found (%)): C (49.95, 50.00), H (4.57, 4.63), N (14.12, 14.30).

Synthesis of $[Fe(ImP^{CF_3})_2](PF_6)$ 16f

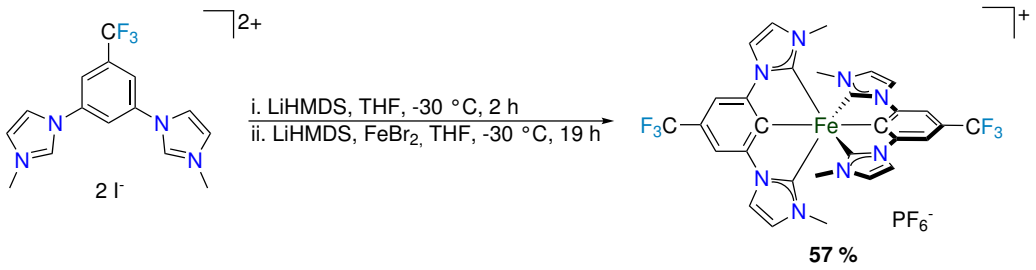

To a cooled solution (-30 °C) of **15f** (0.56 g, 1.00 mmol) in THF (10 mL), LiHMDS (0.35 g, 2.10 mmol) in THF (4 mL) was added, while to a solution of $FeBr_2$ (0.14 g, 0.63 mmol) in THF (6 mL) another solution of LiHMDS (0.22 g, 1.30 mmol) in THF (2 mL) was added in the glovebox. After stirring for 2 h, the solutions were combined and stirred for 19 h. Afterwards, methanol was added to quench the reaction. The volatiles were removed under reduced pressure and the dark residue was redissolved in acetone. An excess KPF_6 was added and after stirring for 10 minutes water was added. The precipitate was filtered off and purified over a silica column (DCM:MeCN, 8:1), yielding the dark **16f** (0.23 g, 0.28 mmol, **57 %**).

^{1}**H NMR** (500 MHz, CD_3CN): δ = 22.19 (s, 4H), 11.34 (s, 12H), 2.72 (s, 4H), -3.82 (s, 4H).

ESI-MS: Calculated for $[\mathbf{16f}\text{-}PF_6]^+$ ($C_{30}H_{24}F_6FeN_8$) 666.1387, found 666.1373.

Elemental Analysis for $C_{30}H_{24}F_{12}FeN_8P \cdot 0.5\ C_3H_6O$ (0.5 eq. acetone) (Calculated, Found (%)): C (45.02, 45.14), H (3.24, 3.29), N (13.33, 13.28).

Synthesis of $[Fe(ImP^{OCF_3})_2](PF_6)$ 16g

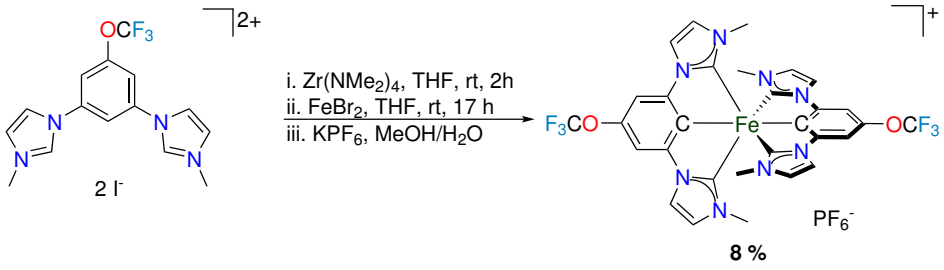

Tetrakis(dimethylamino)zirconium (0.21 g, 0.8 mmol) and **15g** (0.44 g, 0.76 mmol) were suspended in THF (10 mL) in the glovebox and stirred for 2 h. Iron(II) bromide (0.082 g, 0.38 mmol) was added to the yellow suspension, which was stirred for another 17 h, before methanol was added outside the box for quenching. The solution was stirred for 1 h under atmospheric conditions, before the solids were filtered off. The residue was washed with acetone until the filtrate ran clear. The solvent of the filtrate was removed under reduced pressure and redissolved in acetone. An excess KPF_6 was added and stirred for 10 minute, before water was added. The precipitate was collected by filtration and washed with water. Raw **16g** was purified by column chromatography (Silica, DCM:MeCN 5:1), yielding a dark solid (26 mg, 0.031 mmol, **8 %**)

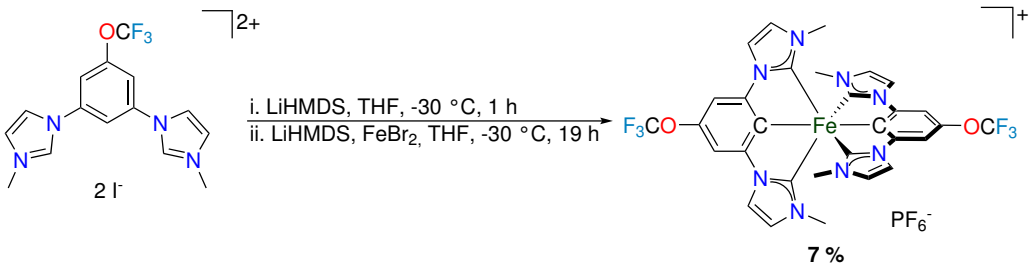

To a cooled solution (-30 °C) of **15g** (0.58 g, 1.00 mmol) in THF (8 mL), LiHMDS (0.35 g, 2.10 mmol) in THF (4 mL) was added, while to a solution of $FeBr_2$ (0.14 g, 0.63 mmol) in THF (4 mL) another solution of LiHMDS (0.22 g, 1.30 mmol) in THF (2 mL) was added in the glovebox. After stirring for 1 h, the solutions were combined and stirred for 19 h. Afterwards, methanol was added to quench the reaction. The volatiles were removed

under reduced pressure and the dark residue was redissolved in acetone. An excess KPF_6 was added and after stirring for 10 minutes water was added. The precipitate was filtered off and purified over a silica column (DCM:MeCN, 5:1), yielding the dark **16g** (31 mg, 0.037 mmol, **7 %**).

^{1}**H NMR** (500 MHz, CD_3CN): δ = 22.19 (s, 4H), 11.34 (s, 12H), 2.72 (s, 4H), -3.82 (s, 4H).

ESI-MS: Calculated for [**16g**-PF_6]$^+$ ($C_{30}H_{24}F_6FeN_8O_2$) 698.1276, found 698.1294.

Elemental Analysis for $C_{30}H_{24}F_{12}FeN_8O_2P$ (Calculated, Found (%)): C (42.72, 48.86), H (2.87, 7.49), N (13.29, 5.36).

Synthesis of $[Fe(ImP^{CN})_2](PF_6)$ 16h

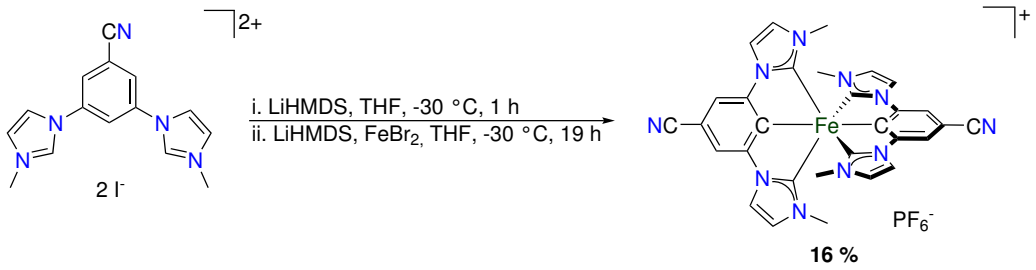

To a cooled solution (-30 °C) of **15h** (0.42 g, 0.80 mmol) in THF (4 mL), LiHMDS (0.28 g, 1.68 mmol) in THF (4 mL) was added, while to a solution of $FeBr_2$ (0.11 g, 0.50 mmol) in THF (4 mL) another solution of LiHMDS (0.17 g, 1.04 mmol) in THF (4 mL) was added in the glovebox. After stirring for 1 h, the solutions were combined and stirred for 19 h. Afterwards, the solvent was removed under vacuum. The dark residue was washed with a mixture of hexanes and diethylether (1:1, 15 mL) and then with hexanes (3 mL). Outside the glovebox, methanol was added to the reaction mixture. The solvent was removed afterwards under reduced pressure and the solid was redissolved in acetone and filtrated. Excess KPF_6 was added to the filtrate and water was added. The mixture was filtrated again and the green solid was purified over a silica column (DCM:MeCN, 5:1), yielding the dark **16h** (42 mg, 0.06 mmol, **16 %**).
^{1}H NMR (500 MHz, CD_3CN): δ = 22.19 (s, 4H), 11.34 (s, 12H), 2.72 (s, 4H), -3.82 (s, 4H).
ESI-MS: Calculated for [**16h**-PF_6]$^+$ ($C_{30}H_{24}FeN_{10}$) 580.1535, found 580.1533.
Elemental Analysis for $C_{30}H_{24}F_6FeN_{10}P$ (Calculated, Found (%)): C (49.67, 49.45), H (3.33, 3.49), N (19.31, 18.98).

5.3.3. Catalysis

The catalytic reactions were carried out according to a procedure which is exemplarily given for optimizing electron donors.
In a vial, the previously mortared $[Fe(ImP)_2]PF_6$ (**16a**, 1.4 mg, 2.1 μmol), benzaldehyde (22.3 mg, 0.21 mmol) and a electron donor (0.63 mmol) were dissolved in dry acetonitrile (2.1 mL). The solution was transferred into a schlenk flask and degassed *via* freeze-pump-thaw. The degassed solution was divided into three J. Young NMR tubes under argon and

irradiated with a 300 W Xenon lamp equipped with an AM 1.5 filter for 17 h. Afterwards, the conversion was determined by ^{1}H NMR.

References

[1] UN, *Tracking SDG 7 - The energy progress report 2021*. https://unstats.un.org/unsd/energystats/pubs/documents/sdg_7.pdf.

[2] *Sechster IPCC-Sachstandsbericht (AR6) Beitrag von Arbeitsgruppe II: Folgen, Anpassung und Verwundbarkeit*. https://www.de-ipcc.de/media/content/Hauptaussagen_AR6-WGII.pdf.

[3] Industriegewerkschaft Bergbau, Chemie, Energie, Verband der Chemischen Industrie e.V., *Gemeinsame Strategie von IG BCE und VCI zu einer Wasserstoffwirtschaft*, **2020**. https://www.vci.de/vci/downloads-vci/2020-09-29-ig-bce-vci-h2-strategie-final.pdf.

[4] E. Amouyal, *Sol. Energ. Mat. Sol. Cells* **1995**, *38*, 249–276.

[5] K. T. Møller, T. R. Jensen, E. Akiba, H.-w. Li, *Progress in Natural Science: Materials International* **2017**, *27*, 34–40.

[6] David R. Lide, *CRC handbook of chemistry and physics: A ready-reference book of chemical and physical data 84th ed.*, CRC Press, Boca Raton, **2003**.

[7] E. Hahne, *Technische Thermodynamik*, Oldenbourg Verlag, **2010**.

[8] S. McAllister, *Fundamentals of Combustion Processes*, of *SpringerLink Bücher*, Springer New York, New York, NY, **2011**.

[9] J. R. Darwent, P. Douglas, A. Harriman, G. Porter, M.-C. Richoux, *Coordination Chemistry Reviews* **1982**, *44*, 83–126.

[10] F. Gärtner, A. Boddien, E. Barsch, K. Fumino, S. Losse, H. Junge, D. Hollmann, A. Brückner, R. Ludwig, M. Beller, *Chemistry - A European Journal* **2011**, *17*, 6425–6436.

[11] J. I. Goldsmith, W. R. Hudson, M. S. Lowry, T. H. Anderson, S. Bernhard, *J. Am. Chem. Soc.* **2005**, *127*, 7502–7510.

[12] H. Ozawa, K. Sakai, *Chem. Comm.* **2011**, *47*, 2227–2242.

[13] L. L. Tinker, S. Bernhard, *Inorganic chemistry* **2009**, *48*, 10507–10511.

[14] M. Wang, Y. Na, M. Gorlov, L. Sun, *Dalton transactions* **2009**, 6458–6467.

[15] D. R. Whang, K. Sakai, S. Y. Park, *Angew. Chem., Int. Ed.* **2013**, *52*, 11612–11615.

[16] T. Lazarides, T. McCormick, P. Du, G. Luo, B. Lindley, R. Eisenberg, *J. Am. Chem. Soc.* **2009**, *131*, 9192–9194.

[17] C. K. Prier, D. A. Rankic, D. W. MacMillan, *Chemical reviews* **2013**, *113*, 5322–5363.

[18] R. A. Angnes, Z. Li, C. R. D. Correia, G. B. Hammond, *Org. Biomol. Chem.* **2015**, *13*, 9152–9167.

[19] Verband der Chemischen Industrie e.V., *Energiestatistik für die Chemie- und Pharmaindustrie*, **2021**. `https://www.vci.de/ergaenzende-downloads/energiestatistik-daten-fakten.pdf`.

[20] J. J. Douglas, M. J. Sevrin, C. R. J. Stephenson, *Organic Process Research & Development* **2016**, *20*, 1134–1147.

[21] Y. Yu, L.-K. Zhang, A. V. Buevich, G. Li, H. Tang, P. Vachal, S. L. Colletti, Z.-C. Shi, *Journal of the American Chemical Society* **2018**, *140*, 6797–6800.

[22] N. Ichiishi, J. P. Caldwell, M. Lin, W. Zhong, X. Zhu, E. Streckfuss, H.-Y. Kim, C. A. Parish, S. W. Krska, *Chemical Science* **2018**, *9*, 4168–4175.

[23] P. Li, J. A. Terrett, J. R. Zbieg, *ACS Medicinal Chemistry Letters* **2020**, *11*, 2120–2130.

[24] M. A. Ischay, M. E. Anzovino, J. Du, T. P. Yoon, *Journal of the American Chemical Society* **2008**, *130*, 12886–12887.

[25] D. A. Nicewicz, D. W. C. MacMillan, *Science* **2008**, *322*, 77–80.

[26] J. M. R. Narayanam, J. W. Tucker, C. R. J. Stephenson, *Journal of the American Chemical Society* **2009**, *131*, 8756–8757.

[27] J. J. Douglas, K. P. Cole, C. R. J. Stephenson, *The Journal of Organic Chemistry* **2014**, *79*, 11631–11643.

[28] T. Wan, Z. Wen, G. Laudadio, L. Capaldo, R. Lammers, J. A. Rincón, P. García-Losada, C. Mateos, M. O. Frederick, R. Broersma, T. Noël, *ACS central science* **2022**, *8*, 51–56.

[29] F. Strieth-Kalthoff, M. J. James, M. Teders, L. Pitzer, F. Glorius, *Chemical Society reviews* **2018**, *47*, 7190–7202.

[30] F. Strieth-Kalthoff, F. Glorius, *Chem* **2020**, *6*, 1888–1903.

[31] J. R. Lakowicz, *Principles of fluorescence spectroscopy 3rd ed.*, Springer, New York, **2006**.

[32] M. Zamadar, A. Greer in *Handbook of synthetic photochemistry*, A. Albini, M. Fagnoni (Eds.), Wiley-VCH Verlag GmbH & Co. KGaA, Weinheim, **2010**, pp. 353–386.

[33] N. Boens, W. Qin, N. Basarić, J. Hofkens, M. Ameloot, J. Pouget, J.-P. Lefèvre, B. Valeur, E. Gratton, M. vandeVen, N. D. Silva, Y. Engelborghs, K. Willaert, A. Sillen, G. Rumbles, D. Phillips, A. J. W. G. Visser, A. van Hoek, J. R. Lakowicz, H. Malak, I. Gryczynski, A. G. Szabo, D. T. Krajcarski, N. Tamai, A. Miura, *Analytical Chemistry* **2007**, *79*, 2137–2149.

[34] V. E. Korobov, V. V. Shubin, A. K. Chibisov, *Chemical Physics Letters* **1977**, *45*, 498–501.

[35] S. F. McClanahan, J. R. Kincaid, *Journal of the American Chemical Society* **1986**, *108*, 3840–3841.

[36] K. Kalyanasundaram, *Coordination Chemistry Reviews* **1982**, *46*, 159–244.

[37] O. Ciocirlan, O. Iulian, *Journal of Chemical & Engineering Data* **2012**, *57*, 3142–3148.

[38] J. R. Lakowicz, G. Weber, *Biochemistry* **1973**, *12*, 4161–4170.

[39] M. R. McDevitt, A. W. Addison, *Inorganica Chimica Acta* **1993**, *204*, 141–146.

[40] Q. Li, C. Batchelor-McAuley, N. S. Lawrence, R. S. Hartshorne, R. G. Compton, *Journal of Electroanalytical Chemistry* **2013**, *688*, 328–335.

[41] M. Cherevatskaya, M. Neumann, S. Füldner, C. Harlander, S. Kümmel, S. Dankesreiter, A. Pfitzner, K. Zeitler, B. König, *Angewandte Chemie International Edition* **2012**, *51*, 4062–4066.

[42] D. C. Fabry, J. Zoller, M. Rueping, *Organic Chemistry Frontiers* **2019**, *6*, 2635–2639.

[43] A. Savateev, M. Antonietti, *ACS Catalysis* **2018**, *8*, 9790–9808.

[44] S. M. Fatur, S. G. Shepard, R. F. Higgins, M. P. Shores, N. H. Damrauer, *J. Am. Chem. Soc.* **2017**, *139*, 4493–4505.

[45] G. A. Parada, L. A. Fredin, M.-P. Santoni, M. Jäger, R. Lomoth, L. Hammarström, O. Johansson, P. Persson, S. Ott, *Inorganic chemistry* **2013**, *52*, 5128–5137.

[46] W.-S. Tai, P. Gnanasekaran, Y.-Y. Chen, W.-Y. Hung, X. Zhou, T.-C. Chou, G.-H. Lee, P.-T. Chou, C. You, Y. Chi, *ACS applied materials & interfaces* **2021**.

[47] M. S. Lowry, S. Bernhard, *Chemistry - A European Journal* **2006**, *12*, 7970–7977.

[48] P. Coppo, E. A. Plummer, L. de Cola, *Chem. Comm.* **2004**, 1774–1775.

[49] T. Tsuzuki, N. Shirasawa, T. Suzuki, S. Tokito, *Advanced Materials* **2003**, *15*, 1455–1458.

[50] W. Lu, B.-X. Mi, M. C. W. Chan, Z. Hui, C.-M. Che, N. Zhu, S.-T. Lee, *J. Am. Chem. Soc.* **2004**, *126*, 4958–4971.

[51] N. H. Damrauer, J. K. McCusker, *The Journal of Physical Chemistry A* **1999**, *103*, 8440–8446.

[52] Kristjan Kunnus, Morgane Vacher, Tobias C. B. Harlang, Kasper S. Kjær, Kristoffer Haldrup, Elisa Biasin, Tim B. van Driel, Mátyás Pápai, Pavel Chabera, Yizhu Liu, Hideyuki Tatsuno, Cornelia Timm, Erik Källman, Mickaël Delcey, Robert W. Hartsock, Marco E. Reinhard, Sergey Koroidov, Mads G. Laursen, Frederik B. Hansen, Peter Vester, Morten Christensen, Lise Sandberg, Zoltán Németh, Dorottya Sárosiné Szemes, Éva Bajnóczi, Roberto Alonso-Mori, James M. Glownia, Silke Nelson, Marcin Sikorski, Dimosthenis Sokaras, Henrik T. Lemke, Sophie E. Canton, Klaus B. Møller, Martin M. Nielsen, György Vankó, Kenneth Wärnmark, Villy Sundström, Petter Persson, Marcus Lundberg, Jens Uhlig, Kelly J. Gaffney, *Nature Communications* **2020**, *11*, 1–11.

[53] K. S. Kjær, K. Kunnus, T. C. B. Harlang, T. B. van Driel, K. Ledbetter, R. Hartsock, M. E. Reinhard, S. Koroidov, L. Li, M. G. Laursen, E. Biasin, F. B. Hansen, P. Vester, M. Christensen, K. Haldrup, M. M. M. Nielsen, P. Chabera, Y. Liu, H. Tatsuno, C. Timm, J. Uhlig, V. Sundstrom, Z. Németh, D. Sárosiné Szemes, É. Bajnóczi, G. Vanko, R. A. Mori, J. M. Glownia, S. Nelson, M. Sikorski, D. Sokaras, H. T. Lemke, S. E. Canton, K. Warnmark, P. Persson, A. cordones, K. Gaffney, *Physical Chemistry Chemical Physics* **2018**.

[54] F. Reichenauer, C. Wang, C. Förster, P. Boden, N. Ugur, R. Báez-Cruz, J. Kalmbach, L. M. Carrella, E. Rentschler, C. Ramanan, G. Niedner-Schatteburg, M. Gerhards, M. Seitz, U. Resch-Genger, K. Heinze, *Journal of the American Chemical Society* **2021**, *143*, 11843–11855.

[55] D. P. Hari, B. König, *Chem. Commun.* **2014**, *50*, 6688–6699.

[56] I. Ghosh, L. Marzo, A. Das, R. Shaikh, B. König, *Accounts for Chemical Research* **2016**, *49*, 1566–1577.

[57] I. Ghosh, T. Ghosh, J. I. Bardagi, B. König, *Science* **2014**, *346*, 725–728.

[58] R. Lechner, S. Kümmel, B. König, *Photochemical & Photobiological Sciences* **2010**, *9*, 1367.

[59] A. Juris, V. Balzani, F. Barigelletti, S. Campagna, P. Belser, A. von Zelewsky, *Coordination Chemistry Reviews* **1988**, *84*, 85–277.

[60] G. A. Crosby, J. N. Demas, *Journal of the American Chemical Society* **1971**, *93*, 2841–2847.

[61] E. Deponti, M. Natali, *Dalton Transactions* **2016**, *45*, 9136–9147.

[62] L. Flamigni, A. Barbieri, C. Sabatini, B. Ventura, F. Barigelletti in *Photochemistry and Photophysics of Coordination Compounds II*, of *Topics in Current Chemistry*, V. Balzani, S. Campagna (Eds.), Springer Berlin Heidelberg, Berlin, Heidelberg, **2007**, pp. 143–203.

[63] J. Mabiza-ma Mabiza, C. Mbohwa in *Transactions on Engineering Technologies*, *Vol. 31*, S.-i. Ao, G.-C. Yang, L. Gelman (Eds.), Springer Singapore, Singapore, **2016**, pp. 273–283.

[64] P. Dierks, Y. Vukadinovic, M. Bauer, *Inorganic Chemistry Frontiers* **2022**, *9*, 206–220.

[65] M. Ruthkosky, F. N. Castellano, G. J. Meyer, *Inorganic chemistry* **1996**, *35*, 6406–6412.

[66] M. Pirtsch, S. Paria, T. Matsuno, H. Isobe, O. Reiser, *Chemistry - A European Journal* **2012**, *18*, 7336–7340.

[67] M. Hashimoto, S. Igawa, M. Yashima, I. Kawata, M. Hoshino, M. Osawa, *Journal of the American Chemical Society* **2011**, *133*, 10348–10351.

[68] L. A. Büldt, O. S. Wenger, *Dalton transactions (Cambridge, England : 2003)* **2017**, *46*, 15175–15177.

[69] L. A. Büldt, X. Guo, R. Vogel, A. Prescimone, O. S. Wenger, *Journal of the American Chemical Society* **2017**, *139*, 985–992.

[70] M. Dorn, J. Kalmbach, P. Boden, A. Päpcke, S. Gómez, C. Förster, F. Kuczelinis, L. M. Carrella, L. A. Büldt, N. H. Bings, E. Rentschler, S. Lochbrunner, L. González, M. Gerhards, M. Seitz, K. Heinze, *J. Am. Chem. Soc.* **2020**, *142*, 7947–7955.

[71] S. Otto, M. Grabolle, C. Förster, C. Kreitner, U. Resch-Genger, K. Heinze, *Angewandte Chemie International Edition* **2015**, *54*, 11572–11576.

[72] K. S. Egorova, V. P. Ananikov, *Organometallics* **2017**, *36*, 4071–4090.

[73] F. Lafolet, J. Chauvin, M.-N. Collomb, A. Deronzier, H. Laguitton-Pasquier, J.-C. Leprêtre, J.-C. Vial, B. Brasme, *Physical Chemistry Chemical Physics* **2003**, *5*, 2520.

[74] J. K. McCusker, *Science* **2019**, *363*, 484–488.

[75] Pekka Pyykkö, *Phys. Scr.* **1979**, *20*, 647–651.

[76] M. Kaupp, *Journal of computational chemistry* **2007**, *28*, 320–325.

[77] G. Auböck, M. Chergui, *Nature Chemistry* **2015**, *7*, 629–633.

[78] J. Nance, D. N. Bowman, S. Mukherjee, C. T. Kelley, E. Jakubikova, *Inorganic chemistry* **2015**, *54*, 11259–11268.

[79] M. Nakaya, R. Ohtani, L. F. Lindoy, S. Hayami, *Inorganic Chemistry Frontiers* **2021**, *8*, 484–498.

[80] M. D. Woodhouse, J. K. McCusker, *Journal of the American Chemical Society* **2020**, *142*, 16229–16233.

[81] P. Dierks, A. Kruse, O. S. Bokareva, M. J. Al-Marri, J. Kalmbach, M. Baltrun, A. Neuba, R. Schoch, S. Hohloch, K. Heinze, M. Seitz, O. Kühn, S. Lochbrunner, M. Bauer, *Chem. Commun.* **2021**, *57*, 6640–6643.

[82] L. L. Jamula, A. M. Brown, D. Guo, J. K. McCusker, *Inorganic chemistry* **2014**, *53*, 15–17.

[83] M. Abrahamsson, M. Jager, T. Osterman, L. Eriksson, P. Persson, H.-C. Becker, O. Johansson, L. Hammarstrom, *J. Am. Chem. Soc.* **2006**, *128*, 12616–12617.

[84] A. K. C. Mengel, C. Förster, A. Breivogel, K. Mack, J. R. Ochsmann, F. Laquai, V. Ksenofontov, K. Heinze, *Chemistry - A European Journal* **2015**, *21*, 704–714.

[85] M. Darari, A. Francés-Monerris, B. Marekha, A. Doudouh, E. Wenger, A. Monari, S. Haacke, P. C. Gros, *Molecules* **2020**, *25*, 5991.

[86] Y. Liu, T. Harlang, S. E. Canton, P. Chábera, K. Suárez-Alcántara, A. Fleckhaus, D. A. Vithanage, E. Göransson, A. Corani, R. Lomoth, V. Sundström, K. Wärnmark, *Chem. Comm.* **2013**, *49*, 6412–6414.

[87] L. A. Fredin, M. Pápai, E. Rozsályi, G. Vankó, K. Wärnmark, V. Sundström, P. Persson, *The journal of physical chemistry letters* **2014**, *5*, 2066–2071.

[88] T. C. B. Harlang, Y. Liu, O. Gordivska, L. A. Fredin, C. S. Ponseca, P. Huang, P. Chábera, K. S. Kjaer, H. Mateos, J. Uhlig, R. Lomoth, R. Wallenberg, S. Styring, P. Persson, V. Sundström, K. Wärnmark, *Nature Chemistry* **2015**, *7*, 883–889.

[89] L. Liu, T. Duchanois, T. Etienne, A. Monari, M. Beley, X. Assfeld, S. Haacke, P. C. Gros, *Physical Chemistry Chemical Physics* **2016**, *18*, 12550–12556.

[90] M. Darari, E. Domenichini, A. Francés-Monerris, C. Cebrián, K. Magra, M. Beley, M. Pastore, A. Monari, X. Assfeld, S. Haacke, P. C. Gros, *Dalton transactions* **2019**, *48*, 10915–10926.

[91] T. Reuter, A. Kruse, R. Schoch, S. Lochbrunner, M. Bauer, K. Heinze, *Chem. Commun.* **2021**, *57*, 7541–7544.

[92] P. Zimmer, P. Müller, L. Burkhardt, R. Schepper, A. Neuba, J. Steube, F. Dietrich, U. Flörke, S. Mangold, M. Gerhards, M. Bauer, *Eur. J. Inorg. Chem.* **2017**, *2017*, 1504–1509.

[93] M. Huber-Gedert, M. Nowakowski, A. Kertmen, L. Burkhardt, N. Lindner, R. Schoch, R. Herbst-Irmer, A. Neuba, L. Schmitz, T.-K. Choi, J. Kubicki, W. Gawelda, M. Bauer, *Chemistry (Weinheim an der Bergstrasse, Germany)* **2021**, *27*, 9905–9918.

[94] P. Zimmer, L. Burkhardt, A. Friedrich, J. Steube, A. Neuba, R. Schepper, P. Müller, U. Flörke, M. Huber, S. Lochbrunner, M. Bauer, *Inorganic chemistry* **2018**, *57*, 360–373.

[95] P. Chabera, K. S. Kjær, O. Prakash, A. Honarfar, Y. Liu, L. A. Fredin, T. B. Harlang, S. Lidin, J. Uhlig, V. Sundstrom, R. Lomoth, P. Persson, K. Wärnmark, P. Chábera, K. S. Kjaer, T. C. B. Harlang, V. Sundström, *The journal of physical chemistry letters* **2018**, *9*, 459–463.

[96] Y. Liu, P. Persson, V. Sundstrom, K. Wärnmark, *Accounts for Chemical Research* **2016**, *49*, 1477–1485.

[97] D. J. Nelson, S. P. Nolan in *N-Heterocyclic carbenes*, S. P. Nolan (Ed.), Wiley-VCH, Weinheim an der Bergstrasse, Germany, **2014**, pp. 1–24.

[98] L. L. Tinker, N. D. McDaniel, P. N. Curtin, C. K. Smith, M. J. Ireland, S. Bernhard, *Chemistry - A European Journal* **2007**, *13*, 8726–8732.

[99] P. G. Bomben, K. C. D. Robson, P. A. Sedach, C. P. Berlinguette, *Inorganic chemistry* **2009**, *48*, 9631–9643.

[100] P. G. Bomben, K. C. Robson, B. D. Koivisto, C. P. Berlinguette, *Coordination Chemistry Reviews* **2012**, *256*, 1438–1450.

[101] R. Kaneko, G. Wu, K. Sugawa, J. Otsuki, A. Islam, L. Han, I. Bedja, R. K. Gupta, *J. Organomet. Chem.* **2017**, *833*, 61–70.

[102] H. Kisserwan, A. Kamar, T. Shoker, T. H. Ghaddar, *Dalton transactions* **2012**, *41*, 10643–10651.

[103] T. C. Motley, L. Troian-Gautier, M. K. Brennaman, G. J. Meyer, *Inorganic chemistry* **2017**, *56*, 13579–13592.

[104] S. Mukherjee, D. N. Bowman, E. Jakubikova, *Inorganic chemistry* **2015**, *54*, 560–569.

[105] I. M. Dixon, F. Alary, M. Boggio-Pasqua, J.-L. Heully, *Dalton transactions* **2015**, *44*, 13498–13503.

[106] W. Leis, M. A. Argüello Cordero, S. Lochbrunner, H. Schubert, A. Berkefeld, *Journal of the American Chemical Society* **2022**, *144*, 1169–1173.

[107] A. S. Estrada-Montaño, A. D. Ryabov, A. Gries, C. Gaiddon, R. Le Lagadec, *Eur. J. Inorg. Chem.* **2017**, *2017*, 1673–1678.

[108] P. Chabera, Y. Liu, O. Prakash, E. Thyrhaug, A. E. Nahhas, A. Honarfar, S. Essen, L. A. Fredin, T. C. B. Harlang, K. S. Kjaer, K. Handrup, F. Ericson, H. Tatsuno, K. Morgan, J. Schnadt, L. Haggstrom, T. Ericsson, A. Sobkowiak, S. Lidin, P. Huang, S. Styring, J. Uhlig, J. Bendix, R. Lomoth, V. Sundstrom, P. Persson, K. Wärnmark, *Nature* **2017**, *543*, 695–699.

[109] K. S. Kjær, N. Kaul, O. Prakash, P. Chábera, N. W. Rosemann, A. Honarfar, O. Gordivska, L. A. Fredin, K.-E. Bergquist, L. Häggström, T. Ericsson, L. Lindh, A. Yartsev, S. Styring, P. Huang, J. Uhlig, J. Bendix, D. Strand, V. Sundström, P. Persson, R. Lomoth, K. Wärnmark, *Science* **2019**, *363*, 249–253.

[110] P. Chábera, L. Lindh, N. W. Rosemann, O. Prakash, J. Uhlig, A. Yartsev, K. Wärnmark, V. Sundström, P. Persson, *Coordination Chemistry Reviews* **2021**, *426*, 213517.

[111] J. J. Adams, N. Arulsamy, B. P. Sullivan, D. M. Roddick, A. Neuberger, R. H. Schmehl, *Inorganic chemistry* **2015**, *54*, 11136–11149.

[112] S. Chatterjee, A. S. Del Negro, F. N. Smith, Z. Wang, S. E. Hightower, B. P. Sullivan, W. R. Heineman, C. J. Seliskar, S. A. Bryan, *The journal of physical chemistry. A* **2013**, *117*, 12749–12758.

[113] Y. F. Lee, J. R. Kirchhoff, *J. Am. Chem. Soc.* **1994**, *116*, 3599–3600.

[114] A. Vogler, H. Kunkely, *Inorganica Chimica Acta* **1981**, *53*, L215–L216.

[115] N. W. Rosemann, P. Chábera, O. Prakash, S. Kaufhold, K. Wärnmark, A. Yartsev, P. Persson, *Journal of the American Chemical Society* **2020**, *142*, 8565–8569.

[116] A. Aydogan, R. E. Bangle, A. Cadranel, M. D. Turlington, D. T. Conroy, E. Cauët, M. L. Singleton, G. J. Meyer, R. N. Sampaio, B. Elias, L. Troian-Gautier, *Journal of the American Chemical Society* **2021**, *143*, 15661–15673.

[117] M. Albrecht, *Chemical reviews* **2010**, *110*, 576–623.

[118] M. Puri, S. Gatard, D. A. Smith, O. V. Ozerov, *Organometallics* **2011**, *30*, 2472–2482.

[119] A. O. King, N. Okukado, E.-i. Negishi, *Journal of the Chemical Society, Chemical Communications* **1977**, 683.

[120] M. Kumada, *Organic Syntheses* **1978**, *58*, 127.

[121] J. K. Stille, *Angewandte Chemie* **1986**, *98*, 504–519.

[122] N. Miyaura, A. Suzuki, *Chemical reviews* **1995**, *95*, 2457–2483.

[123] E. McNeill, T. Ritter, *Accounts for Chemical Research* **2015**, *48*, 2330–2343.

[124] S. C. Rasmussen, *ChemTexts* **2021**, *7*.

[125] D. L. Jameson, L. E. Guise, *Tetrahedron Letters* **1991**, *32*, 1999–2002.

[126] A. Sandleben, N. Vogt, G. Hörner, A. Klein, *Organometallics* **2018**.

[127] N. Vogt, A. Sandleben, L. Kletsch, S. Schäfer, M. T. Chin, D. A. Vicic, G. Hörner, A. Klein, *Organometallics* **2021**, *40*, 1776–1785.

[128] A. Klein, B. Rausch, A. Kaiser, N. Vogt, A. Krest, *J. Organomet. Chem.* **2014**, *774*, 86–93.

[129] T. W. Rees, J. Liao, A. Sinopoli, L. Male, G. Calogero, B. F. E. Curchod, E. Baranoff, *Inorganic chemistry* **2017**, *56*, 9903–9912.

[130] TCI Chemicals, *6-Bromo-2,2'-bipyridyl*. `https://www.tcichemicals.com/DE/de/p/B4114`.

[131] G. S. Hanan, U. S. Schubert, D. Volkmer, E. Rivière, J.-M. Lehn, N. Kyritsakas, J. Fischer, *Canadian Journal of Chemistry* **1997**, *75*, 169–182.

[132] Y.-Q. Fang, G. S. Hanan, *Synlett* **2003**, 852–854.

[133] I. M. Dixon, S. Khan, F. Alary, M. Boggio-Pasqua, J.-L. Heully, *Dalton transactions* **2014**, *43*, 15898–15905.

[134] E. C. Constable, T. A. Leese, *J. Organomet. Chem.* **1987**, *335*, 293–299.

[135] R. Kumar, C. Nevado, *Angewandte Chemie International Edition* **2017**, *56*, 1994–2015.

[136] M. T. DuPriest, C. L. Schmidt, D. Kuzmich, S. B. Williams, *The Journal of Organic Chemistry* **1986**, *51*, 2021–2023.

[137] R. Shang, L. Ilies, E. Nakamura, *Chemical reviews* **2017**.

[138] A. S. Estrada-Montaño, A. Gries, J. A. Oviedo-Fortino, C. Torres-Gutierrez, A. Grain-Hayton, R. Marcial-Hernández, L. Shen, A. D. Ryabov, C. Gaiddon, R. Le Lagadec, *Organometallics* **2020**, *39*, 1842–1854.

[139] H. G. O. Becker, *Organikum: Organisch-chemisches Grundpraktikum 21st ed.*, Wiley-VCH, Weinheim, **2001**.

[140] A. Krasovskiy, V. Krasovskaya, P. Knochel, *Angew. Chem., Int. Ed.* **2006**, *45*, 2958–2961.

[141] R. A. Andersen, K. Faegri, J. C. Green, A. Haaland, M. F. Lappert, W. P. Leung, K. Rypdal, *Inorganic chemistry* **1988**, *27*, 1782–1786.

[142] S. H. Wunderlich, P. Knochel, *Angew. Chem., Int. Ed.* **2009**, *48*, 9717–9720.

[143] H.-F. Klein, S. Camadanli, R. Beck, U. Flörke, *Chem. Comm.* **2005**, 381–382.

[144] H.-F. Klein, S. Camadanli, R. Beck, D. Leukel, U. Flörke, *Angewandte Chemie International Edition* **2005**, *44*, 975–977.

[145] S. Camadanli, R. Beck, U. Flörke, H.-F. Klein, *Organometallics* **2009**, *28*, 2300–2310.

[146] J. Steube, L. Burkhardt, A. Päpcke, J. Moll, P. Zimmer, R. Schoch, C. Wölper, K. Heinze, S. Lochbrunner, M. Bauer, *Chemistry - A European Journal* **2019**, *25*, 11826–11830.

[147] Z. Tang, X.-Y. Chang, Q. Wan, J. Wang, C. Ma, K.-C. Law, Y. Liu, C.-M. Che, *Organometallics* **2020**, *39*, 2791–2802.

[148] A. Collado, J. Bohnenberger, M.-J. Oliva-Madrid, P. Nun, D. B. Cordes, A. M. Z. Slawin, S. P. Nolan, *Eur. J. Inorg. Chem.* **2016**, *2016*, 4111–4122.

[149] R. J. Rubio, G. T. S. Andavan, E. B. Bauer, T. K. Hollis, J. Cho, F. S. Tham, B. Donnadieu, *Journal of Organometallic Chemistry* **2005**, *690*, 5353–5364.

[150] T. K. Hollis, C. E. Webster, *Unsymmetrical Salts, CCC-NHC Pincer Metal Complexes and Methods of Making the Same: International Patent*, **2018**. https://worldwide.espacenet.com/publicationDetails/biblio?FT=D&date=20180927&DB=&locale=en_EP&CC=WO&NR=2018175659A1&KC=A1&ND=5.

[151] M. Nakajima, E. Fava, S. Loescher, Z. Jiang, M. Rueping, *Angew. Chem., Int. Ed.* **2015**, *54*, 8828–8832.

[152] K. Li, Q. Wan, C. Yang, X.-Y. Chang, K.-H. Low, C.-M. Che, *Angew. Chem., Int. Ed.* **2018**, *57*, 14129–14133.

[153] Merck KGaA, *Safety Data Sheet for Triethanolamin 822341*, **2021**. https://www.merckmillipore.com/DE/de/product/msds/MDA_CHEM-822341.

[154] Merck KGaA, *Safety Data Sheet for Tributylamin 808358*, **2021**. https://www.merckmillipore.com/DE/de/product/msds/MDA_CHEM-808358.

[155] M. Jeganmohan, P. Knochel, *Angewandte Chemie (International ed. in English)* **2010**, *49*, 8520–8524.

[156] J. Steube, A. Kruse, O. S. Bokareva, T. Reuter, S. Demeshko, R. Schoch, M. A. Argüello Cordero, A. Krishna, S. Hohloch, F. Meyer, K. Heinze, O. Kühn, S. Lochbrunner, M. Bauer, *Nature Chemistry* **2023**.

[157] L. Pause, M. Robert, J.-M. Savéant, *Journal of the American Chemical Society* **1999**, *121*, 7158–7159.

[158] E. Fišerová, M. Kubala, *Journal of Luminescence* **2012**, *132*, 2059–2064.

[159] G. Zatryb, M. M. Klak, *Journal of physics. Condensed matter : an Institute of Physics journal* **2020**, *32*.

[160] A. Sillen, Y. Engelborghs, *Photochemistry and Photobiology* **1998**, *67*, 475–486.

[161] D. B. G. Williams, M. Lawton, *The Journal of organic chemistry* **2010**, *75*, 8351–8354.

[162] G. R. Fulmer, A. J. M. Miller, N. H. Sherden, H. E. Gottlieb, A. Nudelman, B. M. Stoltz, J. E. Bercaw, K. I. Goldberg, *Organometallics* **2010**, *29*, 2176–2179.

[163] R. S. Nicholson, I. Shain, *Analytical Chemistry* **1964**, *36*, 706–723.

[164] J. Heinze, *Angewandte Chemie* **1984**, *96*, 823–840.

[165] J. E. B. Randles, *Trans. Faraday Soc.* **1948**, *44*, 327–338.

[166] F. Scholz, A. M. Bond, R. G. Compton, D. A. Fiedler, G. Inzelt, H. Kahlert, Š. Komorsky-Lovrić, H. Lohse, M. Lovrić, F. Marken, A. Neudeck, U. Retter, F. Scholz, Z. Stojek, *Electroanalytical Methods*, Springer Berlin Heidelberg, Berlin, Heidelberg, **2010**.

[167] E. Ioachim, E. A. Medlycott, M. I. J. Polson, G. S. Hanan, *European Journal of Organic Chemistry* **2005**, *2005*, 3775–3780.

[168] C. Li, C. Gao, J. Lan, J. You, G. Gao, *Org. Biomol. Chem.* **2014**, *12*, 9524–9527.

[169] D. Samanta, A. Chowdhury, P. S. Mukherjee, *Inorganic chemistry* **2016**, *55*, 1562–1568.

[170] J. Liu, T.-L. Lam, M.-K. Sit, Q. Wan, C. Yang, G. Cheng, C.-M. Che, *Journal of Materials Chemistry C* **2022**, *10*, 10271–10283.

[171] A. Aijaz, E. C. Sañudo, P. K. Bharadwaj, *Crystal Growth & Design* **2011**, *11*, 1122–1134.

List of Figures

List of Schemes

List of Tables

Appendix

A. Spectra

1a: ^{1}H-NMR

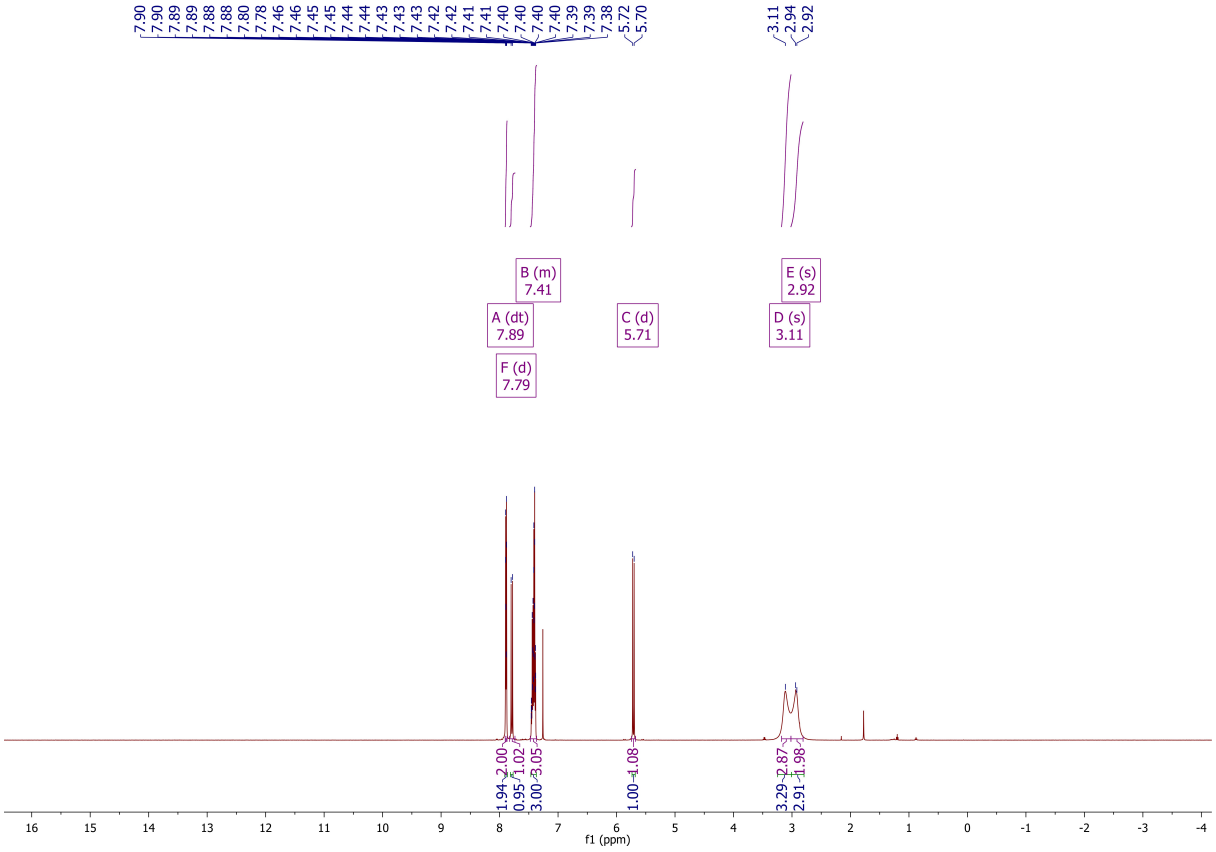

2: ^{1}H-NMR, ^{13}C-NMR, ^{15}N-NMR

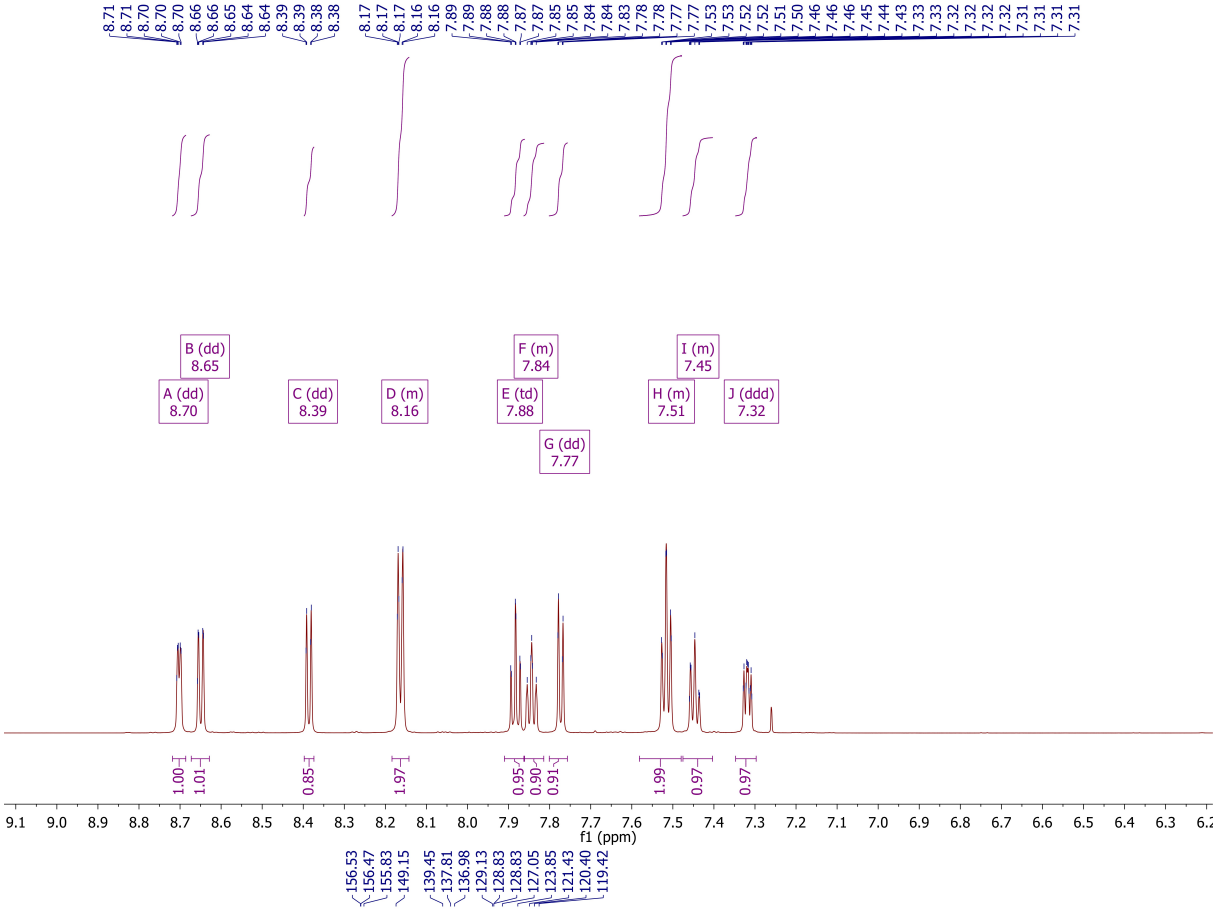

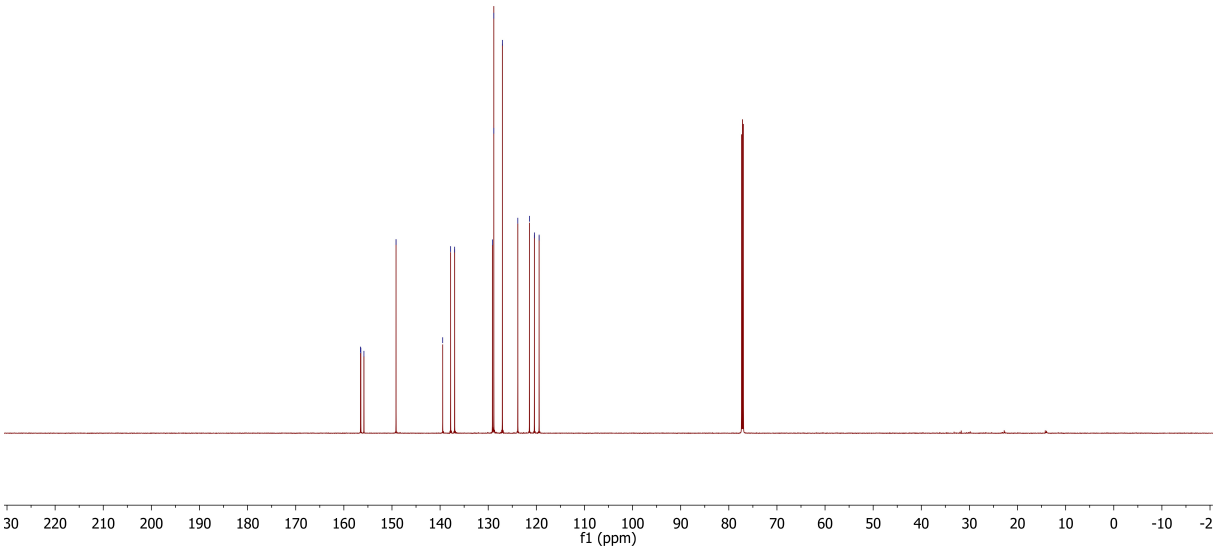

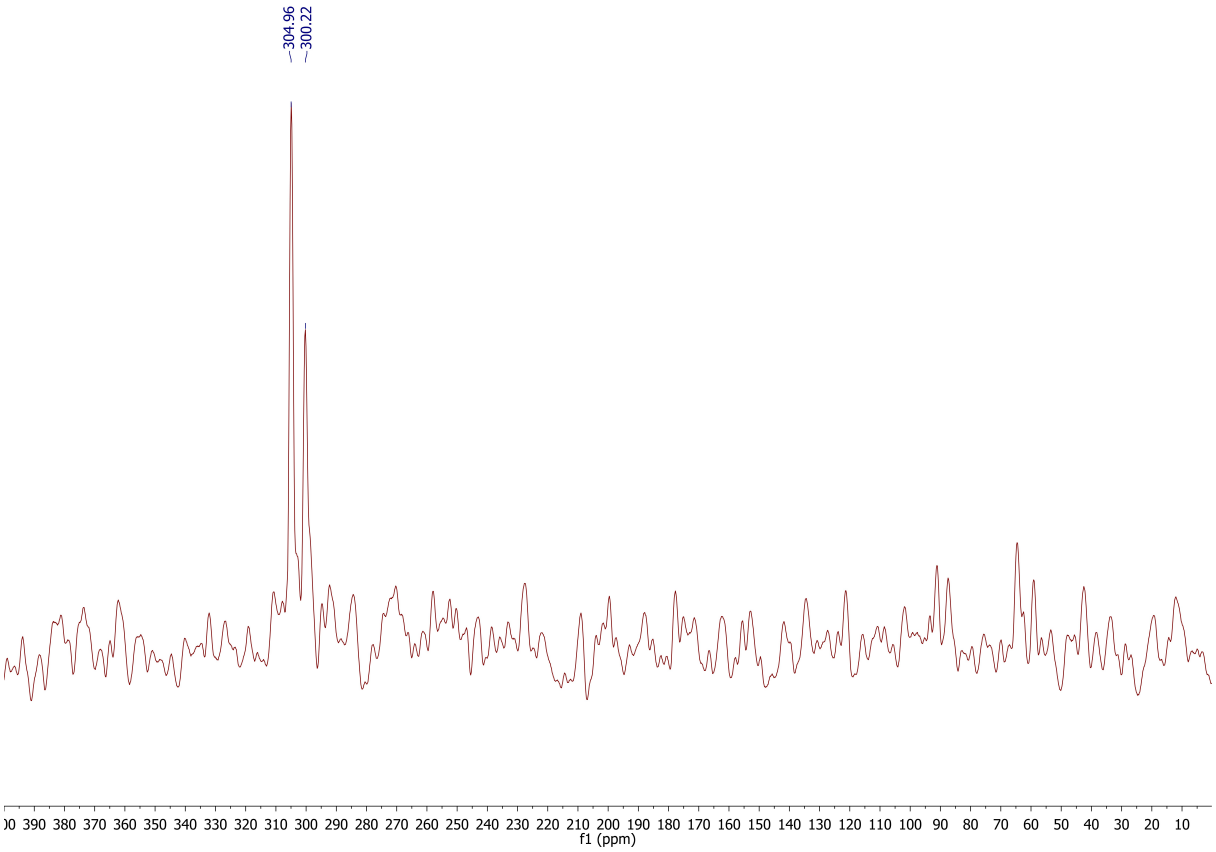

3: ^{1}H-NMR, ^{13}C-NMR,

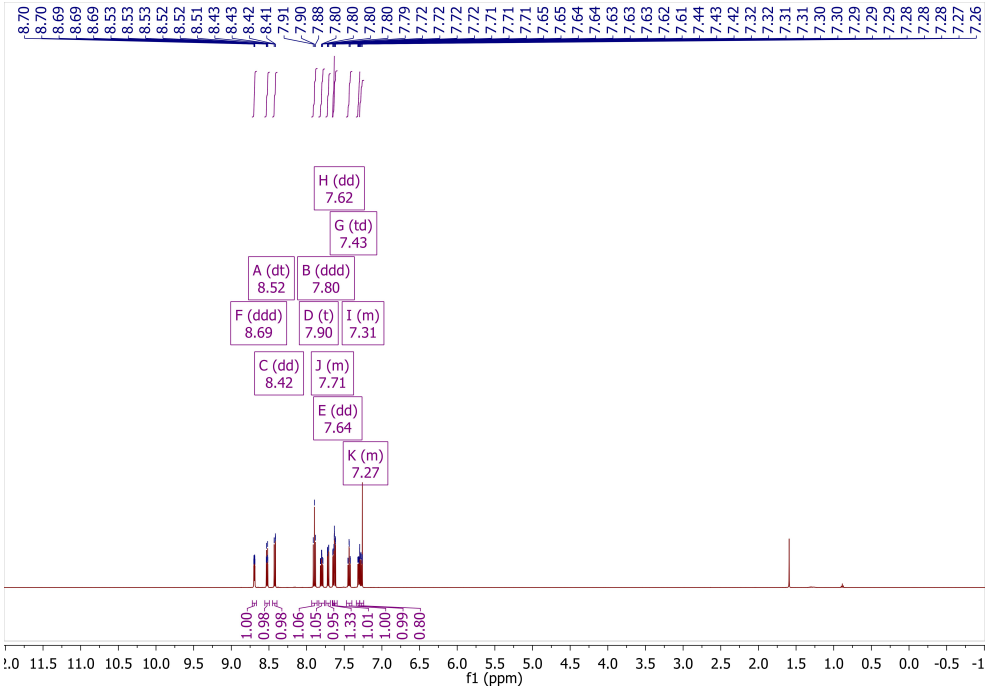

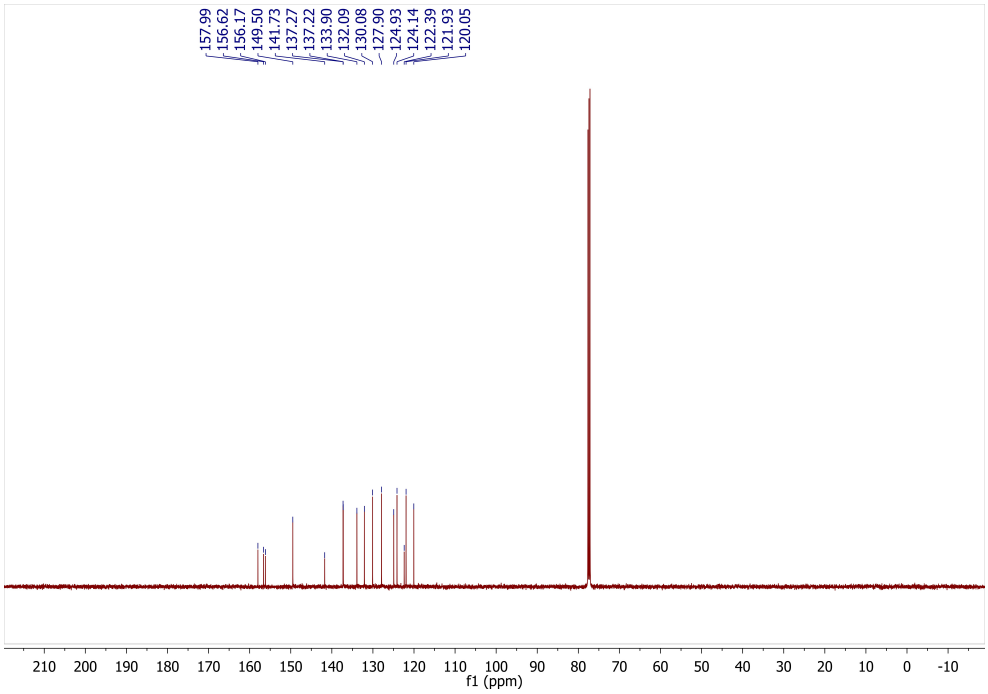

4,4'-bis(trifluoromethyl)-2,2'-bipyridine: ^{1}H-NMR, ^{13}C-NMR, ^{19}F-NMR

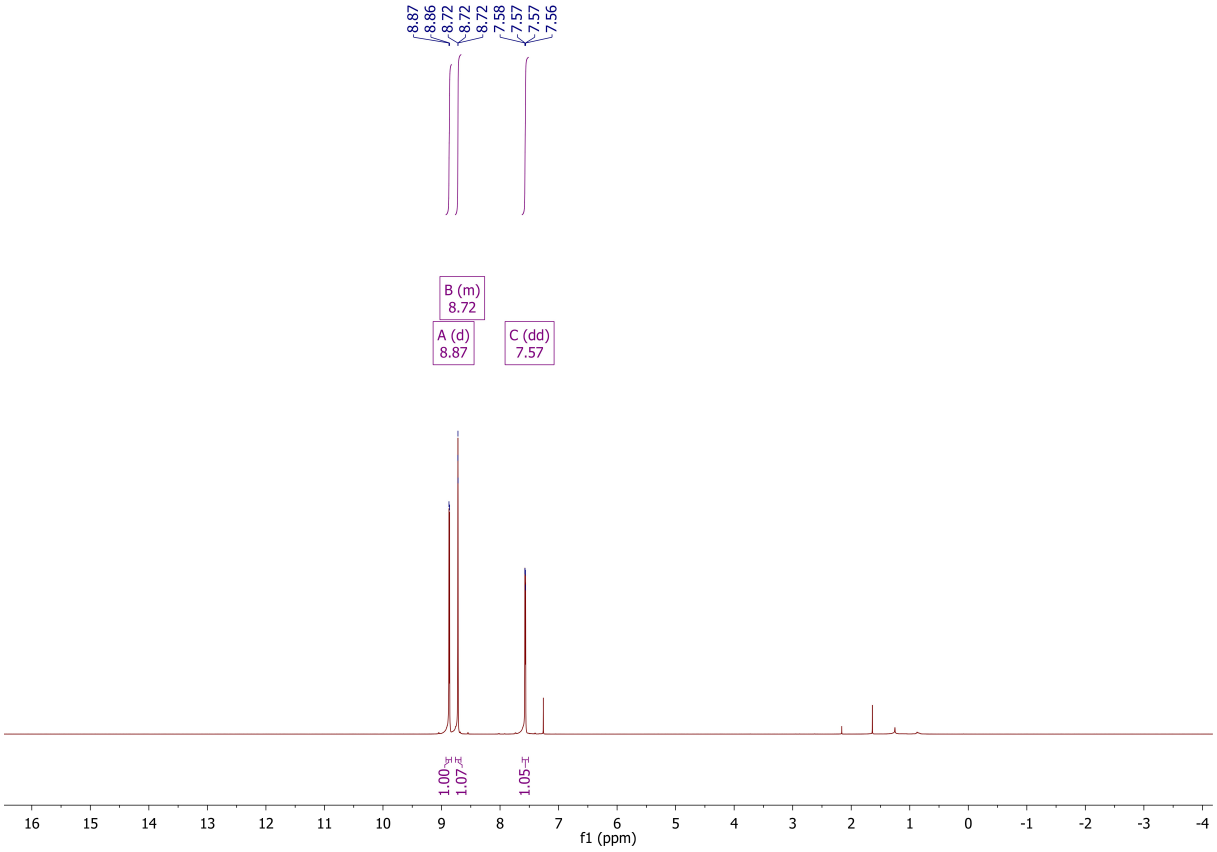

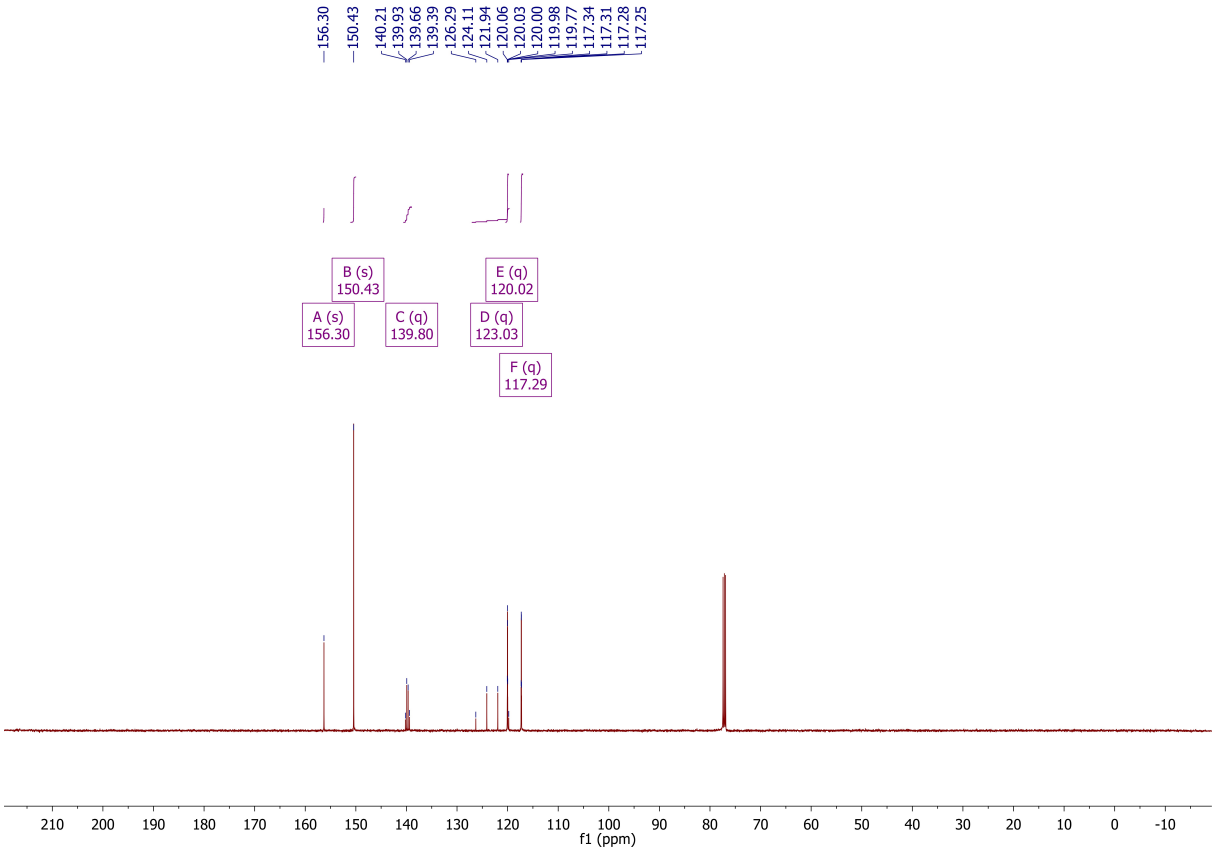
156.30
150.43
140.21
139.93
139.66
139.39
126.29
124.11
121.94
120.06
120.03
120.00
119.98
119.77
117.34
117.31
117.28
117.25
B (s)
150.43
E (q)
120.02
A (s)
156.30
C (q)
139.80
D (q)
123.03
F (q)
117.29
210 200 190 180 170 160 150 140 130 120 110 100 90 80 70 60 50 40 30 20 10 0 -10
f1 (ppm)

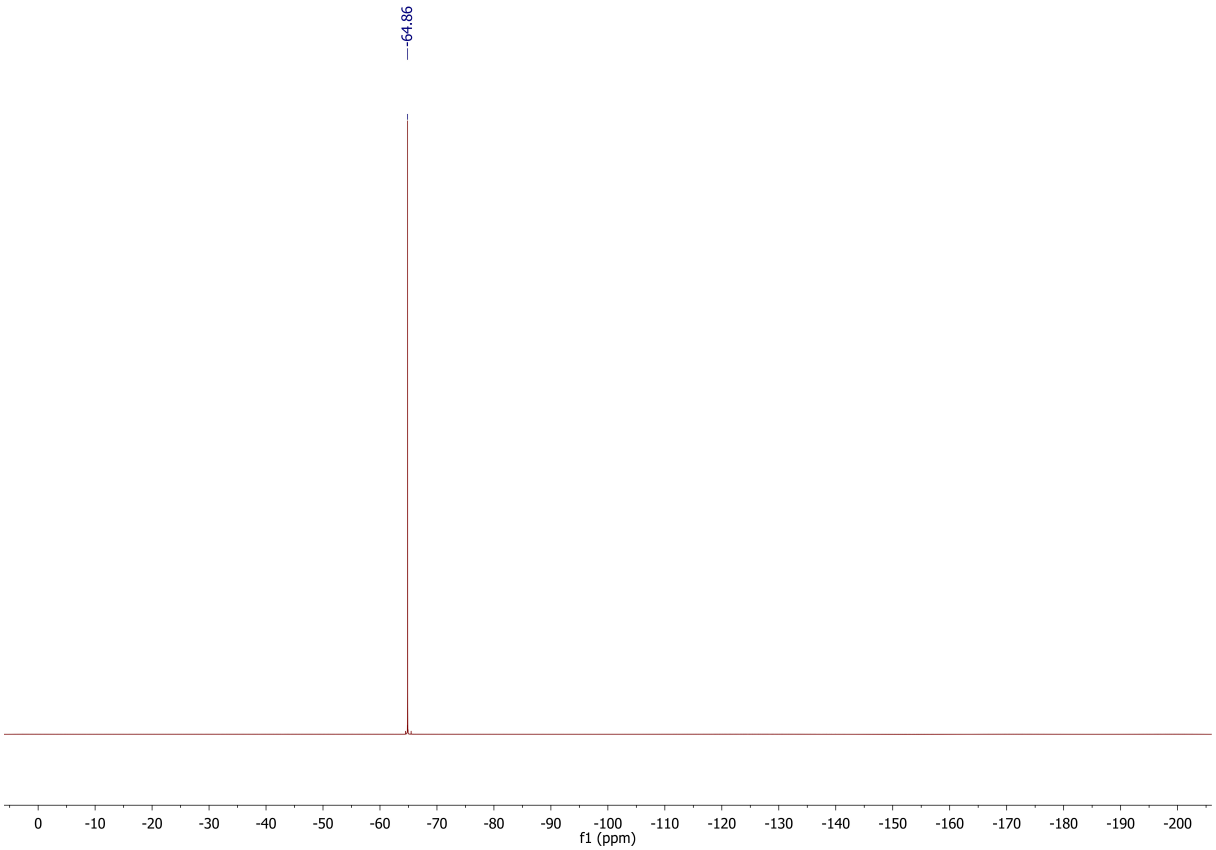
-64.86
0 -10 -20 -30 -40 -50 -60 -70 -80 -90 -100 -110 -120 -130 -140 -150 -160 -170 -180 -190 -200
f1 (ppm)

6b: ^{1}H-NMR, ^{13}C-NMR, ^{19}F-NMR

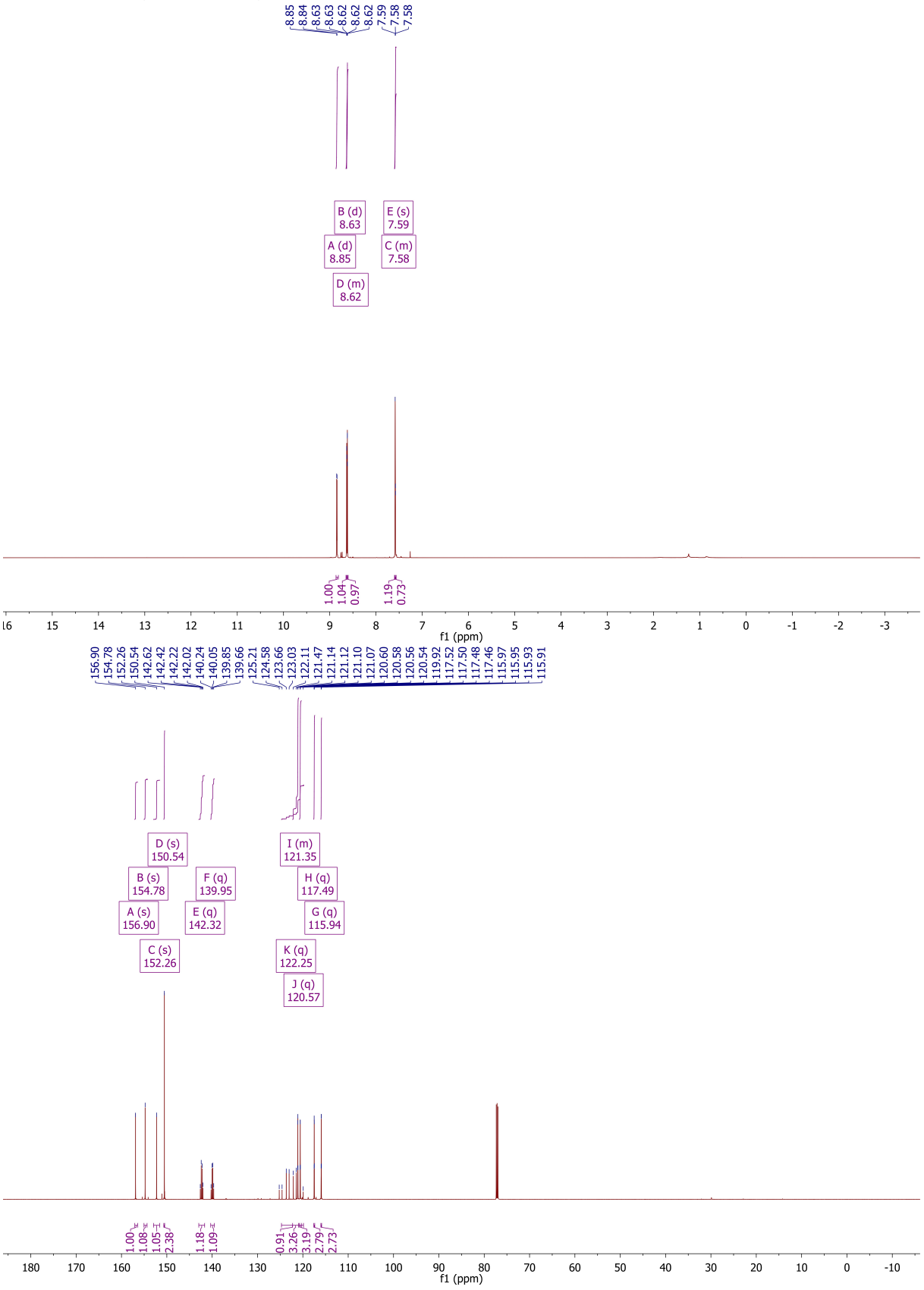

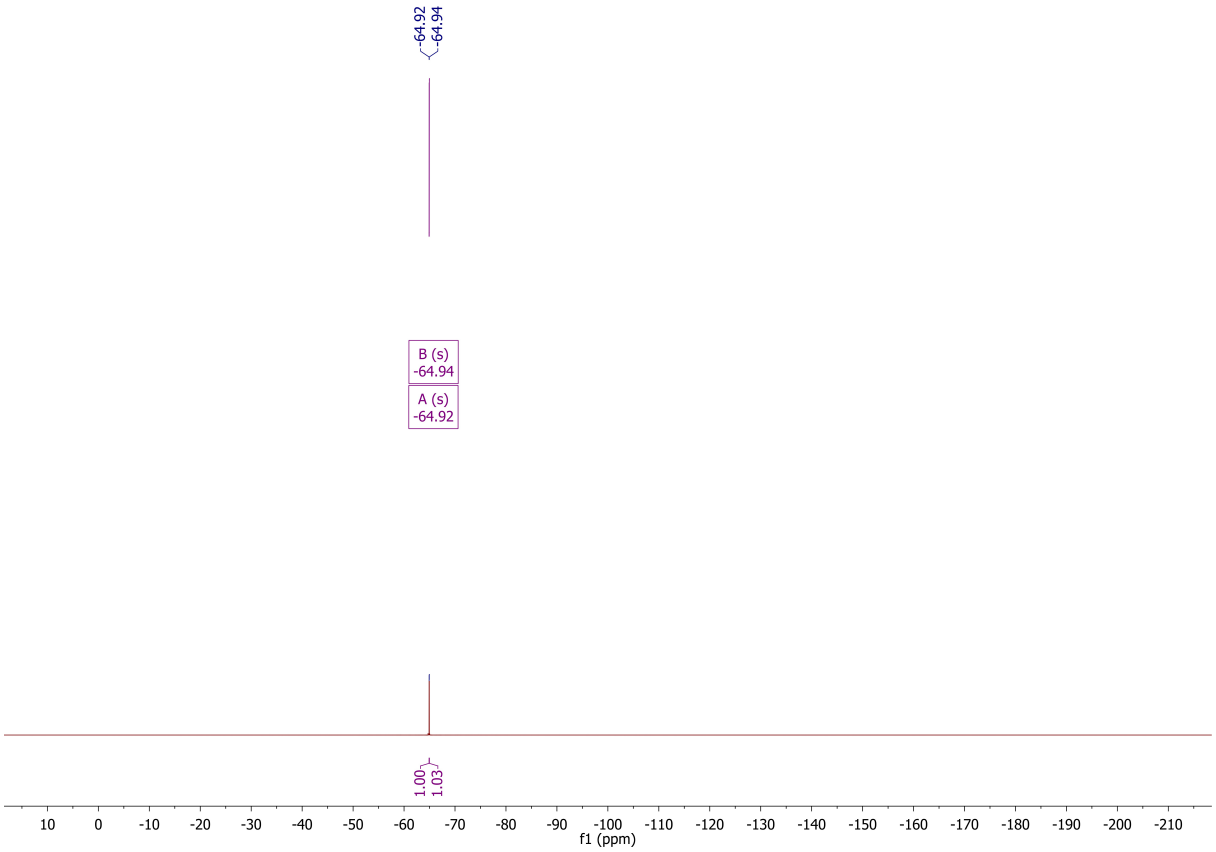

2a: ^{1}H-NMR, ^{13}C-NMR

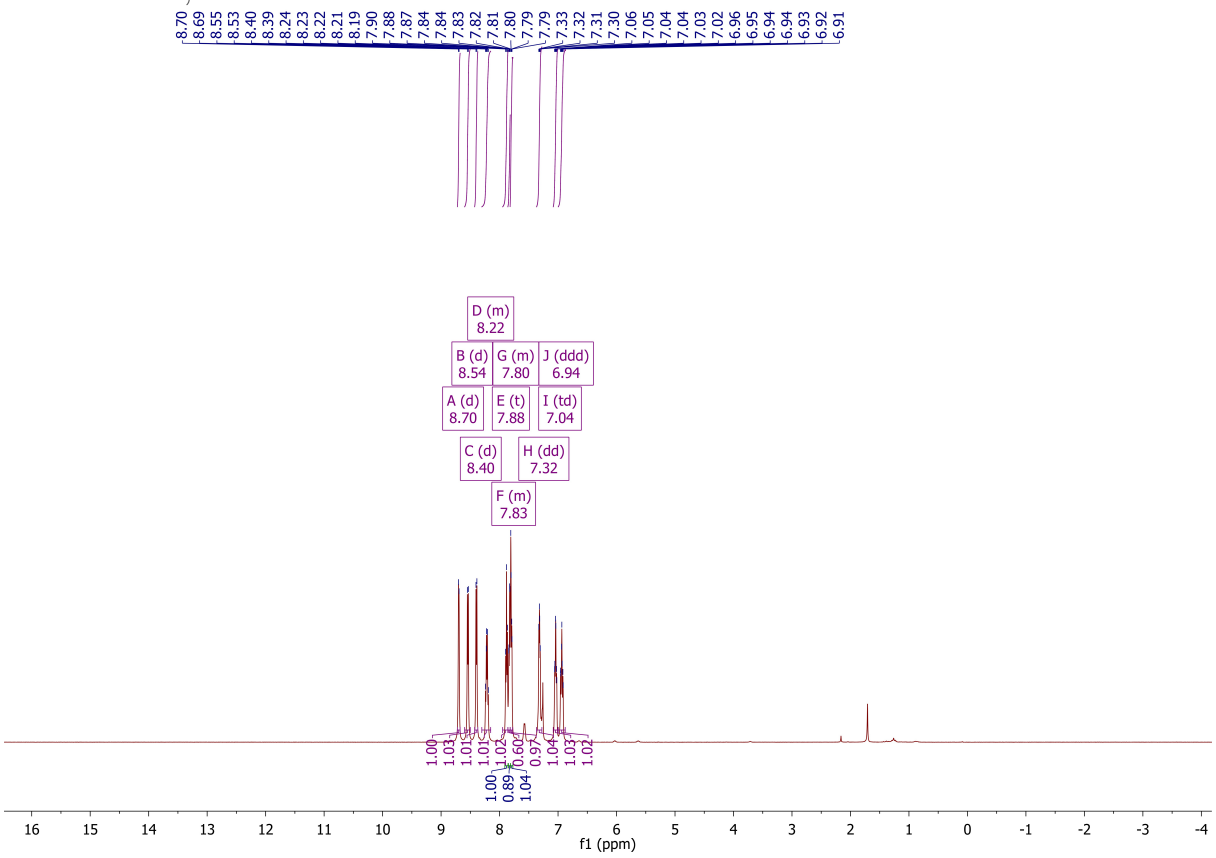

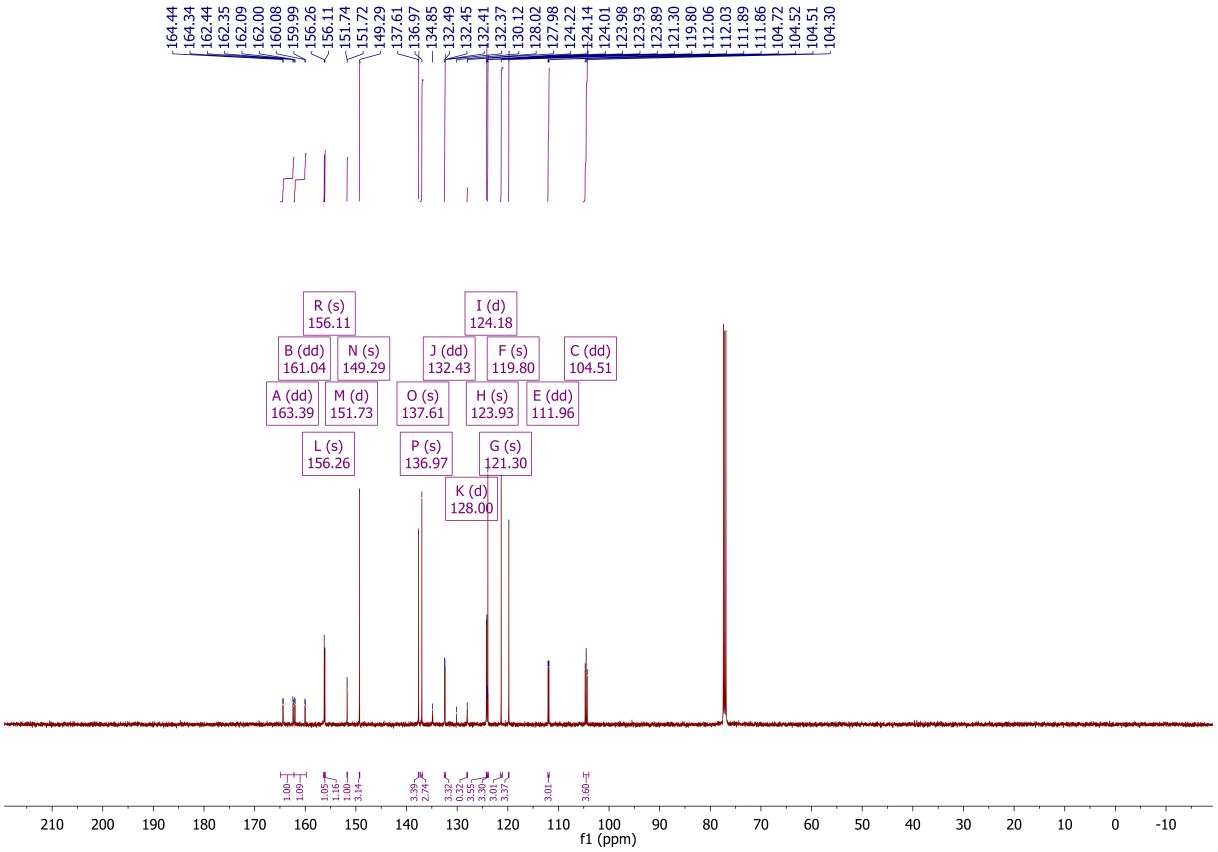

2b: ^{1}H-NMR, ^{19}F-NMR

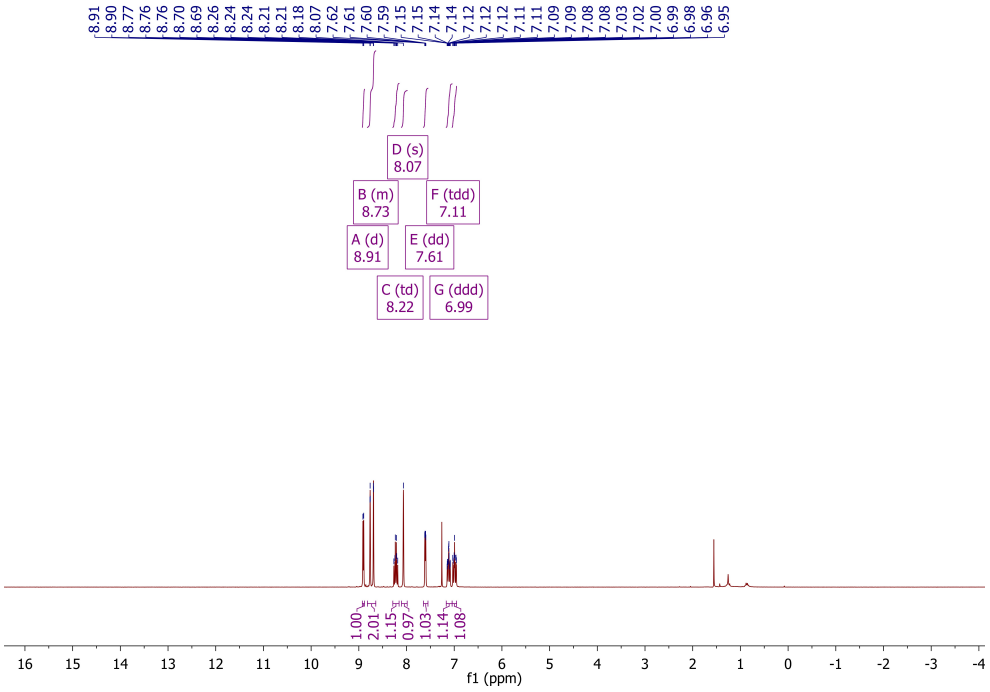

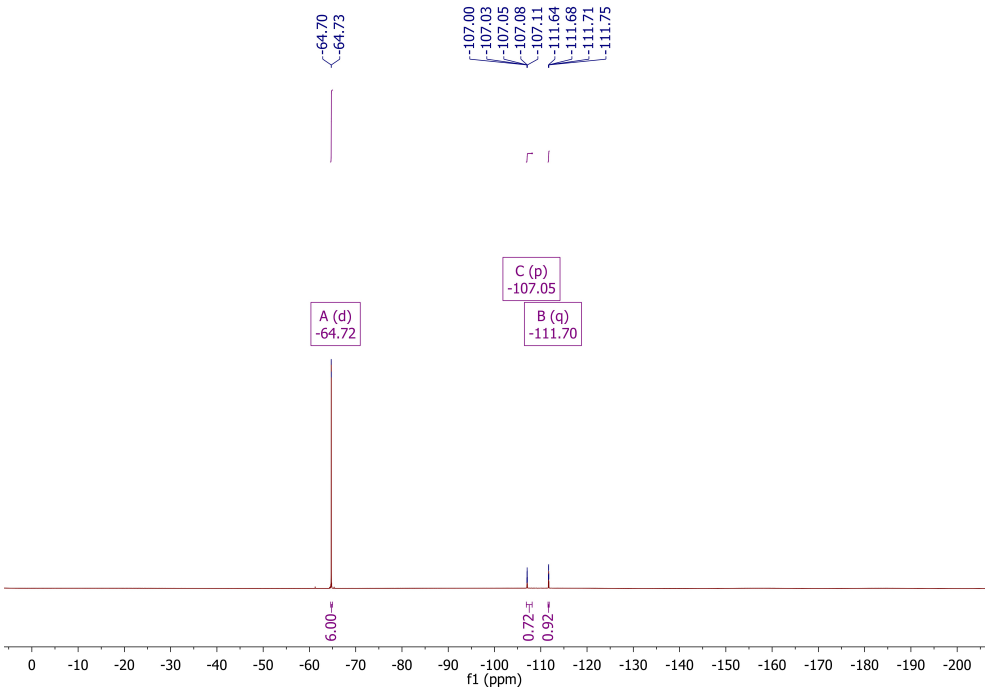

2c: ^{1}H-NMR, ^{19}F-NMR

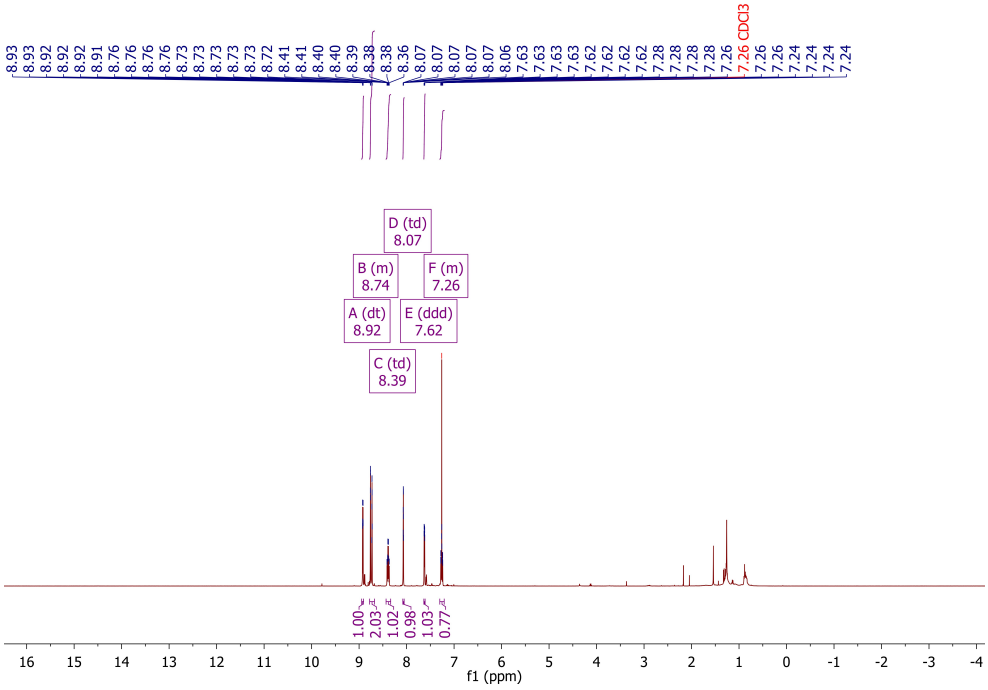

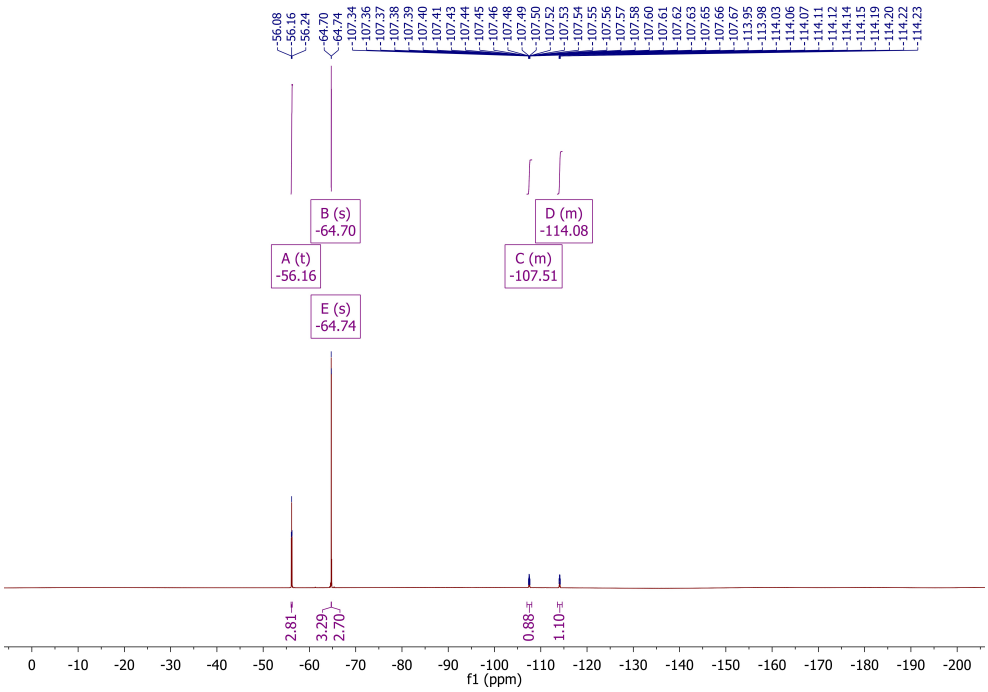
B (s)
-64.70
A (t)
-56.16
E (s)
-64.74
D (m)
-114.08
C (m)
-107.51
2.81
3.29
2.70
0.88
1.10
f1 (ppm)

14a: ^{1}H-NMR

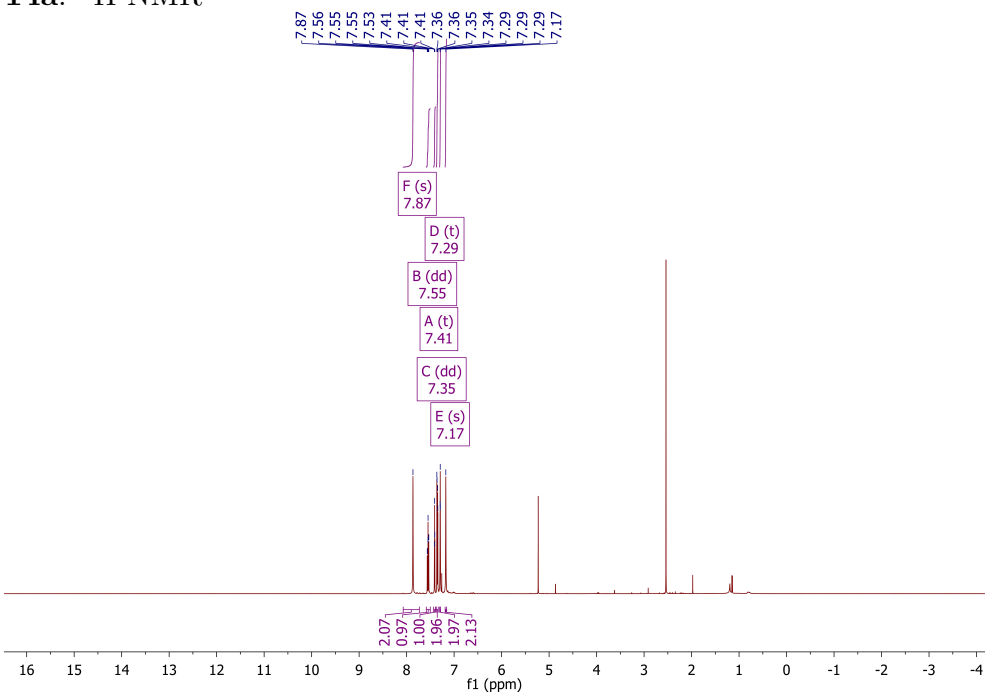
F (s)
7.87
D (t)
7.29
B (dd)
7.55
A (t)
7.41
C (dd)
7.35
E (s)
7.17
2.07
0.97
1.00
1.96
1.97
2.13
f1 (ppm)

14b: ^{1}H-NMR

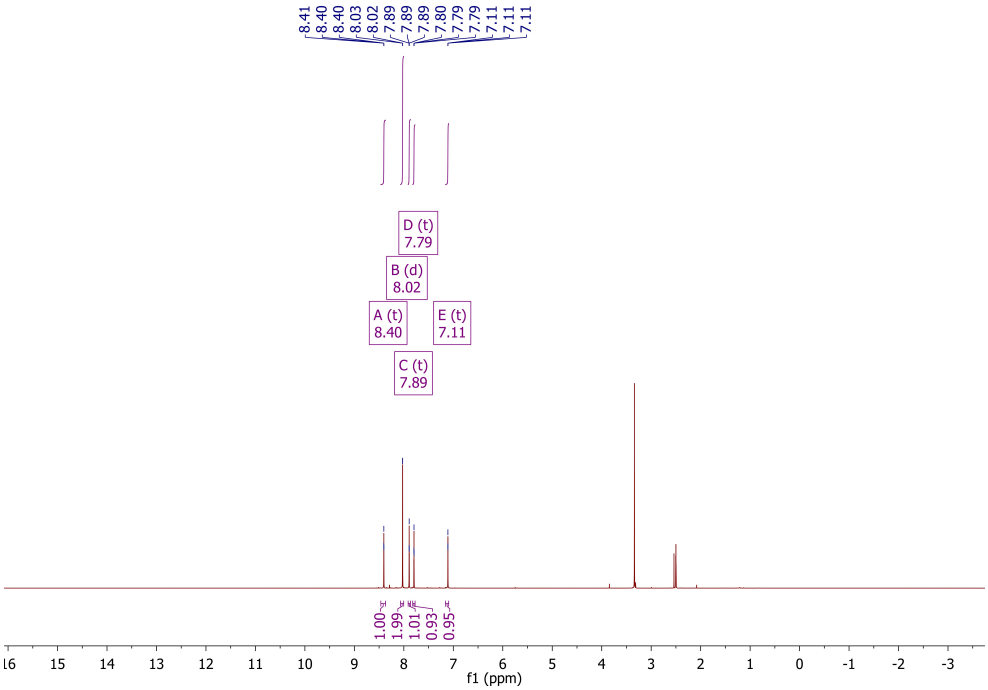

14c: ^{1}H-NMR

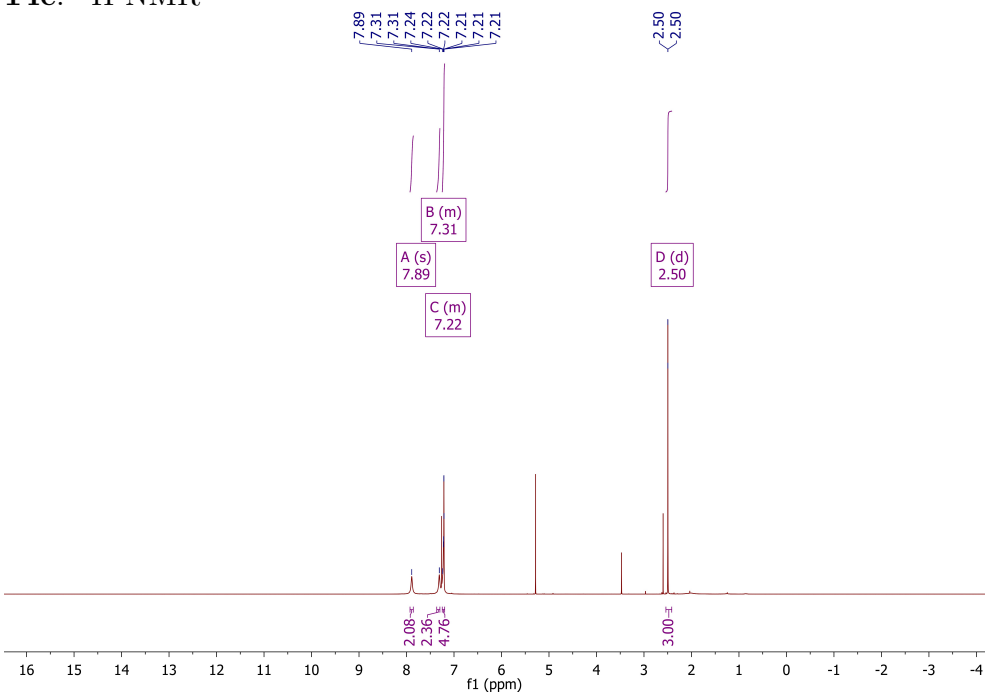

14d: ^{1}H-NMR

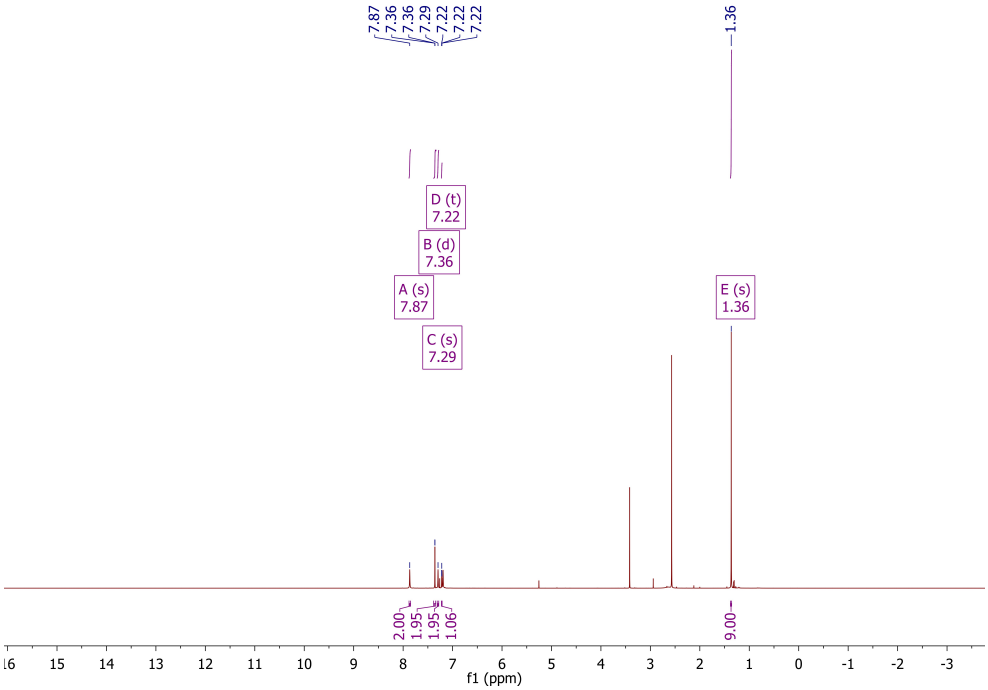

14e: ^{1}H-NMR, ^{13}C-NMR

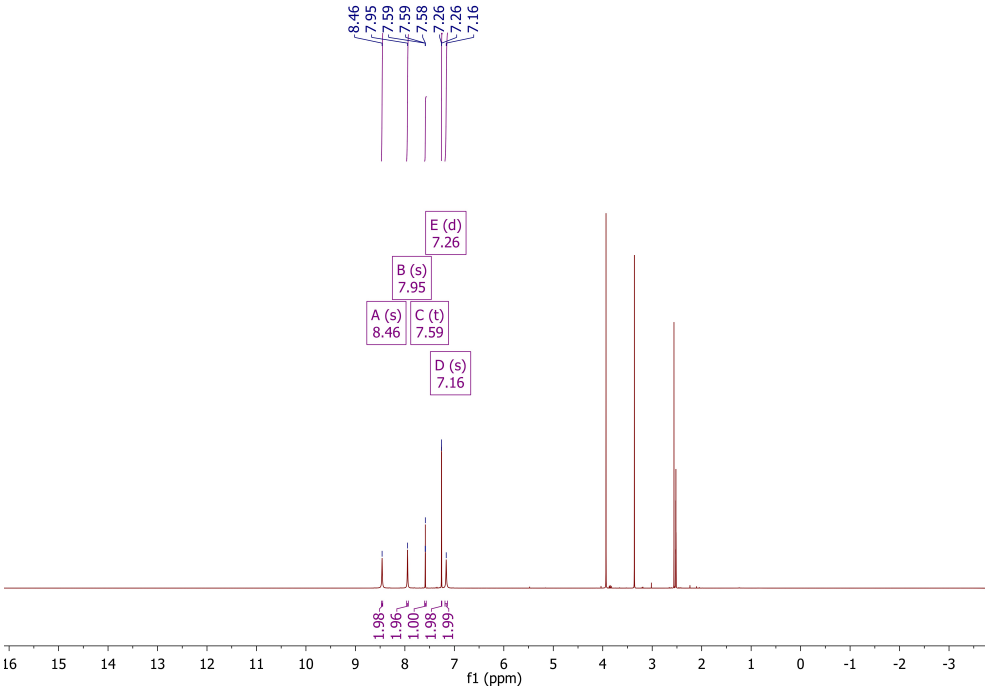

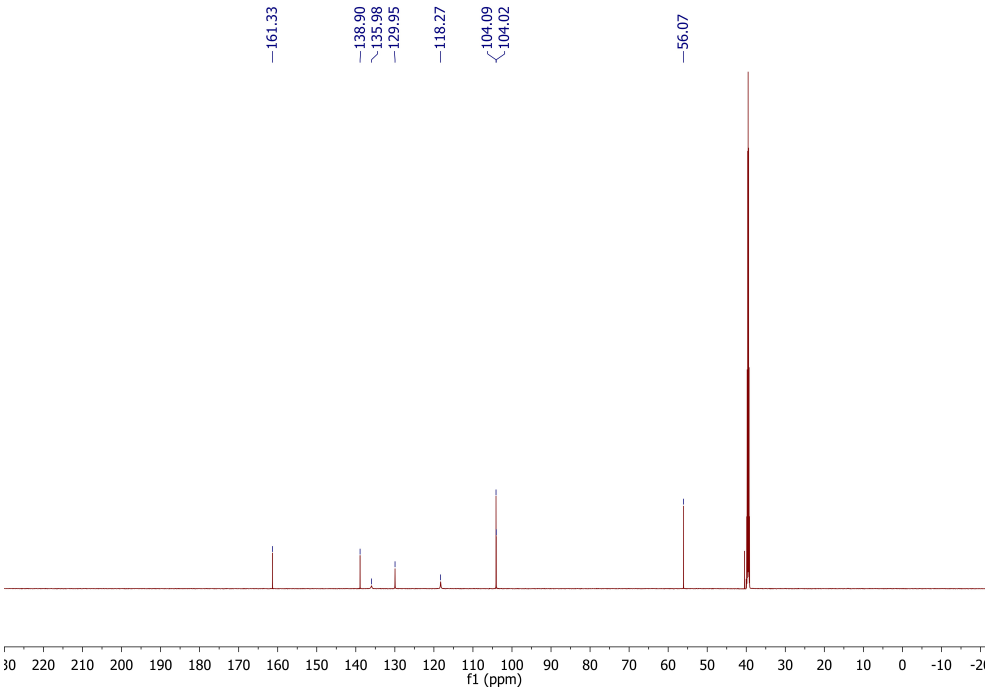
161.33
138.90
135.98
129.95
118.27
104.09
104.02
56.07
f1 (ppm)

14f: ^{1}H-NMR

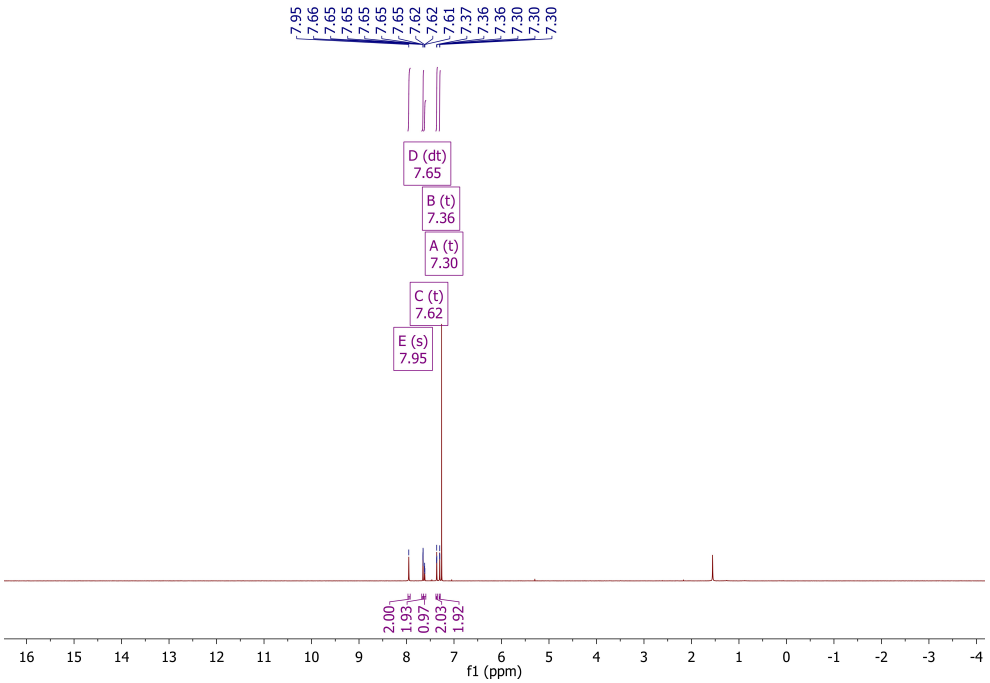
7.95
7.66
7.65
7.65
7.65
7.65
7.65
7.62
7.62
7.61
7.37
7.36
7.36
7.30
7.30
7.30
D (dt)
7.65
B (t)
7.36
A (t)
7.30
C (t)
7.62
E (s)
7.95
2.00
1.93
0.97
2.03
1.92
f1 (ppm)

14g: ^{1}H-NMR, ^{13}C-NMR, ^{19}F-NMR

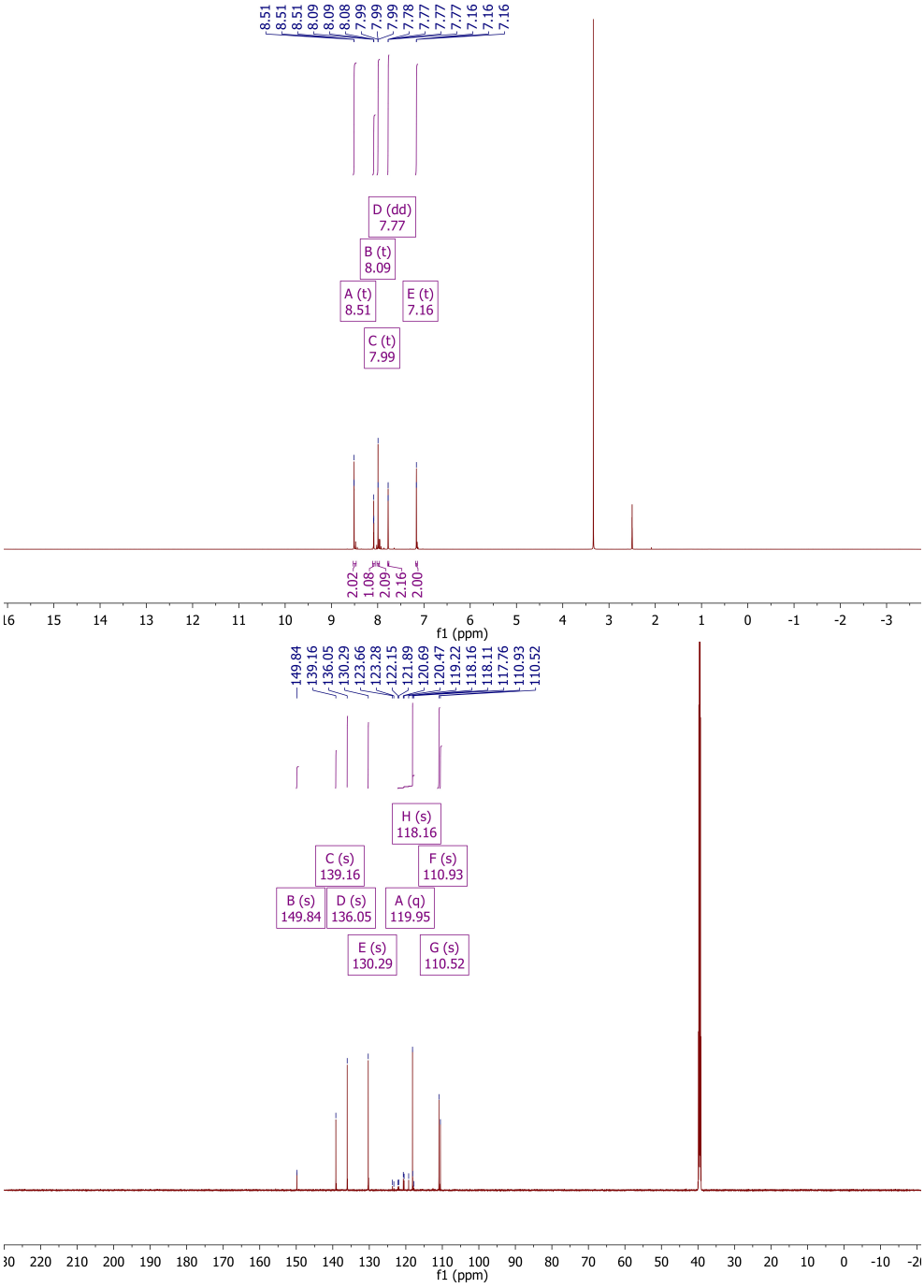

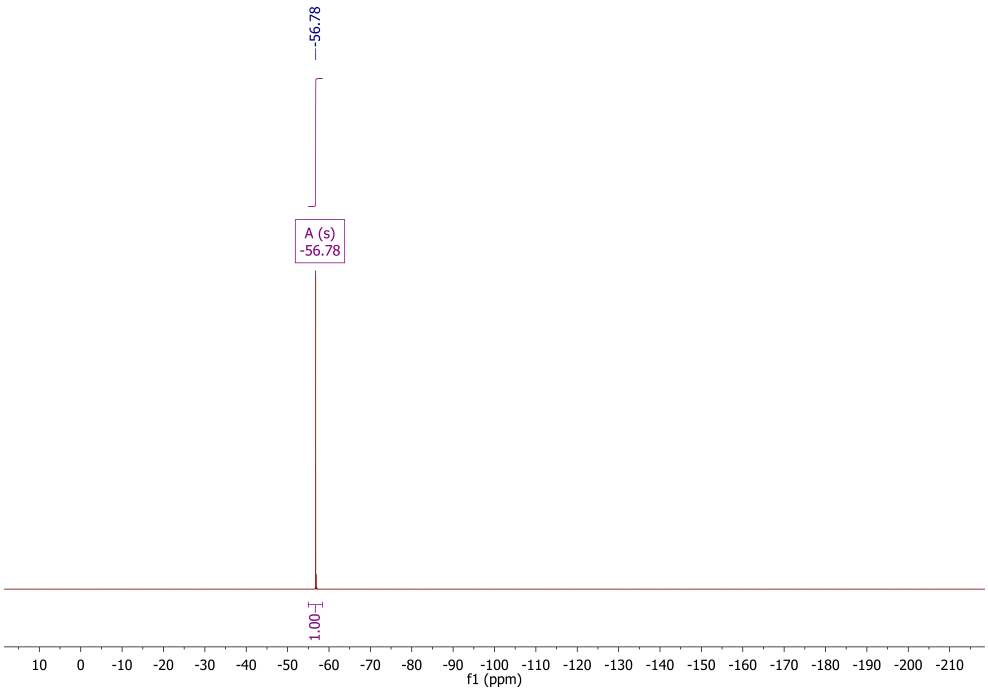
-56.78
A (s)
-56.78
1.00
10 0 -10 -20 -30 -40 -50 -60 -70 -80 -90 -100 -110 -120 -130 -140 -150 -160 -170 -180 -190 -200 -210
f1 (ppm)

14h: ^{1}H-NMR

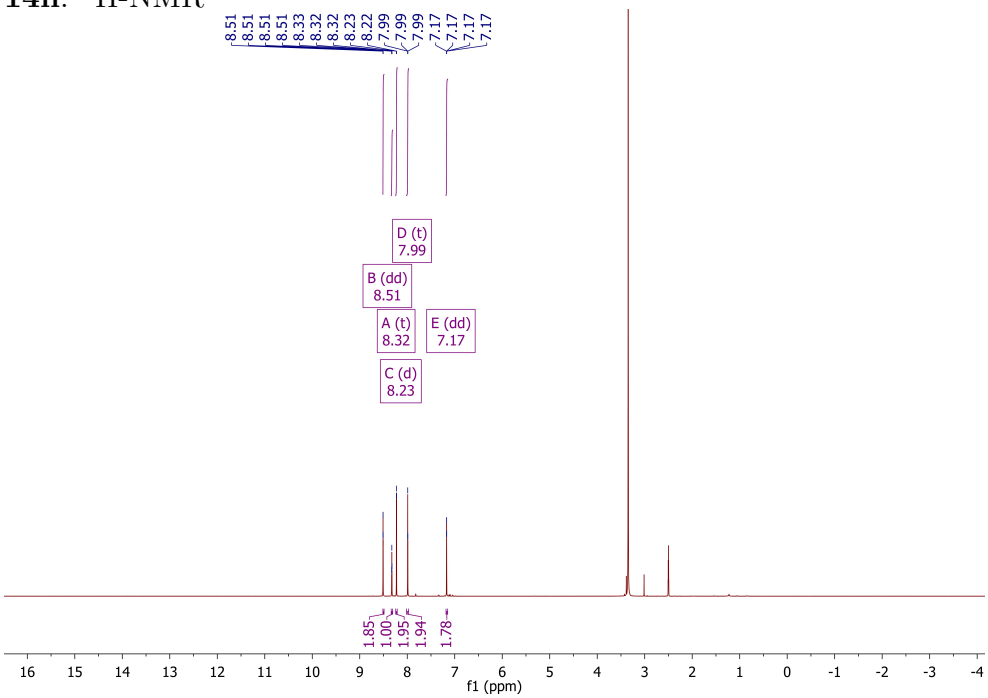
8.51
8.51
8.51
8.51
8.33
8.32
8.32
8.23
8.22
7.99
7.99
7.99
7.17
7.17
7.17
7.17
D (t)
7.99
B (dd)
8.51
A (t)
8.32
E (dd)
7.17
C (d)
8.23
1.85
1.00
1.95
1.94
1.78
16 15 14 13 12 11 10 9 8 7 6 5 4 3 2 1 0 -1 -2 -3 -4
f1 (ppm)

15a: ^{1}H-NMR

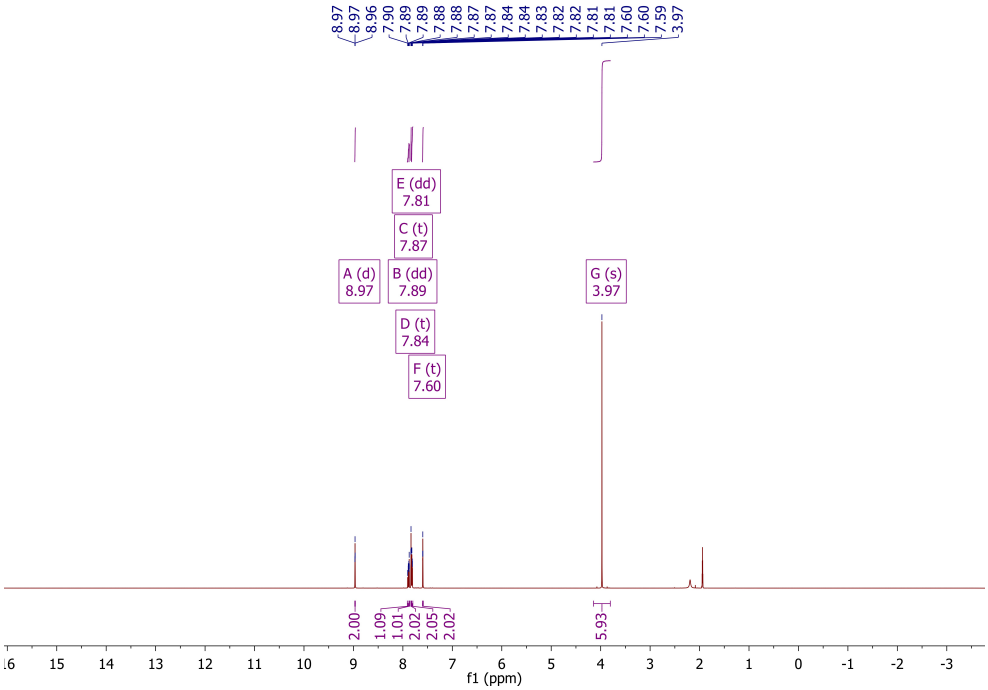

15b: ^{1}H-NMR

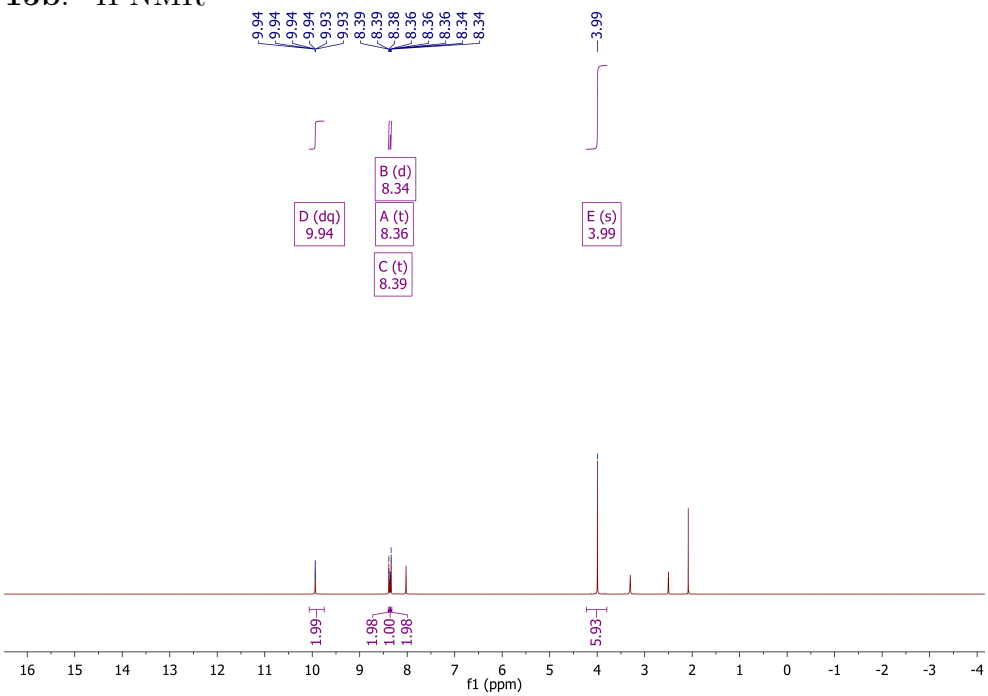

15c: ^{1}H-NMR

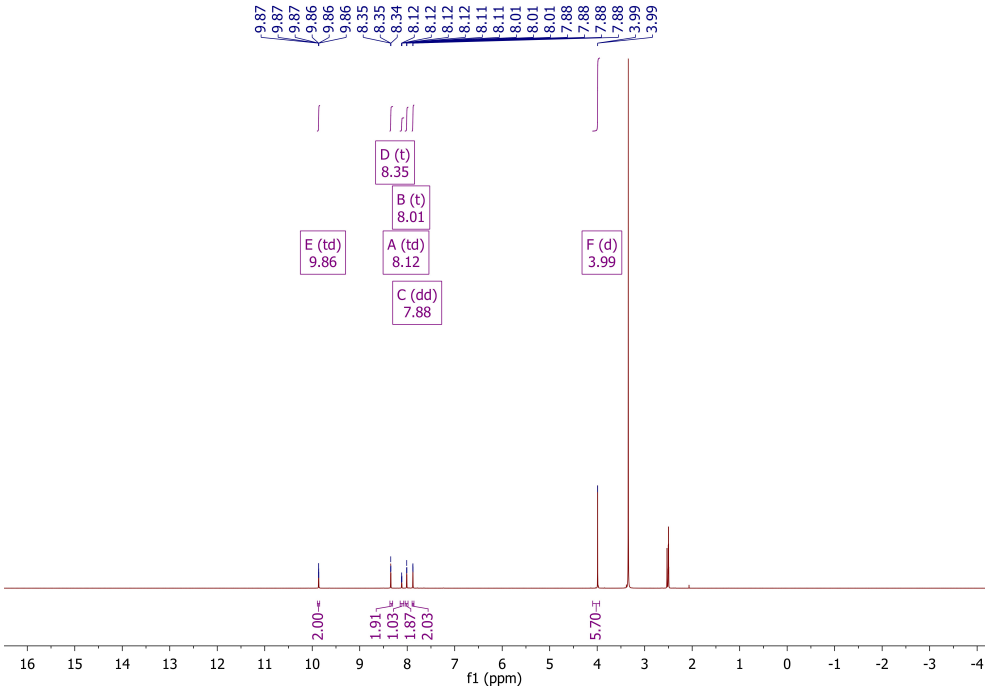

15d: ^{1}H-NMR

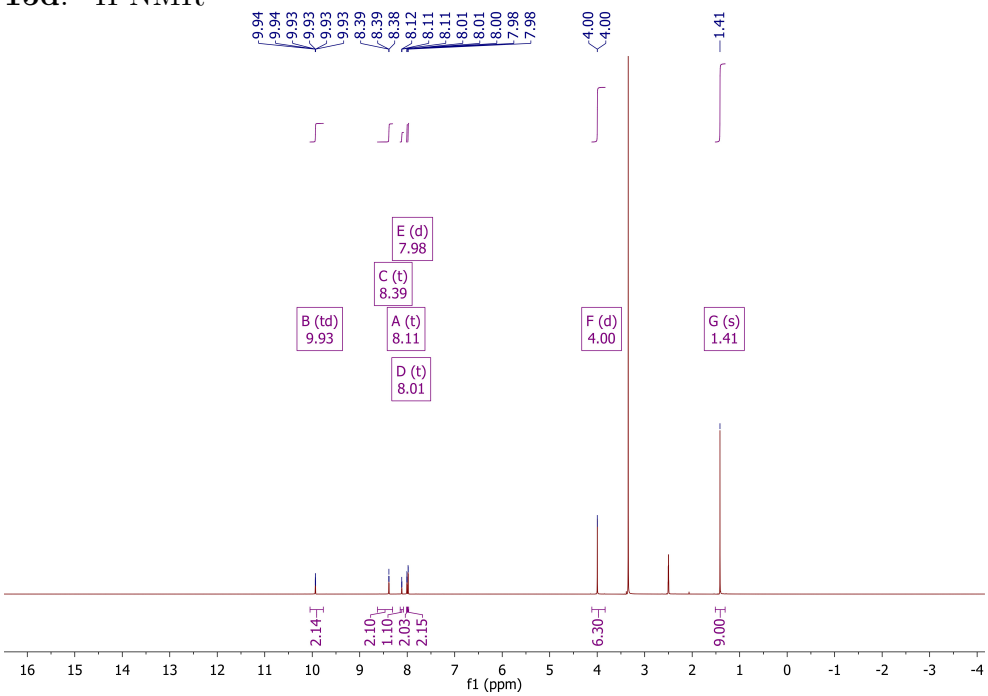

15e: ^{1}H-NMR

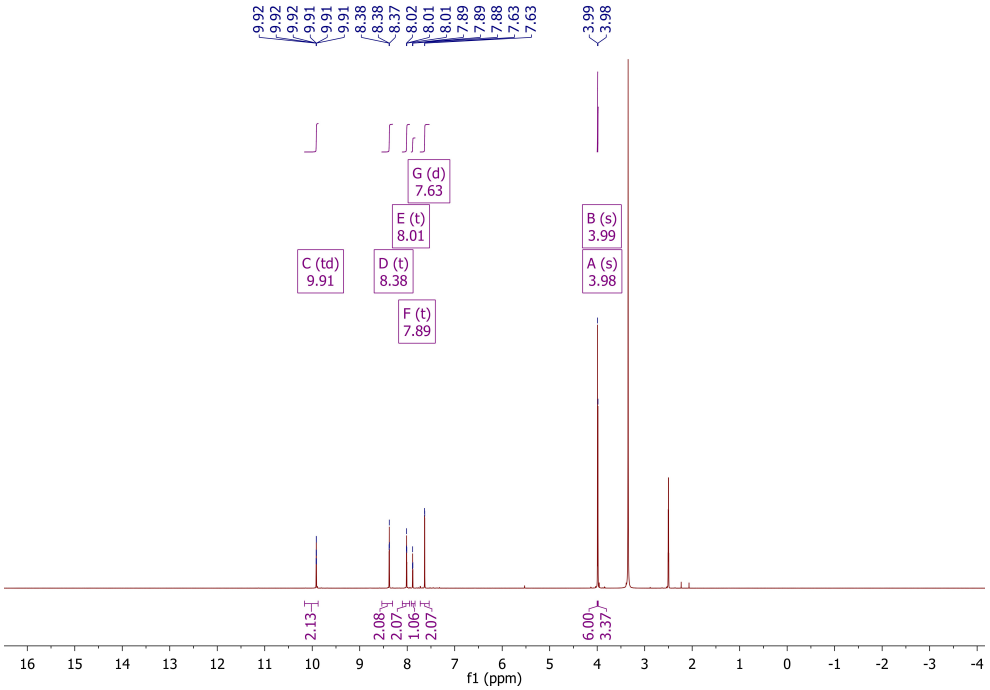

15f: ^{1}H-NMR

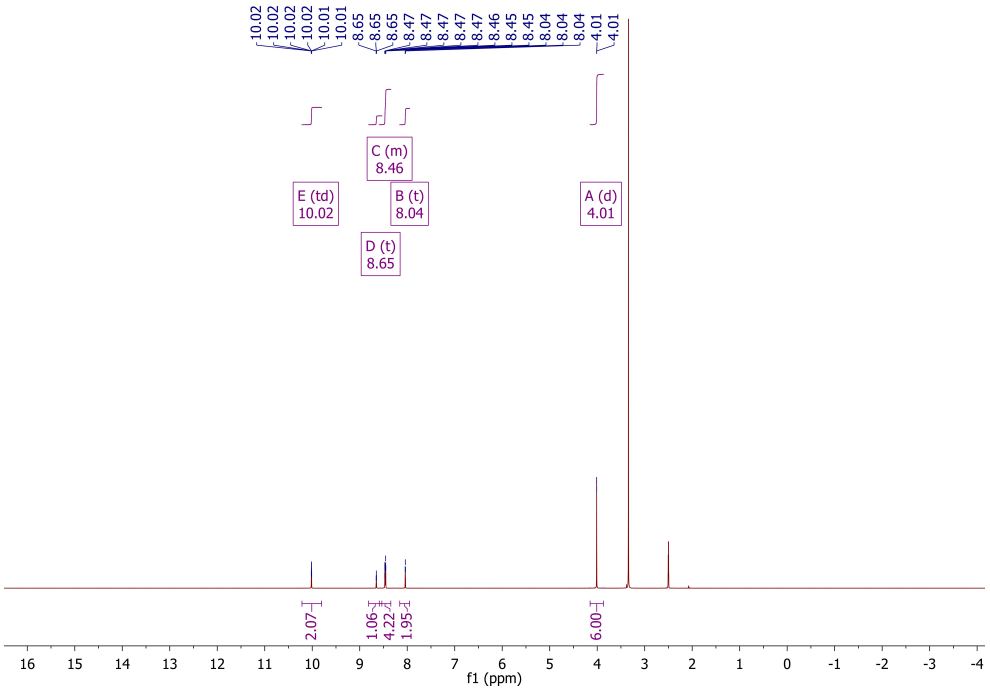

15g: ^{1}H-NMR, ^{13}C-NMR

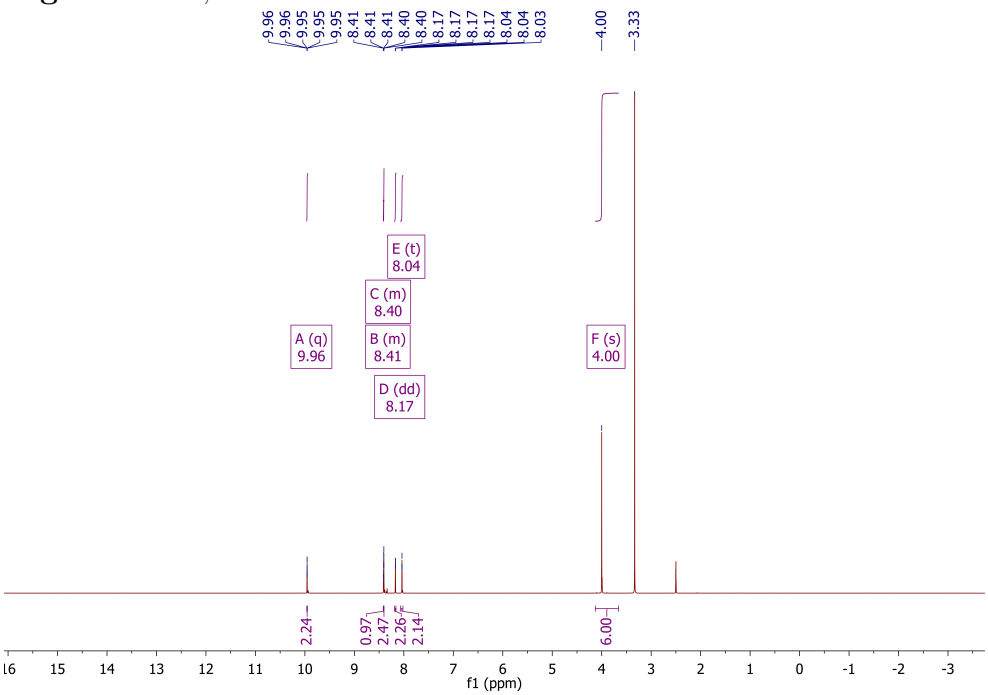

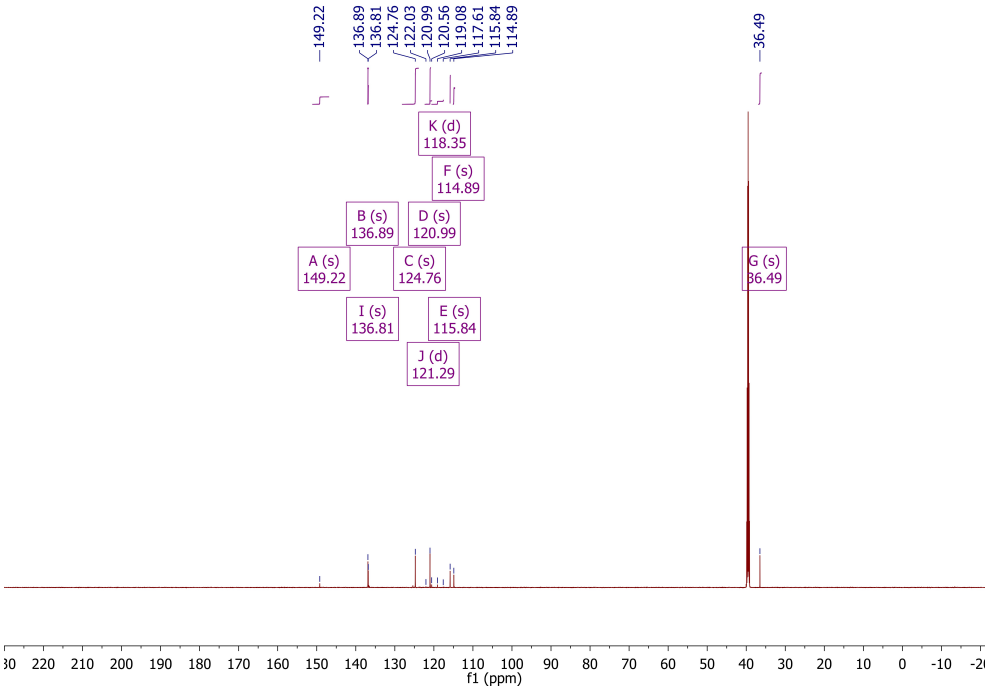

15h: ^{1}H-NMR

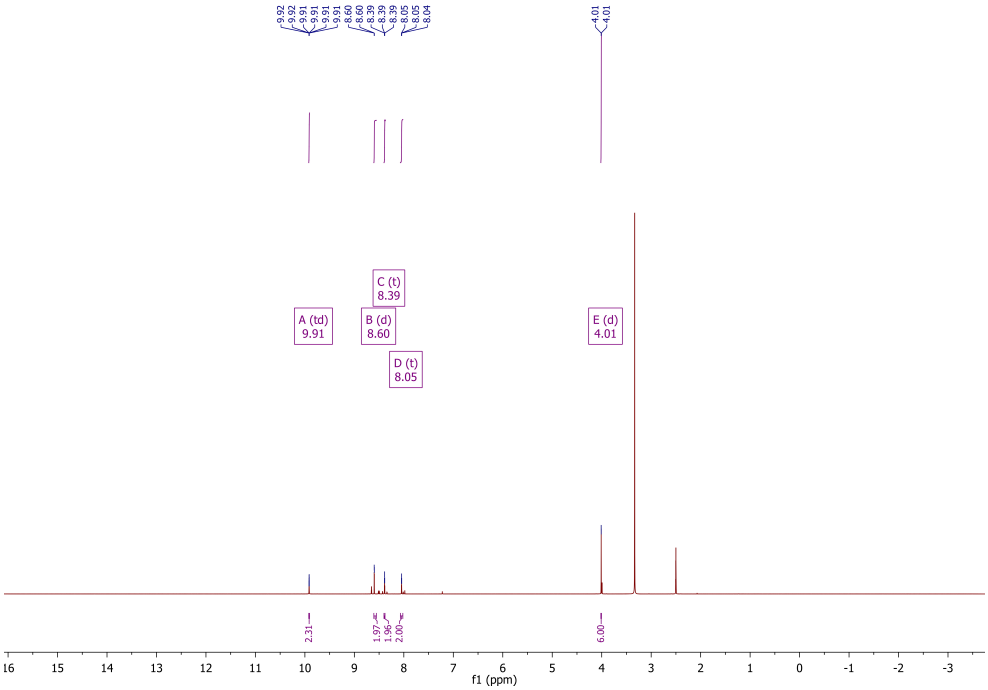

8a: ^{1}H-NMR

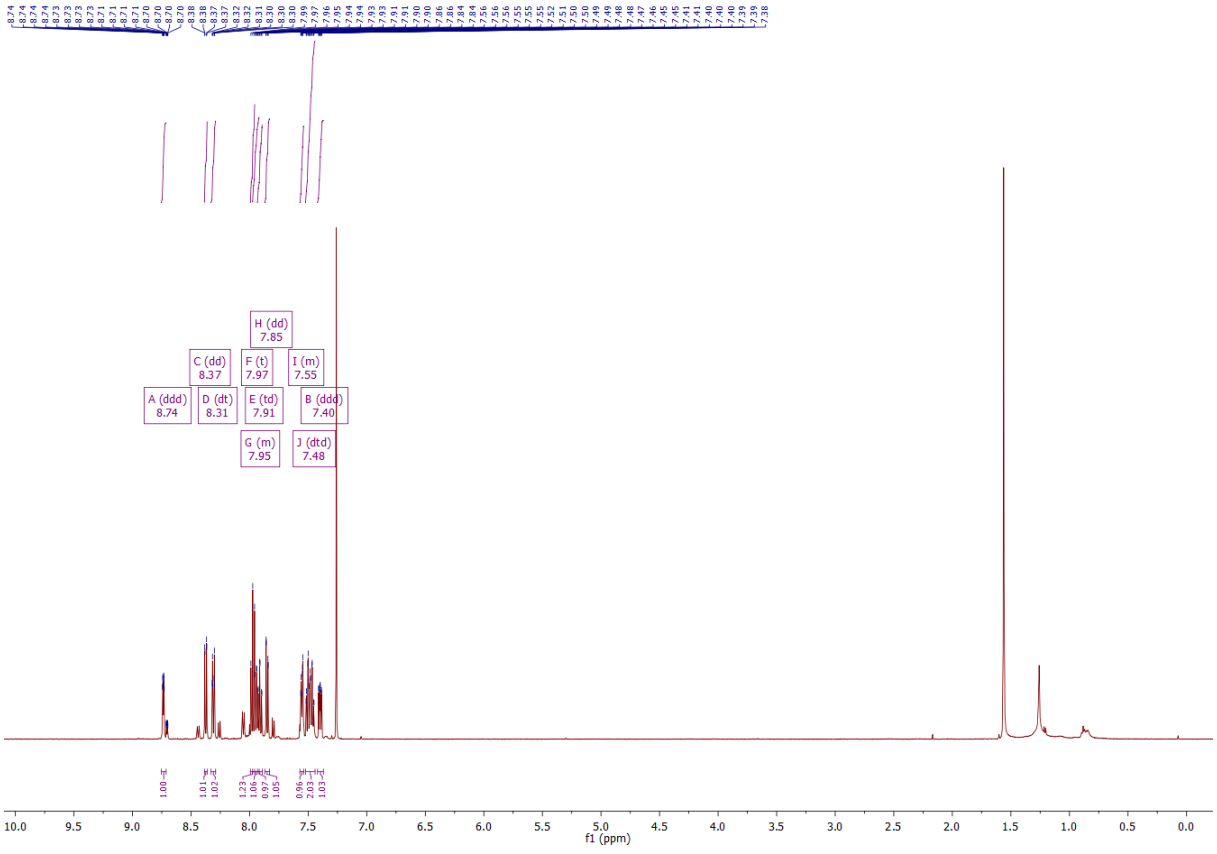

9: ESI-MS

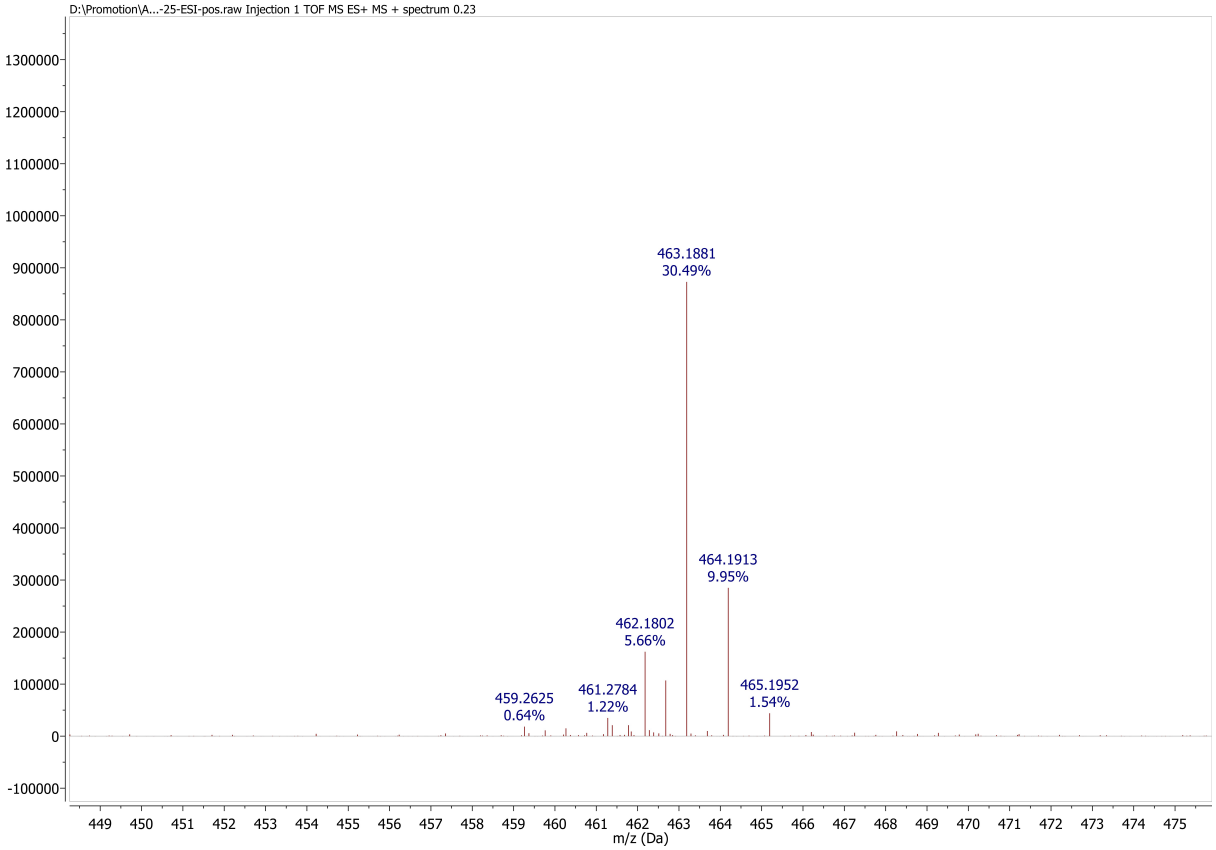

16b: ^{1}H-NMR, ESI-MS

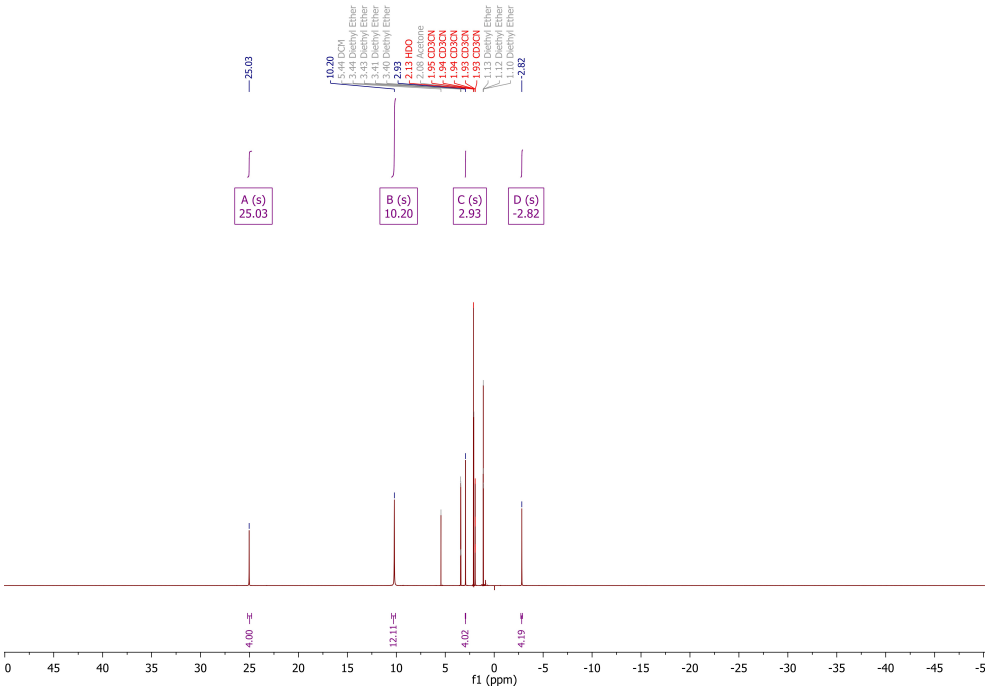

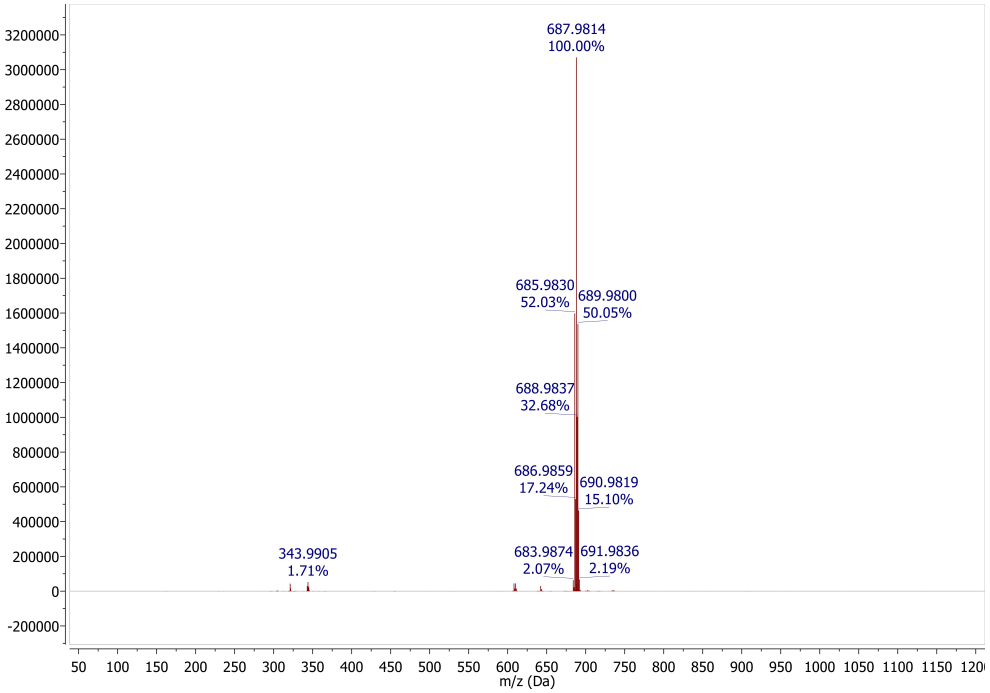

16c: ^{1}H-NMR, ESI-MS

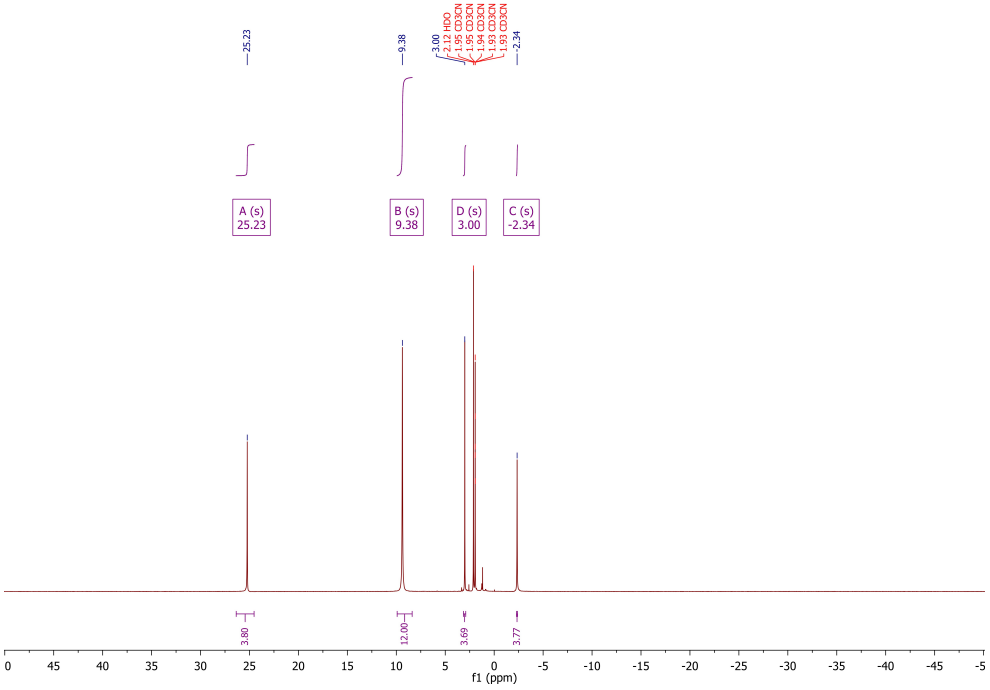

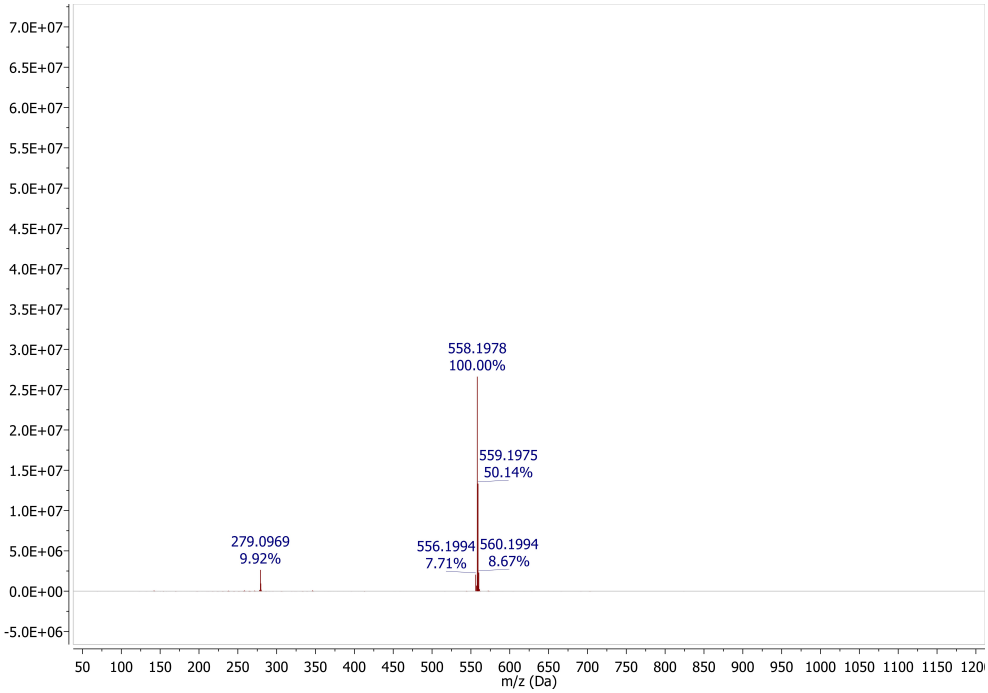

16d: ^{1}H-NMR, ESI-MS

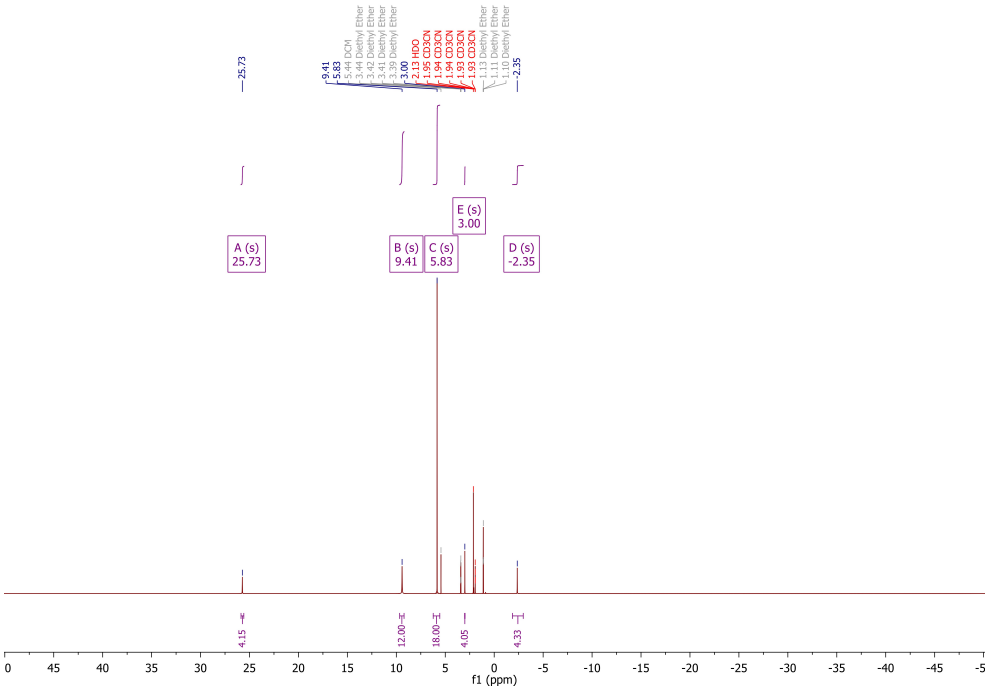

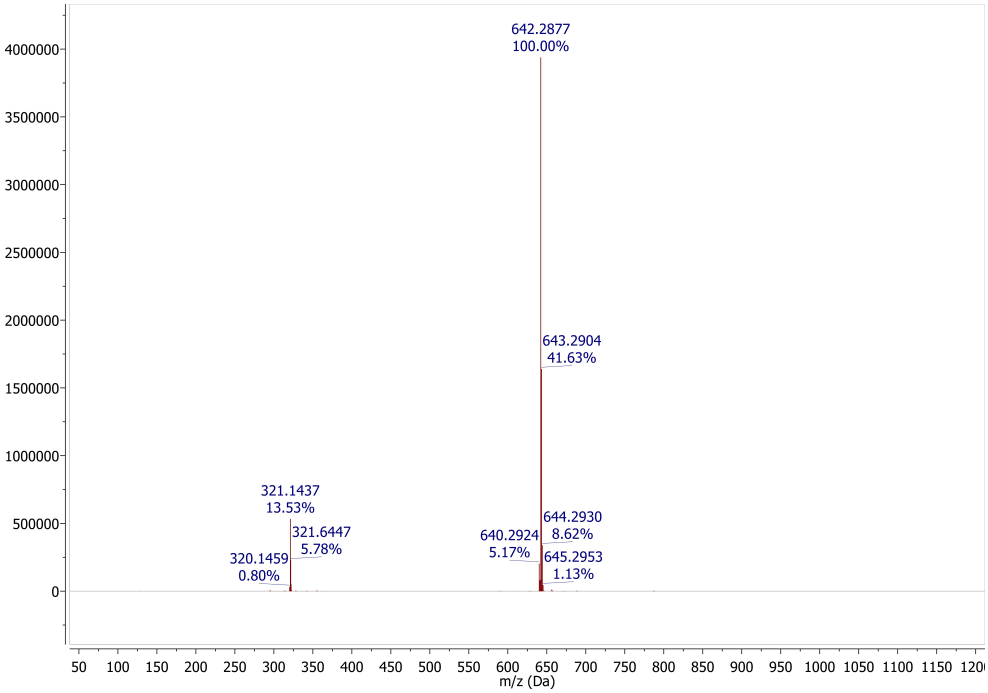

16e: ^{1}H-NMR, ESI-MS

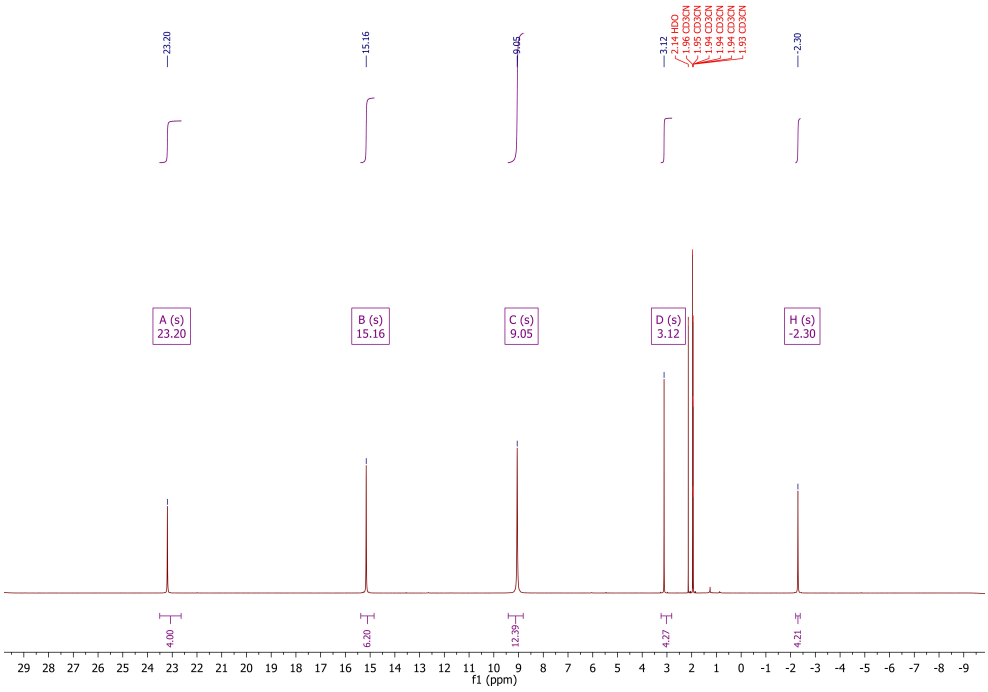

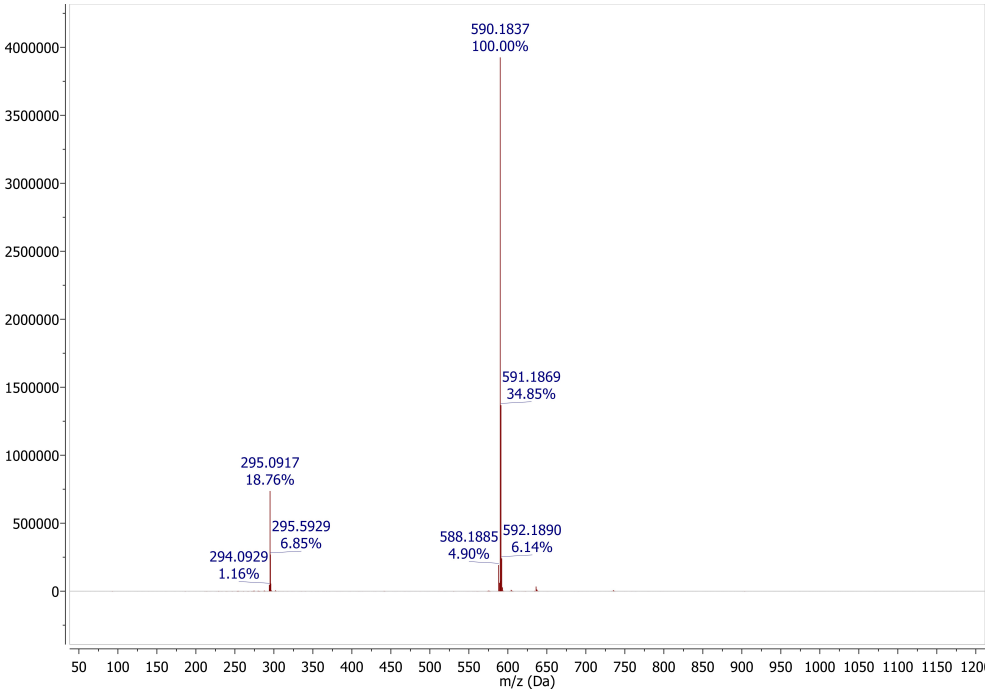

16f: ^{1}H-NMR, ESI-MS

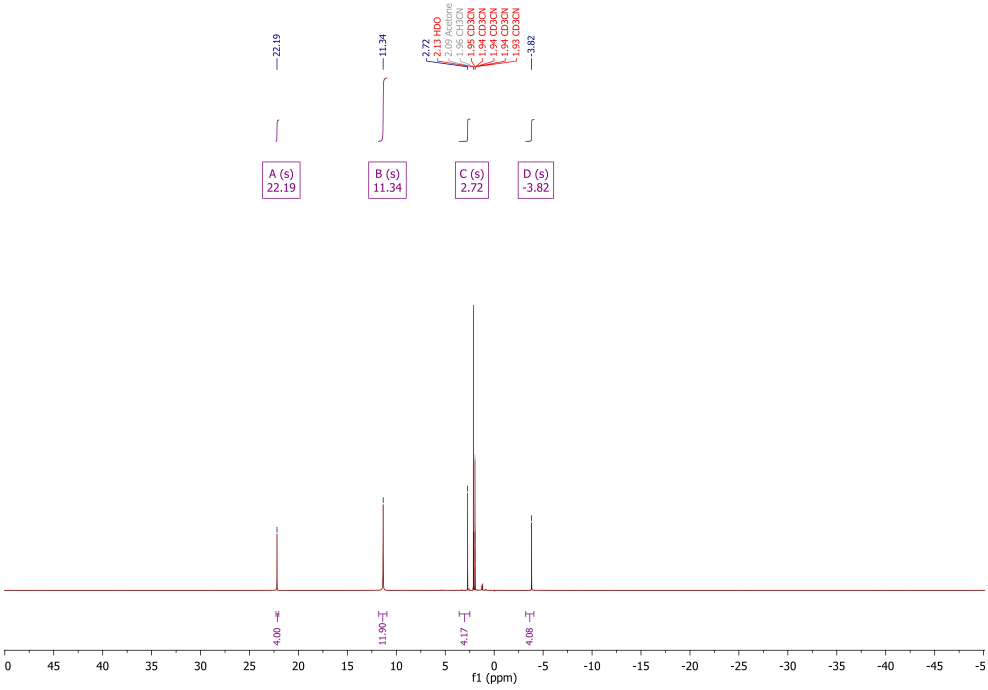

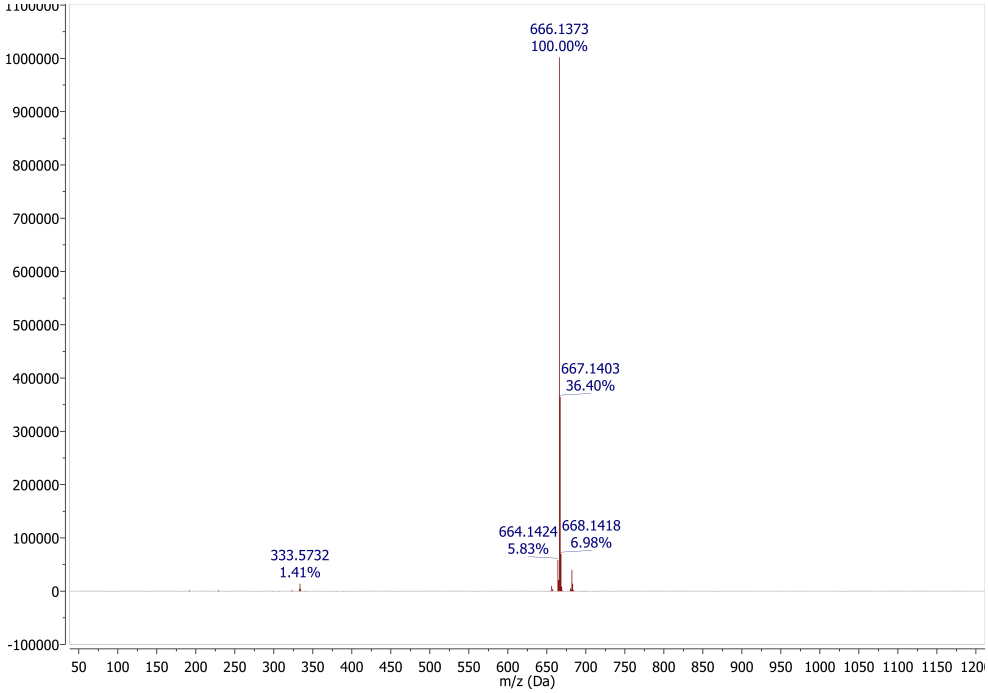

16g: ^{1}H-NMR, ESI-MS

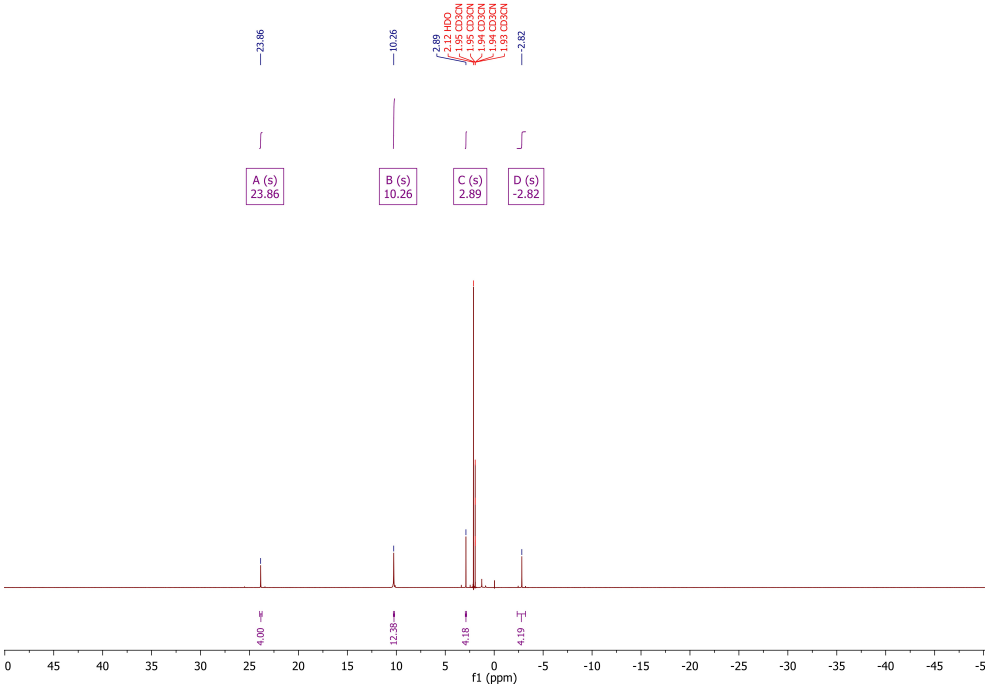

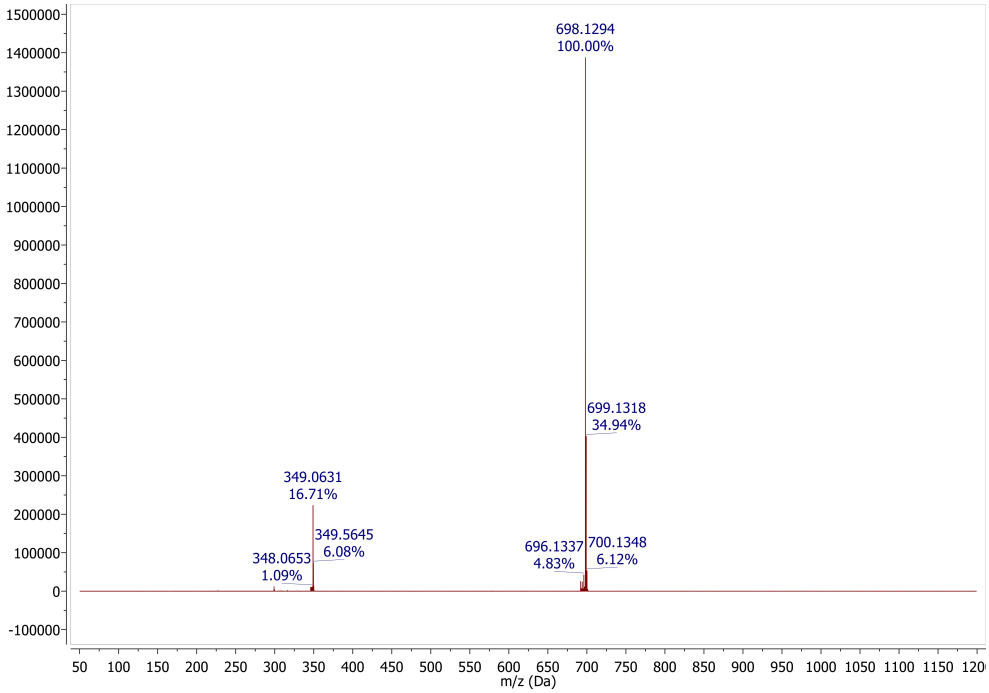

16h: ^{1}H-NMR, ESI-MS

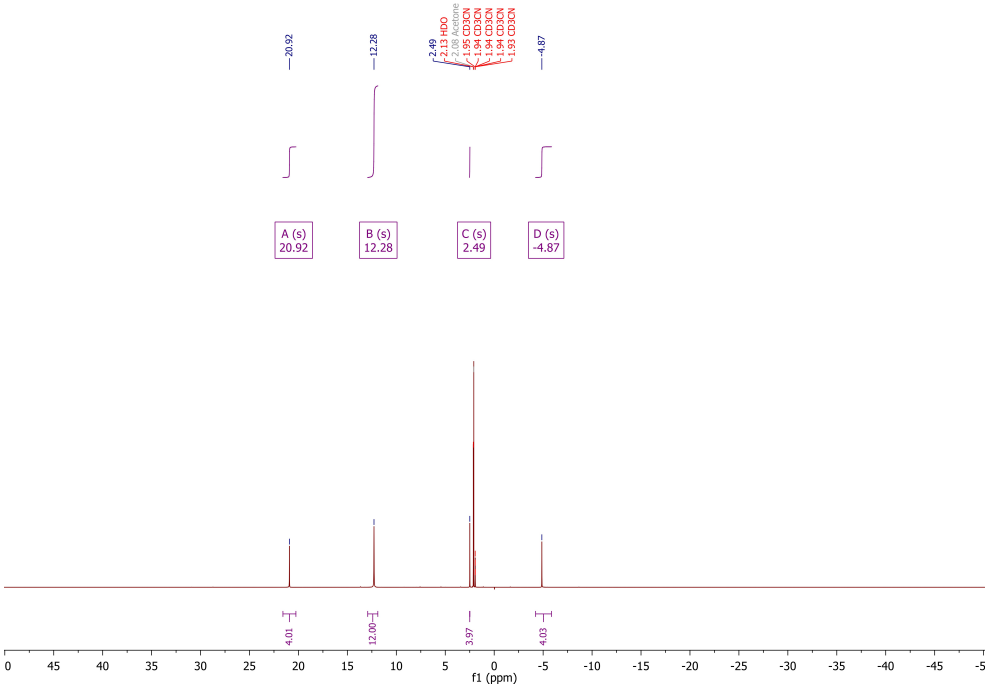

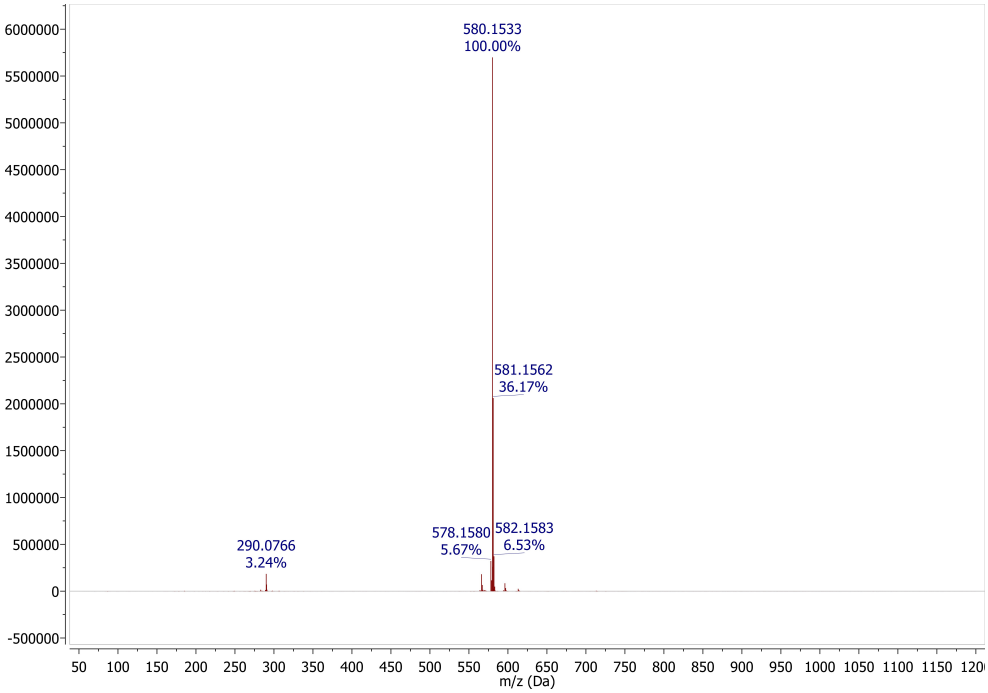
580.1533
100.00%
581.1562
36.17%
582.1583
6.53%
578.1580
5.67%
290.0766
3.24%
6000000
5500000
5000000
4500000
4000000
3500000
3000000
2500000
2000000
1500000
1000000
500000
0
-500000
50 100 150 200 250 300 350 400 450 500 550 600 650 700 750 800 850 900 950 1000 1050 1100 1150
m/z (Da)

B. Crystal Data

11

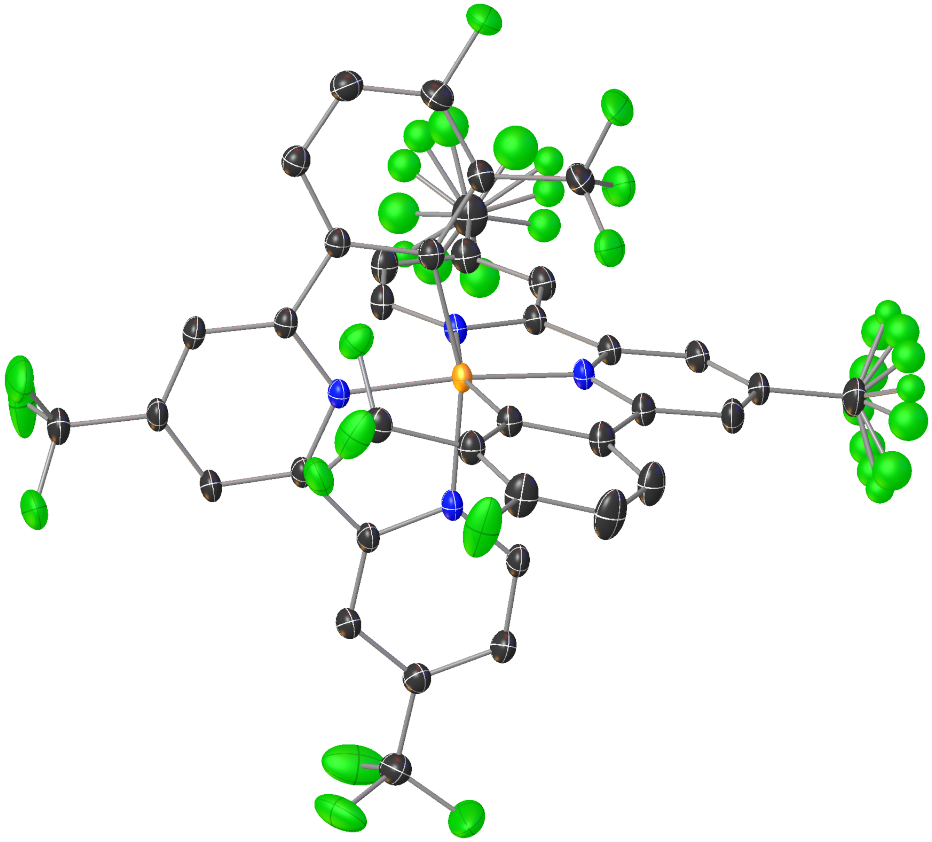

Identification code	mo_JS_0213n_0m_a	
Empirical formula	C39 H15 Cl3 F20 Fe N4	
Formula weight	1081.75	
Temperature	120(2) K	
Wavelength	0.71073 Å	
Crystal system	Triclinic	
Space group	P-1	
Unit cell dimensions	a = 10.5544(5) Å	α= 77.875(2)°.
	b = 11.4360(5) Å	β= 82.802(2)°.
	c = 17.1654(7) Å	γ = 76.558(2)°.
Volume	1963.77(15) $Å^3$	
Z	2	
Density (calculated)	1.829 Mg/m^3	
Absorption coefficient	0.722 mm^{-1}	
F(000)	1068	
Crystal size	0.240 x 0.060 x 0.020 mm^3	
Theta range for data collection	1.990 to 30.544°.	
Index ranges	-15<=h<=15, -16<=k<=16, -24<=l<=24	
Reflections collected	241771	
Independent reflections	12023 [R(int) = 0.0455]	
Completeness to theta = 25.242°	99.9 %	
Absorption correction	Semi-empirical from equivalents	
Refinement method	Full-matrix least-squares on F^2	
Data / restraints / parameters	12023 / 2 / 654	
Goodness-of-fit on F^2	1.065	
Final R indices [I>2sigma(I)]	R1 = 0.0487, wR2 = 0.1232	
R indices (all data)	R1 = 0.0605, wR2 = 0.1346	
Extinction coefficient	n/a	
Largest diff. peak and hole	0.992 and -0.800 $e.Å^{-3}$	

16b

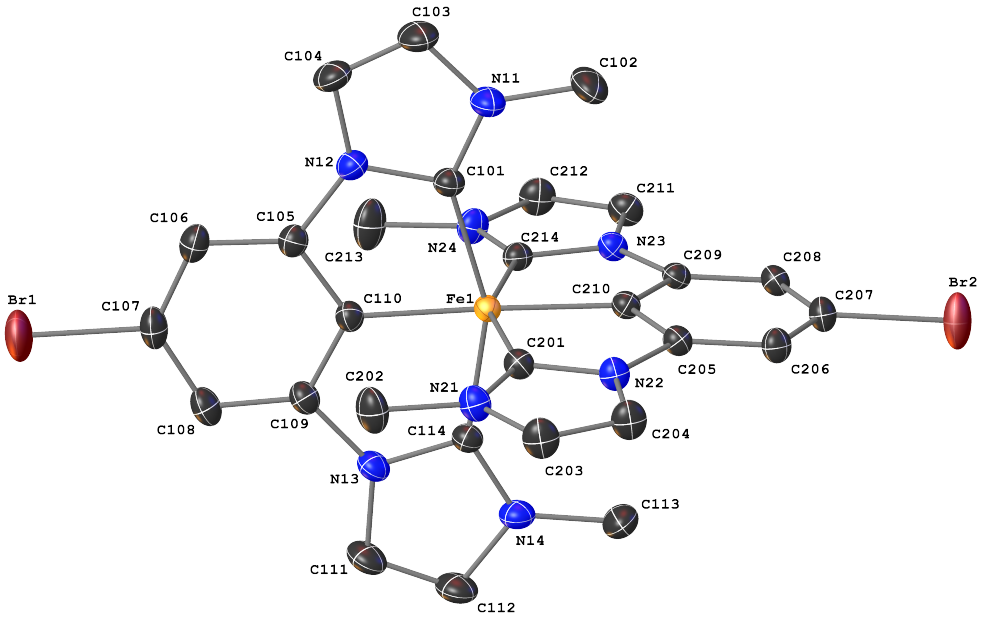
C103
C104
N11
C102
N12
C101
C212
C211
C106
C105
C213
N24
C214
N23
C209
C208
Br1
C107
C110
Fe1
C210
C207
Br2
C201
C205
C206
C202
N21
N22
C108
C109
C114
C204
C203
N13
C113
N14
C111
C112

Identification code	mo_JS_0160n_0m_a	
Empirical formula	C31 H30 Br2 Cl6 F6 Fe N8 P	
Formula weight	1087.97	
Temperature	120(2) K	
Wavelength	0.71073 Å	
Crystal system	Monoclinic	
Space group	$P2_1/c$	
Unit cell dimensions	a = 10.5000(9) Å	α= 90°.
	b = 20.3490(17) Å	β= 90.401(3)°.
	c = 18.8945(16) Å	γ = 90°.
Volume	4037.0(6) $Å^3$	
Z	4	
Density (calculated)	1.790 Mg/m^3	
Absorption coefficient	2.855 mm^{-1}	
F(000)	2156	
Crystal size	0.280 x 0.240 x 0.200 mm^3	
Theta range for data collection	2.002 to 33.206°.	
Index ranges	-16<=h<=16, -31<=k<=30, -29<=l<=29	
Reflections collected	606322	
Independent reflections	15436 [R(int) = 0.0579]	
Completeness to theta = 25.242°	99.9 %	
Absorption correction	Semi-empirical from equivalents	
Refinement method	Full-matrix least-squares on F^2	
Data / restraints / parameters	15436 / 24 / 556	
Goodness-of-fit on F^2	1.038	
Final R indices [I>2sigma(I)]	R1 = 0.0375, wR2 = 0.0929	
R indices (all data)	R1 = 0.0476, wR2 = 0.0987	
Extinction coefficient	n/a	
Largest diff. peak and hole	1.225 and -1.076 $e.Å^{-3}$	

16c

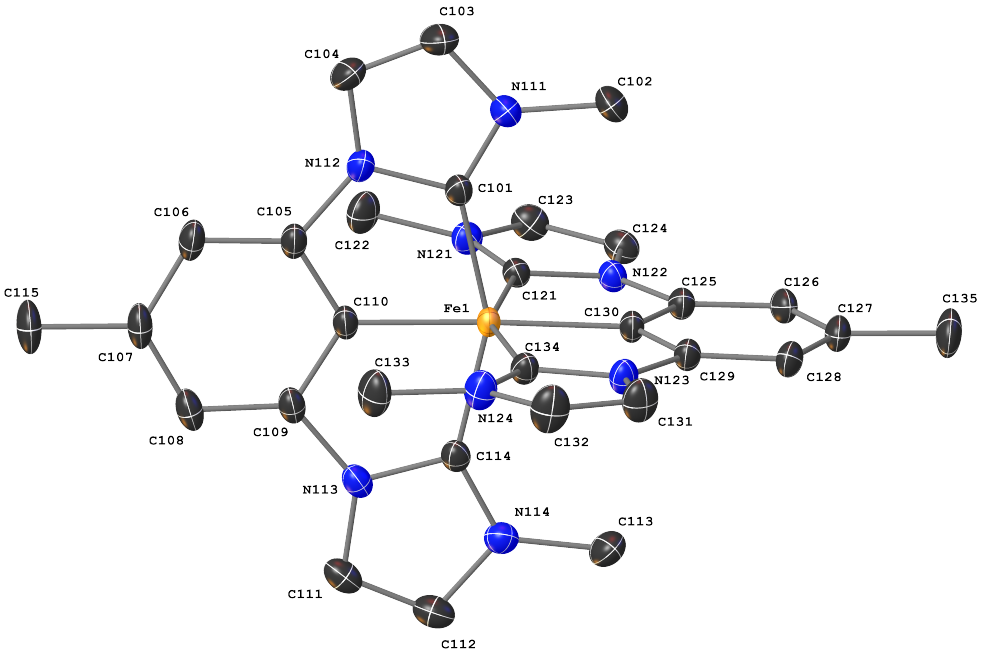
C103
C104
N111
C102
N112
C101
C123
C106
C105
C122
N121
C124
N122
C125
C126
C115
C110
Fe1
C121
C130
C127
C135
C107
C134
C133
N123
C129
C128
N124
C131
C108
C109
C132
C114
N113
N114
C113
C111
C112

Identification code	mo_js_0167n_0m_a_sq	
Empirical formula	C63 H66 Br0.34 Cl6 F9.96 Fe2 N16 P1.66	
Formula weight	1639.54	
Temperature	120(2) K	
Wavelength	0.71073 Å	
Crystal system	Monoclinic	
Space group	$P2_1/c$	
Unit cell dimensions	a = 11.6448(7) Å	α= 90°.
	b = 23.8559(14) Å	β= 96.6000(10)°.
	c = 26.8763(16) Å	γ = 90°.
Volume	7416.7(8) $Å^3$	
Z	4	
Density (calculated)	1.468 Mg/m^3	
Absorption coefficient	0.902 mm^{-1}	
F(000)	3346	
Crystal size	0.260 x 0.220 x 0.160 mm^3	
Theta range for data collection	1.870 to 32.115°.	
Index ranges	-17<=h<=17, -35<=k<=35, -40<=l<=40	
Reflections collected	921069	
Independent reflections	25948 [R(int) = 0.0559]	
Completeness to theta = 25.242°	99.9 %	
Absorption correction	Semi-empirical from equivalents	
Refinement method	Full-matrix least-squares on F^2	
Data / restraints / parameters	25948 / 1 / 951	
Goodness-of-fit on F^2	1.126	
Final R indices [I>2sigma(I)]	R1 = 0.0454, wR2 = 0.1229	
R indices (all data)	R1 = 0.0523, wR2 = 0.1278	
Extinction coefficient	n/a	
Largest diff. peak and hole	1.396 and -0.737 $e.Å^{-3}$	

16d

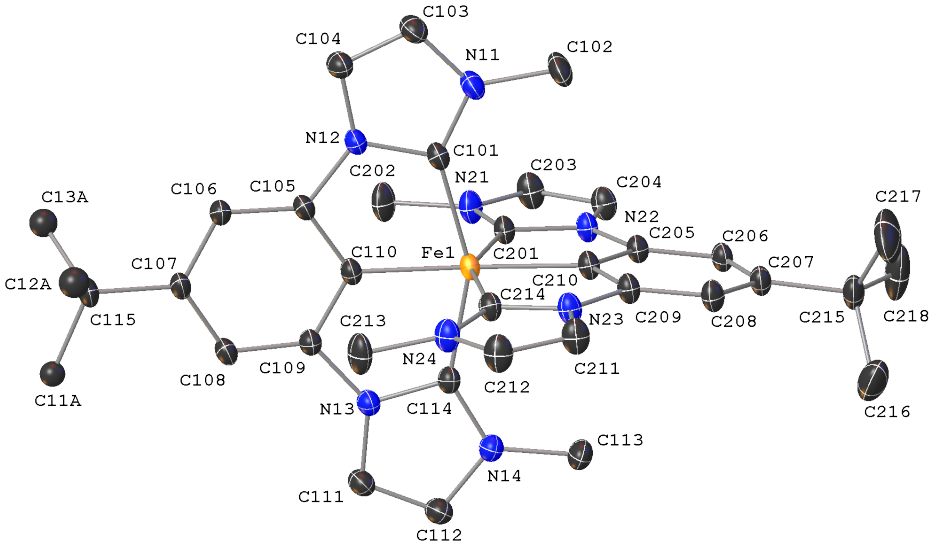
C103
C104
N11
C102
N12
C101
C202
N21
C203
C204
C13A
C106
C105
N22
C205
C206
C217
C107
C110
Fe1
C201
C207
C12A
C210
C214
C115
C213
N23
C209
C208
C215
C218
N24
C211
C109
C108
C212
C11A
N13
C114
C216
C113
N14
C111
C112

Identification code	mo_JS_210n_0m_a	
Empirical formula	C39 H48 F6 Fe N8 O P	
Formula weight	845.67	
Temperature	120(2) K	
Wavelength	0.71073 Å	
Crystal system	Monoclinic	
Space group	$P2_1/n$	
Unit cell dimensions	a = 16.8918(8) Å	α= 90°.
	b = 12.7147(6) Å	β= 99.427(2)°.
	c = 19.3838(10) Å	γ = 90°.
Volume	4106.9(3) $Å^3$	
Z	4	
Density (calculated)	1.368 Mg/m^3	
Absorption coefficient	0.475 mm^{-1}	
F(000)	1764	
Crystal size	0.300 x 0.220 x 0.180 mm^3	
Theta range for data collection	2.015 to 32.071°.	
Index ranges	-24<=h<=25, -18<=k<=18, -28<=l<=28	
Reflections collected	169480	
Independent reflections	14300 [R(int) = 0.0402]	
Completeness to theta = 25.242°	99.8 %	
Absorption correction	Semi-empirical from equivalents	
Refinement method	Full-matrix least-squares on F^2	
Data / restraints / parameters	14300 / 37 / 535	
Goodness-of-fit on F^2	1.066	
Final R indices [I>2sigma(I)]	R1 = 0.0428, wR2 = 0.1071	
R indices (all data)	R1 = 0.0591, wR2 = 0.1222	
Extinction coefficient	n/a	
Largest diff. peak and hole	0.663 and -0.477 $e.Å^{-3}$	

16e

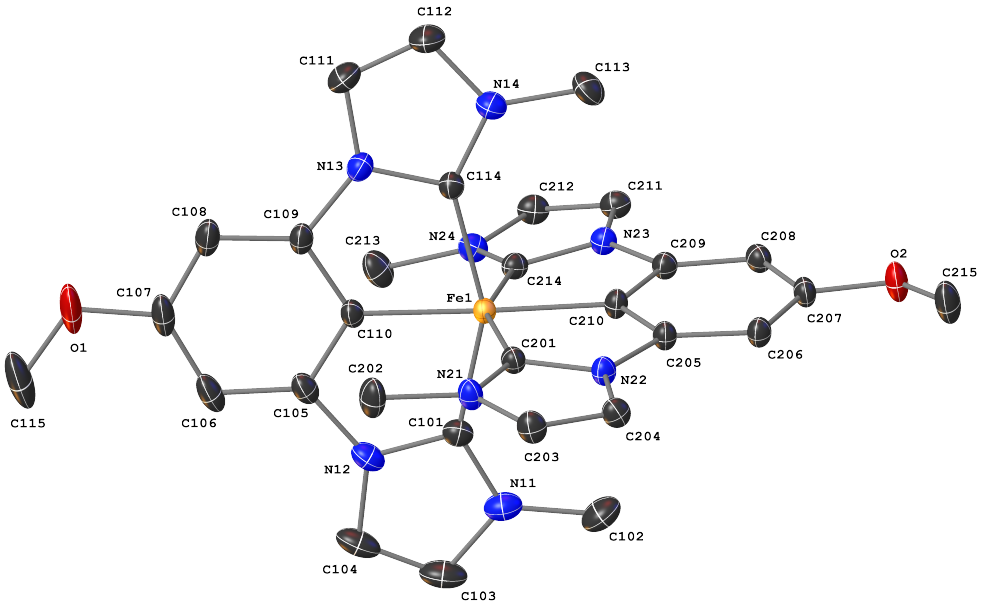
C112
C111
C113
N14
N13
C114
C212
C211
C108
C109
C213
N24
N23
C209
C208
O2
C215
C214
C107
Fe1
C210
C207
O1
C110
C201
C205
C206
C202
N21
N22
C115
C106
C105
C101
C204
C203
N12
N11
C102
C104
C103

Identification code	mo_JS_0159n_0ma_a	
Empirical formula	C31 H32 Cl2 F6 Fe N8 O2 P	
Formula weight	820.36	
Temperature	120(2) K	
Wavelength	0.71073 Å	
Crystal system	Orthorhombic	
Space group	$Pna2_1$	
Unit cell dimensions	a = 15.9372(17) Å	α= 90°.
	b = 14.8224(16) Å	β= 90°.
	c = 14.3300(15) Å	γ = 90°.
Volume	3385.1(6) $Å^3$	
Z	4	
Density (calculated)	1.610 Mg/m^3	
Absorption coefficient	0.728 mm^{-1}	
F(000)	1676	
Crystal size	0.280 x 0.220 x 0.160 mm^3	
Theta range for data collection	2.354 to 33.208°.	
Index ranges	-24<=h<=24, -22<=k<=22, -22<=l<=22	
Reflections collected	499894	
Independent reflections	12937 [R(int) = 0.0466]	
Completeness to theta = 25.242°	99.6 %	
Absorption correction	Semi-empirical from equivalents	
Refinement method	Full-matrix least-squares on F^2	
Data / restraints / parameters	12937 / 1 / 466	
Goodness-of-fit on F^2	1.062	
Final R indices [I>2sigma(I)]	R1 = 0.0326, wR2 = 0.0905	
R indices (all data)	R1 = 0.0364, wR2 = 0.0959	
Absolute structure parameter	0.0022(17)	
Extinction coefficient	n/a	
Largest diff. peak and hole	0.866 and -0.623 $e.Å^{-3}$	

16f

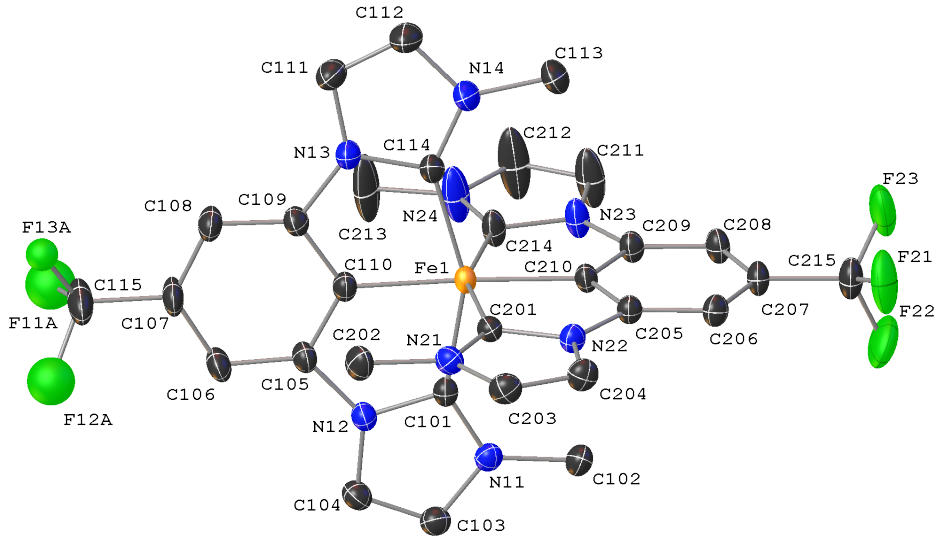
C112
C111
N14
C113
N13
C114
C212
C211
F23
C108
C109
N24
N23
C209
C208
F13A
C213
C214
F21
C115
C110
Fe1
C210
C215
C201
C207
F11A
C107
C202
N21
N22
C205
C206
F22
C106
C105
C204
F12A
N12
C101
C203
N11
C102
C104
C103

Identification code	mo_JS_209n_2_0m_a	
Empirical formula	C33 H30 F12 Fe N8 O P	
Formula weight	869.47	
Temperature	120(2) K	
Wavelength	0.71073 Å	
Crystal system	Monoclinic	
Space group	C2/c	
Unit cell dimensions	a = 27.8080(13) Å	α= 90°.
	b = 12.2257(5) Å	β= 110.0830(10)°.
	c = 23.3836(10) Å	γ = 90°.
Volume	7466.4(6) $Å^3$	
Z	8	
Density (calculated)	1.547 Mg/m^3	
Absorption coefficient	0.547 mm^{-1}	
F(000)	3528	
Crystal size	0.200 x 0.140 x 0.100 mm^3	
Theta range for data collection	1.935 to 32.040°.	
Index ranges	-40<=h<=41, -18<=k<=18, -34<=l<=34	
Reflections collected	130894	
Independent reflections	12950 [R(int) = 0.0578]	
Completeness to theta = 25.242°	99.9 %	
Absorption correction	Semi-empirical from equivalents	
Refinement method	Full-matrix least-squares on F^2	
Data / restraints / parameters	12950 / 37 / 535	
Goodness-of-fit on F^2	1.049	
Final R indices [I>2sigma(I)]	R1 = 0.0634, wR2 = 0.1556	
R indices (all data)	R1 = 0.0979, wR2 = 0.1859	
Extinction coefficient	n/a	
Largest diff. peak and hole	1.365 and -1.073 $e.Å^{-3}$	

C. Supplementary Information of the publications

C.1. Supplementary Information of "Excited-State Kinetics of an Air-Stable Cyclometalated Iron(II) Complex"

Supporting Information

Content

Experimental Section

The reactions were carried out under argon atmosphere using standard Schlenk techniques. Dry THF was obtained from reflux and subsequent distillation over potassium. Solvents were degassed prior to use. Chemicals were purchased from Sigma Aldrich, TCI or ACROS and used without purification. NMR spectra were recorded using a Bruker Avance 500 spectrometer. ESI-MS spectra were measured with a Waters Synapt G2 quadropole – Time of flight spectrometer.
Spectroelectrochemical measurements were carried out on a BioLogic SP-50 and SP-200 voltammetric analyzer, respectively in a Specac omni-cell liquid transmission cell with CaF_2 windows equipped with a Pt gauze working electrode, a Pt counter electrode and a Ag pseudoreference electrode, melt-sealed in a polyethylene spacer (path length 1 mm for oxidation and 0.5 mm for reduction experiments) using 0.1 M [*n*-Bu_4N][PF_6] as the supporting electrolyte in MeCN. UV/Vis/NIR spectro-electrochemical absorption spectra were measured on a Jasco V-770 spectrometer for oxidation measurements and on a Varian Cary 5000 spectrometer for reduction experiments.

Cyclic and square-wave voltammograms were carried out at room-temperature using a compactstat potentiostat from Ivium with an analyte concentration of 10^{-3} M in a MeCN/0.1 M [*n*-Bu_4N][PF_6] electrolyte. In a three-electrode configuration, a Pt working electrode (1 mm diameter), Ag/0.01 M $AgNO_3$, 0.1 M [*n*-Bu_4N][PF_6] in MeCN as reference and a Pt plate (~1 cm^2 surface area) as a counter electrode were used. Ferrocene was used as an internal standard and added after the measurements to refernce them to the respective $Fc^{0/+}$ couple. The resulting spectra were analyzed using the Iviumsoft software (v. 2.794). The redox transitions were checked for reversibility using the diagnostic criteria from Nicholson[1] and the Randles-Sevcik equation.[2]
Standard UV-Vis absorption spectra were recorded on a Varian Cary 50 spectrometer at a concentration of 10^{-5} M.

The crystallographic data of [Fe(tpy)(pbpy)]BPh_4 **2 BPh4** were recorded using a Bruker SMART CCD area detector diffractometer working with graphite monochromated MoK_α radiation (λ = 0.71073Å) at T = 130(2) K. The measurement of [Fe(pbpy)(PMe_3)$_2$Cl]PF_6 **1a Cl** was carried out using a Bruker D8 Kappa II applied with an APEX II detector and monochromated MoK_α radiation (λ = 0.71073Å) at T = 100(2) K. Structure solutions were carried out by direct methods,[3] full matrix least squares refinement based on F^2.[3] All not-hydrogen atoms were refined anisotropically, hydrogen positions were derived from geometrical reasons and afterwards refined at idealized positions riding on the carbon atoms with isotropic displacement parameters $U_{iso}(H) = 1.2U_{eq}(C)$ and d(C-H) = 0.96 Å. The methyl groups are idealized with tetrahedral angles in a combined rotating and rigid group refinement with the 1.5 fold isotropic displacement parameters of the equivalent U_{ij} of the corresponding carbon atom.

Transient absorption spectra of complex **2** were obtained by a pump-probe setup with a time resolution of 50 fs using a non-collinear optical parametric amplifier (NOPA) tuned to a center wavelength of 615 nm for pumping and a white light continuum for probing. Both the white light generation and the NOPA were pumped by a regenerative Ti:sapphire laser system operating at 775 nm and a repetition rate of 1 kHz. The polarizations of the pump and probe pulses were set to magic angle with respect to each other to avoid effects due to orientational relaxation. Pump and probe beam were focused onto the sample to overlapping spots with diameters of approximately 460 µm and 140 µm, respectively. The sample solution was measured in a fused silica cuvette with a thickness of 100 µm.

Synthesis

Tetrakis(trimethylphosphine)iron(0) and 2,2':6',2"-terpyridine were prepared according to the literature.[4]

3-(Dimethylamino)-1-(2-pyridinyl)-2-propenone

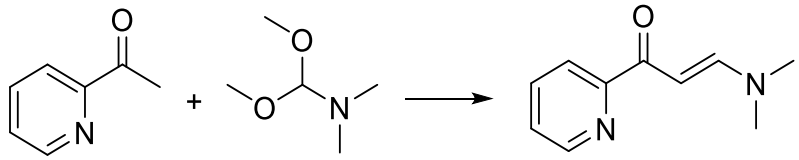

2-Acetylpyridine (9.0 mL, 80 mmol) and *N*,*N*-dimethylformamide dimethyl acetal (11.2 mL, 80 mmol) were heated under air under reflux for 6 h. After cooling to room temperature, the dark suspension was filtered. The solids were washed with pentane (50 mL) and a mixture of pentane and diethylether (2:1, 80 mL) and dried in vacuo. The product was isolated as a light green powder (**70 %**, 9.87 g, 56 mmol).

^{1}H NMR (500 MHz, $CDCl_3$) δ (ppm) = 8.55 (ddd, *J*=4.8, 1.8, 0.9, 1H), 8.06 (dt, *J*=7.9, 1.1, 1H), 7.83 (d, *J*=12.7, 1H), 7.71 (td, *J*=7.7, 1.8, 1H), 7.28 (ddd, *J*=7.5, 4.7, 1.3, 1H), 6.38 (d, *J*=12.7, 1H), 3.08 (s, 3H), 2.90 (s, 3H).
^{13}C NMR (126 MHz, $CDCl_3$) δ (ppm) = 186.82, 156.24, 154.65, 148.22, 136.63, 125.32, 121.95, 91.21, 45.03, 37.40.

6-(2-Bromophenyl)-2,2'-bipyridine

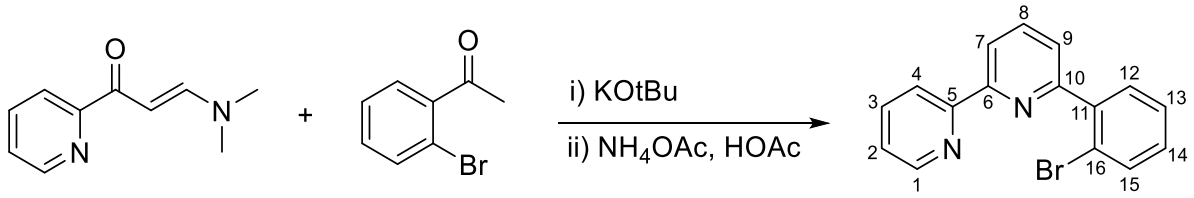

Under argon, a flask was charged with potassium tert-butoxide (8.98 g, 80 mmol) and dry THF (140 mL). Subsequently 2'-bromoacetophenone (7.96 g, 40 mmol) was added. The mixture was stirred for 2 h and 3-(dimethylamino)-1-(2-pyridyl)-2-propenone (7.05 g, 40 mmol) was added in counterstream. The reaction mixture was stirred for further 14 h. Afterwards, ammonium acetate (30.8 g, 400 mmol) and acetic acid (50 mL) were added under air. The mixture was heated and the THF was distilled over in 2 h. The Acetic Acid was removed via rotary evaporator. The black oil was diluted with water (100 mL) and neutralized with sodium carbonate. The suspension was extracted with DCM (3 x 40 mL) and the solvent of the organic phase was removed. To the dark oil toluene (40 mL) was added and was filtered over celite and was washed with a small amount of toluene. The black solution was passed over a small column of silica and washed further with toluene. The resulting red solution was adsorbed on silica gel and purified using column chromatography (7 % ethyl acetate in hexane). A yellow oil could be obtained, which was recrystallized from hexane. The product was isolated as colorless needles (**25** %, 3.59 g 11.5 mmol).

^{1}H NMR (500 MHz, $CDCl_3$) δ (ppm) = 8.69 (ddd, *J* = 4.8, 1.8, 0.9 Hz, 1H, **1**), 8.52 (dt, *J* = 8.0, 1.1 Hz, 1H, **4**), 8.42 (dd, *J* = 7.9, 1.0 Hz, 1H, **7**), 7.90 (t, *J* = 7.8 Hz, 1H, **8**), 7.80 (ddd, *J* = 8.0, 7.5, 1.8 Hz, 1H, **3**), 7.74 – 7.69 (m, 1H, **12**), 7.64 (dd, *J* = 7.7, 1.9 Hz, 1H, **15**), 7.62 (dd, *J* = 7.7, 1.0 Hz, 1H, **9**), 7.43 (td, *J* = 7.5, 1.2 Hz, 1H, **14**), 7.34 – 7.29 (m, 1H, **2**), 7.30 – 7.24 (m, 1H, **13**).
^{13}C NMR (126 MHz, $CDCl_3$) δ (ppm) = 157.99 (**10**), 156.62 (**5**), 156.17 (**6**), 149.50 (**1**), 141.73 (**11**), 137.27 (**3**), 137.22 (**8**), 133.90 (**12**), 132.09 (**15**), 130.08 (**13**), 127.90 (**14**), 124.93 (**9**), 124.14 (**2**), 122.39 (**16**), 121.93 (**4**), 120.05 (**7**).

Calculated for $C_{16}H_{11}BrN_2$: C = 61.76, H = 3.56 N = 9.00
Found: C = 61.76, H = 3.58, N = 9.08

[Fe(pbpy)(PMe$_3$)$_2$Br] (1)

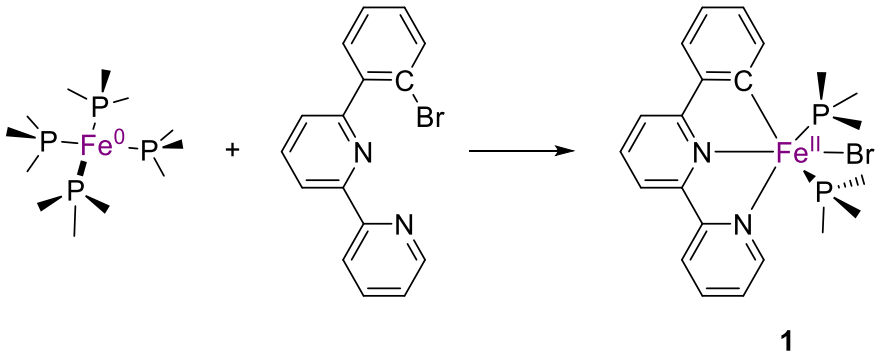

1

A flask was charged with tetrakis(trimethylphosphine)iron(0) (360 mg, 1 mmol) and dry THF (10 mL) and cooled to -80 °C in a N_2/EtOH bath. 6-(2-Bromophenyl)-2,2'-bipyridine (311 mg, 1 mmol) in THF (8 mL) was added to the yellow solution and stirred for 2 h.

For isolation of this intermediate, the solution was stirred for further 16 h, while allowing to warm to room temperature. Subsequently the solvent was removed in vacuo and the resulting brown orange solid was dried thoroughly to remove residual PMe_3. The raw product was dissolved in dry toluene (25 mL) and filtered. The solvent was removed from the filtrate to yield **1** as a dark brown solid (190 mg, 0.37 mmol, **21 %**).

^{1}H NMR (500 MHz, Benzene-d_6) δ (ppm) = 10.09 (d, *J* = 5.7 Hz, 1H), 8.65 (d, *J* = 7.6 Hz, 1H), 7.76 (d, *J* = 7.6 Hz, 1H), 7.42 – 7.18 (m, 4H), 7.01 (d, *J* = 8.0 Hz, 2H), 6.88 (dd, *J* = 16.4, 7.7 Hz, 2H), 0.51 (t, *J* = 3.8 Hz, 18H).
^{31}P NMR (202 MHz, C_6D_6) δ (ppm) = -43.00.

Due to the reactivity towards oxygen, this intermediate readily oxidizes but is stable towards water. Most of the residue obtained from the filtration is the oxidized complex of **1** (Fe^{III} instead of Fe^{II}), **1a** with an unknown anion, which was later converted into the PF_6 salt (yield not determined).
The ^{1}H-NMR spectrum shows only minor impurities, mostly residual solvent. One characteristic triplet of the methyl groups at 0.51 ppm and only a single resonance in the ^{31}P-NMR spectrum indicates that the two PMe_3 ligands are in *trans*-position.

It is yet unclear if there is any reactivity of **1** towards C-Cl bonds, but after work up of the first reaction using chloroform and dichloromethane following the further reaction with terpyridine (see synthesis of **2**), compound **1a-Cl** was obtained, where a chlorido ligand is coordinated to iron instead of a bromido ligand (**1a**). Crystals of the chlorido complex suitable for X-ray diffraction were obtained by slowly

diffusing pentane into a solution containing both **1a-Cl** and **2** (cf. fig. S1). The crystal structure confirms the *trans* position of the trimethyl phosphane ligands.

[Fe(pbpy)(tpy)]PF_6 (2)

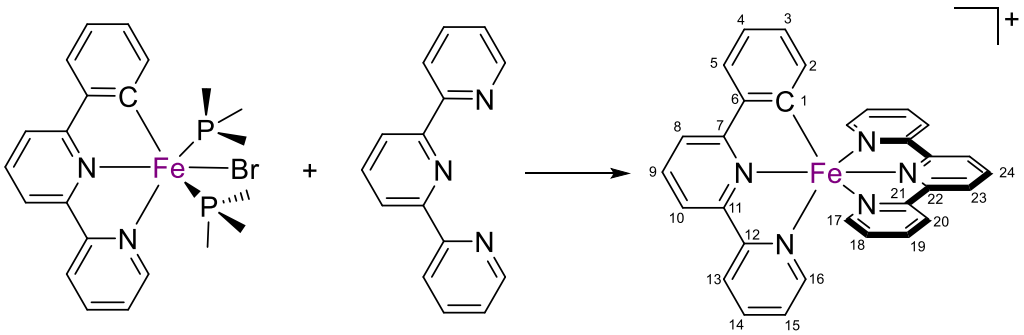

1 **2**

To the reaction mixture of [FeBr(pbpy)(PMe_3)$_2$] **(1)**, terpyridine (233 mg, 1 mmol) was added and the solution was stirred overnight and allowed to warm to room temperature. The solvent was removed and the dark residue was redissolved in a minimal amount of methanol (15 mL) under air. The dark solution was added dropwise to a large excess of diethylether (200 mL). The suspension was stirred for 20 minutes and filtered.

The purple residue was washed with water to remove the bis(terpyridine) complex **3**, until the filtrate acquired a pale blue color. This indicated that only **2** Br was left which has a low solubility in water. For yield maximation it is possible to extract the aqueous phase with DCM. The residue was dissolved in methanol (20 mL) and stirred with KPF_6 (2 eq. 368 mg) for 30 minutes, after which 80 mL water were added. The green precipitate was purified using reversed phase column chromatography (C18 Silica, 17 % C) with methanol as eluent. The eluting green band was collected. This chromatographic procedure was repeated two times. The green raw product was crystallized from acetone/pentane to yield dark green crystals of **2** (**26 %**, 171 mg, 0.26 mmol) based on [Fe(PMe_3)$_4$].

^{1}H NMR (500 MHz, Acetone-d_6) δ (ppm) = 8.89 (d, *J* = 7.9 Hz, 2H, **23**), 8.67 (d, *J* = 2.9 Hz, 1H, **10**), 8.66 (d, *J* = 3.1 Hz, 1H, **13**), 8.52 (d, *J* = 8.0 Hz, 2H, **17**), 8.46 (d, *J* = 8.0 Hz, 1H, **8**), 8.38 – 8.34 (m, 1H, **9**), 8.34 – 8.31 (m, 1H, **24**), 7.98 – 7.93 (m, 1H, **14**), 7.93 – 7.90 (m, 1H, **5**), 7.73 (td, *J* = 7.7, 1.5 Hz, 2H, **18**), 7.64 (d, *J* = 5.4 Hz, 1H, **16**), 7.18 (ddd, *J* = 7.1, 5.5, 1.2 Hz, 1H, **15**), 7.09 (d, *J* = 5.7 Hz, 2H, **20**), 7.00 (ddd, *J* = 7.2, 5.7, 1.3 Hz, 2H, **19**), 6.75 (td, *J* = 7.4, 1.2 Hz, 1H, **4**), 6.47 (td, *J* = 7.3, 1.3 Hz, 1H, **3**), 5.70 (dd, *J* = 7.5, 1.1 Hz, 1H, **2**).

^{13}C NMR (126 MHz, Acetone-d_6) δ (ppm) = 196.84 (**1**), 168.69 (**7**), 158.53 (**21**), 158.51 (**11**), 158.05 (**12**), 157.53 (**22**), 151.89 (**16**), 151.00 (**20**), 147.80 (**6**), 138.29 (**14**), 137.05 (**9**), 136.06 (**2**), 135.48 (**18**), 130.29 (**24**), 128.94 (**3**), 126.99 (**15**), 126.13 (**19**), 124.84 (**5**), 123.71 (**13**), 123.12 (**4**), 122.83 (**17**), 121.96 (**23**), 119.64 (**10**), 118.73 (**8**).

HRMS (ESI): *m/z* $[M\text{-}PF_6]^+$calculated for $C_{31}H_{22}FeN_5$: 520.1225, found: 520.1283 m/z

Elemental analysis calculated for $C_{31}H_{22}F_6FeN_5P$: C = 55.96, H = 3.33, N = 10.59
Found: C = 55.71, H = 3.47, N = 10.51
UV-Vis (MeCN)**:** λ (ε) = 416 nm (0.77 10^4 M^{-1} cm^{-1}), 618 nm, (0.92 10^4 M^{-1} cm^{-1}), 670 nm (0.76 10^4 M^{-1} cm^{-1}), 806 nm (0.17 10^4 M^{-1} cm^{-1})

[Fe(pbpy)(tpy)](BPh$_4$) (**2** BPh$_4$)
[Fe(pbpy)(tpy)](PF_6) (0.006 mmol, 3.6 mg) was dissolved in MeOH (2 mL) and $NaBPh_4$ (4 eq., 0.024 mmol, 8.2 mg) was added. The green precipitate was filtered off and washed thoroughly with water. The product was dissolved in a miniscule amount of DCM and layered with n-hexane. Single crystals of **2**BPh$_4$ were obtained after a few days (3.8 mg, 0.0045 mmol, 75 %).

Quantum chemical calculations

All calculations presented here were performed using the ORCA program system (version 4.0.1).[7] Unconstrained geometry optimizations were conducted via the PBEh-3c method of the Grimme group.[8] All presented optimized structures are confirmed to be minima structures by numerical frequency calculations and the absence of negative frequencies. Correction for dispersion interaction was included by DFT-D3 with Becke-Johnson damping (D3BJ)[9] for all calculations presented here.

TD-DFT XANES[10] and DFT VtC-XES[11] calculations were accomplished using a modified TPSSh[12] functional, with an adjusted Hartree-Fock exchange of 12.5 %[13–16] in conjunction with the RIJCOSX approximation and the def2-TZVP[17]basis set, combined with the def2-TZVP/J[18] auxiliary basis set (with a special integration accuracy of 5) on all atoms except Fe, for which the expanded CP(PPP) basis set[19] (with a special integration accuracy of 7) was used.

TD-DFT UV/VIS calculations were accomplished using a modified TPSSh functional, with an adjusted Hartree-Fock exchange of 5 % in conjunction with the RIJCOSX approximation and the def2-TZVP basis set,[17] combined with the def2-TZVP/J[18] auxiliary basis set (with a special integration accuracy of 5) on all atoms. It has been shown in a previous computational study of complexes **2** and **3** that the non-hybrid functional TPSS[12] outperforms the hybrid functional TPSSh (10 % Hartree-Fock exchange).[20] Nevertheless, we observed a benefit of a slight inclusion of only 5 % Hartree-Fock exchange in respect to the overall accuracy of modelling the whole UV/VIS spectra (see figure S15), especially concerning the splitting between MLCT features and ligand localized features for both complexes (**2** and **3**).

TD-DFT UV/VIS transitions were broadened by a 1750 cm^{-1} Gaussian (fwhm) and shifted by -1900 cm^{-1}. Kohn-Sham orbitals were visualized with the IboView program (version 20150427).[21] Orbital populations were extracted via Löwdin Reduced Orbital Population Analysis using MOAnalyzer (version 1.2).[22]

DFT levels shown in the manuscript were calculated using the TPSSh functional in conjunction with the def2-TZVPP basis set using very tight SCF convergence criteria (energy change of 10^{-9} au). Solvation by acetonitrile is covered by the SMD solvation model.[23]

X-Ray spectroscopy

CtC-XES

Core-to-core X-ray emission spectroscopy (CtC-XES, K$\beta_{1,3}$ emission),[24,25–27] valence-to-core X-ray emission spectroscopy (VtC-XES, K$\beta_{2,5}$ emission)[28a–c,11,28d] and high energy resolution fluorescence

detected XANES (HERFD-XANES)[29] were performed in the solid state and the results compared to the reference complex **3**.

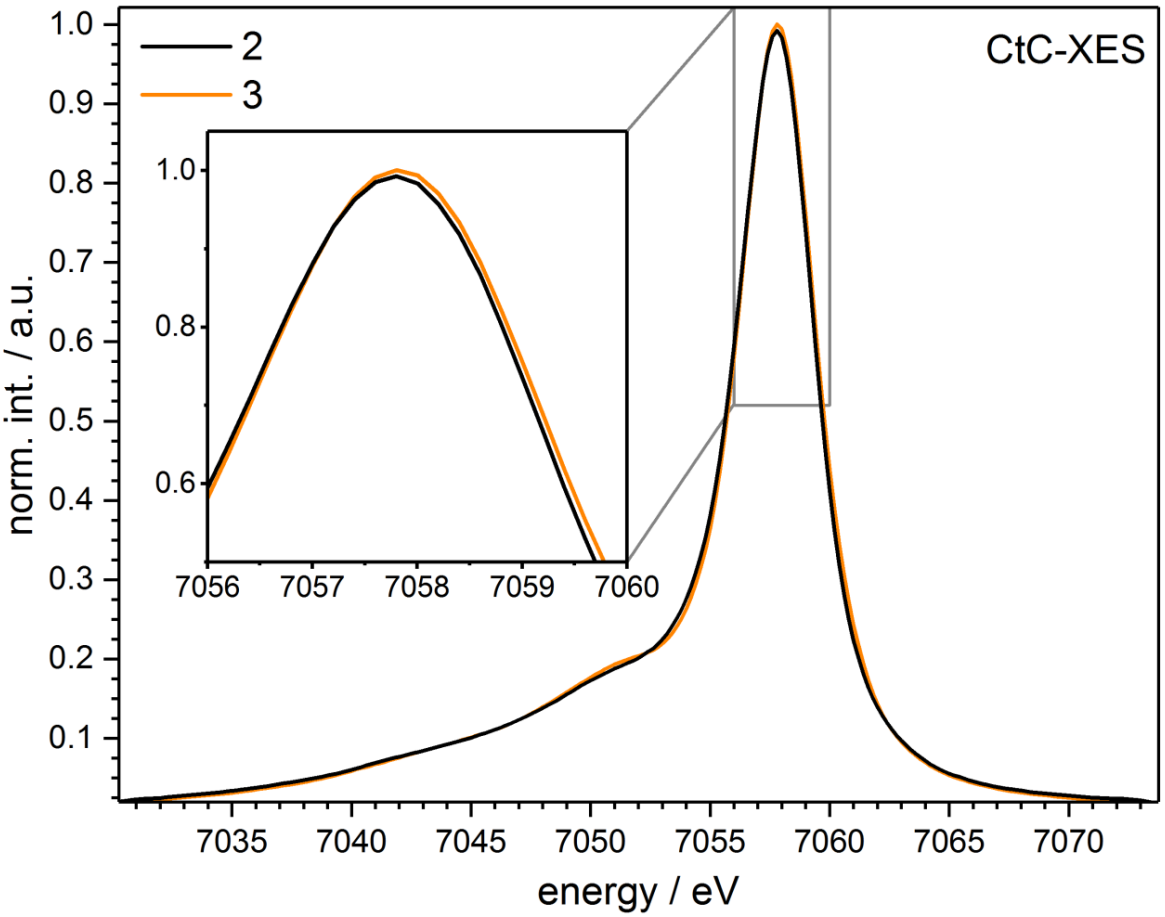

Figure S1: Experimental CtC-XES spectra of complexes **2** and **3**

The obtained CtC-XES spectrum of **2** is compared to the spectrum of the reference complex **3** in figure S3. Both complexes (**2**, **3**) are clearly in a low-spin configuration (LS, S = 0), since the satellite (Kβ') is not separated from the mainline (K$\beta_{1,3}$) and the intensity ratio between both signals (Kβ'/K$\beta_{1,3}$) is small.[27]

Nevertheless, the mainline is slightly red shifted for complex **2** in relation to **3**. Since both complexes are in a Fe $3d^6$ LS configuration, this shift is interpreted as an increased covalency between the central Fe atom and the pbpy ligand (**2**) compared to tpy (**3**).[25–27]

HERFD-XANES

In general, a well-resolved, asymmetrical pre-edge feature A at around 7114 eV and three near-edge features B (at around 7118 eV), C (at around 7123 eV) and D (at around 7125 eV), are observed (see figure S4, top). Since near-edge features are caused by transition to higher LUMO levels, we will focus on the pre-edge feature A. A slightly increased pre-edge energy is observed for **2** (7113.8 eV), in comparison to **3** (7113.6 eV). To understand the quantum mechanical origin of the observed HERFD-

XANES features, TD-DFT XANES calculations applying the TPSSh functional with an adjusted Hartree-Fock exchange of 12.5 % were performed (Figure S4, bottom).[13–16] Since an excellent agreement between experiment and theory is obtained, further information of the underlying transitions can be extracted. For both **2** and **3** the pre-edge feature A consists mainly of Fe 1s → e_g* transitions, superimposed by contributions of tpy π* dominated acceptor orbitals (predominant acceptor orbitals of predominant core-excited states S1 to S5 are shown in figure S4). Therefore, the experimentally observed blue shift of pre-edge feature A of complex **2** in relation to **3** is attributed to a destabilization of the e_g* and / or tpy π* energies.

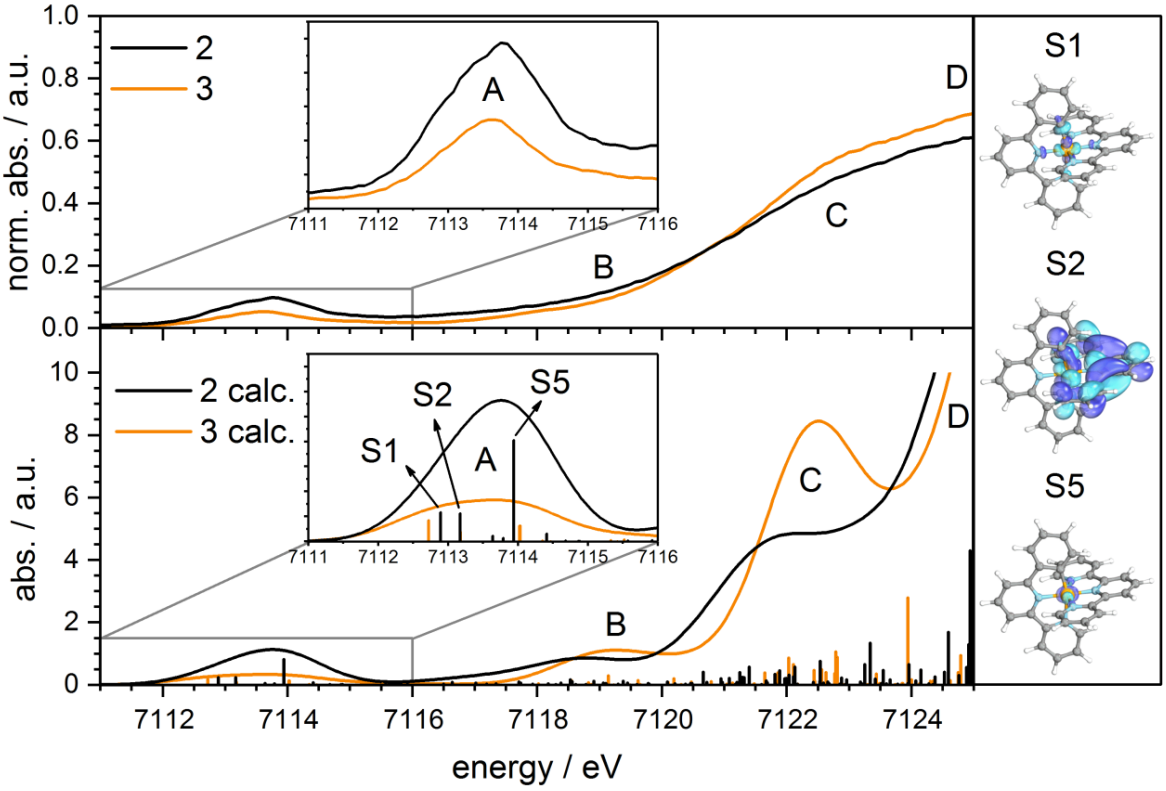

Figure S2: Experimental Fe K-edge HERFD-XANES spectra of complexes **2** and **3** (top) in comparison to theoretical Fe K-edge XANES spectra (bottom).

VtC-XES

Complementary to HERFD-XANES, VtC-XES was applied to characterize the HOMO states of **2**. Experimental spectra are shown in figure S5 (top). The VtC-XES spectrum is dominated by a strong band, which can be divided into four spectral regions: low-energy shoulder A, main feature B, shoulder C and high-energy feature D. The low-energy shoulder A and the main feature B of **2** are decreased in intensity and red shifted in relation to **3**. The high-energy shoulder C is only observed for the

cyclometalated complex **2** and is not expected to appear in Fe^{II} polypyridyl/NHC complexes,[16] since it is connected to the interaction of the pbpy ligand and the Fe center (cf. figure S5, bottom).

The VtC-XES spectra were simulated by DFT calculations using an adjusted TPSSh functional (for details see quantum-chemical calculations section). Theory and experiment agree very well (see Figure S5). The low-energy shoulder A is caused by phenyl/polypyridyl σ donor orbitals, while the main feature B originates from a superposition phenyl/polypyridyl σ/π donor orbitals (donor orbitals of the predominant transitions of VtC-XES features A - D are shown in Figure S5), in line with previous studies on similar compounds.[16] Therefore, the observed redshift of feature A and B of complex **2** is led back to a stabilization of the phenyl/polypyridyl σ and π levels in relation to **3**. The additional feature C is caused by a single transition of a donor orbital which reflects the σ bonding interaction of the $pbpy^-$ ligand and the Fe $3d_{z^2}$ orbital.

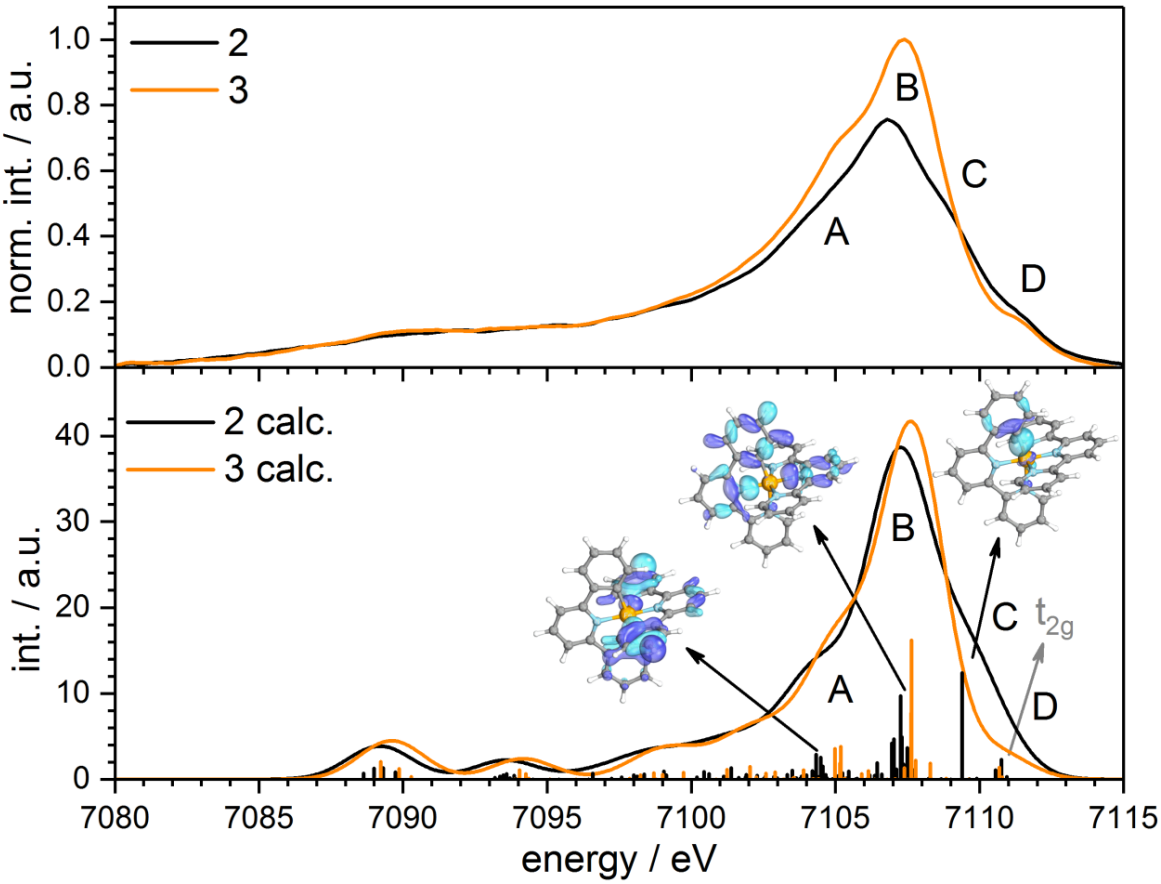

Figure S3: Experimental Fe K-edge VtC-XES spectra of complexes **2** and **3** (top) in comparison to theoretical Fe K-edge VtC-XES spectra (bottom).

Electrochemistry

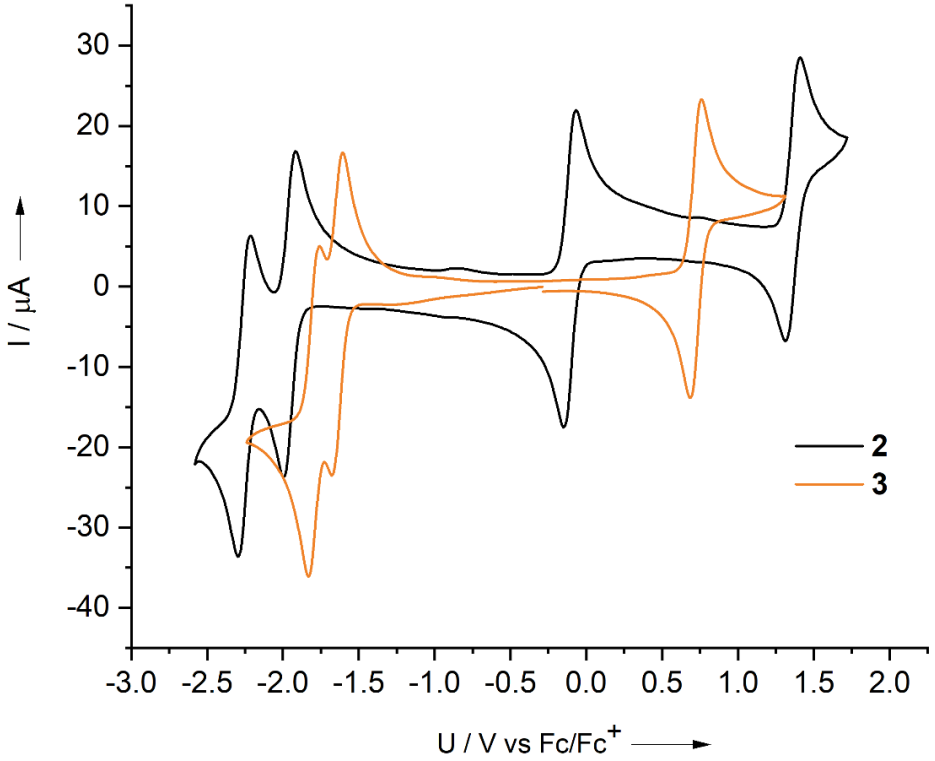

Figure S4: Cyclic voltammogram of **2** and **3** (scan rate 100 mV/s, MeCN).

The data for the $[Fe(tpy)_2](PF_6)_2$ complex **3** was already published.[30]

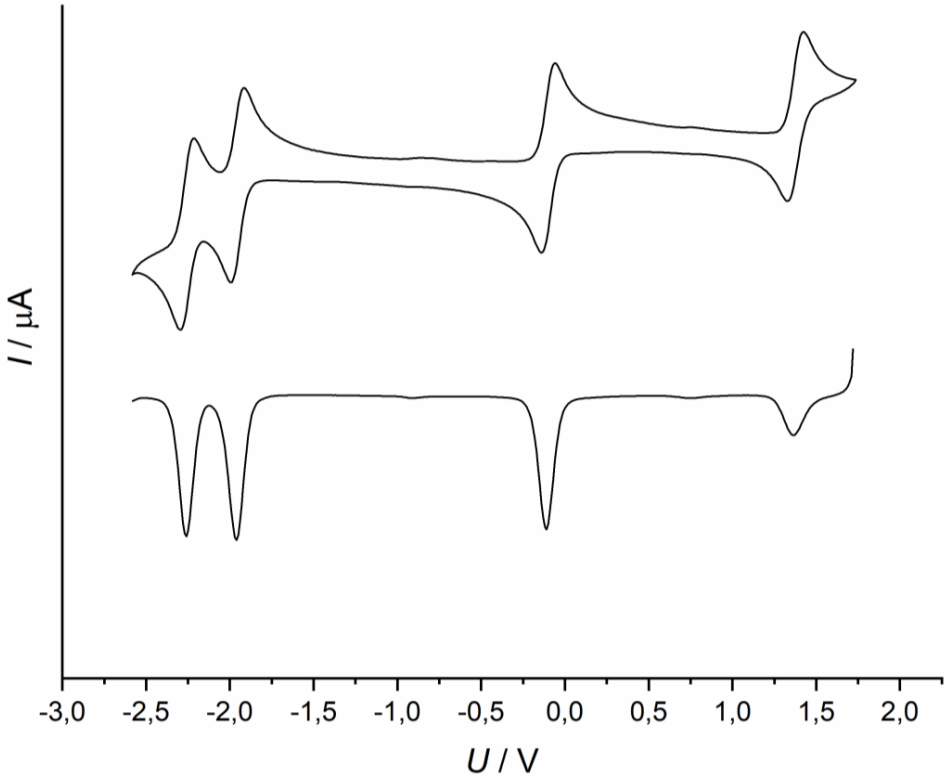

Figure S5: Cyclic voltammogram (scan rate 100 mV/s) and square-wave voltammogram (25 Hz) of $[Fe(pbpy)(tpy)]PF_6$ **2** in MeCN.

Table S 1: Electrochemical data for the reversible oxidation at $E^0_{1/2}$ = -0.11 V vs. $Fc^{0/+}$ of complex **2**.

v / mV/s	50	100	200	400	600	800	1000
E_{pc} / V	-0.15	-0.15	-0.15	-0.15	-0.15	-0.15	-0.16
E_{pa} / V	-0.07	-0.07	-0.07	-0.07	-0.07	-0.06	-0.06
$E_{1/2}$ /V	-0.11	-0.11	-0.11	-0.11	-0.11	-0.11	-0.11
I_{pc} / µA	-1.23	-1.71	-2.49	-3.60	-4.42	-5.14	-5.68
I_{pa} / µA	1.22	1.73	2.57	3.75	4.47	5.19	5.85
ΔE / mV	85	-80	-75	-75	-85	-90	-95
$\|I_c/I_a\|$	1.01	0.99	0.97	0.96	0.99	0.99	0.97
$\|I_{pc}/v^{1/2}\|$	0.17	0.17	0.18	0.18	0.18	0.18	0.18
$\|I_{pa}/v^{1/2}\|$	0.17	0.17	0.18	0.19	0.18	0.18	0.18

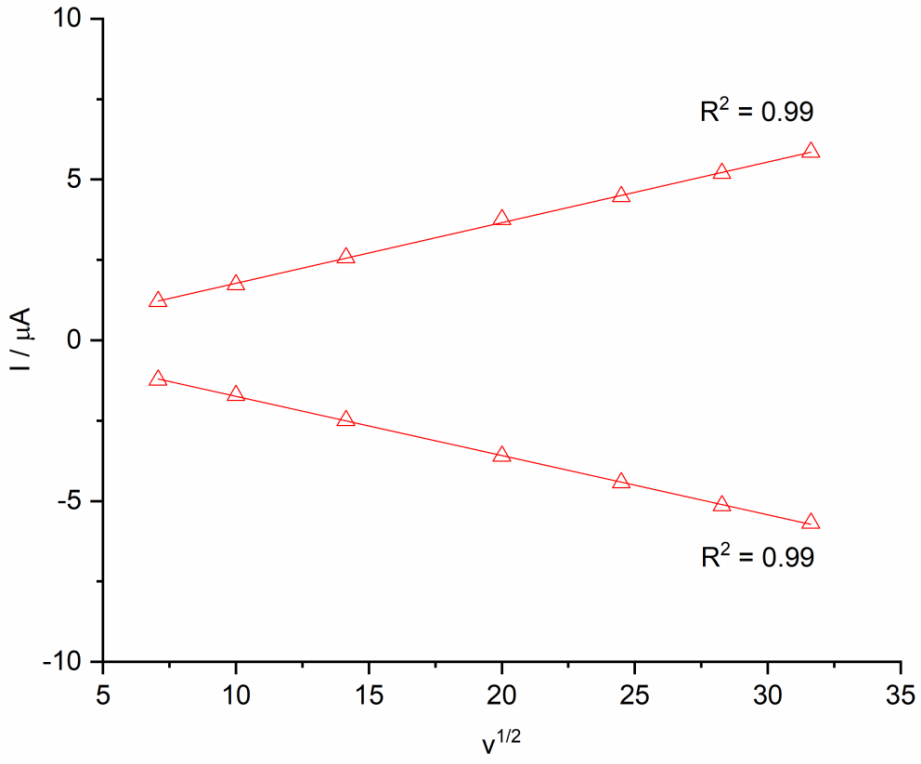

Figure S6: Linear dependence of forward current peaks I_{pc} and I_{pa} versus the square root of the scan rate v for the reversible oxidation at $E^0_{1/2}$ = -0.11 V vs. $Fc^{0/+}$ of complex **2**.

Table S2: Electrochemical data for the irreversible oxidation at $E^0_{1/2}$ = 1.37 V vs. $Fc^{0/+}$ of complex **2**.

v / mV/s	50	100	200	400	600	800	1000
E_{pc} / V	1.31	1.31	1.30	1.30	1.29	1.28	1.27
E_{pa} / V	1.42	1.42	1.43	1.44	1.45	1.46	1.47
$E_{1/2}$ /V	1.37	1.37	1.37	1.37	1.37	1.37	1.37
I_{pc} / µA	-1.03	-1.39	-1.89	-2.43	-2.72	-3.00	-3.12
I_{pa} / µA	1.06	1.46	1.96	2.55	2.92	3.17	3.33
ΔE / mV	110	110	130	140	160	180	200
$\lvert I_c/I_a \rvert$	0.97	0.96	0.96	0.95	0.93	0.95	0.94
$\lvert I_{pc}/v^{1/2} \rvert$	0.15	0.14	0.13	0.12	0.11	0.11	0.10
$\lvert I_{pa}/v^{1/2} \rvert$	0.15	0.15	0.14	0.13	0.12	0.11	0.11

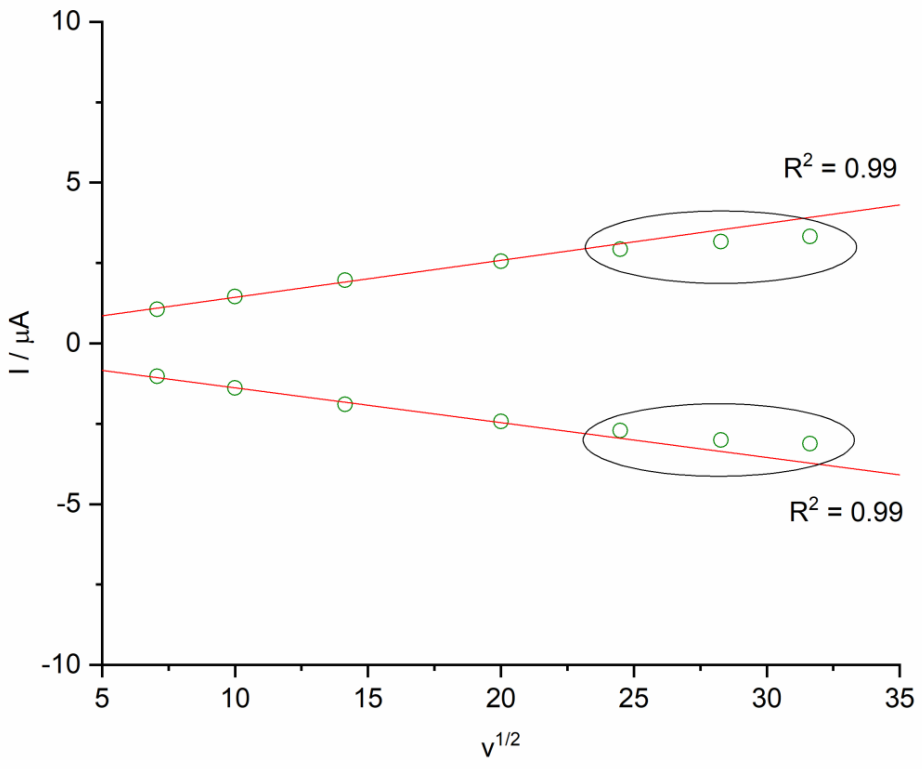

Figure S7: Linear dependence of forward current peaks I_{pc} and I_{pa} versus the square root of the scan rate v for the irreversible oxidation at $E^0_{1/2}$ = 1.37 V vs. $Fc^{0/+}$ of complex **2**. Encircled data points (v = 600, 800, 1000 mv/s) are excluded from the linear fit. This means that the Randles-Sevcik equation is only valid for the 50-400 mV/s scan rates.

Table S3: Electrochemical data for the quasireversible reduction at $E^0_{1/2}$ = -1.96 V vs. $Fc^{0/+}$ of complex **2**.

v / mV/s	50	100	200	400	600	800	1000
E_{pc} / V	-2.00	-2.00	-2.00	-2.00	-2.00	-2.01	-2.01
E_{pa} / V	-1.91	-1.92	-1.92	-1.92	-1.92	-1.92	-1.91
$E_{1/2}$ /V	-1.96	-1.96	-1.96	-1.96	-1.96	-1.96	-1.96
I_{pc} / µA	-1.04	-1.50	-2.39	-3.46	-4.00	-4.64	-4.81
I_{pa} / µA	1.08	1.58	2.25	3.29	3.89	4.32	4.81
ΔE / mV	90	80	75	80	80	90	100
$\|I_c/I_a\|$	1.04	1.05	0.94	0.95	0.97	0.93	1.00
$\|I_{pc}/v^{1/2}\|$	0.15	0.15	0.17	0.17	0.16	0.16	0.15
$\|I_{pa}/v^{1/2}\|$	0.15	0.16	0.16	0.16	0.16	0.15	0.15

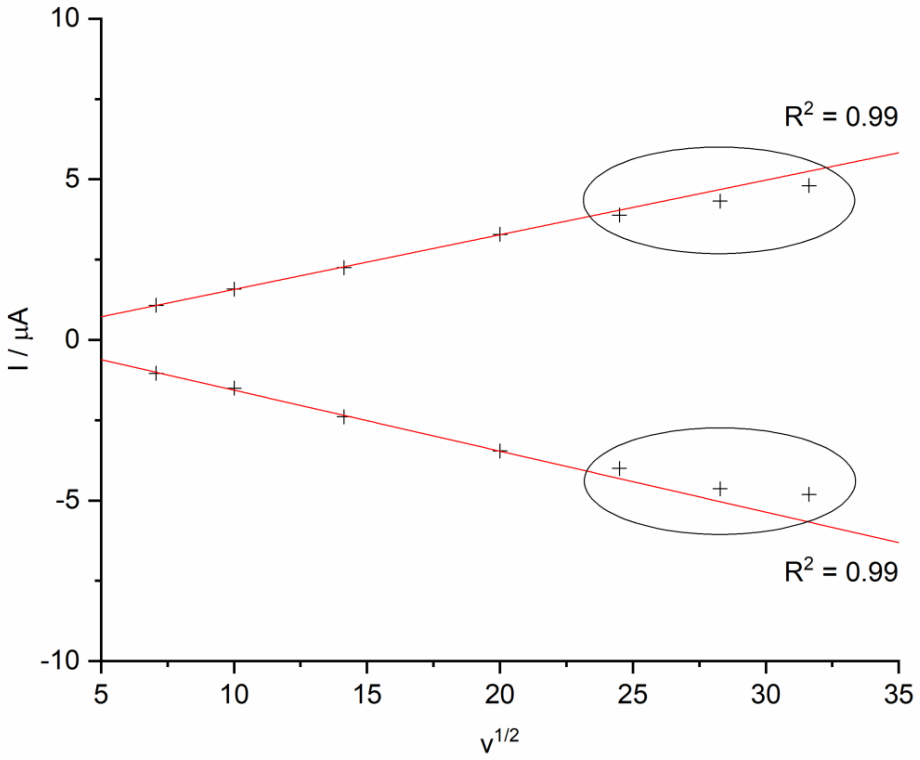

Figure S8: Linear dependence of forward current peaks I_{pc} and I_{pa} versus the square root of the scan rate v for the quasireversible reduction at $E^0_{1/2}$ = -1.96 V vs. $Fc^{0/+}$ of complex **2**. Encircled data points (v = 600, 800, 1000 mv/s) are excluded from the linear fit. This means that the Randles-Sevcik equation is only valid for the 50-400 mV/s scan rates.

Table S4: Electrochemical data for the quasireversible reduction at $E^0_{1/2}$ = -2.25 V vs. $Fc^{0/+}$ of complex **2**.

v / mV/s	50	100	200	400	600	800	1000
E_{pc} / V	-2.30	-2.30	-2.29	-2.29	-2.30	-2.30	-2.31
E_{pa} / V	-2.21	-2.22	-2.22	-2.22	-2.22	-2.21	-2.21
$E_{1/2}$ /V	-2.25	-2.26	-2.25	-2.26	-2.26	-2.26	-2.26
I_{pc} / µA	-1.14	-1.41	-2.16	-3.24	-3.89	-4.56	-4.89
I_{pa} / µA	1.05	1.43	2.24	3.34	3.91	4.50	4.96
ΔE / mV	85	80	75	70	80	90	100
$\|I_c/I_a\|$	0.92	1.01	1.04	1.03	1.01	0.99	1.01
$\|I_{pc}/v^{1/2}\|$	0.16	0.14	0.15	0.16	0.16	0.16	0.15
$\|I_{pa}/v^{1/2}\|$	0.15	0.14	0.16	0.17	0.16	0.16	0.16

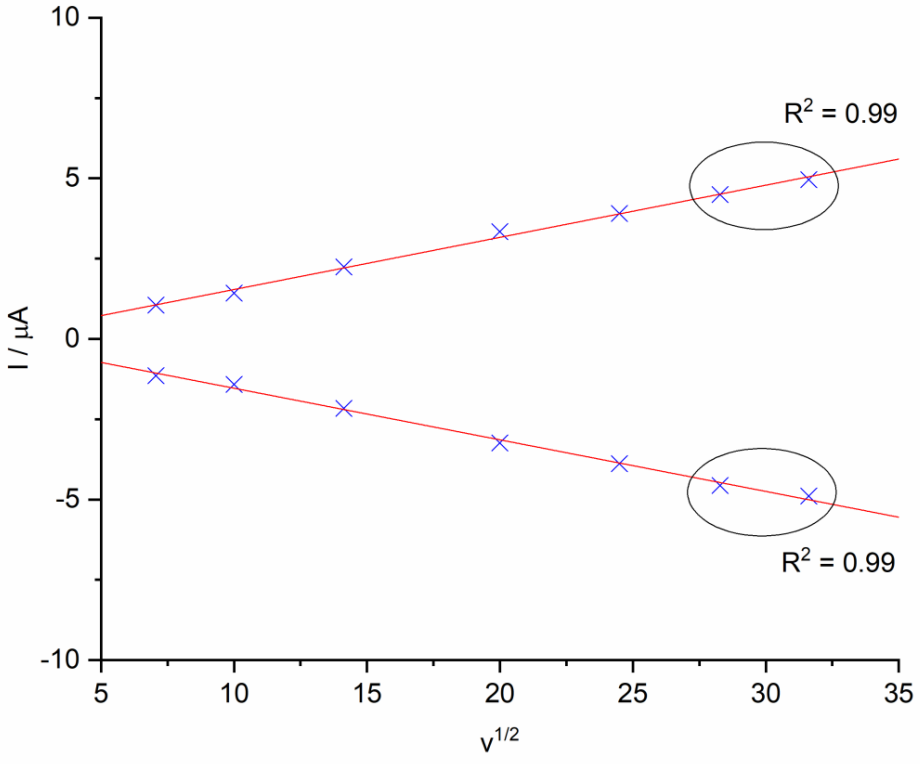

Figure S9: Linear dependence of forward current peaks I_{pc} and I_{pa} versus the square root of the scan rate v for the quasireversible reduction at $E^0_{1/2}$ = -2.25 V vs. $Fc^{0/+}$ of complex **2**. Encircled data points (v = 800, 1000 mv/s) are excluded from the linear fit. This means that the Randles-Sevcik equation is only valid for the 50-600 mV/s scan rates.

UV-Vis Spectroscopy

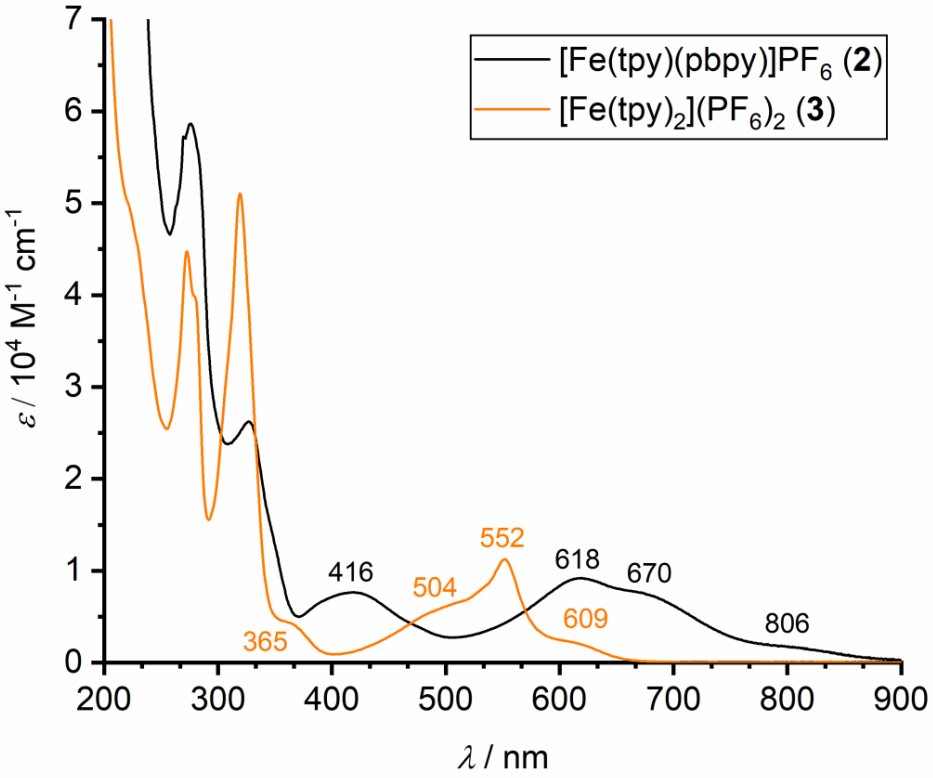

Figure S10: Electronic absorption spectra of **2** and **3** in MeCN

The data for the $[Fe(tpy)_2](PF_6)_2$ complex **3** was already published.[30]

The absorption properties of **2** and **3** are quite different. While the absorption maximum in **3** is located at 552 nm, the absorption maximum in **2** is bathochromically shifted to 618 nm. The absorption itself reaches up into the NIR with shoulders at 670 and 806 nm.
The bands below 375 nm are caused by ligand localized transitions. The bands above 375 nm are expected to be MLCT-based transitions. The exact assignment was done via TD-DFT calculations and is further discussed in the "quantum chemical calculations" paragraph. Table S5 summarizes the main donor and acceptor orbitals from the transitions in the 500-900 nm region.

The complex was also examined for solvatochromism, as shown in figure S13. UV-Vis absorption spectra were recorded in methanol, ethanol, acetonitrile (MeCN), dichloromethane (DCM), dimethylsulfoxide (DMSO), and acetone at a respective concentration of 10^{-5} M and normalized to the MLCT-absorption maximum. Beside of DMSO, the spectral position of the absorption maximum correlates linearly with the permittivity ε of the solvents and increasing the permittivity by going from

DCM to MeCN results in a small hypsochromic shift ($\Delta\lambda$ = -9 nm; +232 cm^{-1} difference) (figure S14). Using ET(30) values[31] no such correlation with shifts of the absorption band is found.

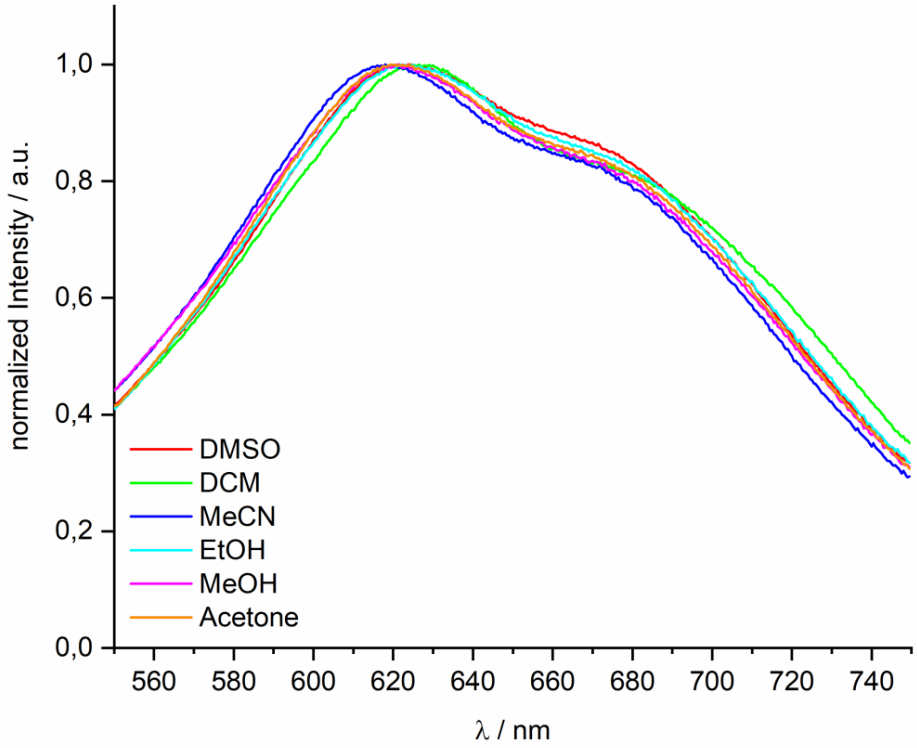

Figure S11: MLCT-absorption maxima normalized to 1 of (**2**) in different solvents (10^{-5} mol L^{-1}).

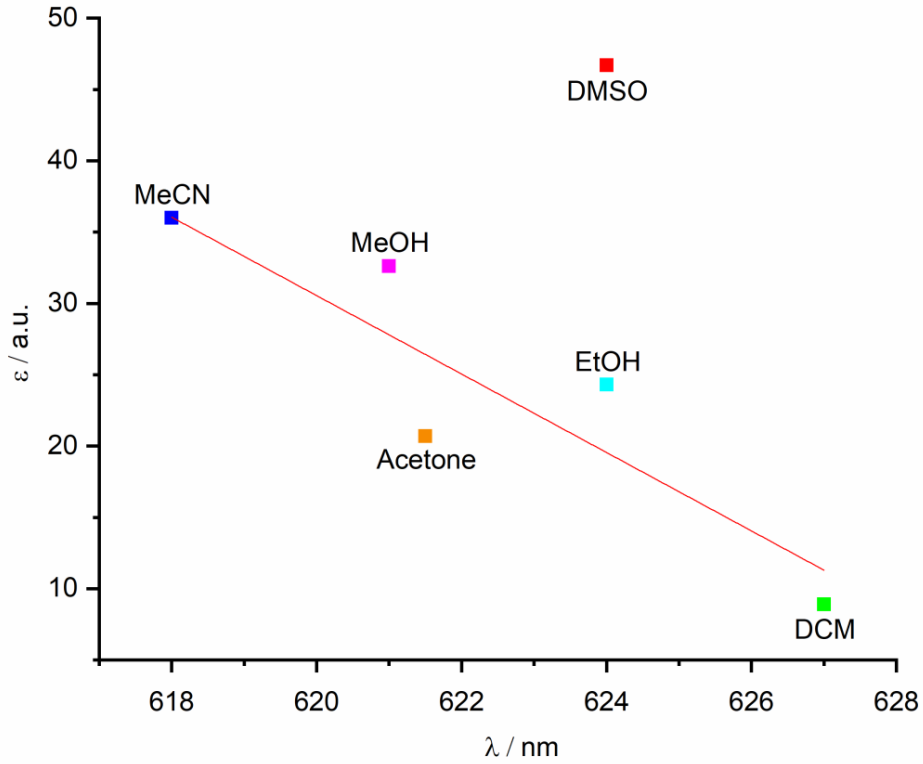

Figure S12: Wavelength of the MLCT absorption maxima of (**2**) in different solvents plotted versus the relative permittivity of the respective solvent. The linear fit excludes the data point of DMSO since it severely deviates from the overall trend.

Calculated UV/VIS spectra

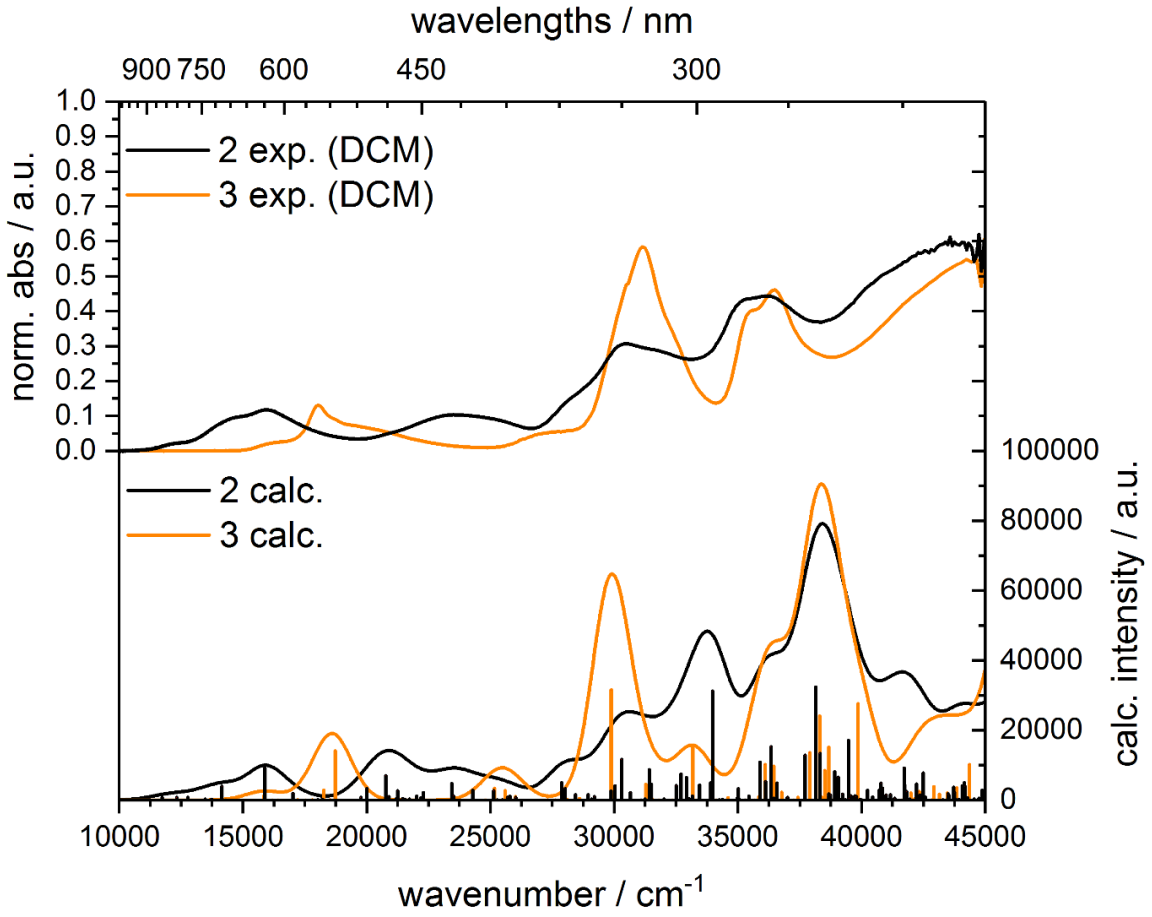

Figure S13: Experimental UV/VIS/NIR spectra of **2** and **3** in DCM (top) in comparison to theoretical UV/VIS/NIR spectra (bottom).

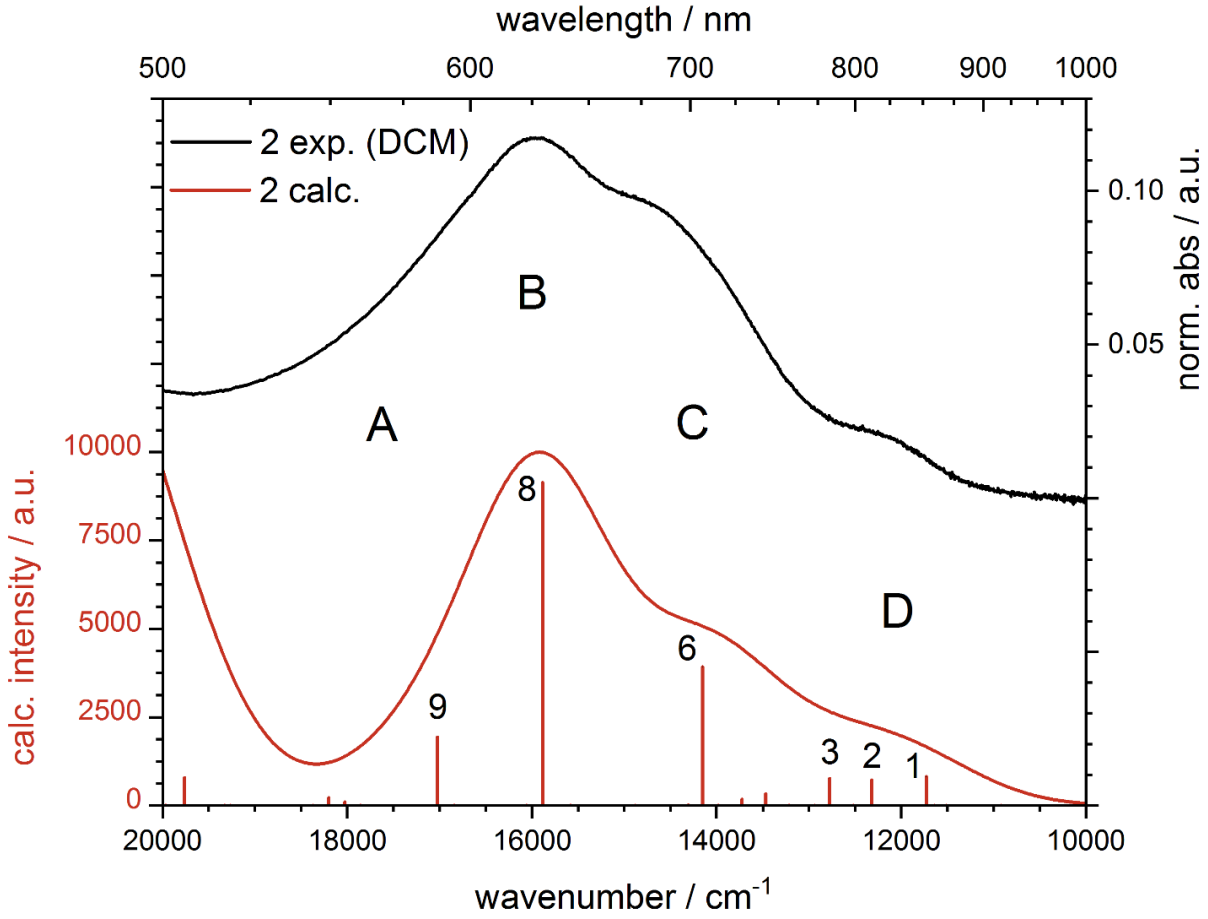

Figure S14: Experimental UV/VIS of **2** in DCM (top) in comparison to theoretical UV/VIS spectrum (bottom). Predominant transitions are labeled by their singlet excited state order, with 1 being the transition to singlet excited state of lowest energy.

The theoretical UV/VIS spectra of **2** and **3** were calculated by TDDFT using the TPSSh functional with an adjusted Hartree-Fock exchange to 5 %. An overall impressive agreement could be achieved (as shown in figure S15), especially in the low-energy region from 500 – 900 nm (figure S16, which allows an extraction of detailed information about the involved molecular levels and their chemical nature. Since our main interest here is the MLCT region, we will focus on the low-energy signal of complex **2** for clarity, located between 500 and 900 nm.

In general, four spectral features are observed in the MLCT region, starting with the high-energy shoulder A, followed by main feature B and low-energy shoulders C and D. All underlying predominant transitions (figure S16, labeled transitions 1 – 9) are caused by Fe localized donor orbitals, which reflect the Fe t_{2g} orbitals (HOMO-2, HOMO-1, HOMO; detailed information about the excited state composition is given in table S5; acceptor and donor orbital compositions are given in table S5). High-energy shoulder A is solely caused by a transition to singlet excited state 9, whose predominant acceptor orbital is the LUMO+3, reflecting a pbpy π* orbital. Only minor proportions of the LUMO+1 reflecting

the antibonding Fe $3d_{xz/yz}$ – tpy π* and the LUMO+2, reflecting the Fe $3d_{xy}$ – bpy π* interaction are contributing to excited state 9 (see supporting information table S6). Main feature B is evoked by transition 8, which is composed of the LUMO+2 (Fe $3d_{xy}$ – bpy π*) as the predominant acceptor and the LUMO+1 (Fe $3d_{xz/yz}$ – tpy π*) as the minor acceptor. Transition 6 is causing shoulder C, with the LUMO as the main acceptor, which reflects a tpy π* orbital and the LUMO+2 (Fe $3d_{xy}$ – bpy π*) as secondary acceptor. Low-energy shoulder D is caused by three transitions, 1, 2 and 3 (see table S5), with the predominant acceptors LUMO+1 (Fe $3d_{xz/yz}$ – tpy π*), LUMO (tpy π*) and LUMO+2 (Fe $3d_{xy}$ – bpy π*). No additional significant secondary contributions to the excited states 1, 2 and 3 are observed.

Table S5: Detailed information about the excited state composition of predominant transition causing low-energy UV/VIS/NIR features A – D of complex **2** (Figure S21). Only transitions occupying at least 10 % of the excited state composition are taken into account for clarity.

Feature	Order	Excited state composition
A	9	HOMO → LUMO+3 (0.55)
		HOMO-1 → LUMO+1 (0.16)
		HOMO-2 → LUMO+2 (0.10)
B	8	HOMO-2 → LUMO+2 (0.55)
		HOMO-1 → LUMO+1 (0.28)
C	6	HOMO-1 → LUMO (0.61)
		HOMO-1 → LUMO+2 (0.23)
D	3	HOMO → LUMO+2 (0.90)
	2	HOMO → LUMO (0.92)
	1	HOMO → LUMO+1 (0.92)

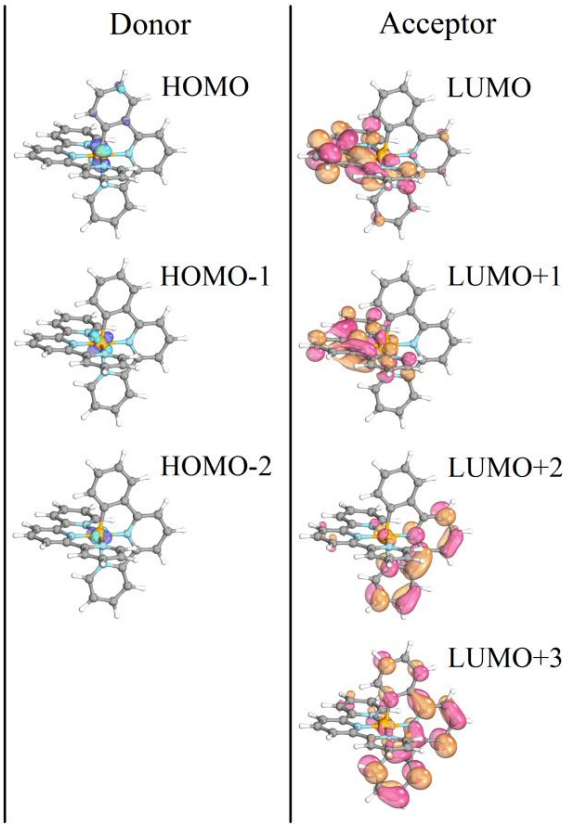

Table S6: AO populations of predominant acceptor and donor orbitals of the MLCT transitions in the UV/VIS/NIR spectrum.

Element / ligand / fragment	Population[a] / %						
	H-2[b]	H-1[b]	H[b]	L[c]	L+1[c]	L+2[c]	L+3[c]
Fe 3d	78.7	71.7	65.7	1.4	12.9	6.3	2.1
tpy	2.1	14.7	6.6	62.2	59.8	7.1	7.6
bpy (pbpy)	8.6	1.1	5	7.7	1.5	59.4	52.5
ph (pbpy)	2.5	2.1	13.1	0.3	0.7	0.4	10.2
[a] Population of the given element via Loewdin reduced orbital population analysis. All given values are the sum over all AOs of a given element or fragment.							
[b] H : HOMO, [c] L : LUMO							

XYZ coordinates of all optimized structures:

Optimized structure of **3:**

59

C	5.04873391857648	2.90881959139104	-4.30698938987414
C	6.11165793721858	2.05310485324152	-4.05703785731485
C	6.37638753986199	1.62060597526765	-2.76576830958664
C	5.55423294314135	2.06569013456251	-1.74039936975324
N	4.53995155575388	2.88753012196515	-2.00566617263250
C	4.26538233180264	3.31640980298293	-3.23662562706555
C	3.09854604370143	4.21264589894118	-3.28206158452367
C	5.65776972209847	1.72889107217986	-0.31121747425080
C	6.63212162070624	0.89816469702652	0.21484310183638
C	6.63956788666347	0.64474492549012	1.57738126971416
C	5.67009158734726	1.23169848673194	2.36997752188489
C	4.72834646630151	2.05179370867612	1.77051935150979
N	4.71590081425521	2.29899028287865	0.46627775644637
C	1.51107374898522	5.62302784741817	-4.37610888844452
C	2.61860210795344	4.79258639307887	-4.44376420379448
N	2.51768985671111	4.43376436455490	-2.08605652948038
C	1.45721553620322	5.23021204324965	-2.02817834537639
C	0.91928423947501	5.84617513215441	-3.14621258378318
Fe	3.42648682850047	3.46403047061360	-0.56441880189273
C	2.63431401913328	5.14835137543843	1.53378968280025
N	2.31052411143759	4.03555153194229	0.87702286744759
C	1.24105756118405	3.30390500043642	1.18624584166730
C	0.41079295662243	3.69026326855477	2.22878643938646
C	0.72631019847266	4.84582592311539	2.92853074722173
C	1.84616933610325	5.58989788504347	2.58696215893623
C	1.08947475261901	2.12077080228129	0.32369167878132
C	3.85563766368586	5.78378698451933	1.01306410842467
N	2.04810593489426	1.98689166131232	-0.61423673752151
C	1.99421935341340	0.94808107241297	-1.43903920121182
C	0.99320132457794	-0.00745785197328	-1.37830368197635
C	0.00681464045214	0.12475768944686	-0.41795743910423
C	0.05696551216582	1.20692286159302	0.44644919358886
C	6.12908824158791	6.79652352055865	-0.10094629038933

C	5.53028737619034	5.63484279666717	-0.56007394155931
N	4.42367972287162	5.13541456825054	-0.02308400013848
C	4.39536343024871	6.95006953873171	1.52750167419909
C	5.55084531963741	7.46586493075097	0.96221248871001
H	6.73727317085112	1.72057764736325	-4.87395474784508
H	4.84690706876410	3.24142972941077	-5.31492169664719
H	7.20489650141915	0.95321106684960	-2.57746869844870
H	7.38084562966121	0.44968585551355	-0.42253008002359
H	7.39184852239768	-0.00100140815501	2.00886912034962
H	5.63643762771616	1.06264112091537	3.43652897290001
H	3.95877476451813	2.52417109538803	2.36569772795763
H	3.09647295731823	4.60496087471390	-5.39475461352339
H	1.11998080491300	6.08622193485259	-5.27142504923848
H	0.05446923124751	6.48581654897691	-3.04521730340792
H	1.01499352183180	5.38640641805557	-1.05367147207593
H	5.96060432320803	5.09072124597273	-1.38978530031311
H	7.02969857256080	7.16131913098172	-0.57324430486679
H	5.98907830047317	8.37569174260503	1.34855526055099
H	3.92710004246005	7.45738226817046	2.35895324536066
H	2.08705940414004	6.48876477325191	3.13587608983056
H	0.09544646007580	5.16843382013609	3.74538811160930
H	-0.46262636926466	3.11495989635580	2.49990820339273
H	-0.70358167420050	1.32950247603287	1.20435336324951
H	-0.79095008377397	-0.60083936023412	-0.33939277496416
H	0.99506326864025	-0.83451621889679	-2.07344650283500
H	2.77832881448821	0.86968898025268	-2.17972900389262

Optimized structure of **2**:

59

C	-3.46611127795230	0.02295240893246	2.65466417803603
C	-3.54683337654611	-1.23072056929200	2.06805770749277
C	-2.90391529377373	-1.43701544686603	0.85608411214570
N	-2.22116012104150	-0.44882707888722	0.27760001747021
C	-2.14279089461917	0.76767533827102	0.81710932017977
C	-2.76289467725263	1.04024519420368	2.02788805212421
C	-2.89240802668868	-2.66838095646685	0.05710234657080
C	-3.53575133970865	-3.83916459575320	0.42660388052777

C	-3.48016625485121	-4.93337104723917	-0.41834323901660
C	-2.78377210733400	-4.81998125340261	-1.60908622538935
C	-2.16620423032035	-3.61804566962395	-1.90783828500214
N	-2.21162348456606	-2.56627517152483	-1.09907080657092
C	-1.38279076174888	1.70401440000740	-0.01969104729382
N	-0.92341248724693	1.16805943821642	-1.16528623391734
C	-0.24774790641287	1.94210413832280	-2.00595955231725
C	0.01189590770076	3.27732186632204	-1.75086830384102
C	-0.45172429087026	3.83262197894586	-0.57087914731887
C	-1.16111349849053	3.03262294711889	0.30721981976305
N	-0.66213714306044	-1.04696355356477	-3.14801295599806
C	0.59444973144660	-1.48110268096433	-3.24887910696832
C	1.17460488969588	-1.70373301600302	-4.48545762369182
C	0.40146823520324	-1.45869355731285	-5.61595315799163
C	-0.89836151974957	-1.00873067931405	-5.49208222421214
C	-1.43156746908281	-0.80139363494114	-4.21682084324274
C	-2.76513485231464	-0.33507700673651	-3.85937568977690
C	-3.73521141577559	-0.01746526867074	-4.81113941915589
C	-4.97895788405946	0.41904593816163	-4.39803971546044
C	-5.24081155298557	0.53383325945675	-3.03720800286054
C	-4.26700545718864	0.21476327045372	-2.09941729021028
C	-2.99818125990160	-0.22965524135005	-2.46930329236614
C	1.23513417899573	-1.67642430162355	-1.93688523090944
N	0.45039838068293	-1.38865591584573	-0.88393150422584
C	0.93988555688867	-1.53361697416463	0.34140834965741
C	2.22973354374692	-1.96987005179162	0.58861325802782
C	3.04398836320798	-2.26756425533391	-0.49083298114465
C	2.53937867281019	-2.11858830673732	-1.77072918871564
Fe	-1.42629679440046	-0.75269014290155	-1.40557089460140
H	-3.96009139067870	0.21016547422581	3.59785498715730
H	-4.10654660115763	-2.02035746319583	2.54832640020207
H	-2.71122846037305	2.02175796194621	2.47665849814632
H	-4.07911141470793	-3.89852902086070	1.35892582433464
H	-3.97694341938523	-5.85608120277780	-0.15244681371976
H	-2.71901839925349	-5.64467001320198	-2.30391804027905
H	-1.62312629826953	-3.49509359681515	-2.83453602644506
H	0.09296899271918	1.48193433265281	-2.92298101587970

H	0.56378773442380	3.86450261457521	-2.47040530332293
H	-0.26946610965814	4.87265517155604	-0.33850977872452
H	-1.54032401762769	3.44330958715241	1.23219061572283
H	2.19115202147110	-2.05579040978836	-4.58293426997288
H	0.82286470054241	-1.62221996590752	-6.59864702304583
H	-1.49498501204473	-0.81981946205211	-6.37275725776805
H	-3.53231226695483	-0.10637630672708	-5.87223266800146
H	-5.73949642550313	0.66833348938425	-5.12534538704842
H	-6.21491724419055	0.87573304916170	-2.70915360902219
H	-4.52497320832202	0.32238527572942	-1.04981659246546
H	0.27563411073166	-1.29160237915295	1.16080297544997
H	2.58117351961393	-2.07140121788109	1.60515150388080
H	4.05821615336400	-2.61104227070333	-0.34038923684520
H	3.15700095282430	-2.34492744942096	-2.62803686214980

Spectroelectrochemistry

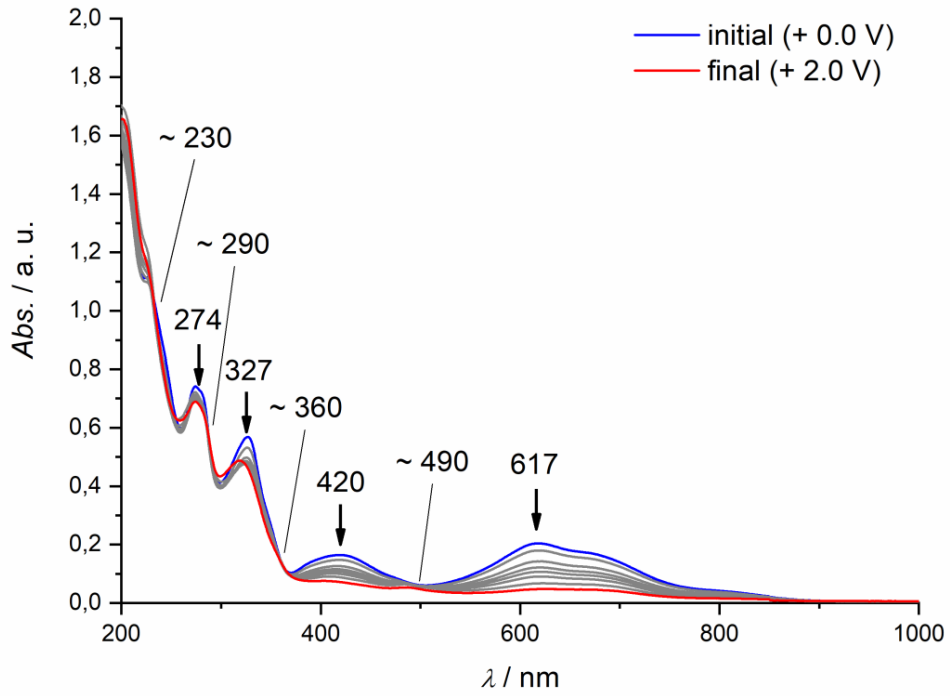

Figure S15: Changes in the UV/vis/NIR spectra during the oxidation of **2** to $\mathbf{2}^+$ (0.0 V → 2.0 V) in MeCN/[*n*-Bu_4N][PF_6] during OTTLE spectroelectrochemistry. Maxima and isosbestic points indicated.

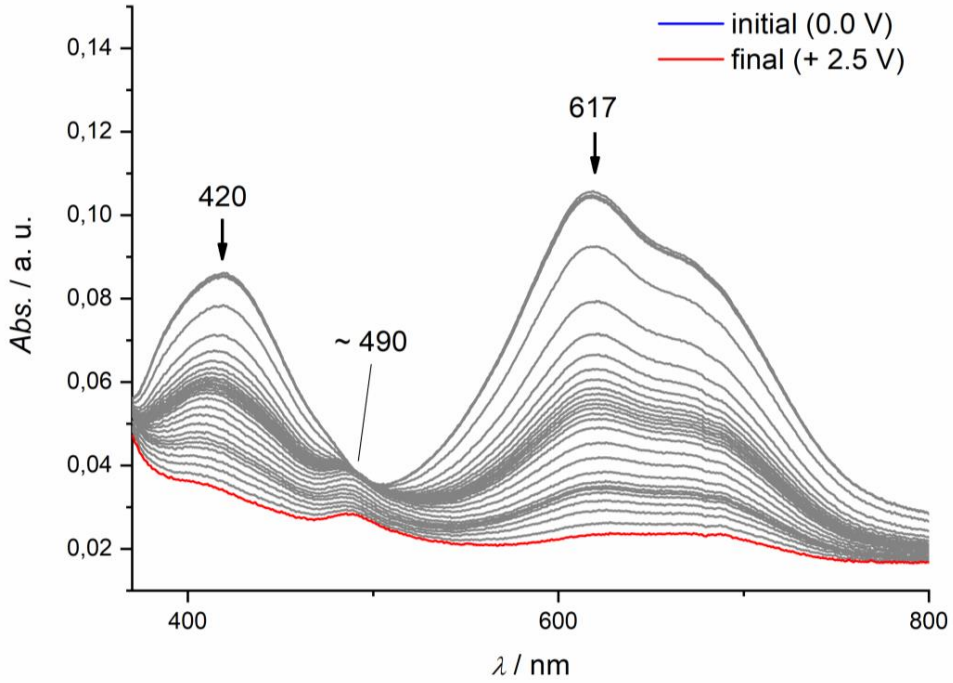

Figure S16: Changes in the UV/vis/NIR spectra during the oxidation of **2** to $\mathbf{2}^{+}$ (0.0 V → 2.5 V) in MeCN/[*n*-Bu_4N][PF_6] during OTTLE spectroelectrochemistry (zoom in the CT region). Maxima and isosbestic points indicated.

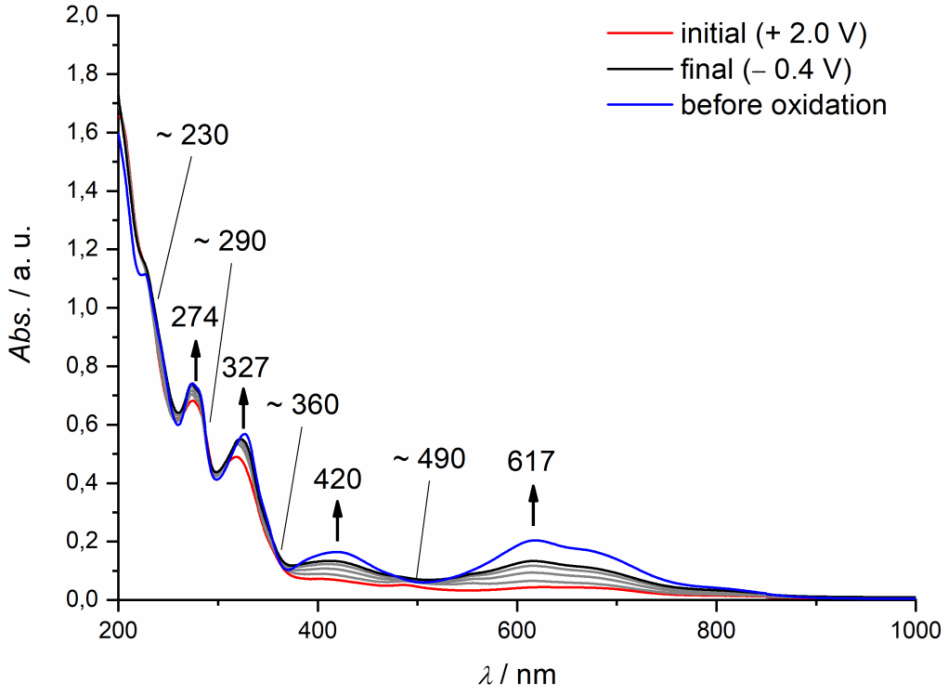

Figure S17: Changes in the UV/vis/NIR spectra during the re-reduction of $\mathbf{2}^{+}$ to **2** (2.0 V → –0.4 V) in MeCN/[*n*-Bu_4N][PF_6] during OTTLE spectroelectrochemistry. Maxima and isosbestic points indicated.

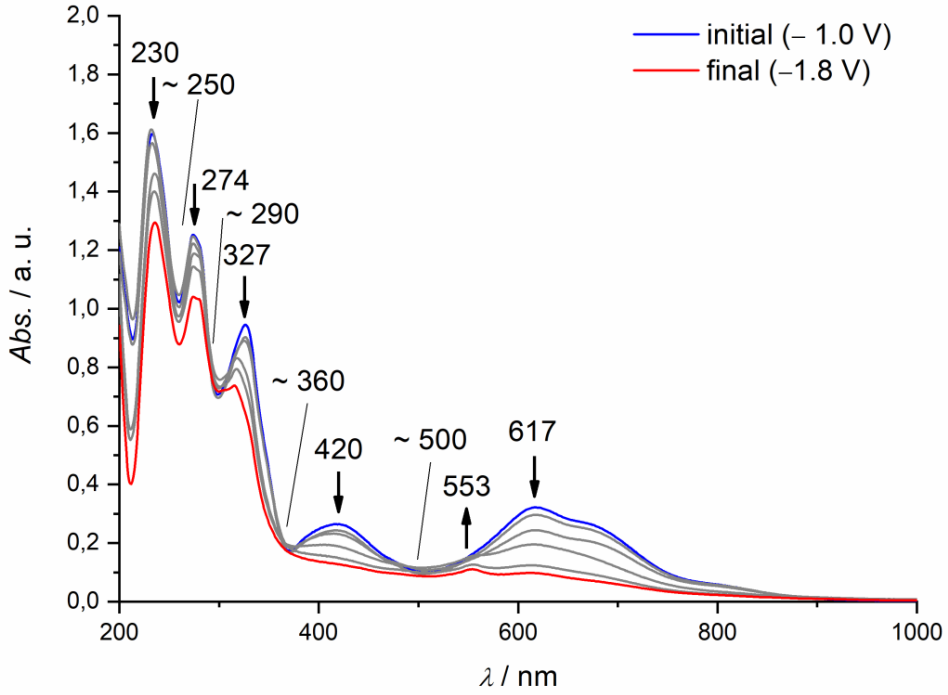

Figure S18: Changes in the UV/vis/NIR spectra during the reduction of **2** to **2**$^{-}$ (-1.0 V → -1.8 V) in MeCN/[*n*-Bu_4N][PF_6] during OTTLE spectroelectrochemistry. Maxima and isosbestic points indicated.

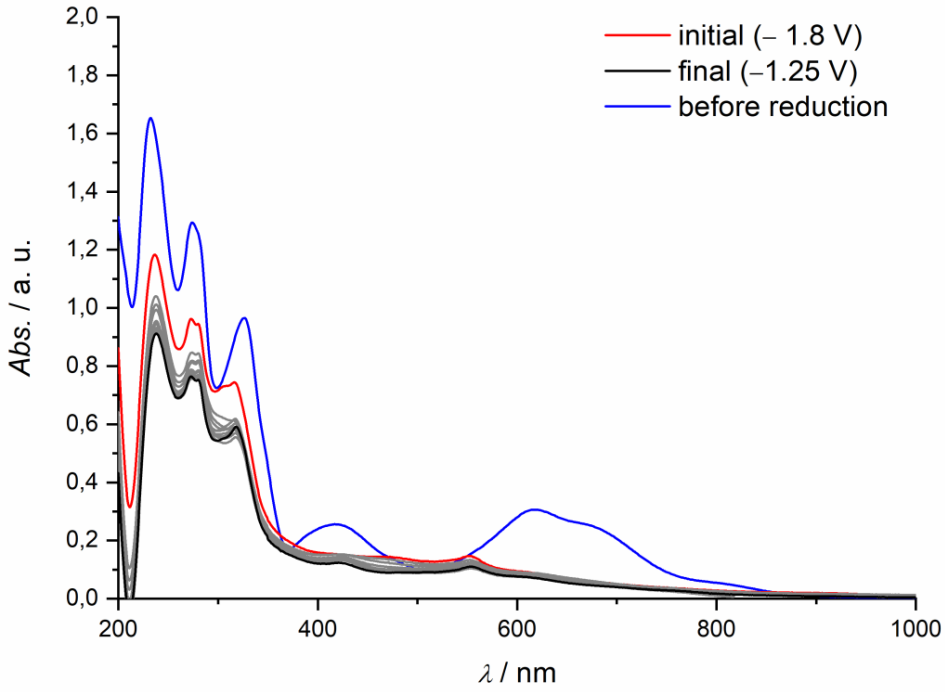

Figure S19: Changes in the UV/vis/NIR spectra during the attempted re-oxidation of $\mathbf{2}^-$ to **2** (-1.8 V → -1.25 V) in MeCN/[*n*-Bu_4N][PF_6] during OTTLE spectroelectrochemistry. Clearly, the reduction is irreversible on the timescale of the spectroelectrochemical experiment.

Ultrafast Pump-Probe Spectroscopy

Ultrafast pump-probe measurements were performed on **2** dissolved in acetonitrile applying excitation pulses centered at 615 nm. Figure S22 a) shows recorded transient spectra for the specified delay times between probe and pump. The data were analyzed by a global double exponential fit. The resulting decay associated amplitude spectra (DAS) are depicted in Figure S22 b) and labelled with the obtained decay times.

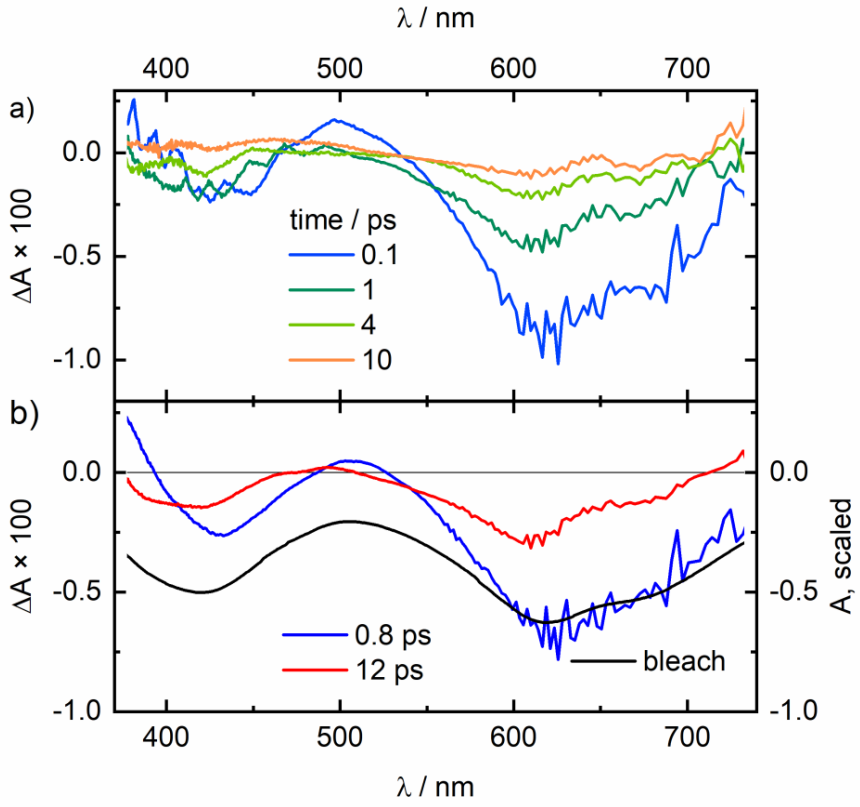

Figure S20: (a) Transient absorption spectra of **2** in acetonitrile at the specified delay times after optical excitation at 615 nm. (b) DAS of two exponential components with time constants of 0.8 ps and 12 ps obtained by a double exponential global fit (left scale). The DAS are compared to the scaled bleach (right scale) of complex **2**.

The graph shows for comparison also the scaled bleach, i.e. the inverted ground state absorption spectrum. Both DAS are similar to the bleach with dominating negative signals which means that most of the observed absorption change is due depopulation of the electronic ground state. The DAS of the shorter time constant exhibits at 500 nm and below 400 nm positive contributions demonstrating that also excited state absorption (ESA) is present. The observation of two steps in the excited state dynamics points to the following relaxation scenario. The ^{1}MLCT singlet state excited. However, iron(II) complexes exhibit typically an extremely fast intersystem crossing[16,32] and the ^{3}MLCT triplet state is

most probably populated within the time resolution of our pump-probe measurements. This notion is supported by the absence of any fluorescence. The short time constant of 0.8 ps reflects the depopulation of the ^{3}MLCT state into the ^{3}MC state. The latter decays with a lifetime of 12 ps back to the electronic ground state resulting thereafter in a completely recovered ground state absorption.

To check for solvent effects, additional transient absorption measurements were performed with **2** dissolved in dichloromethane and methanol. There, a very similar behavior as for MeCN was observed, although with somewhat different time constants. The results are shown in Figure S23. Since the solubility of **2** is lower in methanol, the measurement was in this case performed with a lower concentration. The concentrations read as follows:

2 in acetonitrile: c = 0.62 mol/L; in dichloromethane: c = 0.78 mol/L; in methanol: c = 0.18 mol/L

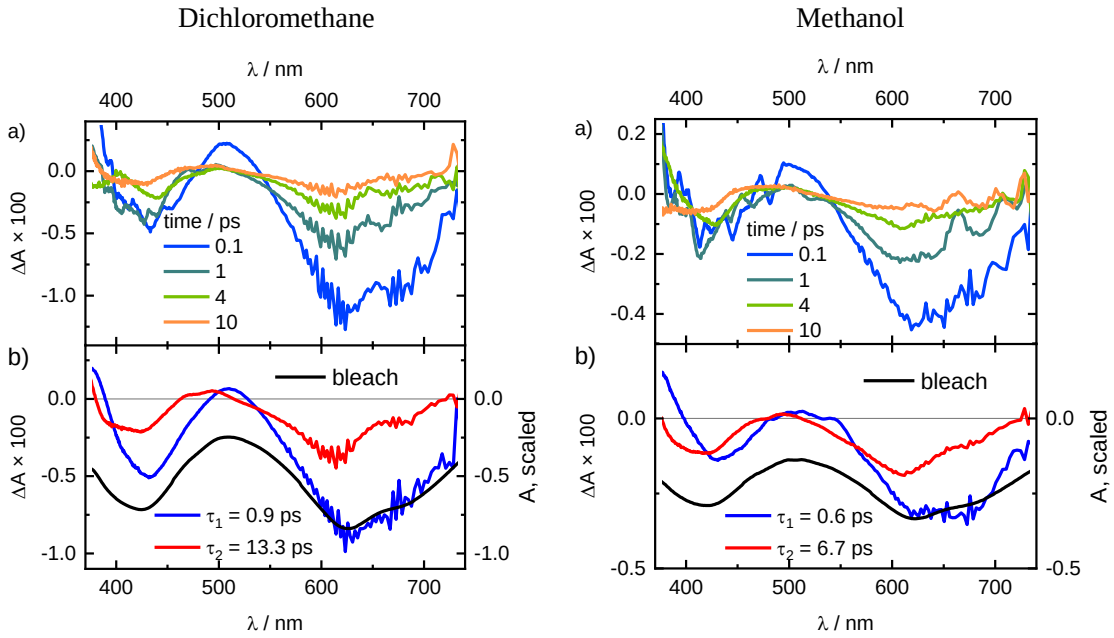

Figure S21: Transient absorption spectra of **2** in dichloromethane (left) and methanol (right) at different times after excitation with pulses at 615 nm (top, part a)) and the corresponding decay associated amplitude spectra of the exponential decay components labelled with the respective time constants (bottom, part b)). While the decay times in acetonitrile (*cf.* Figure S22) and dichloromethane are quite similar, they are significantly shorter in methanol.

In general, the transient absorption measurements were carried out with magic angle (55°) between the polarizations of the pump and probe pulses to avoid effects due to rotational diffusion of the molecules. In acetonitrile the sample was in addition also investigated with parallel and perpendicular polarizations. But no significant differences to the magic angle configuration were observed, see Figure S24.

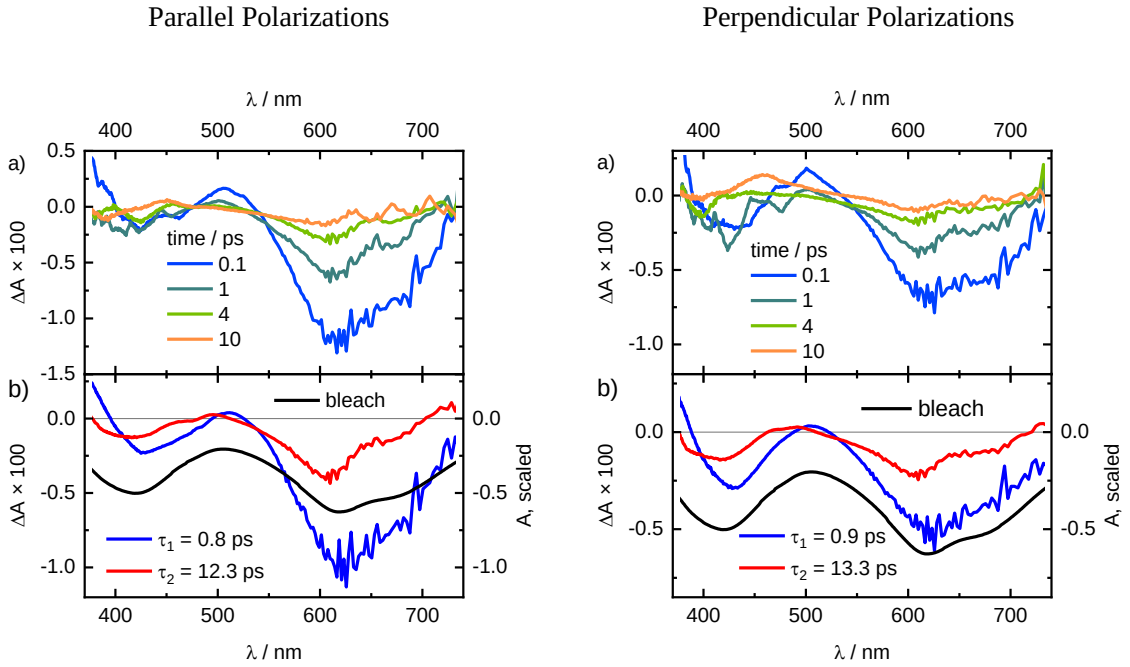

Figure S22: fs-Transient absorption measurements of **2** in MeCN with different polarizations: parallel (left) and perpendicular (right). Top, part a) Transient spectra at different times after excitation with pulses at 615 nm. Bottom, part b) DASs of the decay components labelled with the respective time constants.

NMR Spectra

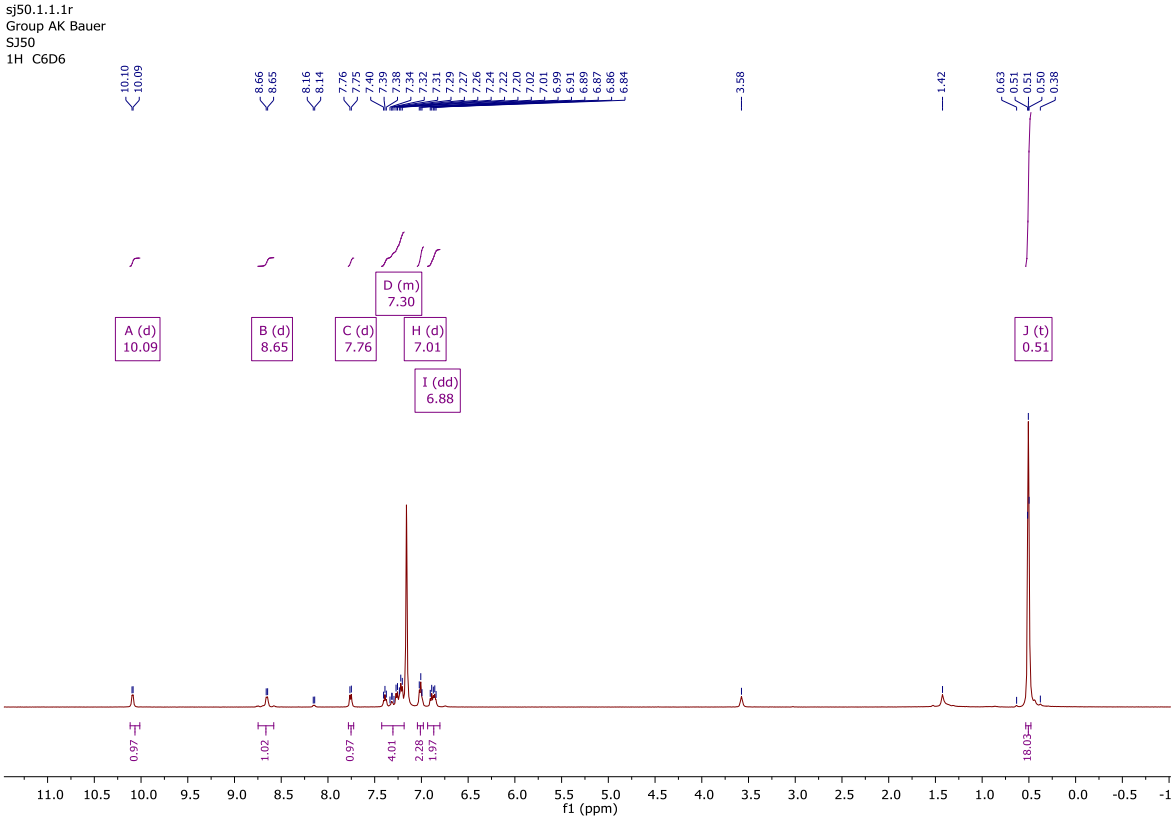

Figure S23: ^{1}H-NMR spectrum of [Fe(pbpy)$(PMe_3)_2$Br] **1** in C_6D_6

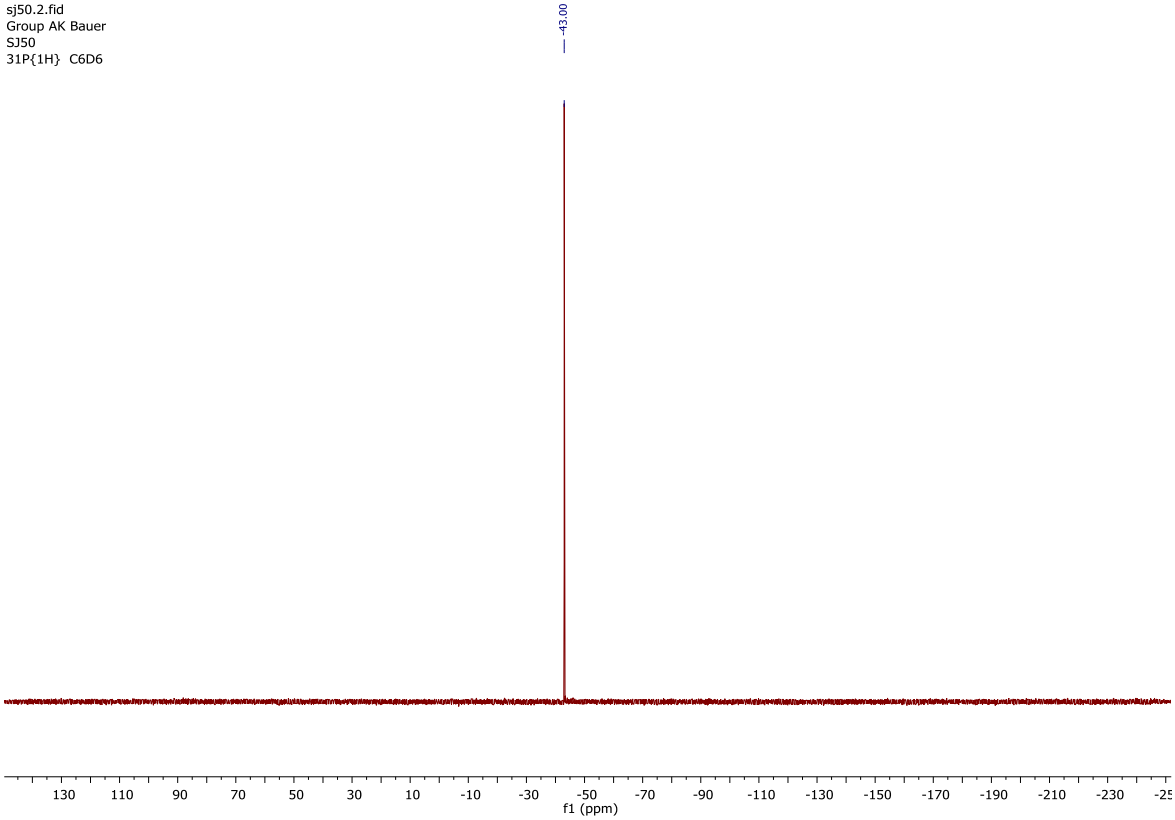

Figure S24: ^{31}P-NMR spectrum of [Fe(pbpy)(PMe$_3$)$_2$Br] **1** in C_6D_6

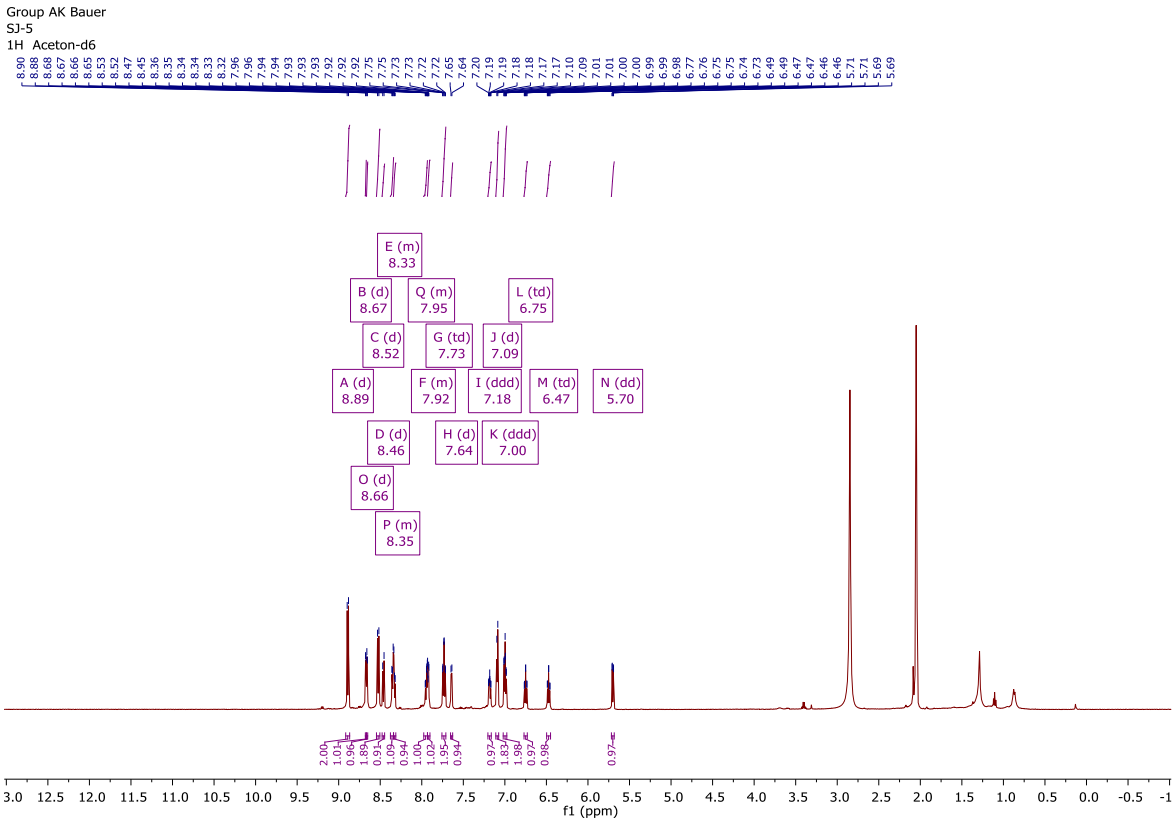

Figure S25: ^{1}H-NMR spectrum of [Fe(pbpy)(tpy)]PF$_6$ **2** in Acetone-d$_6$

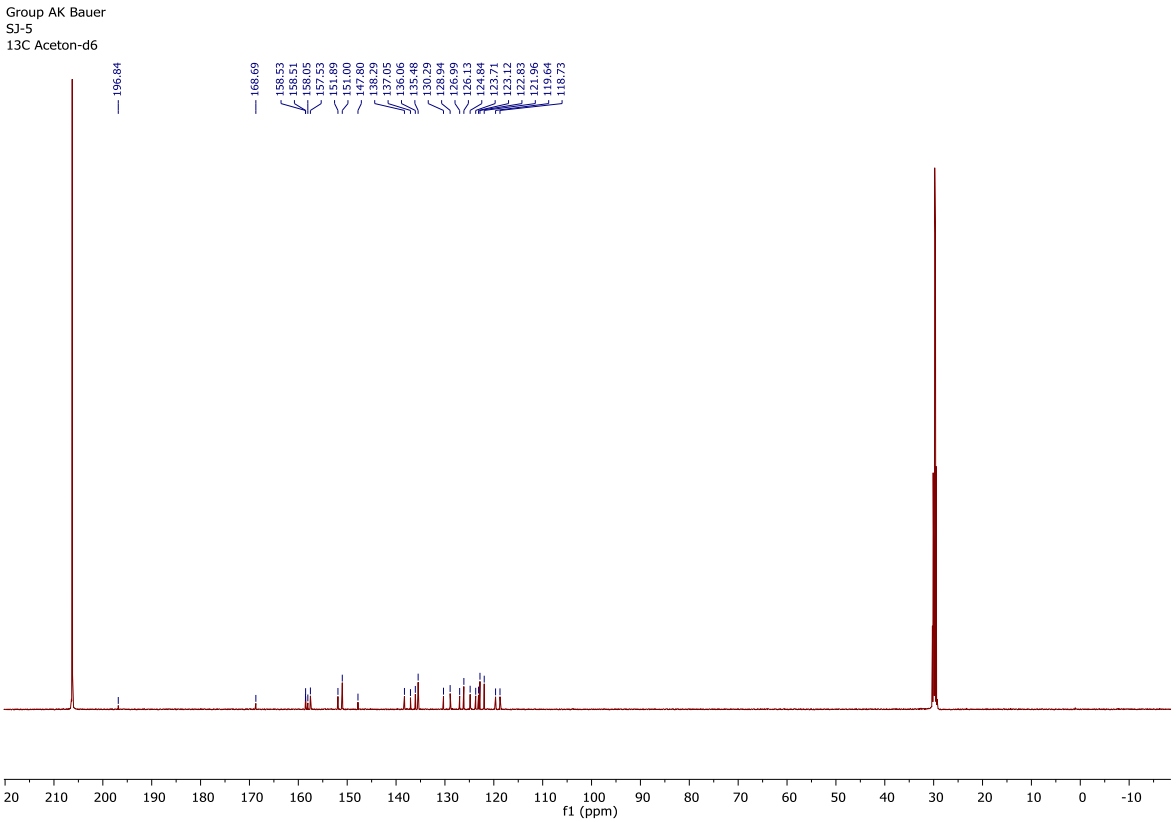

Figure S26: ^{13}C-NMR spectrum of [Fe(pbpy)(tpy)]PF_6 **2** in Acetone-d_6

References

[1] a) R. S. Nicholson, I. Shain, *Anal. Chem.* **1964**, *36*, 706; b) J. Heinze, *Angew. Chem.* **1984**, *96*, 823.

[2] a) J. E. B. Randles, *Trans. Faraday Soc.* **1948**, *44*, 327; b) F. Scholz, A. M. Bond, R. G. Compton, D. A. Fiedler, G. Inzelt, H. Kahlert, Š. Komorsky-Lovrić, H. Lohse, M. Lovrić, F. Marken et al., *Electroanalytical Methods*, Springer Berlin Heidelberg, Berlin, Heidelberg, **2010**.

[3] G. M. Sheldrick, *Acta Crystallogr., Sect. A: Found. Crystallogr.* **2008**, *64*, 112.

[4] a) P. Bhattacharya, J. A. Krause, H. Guan, *Organometallics* **2011**, *30*, 4720; b) D. L. Jameson, L. E. Guise, *Tetrahedron Lett.* **1991**, *32*, 1999.

[5] D. Kratzert, J. J. Holstein, I. Krossing, *Journal of applied crystallography* **2015**, *48*, 933.

[6] a) A. L. Spek, *Acta crystallographica. Section D, Biological crystallography* **2009**, *65*, 148; b) A. L. Spek, *Acta crystallographica. Section C, Structural chemistry* **2015**, *71*, 9.

[7] F. Neese, *WIREs Comput Mol Sci* **2017**, *2*, e1327.

[8] S. Grimme, J. G. Brandenburg, C. Bannwarth, A. Hansen, *The Journal of chemical physics* **2015**, *143*, 54107.

[9] a) L. Goerigk, S. Grimme, *Physical chemistry chemical physics : PCCP* **2011**, *13*, 6670; b) S. Grimme, S. Ehrlich, L. Goerigk, *Journal of computational chemistry* **2011**, *32*, 1456; c) S. Grimme, J. Antony, S. Ehrlich, H. Krieg, *The Journal of chemical physics* **2010**, *132*, 154104.

[10] a) S. DeBeer George, T. Petrenko, F. Neese, *J. Phys. Chem. A* **2008**, *112*, 12936; b) S. DeBeer George, T. Petrenko, F. Neese, *Inorganica Chimica Acta* **2008**, *361*, 965.

[11] N. Lee, T. Petrenko, U. Bergmann, F. Neese, S. DeBeer, *J. Am. Chem. Soc.* **2010**, *132*, 9715.

[12] J. Tao, J. P. Perdew, V. N. Staroverov, G. E. Scuseria, *Physical review letters* **2003**, *91*, 146401.

[13] L. Burkhardt, M. Holzwarth, B. Plietker, M. Bauer, *Inorg. Chem.* **2017**, *56*, 13300.

[14] P. Zimmer, L. Burkhardt, R. Schepper, K. Zheng, D. Gosztola, A. Neuba, U. Flörke, C. Wölper, R. Schoch, W. Gawelda et al., *Eur. J. Inorg. Chem.* **2018**, *2018*, 5203.

[15] N. J. Vollmers, P. Müller, A. Hoffmann, S. Herres-Pawlis, M. Rohrmüller, W. G. Schmidt, U. Gerstmann, M. Bauer, *Inorganic chemistry* **2016**, *55*, 11694.

[16] P. Zimmer, L. Burkhardt, A. Friedrich, J. Steube, A. Neuba, R. Schepper, P. Müller, U. Flörke, M. Huber, S. Lochbrunner et al., *Inorg. Chem.* **2018**, *57*, 360.

[17] F. Weigend, R. Ahlrichs, *Phys. Chem. Chem. Phys.* **2005**, *7*, 3297.

[18] F. Weigend, *Phys. Chem. Chem. Phys.* **2006**, *8*, 1057.

[19] F. Neese, *Inorganica Chimica Acta* **2002**, *337*, 181.

[20] I. M. Dixon, S. Khan, F. Alary, M. Boggio-Pasqua, J.-L. Heully, *Dalton Trans.* **2014**, *43*, 15898.

[21] G. Knizia, *iboview*.

[22] M. U. Delgado-Jaime, S. DeBeer, *Journal of computational chemistry* **2012**, *33*, 2180.

[23] A. V. Marenich, C. J. Cramer, D. G. Truhlar, *J. Phys. Chem. B* **2009**, *113*, 6378.

[24] a) G. Vankó, T. Neisius, G. Molnar, F. Renz, S. Karpati, A. Shukla, F. M. F. de Groot, *J. Phys. Chem. B* **2006**, *110*, 11647; b) U. Bergmann, P. Glatzel, *Photosynthesis research* **2009**, *102*, 255.

[25] C. J. Pollock, M. U. Delgado-Jaime, M. Atanasov, F. Neese, S. DeBeer, *J. Am. Chem. Soc.* **2014**, *136*, 9453.

[26] S. D. Gamblin, D. S. Urch, *Journal of Electron Spectroscopy and Related Phenomena* **2001**, *113*, 179.

[27] P. Glatzel, U. Bergmann, *Coord. Chem. Rev.* **2005**, *249*, 65.

[28] P. Zimmer, P. Müller, L. Burkhardt, R. Schepper, A. Neuba, J. Steube, F. Dietrich, U. Flörke, S. Mangold, M. Gerhards et al., *Eur. J. Inorg. Chem.* **2017**, *2017*, 1504.

[29] a) G. Smolentsev, A. V. Soldatov, J. Messinger, K. Merz, T. Weyhermüller, U. Bergmann, Y. Pushkar, J. Yano, V. K. Yachandra, P. Glatzel, *J. Am. Chem. Soc.* **2009**, *131*, 13161; b) C. J. Pollock, S. DeBeer, *Acc. Chem. Res.* **2015**, *48*, 2967; c) C. J. Pollock, S. DeBeer, *J. Am. Chem. Soc.* **2011**, *133*, 5594; d) M. U. Delgado-Jaime, S. DeBeer, M. Bauer, *Chem. Eur. J.* **2013**, *19*, 15888.

[30] a) M. Bauer, *Phys. Chem. Chem. Phys.* **2014**, *16*, 13827; b) A. J. Atkins, M. Bauer, C. R. Jacob, *Phys. Chem. Chem. Phys.* **2013**, *15*, 8095; c) T. E. Westre, P. Kennepohl, J. G. DeWitt, B. Hedman, K. O. Hodgson, E. I. Solomon, *J. Am. Chem. Soc.* **1997**, *119*, 6297.

[31] a) Y. Liu, T. Harlang, S. E. Canton, P. Chábera, K. Suárez-Alcántara, A. Fleckhaus, D. A. Vithanage, E. Göransson, A. Corani, R. Lomoth et al., *Chem. Comm.* **2013**, *49*, 6412; b) Y. Liu, P. Persson, V. Sundstrom, K. Wärnmark, *Acc. Chem. Res.* **2016**, *49*, 1477; c) T. Duchanois, T. Etienne, C. Cebrián, L. Liu, A. Monari, M. Beley, X. Assfeld, S. Haacke, P. C. Gros, *Eur. J. Inorg. Chem.* **2015**, *2015*, 2469; d) L. Liu, T. Duchanois, T. Etienne, A. Monari, M. Beley, X. Assfeld, S. Haacke, P. C. Gros, *Phys. Chem. Chem. Phys.* **2016**, *18*, 12550.

C.2. Supplementary Information of "Janus-type emission from a cyclometalated iron(III) complex"

Supplementary Information for

Janus-type Emission from a Cyclometalated Iron(III) Complex

Jakob Steube[1], Ayla Kruse[2], Olga S. Bokareva[3,4], Thomas Reuter[5], Serhiy Demeshko[6], Roland Schoch[1], Miguel A. Argüello Cordero[2], Athul Krishna[1], Stephan Hohloch[7], Franc Meyer[6], Katja Heinze[5], Oliver Kühn[2], Stefan Lochbrunner[2], Matthias Bauer[1*]

1 Institute of Inorganic Chemistry and Center for Sustainable Systems Design (CSSD), Paderborn University, Warburger Straße 100, 33098 Paderborn, Germany

2 Institute of Physics and Department for Life, Light and Matter, University of Rostock, 18051 Rostock, Germany

3 Institute of Physics, University of Rostock, 18051 Rostock, Germany

4 Institute of Physics, University of Kassel, Heinrich-Plett-Str. 40, 34132, Kassel, Germany

5 Department of Chemistry, Johannes Gutenberg University, Duesbergweg 10–14, 55128 Mainz, Germany

6 Institute of Inorganic Chemistry, University of Göttingen, Tammannstrasse 4, 37077 Göttingen, Germany

7 Institute of General, Inorganic and Theoretical Chemistry, University of Innsbruck, Innrain 80-82, 6020 Innsbruck, Austria

Content

Synthesis, NMR and mass spectrometry

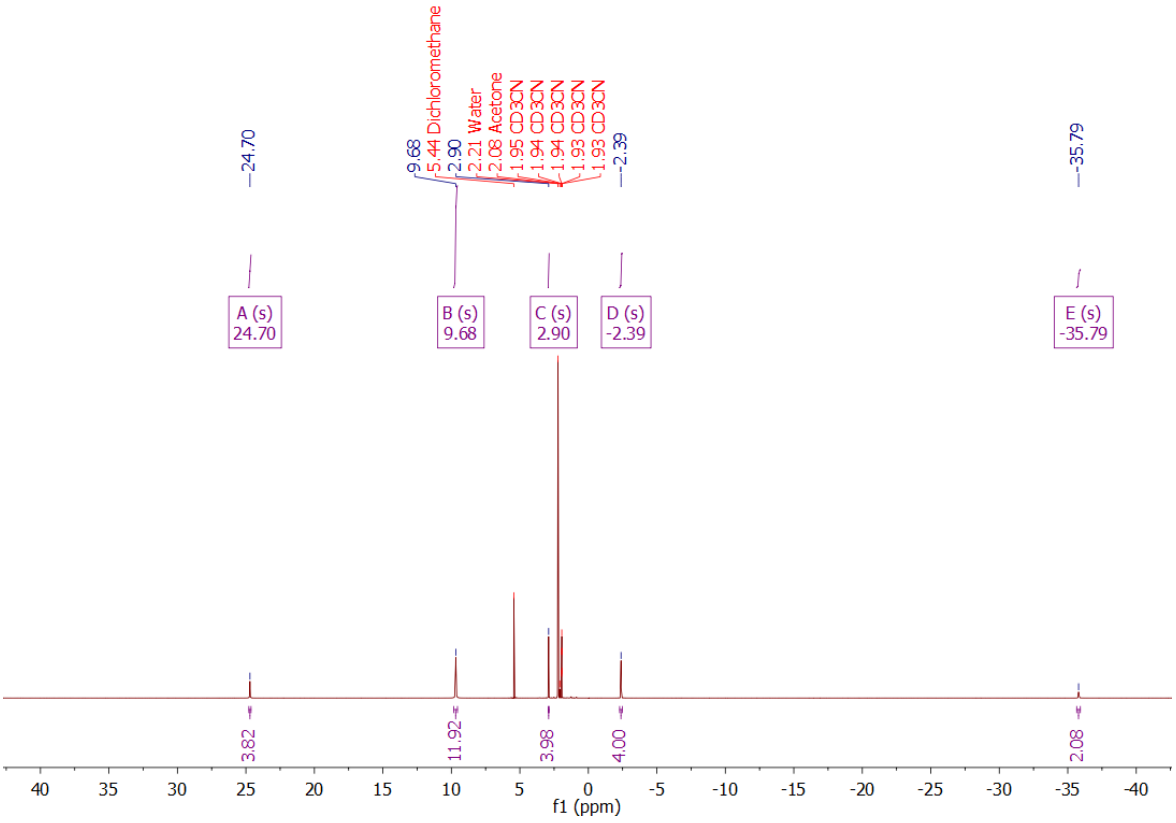

Supplementary Figure 1| ^{1}H NMR characterization of [Fe(ImP)$_2$][PF$_6$]. The spectrum was recorded in deuterated acetonitrile on a scan range from -50 – 50 ppm. The spectrum shows the expected number of resonances and integrals of **1** (26 H nuclei in total) and resonances of the residual solvents.

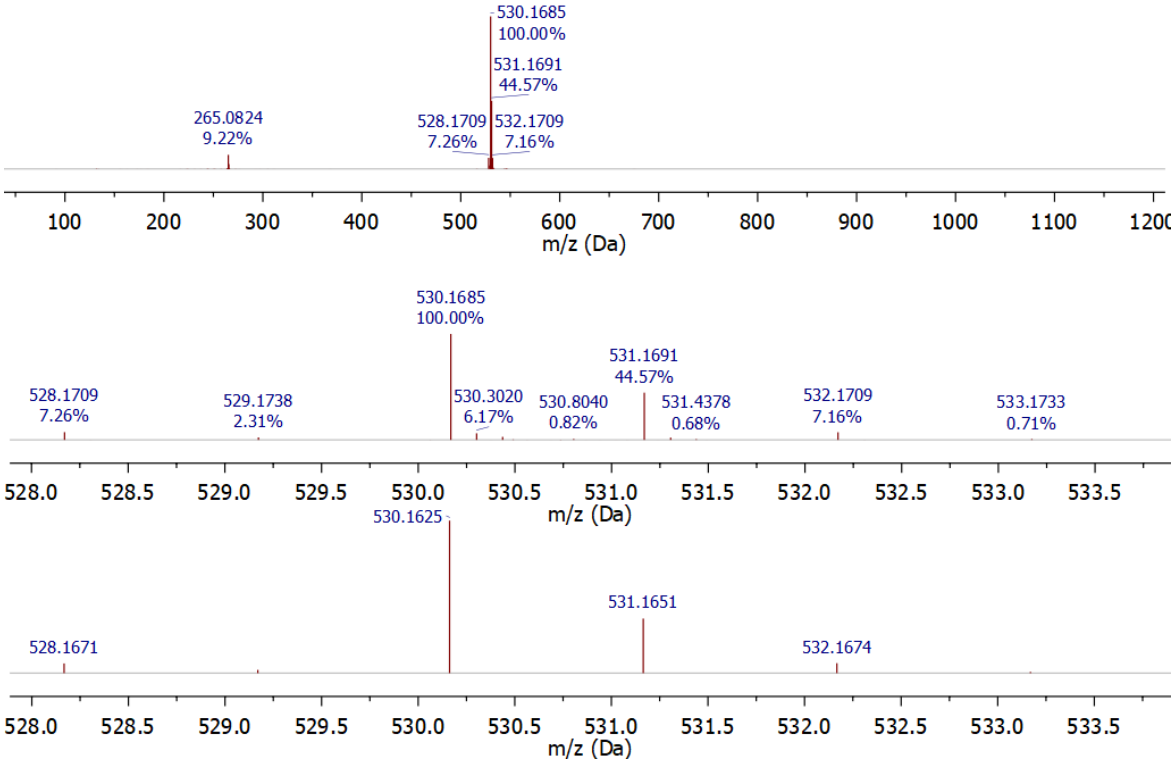

Supplementary Figure 2| ESI mass spectrometry measurement of $[Fe(ImP)_2][PF_6]$. Top: Full spectrum over the whole measurement range, showing $[M\text{-}PF_6]^+$ at 530.1685 m/z and the ESI-oxidized $[M\text{-}PF_6]^{2+}$ species at 265.0824 m/z. Middle: Enlargement on the $[M\text{-}PF_6]^+$ range. Bottom: Simulation of $[M\text{-}PF_6]^+$ shows good agreement to the experimental isotopic pattern.

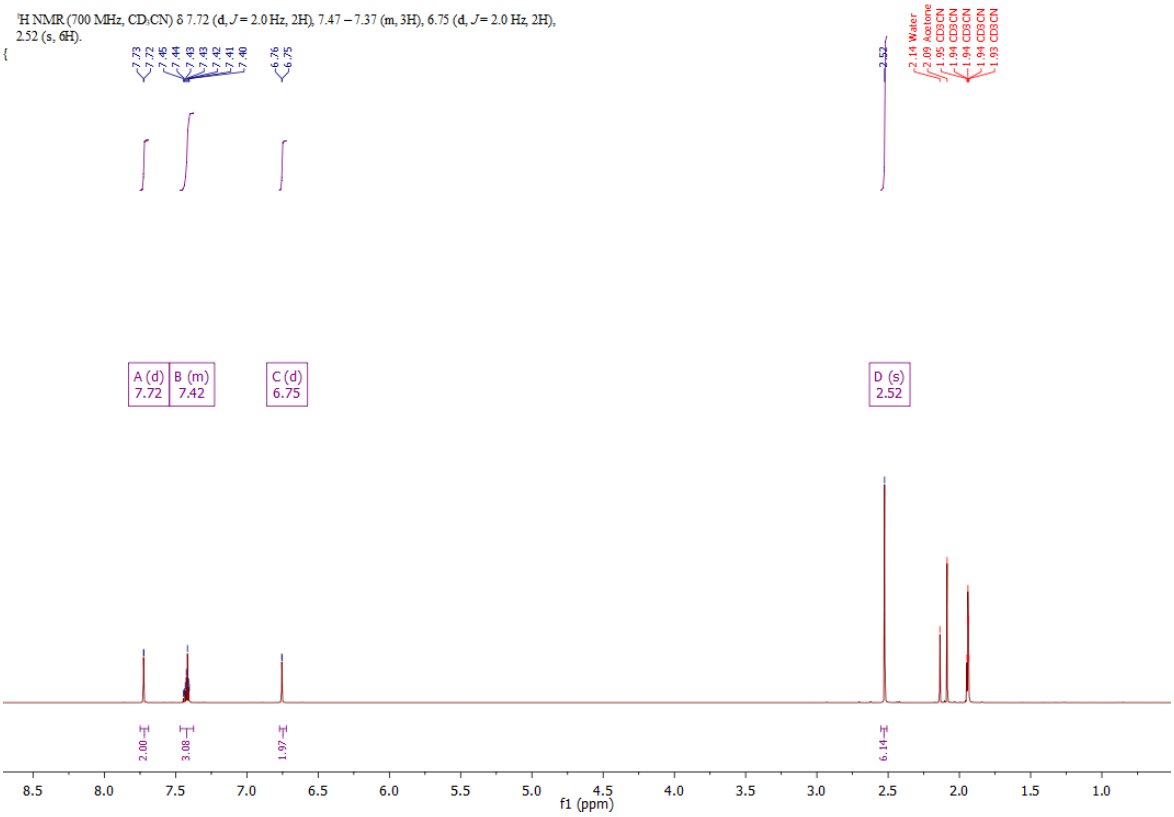

Supplementary Figure 3| ^{1}H NMR characterization of [Co(ImP)$_2$][PF$_6$]. The spectrum was recorded in deuterated acetonitrile. The spectrum shows the expected number of resonances and integrals (13 H nuclei in total for the half complex of [Co(ImP)$_2$][PF$_6$]).

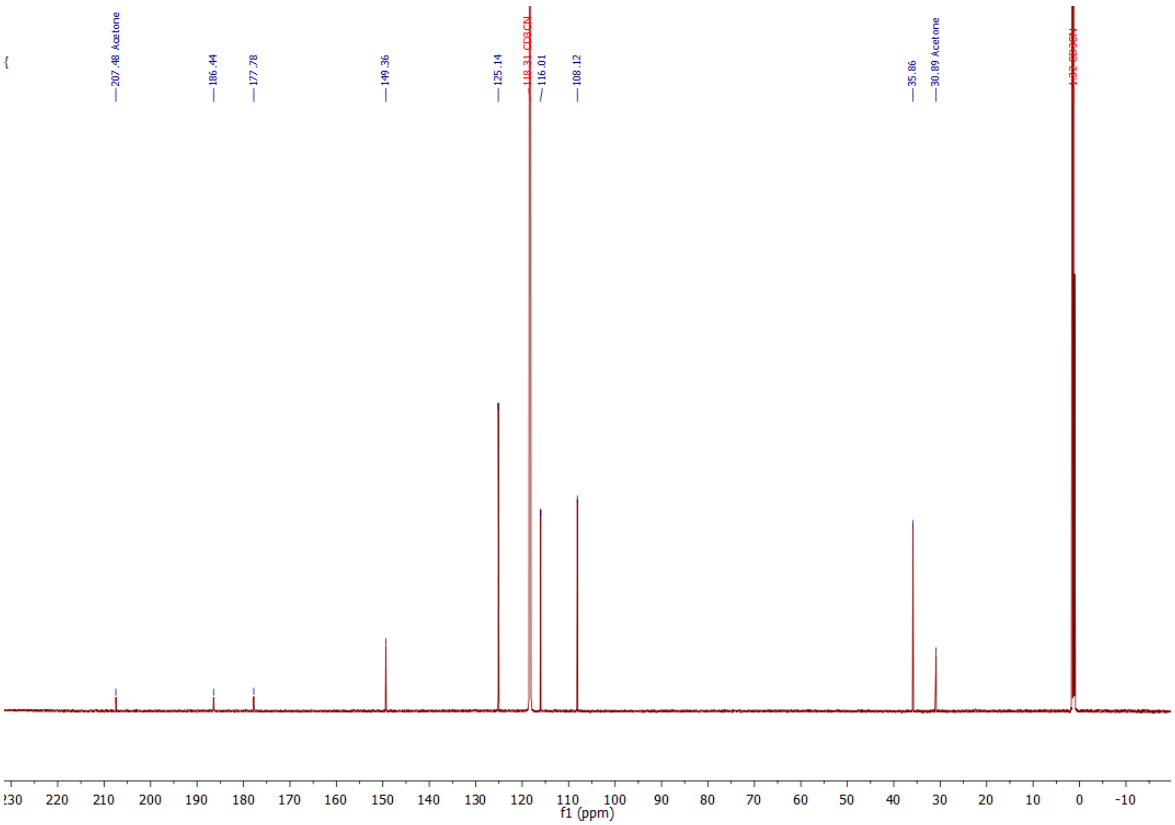

Supplementary Figure 4| ^{13}C NMR characterization of [Co(ImP)$_2$][PF$_6$]. The spectrum was recorded in deuterated acetonitrile. The spectrum shows the expected number of resonances and resonances of the residual solvent.

X-ray diffraction analysis and crystallographic data deposition

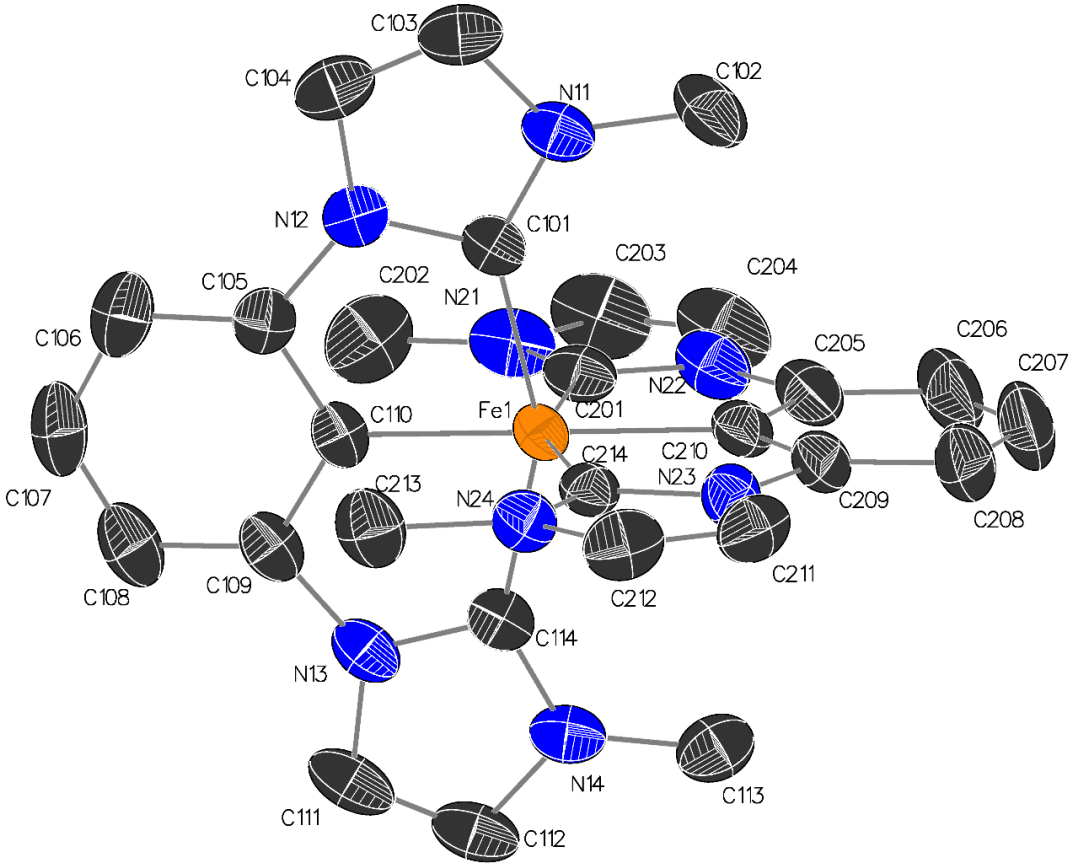

Supplementary Figure 5| Ortep plot of [Fe(ImP)$_2$][PF$_6$]. Structure of the cation of **1** as determined by X-ray diffraction, hydrogen atoms and counter ion are omitted for clarity. Crystallographic data have been deposited at the Cambridge Crystallographic Data Centre, assigned to the deposition number CCDC 2002774. Copies are available free of charge via www.ccdc.cam.ac.uk.

Mößbauer spectroscopy and magnetic susceptibility measurements

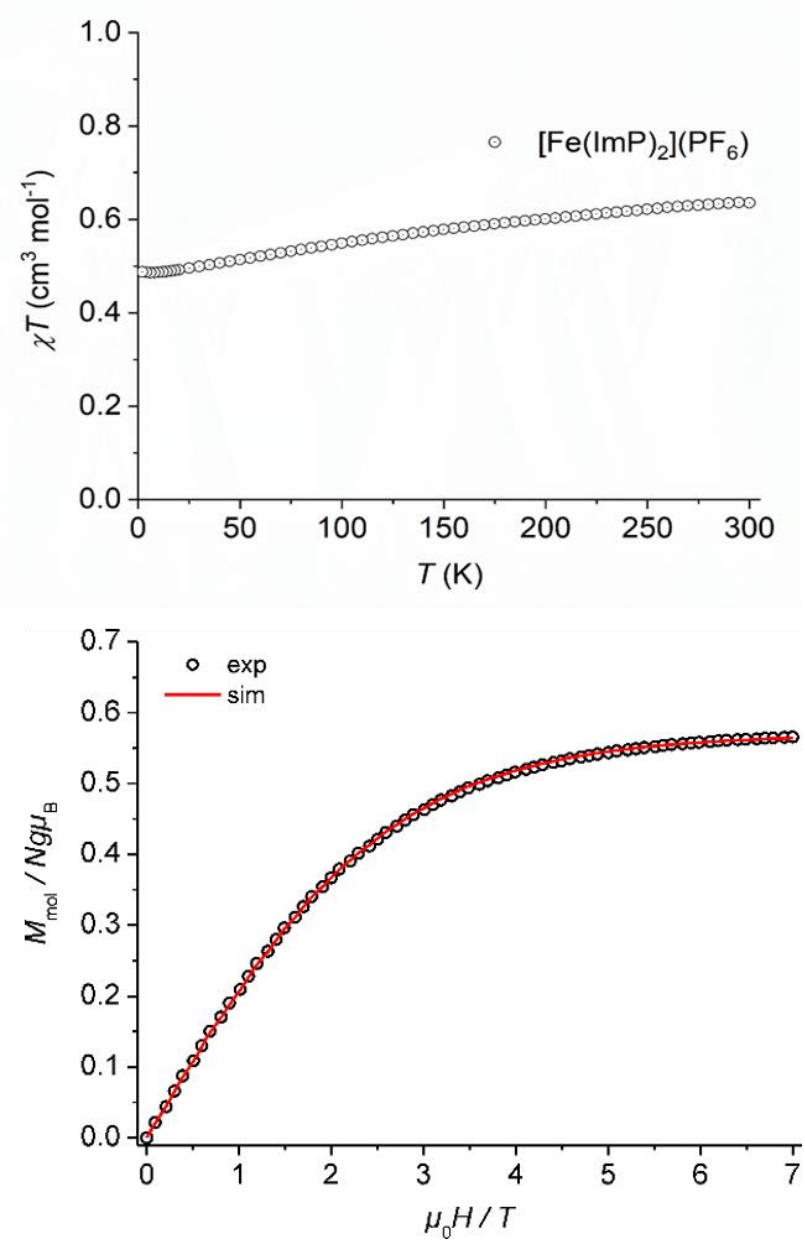

Supplementary Figure 6| Magnetic characterization of [Fe(ImP)$_2$][PF$_6$]. Top: Magnetic susceptibility data as the temperature dependence of $\chi_M T$ in the range of 2 – 300 K at 0.5 T, showing the typical behavior of metal complexes with $(t_{2g})^5$ electron configuration ($^2T_2$) with significantly higher $\chi_M T$ values than expected for a conventional S = ½ spin system (spin-only) due to spin-orbit coupling. Bottom: Plot of the magnetization vs. field at 2 K. The simulation was performed for S = ½ with g = 2.28 (fixed).

Cyclic and square wave voltammetry

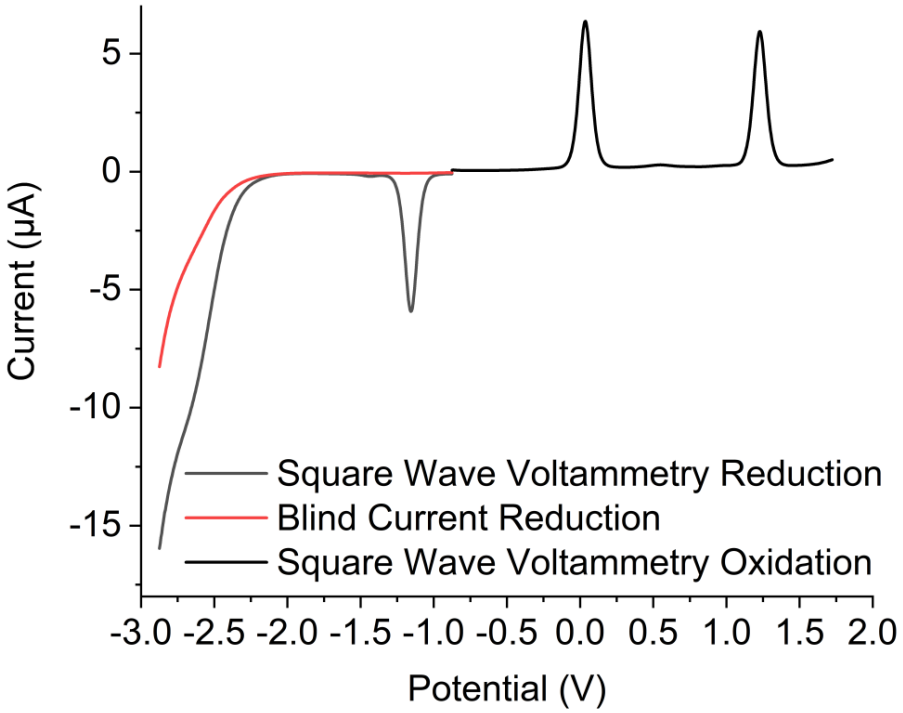

Supplementary Figure 7| Square wave voltammetry of [Fe(ImP)$_2$][PF$_6$]. Square wave voltammogram of **1** in CH_3CN/[*n*Bu_4N][PF_6] of the reduction up to -2.85 V vs $FcH^{0/+}$ compared with the blind current during that process at a scan rate of 100 mV s^{-1}. This indicates that the ligand reduction is observed at around -2.7 V.

Absorption spectroscopy (steady-state)

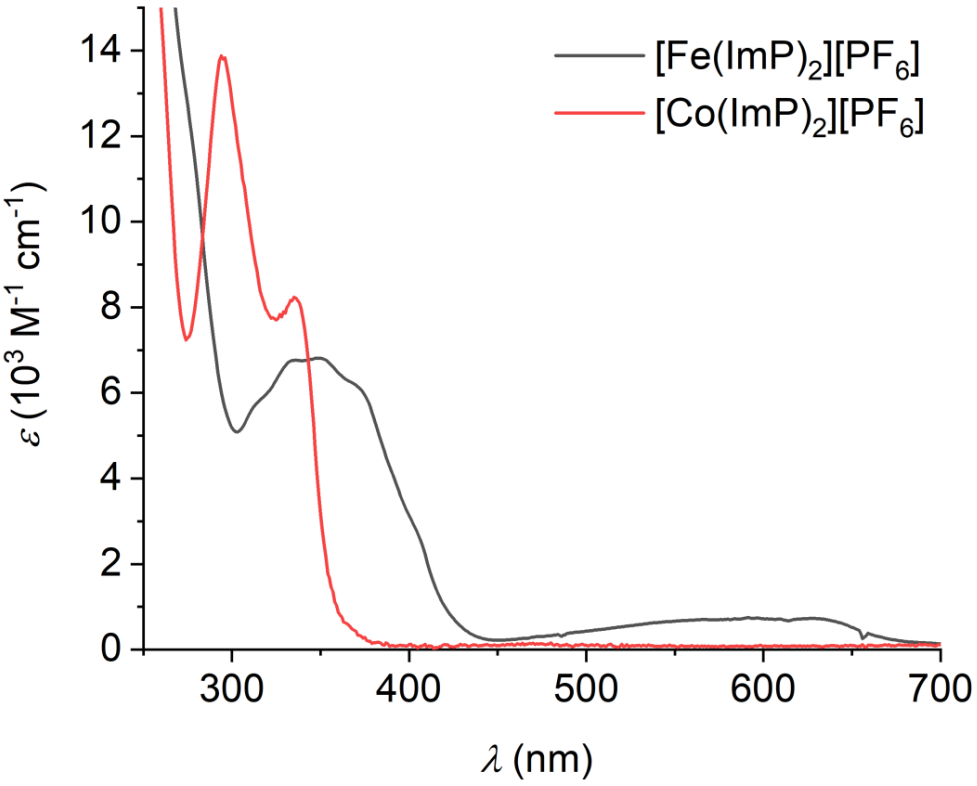

Supplementary Figure 8| Absorption spectra of $[Fe(ImP)_2][PF_6]$ and $[Fe(ImP)_2][PF_6]$. Absorption spectra in the region between 250 nm and 700 nm.

Theoretical Calculations

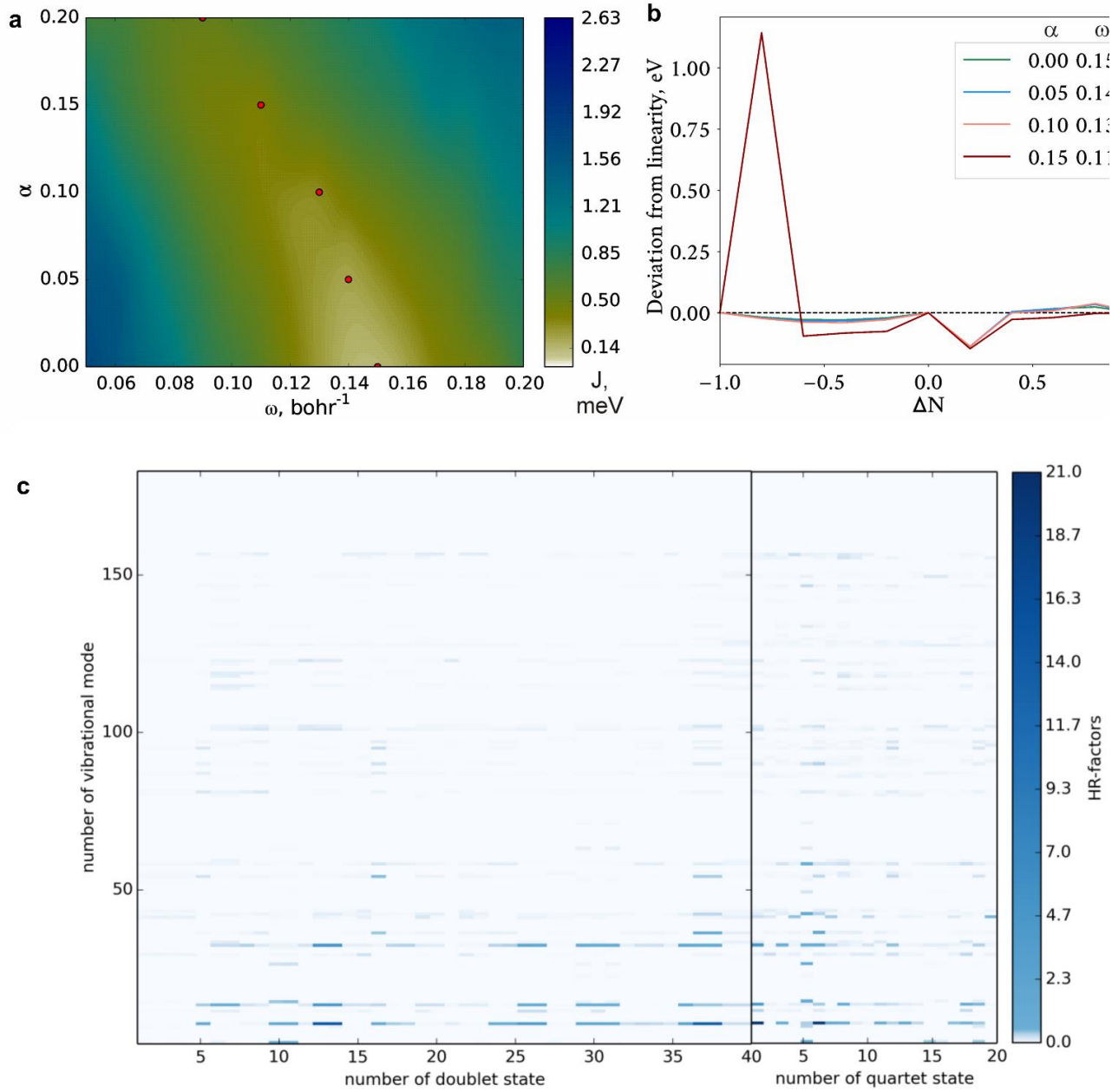

Supplementary Figure 9| Theoretical investigations of $[Fe(ImP)_2][PF_6]$. a,b, Tuning of the LC-BLYP functional for DFT calculations. **a,** functional $J^*(\alpha,\omega) = \sqrt{J_0^2 + J_1^2}$, $J_0 = |\varepsilon_{HOMO}(N) + IP(N)|$ and $J_1 = |\varepsilon_{HOMO}(N+1) + EA(N)|$ showing the deviation from Koopman's theorem for ionization potential (IP) and electron affinity (EA) for the system with N electrons. The red points denote the minima of the J*-functional at constant α values. **b,** the deviation from linearity of energy dependence between integer number of electrons. As a result of tuning, the parameters α=0.0 and ω=0.15 Bohr^{-1} were found. **c,** Huang-Rhys factors for the lowest 40 doublet and 20

quartet states as calculated using TDDFT. The mode shown in Fig. 4 of the main text corresponds to the mode with index 7 ($\omega/(2\pi c)$=126 cm^{-1}). It has the largest Huang-Rhys factor among the lowest 15 doublet states.

Supplementary Table 1: Main orbital densities in **1**$^{-}$, **1,** and **1**$^{+}$.

Orb. Nr.	**1**$^{-}$ Fe^{II} (singlet)		**1** Fe^{III} (doublet)				**1**$^{+}$ Fe^{IV} (triplet)			
	Orbital (↑↓)		Orbital (α, ↑)		Orbital (β, ↓)		Orbital (α, ↑)		Orbital (β, ↓)	
136	HOMO-2	Fe (t_{2g})	SOMO-2	Fe (t_{2g})	SOMO-1	Fe (t_{2g})	SOMO-2	Ligand	SOMO	Fe (t_{2g})
137	HOMO-1	Fe (t_{2g})	SOMO-1	Fe (t_{2g})	SOMO	Fe (t_{2g})	SOMO-1	Ligand	SUMO	Fe (t_{2g})
138	HOMO	Fe (t_{2g})	SOMO	Fe (t_{2g})	SUMO	Fe (t_{2g})	SOMO	Fe (t_{2g})*	SUMO+1	Fe (t_{2g})
139	LUMO	Ligand	SUMO	Ligand	SUMO+1	Ligand	SUMO	Ligand	SUMO+2	Ligand
140	LUMO+1	Ligand	SUMO+2	Ligand	SUMO+2	Ligand	SUMO+2	Ligand	SUMO+3	Ligand

Orbital densities were calculated on the respective optimized structure (**1**$^{-}$, **1,** and **1**$^{+}$ as singlet, doublet, and triplet, respectively) to show the metal character of the reduction and oxidation. In the three doubly occupied HOMOs, the density is mainly located on the iron. In the oxidized species (**1**$^{+}$), the density of the α-orbitals is mainly delocalized on the ligands with partial Fe-fraction. The β-orbitals show more of a "t_{2g}-behavior", with the SOMO and the SUMO/SUMO+1 (singly occupied/unoccupied molecular orbital) orbital representing the t_{2g}-orbitals, indicating metal-based oxidation.

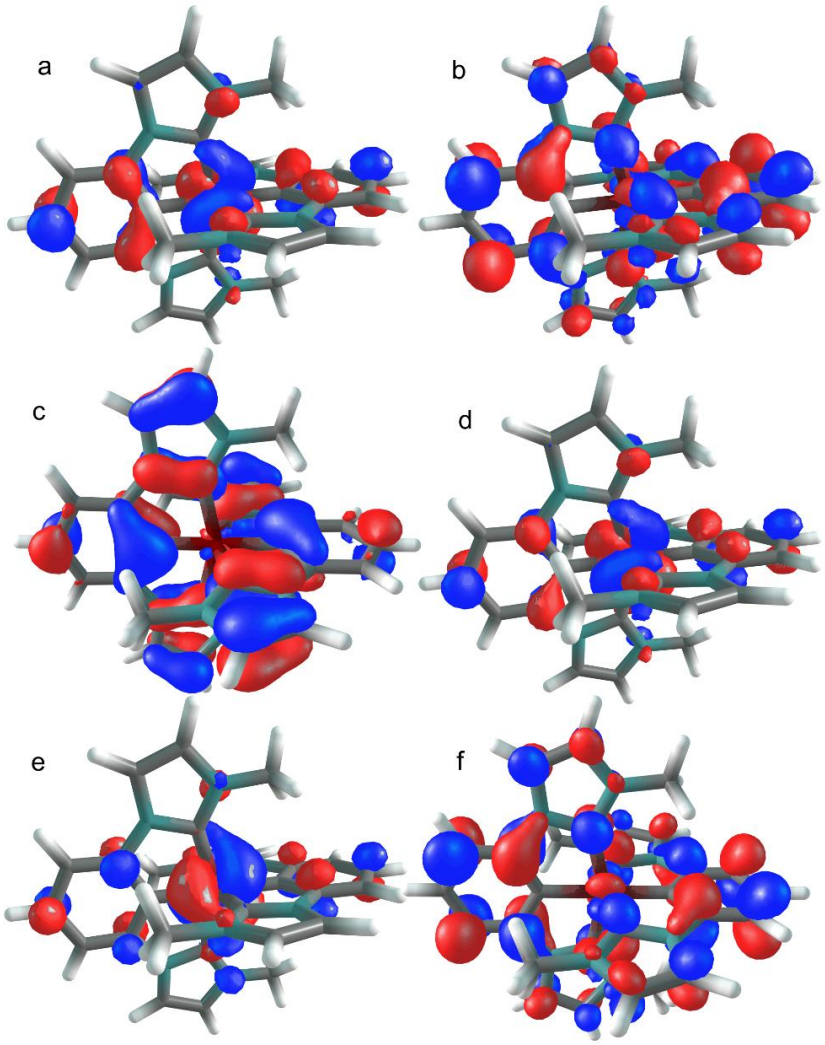

Supplementary Figure 10| Orbitals involved in the electronic transitions. a, Orbital a138. **b,** Orbital a139. **c,** Orbital b135. **d,** Orbital b137. **e,** Orbital b138. **f,** Orbital b139.

Supplementary Table 2: Vertical excitation energies predicted with tuned LC-BLYP. Note that only the most important contributions are presented, and therefore the sum of weights for a given state may be less than 1. The letters S and V describe the singly (S) and vacant (V) orbitals.

No.	E, eV	Osc.str.	Weight	Involved orbitals					No.	E, eV	Osc.str.	Weight	Involved orbitals				
1	0.18	0.0023	1.03	137	→	S	1	β	17	3.43	0.0012	0.38	127	→	S	1	β
2	0.26	0.0009	1.01	136	→	S	1	β				0.15	136	→	V	4	β
3	1.88	0.0009	0.85	131	→	S	1	β				0.15	137	→	V	2	β
			0.13	134	→	S	1	β				0.11	137	→	V	7	β
4	1.97	0.0115	0.96	135	→	S	1	β	18	3.45	0.0018	0.63	137	→	V	4	β

5	2.08	0.0000	0.97	133	→	S	1	β
6	2.24	0.0000	0.86	134	→	S	1	β
			0.13	131	→	S	1	β
7	2.46	0.0056	0.97	132	→	S	1	β
8	2.68	0.0164	0.89	129	→	S	1	β
9	2.85	0.0000	0.88	128	→	S	1	β
10	2.89	0.0110	0.97	130	→	S	1	β
11	3.09	0.0000	0.63	136	→	V	1	β
			0.20	137	→	V	1	α
12	3.10	0.0040	0.80	137	→	V	1	β
			0.09	S1	→	V	1	α
13	3.24	0.0043	0.62	137	→	V	2	β
			0.15	137	→	V	7	β
			0.08	S1	→	V	5	α
			0.06	S1	→	V	2	α
14	3.31	0.0112	0.60	136	→	V	2	β
			0.14	136	→	V	7	β
			0.08	137	→	V	2	α
			0.07	137	→	V	5	α
15	3.39	0.0000	0.68	137	→	V	3	α
			0.16	S1	→	V	4	α
16	3.40	0.0025	0.85	124	→	S	1	β
26	3.70	0.0129	0.46	137	→	V	1	α
			0.20	136	→	V	1	β
			0.09	S1	→	V	4	α
			0.07	134	→	V	1	α
			0.06	136	→	V	7	β
27	3.71	0.0384	0.65	S1	→	V	2	α
			0.15	136	→	V	1	α
			0.06	137	→	V	2	β
28	3.74	0.0007	0.33	137	→	V	9	β
			0.17	S1	→	V	6	α
			0.15	137	→	V	6	β
			0.08	S1	→	V	8	α
			0.07	137	→	V	13	β
29	3.86	0.0861	0.53	S1	→	V	3	α
			0.11	137	→	V	2	α
			0.11	137	→	V	4	β
30	3.86	0.0008	0.80	122	→	S	1	β
			0.10	125	→	S	1	β
31	3.88	0.0338	0.70	137	→	V	3	α
			0.07	136	→	V	4	β
32	3.92	0.0000	0.21	137	→	V	6	α
			0.19	136	→	V	6	β
			0.15	136	→	V	9	β
			0.05	136	→	V	5	β
			0.11	S1	→	V	3	α
			0.06	136	→	V	7	β
19	3.48	0.0096	0.27	S1	→	V	5	α
			0.23	127	→	S	1	β
			0.18	137	→	V	7	β
			0.12	137	→	V	2	β
20	3.52	0.0117	0.52	S1	→	V	1	α
			0.28	136	→	V	3	β
			0.10	137	→	V	1	β
21	3.53	0.0187	0.29	137	→	V	5	α
			0.24	136	→	V	7	β
			0.21	136	→	V	2	β
			0.10	137	→	V	4	β
22	3.62	0.0280	0.50	136	→	V	3	β
			0.26	S1	→	V	1	α
23	3.64	0.0040	0.60	136	→	V	4	β
			0.29	127	→	S	1	β
24	3.66	0.0018	0.74	126	→	S	1	β
			0.17	123	→	S	1	β
25	3.67	0.0000	0.46	137	→	V	1	α
			0.20	136	→	V	1	β
			0.09	S1	→	V	4	α
34	3.97	0.0000	0.18	136	→	V	9	β
			0.11	132	→	V	1	α
			0.10	137	→	V	8	α
			0.09	134	→	V	2	β
			0.08	134	→	V	2	α
			0.08	137	→	V	1	α
			0.08	132	→	V	1	β
35	4.00	0.0232	0.36	137	→	V	5	α
			0.28	136	→	V	7	β
			0.10	S1	→	V	3	α
36	4.01	0.0003	0.68	120	→	S	1	β
			0.08	136	→	V	5	α
			0.06	136	→	V	2	α
			0.05	137	→	V	4	α
37	4.06	0.0071	0.34	137	→	V	4	α
			0.09	135	→	V	1	α
			0.08	120	→	S	1	β
			0.08	136	→	V	2	α
			0.08	135	→	V	1	β
38	4.06	0.0040	0.25	136	→	V	1	α
			0.15	S1	→	V	2	α
			0.12	135	→	V	2	α
			0.09	135	→	V	2	β
			0.08	133	→	V	1	β

33	3.93	0.0097	0.38	137	→	V	4	α
			0.12	135	→	V	1	α
			0.11	136	→	V	3	β
			0.09	136	→	V	2	α
			0.06	135	→	V	1	β
			0.05	132	→	V	2	α
			0.05	135	→	V	3	α
40	4.13	0.0000	0.53	S1	→	V	4	α
			0.11	137	→	V	3	β
			0.05	136	→	V	1	β
41	4.18	0.0000	0.20	125	→	S	1	β
			0.15	136	→	V	3	α
			0.08	135	→	V	4	α
			0.06	135	→	V	3	β
42	4.20	0.0008	0.43	S1	→	V	5	α
			0.31	137	→	V	7	β
43	4.21	0.0209	0.20	123	→	S	1	β
			0.10	132	→	V	2	α
			0.08	132	→	V	2	β
			0.07	136	→	V	4	α
			0.07	134	→	V	1	α
			0.06	134	→	V	1	β
			0.05	137	→	V	2	α
			0.05	137	→	V	5	β
			0.05	126	→	S	1	β
			0.05	S1	→	V	7	α
44	4.23	0.0001	0.32	S1	→	V	6	α
			0.13	137	→	V	9	β
			0.10	136	→	V	2	α
			0.08	S1	→	V	8	α
			0.06	136	→	V	5	α
			0.05	135	→	V	1	β
45	4.27	0.0198	0.34	136	→	V	1	α
			0.11	133	→	V	1	α
			0.05	135	→	V	3	α
53	4.52	0.0098	0.27	137	→	V	5	β
			0.13	136	→	V	12	β
			0.07	137	→	V	6	β
			0.06	137	→	V	12	α
			0.05	135	→	V	3	α
54	4.54	0.0008	0.04	130	→	V	2	α
			0.11	137	→	V	6	α
			0.11	136	→	V	3	α
			0.11	133	→	V	3	α
			0.05	136	→	V	6	β
			0.05	133	→	V	4	β
			0.07	137	→	V	3	α
39	4.07	0.0020	0.21	137	→	V	2	α
			0.10	137	→	V	5	α
			0.10	S1	→	V	3	α
			0.07	136	→	V	4	α
			0.10	133	→	V	1	β
			0.09	135	→	V	2	β
46	4.29	0.0144	0.22	137	→	V	6	β
			0.16	S1	→	V	8	α
			0.12	136	→	V	2	α
			0.06	137	→	V	5	β
			0.05	133	→	V	2	α
47	4.33	0.0000	0.17	136	→	V	6	β
			0.12	137	→	V	8	α
			0.09	125	→	S	1	β
			0.05	132	→	V	1	α
48	4.37	0.0096	0.24	137	→	V	9	β
			0.14	137	→	V	6	β
			0.14	136	→	V	2	α
			0.07	135	→	V	1	β
49	4.37	0.0227	0.49	123	→	S	1	β
			0.13	126	→	S	1	β
			0.09	137	→	V	5	β
			0.06	136	→	V	4	α
50	4.39	0.0000	0.53	125	→	S	1	β
			0.12	136	→	V	3	α
51	4.48	0.0073	0.43	136	→	V	5	β
			0.12	136	→	V	6	β
			0.07	136	→	V	11	β
52	4.49	0.0058	0.15	137	→	V	5	β
			0.08	136	→	V	12	β
			0.07	134	→	V	1	α
			0.05	130	→	V	1	β
			0.05	130	→	V	1	α
			0.06	132	→	V	4	α
58	4.60	0.0221	0.30	131	→	V	1	α
			0.14	136	→	V	4	α
			0.13	131	→	V	1	β
			0.07	136	→	V	12	β
59	4.61	0.0048	0.51	131	→	V	1	α
			0.11	136	→	V	4	α
60	4.62	0.0007	0.27	136	→	V	10	β
			0.07	137	→	V	10	α
			0.07	135	→	V	1	α
61	4.63	0.0000	0.31	137	→	V	8	β
			0.24	137	→	V	10	β

55	4.54	0.0103	0.13	133	→	V	1	β
			0.12	135	→	V	2	β
			0.09	134	→	V	4	α
			0.09	137	→	V	7	α
			0.08	132	→	V	3	α
			0.06	135	→	V	2	α
			0.05	133	→	V	1	α
56	4.56	0.0000	0.45	121	→	S	1	β
			0.08	134	→	V	3	α
			0.07	132	→	V	4	α
			0.05	132	→	V	3	β
			0.05	136	→	V	10	β
57	4.57	0.0129	0.19	135	→	V	1	β
			0.18	135	→	V	1	α
			0.07	133	→	V	2	β
			0.07	133	→	V	2	α
			0.07	137	→	V	6	β
66	4.72	0.0001	0.08	134	→	V	3	α
			0.50	136	→	V	5	α
			0.08	120	→	S	1	β
			0.05	136	→	V	2	α
67	4.74	0.0000	0.45	131	→	V	2	α
			0.28	131	→	V	2	β
68	4.76	0.0442	0.15	134	→	V	4	α
			0.14	136	→	V	5	β
			0.10	137	→	V	12	β
			0.09	134	→	V	3	β
			0.08	132	→	V	3	α
			0.06	132	→	V	4	β
69	4.79	0.0000	0.46	131	→	V	2	β
			0.28	131	→	V	2	α
			0.05	134	→	V	2	β
70	4.82	0.0303	0.24	131	→	V	3	α
			0.11	S1	→	V	8	α
			0.10	136	→	V	8	β
			0.08	131	→	V	4	β
			0.08	S1	→	V	6	α
			0.06	136	→	V	2	α
			0.05	134	→	V	3	α
71	4.82	0.0005	0.21	136	→	V	4	α
			0.10	S1	→	V	7	α
			0.06	133	→	V	4	α
			0.05	128	→	V	4	α
			0.05	136	→	V	9	α
72	4.83	0.0001	0.11	137	→	V	8	β
			0.09	136	→	V	3	α
			0.05	136	→	V	3	α
62	4.64	0.0008	0.19	133	→	V	1	α
			0.11	136	→	V	11	β
			0.10	135	→	V	2	α
			0.05	137	→	V	11	α
63	4.64	0.0001	0.41	121	→	S	1	β
			0.18	136	→	V	8	β
			0.08	135	→	V	1	α
			0.07	136	→	V	5	α
			0.05	136	→	V	10	β
64	4.66	0.0395	0.70	131	→	V	1	β
			0.06	131	→	V	1	α
			0.05	136	→	V	4	α
65	4.67	0.0001	0.32	137	→	V	6	α
			0.19	136	→	V	9	β
			0.11	136	→	V	3	α
			0.06	137	→	V	8	α
			0.08	136	→	V	7	α
			0.06	131	→	V	2	β
73	4.84	0.0095	0.34	131	→	V	3	α
			0.21	S1	→	V	8	α
			0.12	S1	→	V	6	α
			0.10	131	→	V	4	β
74	4.84	0.0097	0.51	136	→	V	6	α
			0.14	136	→	V	8	α
75	4.88	0.0029	0.36	137	→	V	12	β
			0.22	131	→	V	4	α
			0.19	131	→	V	3	β
76	4.88	0.0589	0.28	S1	→	V	7	α
			0.22	134	→	V	1	α
			0.09	135	→	V	4	β
			0.06	134	→	V	1	β
			0.06	133	→	V	3	β
77	4.89	0.0507	0.18	131	→	V	4	α
			0.14	119	→	S	1	β
			0.10	137	→	V	12	β
			0.09	131	→	V	3	β
			0.07	135	→	V	2	α
			0.07	137	→	V	7	α
			0.07	136	→	V	5	β
78	4.91	0.0187	0.20	136	→	V	8	β
			0.13	S1	→	V	8	α
			0.09	S1	→	V	6	α
			0.09	131	→	V	3	α
			0.06	134	→	V	3	α
			0.06	135	→	V	1	β

79	4.92	0.0000	0.24	137	→	V	10	β
			0.09	131	→	V	2	α
			0.06	136	→	V	6	β
			0.05	136	→	V	9	β
			0.05	131	→	V	5	α
80	4.93	0.0015	0.16	137	→	V	12	β
			0.15	135	→	V	2	α
			0.10	131	→	V	4	α
			0.06	136	→	V	8	α
			0.06	135	→	V	5	α
			0.05	131	→	V	3	β
81	4.96	0.0123	0.13	135	→	V	1	α
			0.10	134	→	V	4	β
			0.09	129	→	V	1	β
			0.06	136	→	V	10	β
			0.05	135	→	V	1	β
			0.05	136	→	V	8	β
			0.05	129	→	V	1	α
82	4.97	0.0000	0.22	137	→	V	8	β
			0.21	137	→	V	10	β
			0.16	131	→	V	5	α
			0.09	137	→	V	8	α
83	4.98	0.2584	0.31	S1	→	V	7	α
			0.19	135	→	V	3	α
			0.12	134	→	V	1	β
			0.06	136	→	V	12	β
84	4.99	0.0321	0.73	119	→	S	1	β
			0.05	137	→	V	7	α
85	5.02	0.0000	0.13	S1	→	V	9	α
			0.07	137	→	V	6	α
			0.06	134	→	V	2	α
			0.06	131	→	V	5	α
			0.06	134	→	V	2	β
			0.05	132	→	V	1	β
			0.05	137	→	V	8	β
93	5.12	0.0109	0.22	137	→	V	7	α
			0.10	132	→	V	3	α
			0.07	129	→	V	2	β
			0.05	135	→	V	2	α
			0.05	130	→	V	4	α
			0.05	131	→	V	3	β
			0.05	128	→	V	1	β
94	5.13	0.0007	0.22	131	→	V	5	α
			0.12	137	→	V	8	α
			0.08	S1	→	V	9	α
			0.08	135	→	V	4	α
			0.13	134	→	V	2	α
			0.11	137	→	V	10	β
			0.10	S1	→	V	10	α
			0.09	137	→	V	8	β
			0.09	131	→	V	5	α
			0.06	132	→	V	1	β
			0.06	135	→	V	3	β
86	5.04	0.0049	0.85	137	→	V	11	β
87	5.05	0.0021	0.27	133	→	V	2	α
			0.17	133	→	V	2	β
			0.14	135	→	V	1	β
			0.10	135	→	V	1	α
			0.06	133	→	V	5	α
88	5.06	0.0185	0.32	133	→	V	1	α
			0.23	137	→	V	7	α
			0.12	135	→	V	2	α
89	5.06	0.0010	0.32	131	→	V	4	β
			0.14	134	→	V	4	β
			0.12	134	→	V	3	α
			0.09	131	→	V	3	α
			0.06	132	→	V	3	β
90	5.08	0.0021	0.43	133	→	V	1	β
			0.40	135	→	V	2	β
91	5.10	0.0030	0.32	131	→	V	3	β
			0.23	131	→	V	4	α
			0.13	134	→	V	3	β
			0.09	134	→	V	4	α
92	5.11	0.0000	0.10	137	→	V	8	α
			0.08	134	→	V	5	α
			0.06	S1	→	V	7	α
97	5.15	0.0001	0.76	137	→	V	13	β
			0.12	137	→	V	9	β
98	5.15	0.0002	0.58	135	→	V	5	α
			0.06	134	→	V	3	β
			0.05	136	→	V	8	α
99	5.17	0.0624	0.05	131	→	V	6	α
			0.23	135	→	V	3	α
			0.16	136	→	V	12	β
			0.12	135	→	V	4	β
			0.07	134	→	V	1	α
			0.05	137	→	V	12	α
100	5.18	0.0001	0.14	136	→	V	13	β
			0.14	135	→	V	4	α
			0.12	132	→	V	1	α
			0.09	S1	→	V	9	α
			0.07	131	→	V	7	β

			0.07	S1	→	V	10	α
			0.06	131	→	V	7	β
95	5.13	0.0199	0.22	131	→	V	4	β
			0.15	133	→	V	2	β
			0.12	133	→	V	2	α
			0.09	131	→	V	3	α
			0.07	135	→	V	1	β
			0.07	132	→	V	3	β
96	5.14	0.1789	0.13	134	→	V	1	α
			0.22	136	→	V	12	β
			0.10	134	→	V	1	β
			0.09	137	→	V	12	α
			0.06	131	→	V	5	α
			0.05	132	→	V	1	β
			0.05	136	→	V	9	β

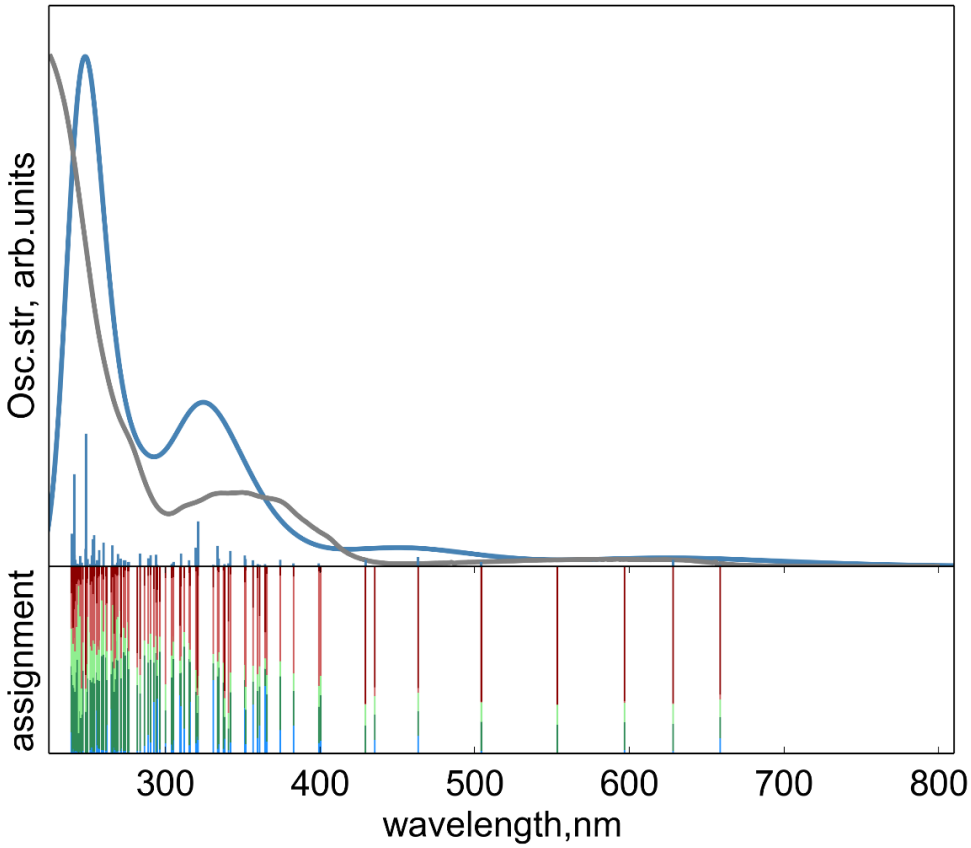

Supplementary Figure 11| Overlay of the simulated optical absorption spectrum (blue line, method: tuned LC-BLYP) and the experimental spectrum (grey line). Broadening: Gaussian line shape, σ=0.2 eV.

Fragment-based excited-states analysis

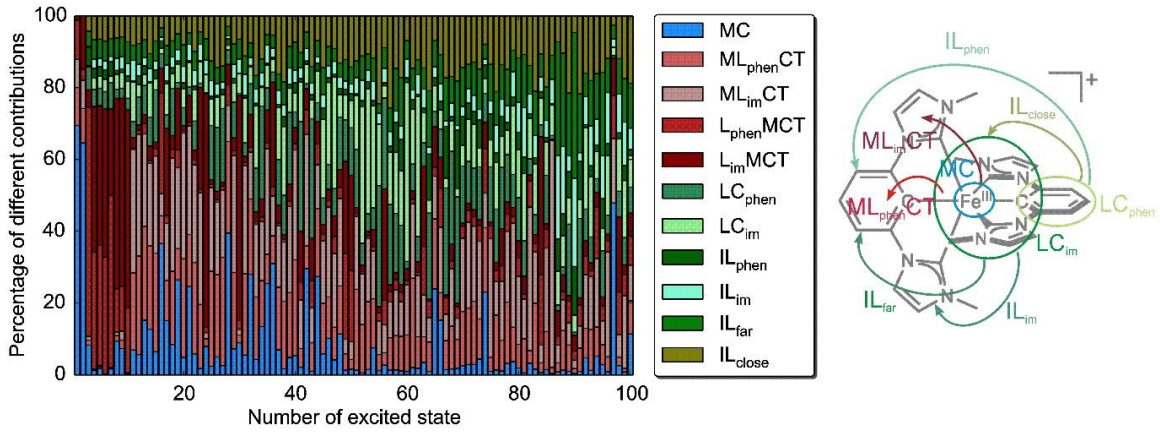

Supplementary Figure 12| Density-matrix analysis of the lowest TDDFT transitions based on the 5 fragments presented in the right part of the figure.

Spectroelectrochemistry

a

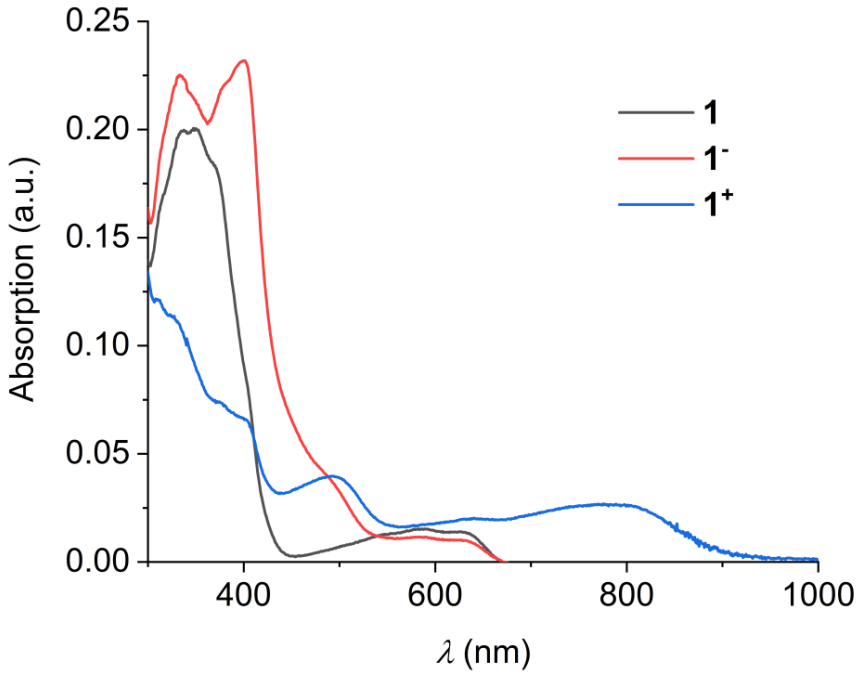

b

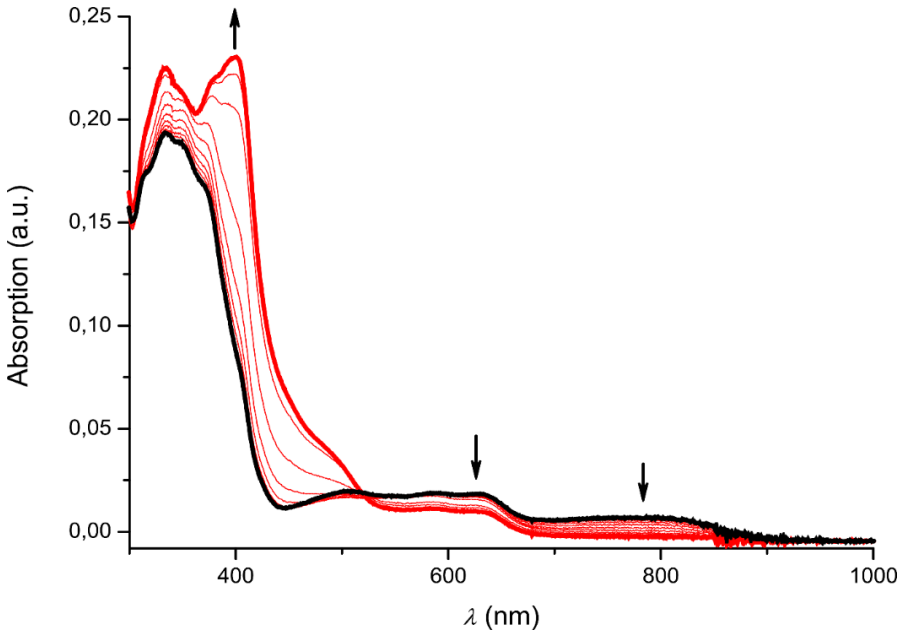

c

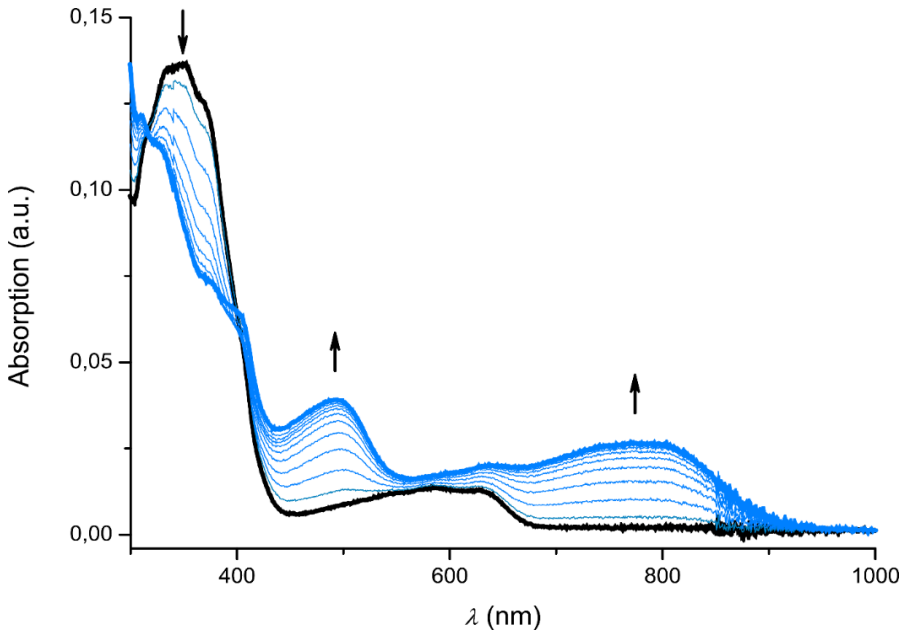

Supplementary Figure 13| Spectroelectrochemical investigations. a) UV-Vis/NIR absorption spectrum of **1** (grey) in comparison with that of $\mathbf{1}^{-}$ (red) and $\mathbf{1}^{+}$ (blue) obtained by spectro-electrochemical measurements in $CH_3CN/[n Bu_4N][PF_6]$. b) Spectra acquired during oxidative SEC. c) Spectra acquired during reductive SEC.

Room temperature emission spectroscopy

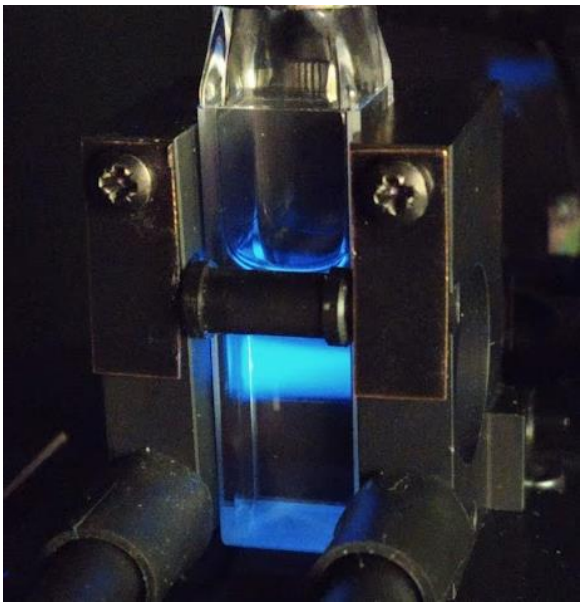

Supplementary Figure 14| Room temperature emission. Observed emission after excitation at 350 nm in degassed acetonitrile.

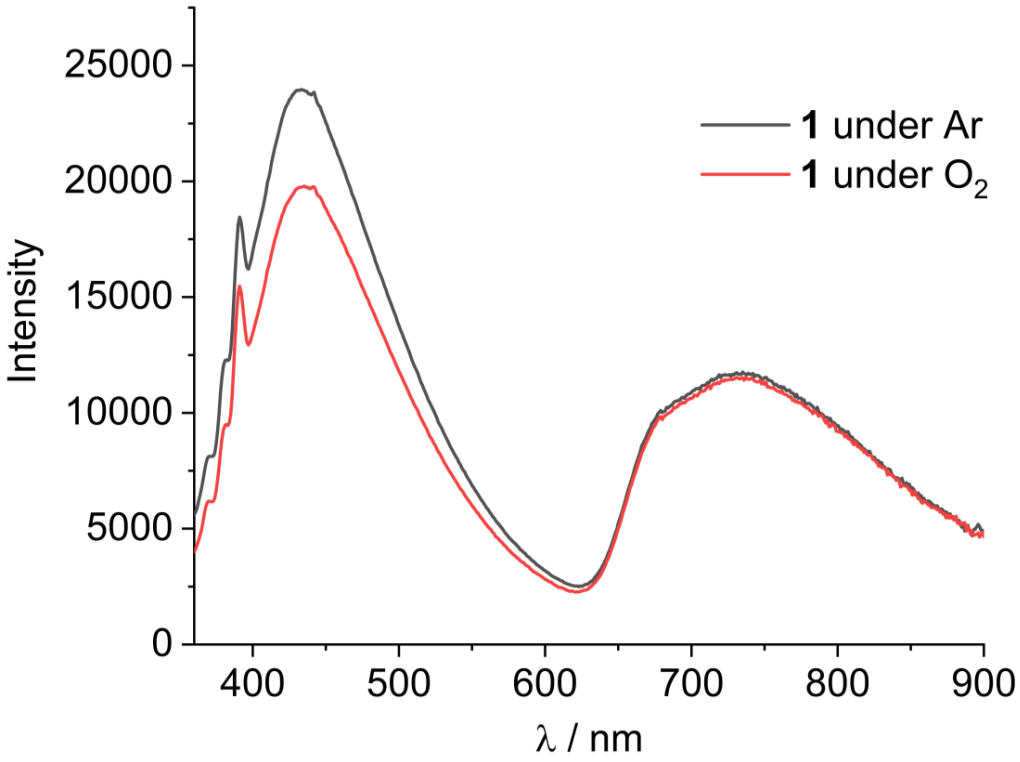

Supplementary Figure 15| Room temperature emission. Emission after excitation at 350 nm in degassed acetonitrile and after being re-aerated under atmosphere.

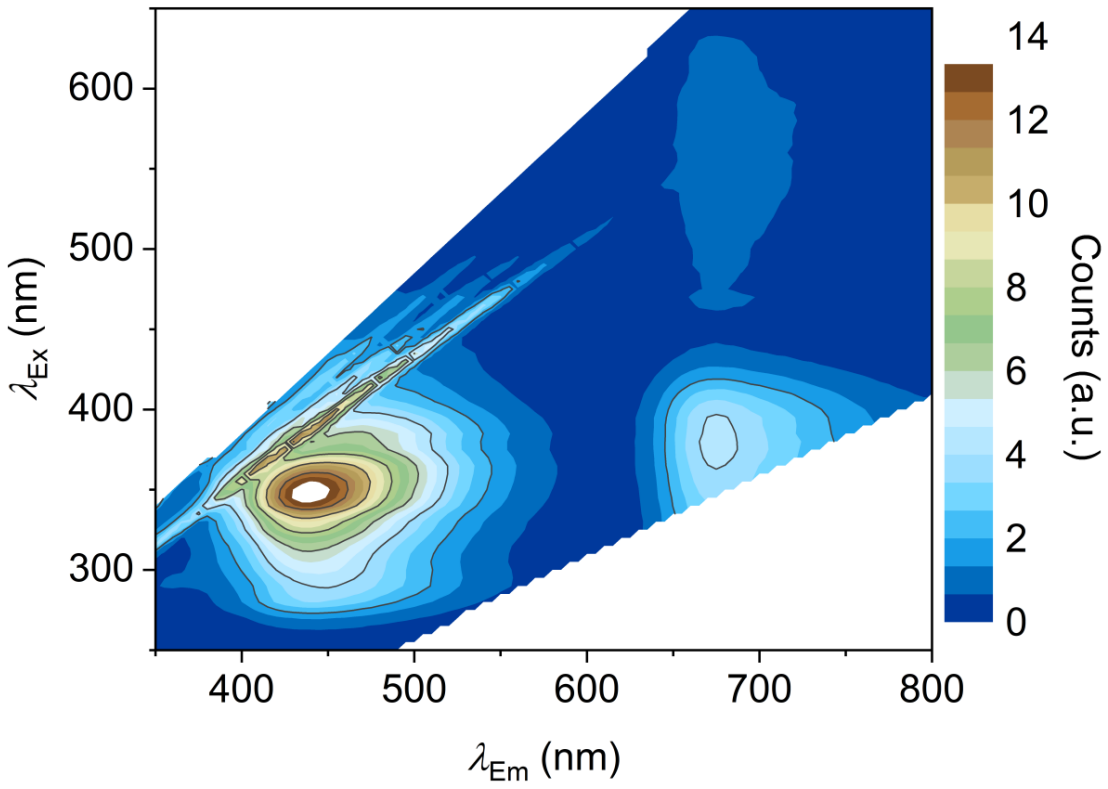

Supplementary Figure 16| Excitation-emission Spectra. Excitation-emission plot for **1**. The plot shows the separation between the MLCT and the LMCT fluorescence. Excitation in the CT-absorption band (310 – 410 nm) shows both MLCT and LMCT emissions. Above this wavelength, the LMCT emission is visible. The narrow diagonal features below 600 nm are caused by Raman signals from the solvent. In this measurement, no correction for the detector sensitivity in the red was employed. Hence the maximum of the LMCT emission is at 675 nm instead of 735 nm.

For the determination of the Stokes shift, the highest intensity features of the respective absorption and emission bands were used. Nonetheless, excitation at lower energies, such as 410 and 630 nm, also led to the observation of the respective MLCT and LMCT emission bands.

Variable temperature emission spectroscopy

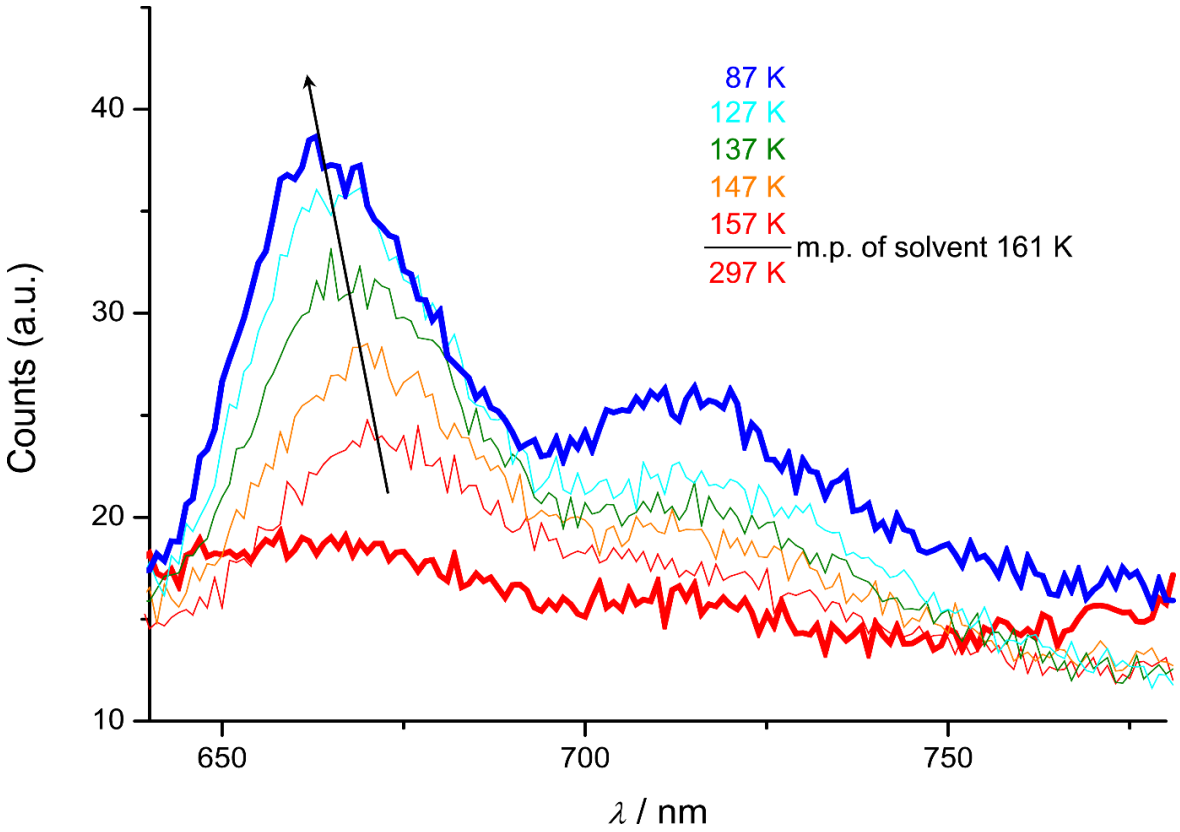

Supplementary Figure 17| Variable Temperature Emission. The spectra of **1** were collected in butyronitrile with an excitation wavelength of 425 nm, showing the intensity increase upon glass formation and further cooling and the blue shift of the LMCT band upon cooling. With this excitation wavelength and with the employed detector, the luminescence in fluid solution is barely visible.

Femtosecond transient absorption spectroscopy

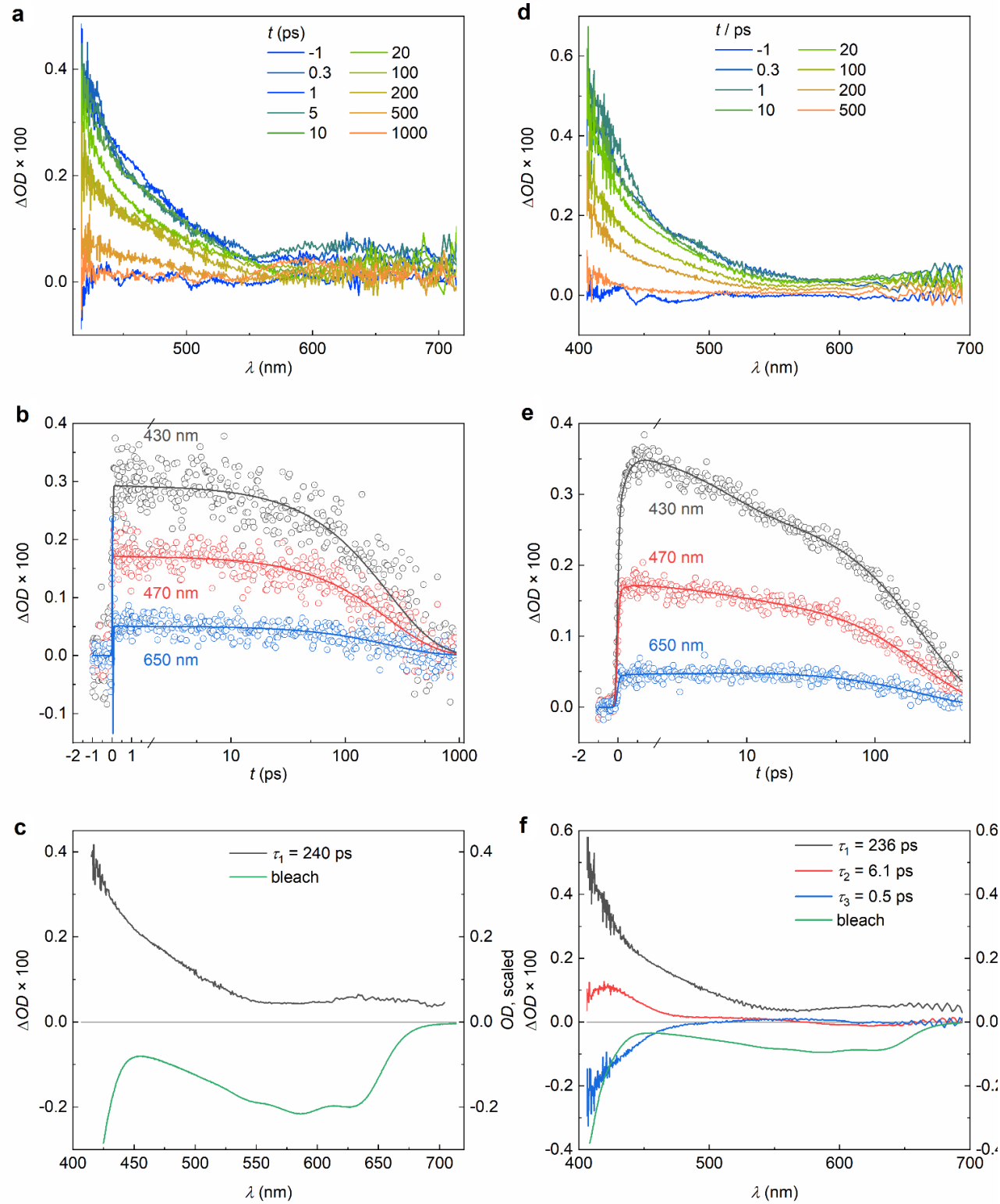

Supplementary Figure 18| Transient absorption (TA) spectra with pump pulses centered at 600 nm and 330 nm, respectively. a, b, c TA data for excitation of complex **1** at 600 nm and corresponding fits. A degassed acetonitrile solution of **1** was used as sample. A global fit, as described in the manuscript, was applied and a pure monoexponential decay with a time constant of τ_1 = 240 ps was found. **a,** TA spectra at the given times after excitation at 600 nm. **b,** Time traces of the transient absorption of **1** at three selected detection wavelengths together with the time curves resulting from the global fit. **c,** Decay associated amplitude spectrum of the single exponential decay in comparison with the ground state bleach, i. e., the scaled negative absorption spectrum. **d, e, f** TA data for excitation of complex **1** at 330 nm and corresponding fits. **d,** TA spectra obtained at the given times after excitation of a degassed solution of **1** in acetonitrile at 330 nm. **e,** Time traces of the transient absorption of **1** at three selected detection wavelengths together with the time curves resulting from the global fit. **f,** Decay associated amplitude spectra for the three components with τ_1 = 236 ps, τ_2 = 6.1 ps, and τ_3 = 0.5 ps in comparison with the ground state bleach, i. e., the scaled negative absorption spectrum.

Time correlated single photon counting and time resolved emission spectroscopy

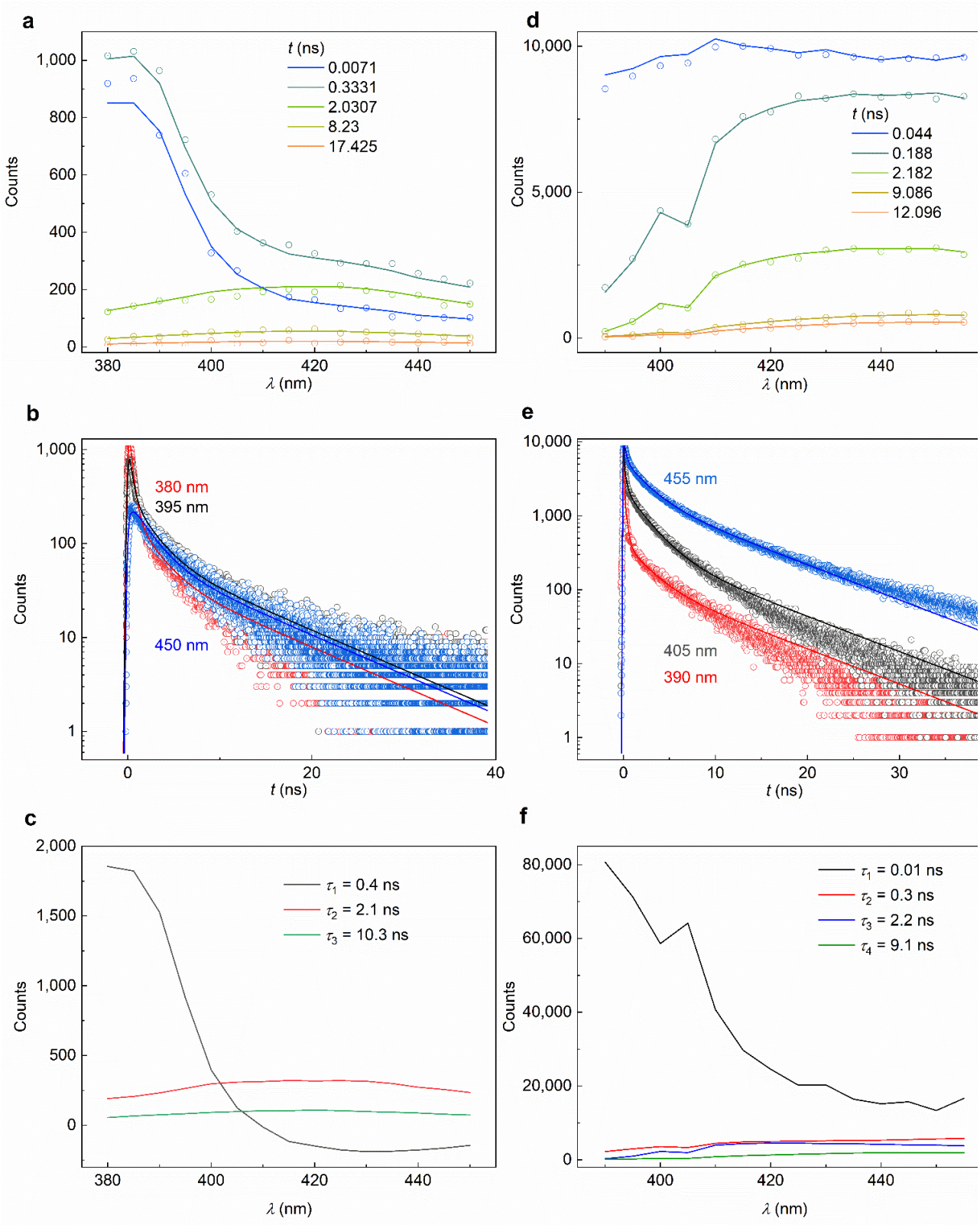

Supplementary Figure 19| TRES Data after excitation at 346 nm and 374 nm. a, b, c, measurements between 380 and 450 nm for 1 h per data point after 346 nm excitation. **a,** Decay of the fluorescence signal over time. **b,** Decay curves (points) at 380, 395 and 450 nm with the corresponding fits (line). **c,** Amplitude spectra of the lifetimes τ_1 = 0.4 ns, τ_2 = 2.1 ns and τ_3 = 10.3 ns obtained from global fitting. If the sub-ns lifetime is ignored, since it is attributed to stray-light of the excitation source, an averaged lifetime of 4.1 ns, comparable to the streak camera measurements is obtained. **d, e, f,** Measurements between 390 and 455 nm for 10k Counts per data point after 374 nm excitation. **d,** Decay of the fluorescence signal over time. **e,** Decay curves (points) at 390 nm, 405 nm and 455 nm with the respective fits (line). **f,** Amplitude spectra of the lifetimes τ_1 = 0.01 ns, τ_2 = 0.3 ns, τ_3 = 2.2 ns and τ_4 = 9.1 ns obtained from global fitting of the decay curves. If the sub-ns lifetimes are ignored here as well, an averaged lifetime of 4.0 ns is obtained.

Quenching experiments

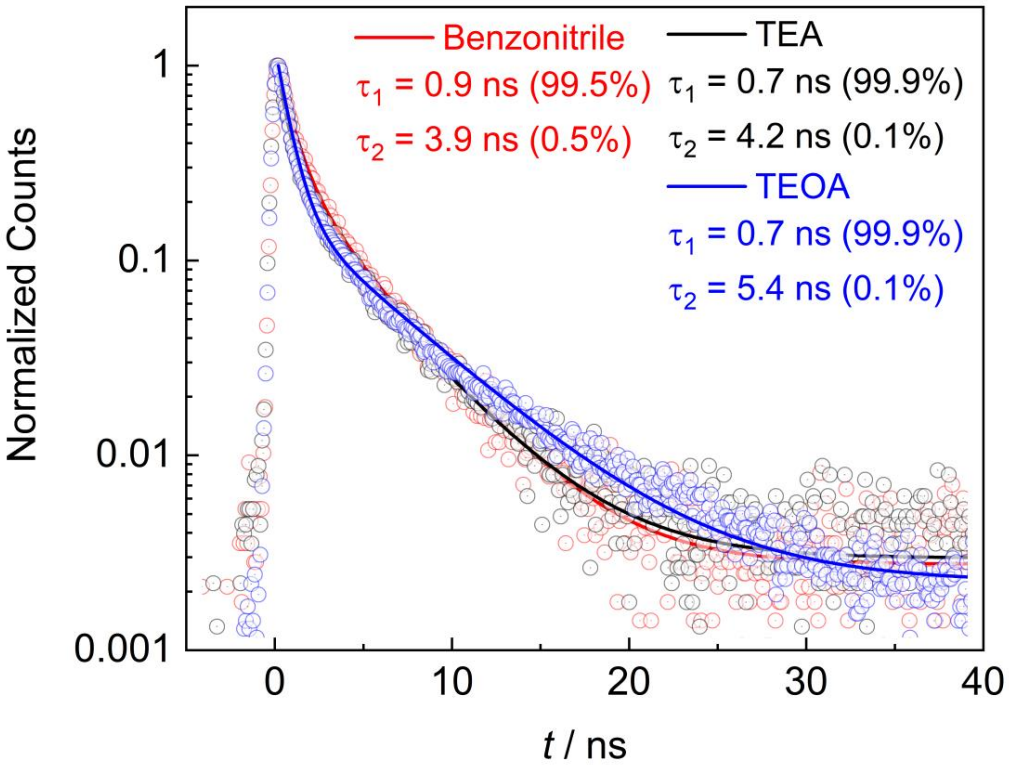

Supplementary Figure 20| Decay curves of the quenching experiments. The decay curves of the quenchers show a significant quenching of the excited state. In

all three quenching experiments, the short time constant dominates the decay, while the long time constant is almost completely quenched.

Singlet oxygen sensitization

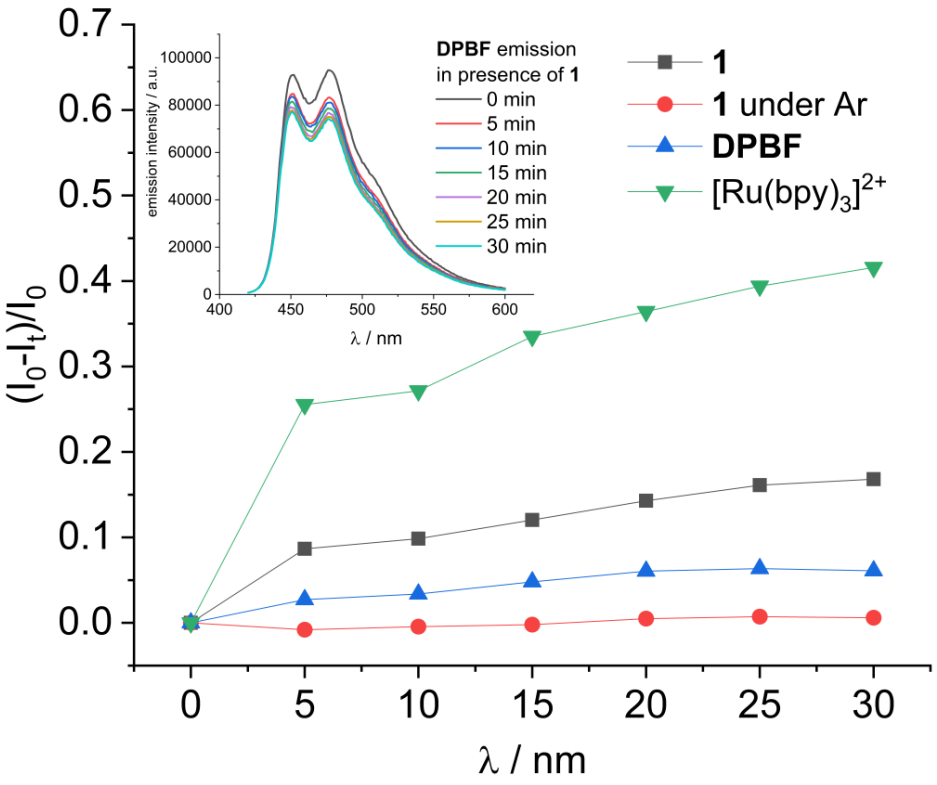

Supplementary Figure 21| DPBF consumption based on the fluorescence intensity as function of irradiation time (λ = 350 nm). Inset: Emission spectra of DPBF during irradiation.

C.3. Supplementary Information of "Isostructural cyclometalated iron complex in three oxidation states"

Supporting Information

Isostructural cyclometalated iron complex in three oxidation states

Contents

Synthesis

All reactions under inert conditions were either performed under standard schlenk techniques using argon as inert gas or in an argon filled glovebox. Dry and degassed solvents were obtained by dynamic drying of the respective solvent over molar sieves in an MBraun SPS solvent purifying system, subsequent degassing by bubbling argon through it and storage over molar sieves. The solvent for the reduction was additionally degassed using three freeze-pump-thaw cycles. All chemicals were used without further purification. NMR spectra were recorded on a Bruker Ascent 700 spectrometer. Assignments were done using 2D spectra. Mass spectra were recorded on a Waters Synapt G2 quadropole TOF spectrometer with Acetonitrile as solvent. Elemental Analysis was performed on a vario MicroCube by elementar. $[Fe(ImP)_2]PF_6$ **1** was synthesized according to literature procedures.[1]

$[Fe(ImP)_2]$ (**1**$^-$)

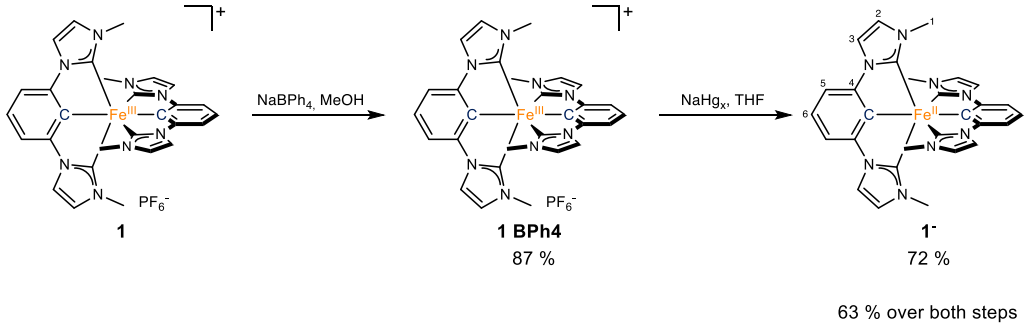

The synthesis of **1**$^-$ started with the preparation of the BPh4$^-$salt of **1**, **1 BPh$_4$**. For this, the starting compound (100 mg, 0.148 mmol) was dissolved in a minimal amount of methanol. $NaBPh_4$ (101 mg, 0.296 mmol, 2 eq.) was added to the dark blue solution and stirred. The dark suspension was filtered, the solids were washed with cold methanol and then washed out of the filter using dichloromethane. After removal of the solvent and thoroughly drying, **1 BPh$_4$** was obtained as a dark blue powder (109 mg, 0.128 mmol, 87 %) and used without further purification.

1 BPh4 (102 mg, 0.12 mmol) was dissolved in dry and degassed THF (15 mL in total) and then transferred to Sodium Amalgam (1.3 %, 849 mg, 0.48 mmol, 4 eq.) under THF (3 mL) in a schlenk flask while stirring. The solution quickly turned green and then slowly orange. After 2h of vigorous stirring, no further change in color was noticeable and the solvent of the orange solution was evaporated off under vacuum. The flask was transferred into a glovebox for further purification. There, the solids were washed with toluene and filtered to obtain an orange solution. The solvent was evaporated off to obtain **3** as fine orange crystals (45 mg, 0.085 mmol, 72 %). Crystals suitable for single crystal analysis were obtained by diffusion of pentane into a solution of **1**$^-$ in dichloromethane, where the orange crystals could be easily separated from residues of **1** which formed due to deterioration of the solution.

Note on the NMR-data: The coordinating carbon atoms were not observed in the ^{13}C-NMR.

^{1}H-NMR: (700 MHz, THF-d_8) δ (ppm) =7.40 (d, *J* = 7.3 Hz, 4H, **5-H**), 7.39 (d, *J* = 2.0 Hz, 4H, **3-H**), 6.44 (d, *J* = 1.9 Hz, 4H, **2-H**), 6.32 (t, *J* = 7.8 Hz, 2H, **6-H**), 2.36 (s, 12H, **1-H**).

^{13}C-NMR: (700 MHz, Acetonitrile-d_3) δ (ppm) =154.72 (**4-C**), 121.96 (**5-C**), 121.27 (**2-C**), 112.35 (**3-C**), 98.66 (**6-C**), 35.07(**1-C**).

$[Fe(ImP)_2](PF_6)_2$ (**1**$^+$)

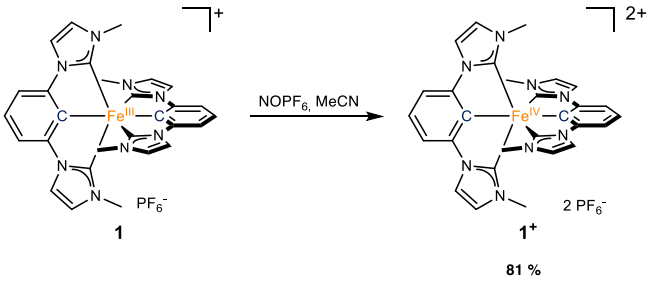

1 **1**$^+$

81 %

In a Schlenk flask, **1** (71.5 mg, 0.106 mmol) was first degassed thoroughly under a vacuum (10^{-3} mbar) for 1 h and then dissolved in dry and degassed Acetonitrile (5 mL). To the blue solution, $NOPF_6$ (20 mg, 0.114 mmol, 1.08 eq.) was added. The solution was stirred under argon overnight, before 1 mL of methanol was added to quench the reaction. The solution was stirred for another 15 minutes under atmosphere. The volatiles were removed at the rotary evaporator. The dark solid was washed thoroughly with chloroform until the blue color disappeared. The purple solid was purified by diffusion of chloroform into a solution of **1**$^+$ in acetone to yield fine purple needles (70 mg, 0.085 mmol, **81 %**). Crystals suitable for single crystal X-Ray analysis were obtained by diffusion of diethyl ether into a solution of **1**$^+$ in methanol, which were also used for Mössbauer spectroscopy and magnetic measurements.

^{1}H-NMR: (700 MHz, Acetonitrile-d_3) δ (ppm) = 38.91 (12H), 26.74 (4H), 8.53 (4H), -35.56 (4H).

ESI-MS: (m/z) $[M\text{-}2PF_6]^{2+}$ 265.0813 (calculated for $C_{28}H_{26}FeN_8^{2+}$: 265.0809), $[M\text{-}2PF_6]^+$ 530.1635 (calculated for $C_{28}H_{26}FeN_8^+$: 530.1630), $[M\text{-}PF_6]^+$ 675.1281 (calculated for $C_{28}H_{26}F_6FeN_8P^+$: 675.1272).

Elemental Analysis: (%) Found (calculated for $C_{28}H_{26}F_{12}FeN_8P_2$): C: 40.93 (41.00) H: 3.42 (3.19) N: 13.50 (13.66).

Single Crystal X-Ray Analysis

X-ray single crystal data of **1** and **2** were recorded using a Bruker SMART CCD area-detector diffractometer equipped with a graphite monochromator. Data of substance **3** were obtained using a Bruker Venture D8 diffractometer applied with a Mo Kα µ-source (λ=0.71073 Å), an Incoatec multilayer monochromator and a Photon III area detector at 120 K. The data were integrated with SAINT and afterwards a multi-scan absorption correction was applied using SADABS.[2] Structure solution was achieved by direct methods in SHELXT[3] and structure refinement was conducted using full-matrix least squares refinement based on F^2.[3] All non-hydrogen-atoms were refined anisotropically and the hydrogen atom positions were refined at idealized positions riding on the carbon atoms with isotropic displacement parameters $U_{iso}(H)=1.2\ U_{eq}(C)$ and C-H bond lengths of 0.93-0.96 Å. In the case of **1** one dichloromethane and of **2** one methanol molecule could not be modelled due to significant disorders and therefore were treated using SQUEEZE from the Platon software package.[4,5]

The Cambridge Crystallographic Data Centre provides the presented structures free of charge via www.ccdc.cam.ac.uk assigned to the deposition numbers 2002774 (**1**), 2108627 ($\mathbf{1}^-$) and 2108628 ($\mathbf{1}^+$).

$\mathbf{1}^-$: ($C_{28}H_{26}N_8Fe$), M_r = 530.42 Da, orange plate, size 0.30 x 0.16 x 0.02 mm³, tetragonal space group $I\bar{4}$ with Z=2, a=8.327(2) Å, b=8.327(2) Å, c=17.946(3) Å, V=1244.4(6) Å³, D_c=1.416 mg/m³, µ=0.640 mm^{-1}, F(000)=552, θ_{max}=33.721°, reflections collected: 85875, independent reflections: 2474, R_{int}=0.0553, refinement converged at R1=0.0312 [I>2σ(I)], wR2=0.0655 [all data], min./max. ΔF: -0.450 eÅ³ (0.75 Å from C1A) / 0.474 eÅ³ (0.75 Å from Fe1), **CCDC No.: 2108627.**

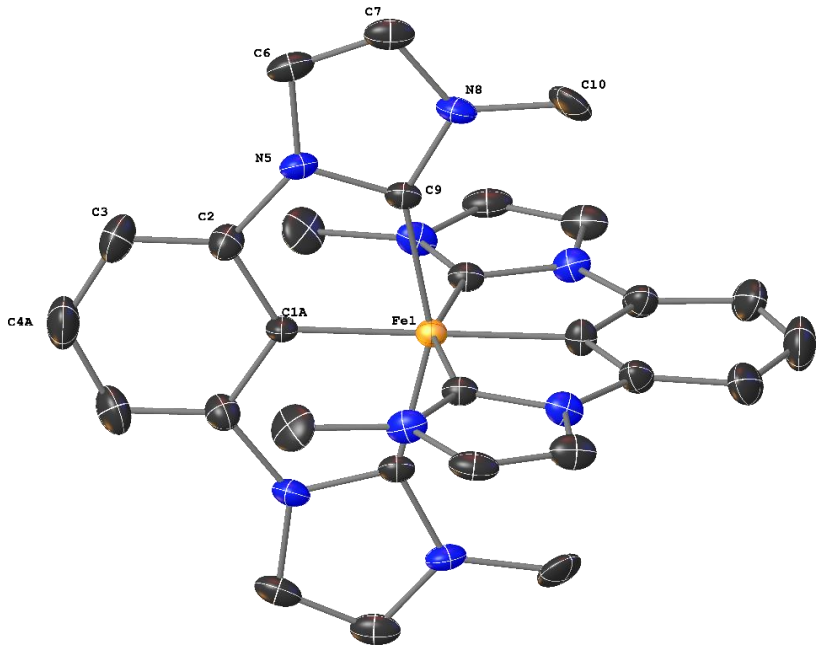

$\mathbf{1}^+$: ($C_{28}H_{26}N_8Fe$)(PF_6)$_2$, M_r = 820.36 Da, black needle, size 0.48 x 0.18 x 0.14 mm³, trigonal space group $P3_221$ with Z=3, a=10.869(3) Å, c=25.087(7) Å, V=2566.4(15) Å³, D_c=1.592 mg/m³, µ=0.634 mm^{-1}, F(000)=1242, θ_{max}=27.110°, reflections collected: 9276, independent reflections: 3765, R_{int}=0.0476,

refinement converged at R1=0.0743 [I>2σ(I)], wR2=0.1683 [all data], min./max. ΔF: -0.632 eÅ³ (0.67 Å from F24) / 0.601 eÅ³ (1.01 Å from C114), **CCDC No.: 2108628.**

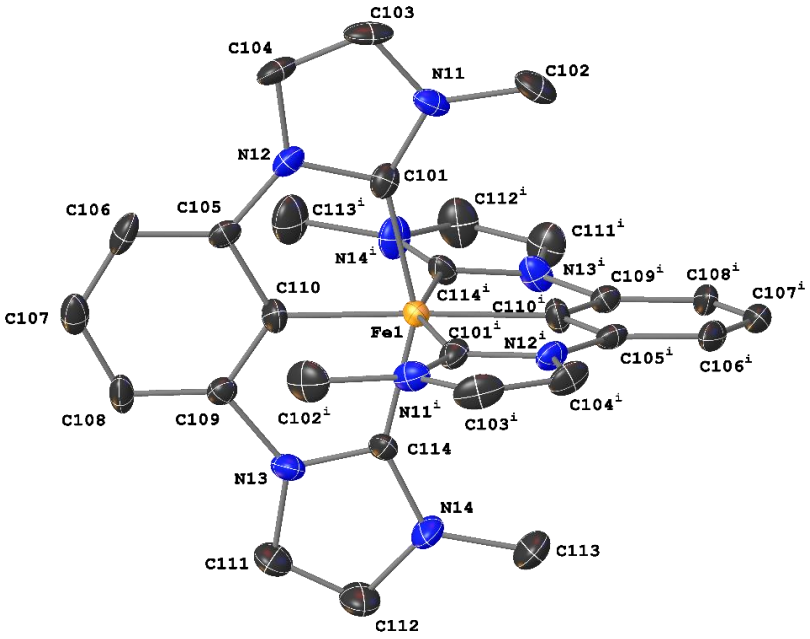

Mössbauer Spectroscopy

Mössbauer spectra were recorded with a ^{57}Co source in a Rh matrix using an alternating constant acceleration *Wissel* Mössbauer spectrometer operated in the transmission mode and equipped with a *Janis* closed-cycle helium cryostat. Isomer shifts are given relative to iron metal at ambient temperature.

Simulation of the experimental data was performed with the *Mfit* program using Lorentzian line doublets: E. Bill, Max-Planck Institute for Chemical Energy Conversion, Mülheim/Ruhr, Germany.

Magnetic Measurements

Temperature-dependent magnetic susceptibility measurements for **1**$^-$ and **1**$^+$ were carried out with a Quantum-Design MPMS3 SQUID magnetometer equipped with a 7 Tesla magnet in the range from 295 to 2.0 K at a magnetic field of 0.5 T. The powdered samples were contained in a polycarbonate capsule and fixed in a non-magnetic sample holder. Each raw data file for the measured magnetic moment was corrected for the diamagnetic contribution of the sample holder and the polycarbonate capsule. The molar susceptibility data were corrected for the diamagnetic contribution.

Experimental temperature dependent and VTVH (variable temperature – variable field) data for **1**$^+$ were simultaneously modelled by using a fitting procedure to the spin Hamiltonian for Zeeman splitting and zero-field splitting, equation (1).

$$\hat{H} = g\mu_B \vec{B}\vec{S} + D\left[\hat{S}_z^2 - \frac{1}{3}S(S+1)\right] \quad (1)$$

For **1**$^-$, the simulation was done for a diamagnetic S =0 spin state assuming 0.1 % impurity with S = 5/2.

Simulations of the experimental magnetic data was performed with the *julX_2s* program: E. Bill, Max-Planck Institute for Chemical Energy Conversion, Mülheim/Ruhr, Germany. Temperature-independent paramagnetism (*TIP*) was included according to $\chi_{calc} = \chi + TIP$ ($TIP = 300 \cdot 10^{-6}$ cm^3mol^{-1}).

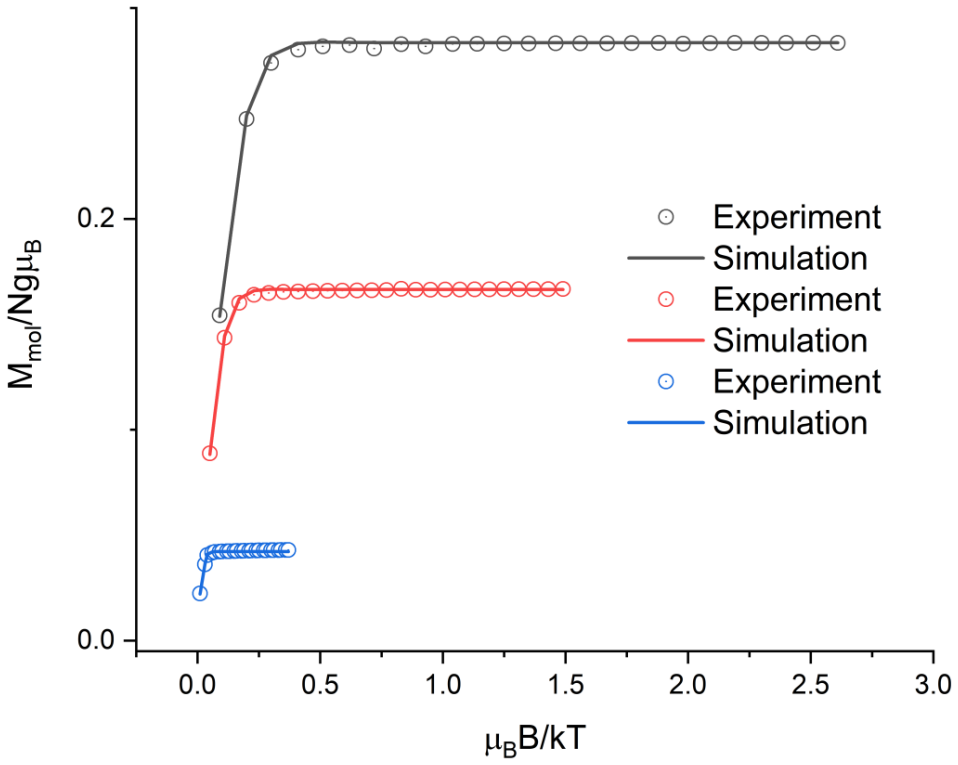

Figure S1: Plot of variable temperature – variable field magnetization measurements for **1**$^+$ at 1 T (blue circles), 4 T (red circles) and 7 T (black circles). The corresponding solid lines represent the global fit with the best parameters g = 2.32 and D = *+39.5 cm^{-1} for* S = *1.*

XANES and Kβ emission data collection, processing, and analysis

All XANES and XES spectra were collected at Beamline P64 of Petra III at DESY (Hamburg, Germany). [6,7] The electron energy of the storage-ring was 6.0 GeV, the ring current was 100 mA. The incident energy was selected using the (311) reflection from a Si double-crystal monochromator using Fe foil for energy calibration. The samples were measured as pure powder at room temperature sealed with Kapton tape against air contact. XANES spectra were recorded in fluorescence mode for 60 s. To obtain reasonable data, 12 spectra, each on a new sample spot, were collected. XES spectra were recorded off-resonant at an excitation energy of 7300 eV in the range of 6930 to 7120 eV with the von Hamos spectrometer of P64, using six Si crystals in the (440) reflection. Also 12 spectra (300 s per scan) were recorded, using a different sample spot for each scan. Comparing XANES spectra before and after irradiation of 300 s no radiation damage can be observed (no change in the spectrum). The VtC-XES spectra are super-imposed by the high-energy slope of the $K\beta_{1,3}$ emission line and were background-

corrected by fitting the slope and subtracted it from the raw spectrum. All spectra were area normalized. Values for the peak maxima of $Fe(CN)_6$ are measured in the same way as for complex row 1 in case of $K\beta_{1,3}$. For $K\beta_{2,5}$ and the pre-peak literature values were used.[8]

Table S1: Parameters of the linear regression between the peak maxima of $K\beta_{1,3}$, $K\beta_{2,5}$ and the $1s \rightarrow e_g$ pre-peak respectively shown in Fig.4.

Line	complex row	function	R^2	corrected R^2
$Kb_{1,3}$	1	f(x) = 1.29 x - 9129.2	1	1
$Kb_{1,3}$	$Fe(CN)_6$	f(x) = 1.11 x - 7859.1	-	-
$Kb_{2,5}$	1	f(x) = 0.52 x - 3670.5	0.988	0.976
$Kb_{2,5}$	$Fe(CN)_6$	f(x) = 0.35 x - 2537.4	-	-
Pre-peak	1	f(x) = 1.42 x - 10094.4	0.993	0.987
Pre-peak	$Fe(CN)_6$	f(x) = 0.83 x - 5927.5	-	-

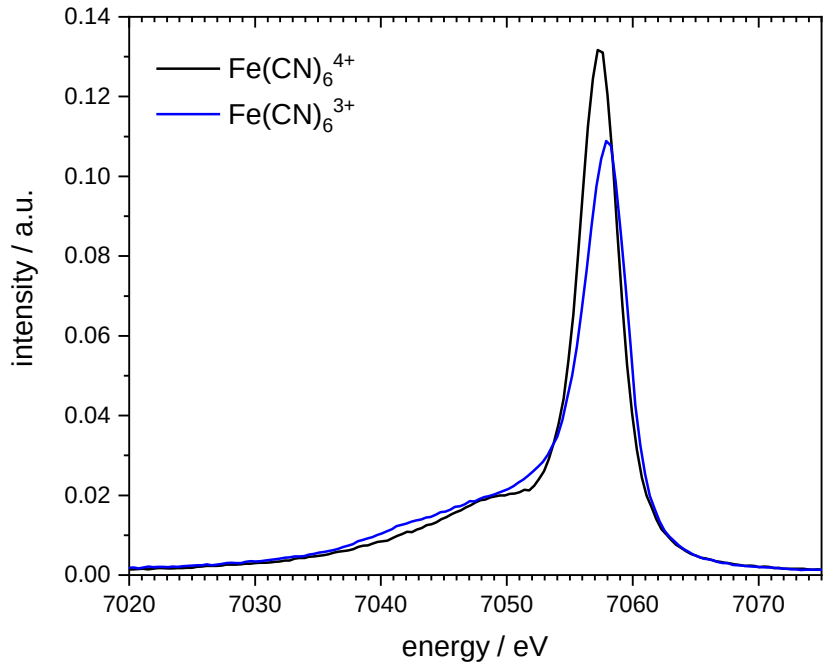

Figure S2: Experimental $K\beta_{1,3}$ spectra of the $Fe(CN)_6^{3+/4+}$ references.

Computational details

Due to the quite rigid structure, the computed geometries only slightly depend on the applied computational protocol within the variety of tested functionals. All minima computed with (U)DFT for differently charged species have been checked for the absence of negative frequencies. Computation of VtC-XES and XANES spectra were performed with ORCA 4.2.1 quantum chemistry package[9], whereas TDDFT calculations of absorption spectra and NBO analysis were done using Gaussian software.[10,11]

VtC-XES and XANES. For the unconstrained geometry optimization the B97-3c method was used.[12] For calculation of VtC-XES spectra, TPSS[13]/def2-TZVP[14] has been chosen. The

TPSSh[13]/def2-TZVP was used to calculate the XANES spectra. Auxiliary basis set def2/J[14] and RIJCOSX approximation[15] for the Hartree-Fock component were used. In all cases, the D3BJ dispersion correction[16] and CP(PPP) basis set[17] for iron were applied. TPPS(h) functionals were previously shown to deliver good performance for XES/XANES spectra.[18–21]

XES spectra were plotted with ORCA Mapspc, using the uniform broadening of 2.5 eV. For the XANES spectra, a linearly increasing broadening to higher energies was chosen, starting from 0.6 (fwhm) at the prepeak. The calculated spectra were shifted to match the prepeak (XANES) or the $K\beta_{2,5}$ peak (VtC-XES) and were normalized to these maxima. The analysis of the individual fractions of the molecular orbitals is based on the Löwdin population analysis, which was extracted from the ORCA output file using MOAnalyzer (version 1.3).[22] Using this, only orbitals with a significant fraction (>10%) were selected for fragment projections of the XES spectra.

For plotting the d-orbital splitting (Fig 4), the Löwdin population analysis was performed. The energy was chosen from the molecular orbital with the highest contribution of a certain d-orbital around the HOMO-LUMO gap, whereas for open shell systems α and β orbitals are averaged. The Kohn-Sham orbitals were visualized with IboView (vers. 20150427).[23]

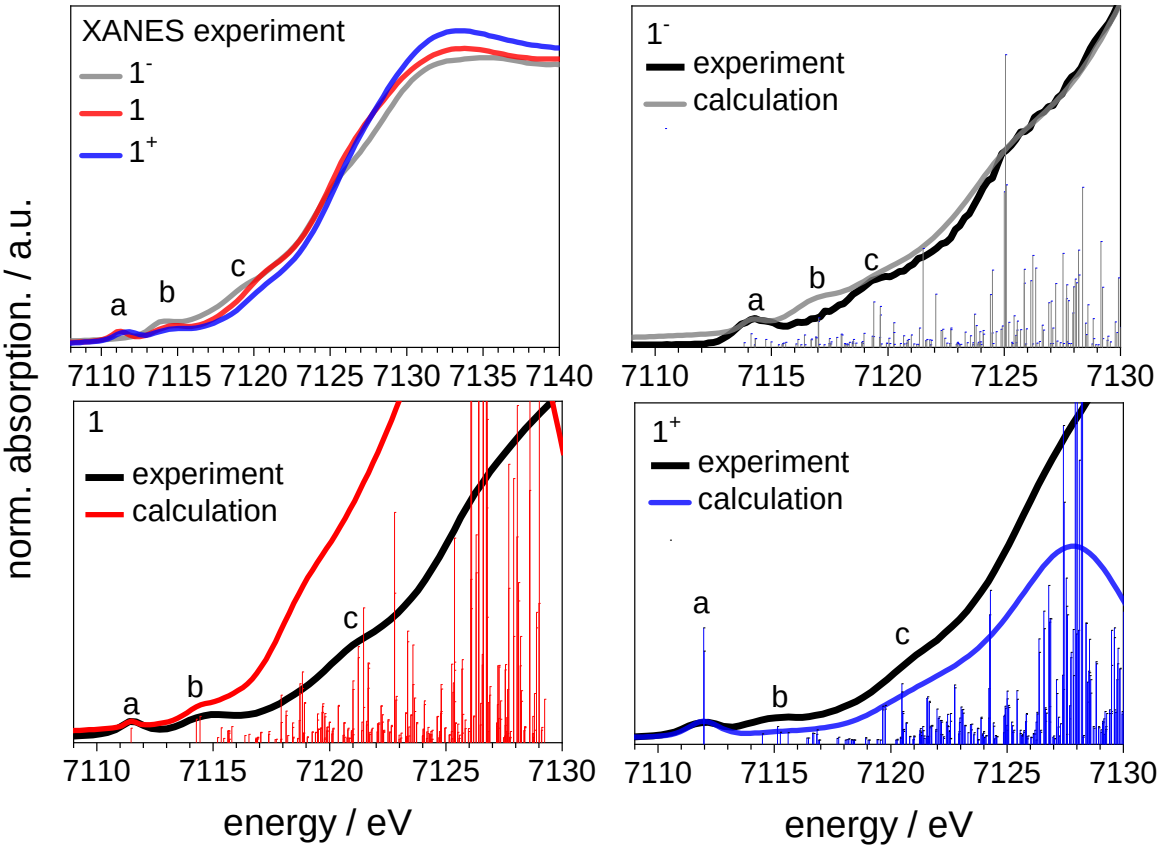

Figure S3: Comparison of experimental and calculated XANES spectra of **1**⁻,**1** and **1**⁺. Single transitions are potted as sticks, whereas the acceptor orbital of the main peaks (a,b,c) are analyzed in Tab. S1

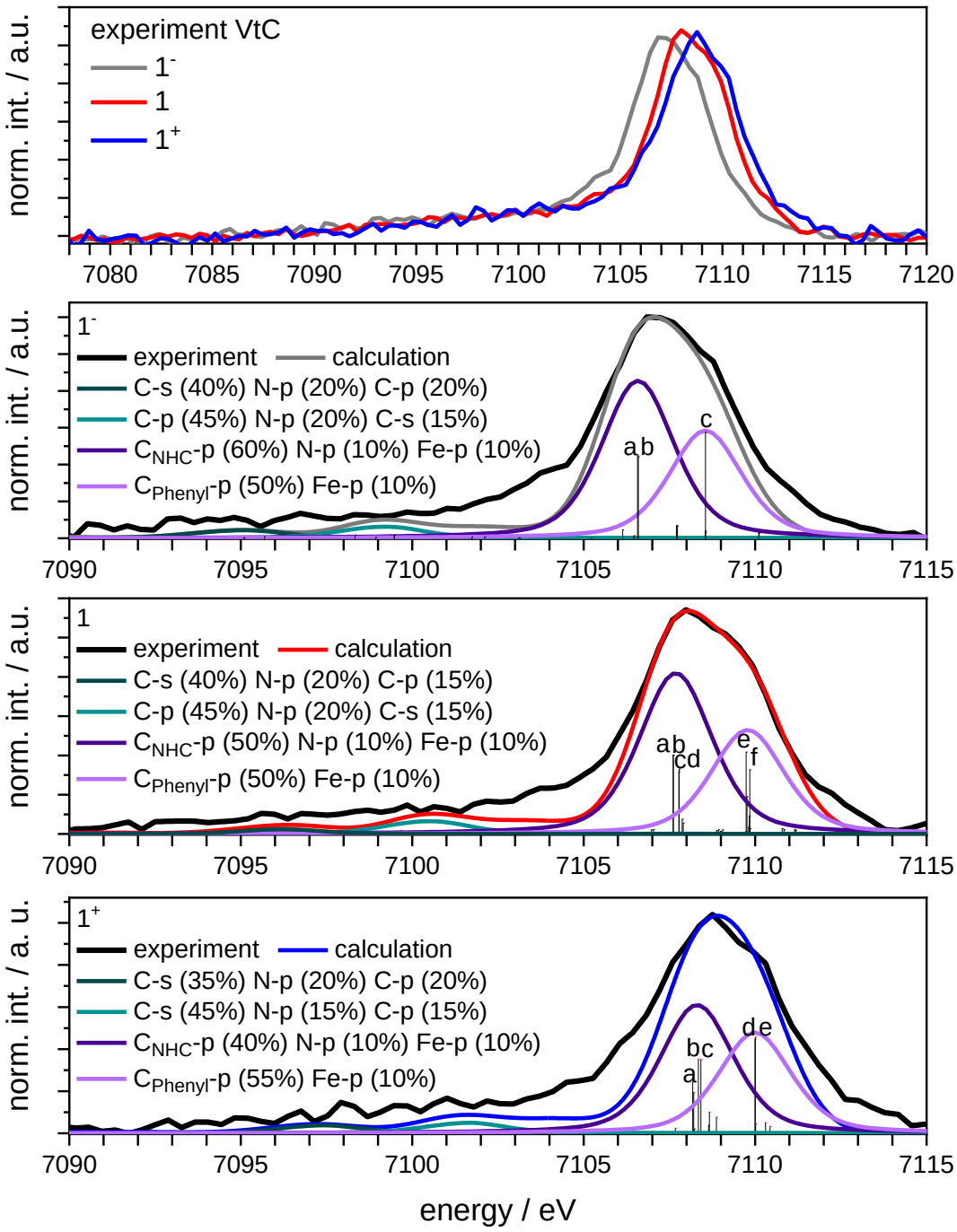

Figure S4: Experimental and calculated VtC spectra of **1**$^{-}$,**1** and **1**$^{+}$ including the analysis of the peak contributions (threshold 10%, rounded on 5%).

Table S2: Calculated fractions of the individual atomic contributions of the acceptor orbitals (XANES) of the most intense transitions. Indication of the orbital fractions in %.

	Peak	acceptor orbital	C		H		N		Fe	
			s	p	s	p	s	p	p	d
1^{-} (Fe^{2+})	a	152	10	17	28	3	0	0	1	28
	b	160	6	27	42	5	0	1	8	0
	c	186	15	26	17	4	0	5	0	0
		191	0	59	3	3	0	3	0	1
1 (Fe^{3+})	a	137 β	0	17	0	0	0	15	0	50

	b	142 α	10	20	1	0	1	2	0	50
		142 β	9	20	1	0	1	3	0	50
	c	186 α	9	42	12	2	1	4	1	0
		186 β	10	43	13	2	1	4	1	0
1^+ (Fe^{4+})	a	136 β	0	19	0	0	0	4	1	61
		137 β	0	18	0	0	0	4	1	62
	b	140 β	5	38	0	0	0	6	0	29
		142 β	6	32	1	0	0	5	0	36
	c	159 α	5	25	40	6	2	1	1	0
		159 β	6	24	43	7	2	1	1	0

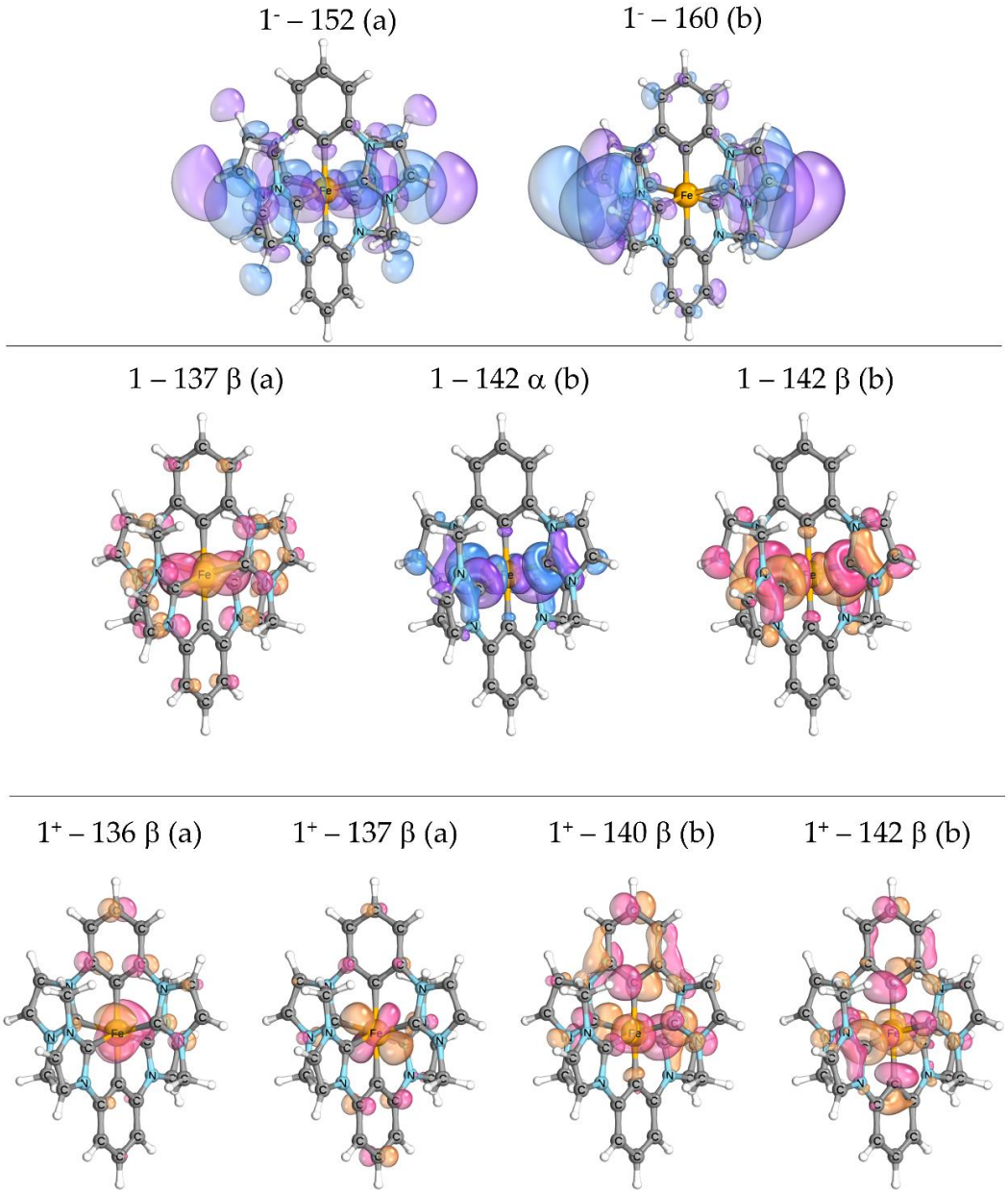

Figure S5: Calculated spatial contribution of the acceptor orbitals (XANES, Tab. S1) of the transitions of the prepeaks (a,b).

Table S3: Calculated fractions of the individual atomic contributions of donor orbitals (VtC) of the most intense transitions. Indication of the orbital fractions in %.

	signal / eV	donor orbital	C		H		N		Fe	
			s	p	s	p	s	p	p	d
1^{-} (Fe^{2+})	7095	59	39	12	11	0	0	26	1	0
		60	39	13	11	2	0	25	1	0
		63	37	26	10	2	2	10	3	0
	7099	72	17	44	11	2	3	16	1	0
		75	12	46	13	2	2	19	1	0
		76	12	45	13	2	2	19	1	0
	7103	84	3	51	27	0	1	6	1	0
		91	6	40	20	0	0	20	1	0
	7106	123 (a)	8	52	1	0	1	11	12	1
		124 (b)	8	52	1	0	1	12	12	1
	7109	134 (c)	5	56	1	0	1	3	12	4
1 (Fe^{3+})	7096	59 β	39	11	10	1	0	27	1	0
		60 β	39	11	10	2	0	27	1	0
		63 β	38	25	11	2	2	10	1	0
	7100	72 β	17	43	11	1	4	16	1	0
		75 β	13	46	12	2	2	18	2	0
		76 β	13	46	12	2	2	18	2	0
	7103	81 β	8	52	19	0	1	9	0	0
		82 α	8	53	19	0	1	9	0	0
		91 α	6	38	20	0	0	21	1	0
	7107	121 α (a)	8	52	1	0	0	12	13	2
		121 β (b)	8	52	1	0	0	11	13	1
		122 α (c)	7	57	1	1	0	8	11	1
		122 β (d)	8	58	0	1	0	8	11	1
	7109	131 β (e)	4	60	1	1	0	3	10	2
		134 α (f)	3	60	1	1	0	5	8	3
1^{+} (Fe^{4+})	7097	59 β	40	13	9	2	0	26	1	0
		60 β	40	12	9	2	0	26	1	0
		63 β	34	23	14	3	3	12	1	0
	7102	71 β	16	43	12	2	3	17	1	0
		75 β	13	46	11	2	2	17	1	0
		76 β	13	46	11	2	3	17	1	0
	7104	81 α	8	52	19	2	1	9	0	0
		82 α	8	52	19	2	1	10	0	0
		89 β	8	37	20	1	0	19	1	0
	7108	123 α (a)	5	37	2	0	0	7	8	24
		122 β (b)	8	52	1	0	1	9	13	4
		123 β (c)	9	53	1	0	1	8	13	4
	7110	129 α (d)	4	58	2	0	1	3	12	3
		129 β (e)	4	58	2	0	0	2	12	4

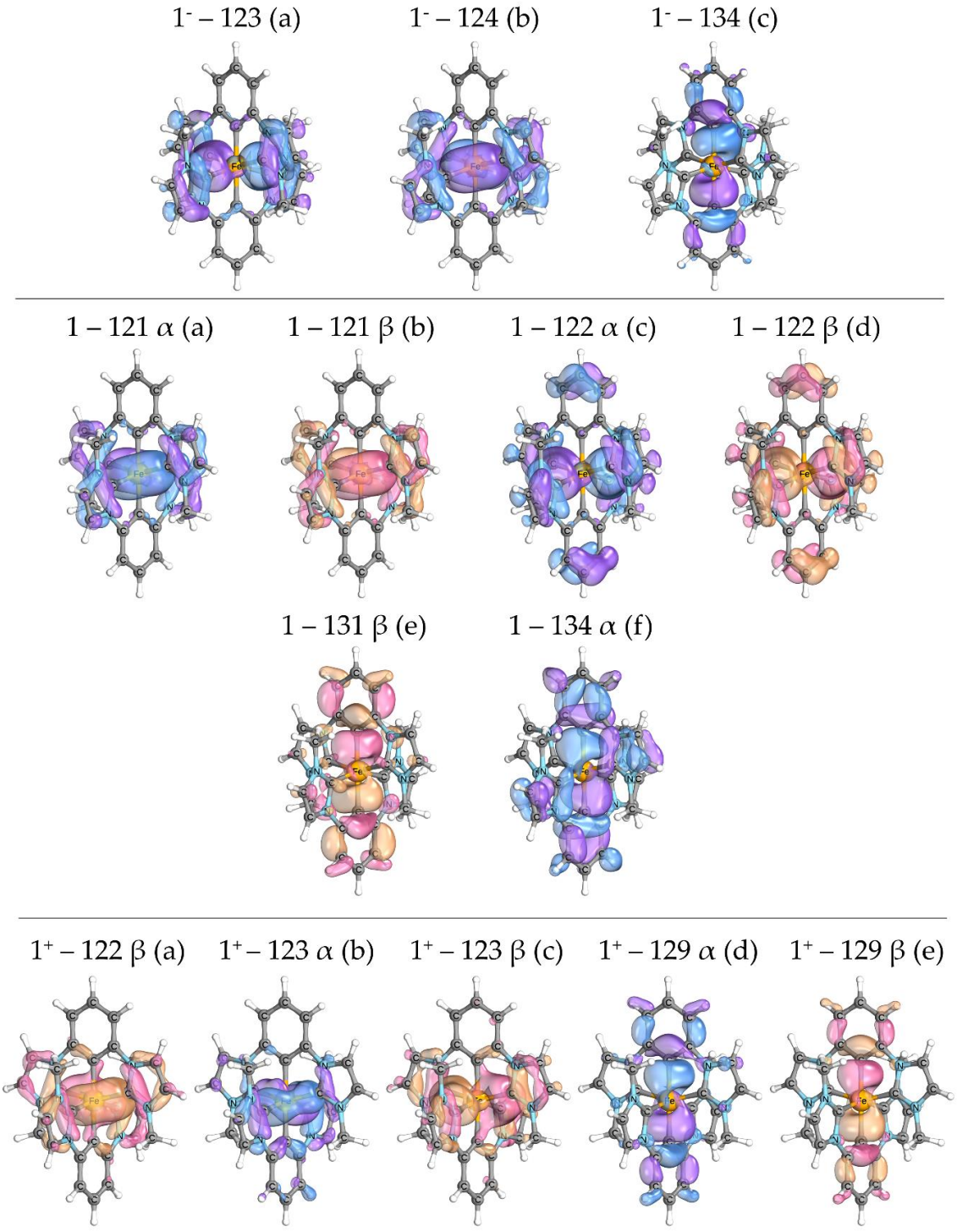

Figure S6: Spatial contribution of the donor orbitals (VtC, Tab. S2) of most intense transitions (a-f) marked in the spectrum Fig. S2.

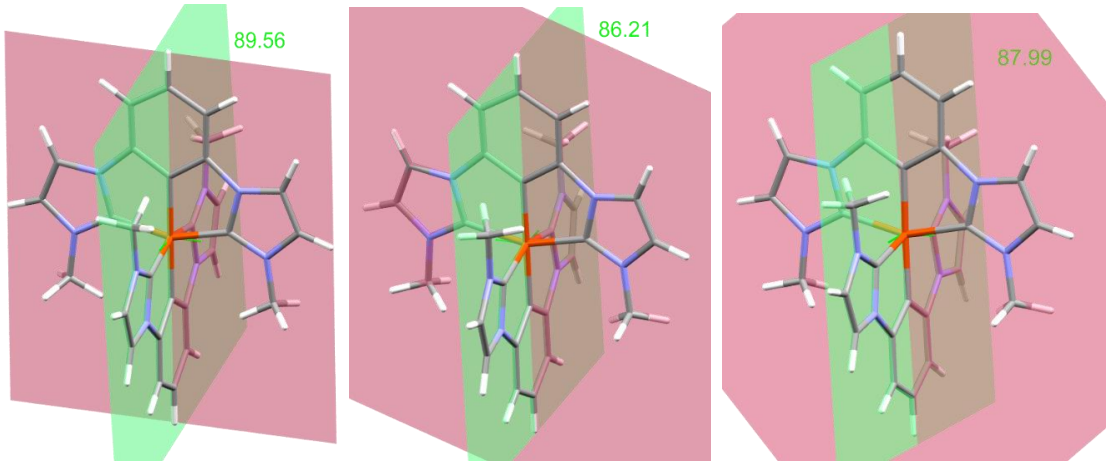

Figure S7: Ligand/ligand torsion angle of the gas phase geometry optimized molecular structures of 1^- (89.56°), 1 (86.21°) and 1^+ (87.99°).

NBO analysis. Analysis of the bonding structure and charge distribution in the three complexes was performed using natural bond orbitals (NBO)[24,25] version 3.1 as implemented in Gaussian 16.[10,26] The geometries of the complexes were optimized with the TPSSH functional and def2-TZVP basis set, and the NBO analysis was performed on the optimized geometries with the same functional and basis set. Table S4 lists the important geometric parameters in the three complexes.

Table S4: Geometric parameters of the optimized geometries of the three complexes. The numbers between brackets indicate the range of the obtained values (maximum minus minimum). Values reported without a range have a span of less than 1 ppm.

	1^-	**1**	**1^+**
Fe-C_{CM}	1.932	1.943	1.953 (0.054)
Fe-C_{NHC}	1.970	2.013	2.062 (0.006)
Bite angle	155.2	155.4	156.6 (4.3)

Characterization of the oxidation state by projection of the wave function.[27]

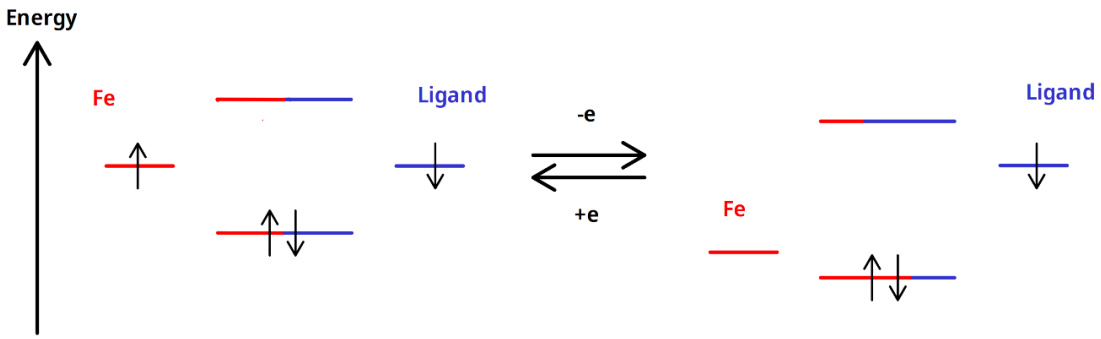

Figure S8: Schematic depiction of the negative feedback charge self-regulation.[28]

For a free ion the assignment of the oxidation state is trivial, and the occupation numbers of the orbitals are either 1 or 0. Here, we take the free Fe atom, with its 5 d-orbitals (ϕ_m), as a reference to facilitate the identification of the oxidation states of the complexes. We now construct a 5 x 5 occupation matrix ($n^{\sigma}_{m,m'}$), obtained by projecting the occupied Kohn-Sham orbitals of the complex (ψ_i^{σ}) onto the atomic d-orbitals of the reference free atom:

$$n^{\sigma}_{m,m'} = \sum_i \langle \psi_i^{\sigma} | \phi_{m'} \rangle \langle \phi_m | \psi_i^{\sigma} \rangle,$$

where the label σ accounts for spin in spin-polarized (open shell) cases. The 5 occupation numbers of the d-orbitals in the complex are then obtained as the eigenvalues of the occupation matrix. This procedure is obviously not sensitive to the choice of the basis set, unlike many of the population analysis methods. As long as the overlap of the d-orbitals with the ligand orbitals is not very strong, only those d-orbitals that would be initially occupied in our reference free ion remain fully occupied (n≈1), all other d-orbital occupations are due to ligand donation to previously empty d-orbitals and are expected to be very low (n≈0). Thus, like in the case of a free atom, only the fully occupied d-orbitals are relevant for determining the oxidation state of the TM in the complex. The oxidation state can be found by simply counting the fully occupied d-orbitals.

NBO analysis results. NBO methods represent chemical structures in a manner that is usually very close to Lewis structures and thus amenable to intuitive chemical reasoning.[25,29,30] Natural bond orbitals are high-occupancy (n≈2) orbitals localized on one center (lone pairs) or two centers (chemical bonds) in the molecule, in a manner that is very similar to Lewis dot-diagrams. The basic idea is to construct a set of orthogonal natural atomic orbitals NAOs (unlike the atomic orbital basis functions, which are generally not orthogonal). The occupancy of these NAOs is the basis of natural population analysis and natural atomic charges. After constructing the NAOs, a search is performed over all possible bonding patterns for these high-occupancy Lewis-type orbitals, leading to the optimal natural Lewis structure pattern and associated natural bond orbitals (NBOs) that optimally describe the total electron density ρ_l. The error of the natural Lewis structure description is quantified by the occupancy (ρ_{nl}) of residual non-Lewis orbitals, which complement the dominant contribution of Lewis orbitals. The higher this error, the less "perfect" is the description of the molecule in terms of a single Lewis structure, for example due to the molecule have other important resonance structures that need to be accounted for.

Natural electron configuration.

Table S5: Natural electron configuration.

		Natural electron configuration
1^{-}		[core] $4S^{0.33}$ $3d^{7.78}$ $4p^{1.29}$
1	Total	[core] $4S^{0.35}$ $3d^{7.32}$ $4p^{1.27}$
	Spin up	[core] $4S^{0.18}$ $3d^{4.14}$ $4p^{0.64}$
	Spin down	[core] $4S^{0.17}$ $3d^{3.18}$ $4p^{0.63}$
1^{+}	Total	[core] $4S^{0.37}$ $3d^{6.96}$ $4p^{1.26}$
	Spin up	[core] $4S^{0.19}$ $3d^{4.35}$ $4p^{0.65}$
	Spin down	[core] $4S^{0.18}$ $3d^{2.60}$ $4p^{0.62}$

Contribution of non-Lewis energy. For a simple covalently-bonded molecule, the occupied NBOs often account for more than 99.9% of the total energy of the molecule. As observable in Table S6, the three complexes have a Lewis energy around 96%, due to both the aromaticity of the complexes and extensive donor-acceptor interactions between bonding and antibonding NBOs.

Table S6: The percentage contribution of Lewis energy to the total energy of each complex.

Molecule	%E (Lewis)
1^-	96.702%
1	96.740%
1^+	96.069%

Contribution of the Fe atom to the six hybrid metal-ligand bonding orbitals.

Table S7: The percentage contribution of the iron to the metal-ligand bonding orbitals.

Complex		Fe-C_{CM}		Fe-C_{NHC}	
		Fe %	Ligand C %	Fe %	Ligand C %
1^+		**34.52%** 4s(17%) 4p(48%) 3d(35%)	**65.48%** 2s(39%) 2p(61%)	**32.81%** 4s(16%) 4p(51%) 3d(33%)	**67.19%** 2s(49%) 2p(51%)
1	Spin up	**36.05%** 4s(17%) 4p(48%) 3d(35%)	**63.95%** 2s(36%) 2p(64%)	**33.63%** 4s(16%) 4p(51%) 3d(33%)	**66.37%** 2s(46%) 2p(54%)
	Spin down	**33.62%** 4s(16%) 4p(48%) 3d(36%)	**66.38%** 2s(38%) 2p(62%)	**32.07%** 4s(17%) 4p(51%) d(32%)	**67.93%** 2s(46%) 2p(54%)
1^-	Spin up	**55.12%** 4s(5%) 4p(10%) 3d(85%)	**44.88%** 2s(33%) 2p(67%)	**51.74%** 4s(5%) 4p(12%) 3d(83%)	**48.26%** 2s(42%) 2p(58%)
	Spin down	**33.91%** 4s(18%) 4p(47%) 3d(35%)	**66.09%** 2s(36%) 2p(64%)	**32.19%** 4s(15%) 4p(51%) 3d(34%)	**67.81%** 2s(45%) 2p(55%)

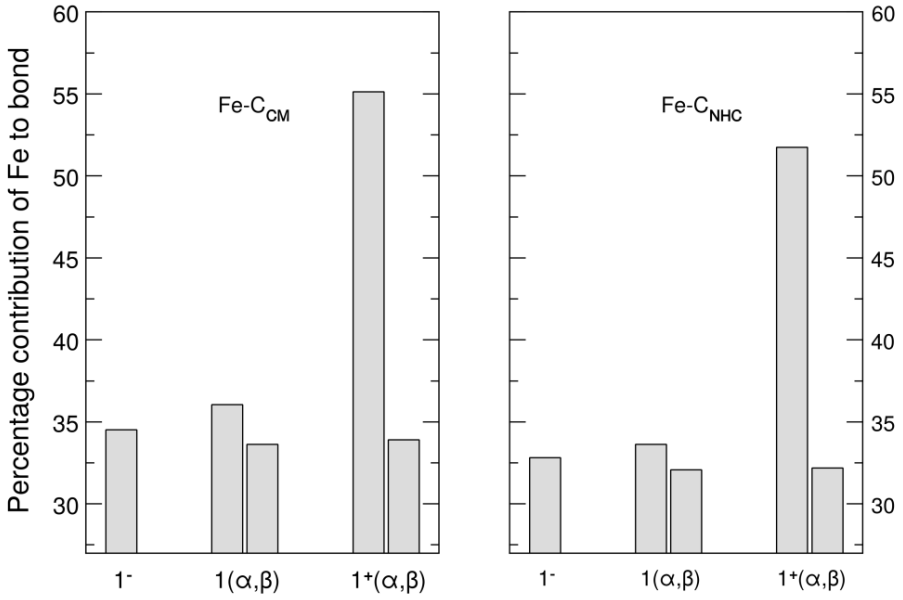

Figure S9: Percentage contribution of the Fe d-orbitals in different complexes to hybrid metal-ligand orbitals. Left: the two Fe-C_{CM} bonds, right: the four Fe-C_{NHC} bonds.

TDDFT absorption spectra. As reliable description of long-range MLCT and LMCT transitions represents a challenge for conventional DFT,[31,32] the non-empirical system-dependent tuning of functional was applied to recover the fundamental properties of exchange-correlation functional and to improve the description of these states. The two-parameter optimal tuning of LC-BLYP was done via the ΔSCF method,[33–35] the details of the present setup can be found in the previous studies.[1,36] The range separations parameters α=0.0 and ω=0.15 Bohr^{-1} were taken for all charged species.

Absorption spectra were computed with the linear-response time-dependent density functional theory (TDDFT) using the optimally-tuned LC-BLYP functional with the solvent effects (acetonitrile) modeled by the polarizable continuum model (PCM)[37]. The 6-31G(d) basis set was used for tuning procedure, while a larger basis set (def2-TZVP on iron and 6-311G(d,p) on other atoms) was employed for calculations of absorption spectra. The broadening of resulting stick spectra was done with Gaussians of FWHM 0.20 eV. Excited state analysis was done using the TheoDORE package,[38] which enables automatic quantitative wavefunction analysis and localization of excitations at predefined molecular moieties. Pre- and post-processing of data was done with homemade programs.

UV-Vis spectroscopy

UV-Vis spectra were recorded at around 10^{-5} M (**1**$^{+}$) and around 10^{-4} M (**1**$^{-}$) on a PerkinElmer Lambda 465 single-beam spectrophotometer. Acetonitrile used for **3** was of HPLC quality from fisher, which was passed over activated neutral alumina and subsequently degassed using three freeze-pump-thaw cycles. The acetonitrile used for **1**$^{+}$ was of spectroscopic quality from VWR.

Transient Absorption Spectroscopy

Transient absorption measurements were realized using a titanium sapphire laser system with a fundamental wavelength of 800 nm and a repetition rate of 1 kHz. For complex **1**$^{+}$ a noncollinear parametric amplifier was applied to obtain the excitation wavelength of 490 nm. The dispersion of the NOPA pulses was minimized by a compressor based on fused silica prisms. The excitation wavelength of 400 nm for complex **1**$^{-}$ was reached by frequency doubling the fundamental wavelength with a BBO-crystal. For probing, a white light continuum was generated with a CaF_2-crystal. To avoid effects caused by orientational relaxation, the polarizations of the pump and probe pulses were set to magic angle with respect to each other. Pump and probe beam were focused onto the sample to overlapping spots with diameters of 530 µm and 120 µm, respectively. Behind the sample the white light continuum was dispersed by a prism. The changes in transient absorption were spectrally resolved recorded by a photodiode array detector. The compounds were dissolved in MeCN under argon and the sample solution was filled into a fused silica cuvette with a thickness of 1 mm. For complex **1**$^{-}$ a glovebox was used to transfer the complex into the cuvette.

Spectra

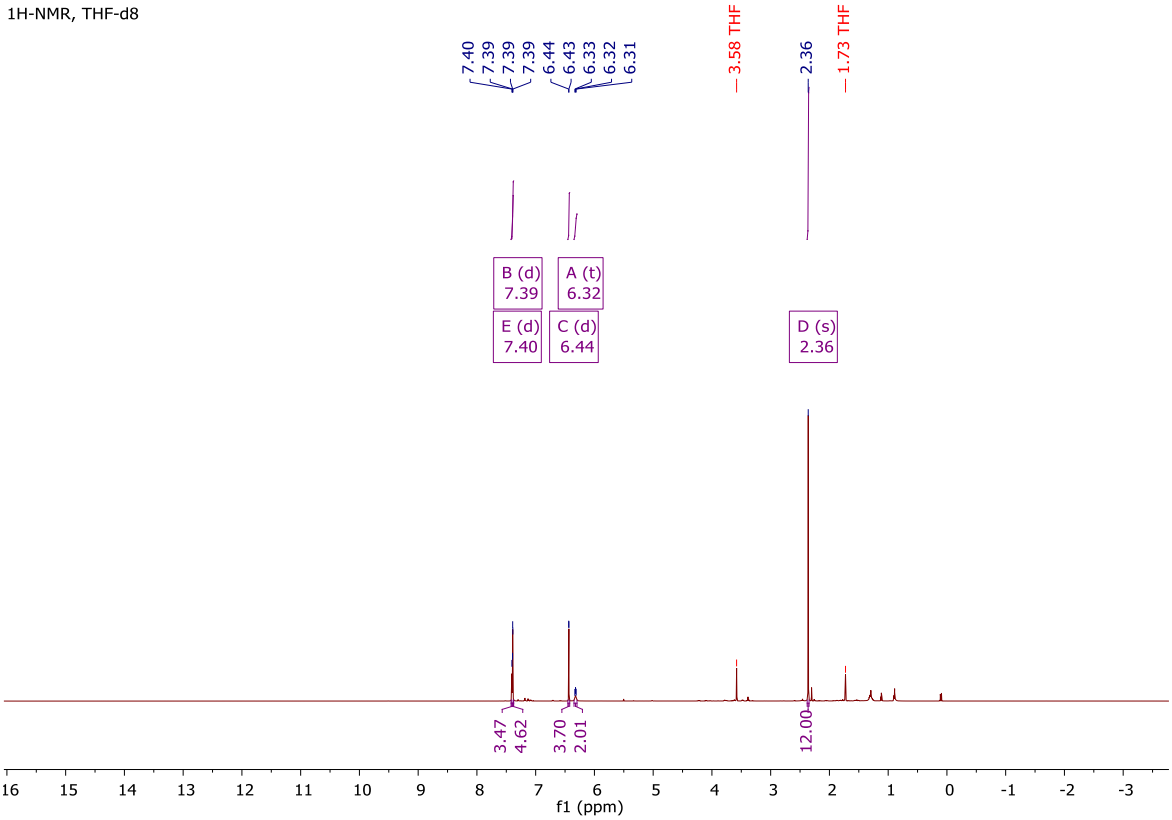

^{1}H-NMR Spectrum of **1**$^{-}$ in THF-d_8

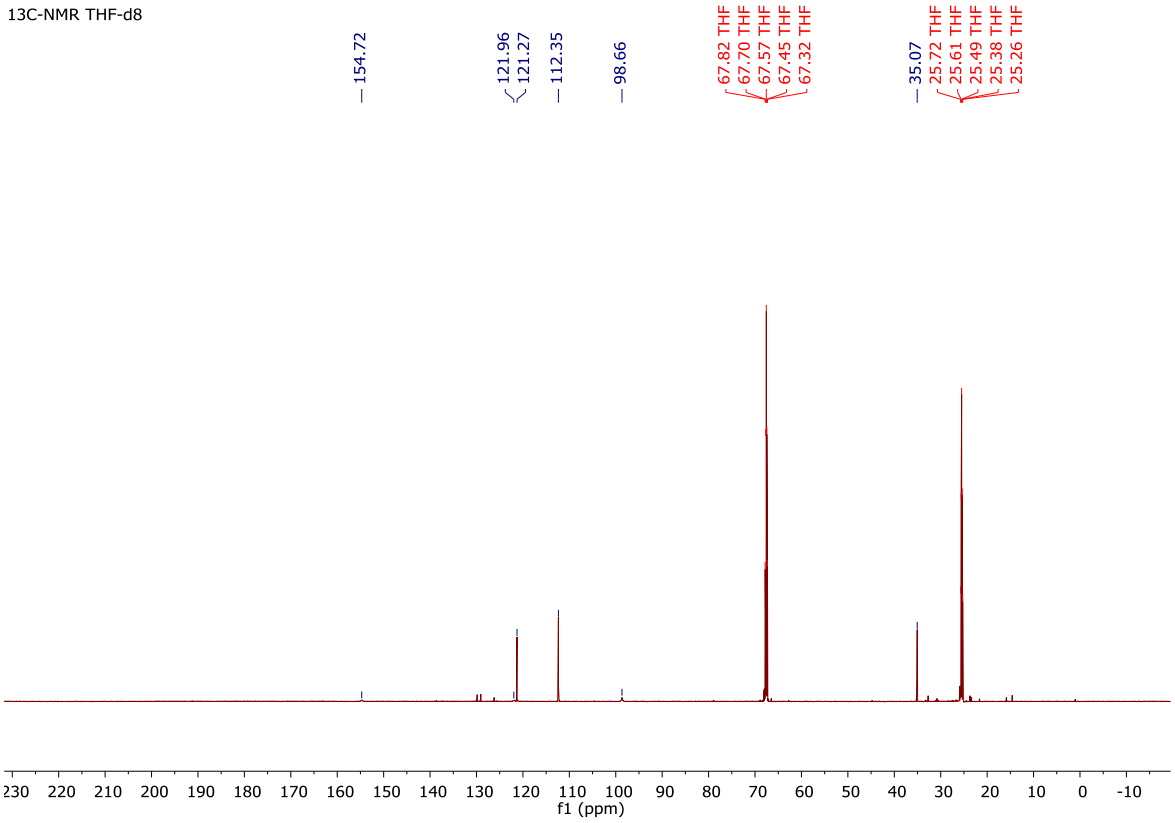

^{13}C-NMR Spectrum of **1**$^{-}$ in THF-d_8

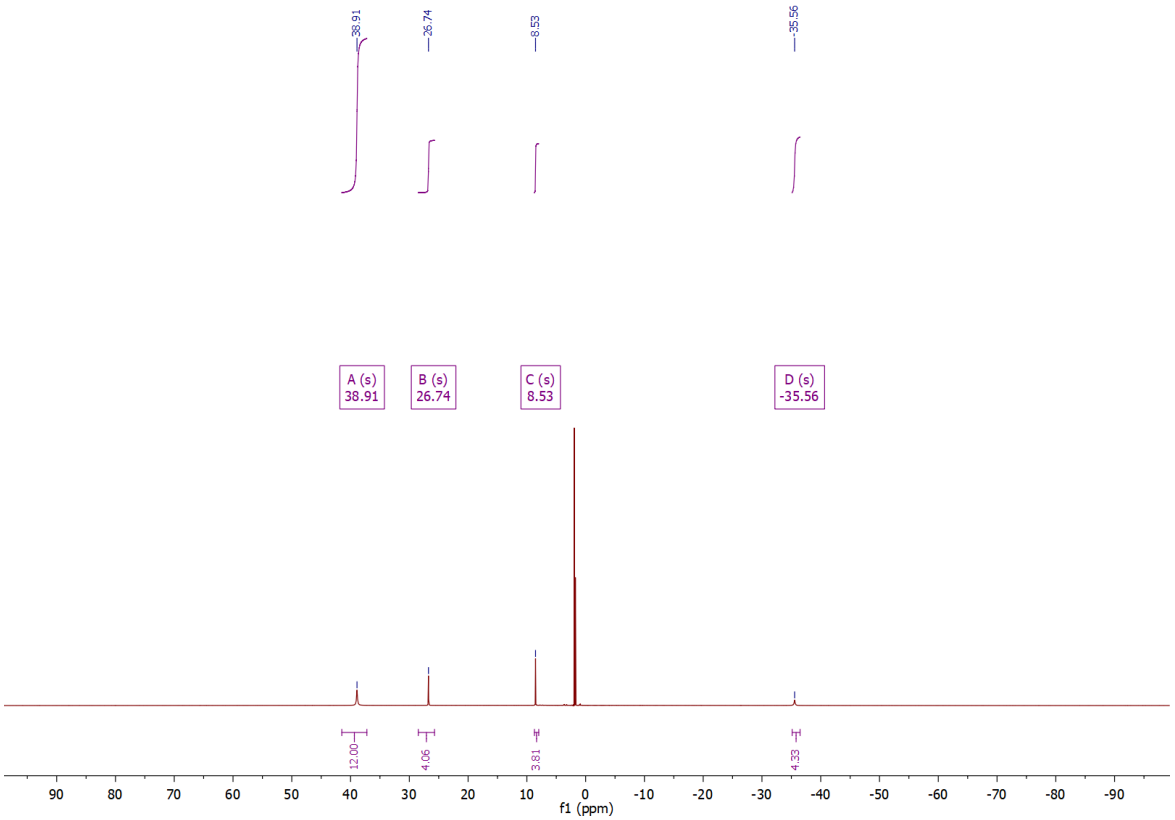

^{1}H-NMR Spectrum of **1**$^{+}$ in MeCN-d_3.

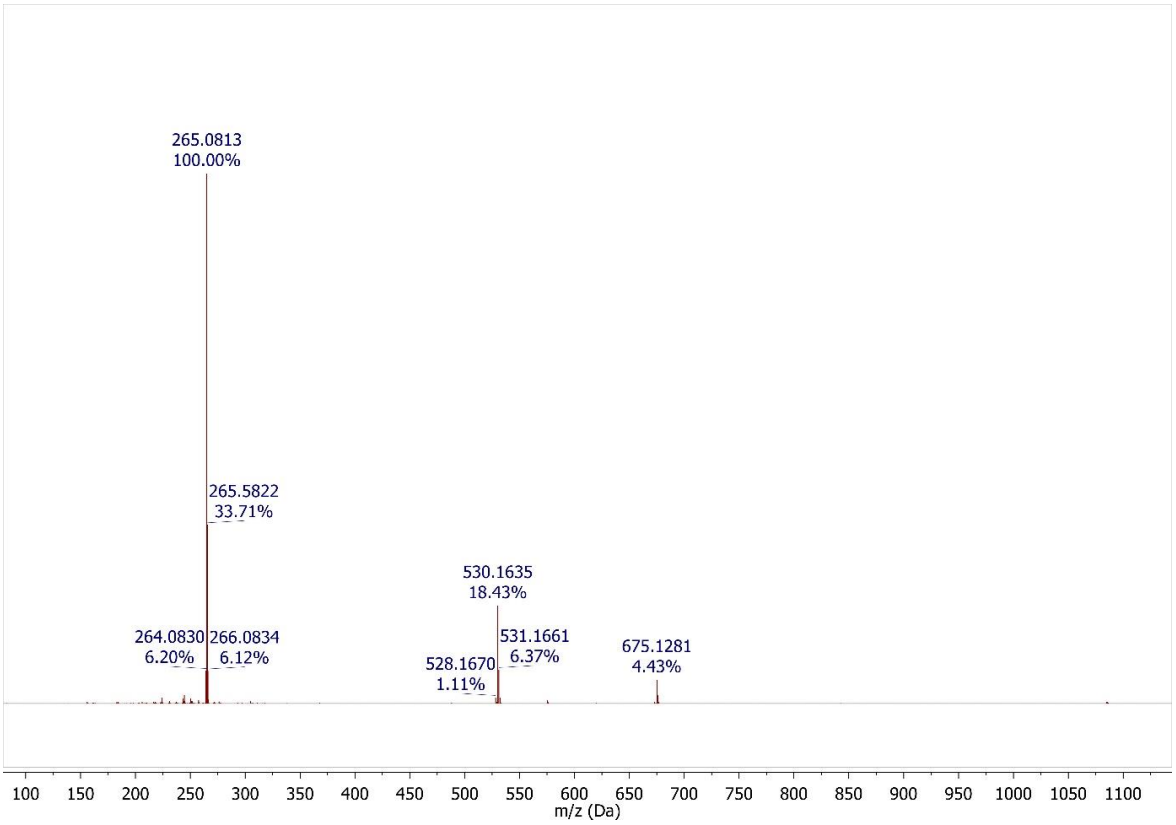

ESI-MS spectrum of $\mathbf{1}^{+}$.

References

(1) Steube, J.; Kruse, A.; Bokareva, O. S.; Reuter, T.; Demeshko, S.; Schoch, R.; Argüello Cordero, M. A.; Krishna, A.; Hohloch, S.; Meyer, F.; Heinze, K.; Kühn, O.; Lochbrunner, S.; Bauer, M. Janus-type emission from a cyclometalated iron(iii) complex. *Nat. Chem.* **2023.** DOI: 10.1038/s41557-023-01137-w.

(2) Krause, L.; Herbst-Irmer, R.; Sheldrick, G. M.; Stalke, D. Comparison of silver and molybdenum microfocus X-ray sources for single-crystal structure determination. *J Appl Crystallogr* **2015**, *48* (1), 3–10. DOI: 10.1107/S1600576714022985.

(3) Sheldrick, G. M. SHELXT – Integrated space-group and crystal-structure determination. *Acta Crystallogr A Found Adv* **2015**, *71* (1), 3–8. DOI: 10.1107/S2053273314026370.

(4) Spek, A. L. Structure validation in chemical crystallography. *Acta Crystallogr. D* **2009**, *65* (Pt 2), 148–155. DOI: 10.1107/S090744490804362X.

(5) Spek, A. L. PLATON SQUEEZE: a tool for the calculation of the disordered solvent contribution to the calculated structure factors. *Acta Crystallogr. C Struct. Chem.* **2015**, *71* (Pt 1), 9–18. DOI: 10.1107/S2053229614024929.

(6) Caliebe, W. A.; Murzin, V.; Kalinko, A.; Görlitz, M. High-flux XAFS-beamline P64 at PETRA III. In ; Author(s), 2019; p 60031. DOI: 10.1063/1.5084662.

(7) Kalinko, A.; Caliebe, W. A.; Schoch, R.; Bauer, M. A von Hamos-type hard X-ray spectrometer at the PETRA III beamline P64. *Journal of synchrotron radiation* **2020**, *27* (Pt 1), 31–36. DOI: 10.1107/S1600577519013638. Published Online: Jan. 1, 2020.

(8) Ross, M.; Andersen, A.; Fox, Z. W.; Zhang, Y.; Hong, K.; Lee, J.-H.; cordones, A.; March, A. M.; Doumy, G.; Southworth, S. H.; Marcus, M. A.; Schoenlein, R. W.; Mukamel, S.; Govind, N.; Khalil, M.

Comprehensive Experimental and Computational Spectroscopic Study of Hexacyanoferrate Complexes in Water: From Infrared to X-ray Wavelengths. *J. Phys. Chem. B* **2018**, *122* (19), 5075–5086. DOI: 10.1021/acs.jpcb.7b12532. Published Online: May. 9, 2018.
(9) Neese, F.; Wennmohs, F.; Becker, U.; Riplinger, C. The ORCA quantum chemistry program package. *J. Chem. Phys.* **2020**, *152* (22), 224108. DOI: 10.1063/5.0004608.
(10) Frisch, M. J.; Trucks, G. W.; Schlegel, H. B.; Scuseria, G. E.; Robb, M. A.; Cheeseman, J. R.; Scalmani, G.; Barone, V.; Petersson, G. A.; Nakatsuji, H.; Li, X.; Caricato, M.; Marenich, A. V.; Bloino, J.; Janesko, B. G.; Gomperts, R.; Mennucci, B.; Hratchian, H. P.; Ortiz, J. V.; Izmaylov, A. F.; Sonnenberg, J. L.; Williams; Ding, F.; Lipparini, F.; Egidi, F.; Goings, J.; Peng, B.; Petrone, A.; Henderson, T.; Ranasinghe, D.; Zakrzewski, V. G.; Gao, J.; Rega, N.; Zheng, G.; Liang, W.; Hada, M.; Ehara, M.; Toyota, K.; Fukuda, R.; Hasegawa, J.; Ishida, M.; Nakajima, T.; Honda, Y.; Kitao, O.; Nakai, H.; Vreven, T.; Throssell, K.; Montgomery Jr., J. A.; Peralta, J. E.; Ogliaro, F.; Bearpark, M. J.; Heyd, J. J.; Brothers, E. N.; Kudin, K. N.; Staroverov, V. N.; Keith, T. A.; Kobayashi, R.; Normand, J.; Raghavachari, K.; Rendell, A. P.; Burant, J. C.; Iyengar, S. S.; Tomasi, J.; Cossi, M.; Millam, J. M.; Klene, M.; Adamo, C.; Cammi, R.; Ochterski, J. W.; Martin, R. L.; Morokuma, K.; Farkas, O.; Foresman, J. B.; Fox, D. J. *Gaussian 16 Rev. C.01*, 2016.
(11) Mao, Y.; Ge, Q.; Horn, P. R.; Head-Gordon, M. On the Computational Characterization of Charge-Transfer Effects in Noncovalently Bound Molecular Complexes. *J. Chem. Theory Comput.* **2018**, *14* (5), 2401–2417. DOI: 10.1021/acs.jctc.7b01256.
(12) Brandenburg, J. G.; Bannwarth, C.; Hansen, A.; Grimme, S. B97-3c: A revised low-cost variant of the B97-D density functional method. *J. Chem. Phys.* **2018**, *148* (6), 64104. DOI: 10.1063/1.5012601.
(13) Staroverov, V. N.; Scuseria, G. E.; Tao, J.; Perdew, J. P. Comparative assessment of a new nonempirical density functional: Molecules and hydrogen-bonded complexes. *The Journal of Chemical Physics* **2003**, *119* (23), 12129–12137. DOI: 10.1063/1.1626543.
(14) Weigend, F.; Ahlrichs, R. Balanced basis sets of split valence, triple zeta valence and quadruple zeta valence quality for H to Rn: Design and assessment of accuracy. *Phys. Chem. Chem. Phys.* **2005**, *7* (18), 3297–3305. DOI: 10.1039/b508541a.
(15) Neese, F.; Wennmohs, F.; Hansen, A.; Becker, U. Efficient, approximate and parallel Hartree–Fock and hybrid DFT calculations. A 'chain-of-spheres' algorithm for the Hartree–Fock exchange. *Chemical Physics* **2009**, *356* (1-3), 98–109. DOI: 10.1016/j.chemphys.2008.10.036.
(16) Becke, A. D.; Johnson, E. R. A density-functional model of the dispersion interaction. *J. Chem. Phys.* **2005**, *123* (15), 154101. DOI: 10.1063/1.2065267.
(17) Neese, F. Prediction and interpretation of the 57Fe isomer shift in Mössbauer spectra by density functional theory. *Inorg. Chim. Acta* **2002**, *337*, 181–192. DOI: 10.1016/S0020-1693(02)01031-9.
(18) Chakraborty, U.; Bügel, P.; Fritsch, L.; Weigend, F.; Bauer, M.; Jacobi von Wangelin, A. Planar Iron Hydride Nanoclusters: Combined Spectroscopic and Theoretical Insights into Structures and Building Principles. *ChemistryOpen* **2021**, *10* (2), 265–271. DOI: 10.1002/open.202000307.
(19) Schoch, A.; Burkhardt, L.; Schoch, R.; Stührenberg, K.; Bauer, M. Hard X-ray spectroscopy: an exhaustive toolbox for mechanistic studies (?). *Faraday Discuss.* **2019**, *220* (0), 113–132. DOI: 10.1039/c9fd00070d.
(20) Besley, N. A. Modeling of the spectroscopy of core electrons with density functional theory. *WIREs Comput Mol Sci* **2021**, *11* (6). DOI: 10.1002/wcms.1527.
(21) Burkhardt, L.; Holzwarth, M.; Plietker, B.; Bauer, M. Detection and Characterization of Hydride Ligands in Iron Complexes by High-Resolution Hard X-ray Spectroscopy and Implications for Catalytic Processes. *Inorg. Chem.* **2017**, *56* (21), 13300–13310. DOI: 10.1021/acs.inorgchem.7b02063.
(22) Delgado-Jaime, M. U.; DeBeer, S. Expedited analysis of DFT outputs: introducing MOAnalyzer. *Journal of computational chemistry* **2012**, *33* (27), 2180–2185. DOI: 10.1002/jcc.23028.